LEVEL

Acrylic Plastic Viewports For Ocean Engineering Applications

by J.D. Stachiw

February 1977
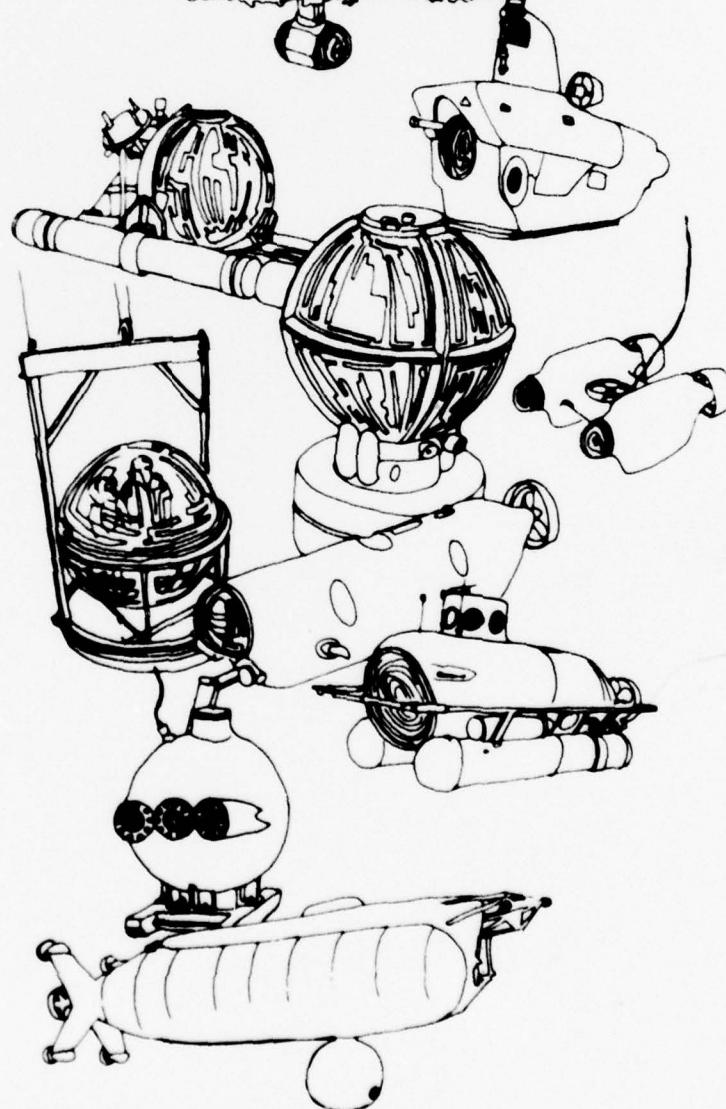
**NAVAL UNDERSEA CENTER
SAN DIEGO, CALIFORNIA 92132**

LEVEL III (12)

(9) Research rept.

(6)

ACRYLIC PLASTIC VIEWPORTS
FOR
OCEAN ENGINEERING APPLICATIONS. Volume II.

by

(10) J. D. Stachiw

(12) 447 p

(14) NUC-TP-562-VOL-2

D D C
JUN 28 1979
A

(11) February 1977
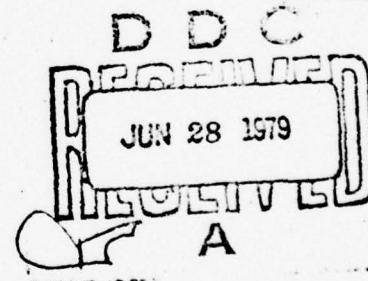
Sponsored By

Naval Facilities Engineering Command
Alexandria, Virginia 22332

390 458

SECTION 11. SPHERICAL SECTOR WINDOWS . . . 11-1

SECTION 11. SPHERICAL SECTOR WINDOWS

11.1 INTRODUCTION

Until the introduction of spherical sector windows into ocean engineering applications (see section 1), the size of plane acrylic plastic windows in the hulls of submersibles and habitats was less than 12 inches (30.48 centimeters). Larger windows could have been built, but their thickness would have made them unacceptable for weight-limited submersibles, i.e., if the thickness were reduced to decrease weight, the magnitude of the tensile stresses would reach an unacceptable level because of flexing.

This dilemma could only be resolved by substituting a curved membrane configuration for a plane membrane configuration. Spherical shell sectors – membranes with double curvature and spherical angle bearing surfaces (figure 11.1) – are ideally suited for resisting external pressure, as all material in the body of the shell goes into compression while under external pressure loading and thus is not sensitive to crack initiators, e.g., inclusions, crazing, scratches, or gouges resulting from improper fabrication procedures, handling, or service in hostile environments (references 11.1 through 11.20). Furthermore, since acrylic plastic has higher strength in compression than it does in tension, a spherical window subjected only to compressive stresses can safely withstand higher pressure loading for a given t/D_i ratio than can a plane window, which is generally subjected to both tensile and compressive stresses.

The magnitude of structural improvement a spherical shell sector window offers over a plane disc window with a conical bearing surface varies with the t/D_i ratio and spherical angle of the sector. The improvement appears to be greatest in the operational depth range of 0 to 5000 feet (0 to 1524 meters). At greater depths, the windows appear to lose some structural superiority, since, when t/D_i is greater than 0.5, the plane disc windows experience only compressive stresses under hydrostatic loading. When t/D_i is less than 0.5, the structural improvement of spherical sectors is impressive. For example, a 90-degree (1.57 radians) spherical sector window with t/D_i equal to 0.25 implodes at critical pressures which are 250 percent higher than those for a 90-degree (1.57 radians) conical frustum window with an identical t/D_i ratio (figure 11.2). The axial displacement of spherical sector windows is also less than that of conical frustums. For example, for a 90-degree (1.57 radians) spherical sector window with t/D_i equal to 0.25, the displacement is approximately 60 percent less (figure 11.3). As a result, spherical sector windows have replaced plane disc windows in all applications where a maximum field-of-vision with a minimum weight penalty is required (figures 11.3, 2.26, 2.28, and 2.29).

Besides being structurally superior, spherical sector windows are optically superior to plane disc windows. Not only are they thinner than plane discs with identical operational depth ratings, but their shapes are those of convex-concave lenses, i.e., all objects in the field-of-view appear smaller, but free of distortion, and thus are ideal for panoramic viewing with a large field-of view (figures 11.5 and 11.6). However, because of this optical effect, submersible pilots must adapt themselves to spherical sector windows in order to judge distances to obstacles correctly. The optical effect is intensified, i.e., objects appear smaller but closer, because of the greater shell thickness and shorter radii of curvature. For t/R_o less than 0.1 the optical effect is not very significant and requires very little adaptation on the part of the pilot. However, the optical effect becomes very noticeable for t/R_o greater than 0.5 and considerable adaptation is required.

Although spherical sector windows represent a structurally optimum shape for resistance to external pressure, there are many applications where it may be desirable for economic or operational reasons to modify this shape. These modifications do not usually improve the structural performance of spherical shell sector windows but make them, or their mountings, less expensive to fabricate, install, or seal. To date only two such modifications have found acceptance (figure 11.7).

One modification consists of substituting a combination of plane and cylindrical bearing surfaces for the conical bearing surfaces. This increases the implosion pressure of spherical shells with an included angle less than 60 degrees (1.04 radians), while lowering fabrication costs for the mounting. The other modification is an equatorial flange for spherical shells with an included angle of 180 degrees (3.14 radians), i.e., hemispheres. The presence of an equatorial flange makes it easier to secure the window to the mounting flange and also makes it feasible to have the window economically fabricated by free-form blowing. Since these modifications represent only special cases of spherical shell sectors they will be discussed at the end of this section.

Of all window configurations used in ocean engineering applications, the spherical shell sector is the most important, not only because it is the key that opened hydrospace to panoramic vision but also because it serves as the gateway to application in hydrospace of other transparent materials with greater compressive strengths, e.g., glass, ceramic, and sapphire (reference 11.1). Because tensile stresses are absent in spherical sectors during hydrostatic loading, brittle materials with low tensile strengths can be used, if the proper bearing gaskets and mounting arrangements are also used. In addition, because of the predominantly compressive stress field, the sectors can tolerate surface discontinuities and inclusions to a much higher degree than can discs or conical frustums with t/D_i less than 0.5. Several proven spherical sector window designs for photo-optical systems have been developed for intermediate and abyssal depths using ceramics, sapphire germanium, and glass (reference 11.2). However, before these designs can be safely applied to manned submersibles, more experimental evaluation is required (figure 11.8).

11.2 SPHERICAL SHELL SECTORS WITH CONICAL BEARING SURFACES

The spherical shell sector with a conical bearing surface and included angle in the 30- to 270-degree (0.5 to 4.7 radians) range is the most popular configuration for spherical shell windows (figure 11.9). The reasons for this popularity are many; however, the most important ones are (1) the absence of tensile stresses under hydrostatic loading and (2) the reliable high-pressure seal that is available with a conical bearing surface. Because the tensile stresses are absent in a statically loaded window, it is very resistant to point-impact and explosive shock loadings. In fact, an increase in depth makes the window more resistant to such loadings, since the statically induced compressive stresses must first be overcome before a tensile crack can be initiated. Similarly, the presence of a conical bearing surface on the window improves the performance of the high-pressure seal with depth. This feature is very valuable as it provides a backup to the primary O-ring, or gasket seal, on the high-pressure face.

11.2.1 Structural Performance

11.2.1.1 DISTRIBUTION OF STRESSES. The spherical shell sector window performs under external hydrostatic loading very much as a spherical shell does where only membrane compressive stresses, whose magnitudes vary with location in the shell thickness, are present. The highest meridional and circumferential stresses are found on the interior surface, while the lowest ones are located on the exterior surface. Lamé's equation for thick-walled spheres provides a good approximation for the distribution of stresses and change of radius in spherical shell sectors of acrylic plastic under short-term loading:

$$S_1 = S_2 = -p \left[\frac{R_o^3 (R_i^3 + 2r^3)}{2r^3 (R_o^3 - R_i^3)} \right] \tag{11.1}$$

$$\Delta R_i = \frac{-p \, R_i}{692 \times 10^3} \left[\frac{3R_o^3}{2 (R_o^3 - R_i^3)} \right]$$

$$S_3 = -p \left[\frac{R_o^3 (r^3 - R_i^3)}{r^3 (R_o^3 - R_i^3)} \right] \quad ,$$

where

ΔR_i = change in internal radius (in inches)

S_1 = meridional membrane stress (in pounds per square inch)

S_2 = equatorial membrane stress (in pounds per square inch)

S_3 = radial wall stress (in pounds per square inch)

p = external hydrostatic pressure (in pounds per square inch)

R_o = external radius of sphere (in inches)

R_i = internal radius of sphere (in inches)

r = radius of point at which stresses are being computed (in inches).

The reasons for considering Lamé's equation as only an approximation are the visco-elastic behavior of the acrylic plastic and the restraining effect of friction between the window and its seat. If the comparison between experimental and calculated values is made under short-term loading conditions for a location at the center of the window, the agreement is very good. However, if the loading condition is of a long-term nature or if the stress location is near the edge of the window, the agreement between the experimental and analytic values becomes very poor.

The stresses measured on a 120-degree (2.09 radians) spherical sector with t/D_i equal to 0.092 and t/R_i equal to 0.159 during short-term external hydrostatic loading are good examples of actual stress distribution (figure 11.10). The restraining effect of the friction between the window and the flange extends less than a spherical angle of 30 degrees (0.52 radian) measured from the edge of the window. This postulate is based on the observation that all anomalous readings are generated at locations 1 and 2 (0 and 15 degrees (0 and 0.26 radian) from the window's edge), while the readings at locations 3, 4, and 5 (30, 45, and 60 degrees (0.52, 0.78, and 1.04 radians) from the window's edge) are very uniform (figures 11.11A, B, C, and D). The largest stress is found on the interior surface at the edge of the window (location 1) measured in the meridional direction (figure 11.11), while the smallest stress is found on the exterior surface at the edge of the window (location 1), also measured in the meridional direction (figure 11.12). Although both the maximum and minimum stresses are compressive, the difference between them is substantial (−6400 pounds per square inch (−44.1 megapascals) versus −500 pounds per square inch (−3.5 megapascals)), indicating the presence of a significant bending moment at the edge.

Because of this bending moment at the edge of the window, the maximum stress of −6400 pounds per square inch (−44.1 megapascals) at interior location 1 is considerably higher than the membrane compressive stress of −4250 pounds per square inch (−29.3 megapascals) on the interior surface at the center of the window. Similar effects of bending moment on the edge of the window have also been observed in a window with a 270-degree (4.7 radians) included angle and a t/R_i ratio of 0.2 (figures 11.12, 11.13, and 11.14). This indicates that bending moments are present in all spherical sectors with conical bearing surfaces regardless of the magnitude of the included window angle or t/R_i ratio. Thus the structural rating of a spherical sector window is determined by the maximum meridional stress on the interior surface of the window at its very edge rather than by the nominal membrane stress calculated by Lamé's equation. Still, equation 11.1 is useful for predicting the magnitudes of short-term radial displacements and strains at the interior apex of the window under short-term loading. i.e., the correlation between calculated and experimental values has been found to be quite good (figure 11.15). In addition, if the stresses calculated by using equation 11.1 are multiplied by a factor of two, the maximum value of the strain at the window's edge can be conservatively approximated.

11.2.1.2 BUCKLING. Spherical shell windows are unique in that they can fracture not only because of material failure but also because of buckling, which may be of elastic or plastic nature, i.e., the spherical shell may fracture at compressive stress levels that are significantly lower than the ultimate compressive strength of acrylic plastic. In this they differ significantly from plane window shapes (discs, frustums, and double-beveled discs) which fracture only when either the tensile or compressive strength of the material is exceeded. For this reason it is imperative in the design of such windows (whether they be true sectors, sectors with plane bearing surfaces, or hemispheres with equatorial flanges) that the engineer not only check the design for possible material failure but also for elastic or plastic instability.

Whether a spherical shell ultimately fails in the buckling mode depends primarily on three parameters: t/R_i ratio, deviation from sphericity, and the size of the spherical sector as defined by the magnitude of the included spherical angle. As a rule, a spherical shell sector will buckle unless the t/R_i ratio is very high (t/R_i greater than 0.5) or the included angle is very small for a given t/R_i ratio. Since it is very difficult to determine in advance whether

implosion will occur, it is prudent to assume that it will and to calculate the critical pressure at which elastic instability will occur.

Because the modulus of elasticity for acrylic plastic not only varies with stress level but also with duration of loading and temperature, it is very difficult to predict accurately the buckling of a spherical shell sector fabricated from acrylic plastic. Experimentally derived curves that relate the magnitude of membrane compressive stress to the modulus of elasticity under short-term loading exist (figures 4.21, 4.22, and 4.25). However, experimentally derived curves that relate both the compressive membrane stress level and duration of loading to the modulus of elasticity are very fragmentary and less than adequate (figure 4.53). For this reason, calculation of elastic or plastic instability under long-term loading is rarely performed. Instead, calculations are performed for the short-term loading condition at ambient room temperature and the resulting critical pressure is divided by a factor of two to give an estimated critical pressure under long-term loading at room temperature environment. For other temperatures, the short-term critical pressure must be divided by factors that are either larger or smaller than two, depending on the temperature.

This basic rule provides a fair approximation of critical pressure for a spherical sector continuously pressurized for 10,000 hours at room temperature. For other temperatures and durations of loadings, either the basic data relating the modulus of elasticity to time and stress must be generated prior to performance of calculations on critical pressure or the pressure must be established experimentally by testing of full- or model-scale sector specimens for a required period of time at the ambient temperature predicted by the operational scenario.

Buckling under short-term loading can be calculated fairly accurately by using the classical analytic expression for perfect spherical shells that was developed by Zoelly (reference 11.3), modified by Krenzke (reference 11.4) for the presence of deviations in sphericity, and adapted by Stachiw (references 11.5 and 11.6) for materials with modulii of elasticity and Poisson's ratios that are functions of stress:

$$p_{cr} = \frac{0.8 \sqrt{E_s E_t} \, (t/R_o)^2}{\sqrt{1-\mu^2}} \, . \qquad (11.2)$$

where

p_{cr} = critical pressure at which instability occurs (in pounds per square inch)

E_s = secant modulus of elasticity corresponding to the maximum compressive membrane stress level at p_{cr} (in pounds per square inch)

E_t = tangent modulus of elasticity corresponding to the maximum compressive membrane stress level at p_{cr} (in pounds per square inch)

μ = Poisson's ratio corresponding to the maximum compressive membrane stress level at p_{cr} (in pounds per square inch)

t = minimum thickness on the shell (in inches)

R_o = maximum external radius on the shell (in inches)

Since the equation cannot be directly solved, as both E_s and E_t are functions of stress, which in turn is a function of pressure, it is solved by repetitive iteration. One assumes some pressure value p, and on this basis calculates with equation 11.1 the maximum membrane stress which is then used to determine the values for μ, E_s, and E_t (figures 4.25, 4.21, and 4.22) that correspond to the magnitude of stress. Now with E_s, E_t, and μ available, equation 11.2 can be solved for p_{cr}. If the calculated p_{cr} is higher than the assumed p, this indicates that the assumed value was too low. If p_{cr} is less than p, this indicates that the assumed value was too high. By repeatedly assuming higher or lower values of p the discrepancy between p_{cr} and p can be reduced to zero. When p equals p_{cr}, the value of p_{cr} represents the predicted implosion pressure caused by elastic or plastic instability under short-term loading.

Although this approach is quite time consuming, the values of critical pressure calculated in this manner have been experimentally proven to be either equal to or higher than the experimental values. As a rule, the correlation between the experimental and calculated values improves with increases in the spherical angle, since in such cases the restraining effect of the seat does not extend to the center of the sector. Because of good correlation with experimental values, equation 11.2 is extensively used to predict the short-term critical pressure of spherical windows for which experimental data cannot be found in the published literature.

11.2.2 Modes of Failure

11.2.2.1 SHORT-TERM LOADING. *Implosion* of spherical sector windows under short-term loading is always of catastrophic nature. Depending on the sector's t/R_i ratio and included angle α, the mechanism of failure may take several forms.

1.   Sectors with a low t/R_i ratio and large spherical angle may fail by either generalized or localized buckling. The type of buckling depends basically on how well the sector approaches the shape of a perfect spherical surface and how far the effect of edge restraint extends (figures 11.16 and 11.17). The buckling may be of an elastic or a plastic nature, depending on the magnitude of the membrane stress level in the sector at which the buckling occurs. Elastic buckling generally occurs suddenly and without warning in the form of non-linear deflection or strain increase. Plastic buckling is also sudden, but is preceded by non-linear increases in the deflections and strains (figure 11.18).

2.   If the sectors have a high t/R_i ratio and a small included angle, buckling will not occur and the sector will be plastically extruded like a conical plug through the opening in the flange. The magnitude of the critical pressure is then determined by the magnitude of stresses and strengths of the material alone (figures 11.19, 11.20, and 11.21). Because buckling is absent the critical pressure is significantly higher, as the ultimate compressive strength of the material under biaxial compression is at least 100 percent higher than that of the yield strength, which is the critical factor in plastic buckling. One advantage of this type of failure is that it is preceded by a series of visible indicators, such as extensive plastic deformation and formation of cracks (figure 11.22). Because of these visible indicators the pressurization can usually be stopped and the sector saved. This is distinctly different from sectors with low t/R_i ratios, where there are no indicators of failure by elastic buckling and from failure by plastic buckling where there are fewer indicators, their magnitudes are smaller, and they occur just prior to implosion (figure 11.18).

The magnitude of critical pressure for catastrophic failure is a function of the t/R_i ratio, included angle α, temperature, and seat overhang ratio D_i/D_f. Although it is possible to predict with acceptable accuracy the critical pressure of a spherical sector design using

material data (section 4) and analytic expressions or finite-element computer programs, the cost generally exceeds that of a full-scale sector tested to destruction. For this reason, the designs of most spherical sector windows in service have been based on empirical data generated by testing model- or full-scale spherical sectors to destruction (figure 11.23). Because the critical pressure of the model-scale sector is the same as that of the full-scale sector, the cost of an experimental program can be kept very low.

Extensive experimental data have been presently generated only for sectors tested at ambient temperature in window seats with a seat overhang ratio equal to 0.9 (figure 11.23 and appendix C). Data show that the critical pressure of a sector is a function of both the t/R_i ratio and included angle for the particular set of test parameters (figure 11.24). For other temperatures and seat overhang ratios, experimental studies must be conducted, if exact values of critical pressure are to be established. It is possible, however, to postulate the effect of these variables without performing tests:

1.   Decreasing the ambient temperature will increase the critical pressure.

2.   Increasing the ambient temperature above room temperature will decrease the critical pressure.

3.   Decreasing the seat overhang ratio will decrease the critical pressure.

4.   Increasing the seat overhang ratio will increase the critical pressure for sectors with high t/R_i ratios and small included angles, but have little or no effect on sectors with low t/R_i ratios and large included angles, since they displace upon the seat only a small amount prior to implosion.

Experimental data have been also generated to substantiate the postulate that the short-term critical pressure of spherical sectors is not decreased by the presence of scratches on the convex or concave surfaces. A series of model-scale spherical sectors with 0.062-inch-deep (0.16 centimeter) machined notches on both viewing surfaces was tested to destruction under short-term pressurization at ambient room temperature, and the critical pressures were compared with those generated with identical sectors without notches. The findings were quite conclusive: stress risers in the form of sharp notches on the viewing surfaces do not decrease the short-term critical pressure of spherical sectors under short-term loading. It is not known whether this is also true for long-term and cyclic loading conditions. It can be postulated, however, that scratches on the concave surface probably do decrease the cyclic fatigue life, since during the relaxation phases the concave surface may be subjected to tensile stresses whose effects are invariably enhanced by the presence of stress risers such as notches. Scratches and notches on the convex surface, however, have no effect on the cyclic fatigue life of sectors, as that surface never experiences tensile stresses during the loading or relaxation phases.

Displacements and deformations of spherical sectors under short-term loading are functions of the t/R_i ratio, temperature, and included angle α (appendix C). They generally increase with temperature and decrease with the t/R_i ratio as it becomes larger (figures 11.25 and 11.26). In addition, a decrease in the included angle is also followed by a decrease in displacement; however, this occurs only for included angles that are less than 90 degrees (1.57 radians).

While discussing displacements, it is worthwhile to differentiate the locations at which they are measured. If they are measured at the apex of the sector they are approximately

100 percent larger than at the edge, reflecting the effect of sliding friction on radial displacement at that location (figures 11.26 and 11.27 and appendix C). Measurements taken at both locations are important for the window designer. Sliding displacement measured with a mechanical dial on the window seat in the mounting at the edge of the sector provides valuable information for selecting the magnitude of the seat overhang. A sector mounted in a flange with insufficient overhang (as defined by the D_i/D_f ratio) will fail sooner than an identical sector in a flange seat with adequate overhang. By the same token, an overhang that is too large will restrict the field-of-view through the opening in the flange. Axial displacement measured at the apex of the sector with a mechanical dial indicates incipient elastic or plastic buckling, i.e., this is the area on the sector farthest from the restraining effect of friction between the sector and the seat. This is particularly valuable in experimental studies where the objective is to pressurize the sector as much as possible without implosion.

Besides axial and sliding-displacement measurement techniques, there is also the average displacement technique. This is generally applied only to sectors with an included angle greater than or equal to 180 degrees (3.14 radians), as in such sectors the effect of edge restraint on the accuracy of the measurement is negligible. Measurement is performed by closing the back of the sector with a bulkhead, filling the interior of the sector with water, and measuring its displacement under pressurization. Using proper analytic expressions relating displaced volume to strain and a decrease in radius, the average radial displacement and membrane strain on the concave surface can be plotted as a function of external pressure loading (figure 11.28). The average membrane strains calculated in this manner agree remarkably well with strains measured by electric-resistance straingages located at the apex (figure 11.29). The displacement of the water-measurement technique is particularly valuable for detecting incipient local buckling which may occur at locations other than the apex.

Extensive displacement data have been generated only for model-scale spherical sectors at ambient room temperature (appendix C). To apply these data to the design of full-scale sectors it is necessary to multiply the displacements by a linear scaling factor based on the ratio of full- and model-scale sector radii (R_i of the full-scale sector to the R_i of the model-scale sector). To obtain displacements and deformations at other than room temperature, an experimental test program must be conducted, since factors for conversion of room temperature displacement data to other temperatures have not yet been validated.

11.2.2.2 LONG-TERM LOADING. *Implosion* under long-term loading is a function of the t/R_i ratio, duration of loading, temperature, included angle, and seat overhang. It always occurs at a pressure lower than that experienced under short-term loading, and the difference between the short- and long-term critical pressures increases with the duration of loading. This static fatigue characteristic of spherical sectors is similar to those previously discussed for acrylic plastic windows of other shapes, e.g., plane discs and conical frustums.

The major difference between spherical sector windows and windows with plane viewing surfaces is that spherical sectors fail because of both material failure and buckling. Although elastic buckling is almost immune to the effects of long-term loading, plastic buckling, particularly that of a local nature, is very sensitive to them because the time-dependent creep of acrylic plastic accentuates local deviations from sphericity. Thus, since the compressive membrane stress at a location which has a "flat spot" (larger radius of sphericity than the rest of the sector) is higher than at locations with shorter radii of sphericity, it

will produce time-dependent creep of larger magnitude and result in an increased radius of curvature, i.e., the flat spot will become flatter. The larger radius of curvature, in turn, generates higher stresses, which, in turn, produce higher creep, which, in turn, further increases the radius of sphericity. This process avalanches until the local radius of curvature increases to such an extent that the short-term buckling resistance of the spherical shell (defined by p_{cr} of equation 11.1) matches the sustained pressure to which the spherical sector has been subjected. At this point the spherical sector fails by local buckling (figure 11.30).

Because time-dependent buckling is so sensitive to local deviations from sphericity, it is hard to relate experimentally short-term buckling to long-term buckling by some empirical factor unless the deviations from sphericity are kept within some specified limit. Experimental data have been generated to relate critical pressure at ambient room temperature to duration of loading for hyperhemispheres with sphericity deviations less than 0.5 percent of the external spherical radius (figure 11.31). Although these data were generated with hyperhemispheres and spheres, they also apply to sectors whose included angles are 180 degrees (3.14 radians) or less. For very small angles (less than 90 degrees (1.57 radians)) the critical pressure of a sector under long-term loading will be higher than that of a hyperhemisphere because of the restraint imposed by the seat. Since the deviation is on the conservative side it can be used with confidence for design purposes, even for sectors with angles less than 90 degrees (1.57 radians).

Experimental data do not exist for spherical sectors under long-term loading at ambient temperatures that differ from room temperature. However, it can be postulated with a high degree of confidence that the critical pressures are raised by decreasing the ambient temperature and lowered by increasing the ambient termperature. This is based on the fact that the creep of acrylic plastic increases with temperature, which means that the rate of flat-spot formation will also increase.

Cracks appear in spherical sectors long before critical implosion. They usually first appear at locations different from the spot where localized buckling or shear cone failure will occur, e.g., they generally first appear on the conical bearing surface of the window (figure 11.32). These cracks propagate radially from the edge of the window while paralleling the spherical curvature of the window. They are deepest near the concave face, while at the convex face they are either very shallow or totally absent (figure 11.33). If sustained loading is continued, cracks coalesce into a conical fracture surface that when completed will divide the sector into two fragments nesting in each other (figures 11.34 and 11.35). Such a fracture plane generally only occurs in sectors with very high t/R_i ratios (t/R_i greater than 1.0). In spherical sectors with medium or low t/R_i ratios, failure by local buckling takes place before a conical fracture surface can form, and thus is rarely observed.

Cracks have been also observed to originate on the concave surface during the depressurization and relaxation phases that follow an extended sustained loading phase under hydrostatic pressure that represents a high fraction of the short-term critical pressure. These cracks are the result of tensile stresses generated on the concave surface by uneven relaxation rates of acrylic plastic inside the body of the sector. To decrease susceptibility to such cracks, discontinuities in the form of surface scratches should be avoided on the concave surface.

11-9

Displacements and deformations of spherical sectors under long-term loading are similar in character to those observed under short-term loading. The only basic difference is that they are functions of pressure and temperature for short-term loading, while for long-term loading they are functions of pressure, temperature, and duration of loading. They are measured at the same locations and by the same techniques.

Under long-term loading, creep occurs at a much higher rate in axial displacement than it does in sliding displacement, as the restraining force of friction does not act upon the sector at this location (figures 11.36 and 11.37). For example, in 90-degree (1.57 radians) spherical sectors with t/R_i equal to 0.364, creep after 15 minutes of sustained loading at a hydrostatic pressure of 11,500 pounds per square inch (79.3 megapascals) will increase the total axial displacement by approximately 100 percent, while it will increase the total sliding displacement by only 35 percent.

The primary value in measuring the displacement or deformation creep is to establish nondestructively in a short time the projected structural life of the spherical sector under a given level of external pressure loading. If the creep rate decreases to a low value after a sustained loading of less than 100 hours, it is a good indication that its life under sustained loading will be definitely in excess of 10 years, which is more than adequate for most applications. For example, the deformations of a 180-degree (3.14 radians) spherical sector with t/R_i equal to 0.8 under sustained loading indicate that this sector is more than adequate for long-term sustained loading service at 5000 pounds per square inch (34.4 megapascals), but not for 10,000 pounds per square inch (68.9 megapascals), although the critical failure, caused by static fatigue, is probably several months away (figure 11.38). For the same sector at a sustained loading of 20,000 pounds per square inch (137.8 megapascals) the rate of creep is so high that failure will occur in a matter of hours.

11.2.2.3 CYCLIC PRESSURIZATION. *Implosion* of spherical sector windows under cyclic pressure loading is primarily the result of the growth of fatigue cracks. Depending on the sector's t/R_i ratio, included angle, ambient temperature, magnitude of hydrostatic pressure, and duration of loading in each cycle, the cracks originate in one of two, or both, locations, i.e., the conical bearing surface and the concave surface at the apex.

The number of pressure cycles required to induce catastrophic failure is not only a function of the sector's structural properties, such as the t/R_i ratio and included angle, but also of the test conditions. High pressures, high temperatures, and long sustained loading cause failure in only a few cycles, while low pressures, low temperatures, and short sustained loadings prolong the cyclic fatigue life. A qualitative relationship between these experimental variables has not been empirically established, and thus a method for conversion or comparison of the cyclic fatigue lives of sectors, established under different sets of experimental conditions, does not exist. As a result, unless the designer can match the operational cyclic fatigue requirements to an existing set of experimental data, a study with the spherical sector must be conducted under test conditions based upon the projected operational scenario.

The cyclic fatigue life of a spherical sector window is usually experimentally established by subjecting several model- or full-scale sectors to a pressure cycling program in which each sector is pressure-cycled to a different pressure level, while the ambient temperature and duration of the cycles remain constant. If the selected pressures are close to the short-term critical

pressure, implosion will occur after a few cycles, or at most in less than 100 cycles. The values obtained in such a program generate a straight line when plotted on log-log coordinates. These are then used to predict the cyclic fatigue life of the particular design for any pressure level (figure 11.39). In this respect, the behavior of spherical sector windows under cyclic pressure loading is similar to that of plane disc and conical frustum windows.

Displacements and deformations resulting from cyclic pressurization vary in magnitude with changes in ambient temperature, magnitude of pressure, length of the individual pressure cycle, and number of cycles. If the strains generated during the sustained loading phase are low and if the relaxation phase is long enough to permit the strains in the material to return to zero, there will be no increase in displacement or deformation with each succeeding cycle. Since there are so many variables in pressure cycling, no firm postulates, with one exception, have been formulated to relate quantitatively the effect of each test parameter to the cyclic fatigue life.

This one exception is a very conservative empirical postulate: to avoid a progressive increase in displacement and deformation with each pressure cycle, the average membrane compressive strain must be kept below 3500×10^{-6} inches per inch and the length of the relaxation phase must be equal to or exceed that of the sustained loading phase of the pressure cycle. All spherical sectors in service exceed this value and thus experience some cumulative increase in displacement and deformation during their useful life. As a result, the fatigue lives of spherical sectors in service have final rather than infinite values. This is quite safe and reasonable (otherwise the sectors would be unwieldy), if their cyclic fatigue lives have been established and the windows are taken out of service before expiration of their cyclic fatigue lives.

An interesting phenomenon has been observed in spherical sectors with high t/R_i ratios that have been subjected to strains in excess of 3500×10^{-6} inches per inch: with each succeeding pressure cycle the compressive strains on the concave surface during the sustained loading phase decrease while the strains during the relaxation phase become tensile and their magnitudes increase with each pressure cycle, i.e., the higher the compressive membrane stress during the sustained loading phase, the higher the rate of tensile stress growth with each cycle (figures 11.40 and 11.41). After the tensile strain reaches a critical value (whose magnitude varies with ambient temperature and duration of relaxation phases), a crack is initiated on the concave surface. For ambient room temperature, the critical value of tensile deformation required to initiate a crack is greater than or equal to $10,000 \times 10^{-6}$ microinches per inch. If surface discontinuities in the form of scratches are present on that surface, the critical strain for crack initiation may decrease by more than 50 percent.

The presence of tensile strains on the concave face of the sectors during the relaxation phases is explained by the presence of negative creep in acrylic plastic during the sustained loading phase. The magnitude of the creep is larger on the concave surface than it is on the convex surface. Because compressive creep during the sustained loading phase is larger on the concave face than on the convex face, the former, being more permanently deformed, goes into tension during the relaxation phase, as the less deformed material near the convex surface attempts to return to its original shape in the absence of hydrostatic loading.

This also explains why the magnitude of tensile strains increases on the concave face during the relaxation phase with changes in temperature, t/R_i ratio, and magnitude of compressive stress. Increases in the t/R_i ratio are followed by increases in the difference between the strains on the concave and convex surfaces, which in turn creates a larger internal strain during the relaxation phase. Larger stresses and higher temperatures aggravate the situation by making permanent deformations larger and further increasing internal strains during relaxation.

There are not sufficient data to allow formulation of empirical rules for minimizing or eliminating the growth of tensile strains during pressure cycling. The only observation that can be made with reasonable certainty is that tensile strains have not been found during the relaxation phases in spherical sectors with $t/R_i \leq 0.153$, providing the nominal compressive stress during the sustained loading phase did not exceed 5000 pounds per square inch (34.5 megapascals) on the concave surface (figure 11.43). In sectors with $t/R_i \geq 0.363$ tensile strains have been found even when the magnitude of compressive stress was only 3750 pounds per square inch (25.9 megapascals) during the sustained loading phase (figure 11.42).

The presence of tensile strains is, in itself, not a bar to utilizing a given sector design for manned application, as other window shapes, e.g., plane discs and conical frustums with t/D_i less than 0.5, always operate with tensile strain fields on their low-pressure faces during the sustained loading phase. What the designer requires is the ability to predict when the strain will reach the value where fracture is initiated on the concave face.

Cracking is usually initiated in spherical sectors under cyclic pressure loading before implosion occurs. There are three locations where cracking can originate, and the location where it first appears is not necessarily the location of implosion. For this reason the appearance of some cracks can be ignored as they do not initiate implosion until they have grown to very large proportions. Cracks generally first appear on the conical bearing surface (figure 11.44). They are preceded by crazing marks oriented circumferentially. The growth of the circumferential cracks is very slow, requiring hundreds of cycles to proceed from their appearance to the point where they endanger the structural integrity of the sector. One characteristic of these cracks is that they propagate by forming mushroom-shaped extensions (figure 11.45). Each pressure cycle causes the mushroom-shaped extension to expand by a series of scallop-shaped steps. The cracks on the bearing surface can be generally ignored until their depth exceeds at least 2 percent of the sector's D_i.

In spherical sector windows with t/R_i greater than 0.35, cracks also appear on the concave surface at the apex of the sector. They are caused by tensile stresses present during the relaxation phase of each cycle. They appear suddenly, without advance warning, during a relaxation phase of the pressure cycle when the window is not under pressure. The depth of these cracks is generally equal to 50 percent of the sector's thickness, and once they appear the window must be replaced. The cracks generally assume the pattern of a cross (figure 11.46). However, if the pressure on the window is so high or the duration of loading is so long that they appear during the first relaxation phase, then the cracks assume a medusa pattern (figure 11.47). Because cracks induced by tensile strains appear during depressurization or relaxation of the window, they do not initiate catastrophic collapse, if the window is taken out of service before the next pressurization.

Cracks can also appear at any location where local buckling will occur in the future. These cracks form a pattern that encircles the local irregularity. This irregularity is generally an area with a higher radius of curvature that is initiated by a local dimensional deviation in thickness or sphericity, generally a product of the manufacturing process. These cracks first appear as faint crazing on the exterior surface. If crazing with a circular pattern surrounding a localized area is detected on the sector, it should be immediately replaced, i.e., the cracks will appear too late to serve as a warning. In such a case, the cracks will appear with local buckling and the resulting local implosion. The crack pattern resulting from a local buckling implosion under cyclic pressure loading is similar to the one observed during sustained long-term pressure loading (figure 11.30).

11.2.2.4 IMPACT LOADING. *Fracture Mechanism:* Because of the presence of high compressive membrane stresses generated by the static pressure loading (figure 11.48), spherical sector windows possess high resistance to crack initiation under impact loading, particularly if they are already under hydrostatic loading. For the crack to initiate, the point loading must be of such magnitude that the tensile component of flexure stress under the point of load application (figure 11.49) exceeds the compressive membrane stress by a value equal to the tensile strength of acrylic plastic under biaxial tension (5000 psi $< \sigma <$ 9000 psi) (34.5 mPa $< \sigma <$ 62 mPa).

Since the magnitude of compressive membrane stress in the spherical sector is directly related to the magnitude of external static pressure, the resistance of spherical sectors to point-impact loading increases linearly with the static pressure. As a result of the favorable superposition of compressing static stresses on tensile dynamic stresses, spherical sector windows are least vulnerable to catastrophic failure under point-impact loading when they are under their static design pressure loading. This means that submersibles and diving bells are least vulnerable to flooding that results from impact when the chances of hitting an underwater obstacle are the highest. They are most vulnerable during launching and retrieval on top of the ocean's surface, where the chances for crew evacuation and salvage of submersibles are the highest.

Fracture prediction: Because impact is a short-term phenomenon where the acrylic plastic behaves elastically, dynamic stresses can be calculated with the analytical methods applicable to elastic materials. Stresses calculated with classical equations or finite-element computer programs agree rather well with experimental data (figure 11.50). The assumption used in experimentally validated calculations is that the magnitude of local window displacement and the resulting flexure stresses under the point of impact are functions of changes in the kinetic energy in the impacting body, e.g., a submersible or diving bell (figures 11.51, 11.52, and 11.53) moving at operational speeds (less than 10 feet (3 meters) per second) comes to a halt after impacting the rigid obstacle.

Because the kinetic energy of a moving object at a given velocity is directly related to the object's mass, the vulnerability of a window to impact-induced fracture increases with the mass of the submersible or diving bell in which it is mounted. Thus, as the size of the submersible system is increased, its operational speed in the vicinity of obstacles must decrease. From a purely practical viewpoint it appears that submersibles cannot

11-13

exceed 1 foot per second (0.3 meter) in the vicinity of obstacles, if catastrophic accidents are to be avoided.

Cracks generated by point-impact loading on spherical sectors have the typical characteristics of local flexure failure. They are star shaped and originate on the concave surface directly under the point of impact (figure 11.54). If the impact is severe, i.e., its kinetic energy exceeds the critical crack initiation energy value by a significant amount, the star-shaped cracks coalesce into a conical fracture surface and the material enclosed by the conical fracture surface spalls off (figure 11.55). Experimental data also indicate that the kinetic energy of the impact must exceed the critical crack initiation energy by at least 100 percent before the window fracture reaches catastrophic proportions, i.e., fracture penetrates the whole window thickness and leakage occurs.

Prediction of critical velocities for initiation of cracks in spherical sectors based on the principle of a change in the kinetic energy in the impacting body is only valid for the typical operational velocities of submersibles. It is not valid for impacts generated by high-velocity projectiles, e.g., bullets or fragments from exploding or imploding containers close to the window. In such cases, the fracture is generally initiated by the reflection of impact-generated compressive waves from the concave surface of the spherical sector. Since the amplitude and velocity of such waves are functions of both impact velocity and kinetic-energy change, calculations based on kinetic-energy change alone will provide erroneous answers.

Fracture prevention: Fractures can be prevented in spherical sector windows by either making the window more impact resistant or placing an impact-resistant guard over the window. Windows can be made resistant to low-velocity impacts, where fracture is only a function of kinetic-energy change, by being made thicker than required by the static design pressure and by keeping the concave surface free of scratches. Doubling the window thickness doubles the velocity change required by the impactor for initiation of fracture. Resistance to high-velocity impacts can be significantly increased by the use of laminated construction. A 0.25-inch-thick (0.6 centimeter) sheet of acrylic plastic laminated to the static load carrying body of the window with a transparent elastomer can be used as a shield layer (or layers if impact protection is required for both convex and concave surfaces). A high-velocity projectile, e.g., a .22 caliber bullet, will fracture the outer shield layer of the acrylic plastic, but will not initiate any cracks in the main body of the window. Although it will have an unsightly fracture in the shield layer, this window will not need to be replaced, as the structural properties of the window's body will not have been impaired. Placing a 0.5-inch-thick (1.27 centimeters) acrylic shield an inch in front of the window will accomplish the same objective. However, the window-flange assembly will weigh significantly more and the optical properties will be significantly degraded by the inability to clean the window's exterior and the shield's interior.

Additional improvements in resistance to low-velocity impacts can only be achieved by adding an external bumper designed to deform elastically or plastically in a controlled manner. Such bumpers are very valuable for protecting large windows from impacts against the side of the ship during launch or retrieval of the submersible system in rough seas. In some cases bumpers have been made from thick acrylic plastic bars that become almost

11-14

invisible underwater. Their drawback, however, is their low-energy absorption capabilities in comparison to those of other materials, e.g., plastic or aluminum.

11.2.2.5 DYNAMIC PRESSURE LOADING. *Fracture Mechanism:* Spherical sector windows possess high resistance to cracks initiated by explosively generated dynamic pressure loading, particularly if they are already under external hydrostatic pressure. This is explained by the presence of high compressive membrane stresses that have been generated on the concave surface by external hydrostatic loading. Since dynamic tensile stresses must be present for fracture initiation, the static compressive membrane stresses must be overcome by the tensile dynamic stress components before the material will fracture. The dynamic tensile stresses are generated on the concave surface by the reflection of a high-velocity compressive wave travelling through the sector from the convex to the concave surface.

The cracks initiated by the dynamic tensile stress on the concave surface are arranged in a star-shaped pattern at the apex of the sector (figure 11.56). If the impulse loading is just of sufficient magnitude to initiate the crack pattern, leakage will not occur as the cracks do not penetrate the full thickness of the sector. Only if the impulse loading exceeds the critical dynamic pressure by a large margin is there complete penetration of the sector wall by the fracture.

Fracture Prediction: The magnitude of the dynamic overpressure required to initiate fracture in a spherical sector is a function of sector thickness, temperature, duration of dynamic overpressure, and magnitude of static compressive membrane stresses. Increasing the wall thickness and magnitude of static pressure loading increases resistance to fracture, while increasing the temperature and duration of dynamic pressure loading decreases resistance.

Although there are little experimental data on dynamic impulse loading of acrylic plastic spherical sectors, several general observations can be made. When a spherical sector is under a static pressure loading less than or equal to 0.01 short-term critical pressure, it requires a dynamic overpressure greater than or equal to 0.5 short-term critical pressure to initiate a fracture. However, if the external static pressure loading is greater than or equal to 0.25, but less than 0.5, of the short-term critical pressure, the dynamic overpressure value required for initiation of fracture increases to more than 1 short-term critical pressure.

It thus appears that the greatest probability for fracture under explosively generated dynamic pressure loading is when the window is not statically pressurized, i.e., when the submersible is floating on the ocean's surface. At operational depths where the static pressure is high, the probability decreases significantly. This is fortunate, as underwater explosions are most likely to occur at operational depths since this is usually the location of the work area where explosively actuated stud drivers or bolt cutters are used. This is also where entanglement can take place and explosively actuated release bolts are used to release the ballast or personnel capsule.

Fracture prevention: No special construction techniques or devices to increase the resistance of spherical sectors to crack initiation under explosively generated dynamic

pressure loading have yet been developed. The only proven approach is an increase in the sector's thickness and the prevention of scratches on the concave surface. Doubling the thickness approximately doubles the dynamic overpressure required to initiate fracture, and the extra thickness increases the resistance to both dynamic overpressure and point-impact loading. Since the extra thickness also increases the static and cyclic fatigue lives of the window under operational conditions, it is considered a good idea to overdesign the sector's thickness, even if this involves extra expense and a small weight penalty.

11.2.3 Prediction of Implosion Pressure

Although it is difficult to predict accurately the failure of any structure made of acrylic plastic, spherical sectors are better suited for analytical calculations than are plane discs with single or twin conical bearing surfaces. The equations for the calculation of the magnitude of membrane stresses (equation 11.1) and critical pressures at general or local instabilities (equation 11.2) under short-term loading have been discussed and their advantages and disadvantages noted. Using these equations and basic data on the behavior of acrylic plastic under compressive loading (section 4), it is feasible to calculate with an accuracy acceptable for engineering structures the short-term critical pressure for sectors with included angles greater than 90 degrees (1.57 radians). However, this is generally not done since an experimentally generated set of curves that relates t/R_i and the included angle to the implosion pressure under short-term loading at ambient temperature already exists (figure 11.24 and section 15).

Knowing the magnitude of the short-term critical pressure at ambient temperature for a selected sector design only tells the designer how high a momentary overpressure the particular sector can tolerate prior to failure. To predict long-term and cyclic fatigue critical pressures under the postulated operational conditions, a major finite-element stress analysis or a major experimental test program must be conducted. Once the critical pressures under long-term and cyclic loading conditions are known, they must then be compared with projected operational loading conditions to determine if there is an acceptable safety margin. If computer techniques are used, there are the problems of cost and validity; if an experimental program is used, there are the problems of cost and a long test schedule. To a designer without much money and time, both approaches thus pose formidable hurdles.

An alternate approach for determining a safe sector design is to focus the selection process on a design that is known to work under projected operational conditions and to ignore its critical pressures under long-term and cyclic service conditions. This approach is distinctly different from the others which focus on determination of critical pressures under short-term, long-term, and cyclic conditions and only look peripherally into the adequacy, i.e., structural reserve, of the design for postulated operational conditions. This alternate approach, which is applicable to acrylic plastic windows of any shape, has been discussed in previous sections for other window shapes and thus will only be summarized here.

The approach is based on the premise that only the short-term critical pressure at ambient temperature of the proposed design needs to be accurately known and that other operational conditions are defined by the maximum expected operational pressure and temperature. This is accomplished by relating the critical pressure under short-term loading to the operational pressure and temperature by means of proven conversion factors.

These factors have been developed by the author by summarizing, correlating, and extrapolating published and unpublished data from test programs and successful spherical window sector designs in service (table 11.1). For some service conditions, e.g., length of pressure cycles and deviations of pressure and temperature from specified maximum values, the conversion factors are overly conservative, while for others they are probably marginal. However, because of the savings in time and money, this approach is considered both cost effective and safe, if its stated limitations on static and cyclic fatigue lives are not exceeded. (For a discussion of these limitations, see section 15.)

Table 11.1. Conversion factors for acrylic plastic spherical sector windows with conical edges and hyperhemispherical windows with conical edges.

Temperature Ranges				
50°F ($\leqslant 10°$C)	75°F ($\leqslant 24°$C)	100°F ($\leqslant 38°$C)	126°F ($\leqslant 52°$C)	151°F ($\leqslant 66°$)
CF = 4	CF ≈ 6	CF = 8	CF = 10	CF = 16

11.2.4 Mounting of Sectors in Flanges

11.2.4.1 SEATING. Spherical sectors require seats with spherical angles that match their included angles. Although conclusive experimental data are not available, it can be postulated with reasonable confidence that the mismatch between the included angle of the bearing surface on the sector and the seating surface on the flange should not exceed 30 minutes (0.009 radian), and if possible it should be kept within 15 minutes (0.004 radian). If a mismatch is present, it is desirable to have the angle on the window's bearing surface exceed the angle on the flange seat (figure 11.57).

In this way, the maximum stress, which is oriented meridionally and located on the concave surface at the edge of the sector, is decreased. At the same time, the minimum stress, which is oriented meridionally and located on the convex surface at the edge of the sector, is increased. If the angle on the bearing surface of the sector is less than the angle on the flange seat, the opposite occurs, i.e., maximum stress increases while minimum stress decreases. Such an angular mismatch makes sealing at the convex surface very difficult or impossible.

The surface on the sector's bearing surface requires a good finish, otherwise circumferential cracks will originate after several pressure cycles. As a rule, a 32-rms finish has been found adequate for the sector's bearing surface. The surface finish on the flange seat must also be good to minimize friction between the sector and the flange. A 63-rms finish has been found to be adequate for such purposes, but a 32-rms finish is more desirable. If the seat is painted, the paint must be very hard, sanded smooth, and liberally greased. Failure to do so will result in stepwise, instead of gradual, sliding of the sector on the seat. Stepwise sliding is considered undesirable from a structural viewpoint and unacceptable from a psychological viewpoint as it is accompanied by significant releases of acoustic energy. Presence of O-ring grooves in either the window's bearing surface or the seat on the flange is not acceptable, since they dramatically decrease the cyclic fatigue life of the spherical

sector. It is acceptable, however, to machine a bevel on the edge of the convex surface for containment of a seal, if the width of the bevel does not exceed 0.1t.

The seating surface on the flange must provide adequate overhang to support the bearing surface of the window during sliding under hydrostatic loading (figure 11.58). The magnitude of overhang should be based on the magnitude of sliding during the most severe episode predicted from the projected operational scenario. This is generally represented by the single longest sustained pressure loading at design temperature expected during the operational life of the pressure vessel in which the window is located.

Since operational scenarios differ from one pressure vessel to another, the seat overhang will differ, although the vessels may be built for the same design pressure and temperature. If a definite scenario is not available, some duration of sustained loading must be selected as the criterion for design of the seat overhang. The recommended duration of loading is 1000 hours at design temperature and pressure. Since experimental data may not be available, a table of recommended seat overhangs, designed on the basis of conversion factors developed by the author (section 15), has been developed for spherical sectors. The recommended overhangs also provide adequate support for the sectors when the vessel is subjected to 50-percent overpressure of short duration during acceptance testing prior to placement in manned service.

11.2.4.2 ATTACHMENT. Retaining rings are required on windows of any shape to keep them in place during relaxation periods of zero pressure loading. The spherical sectors are unique in that for low t/R_i ratios and included angles (less than 90 degrees (1.57 radians)) they also require retaining rings to hold them in place while being pressurized. Experimental data show that when this is not done, the sector may, and often does, rotate in the seat and fails in local shear. To prevent this, the retaining ring must be substantial (t greater than or equal to 0.25 inch (0.6 centimeter)) and held down with screws at close intervals around its circumference (at least every 4 inches (10 centimeters) with screws greater than or equal to 0.3 inch (0.8 centimeter)).

11.2.4.3 SEALING. Spherical sector windows, like windows of any other shape, require two independent seals for safe, positive sealing. High-pressure sealing is accomplished when the conical bearing surface rests on the well greased conical seat of the flange. This provides a reliable seal whose capability increases with the pressure differential across the window. Unfortunately, this capability decreases to zero when a submersible is on the ocean's surface or when divers are locking-out from a bell at operational depths. To seal during these conditions, a separate low-pressure seal is required.

A neoprene gasket squeezed by the retaining ring against the window's convex surface or a molded ring of circular or triangular cross-section wedged between the conical seat on the flange, beveled surface on the window, and the lower face of the retaining ring (figure 11.59) can be used as low-pressure seals. If properly compressed, the seal will perform reliably at zero pressure differential. Although the temptation exists to make the gasket or O-ring as thin as possible, this should not be done as the large window diameter, large thermal coefficient of expansion exhibited by plastic, and large differential between ambient temperatures in operational and fabrication areas make thick seals with large precompression mandatory.

The worst case is that of a spherical sector window mated to a submersible hull in a heated building and subsequently exposed to arctic temperatures on the deck of a ship prior to diving operations. For such a case, elastomeric material with a low coefficient of thermal expansion and a change in hardness should be selected, since an increase in hardness and a decrease in compression will cause the seal to leak at low temperature. Although materials may be selected that minimize this problem, they cannot replace proper precompression of the seal during assembly. The minimum precompression recommended for the low-pressure-face seal on windows with $60 < \alpha < 120$ is equal to $D_i \times \Delta T \times 10^{-5} + 0.030$ inches. In this case, ΔT is measured in degrees Fahrenheit and it represents the temperature differential between the ambient temperature at assembly and the lowest atmospheric ambient temperature predicted for the area of operation.

11.2.5 Fabrication

11.2.5.1 FREE-FORM BLOWING. Spherical sector windows can be fabricated by using one of several proven techniques. The least expensive technique is free-form blowing. Plane circular discs cut from flat acrylic plastic sheets are used as basic stock. The disc is clamped around its circumference, while compressed air is applied to one side of the disc at ambient temperature in excess of $300°F$ ($149°C$) (figures 11.60 and 11.61). The diameter of such a window is controlled by the inner diameter of the clamp ring, while the radius of curvature is controlled by the magnitude of air pressure, temperature, and duration of sustained pressure application.

Major problems with this technique are the variations in thickness and irregularities in sphericity that it produces in the finished sector (figures 11.62 and 11.63). Because the performance of a spherical sector with varying thickness and sphericity is determined by the most significant deviation from nominal sphericity and thickness, the overall pressure rating of a free-blown sector is low. The equatorial flange resulting from the free-form blowing process also presents a problem. For sectors with an included angle less than 180 degrees (3.14 radians), the flange must be cut off, a significant waste of material. For sectors with an included angle of 180 degrees (3.14 radians), i.e., a hemisphere, either an acrylic backup ring must be bonded to the heel of the flange or the flange must be removed or high bending stresses will be present at the heel of the flange. In either case, additional expenses are involved. As a result, free-form blowing is used only rarely, and only for spherical sectors with large diameters for low-pressure applications (figure 11.64).

There is another technique that can be used to produce sectors with an equatorial lip. It is similar in many respects to the free-form blowing process, except a hydraulic ram-actuated plunger is used to extrude the spherical sector from a circular plane disc (figure 11.60). This hot-forming technique produces a sector with an accurate concave surface and a wall thickness that is more uniform than in sectors produced by the free-form blowing technique (figure 11.65). However, its drawbacks have prevented it from becoming popular: The tooling costs are very high for large sectors; powerful hydraulic presses are needed to exert the necessary force on the male plunger; and the extruded sector must have its flange machined off before the sector can be used for medium- or high-pressure service.

11.2.5.2 VACUUM FORMING. The vacuum-forming fabrication technique uses ambient air pressure to force a circular plane disc at temperatures in excess of 300°F (149°C) into a spherical mold that has been subjected to a partial vacuum (figures 11.66 and 11.67). Because the mold provides a positive limit on the deformation of the acrylic plastic disc, the sphericity of the finished product conforms closely to the shape of the mold. Since the mold provides continuous support to the deforming material, deviations from the nominal thickness are minor. For example, a 120-degree (2.09 radians) spherical sector with a 4-inch (10 centimeters) nominal wall thickness and a 29-inch (74 centimeters) inside radius is only 0.160 inch (0.4 centimeter) thinner at the center and 0.125 inch (0.3 centimeter) thicker at the edge than before forming, representing a deviation from the nominal thickness of approximately 4 percent. Most spherical sector windows in submersibles have been built using the vacuum-forming technique followed by machining of the bearing surface to tight dimensional and angular tolerances. Since the depth rating of any spherical sector is always based on the thinnest measured section of the sector at its apex, vacuum-formed windows lose less of the potential depth rating that is inherent in the thickness of an unformed sheet.

Although vacuum forming can produce large, dimensionally tight sectors at a low cost (providing the mold is amortized over many sectors), it also has some drawbacks and limitations. The major drawbacks are significant thinning out at the apex of the sector if the included angle exceeds 120 degrees (2.09 radians) and an inability to produce sectors with included angles greater than or equal to 130 degrees (2.26 radians). Limitations on the vacuum-forming process are twofold. The maximum achievable diameter of the vacuum-formed spherical sector is determined by the 48-inch (122 centimeters) maximum width of stock sheets that exceed 2 inches (5 centimeters) in thickness. As a result, the outside diameter of a thick sector cannot exceed 44 inches (112 centimeters). The plasticity of acrylic plastic at forming temperatures, however, limits the formability of spherical sectors with included angles in the range of $90 \leqslant \alpha \leqslant 120$ degrees ($1.57 \leqslant \alpha \leqslant 2.09$ radians) to sectors with $t/R_i \leqslant 0.2$. For spherical sectors with $t > 2$ inches (5 centimeters) that exceed the included angle of 130 degrees (2.26 radians), the outside diameter of 47 inches (119 centimeters), or a t/R_i of 0.2, a different fabrication technique must be used.

11.2.5.3 CASTING. Spherical sectors of any size, thickness, t/R_i ratio, and included angle can be fabricated by casting in an assembly consisting of both male and female molds. If the molds are machined to close tolerances, the cast sector will show only very minor deviations from nominal dimensions and the only machining required will be on the bearing surface. If the surfaces of the molds are polished, the concave and convex surfaces will satisfy optical requirements without polishing (figure 11.68).

Several spherical sector designs have been cast by manufacturers specializing in this kind of work. They range from small hemispherical castings for deep submergence windows (figure 11.69) to large castings for observation domes (figure 11.70) and submersible hulls (figure 11.71). Only two types of problems have been encountered in the casting of spherical sectors: inclusions in the form of bubbles and significant variations in the physical properties of material cast from different resin chemistries. Both problems must be considered by the designer in establishing specifications for cast spherical sectors. A useful guide is the ANSI/ASME PVHO-1 Safety Standard (section 15). Any deviations from these specifications for technical or economic reasons must be very carefully studied for their impact on the structural performance of the finished product.

11.3 MODIFIED SPHERICAL SHELL SECTORS

11.3.1 Spherical Shell Sectors with Restrained Edges

11.3.1.1 DESIGN. There are many applications where it is not cost-effective to machine a conical seat in a flange because of its size or location on a submersible. Furthermore, there are also applications where large sliding displacements on the window seat cannot be tolerated because of stringent sealing requirements.

For such applications, a design has been developed that replaces the conical bearing surface on the spherical sector window with two bearing surfaces: one a plane surface and the other a cylindrical surface (figure 11.72). The relationship of the bearing surface's dimensions to the thickness of the sector and its included conical angle is given in equations 11.3 and 11.4:

$$h = t \cos \frac{\alpha}{2} \tag{11.3}$$

$$w = t \sin \frac{\alpha}{2} . \tag{11.4}$$

Although other proportions for h and w can be chosen, windows whose bearing surfaces are based on equations 11.3 and 11.4 have been found to perform satisfactorily since these equations consider the magnitude of the reaction force's components acting upon each bearing surface. The plane bearing surface in the flange seat provides the axial component of the reaction force while the cylindrical surface provides the radial component.

11.3.1.2 SEALING. Because it is relatively easy to maintain tight dimensional tolerances on the outer diameter of the window and on the diameter of the cylindrical seat in the flange, it is possible to obtain a very close fit between the window and the seat (figure 11.73). This close fit eliminates for all practical purposes any relative motion between the bearing surfaces, which in turn increases the cyclic fatigue life of the window's bearing surface (figures 11.74 and 11.75). It also eliminates any sealing problems that are typical of spherical sectors with conical bearing surfaces. In addition, a second seal can be incorporated into the assembly in the form of a gasket bonded to the flange (figure 11.76). This gasket not only seals, but it also eliminates point contacts between the window and any unevenness on the plane bearing surface of the flange.

11.3.1.3 STRUCTURAL PERFORMANCE. Because the edge of this spherical sector design is restrained from decreasing its spherical radius under hydrostatic loading, significant flexure moments are imposed on the edge of the window each time that it is pressurized. The flexure moment generated by the restrained edge introduces flexure stresses into the body of the window, and their magnitudes appear to be inversely related to the magnitude of the included angle (figures 11.77 and 11.78). For example, in sectors with included angles less than or equal to 60 degrees (1.04 radians), tensile stresses instead of compressive strains are predominant on the concave surface. The presence of these tensile stresses makes it mandatory that scratches be absent from this surface, otherwise its critical pressure under operational conditions will be substantially lowered. A different case presents itself for a sector

11-21

with a large included angle, e.g., 120 degrees (2.09 radians) (figures 11.79 and 11.80). In such a window, the strains on the concave surface are not only compressive (figures 11.81 and 11.82), but they are higher in magnitude than they are in a window with an identical t/R_i ratio and included angle but with a conical bearing surface (figures 11.10 through 11.14).

The effect of flexure stresses generated by the restrained edge (superimposed on the membrane stresses characteristic of spherical shells) can be also seen in the difference between critical pressures under short-term loading for spherical sectors with restrained edges and those with conical bearing surfaces (figure 11.83). For sectors with a restrained edge and an included angle less than 75 degrees (1.3 radians), the critical pressures are higher; for those with angles of $75 < \alpha < 180$ degrees ($1.3 < \alpha < 3.14$ radians) they are less than for sectors with conical bearing surfaces. This feature makes the sectors with restrained edges very attractive for service where included angles less than 75 degrees (1.3 radians) are specified by the design requirement. In addition, sectors with restrained edges do not have a tendency to rotate in the flange as do those with conical bearing surfaces and included angles less than 90 degrees (1.57 radians). The restrained edge insures that the sectors, regardless of their t/R_i ratio and included angle, will fail by local or general buckling. Since maximum strains are located in the apex area, the center of the local buckling is generally at the apex (figure 11.84).

11.3.1.4 OPERATIONAL PERFORMANCE. For spherical sector windows with restrained edges the critical pressures for included angles of 75 to 180 degrees (1.3 to 3.14 radians) are lower and the stress distributions are less uniform than in spherical sectors with conical bearing surfaces. Therefore, higher conversion factors must be used when basing the design on the short-term critical pressure of spherical sectors with conical edges (table 11.2 and section 15). However, if the new design is qualified by cyclic fatigue and sustained loading tests, there is no need to use conversion factors for establishing the maximum safe working pressure. In this case, the operational pressure rating is based on the results of the experimental test program. To date, only a single experimental program has been conducted at ambient room temperature utilizing scale-model sectors with restrained edges and t/R_i ratios of 0.032, 0.159, and 0.066 for included angles of 30 to 180 degrees (0.5 to 3.14 radians) (figure 11.85).

Table 11.2. Conversion factors for acrylic plastic spherical sector windows with square edges and hemispherical windows with equatorial flanges.

Temperature Ranges				
50°F ($\leqslant 10°$C)	75°F ($\leqslant 24°$C)	100°F ($\leqslant 38°$C)	126°F ($\leqslant 52°$C)	151°F ($\leqslant 66°$C)
CF = 5	CF = 7	CF = 9	CF = 11	CF = 17

11.3.2 Spherical Sector with Equatorial Flange

11.3.2.1 DESIGN. Equatorial flanges on spherical sectors are either placed there by design or are the byproducts of a fabrication process, e.g., the free-form-blowing process. Equatorial flanges have been used in service only on sectors with an included angle of 180 degrees (3.14 radians), i.e., hemispheres. A hemisphere is equipped with an equatorial flange because it provides a secure attachment to the seat in the flange and it allows the interior of the hemisphere to be at a higher pressure than the exterior ambient pressure, both valuable operational features.

Retainment of a hemisphere without an equatorial flange is only feasible at some loss to the visibility of its interior (figure 11.86). Thus, the presence of the flange provides a simple engineering solution to the attachment of the hemisphere to the mounting flange. Furthermore, it allows the incorporation of seals that remain watertight, regardless of the magnitude of window's radial contraction during sustained pressure loading. In addition, this can be done without using an O-ring groove, which would serve as a stress riser into the bearing surface of the window.

The equatorial flange can be shaped in many different ways. However, the most acceptable appears to be a square flange whose (1) thickness and width are both equal to the sector's thickness, (2) heel is sharp, and (3) instep has a radius greater than or equal to 0.25t (figure 11.87). Large radii on the heel should be avoided, as they introduce large bending moments in the transition region from the flange to the hemisphere. Grooves in the bearing surface should also be avoided, as they act as stress risers and dramatically lower the cyclic fatigue life. Bolt holes should not be drilled in the flange, since the presence of many holes and rigidly fixed screws around the flange's circumference will cause it to fracture and separate from the hemisphere at only a fraction of the window's short-term critical pressure under external pressure loading (figure 11.88).

11.3.2.2 STRUCTURAL PERFORMANCE. The presence of the equatorial flange imposes a flexure moment on the edge of the hemisphere. Its magnitude is a function of the flange's thickness and width and the curvatures of the heel and instep. Since there are insufficient experimental data, a general relationship between these structural variables and the magnitude of stresses under hydrostatic loading cannot be formulated at the present time. There exist, however, sufficient data points to formulate some very general postulates.

It appears that the maximum stress is oriented meridionally and is located somewhere between the flange and the apex of the spherical sector. Its exact location is a function of the radial compliance of the flange and heel curvature. Increasing the radius of the heel dramatically increases the magnitude of stress and brings its location closer to the flange (figure 11.89). If the radius of the heel is very large ($r > t$), the meridional stress on the concave surface near the flange becomes tensile while the meridional stress on the convex surface at the same location achieves very high compressive stress values.

This problem is particularly bothersome in thermoformed hemispheres where the radius of the heel always exceeds the thickness of the shell. Unless the flange is either eliminated or backed up with a heel ring, the tensile membrane stresses on the concave surface in the transition area between the flange and the shell may initiate a crack under a pressure

loading that is only a fraction of the short-term critical pressure for a hemisphere without a flange. In an actual application of free-blown hemispheres with flanges, it was found that when the heel backup ring was eliminated the magnitude of tensile and compressive meridional stresses increased 1000 and 64 percent, respectively, although in an attempt to compensate for the expected increase in stress level the thickness of the wall was doubled (figure 11.90).

Short-term critical pressures of hemispheres with sharp-heeled flanges have been found to be identical to those without flanges in the range of $0 < t/R_i < 0.25$. When t/R_i is greater than 0.25, the critical pressure of hemispheres with flanges is somewhat less than that of those without flanges (figure 11.91). The failure mechanism is the same as for hemispheres without flanges. Only if the heel is well rounded ($r > 0.25t$) does the failure occur because of flexure stresses at the flange.

The strains and radial displacements at the apex under short-term loading are the same as those for flangeless hemispheres, if the radius of the heel is less than 0.25t (figure 11.92). There is, however, a significant difference at other locations on the window (figure 11.93), a difference which increases with external pressure loading.

Critical pressures under long-term loading are the same as those for flangeless hemispheres and follow the same time vs. critical pressure relationship (figure 11.94). The basic differences between flanged and flangeless hemispheres are the early appearance of cracks in the bearing surface and the total separation of the flange from the body of the window long before implosion. Thus, from an operational viewpoint the static fatigue life of flanged hemispheres is less than that of flangeless hemispheres, since with the separation of the flange the window ceases to be reliably attached to the mounting (figure 11.95). This problem can be somewhat alleviated by placing a thin neoprene gasket between the window and the mounting.

The cyclic fatigue life of flanged hemispheres is shorter than that for flangeless hemispheres because of fatigue cracks on the bearing surface. These cracks appear after only a few cycles and cause separation of the flange many cycles before implosion, if the window is cycled to a pressure in excess of 0.5 short-term critical pressure. This can basically be alleviated by placing a thin neoprene gasket between the window and the seat in the mounting. The gasket, however, has only a very minimal influence on the formation of meridional tensile cracks originating at the heel of the flange during the relaxation phase of a pressure cycle (figure 11.96). These cracks originate at a lower pressure loading in flanged windows because the strains in the flange on the interior surface are significantly higher than those at the apex. Thus, in a very real sense, nothing can be done to make the cyclic fatigue life of flanged hemispheres equal to that of flangeless windows.

11.3.2.3 OPERATIONAL PERFORMANCE. Because the flanges cause cracks to appear at a lower fraction of the short-term critical pressure than is the case with flangeless windows, the safe pressure ratings for flanged windows are lower than those for flangeless hemispheres with identical t/R_i ratios. The design pressures at which a flanged window design can be safely operated are determined either by conducting an experimental evaluation program composed of short-term, long-term, and cyclic tests or by applying a conversion factor to the short-term critical pressure of a flangeless spherical sector with the same t/R_i ratio.

Conversion factors that have been found safe are identical in magnitude to those used for flangeless windows with restrained edges (table 11.2).

The mounting and sealing of hemispheres with equatorial flanges is a rather simple process (figures 11.97 and 11.98). It requires only that the seat on the mounting be flat within 0.02 inch (0.05 centimeter) and have a finish less than or equal to 63 rms. The seat *overhang* must be provided for the window in the same manner as it is for hemispheres without an equatorial flange. The window is retained in the mounting by a retainer ring which allows the window to displace radially while under hydrostatic loading. To avoid point loadings a neoprene pressure pad is inserted between the top of the acrylic flange and the bottom of the retainer ring lip and a neoprene bearing gasket is placed between the steel seat in the mounting and the acrylic bearing surface on the equatorial flange. An O-ring wedged between the circumference of the acrylic flange, the retaining ring, and the seat on the mounting is the primary seal. A neoprene bearing gasket bonded to the bearing surface of the acrylic flange is the secondary seal. Because both seals can radially displace with the window, the integrity of the seal remains intact during sustained loading or subsequent relaxation.

11.3.3 Spherical Sector with Spherical Bearing Surface

11.3.3.1 DESIGN. Spherical sectors have been built with spherical bearing surfaces for a few special applications (figure 11.99). The reason for substituting spherical surfaces for conical bearing surfaces on both the spherical sector window and its seat in the mounting is to reduce the cost of fabrication. Machining of conical bearing surfaces to the required tight angular tolerances is time consuming and thus expensive. Spherical bearing surfaces on small windows and their mounting seats, however, can be ground to a very exacting spherical radius by using standard lens-grinding equipment and techniques. In addition, it is hoped that spherical bearing surfaces will eliminate cyclic fatigue cracks from the window's bearing surface because the sector will be able to rotate, rather than slide, in its seat in the mounting.

11.3.3.2 STRUCTURAL PERFORMANCE. Since so few of these sector designs have been built, it is very difficult to make any postulates with a reasonable assurance of validity. It appears, however, that there is no significant difference in the structural behavior between a spherical sector with a spherical bearing surface and one with a conical bearing surface, if (1) the included angle of the conical surface is the same as the included angle of an imaginary frustum whose D_o and D_i coincide with the edges of the spherical bearing surface, (2) t/R_i is the same, and (3) D_i is the same.

Cracks under long-term and cyclic pressure loading originate on the spherical bearing surface. Their appearance, location, and method of propagation appear to be the same as for sectors with conical surfaces (figure 11.100). There is a total lack of data, however, on their static and cyclic fatigue lives. Although it is believed that it is the same as for sectors with conical bearing surfaces, until such data become available the designer must experimentally validate the design before the window is placed in manned service.

Mounting and sealing of these sectors is a process similar to the one used for spherical sectors with conical bearing surfaces. Because these windows displace radially like sectors with conical bearing surfaces, adequate overhang must be provided on the seat to provide

adequate support to the displacing window (figure 11.101). Since there is a total absence of data on the magnitude and rate of window displacement, no postulate can be made with any certainty as to whether the displacements are larger or smaller than those of equivalent sectors with conical bearing surfaces. Thus, the only guideline available to the designer is to assume that the displacements will be the same as those for sectors with conical bearing surfaces.

11.3.4 Spherical Sector with Toroidal Bearing Surface

Design of spherical sectors with toroidal bearing surfaces is in many aspects similar to that for spherical sectors with spherical bearing surfaces (figure 11.102). This design has been used only on hemispheres mated to mounting flanges with the same radial compliance as the hemisphere (figure 11.103). If it were used on hemispheres mounted in rigid flanges, severe bending moments would be introduced into the hemisphere around its equator because the toroidal seat in the rigid flange would prevent the window's equator from displacing radially.

The advantage claimed for the toroidal bearing surface resting on a radially compliant mounting is an infinite cyclic fatigue life for the bearing surface. This claim is based on photoelastic studies of the toroidal bearing surface. These studies have shown that there is a significant decrease in the magnitude of tensile and principal shear stresses inside the edge of the window when the shape of the bearing surface is changed from plane to toroidal with a radius equal to 2t (figures 11.104 through 11.108).

This type of design was experimentally evaluated and applied to the glass hemispherical bow window on the two-man submersible DEEPVIEW (figure 11.109). The glass hemisphere (44.5 inch (113 centimeters) outside diameter by 42 inch (107 centimeters) inside diameter) mounted in a compliant titanium mounting flange successfully withstood repeated pressurizations during a laboratory test program to 4000 feet (1219 meters) without cracks appearing on the toroidal bearing surfaces (figures 11.110 and 11.111). The same design philosophy could be used with an acrylic hemisphere mounted in a compliant glass-fiber-reinforced epoxy mounting ring.

No particular advantage is seen for application of toroidal bearing surfaces to spherical sectors with included angle less than 180 degrees (3.14 radians), as it is more expensive to generate accurately a toroidal surface than a spherical surface. The only reason that toroidal surfaces have been applied to hemispheres is that it is physically impossible to generate spherical bearing surfaces on a large hemisphere and the seat of the mounting flange.

If toroidal surfaces were to be utilized on a spherical sector with an included angle less than 180 degrees (3.14 radians), the mounting and sealing arrangement would be similar to that of a sector with spherical bearing surfaces (figure 11.112).

The structural performance of spherical sectors with toroidal bearing surfaces may be the same as, or differ substantially from, that of spherical sectors with conical bearing surfaces, depending on the included angle, magnitude of the radii of bearing surfaces, and location of the centers of these radii with respect to the mean radius of the sector. Because the interrelationship between these variables is not known, the use of spherical sectors with

toroidal bearing surfaces is not recommended (with the exception of hemispheres on radially compliant mountings), unless an extensive experimental evaluation precedes operational utilization.

11.4 CONCLUSION

Although of recent origin, spherical sector windows have found wide application in submersibles, diving bells, habitats, and hyperbaric chambers for several reasons. For any given thickness, a spherical sector window resists static, dynamic, or impact loading more effectively than does a plane window with conical or plane bearing surfaces. In addition, a spherical sector can be modified at the edge to satisfy special performance or mounting requirements. However, the most important source of its popularity is its ability to provide panoramic vision to weight-limited manned and unmanned submersible systems. The current limit in the size of spherical sectors lies not in any structural or fabrication limitation but in the limited imagination of users who ultimately pay for any pressure-resistant structure that incorporates spherical windows. Where now 40-inch-diameter (102 centimeters) spherical sector windows in submersibles are considered large, a 120 inch diameter (305 centimeters) will be considered large in a decade.

11.5 REFERENCES

11.1   Naval Civil Engineering Laboratory, Technical Report R631, "Windows for External or Internal Hydrostatic Pressure Vessels; Part III — Critical Pressure of Acrylic Spherical Shell Windows Under Short Term Pressure Application," by J. D. Stachiw, June 1969.

11.2   Naval Undersea Center, Technical Publication 393, "Glass or Ceramic Spherical Shell Window Assembly for 20,000-psi Operational Pressure," by J. D. Stachiw, May 1974.

11.3   Zoelly, R., *Ueber Ein Knickungs Problem an der Kugelschale*, Dissertation, Zurich, 1915.

11.4   David Taylor Model Basin, Technical Report 1741, "Tests of Stiffened and Un-stiffened Machined Spherical Shells Under External Hydrostatic Pressure," by M. A. Krenzke and J. T. Kiernan, August 1963.

11.5   Ordnance Research Laboratory, State College, Pennsylvania, Technical Memorandum 26.3420-41, "*Experimental Evaluation of Shell Designs Using Miniature Acrylic Resin Shells as Test Specimens*," by J. D. Stachiw, July 1960.

11.6   Naval Civil Engineering Laboratory, Technical Report R676, "Development of a Spherical Acrylic Plastic Pressure Hull for Hydrospace Application," by J. D. Stachiw, April 1970.

11.7   Naval Undersea Center, Technical Publication 410, "Development of a Precision Casting Process for Acrylic Plastic Spherical Shell Windows Applicable to High Pressure Service," by J. D. Stachiw, May 1974.

11.8   Naval Undersea Center, Technical Publication 453, "Spherical Shell Sector Windows of Acrylic Plastic with 12,000 Foot Operational Depth Capability for Submersible ALVIN," by J. D. Stachiw and R. Sletten, May 1975.

11.9   Civil Engineering Laboratory, Technical Report N-1468, "Flanged Acrylic Plastic Hemispherical Shells for Undersea Systems – Static and Cyclic Fatigue Life Under Hydrostatic Loading," by J. D. Stachiw and R. Sletten, January 1977.

11.10   Stachiw, J. D., "Spherical Pressure Hulls for Undersea Exploration," *Journal of Engineering for Industry*, Trans. ASME, May 1971.

11.11   Naval Undersea Center, Technical Publication 486, "Acrylic Plastic Spherical Shell Windows Under Point Impact Loading," by J. D. Stachiw and O. H. Burnside, July 1976.

11.12   Naval Undersea Center, Technical Publication 505, "Spherical Acrylic Plastic Hulls Under External Explosive Loading," by J. D. Stachiw, March 1976.

11.13   Naval Undersea Center, Technical Publication 383, "Cast Acrylic Plastic Dome for Undersea Applications," by J. D. Stachiw, January 1974.

11.14   Naval Undersea Center, Technical Publication 315, "Acrylic Plastic Hemispherical Shells for NUC Undersea Elevator," by J. D. Stachiw, September 1972.

11.15   Naval Undersea Center, Technical Publication 508, "Spherical Sector Windows with Restrained Edges for Undersea Applications," by J. D. Stachiw, December 1975.

11.16   Naval Undersea Center, Technical Publication 355, "Flanged Acrylic Plastic Hemispherical Shells for Undersea Systems," by J. D. Stachiw and J. R. Maison, September 1973.

11.17   Naval Undersea Center, Technical Publication 493, "Improved Fabrication Process for Plastic Submersible Hulls," by J. D. Stachiw, December 1975.

11.18   Lones, J., and Stachiw, J. D., "Deep Submergence Windows for Optical Systems," *Proceedings*, Underwater Photo-Optical Instrumentation Applications Seminar, Society of Photo-Optical Instrumentation Engineers, 1971.

11.19   Horn, G. M., "Right Spherical Segment Glass Shell to Metal Joint," United States Patent 3,757,725, September 1973.

11.20   Horn, G. M., "Method of Fabricating Right Spherical Segment Glass Shell to Metal Joint," United States Patent 3,839,109, October 1974.

Figure 11.1. Typical spherical shell sector with conical bearing surface, mounting flange, and matching conical seat; developed for undersea vehicles by Dr. Stachiw.
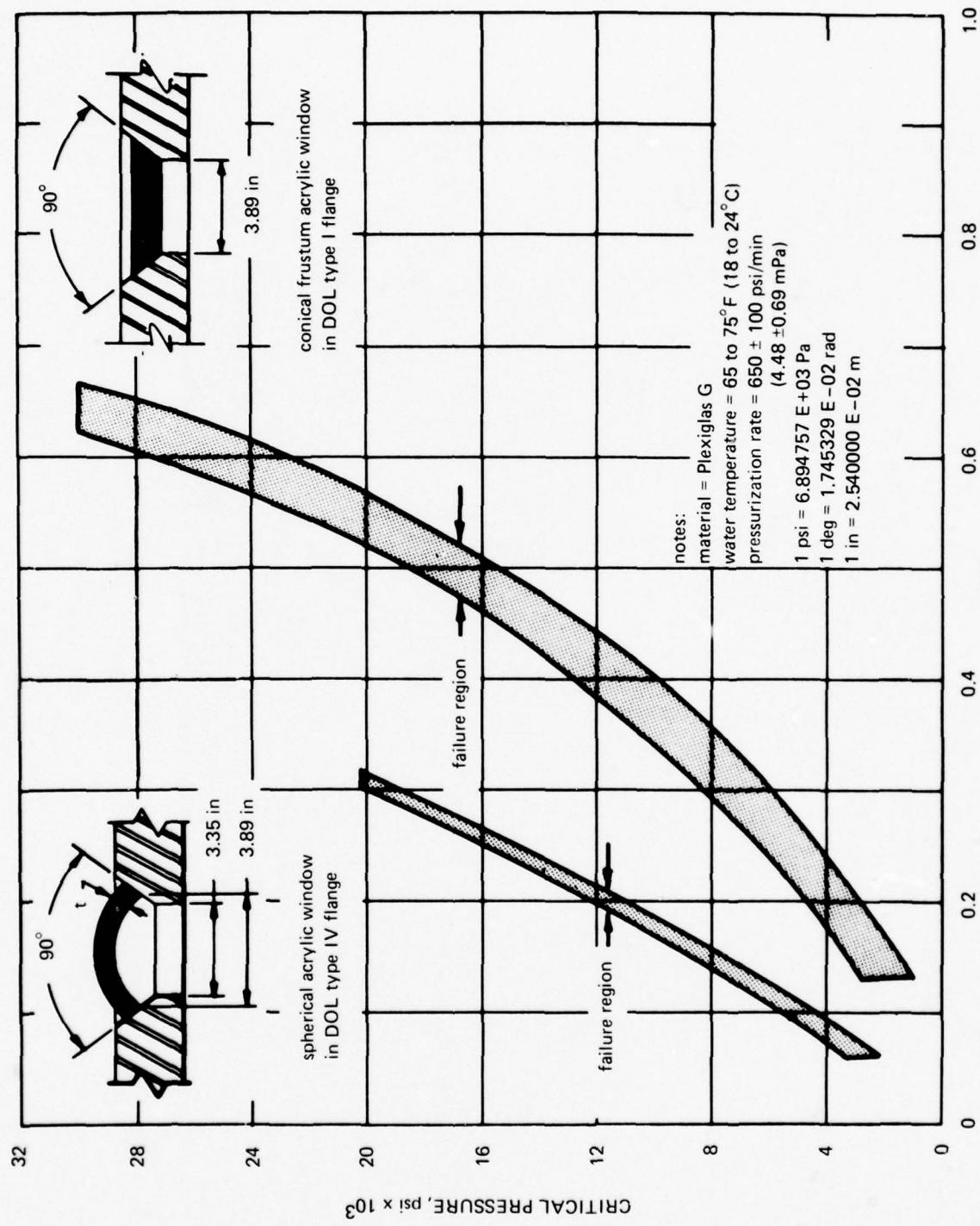
Figure 11.2. Comparison of short-term critical pressures for spherical sectors and conical frustums with the same t/D_i, D_i, and included angle.

PRESSURE, psi x 10³

28

24

20

16

12

8

4

0

0   0.2   0.4   0.6   0.8   1.0

AXIAL DISPLACEMENT, in

notes:
material = Plexiglas G
water temperature = 65 to 75°F (18 to 24°C)
pressurization rate = 650 ± 100 psi/min (4.48 ± 0.69 mPa)
1 psi = 6.894757 E+03 Pa
1 deg = 1.745329 E−02 rad
1 in = 2.540000 E−02 m

spherical acrylic window
in DOL type IV flange

90°

t

3.350 in
3.89 in

t/Dᵢ = 0.25

conical frustum acrylic window
in DOL type I flange

90°

3.89 in

t/Dᵢ = 0.25
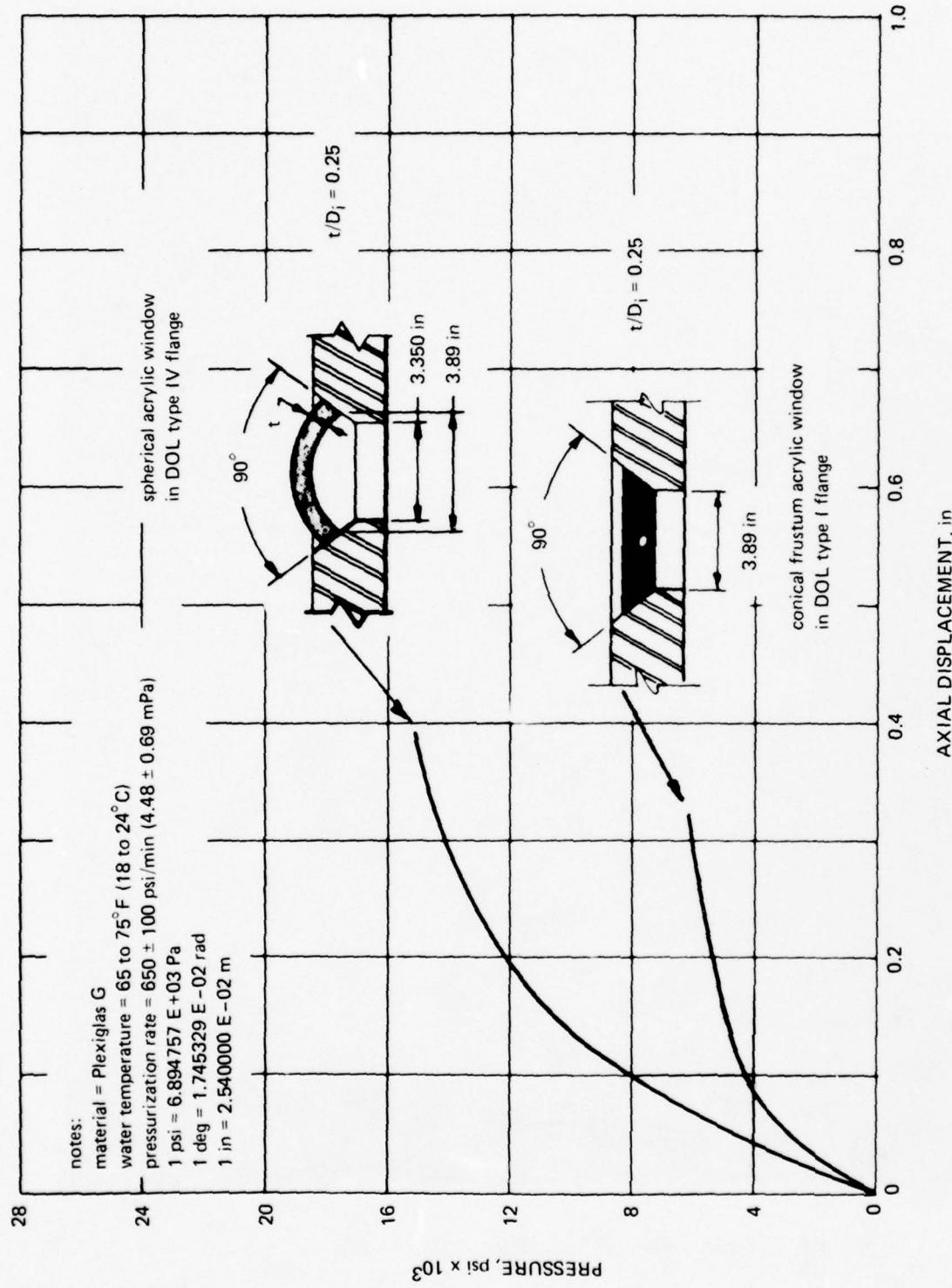
Figure 11.3. Comparison of axial displacements for spherical sectors and conical frustums with the same t/Dᵢ, Dᵢ, and included angle under short-term pressure loading.
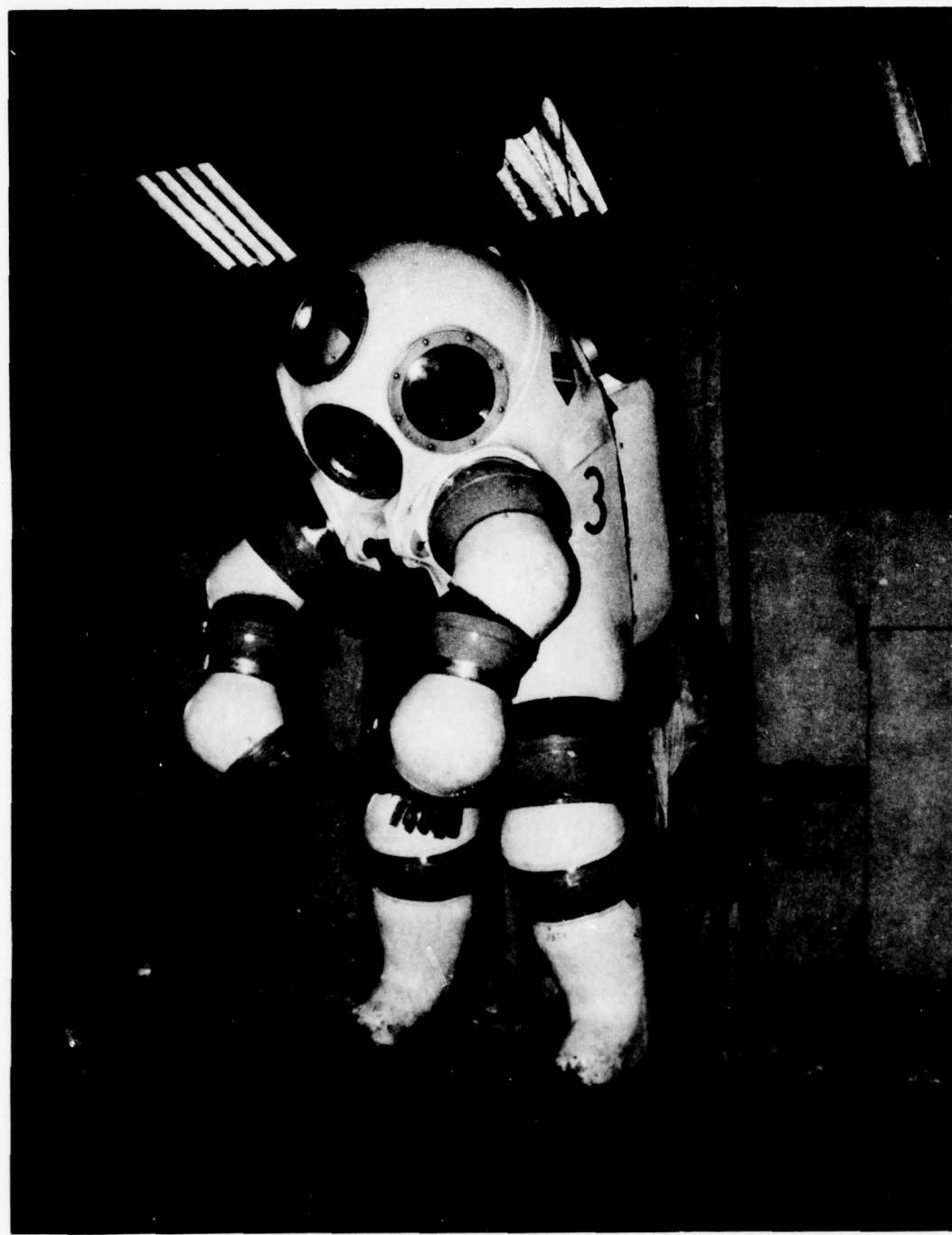
Figure 11.4. Typical application for small spherical sector windows: JIM, the 1-atmosphere articulated hard suit for divers. (Photograph courtesy of Can Dive.)
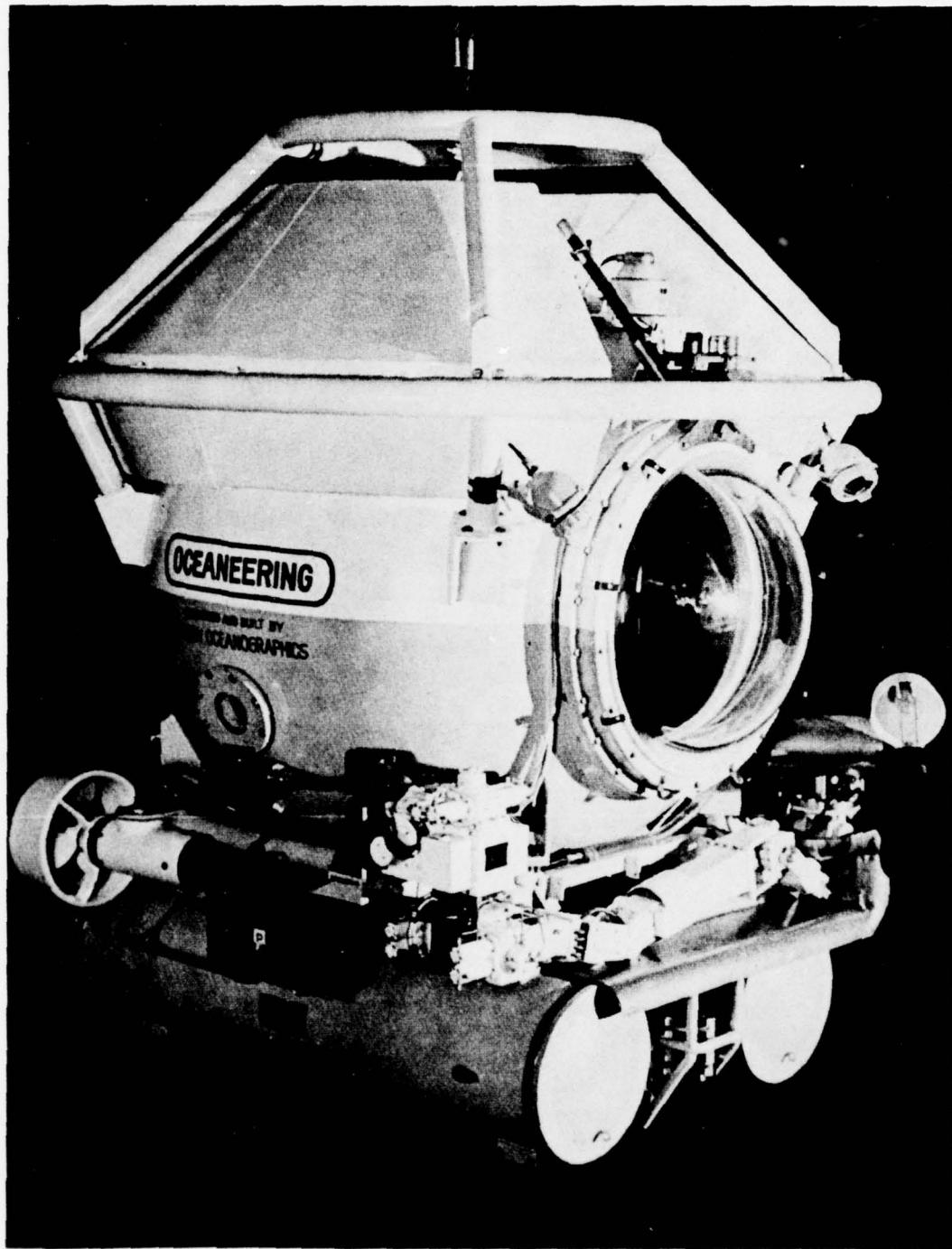
Figure 11.5. Typical application for large spherical sector windows: the 3000-foot (914 meters) Observation Maneuvering Bell, designed and fabricated by Perry Oceanographics for Oceaneering International. (Photograph courtesy of Perry Oceanographics.)

Figure 11.6. Typical optical quality found in spherical sector windows: bow window for Perry's PC-8B submersible. (Photograph courtesy of Swedlow, Inc.)
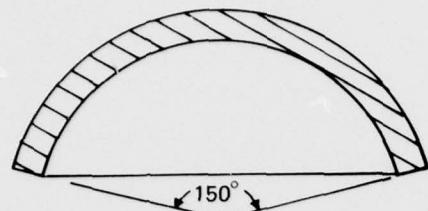
150° spherical sector
conical bearing surface

edge detail

15°
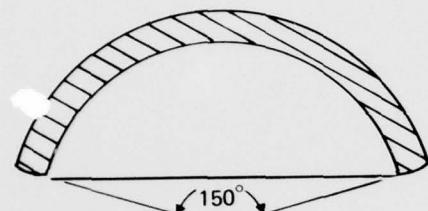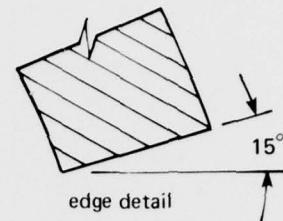
150° spherical sector
spherical bearing surface

edge detail

15°
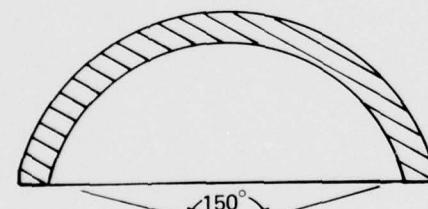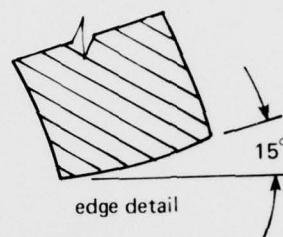
150° spherical sector
square bearing surface

edge detail

15°
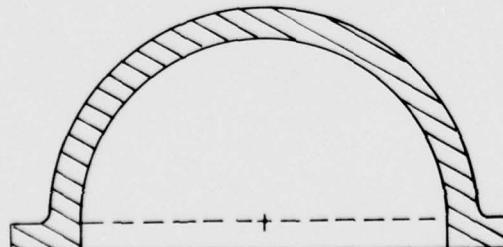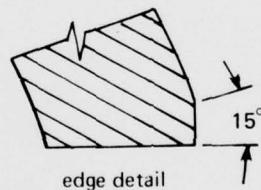
180° spherical sector
flanged bearing surface

edge detail

1 deg = 1.745
329 E-02
rad

Figure 11.7. Spherical shell sectors with different bearing surface designs.

11-35

① WINDOW
② BEARING GASKET-PLASTIC
③ WINDOW SEAL-NEOPRENE
④ CLAMP SCREWS-NYLON

⑤ CLAMP RING-NYLON
⑥ MOUNTING RING-DELRIN
⑦ SEAT SEAL-NEOPRENE
⑧ SEAT-K500 MONEL

A-A
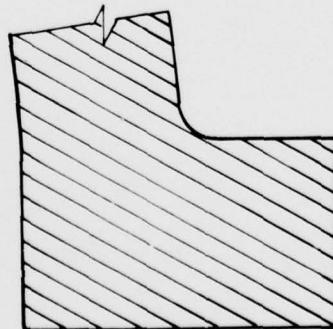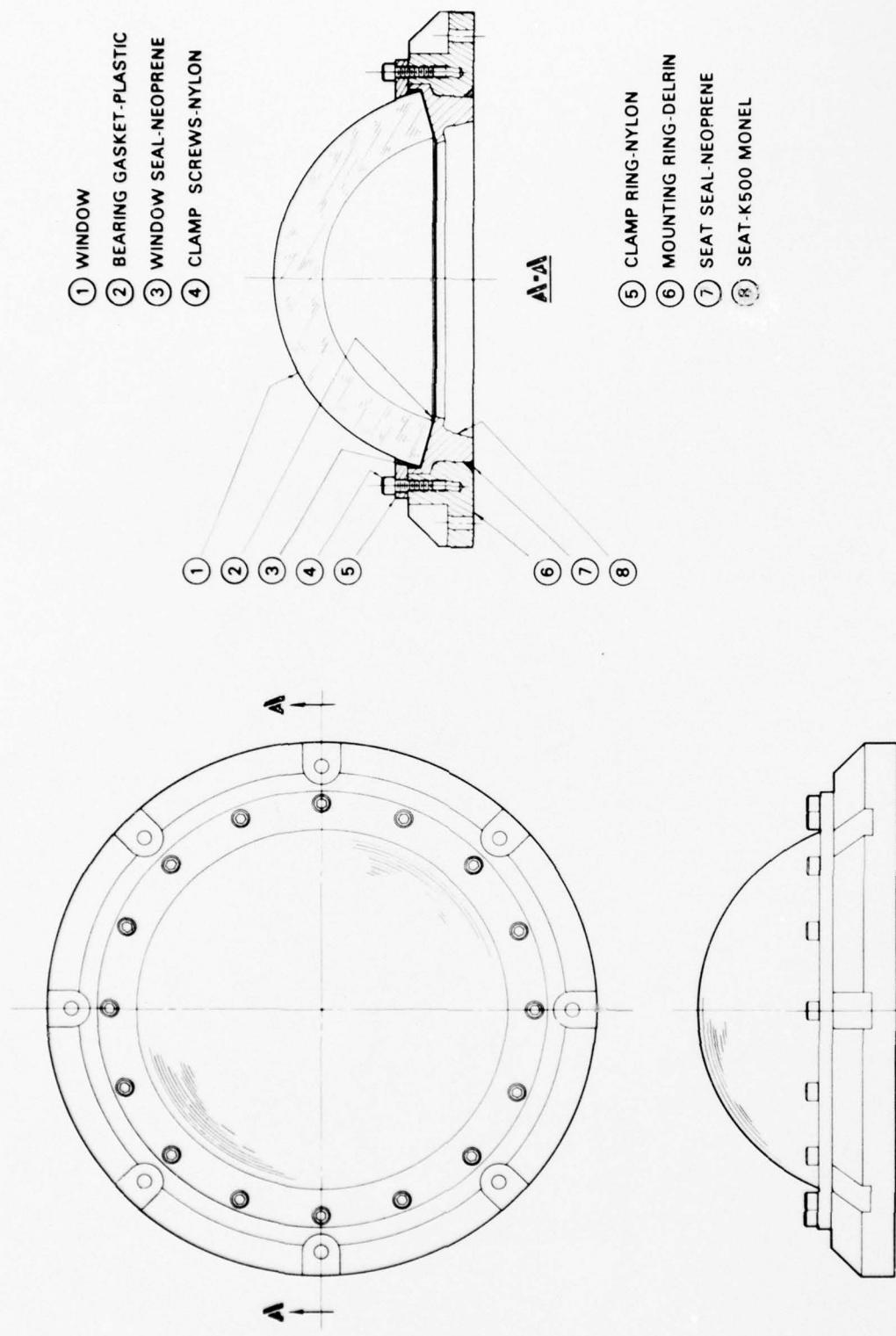
Figure 11.8. Experimentally proven spherical sector designs for 20,000-pound-per-square-inch (138 megapascals) service utilizing glass ceramic, glass, or sapphire windows.

window bearing surface

high-pressure face

low-pressure face

flange bearing surface

spherical sector bevel angle

D_i

D_f

R_o

R_i

α

β

t

note:
$\beta = 90$ deg (1.57 rad)
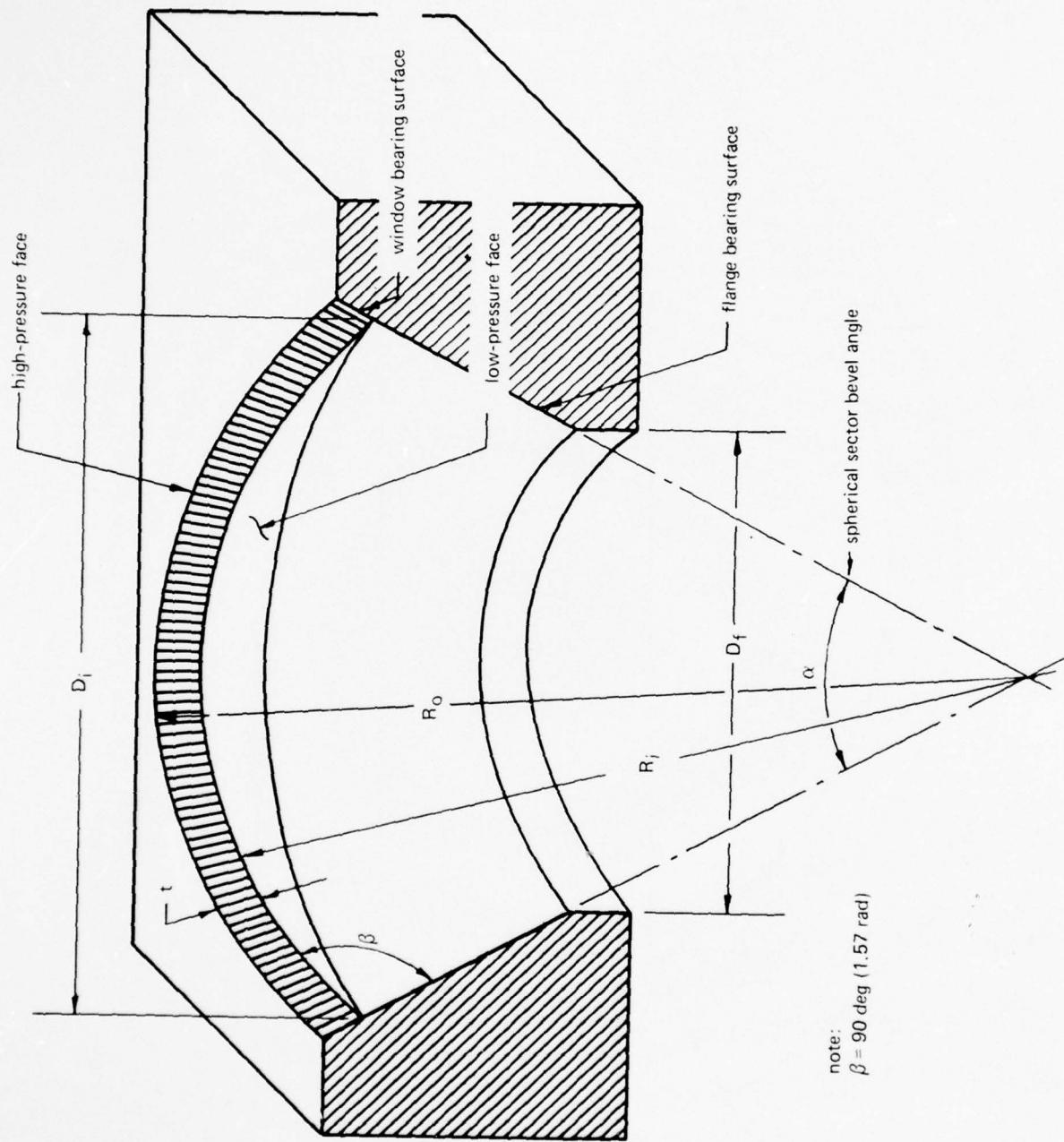
Figure 11.9. Definitions of terms for a spherical shell sector window with conical bearing surface.

polish

$\frac{4.005}{3.995}$ R

$\frac{3.455}{3.445}$ R

$\frac{6.932}{6.923}$ DIA

120° ± 5'

32

notes:
all dimensions in inches
material = acrylic plastic
spherical sector window = 120-deg (2.09 rad) configuration
1 in = 2.540000 E – 02 m
1 deg = 1.745329 E – 02 rad
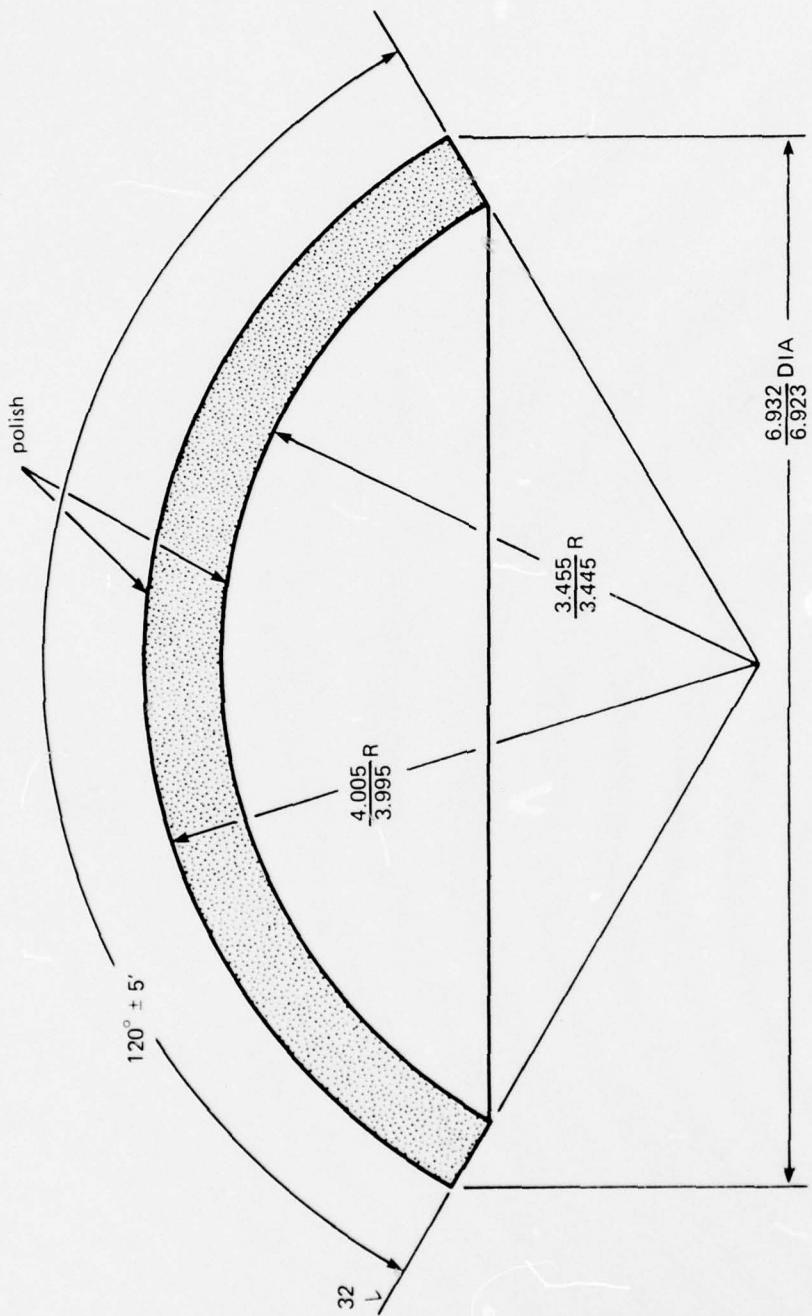
Figure 11.10. Typical model-scale spherical sector window assembly used in experimental test program. $t/D_i = 0.159$; $\alpha = 120$ degrees (2.09 radians); $D_i = 5.97$; $D_f = 5.460$; and $D_i/D_f = 1.093$.

Figure 11.10. Continued.
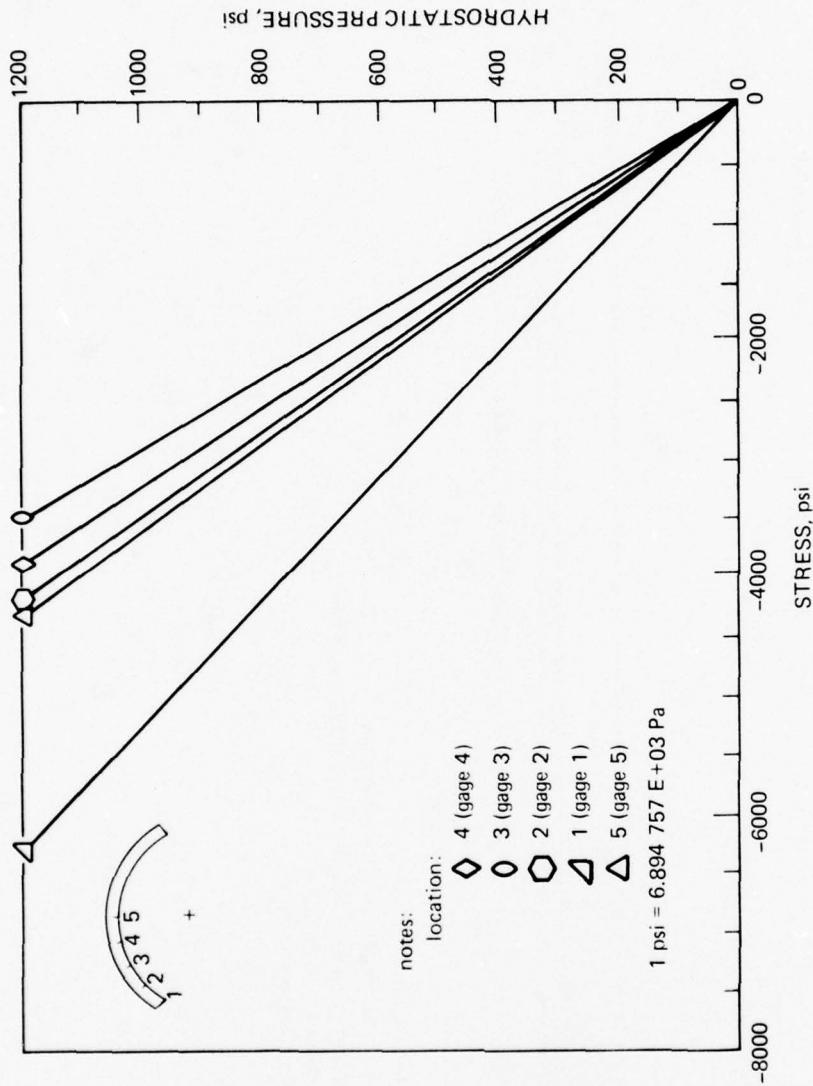
Part A. Distribution of meridional stresses on the concave surface of the spherical sector shown in figure 11.10. Note that the highest stress is at the edge.

Figure 11.11. Distribution of meridional and hoop stresses on concave and convex surfaces of spherical section in figure 11.10.

1200
1000
800
600
400
200
0

HYDROSTATIC PRESSURE, psi

1 2 3 4 5

notes:
location:
⬦ 4-0 (gage 9)
⬯ 3-0 (gage 8)
⬡ 2-0 (gage 7)
◁ 1-0 (gage 6
△ 5-0 (gage 10)

1 psi = 6.894 757 E +03 Pa

-6000   -4000   -2000   0

STRESS, psi
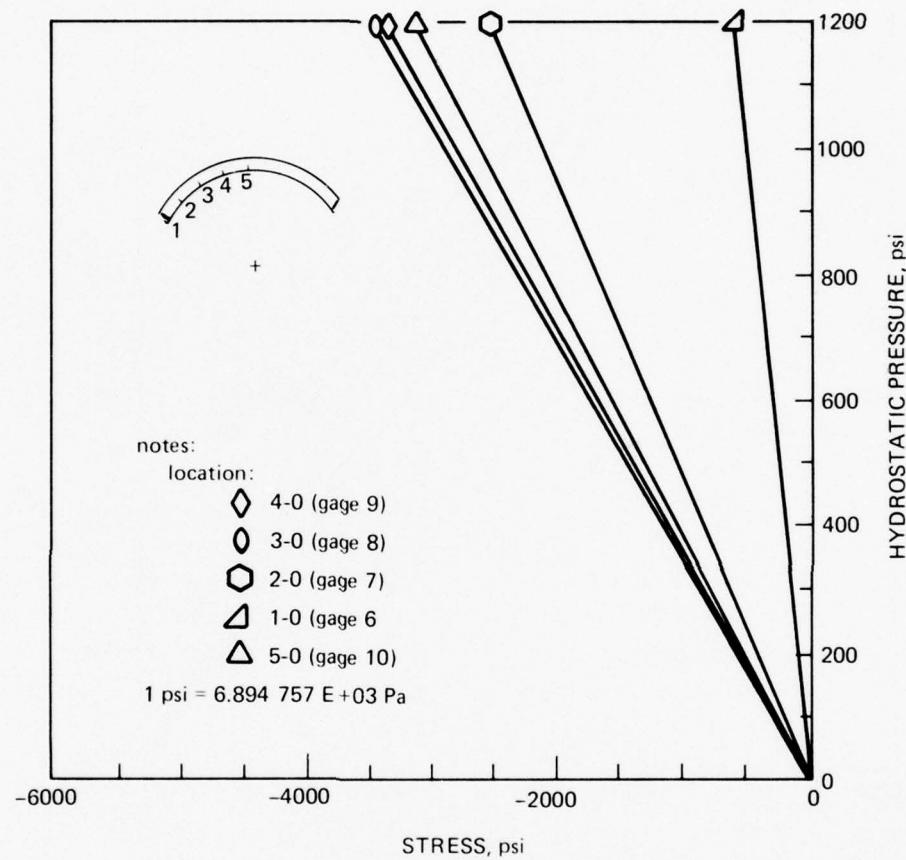
Part B. Distribution of meridional stresses on the convex surface of the spherical
sector shown in figure 11.10. Note that the highest stresses are near the apex
while the lowest one is at the edge of the window.

Figure 11.11. Continued.

11-41
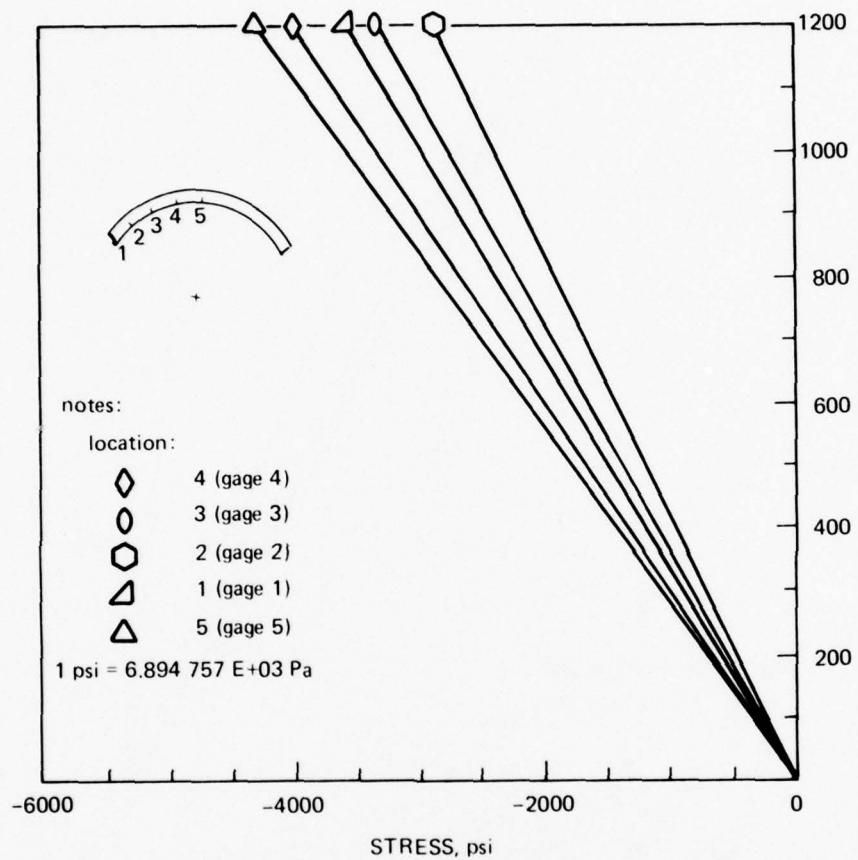
Part C. Distribution of hoop stresses on the concave surface of the spherical sector shown in figure 11.10. Note that the highest stress is at the apex of the window.

Figure 11.11. Continued.

11-42
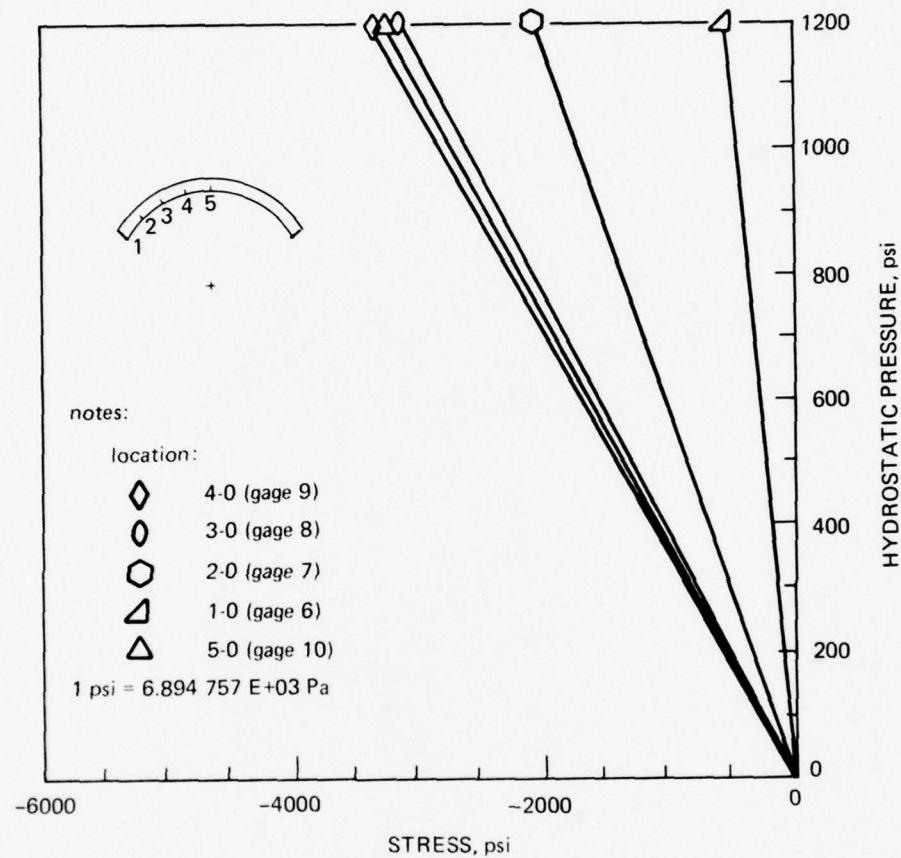
Part D. Distribution of hoop stresses on the convex surface of the spherical sector shown in figure 11.10. Note that the highest stress is at the apex and the lowest stress is at the edge of the window.

Figure 11.11. Continued.

11-43
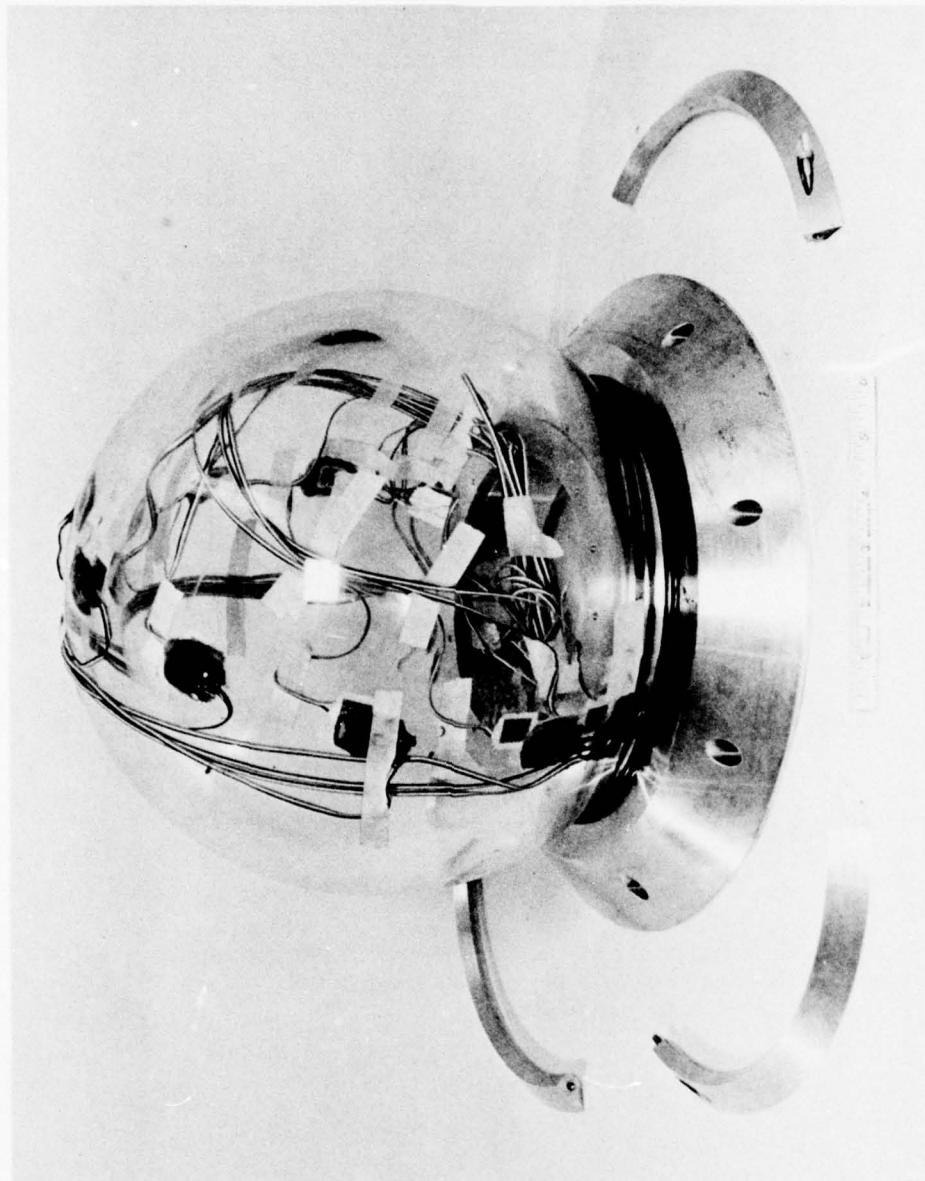
Figure 11.12. Spherical sector with 270-degree (4.7 radians) included angle and t/R_i ratio of 0.2 for operational depth of 4000 feet (1219 meters). The sector is instrumented with electric resistance straingages for measurement of strains.
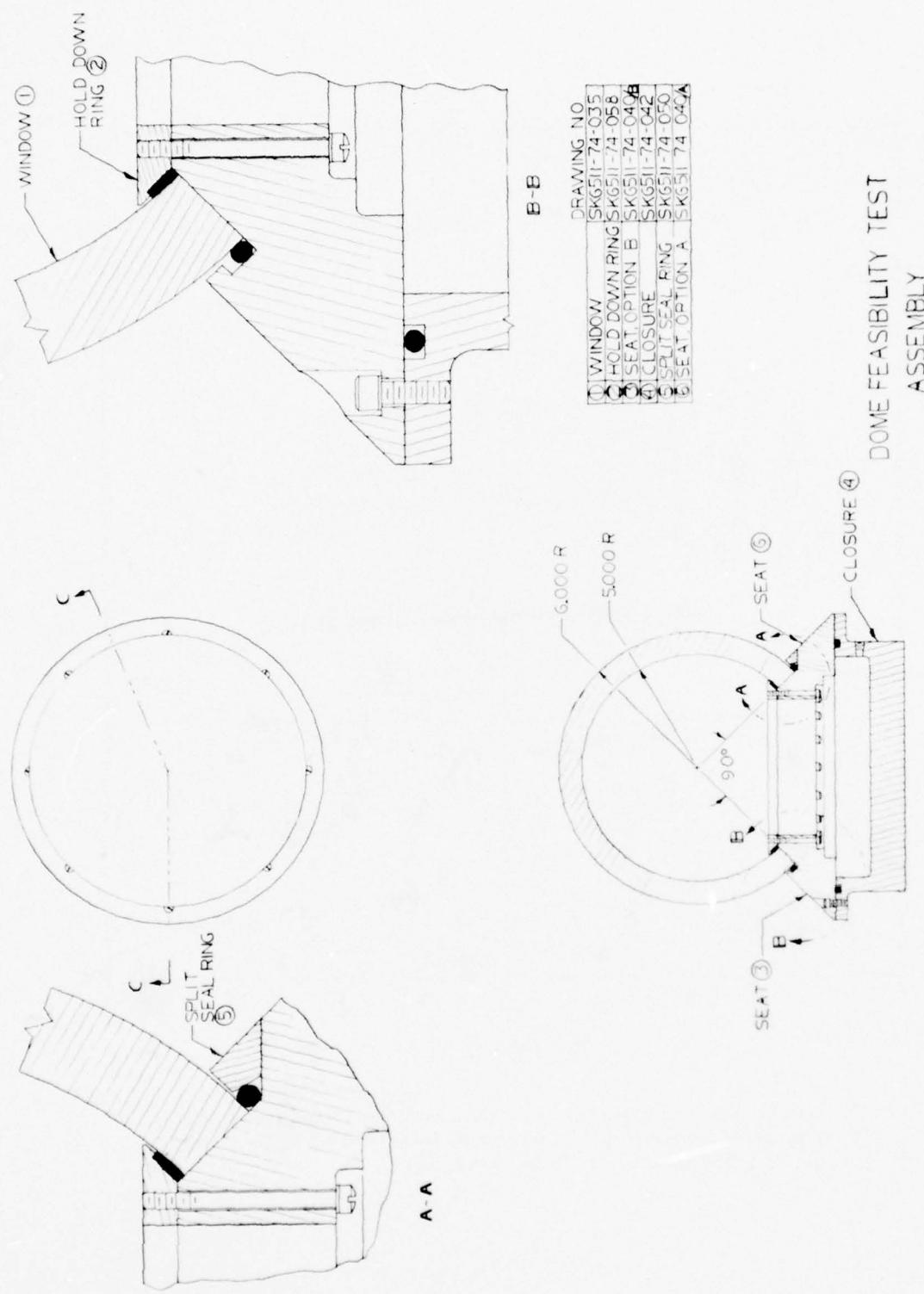
Figure 11.13. Mounting and sealing arrangement for the hyperhemisphere shown in figure 11.12.
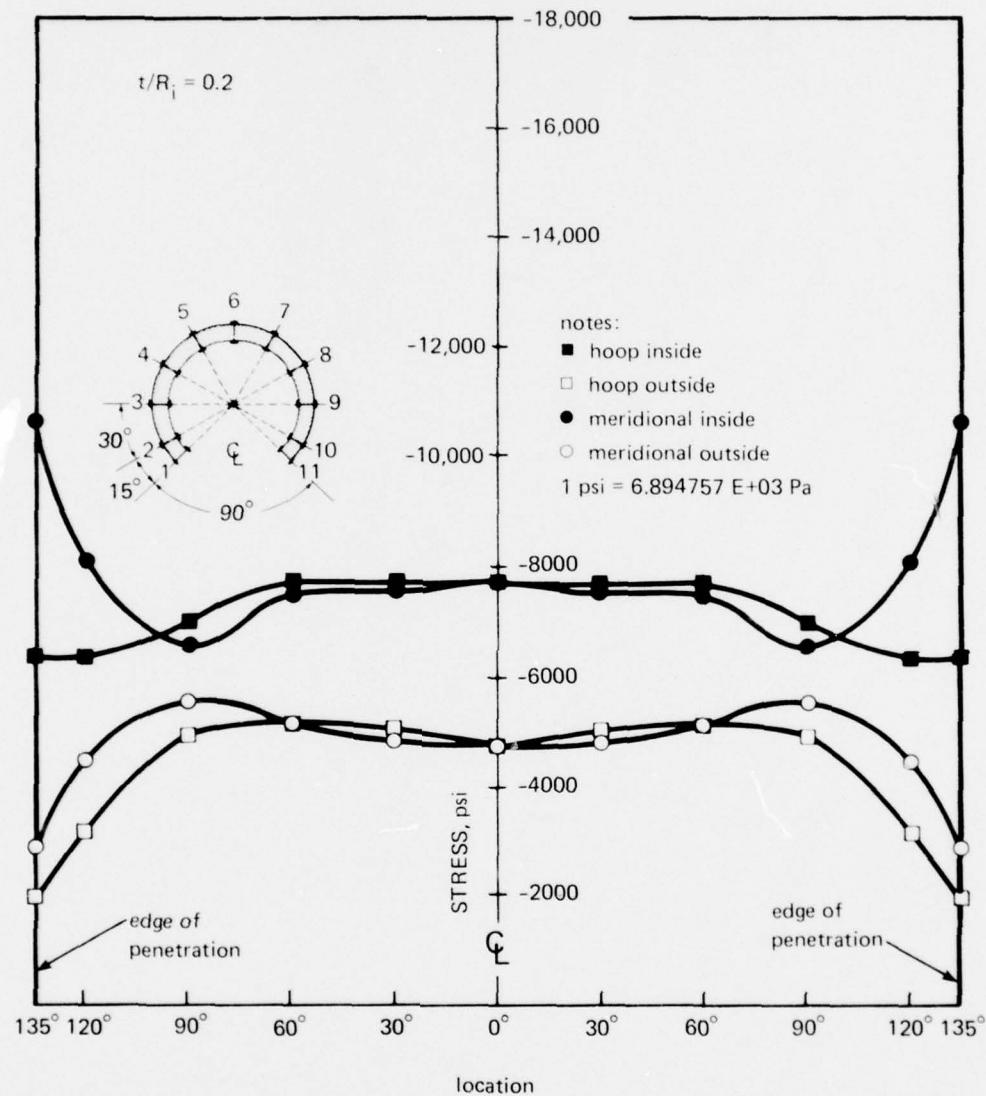
Figure 11.14. Distribution of stresses on the interior surface of the hyperhemisphere shown in figure 11.12 under short-term pressurization of 2000 pounds per square inch (13.7 megapascals) at ambient room temperature.

Lame's equation for hollow spheres

$\nu = 0.3$

$E = 450,000$ psi

$$\frac{\epsilon_t}{P} = \frac{\Delta R_i}{R_i \cdot P} = \frac{1-\nu}{E} \left\{ \frac{1.5}{1 - [1/(1+t/R_i)]^3} \right\}$$

notes:

▲ NCEL R-631

● ALVIN, measured $\Delta R_i/(R_i \cdot P)$

○ ALVIN, measured ϵ_{Ti}/P

□ NUC TP 355, measured ϵ_{Ti}/P

■ CEL (type 1 and 6 domes), measured ϵ_{Ti}/P

★ NUC TP 410, measured $\dfrac{\Delta R_i}{R_i P}$

1 psi = 6.894757 E+03 Pa

ALVIN
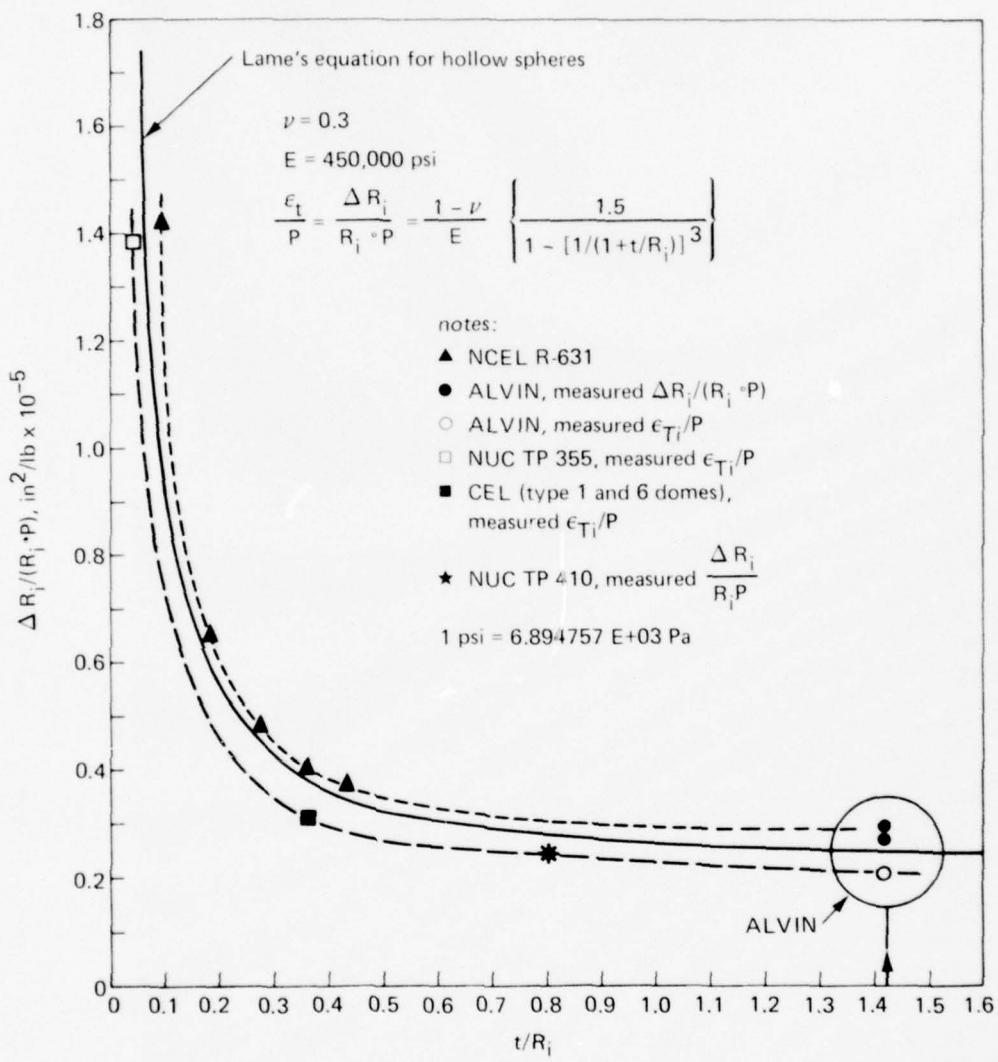
Figure 11.15. Comparison of measured strains and displacements with values calculated on the basis of Lamé's equation for spherical shells.

Part A. Top view.

Figure 11.16. Typical local plastic buckling failure of a spherical sector window with t/D_i equal to 0.182 and an included angle of 180 degrees (3.14 radians). Failure occurred at 15,500 pounds per square inch (107 megapascals) under short-term pressure loading in a 70°F (21°C) ambient temperature environment.
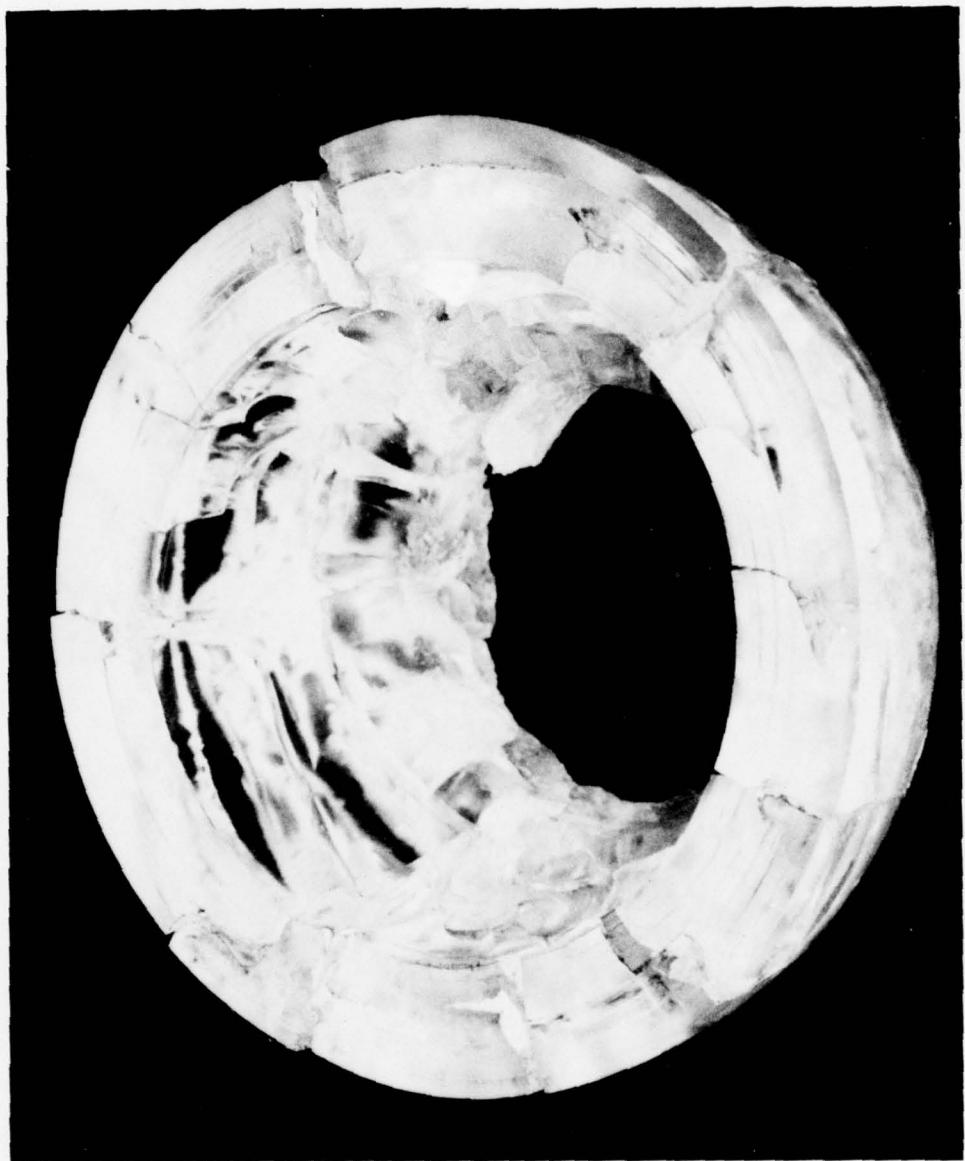
Part B. Bottom view.

Figure 11.16. Continued.

11-49
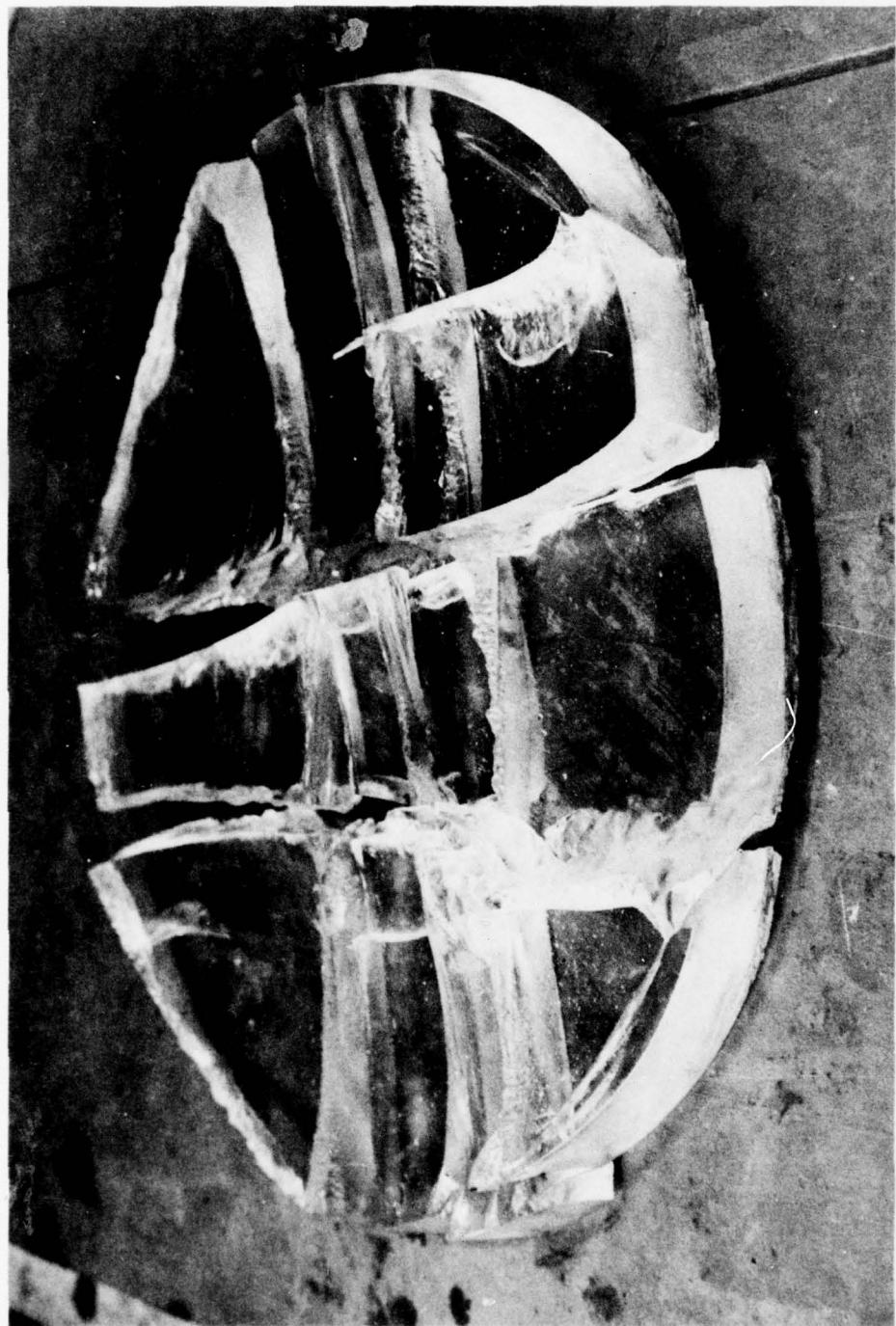
Figure 11.17. Typical general elastic buckling failure of a spherical sector window. $t/D_i = 0.069$; $R = 33$ inches (84 centimeters); $t = 2.5$ inches (6 centimeters); included angle = 72 degrees (1.25 radians); and temperature $70°F$ ($21°C$).

radius of curvature
increases

radius of curvature
decreases

radius of curvature
decreases

phase 1: radius of curvature increases locally

flat spot

tensile cracks

phase 2: cracks appear in areas of high tensile stress

plastically deformed
fragments

phase 3: catastrophic failure takes place
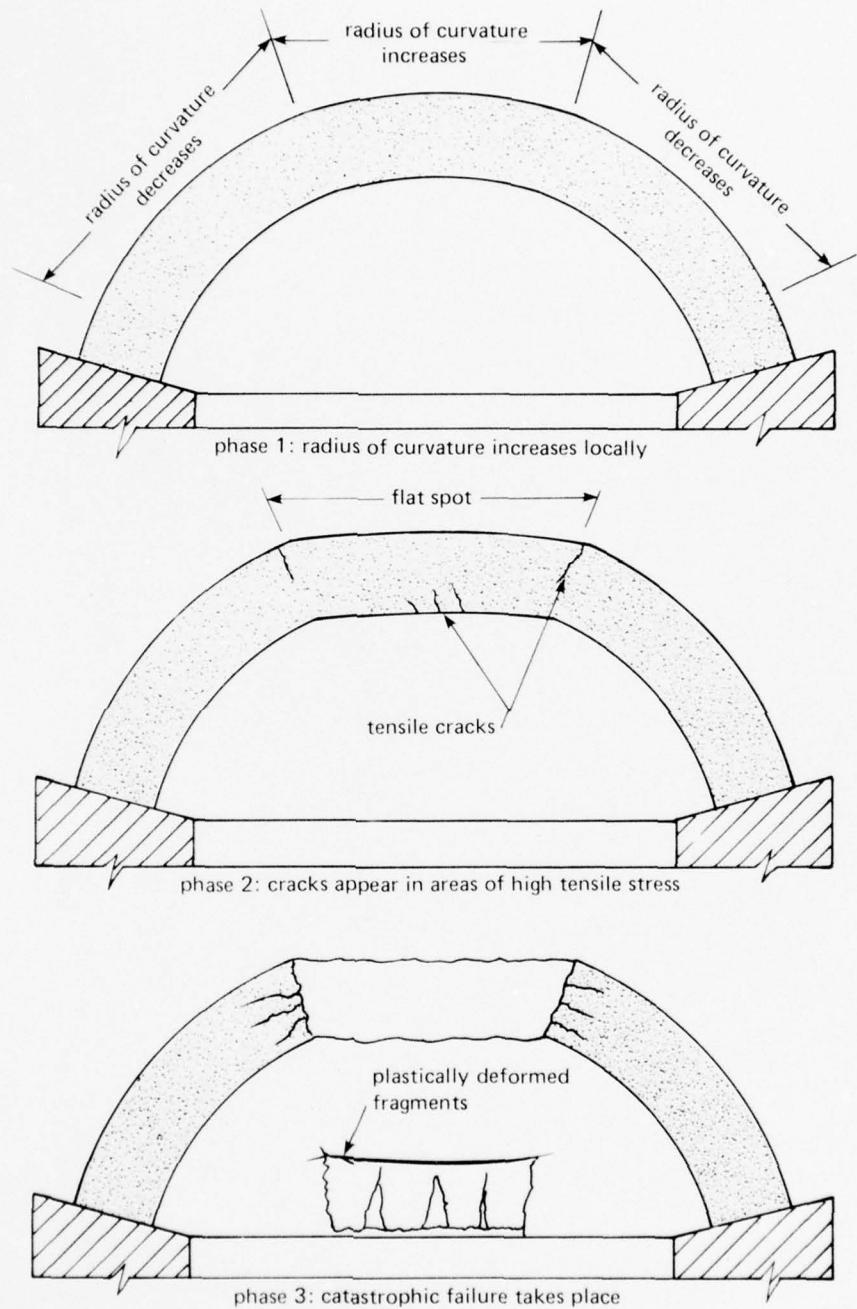
Figure 11.18. Deformation mechanism of a spherical sector
prior to failure by buckling.

11-51
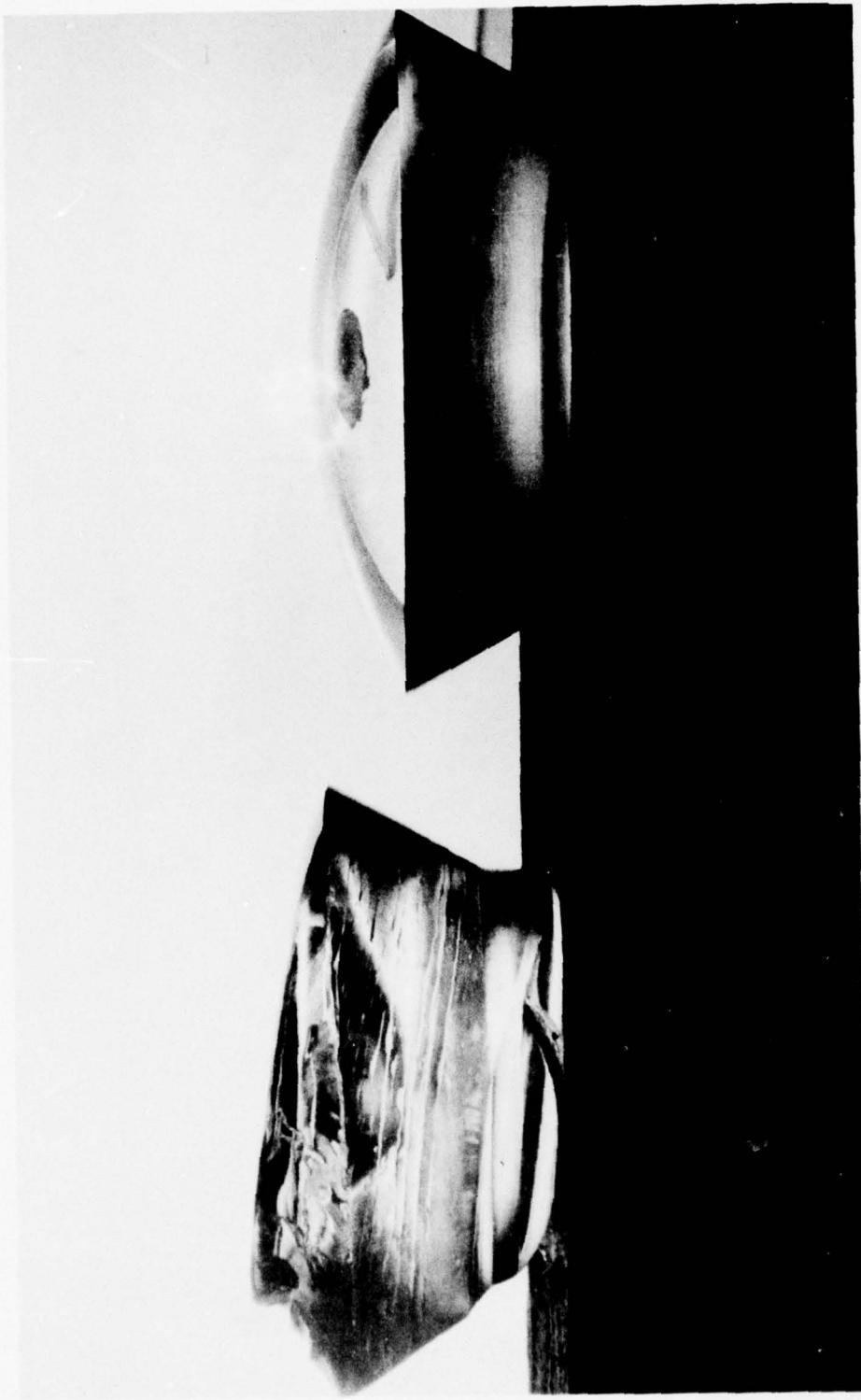
Figure 11.19. Typical plastic extrusion failure of a spherical sector window. $t/D_i = 0.364$; $D_i/D_f = 1.25$; and included angle = 60 degrees (1.04 radians). This photograph was taken at 21,300 pounds per square inch (147 megapascals) prior to catastrophic failure at 70°F (21°C). Note the original shape of the window.
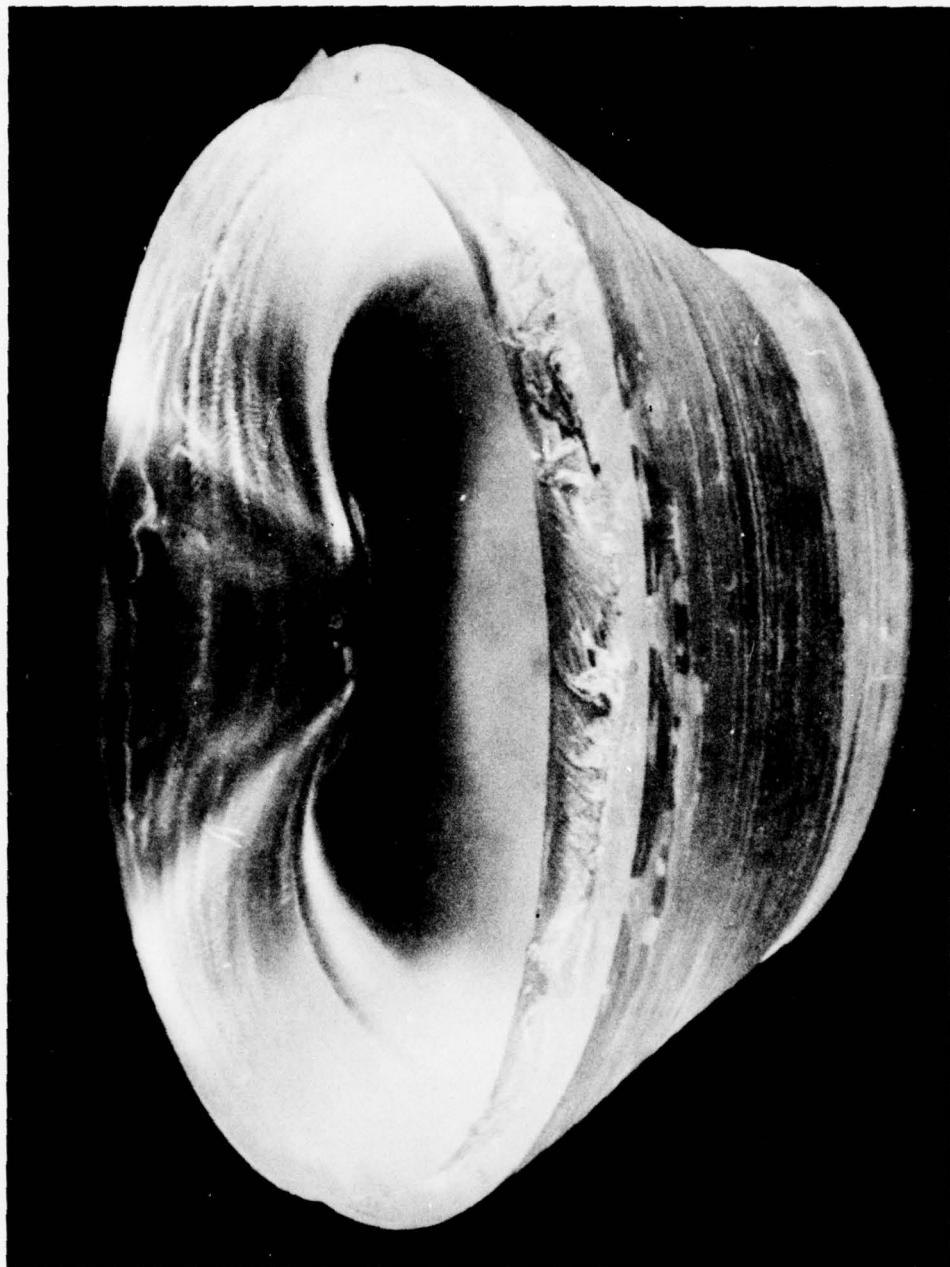
Figure 11.20. Typical deformation of the convex face on a spherical sector window caused by plastic extrusion at 30,000 pounds per square inch (207 megapascals); $t/D_i = 0.436$; $D_i/D_f = 1.61$; included angle = 30 degrees (0.52 radian); and temperature = 70°F (21°C). Note the reversal of curvature at the apex.
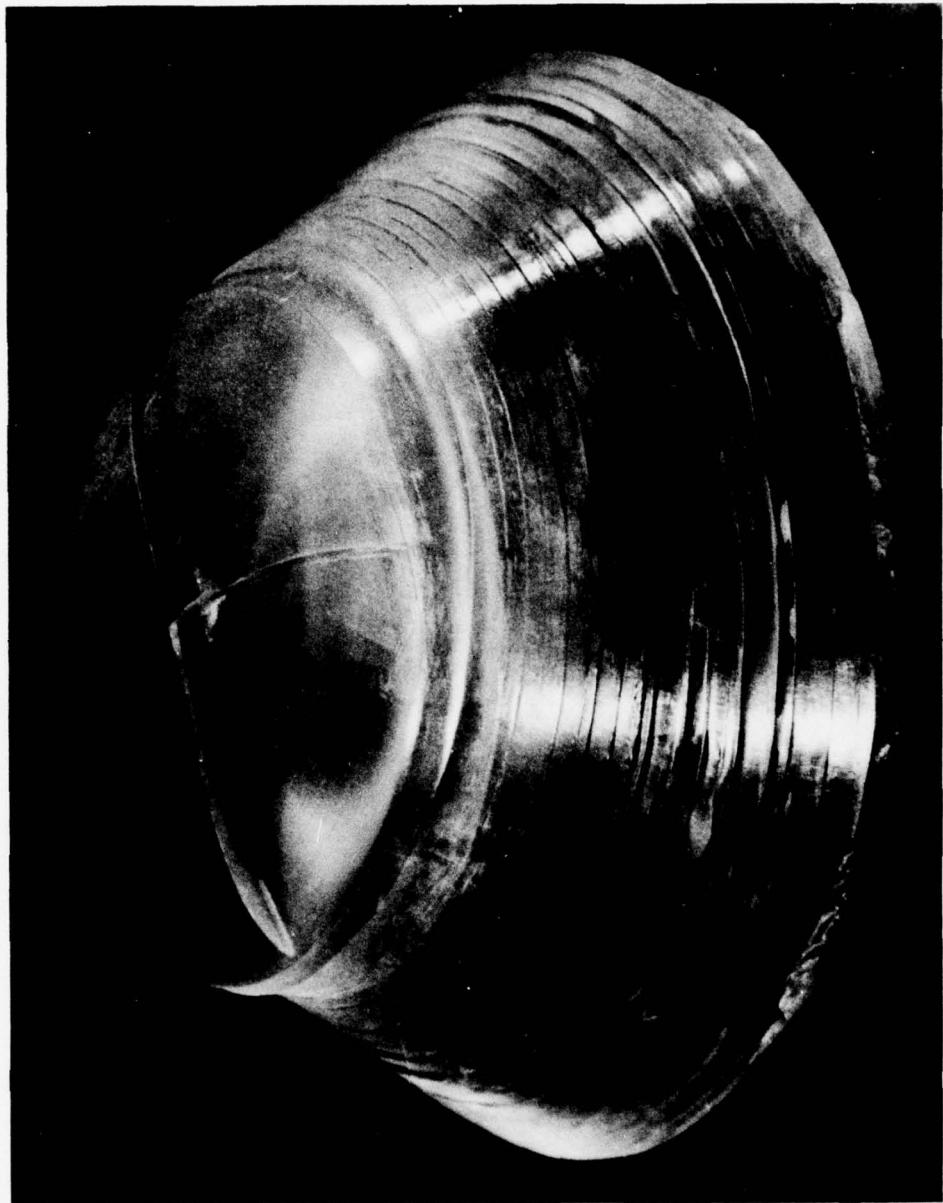
Figure 11.21. Typical deformation of the concave face of the window in figure 11.20 during plastic extrusion. Note the reversal of curvature with the formation of tensile cracks at the apex; also note the numerous shear cracks on the bearing surface.
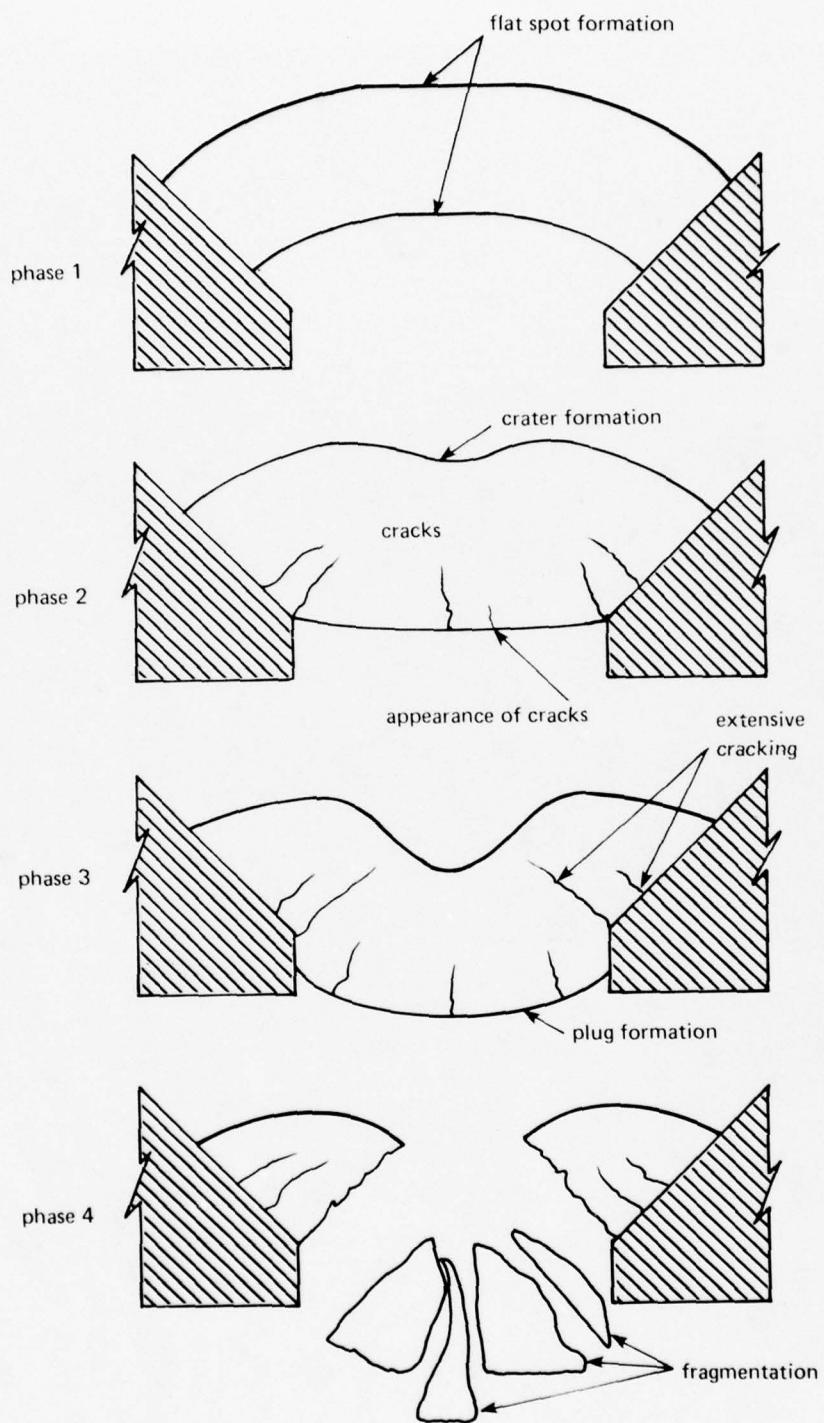
Figure 11.22. Deformation mechanism of a spherical sector prior to failure by plastic extrusion.
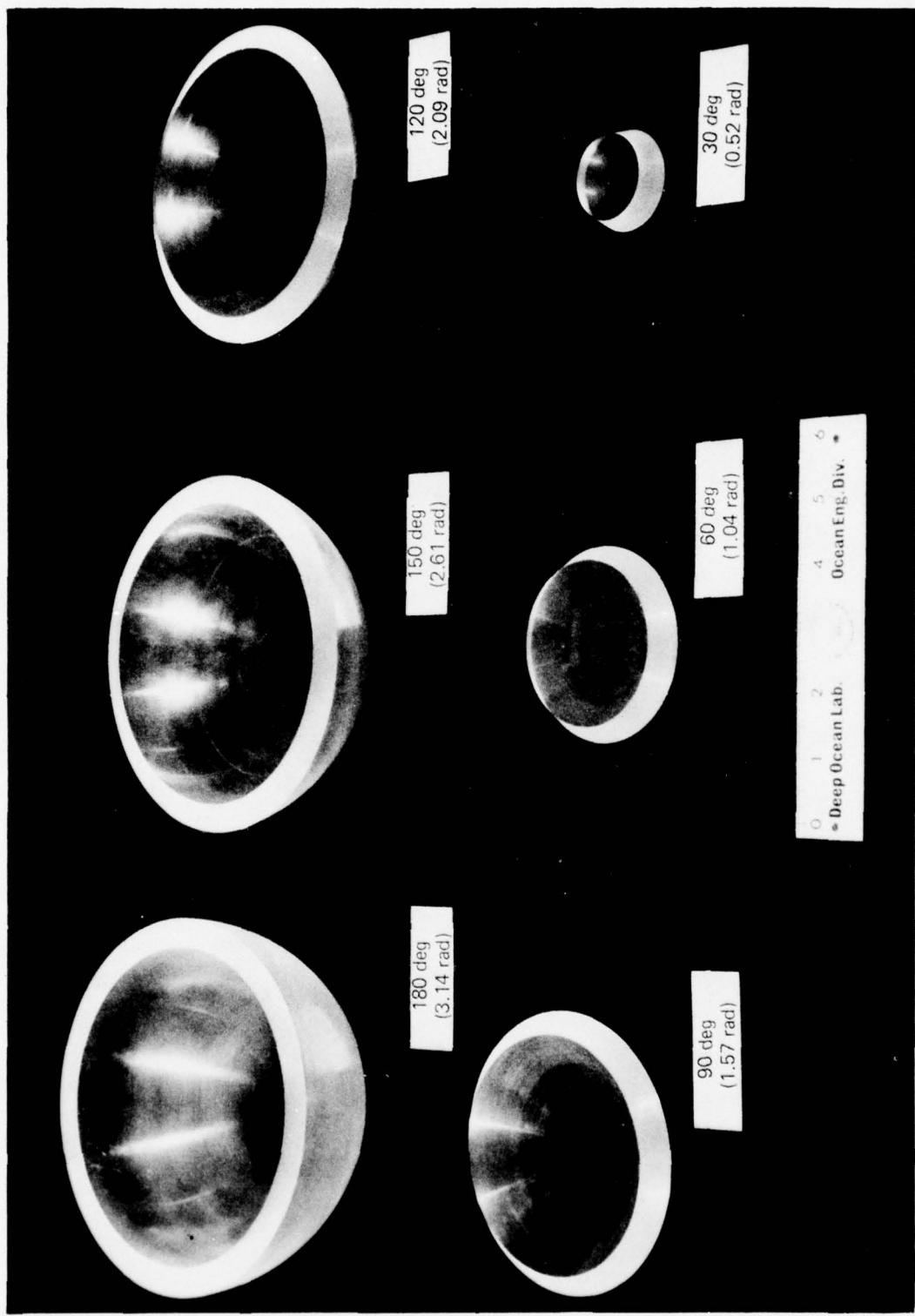
Figure 11.23. Typical acrylic plastic spherical sector test specimens used in experimental programs for determination of short-term critical pressures. R_i = 2.750 inches (6.98 centimeters) and t = 0.5 inch (1.27 centimeters).
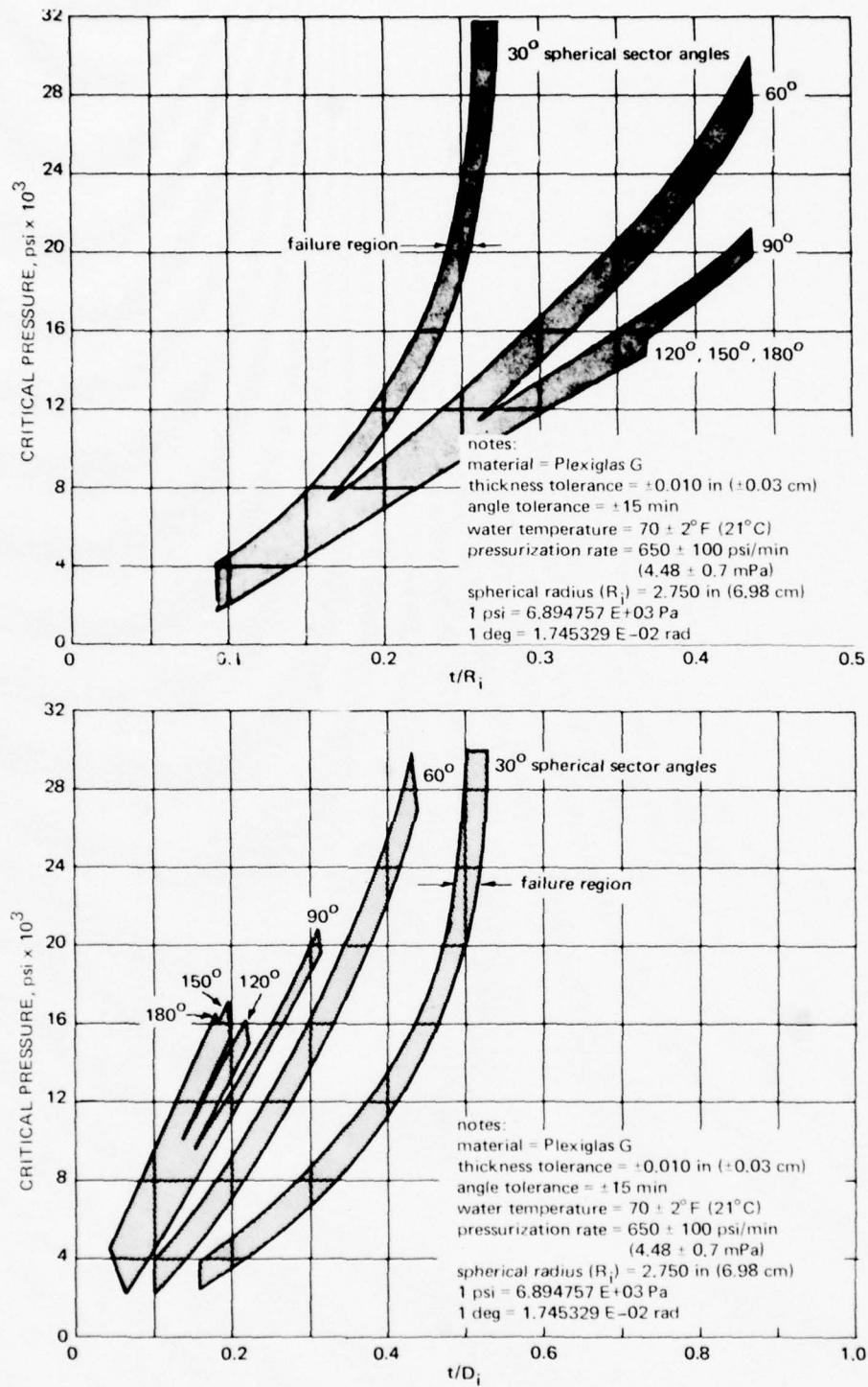
Figure 11.24. Experimentally established short-term critical pressures for acrylic plastic spherical sectors at 70°F (21°C) ambient temperature. The critical pressures of spherical sectors with included angles in excess of 180 degrees (3.14 radians) are the same as those for sectors with 180-degree (3.14 radians) included angles and identical t/R_i ratios.

11-57
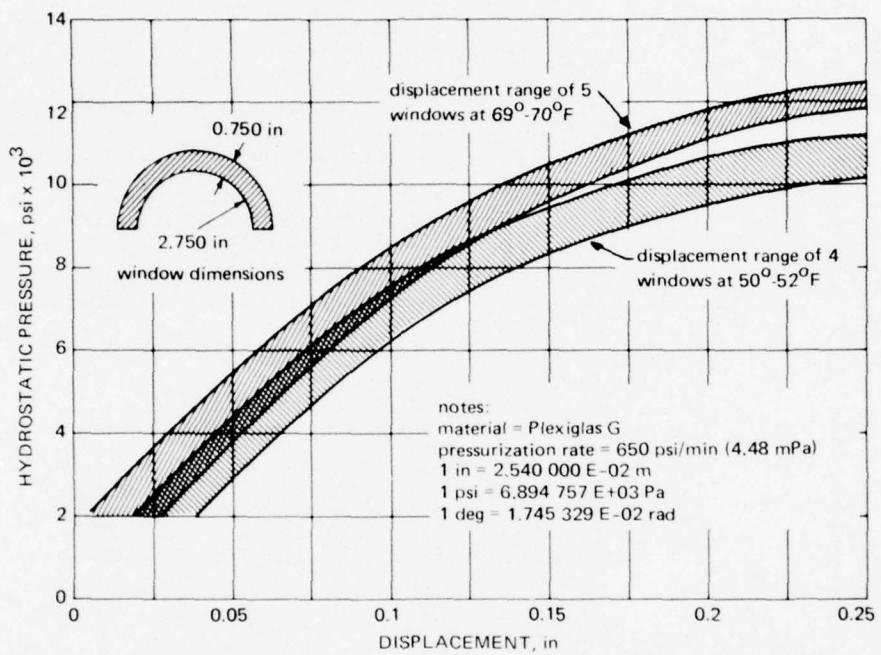
Figure 11.25. Effect of ambient test temperature on the magnitude of axial displacements of acrylic plastic spherical sectors measured at the apex under short-term pressure loading. $t/R_i \approx 0.273$ and included angle = 180 degrees (3.14 radians).
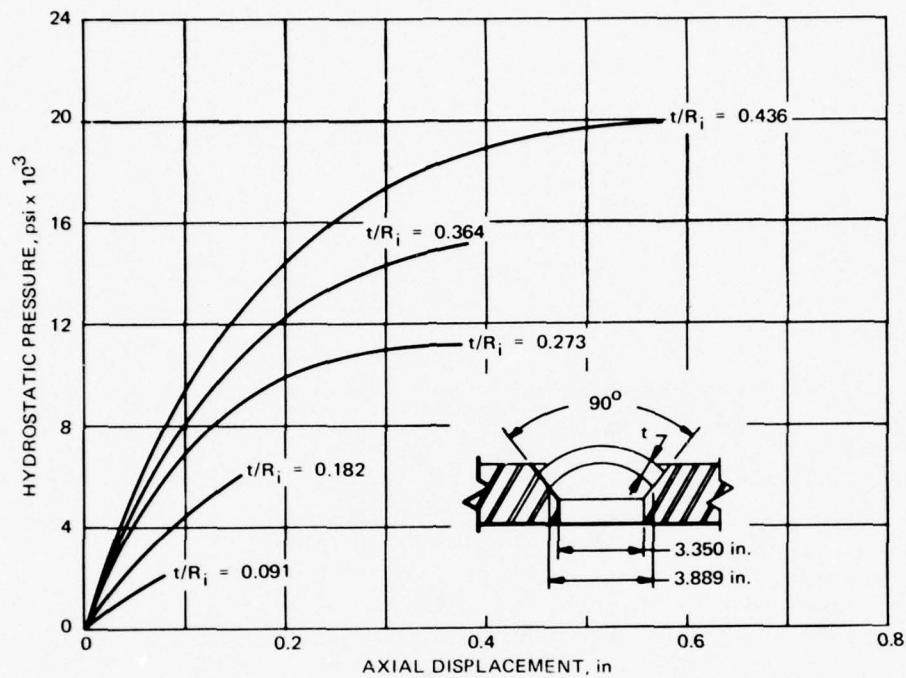
notes:
material = Plexiglas G
thickness tolerance = ±0.010 in (±0.03 cm)
angle tolerance = ±15 min
water temperature = 70 ± 2°F (21°C)
pressurization rate = 650 ± 100 psi/min
(4.48 ± 0.7 mPa)
spherical radius (R_i) = 2.750 in (6.98 cm)

1 psi = 6.894757 E+03 Pa
1 in = 2.540000 E−02 m
1 deg = 1.745329 E−02 rad

axial displacement of the center point on low-pressure face is measured along the vertical axis of the flange opening

each curve is the average value of five window specimens

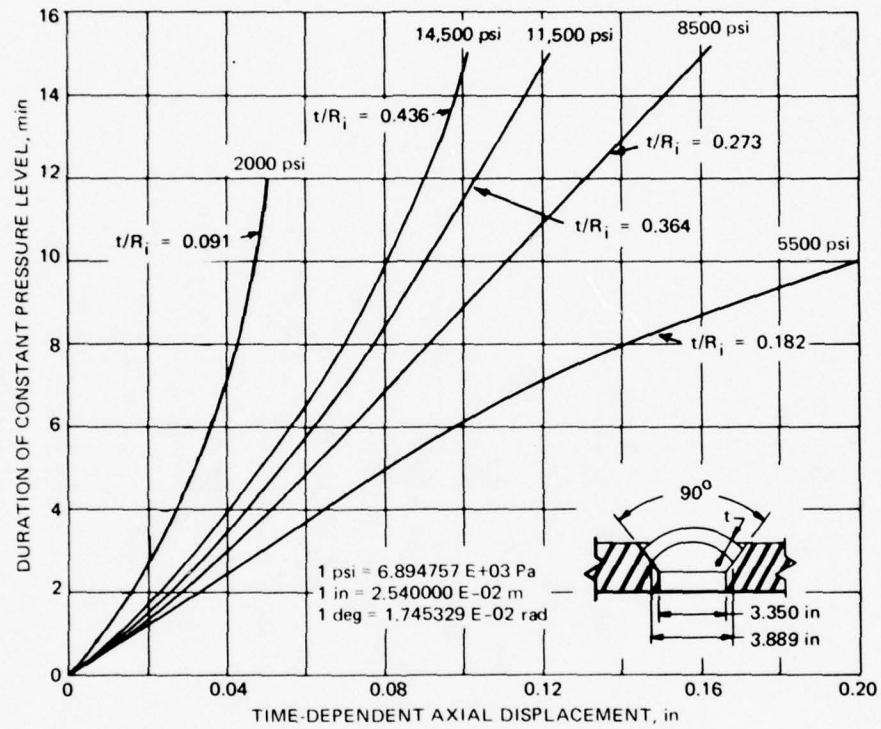Figure 11.26. Axial displacements of a 90-degree (1.57 radians) spherical sector measured at the apex with a mechanical dial indicator under short-term pressure loading at 70°F (21°C) ambient temperature.

Figure 11.27. Sliding displacements of 90-degree (1.57 radians) spherical sectors measured on the conical seat of the mounting flange under short-term pressure loading at 70°F (21°C) ambient temperature. Measurements were made with a mechanical dial indicator.
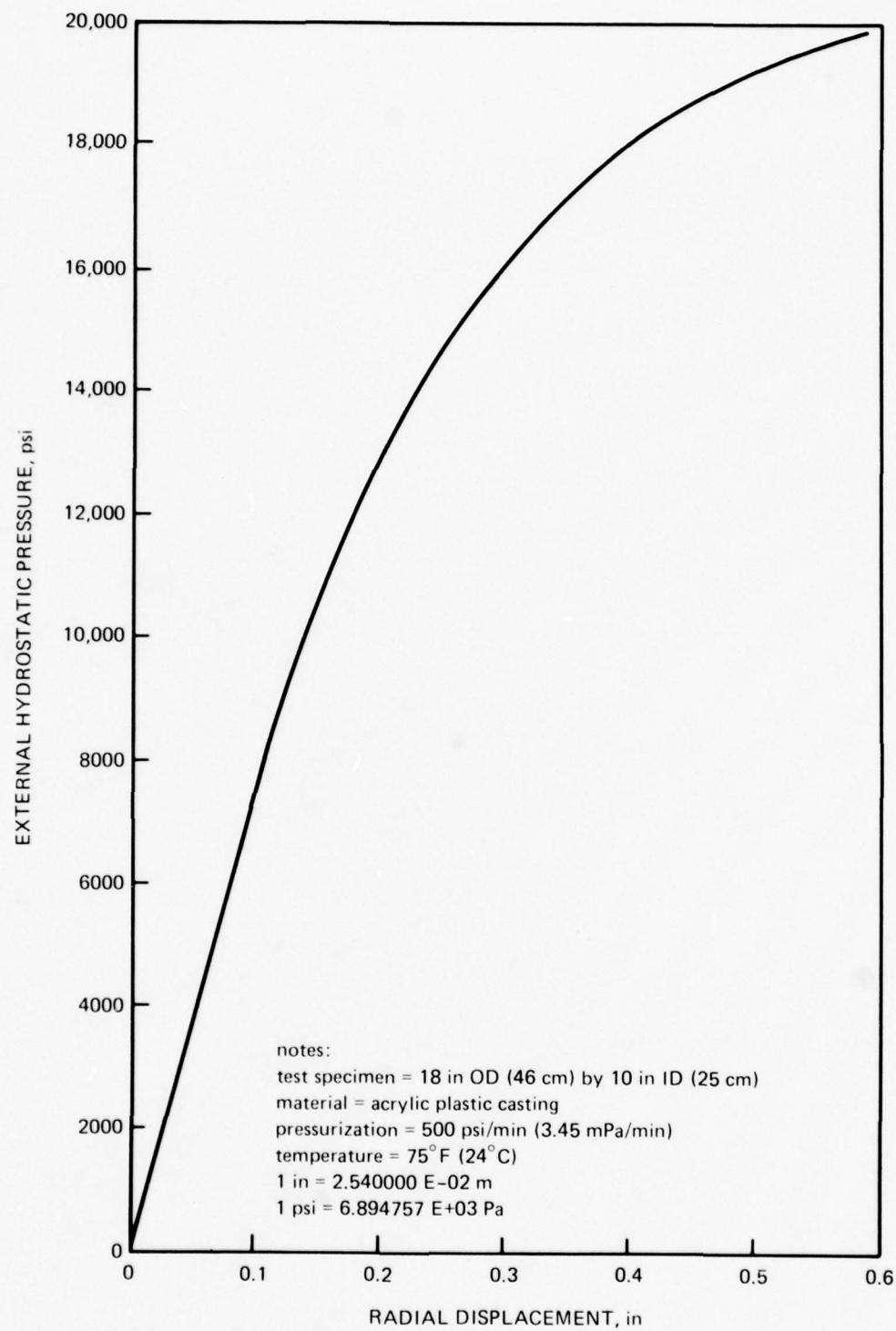
Figure 11.28. Radial displacement of very thick spherical sector under short-term pressure loading at 75°F (24°C) ambient temperature. Measurements made with displaced water technique.

11-61
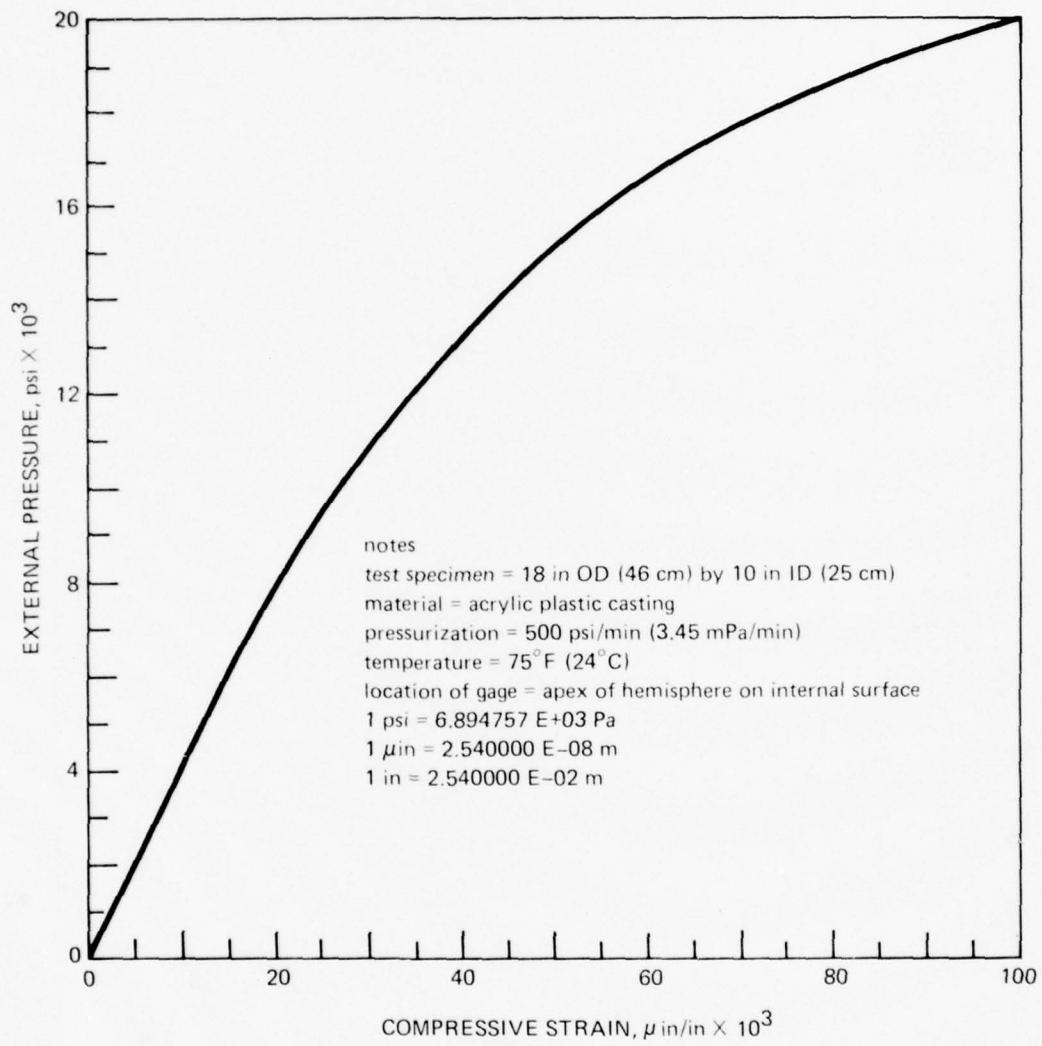
Figure 11.29. Deformation of a very thick spherical sector under short-term pressure loading at 75°F (24°C) ambient temperature. Measurements made with an electric resistance straingage.

Figure 11.30. Localized creep buckling of an acrylic plastic spherical sector with t/R_i equal to 0.161 and an included angle of 120 degrees (2.09 radians) under sustained long-term pressure loading. There are two fracture zones: one at the center and the other around the periphery of the flat spot. The former originated on the concave face, while the latter originated on the convex surface. Catastrophic failure occurred after 800 hours at 2500 pounds per square inch (17.2 megapascals) in a 70°F (21°C) ambient environment.

11-63
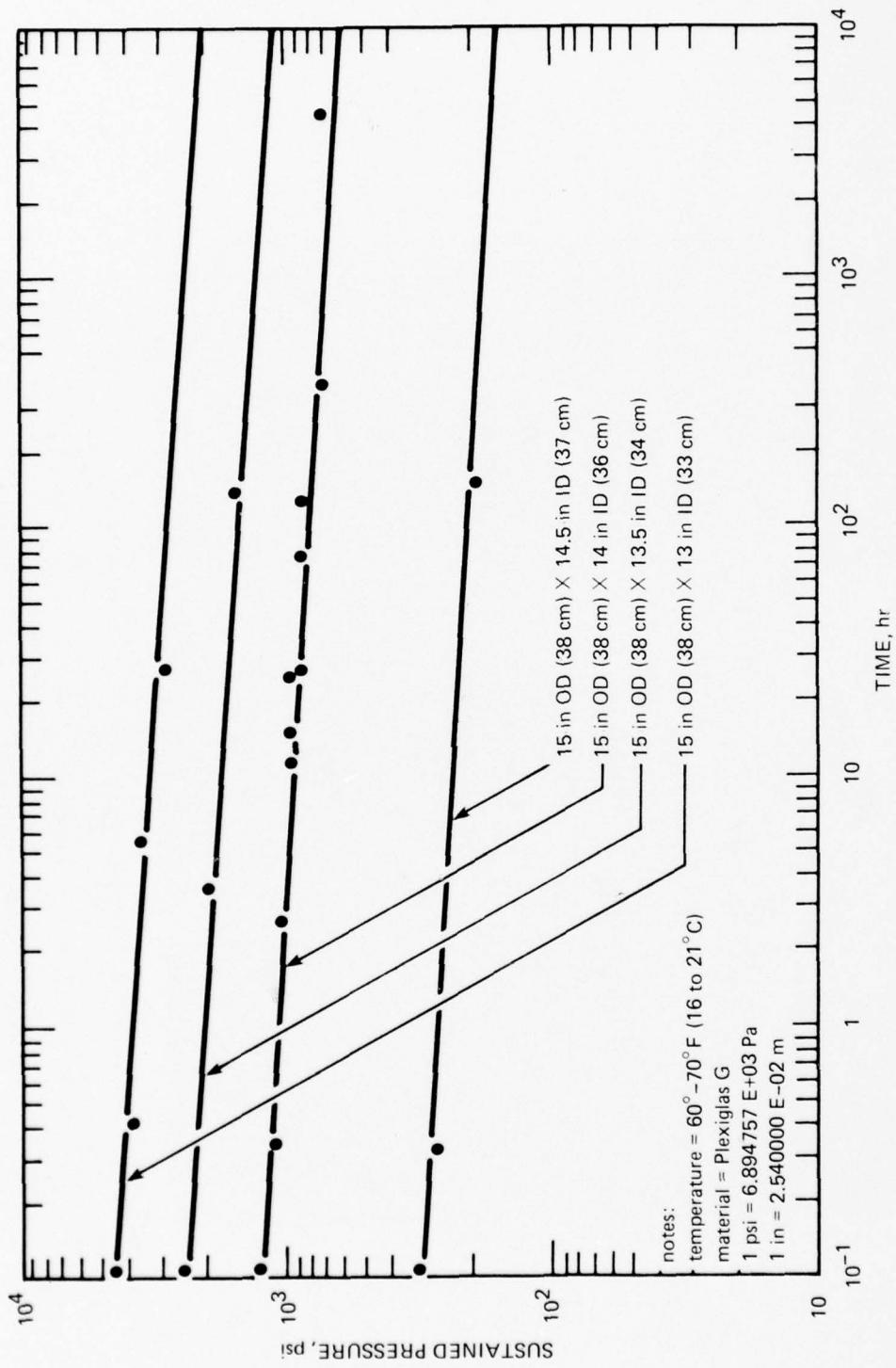
Figure 11.31. Time-dependent creep buckling of acrylic plastic spherical shells under sustained pressure loading at 70°F (21°C). Note that the data were generated with spheres, but the results are applicable to spherical sectors with the same t/R_i ratios (0.034, 0.071, 0.111, and 0.153).

Figure 11.32. Typical shear cracks found on the conical bearing surfaces of spherical sectors under sustained long-term pressure loading.
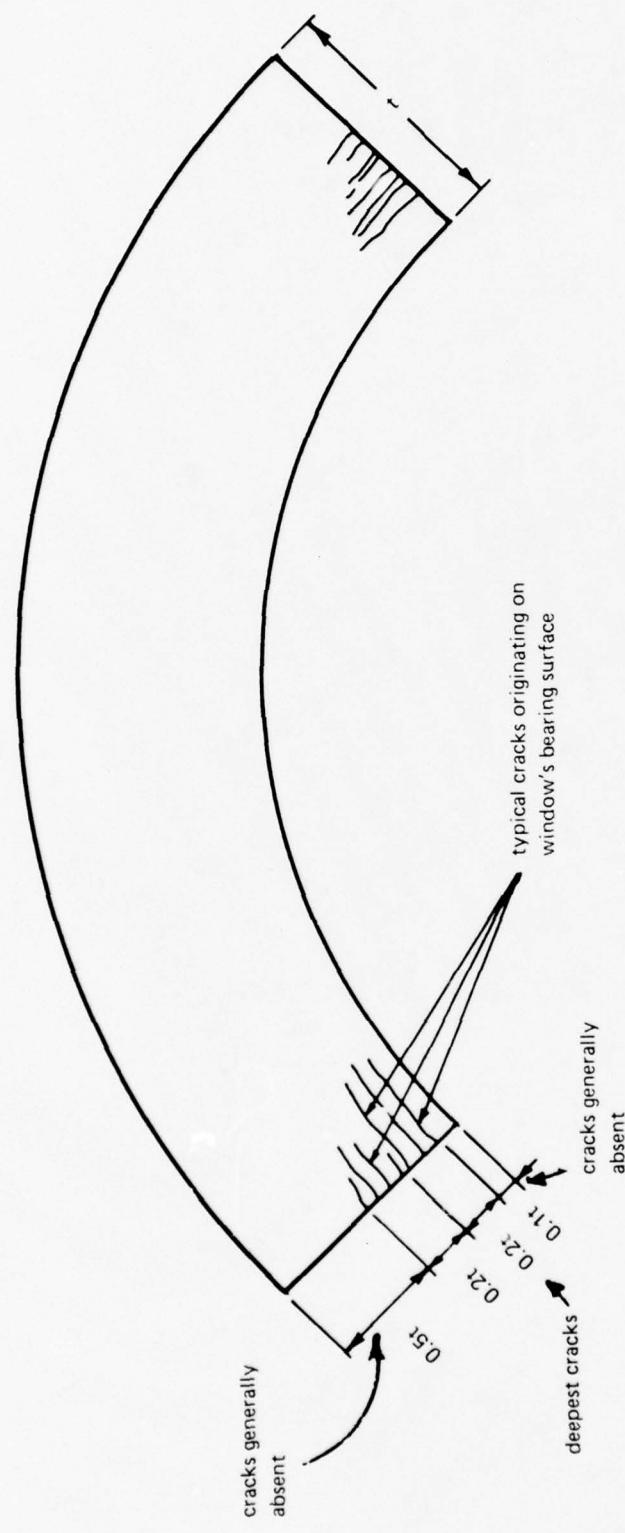
Figure 11.33. Location and relative magnitude of shearing cracks on the conical bearing surface of spherical sectors.

typical cracks originating on window's bearing surface

cracks generally absent

cracks generally absent

deepest cracks

0.1t

0.2t

0.2t

0.5t

Figure 11.34. Top view of the conical fracture surface inside a spherical sector after long-term pressure loading. $t/D_i = 1.0$; $D_i/D_f = 1.0$; temperature = 70°F (21°C); included angle = 90 degrees (1.57 radians); and pressure = 20,000 pounds per square inch (137.8 megapascals) at 100 hours.
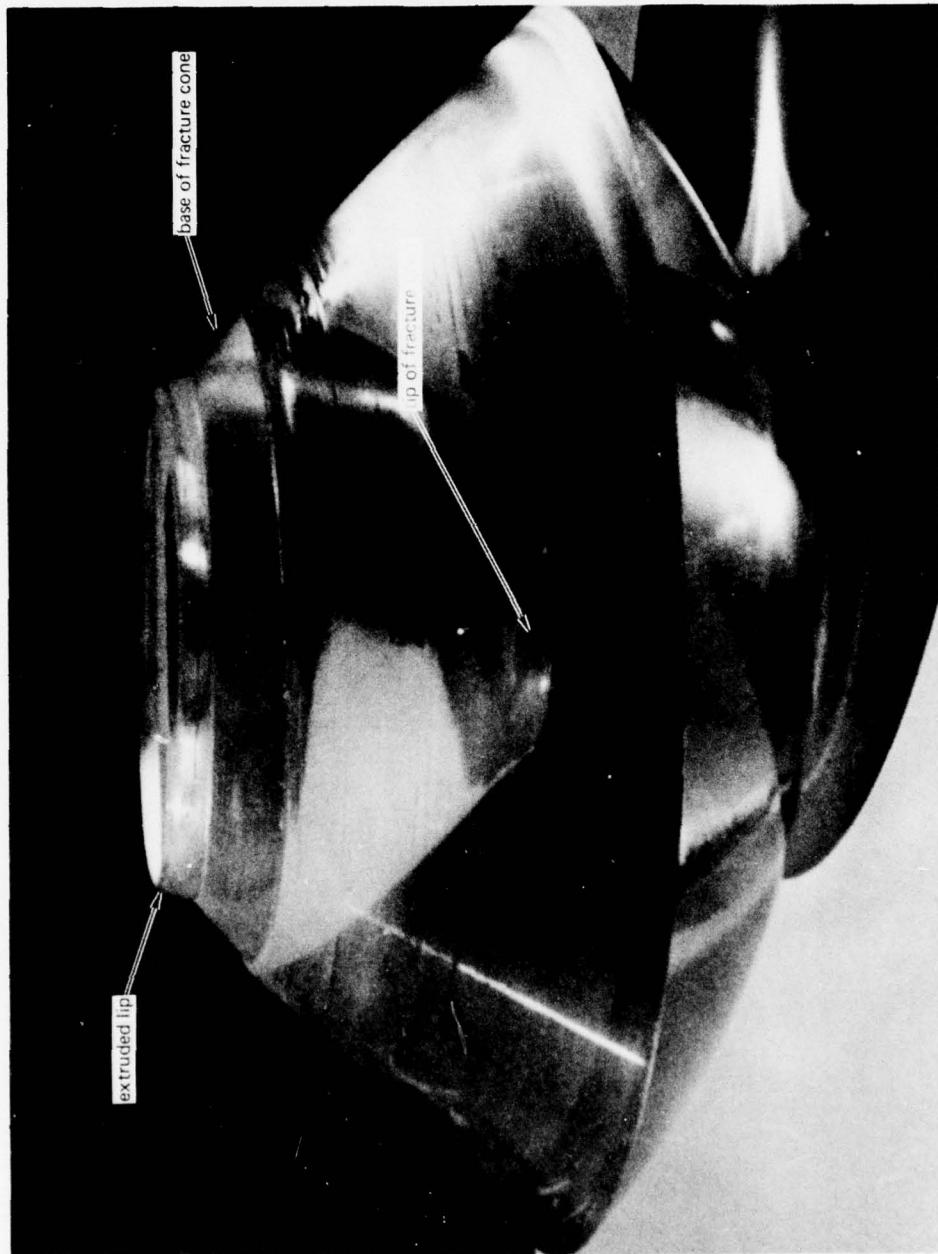
Figure 11.35. Bottom view of conical fracture surface inside the window shown in figure 11.34. Note that the fracture originated on the conical bearing surface close to the concave face and that an extrusion plug has already formed at the low-pressure face.

Figure 11.36. Axial displacement of 90-degree (1.57 radians) spherical sectors
measured at the apex with a mechanical dial indicator under sustained long-term
pressure loading at 70°F (21°C) ambient temperature. Compare these axial
displacements with the short-term axial displacements for identical sectors
shown in figure 11.26. To obtain the total value of axial displacement at
any time during sustained loading, one must add to the value shown in
this figure the short-term axial displacement for the same t/R_i ratio.
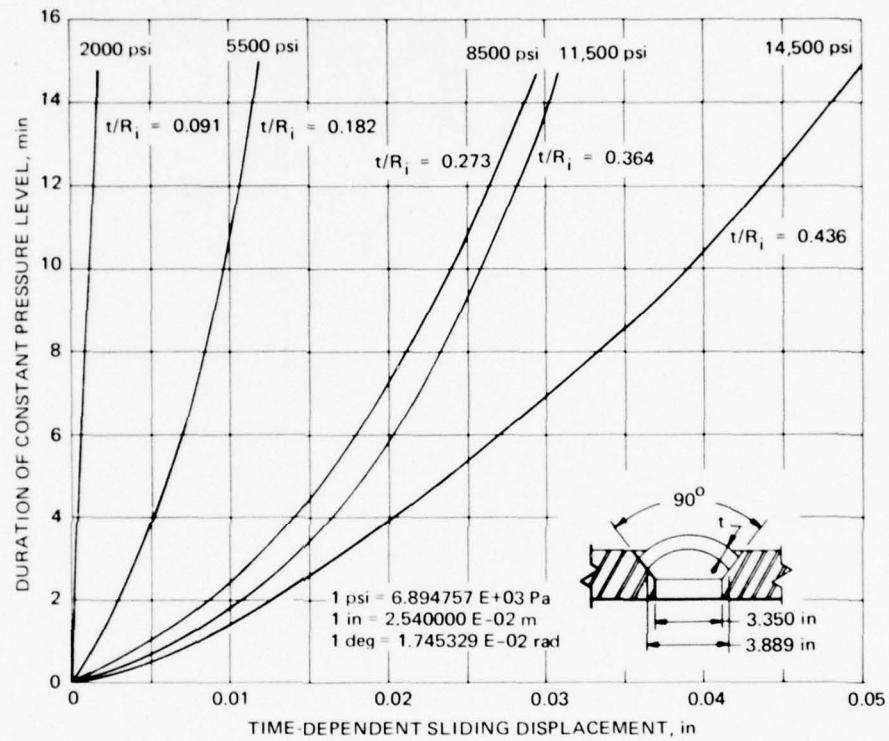
Figure 11.37. Sliding displacement of 90-degree (1.57 radians) spherical sectors measured on the conical seat of the mounting flange under long-term pressure loading at 70°F (21°C) ambient temperature. Compare these sliding displacements with the short-term sliding displacements for identical sectors shown in figure 11.27. To obtain the total value of sliding displacement at any time during sustained loading, one must add to the value shown in this figure the short-term sliding displacement for the same t/R_i ratio.
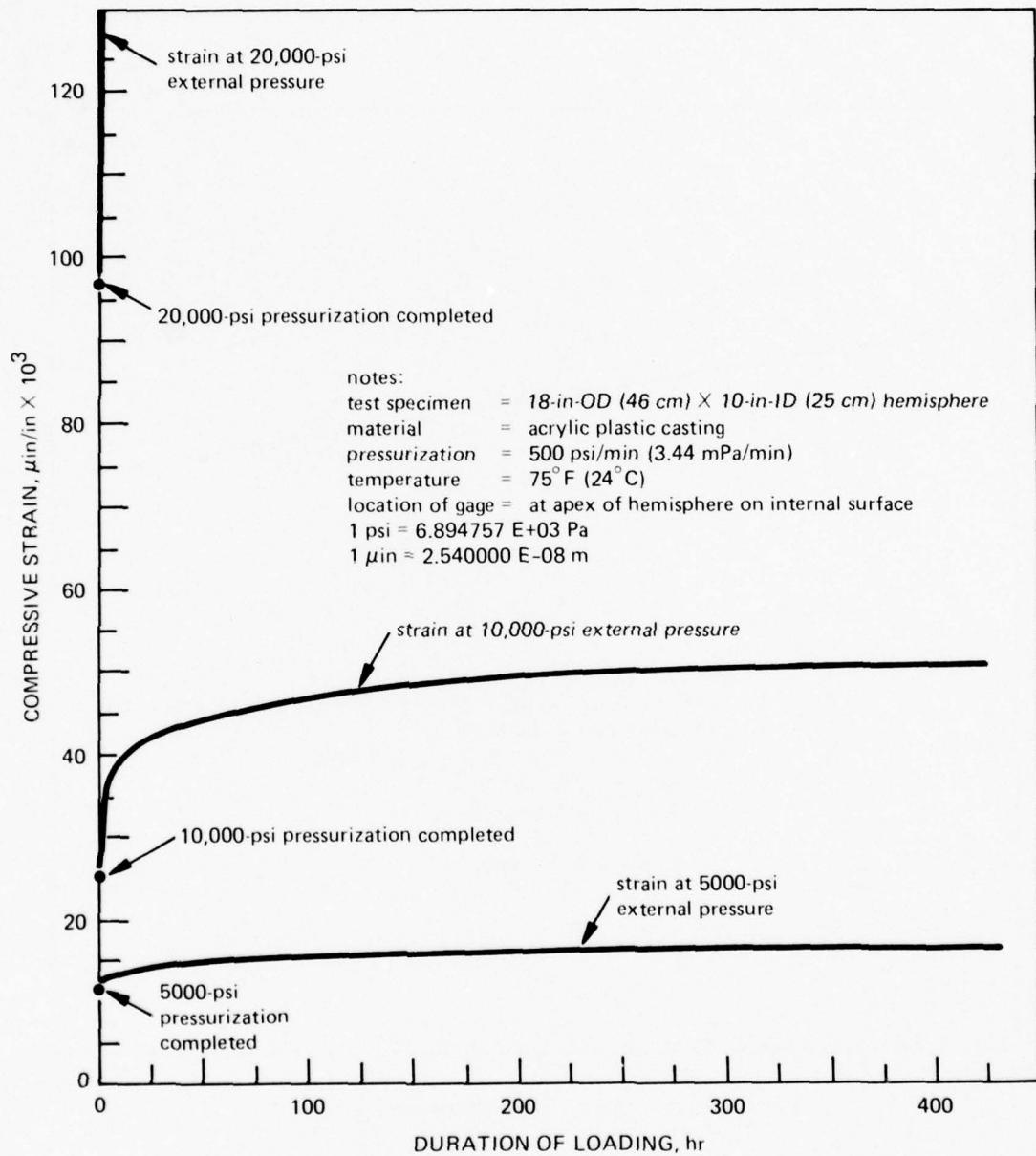
Figure 11.38. Deformation of very thick spherical sectors under sustained long-term loading at 75°F (24°C). Compare these deformations with the short-term deformations in identical sectors in figure 11.29. Note that the creep becomes significant only for pressures greater than 5000 pounds per square inch (34.5 megapascals).
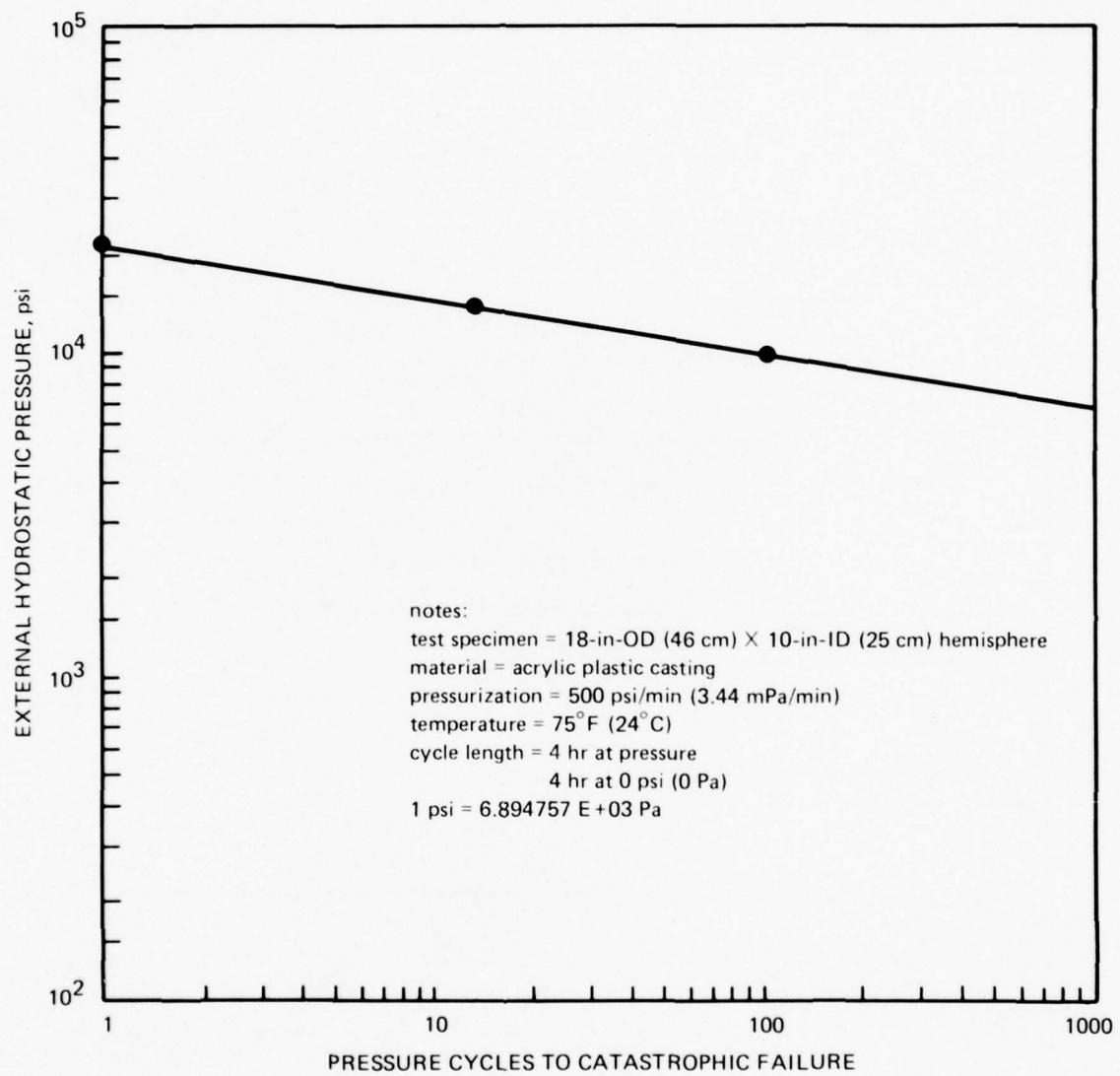
Figure 11.39. Typical cyclic fatigue curve for spherical sectors under repeated long-term pressure cycling. Each point on the curve represents a catastrophic implosion of the test specimen. $t/R_i = 0.8$; $\alpha = 180$ degrees (3.14 radians).

11-72
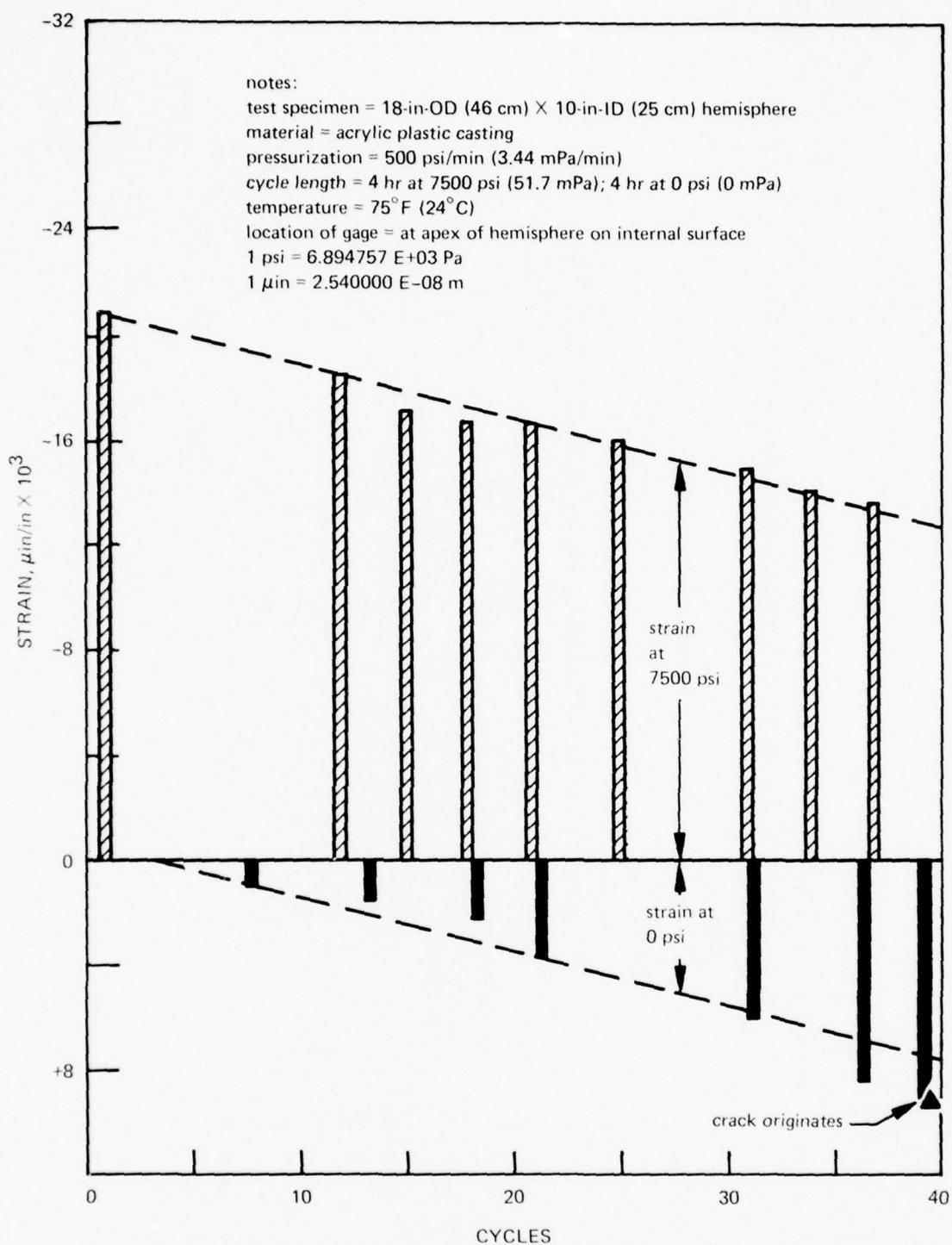
Figure 11.40. Deformations of very thick spherical sectors under cyclic pressure loading from 0 to 7500 pounds per square inch (0 to 51.7 megapascals). The compressive strain at the apex decreases during each successive pressure loading, while the residual tensile strain increases with each relaxation period. $t/R_i = 0.8$; included angle = 180 degrees (3.14 radians). All measurements refer to original dimensions and were taken at the end of successive loading and relaxation periods.

11-73

notes:
test specimen   = 18-in-OD (46 cm) × 10-in-ID (25 cm) hemisphere
material   = acrylic plastic casting
pressurization   = 500 psi/min (3.44 mPa/min)
cycle length   = 4 hr at 10,000 psi (68.9 mPa); 4 hr at 0 psi
                     (0 mPa)
temperature   = 75° F (24°C)
location of gage = at apex of hemisphere on internal surface

1 psi = 6.894
        757 E+03 Pa
1 μin = 2.540
        000 E−08 m

STRAIN, μin/in × 10³

−32

−24

−16

−8

0

+8

strain at
10,000 psi

strain at
0 psi

crack originates

0   10   20   30   40

CYCLES

Figure 11.41. Deformations under cyclic pressure loading to 10,000 pounds per
square inch (68.9 megapascals) of a very thick spherical sector with dimensions
identical to those of the sector in figure 11.40. The compressive and tensile
strains increase with each pressure cycle, but at a greater rate than shown in
figure 11.40.

11-74
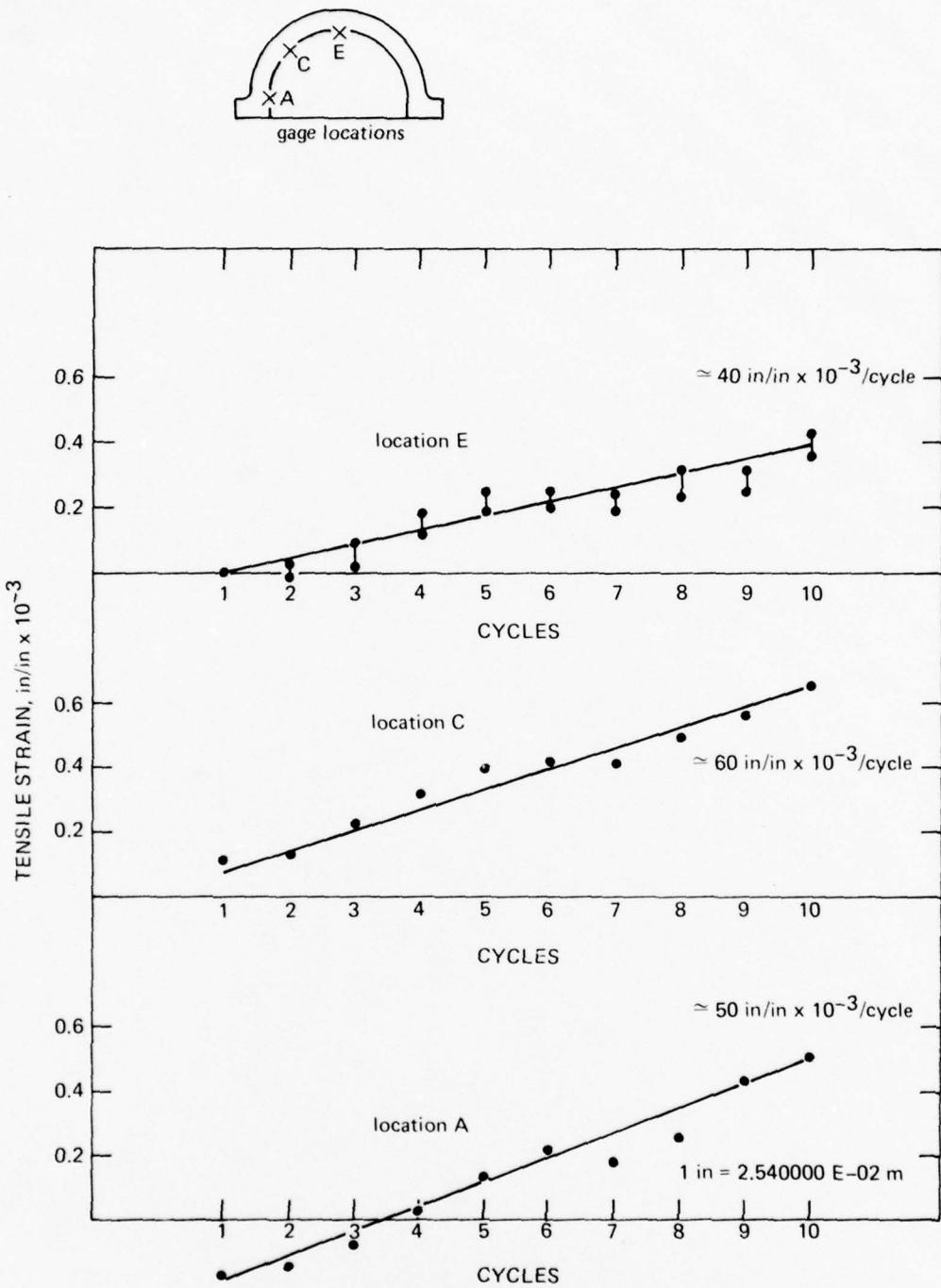
Figure 11.42. Comparison of residual strain rates at various locations on a hemisphere with $t/R_i = 0.363$ under cyclic pressure loading from 0 to 2000 pounds per square inch (13.8 megapascals) at 75°F (24°C) ambient temperature. The magnitudes of the strains are approximately the same regardless of their location on the hemisphere. The strains are measured at the conclusion of a 17-hour relaxation phase, but prior to a 7-hour sustained loading phase, for each pressure cycle.
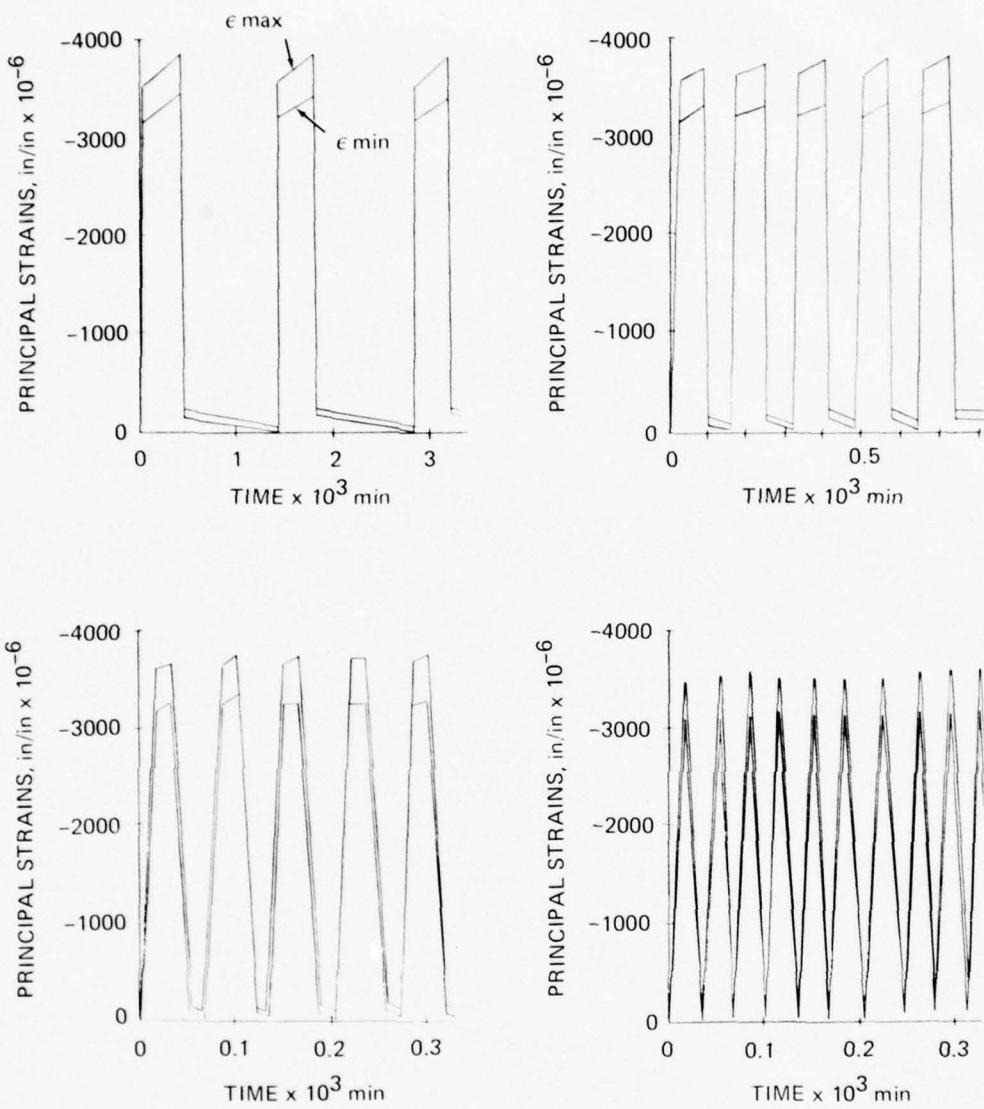
Figure 11.43. Deformations of a thin spherical sector under cyclic pressure loading to 5000 pounds per square inch (34.4 megapascals). $t/R_i = 0.08$; included angle = 180 degrees (3.14 radians). Note that there is no decrease in magnitude of compressive strains between the individual pressure loadings and that the tensile strains are absent during relaxation periods.
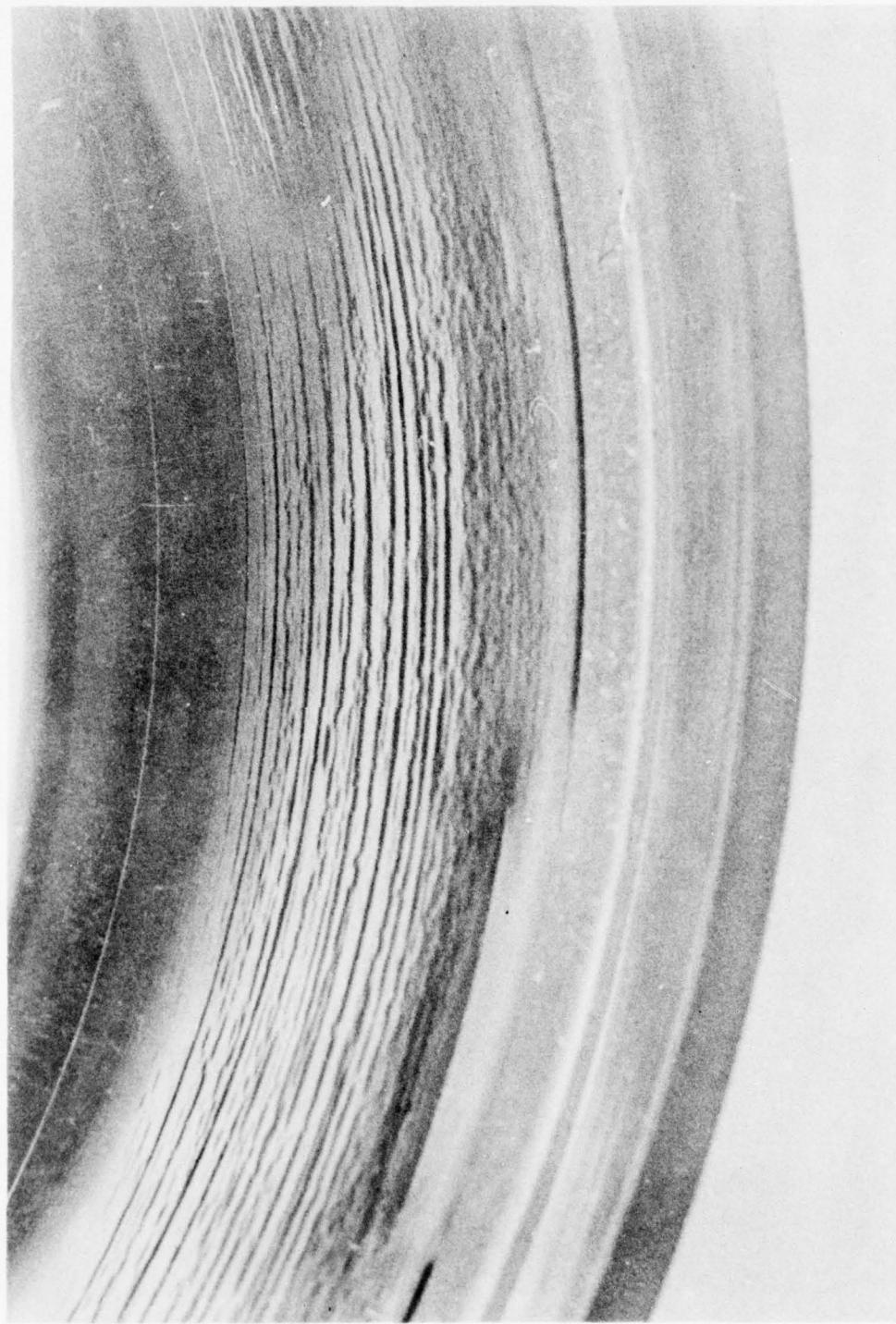
Figure 11.44. Typical cyclic fatigue cracks on the bearing surface of acrylic plastic spherical sectors.

11-77
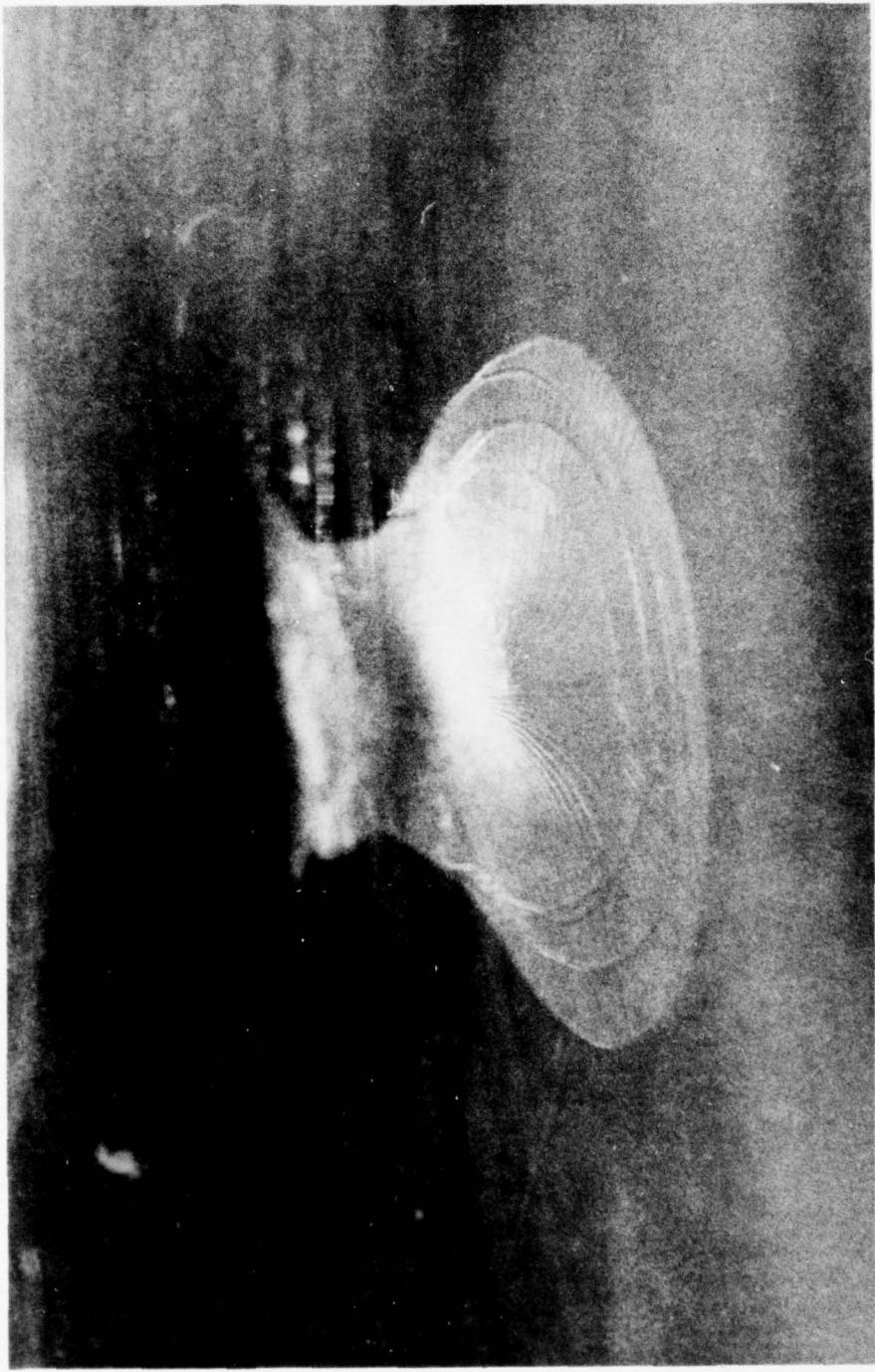
Figure 11.45. Typical mushroom-shaped projection found at the bases of cyclic fatigue cracks in bearing surfaces of spherical sectors under cyclic pressure loading. Note the growth rings on the crack that represent step-wise increases in crack size.

Figure 11.46. Typical star-shaped crack pattern on the concave surface of a thick spherical sector window with $t/R_i = 0.363$ after several cyclic pressure loadings to 2000 pounds per square inch (13.8 megapascals). Note that the cracks originate on the concave surface and propagate towards the convex surface.

Figure 11.47. Typical medusa-shaped crack pattern on the concave surface of a very thick spherical sector window with $t/R_i = 0.8$ after a single pressure loading to 15,000 pounds per square inch (103 megapascals).

11-80

maximum = –455 psi ■

minimum = –6005 psi ●

stress contours at
400-psi intervals

notes:
R_i = 21.75 in
t = 2.25 in

1 psi = 6.894757 E+03 Pa
1 in = 2.540000 E–02 m

hoop stress at 1000-psi external pressure
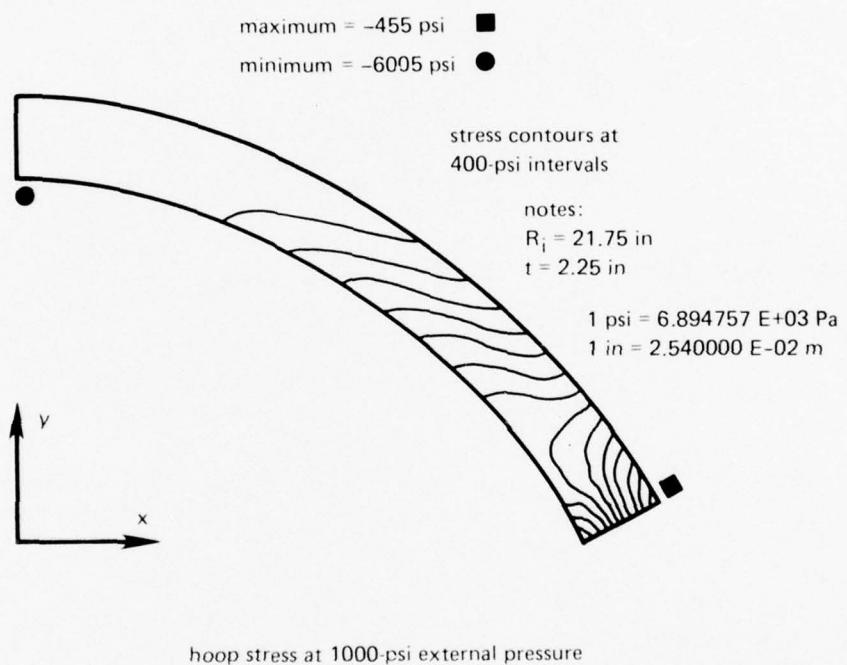
Figure 11.48. Calculated distribution of hoop stresses in a thick
spherical sector under 1000-pound-per-square-inch (6.89 mega-
pascals) external pressure loading. t/R_i = 0.103; included
angle = 117 degrees (2.04 radians).

11-81
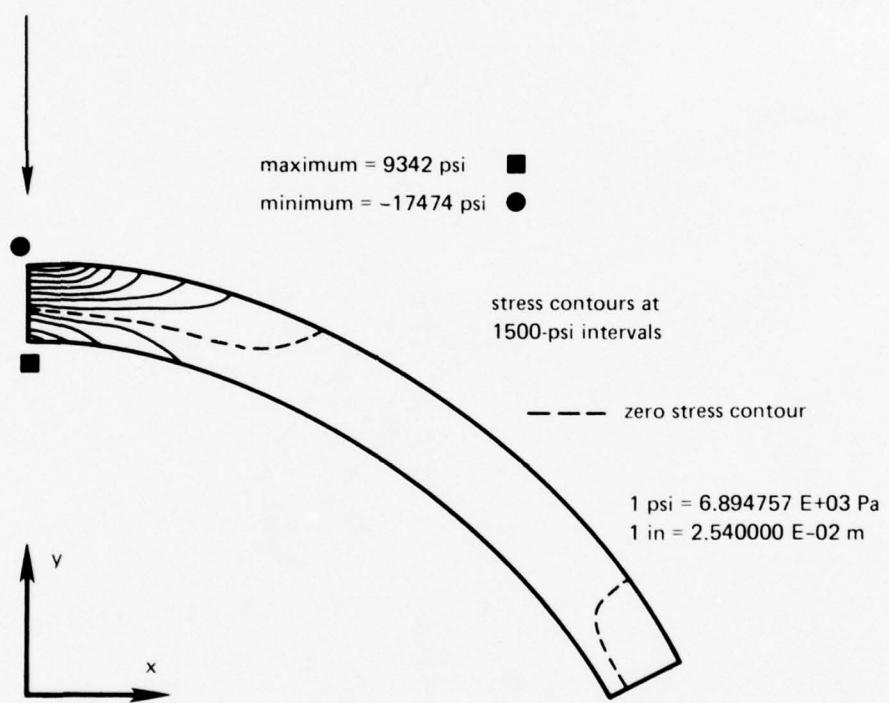
Figure 11.49. Calculated distribution of hoop stresses in the spherical sector shown in figure 11.48 under point-impact loading on the apex with a flat impactor with 689 foot-pounds of kinetic energy.

11-82
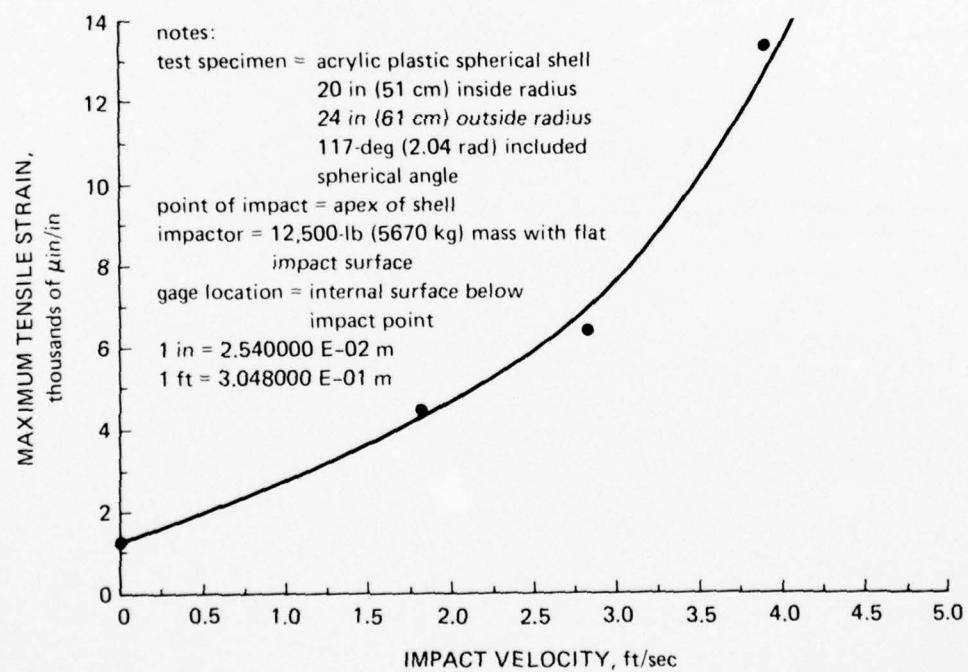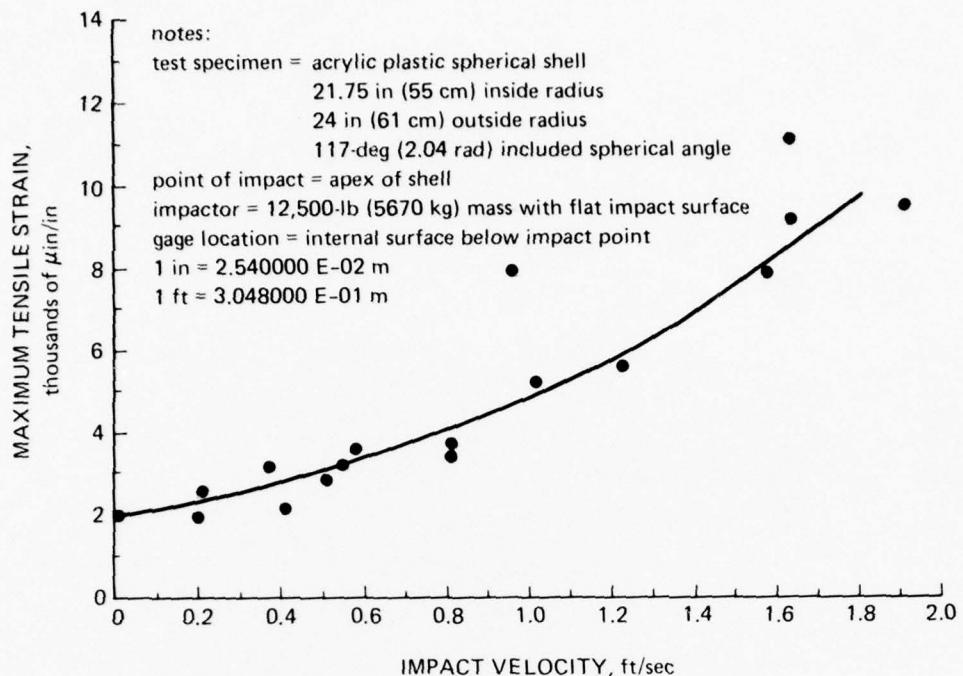
Figure 11.50. Tensile strains experimentally measured on the concave faces of spherical sectors directly below the point of impact. Note how increasing the *thickness of the window by 78 percent* decreases the strain under impacts with identical kinetic energy by approximately 50 percent.
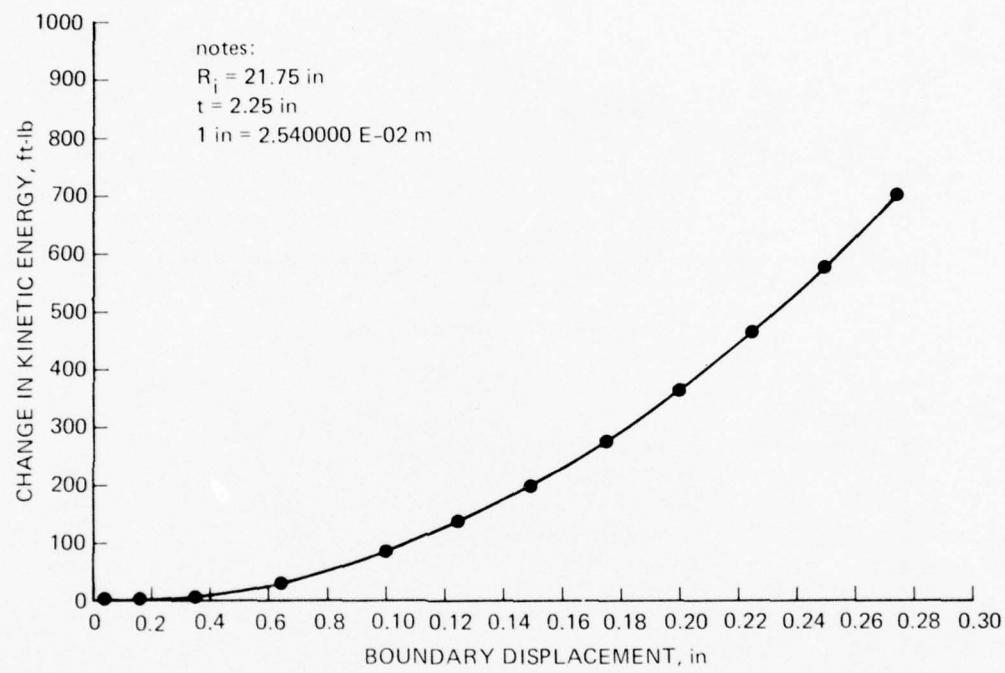
Figure 11.51. Calculated displacement of the apex on the spherical sector in figure 11.48 under point-impact loading.
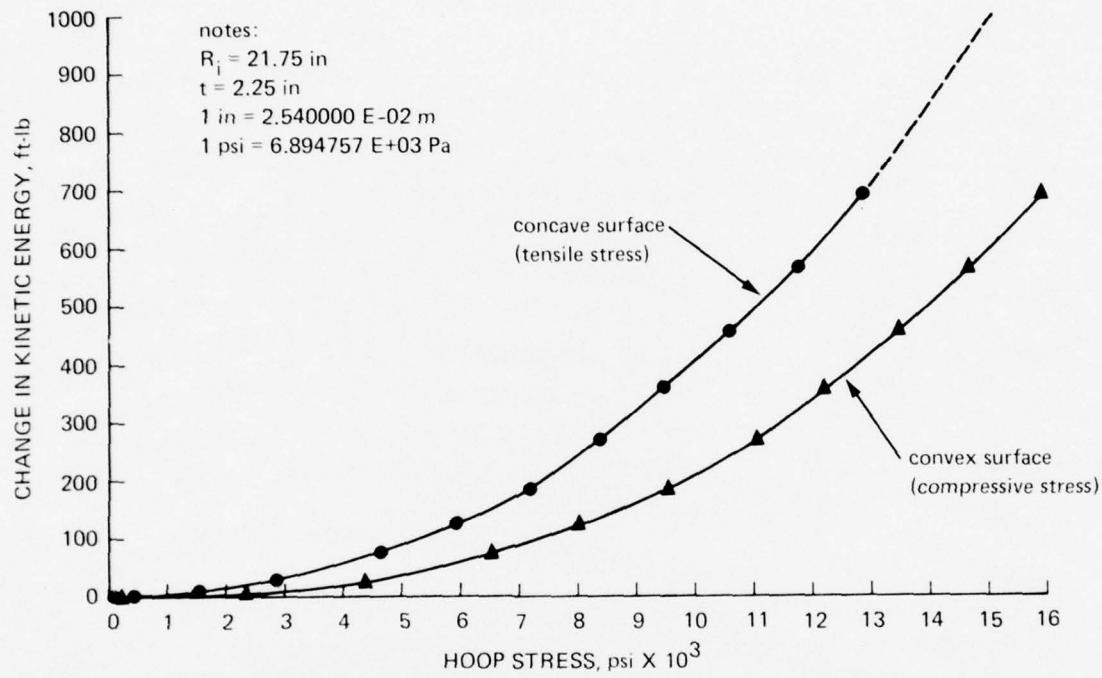
Figure 11.52. Calculated dynamic stresses on the spherical sector in figure 11.48 under point-impact loading with a flat impactor.
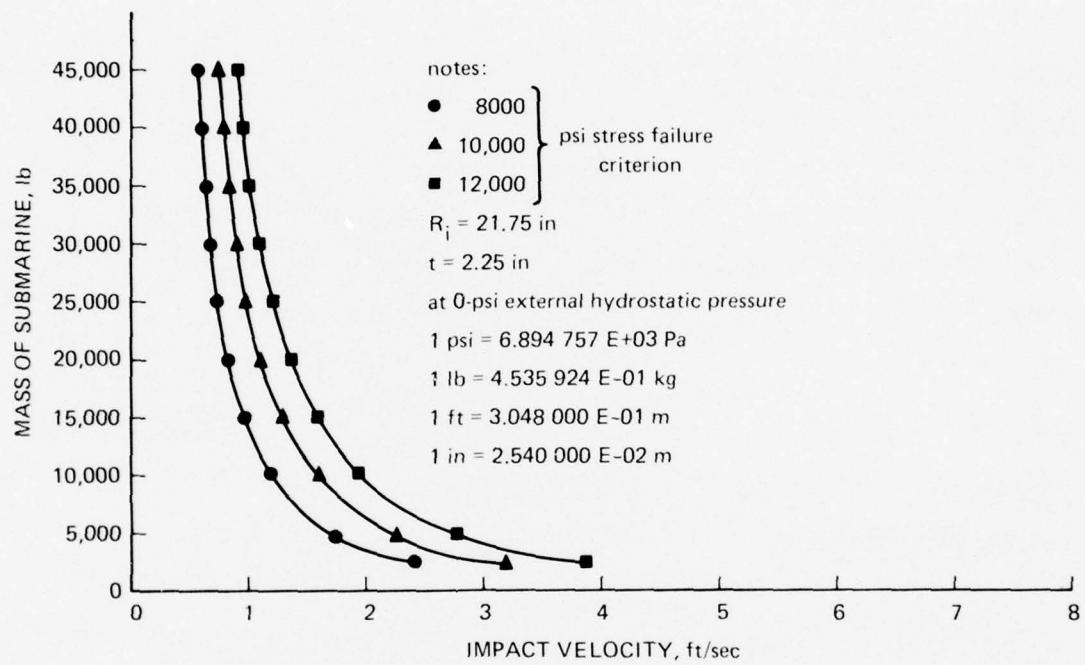
Figure 11.53. Calculated critical impact velocities for spherical sector in figure 11.48 when serving as a bow window in a submarine.
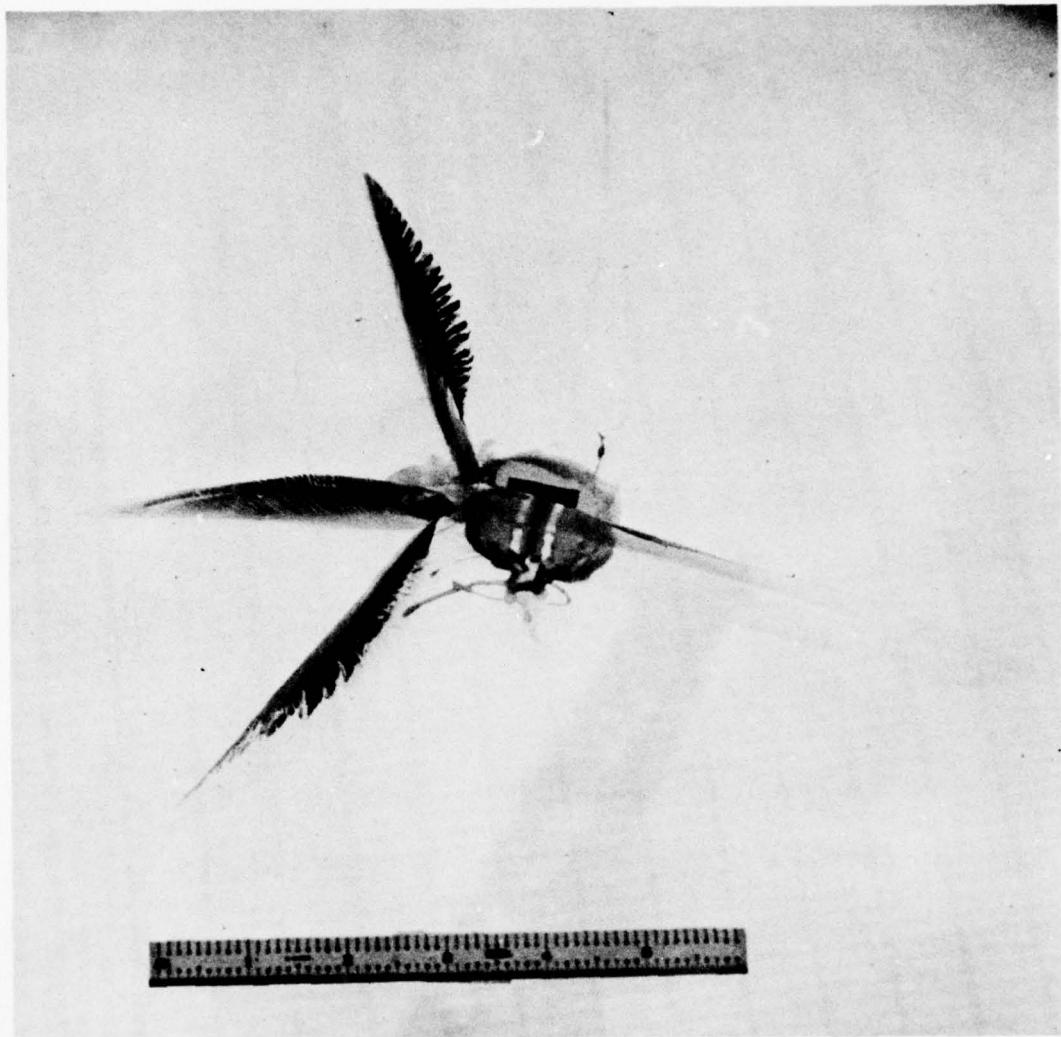
Figure 11.54. Typical crack pattern initiated in a spherical sector by a mild impact with a flat impactor striking the convex surface. The crack originates on the concave surface and propagates towards the convex surface. Note that the window is still pressure tight. $t = 2.25$ inches (5.7 centimeters); $R_i = 21.75$ inches (55 centimeters); included angle = 117 degrees (2.04 radians); $V = 1.6$ feet per second (0.5 meter); $W = 12,500$ pounds (5670 kilograms); hydrostatic pressure = 5 pounds per square inch (0.04 megapascal).

Figure 11.55. Typical fracture surface generated in the spherical sector by a severe impact with a flat impactor striking the convex surface. Note that the material within the fracture cone has spalled off but the window is still pressure tight. $t = 4$ inches (10 centimeters); $R_1 = 20$ inches (51 centimeters); included angle = 117 degrees (2.04 radians); $V = 3.9$ feet per second (1.2 meters); $W = 12,500$ pounds (5670 kilograms); hydrostatic pressure = 5 pounds per square inch (0.04 megapascal).
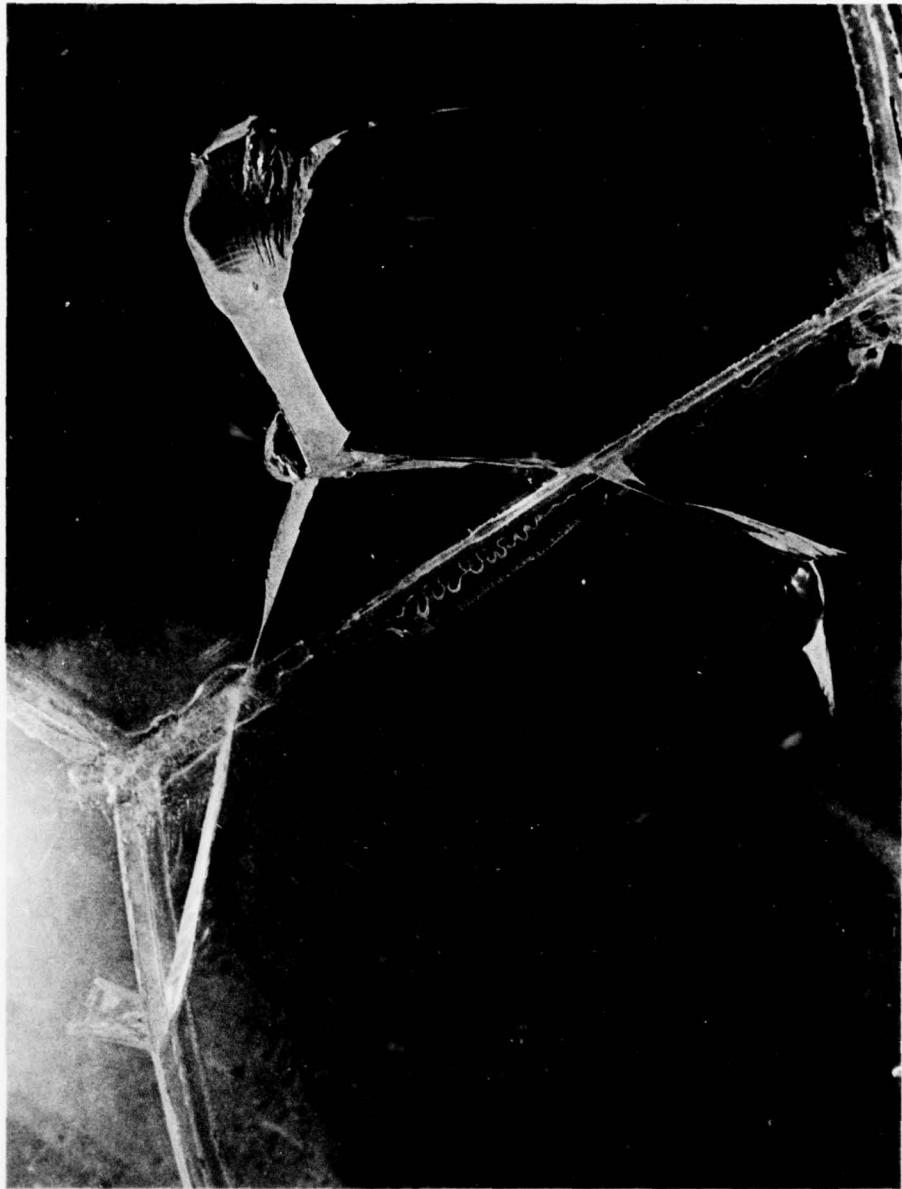
Figure 11.56. Typical crack pattern initiated by underwater explosion in a spherical sector. Note that the cracks do not follow along the bonded joints in the structure.
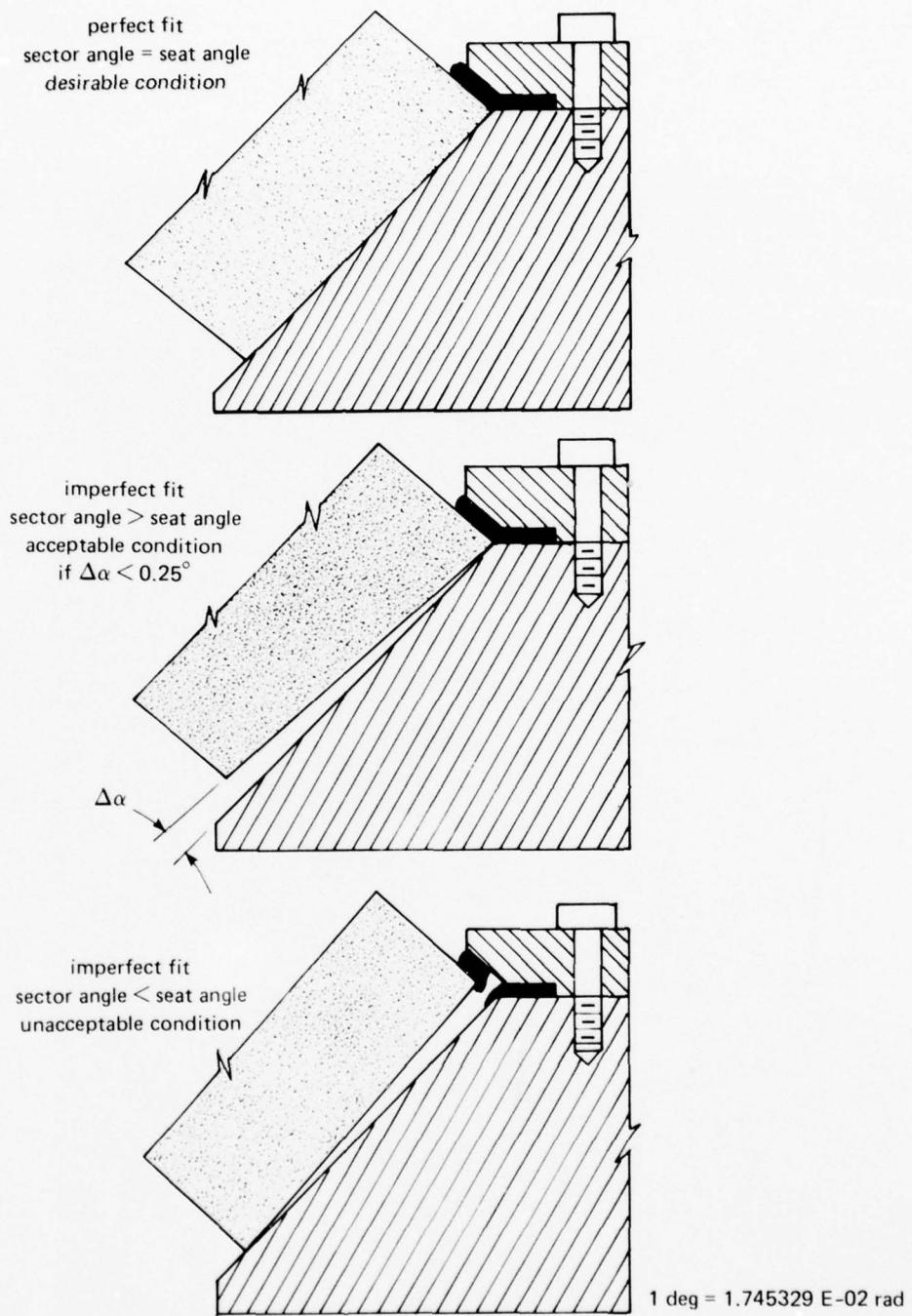
11-89

perfect fit
sector angle = seat angle
desirable condition

imperfect fit
sector angle > seat angle
acceptable condition
if $\Delta\alpha < 0.25°$

$\Delta\alpha$

imperfect fit
sector angle < seat angle
unacceptable condition

1 deg = 1.745329 E-02 rad

Figure 11.57. Typical angular mismatches between spherical
sector and conical seat in mounting flange.

11-90

k = 1

0 psi

optimum overhang for
design pressure

design pressure

k = <1

0 psi

inadequate overhang for
design pressure

design pressure

k = 2

0 psi

excess overhang for
design pressure

design pressure

seat
overhang

k = >4

0 psi

optional overhang for
critical pressure
maximization

300% overpressure

1 psi = 6.894 757 E+03 Pa

unpressurized

pressurized
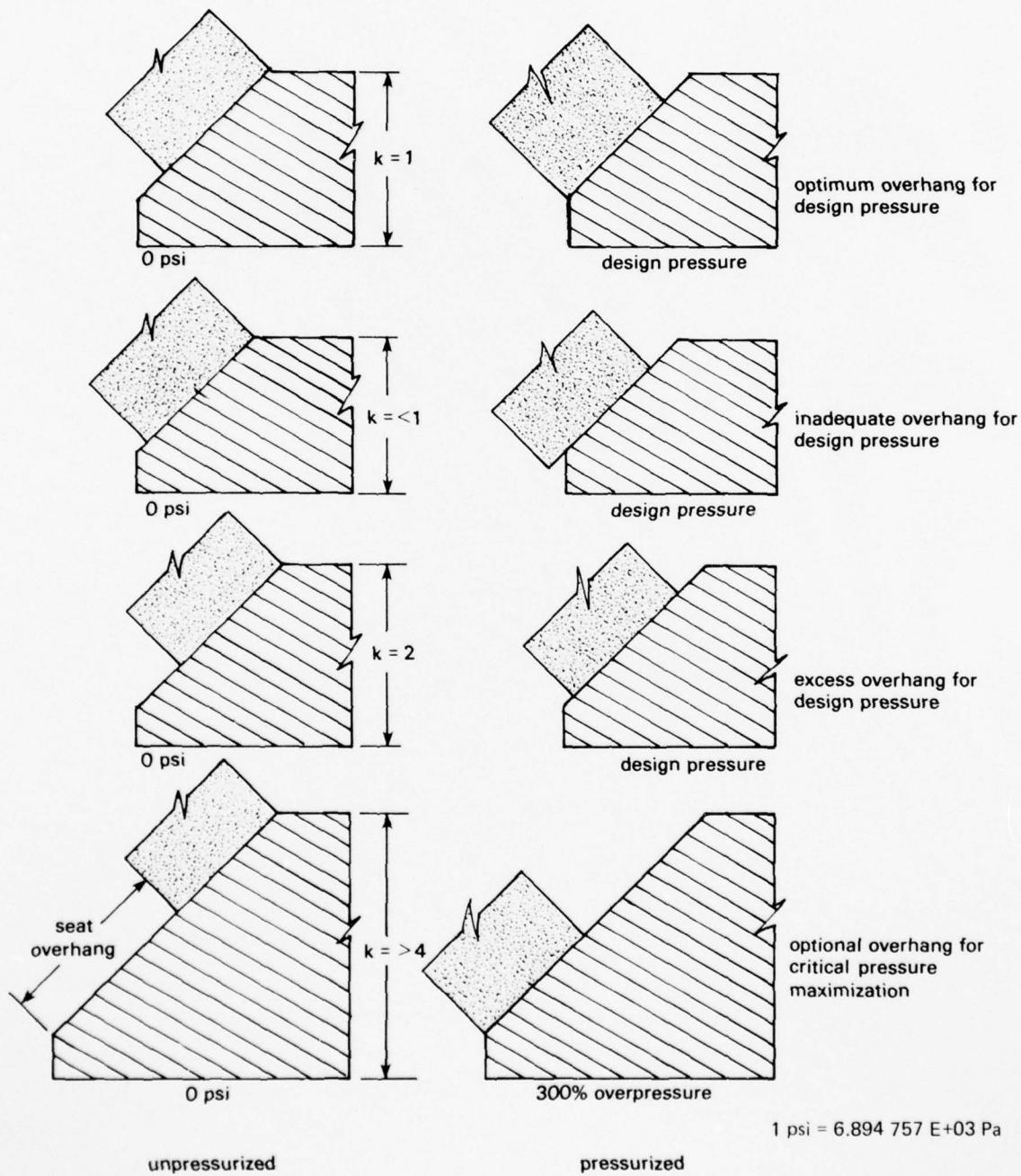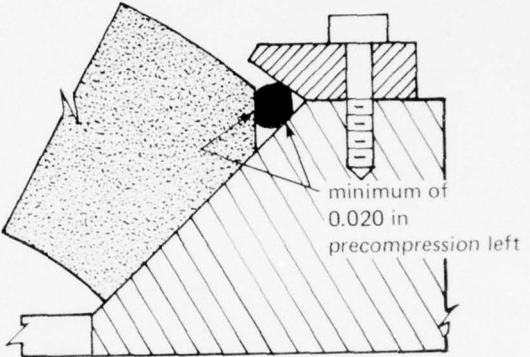
Figure 11.58. Different seat support conditions available for spherical sectors with
conical bearing surfaces.

condition A   conditions B and C

minimum of
0.020 in
precompression left

minimum of
0.020 in
precompression left
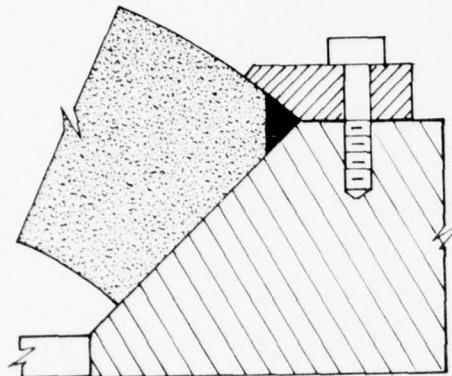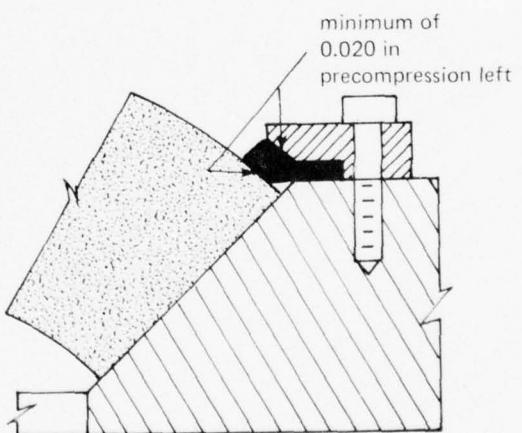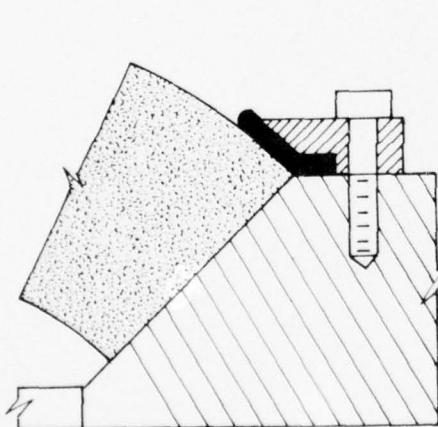
$$1 \text{ in} = 2.540000 \text{ E-02 m}$$
$$1 \ t^{o}_{C} = (t^{o}_{F} - 32)/1.8$$

condition A — after assembly at 75°F ambient air temperature

condition B — initiation of dive at −45°F ambient air temperature

condition C — surfacing after long dive to design depth

Figure 11.59. Typical sealing arrangements for spherical sectors with conical bearing surfaces. Note that the precompression during assembly must be large enough to insure a minimum of precompression at the minimum design temperature and after completion of pressurization to design pressure.

11-92
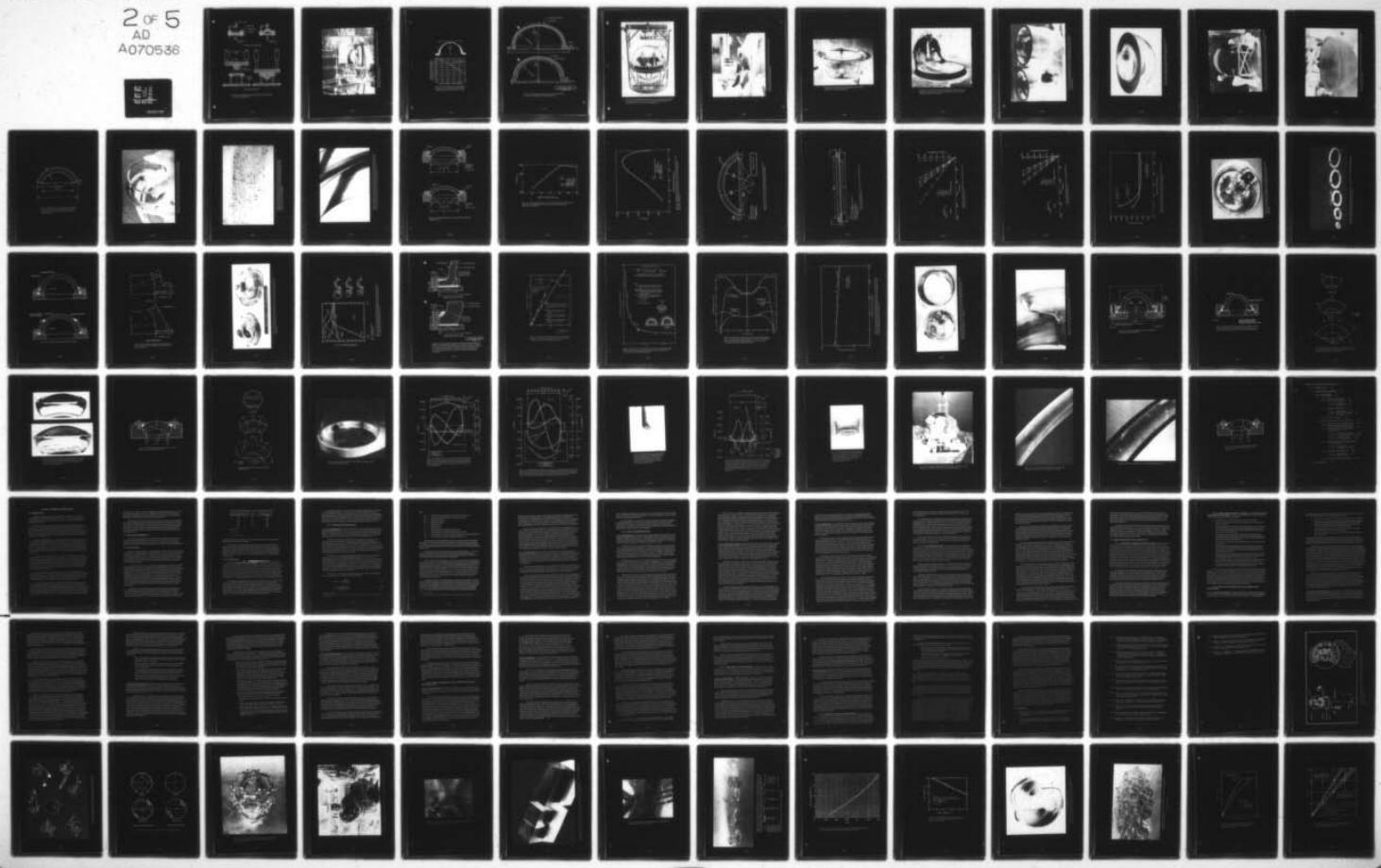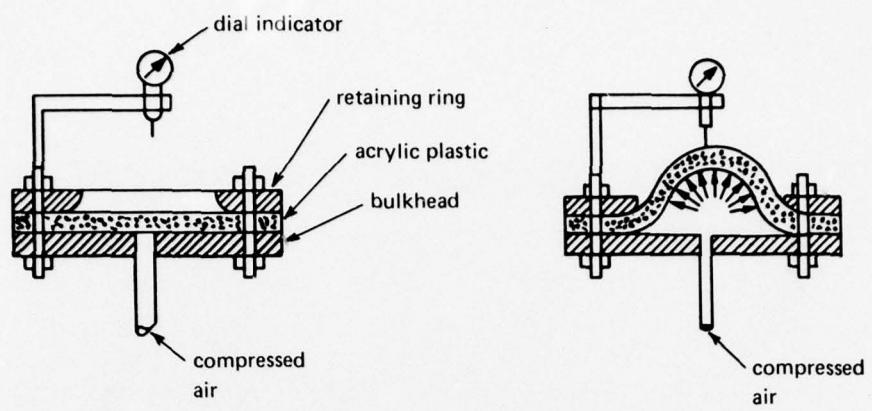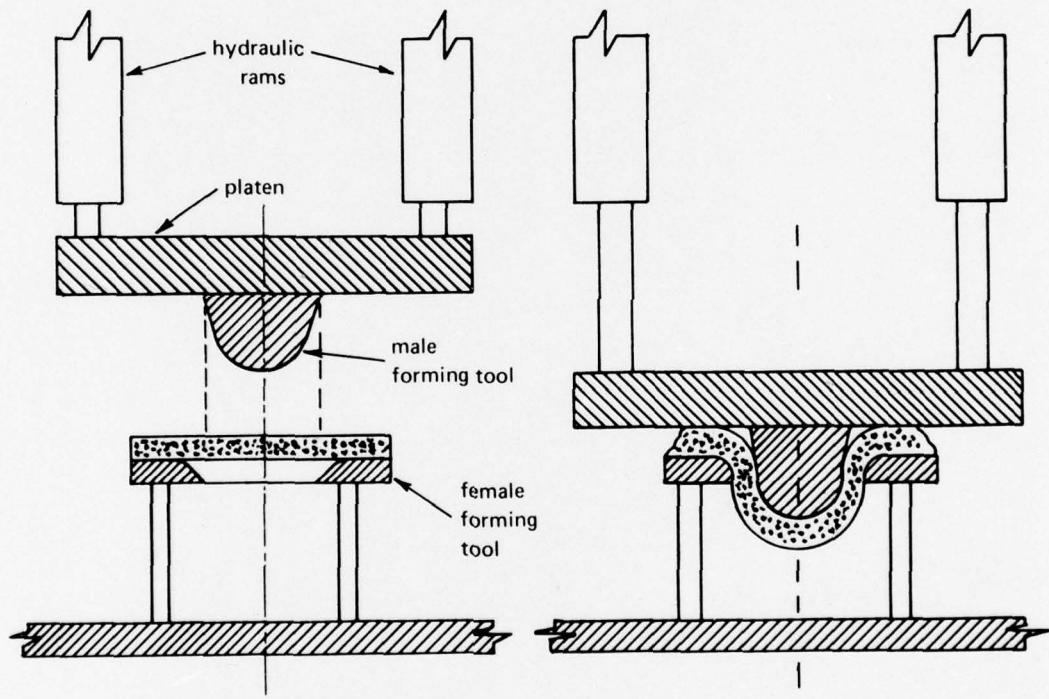
Figure 11.60. Typical thermoforming techniques that produce spherical sectors with equatorial flanges.
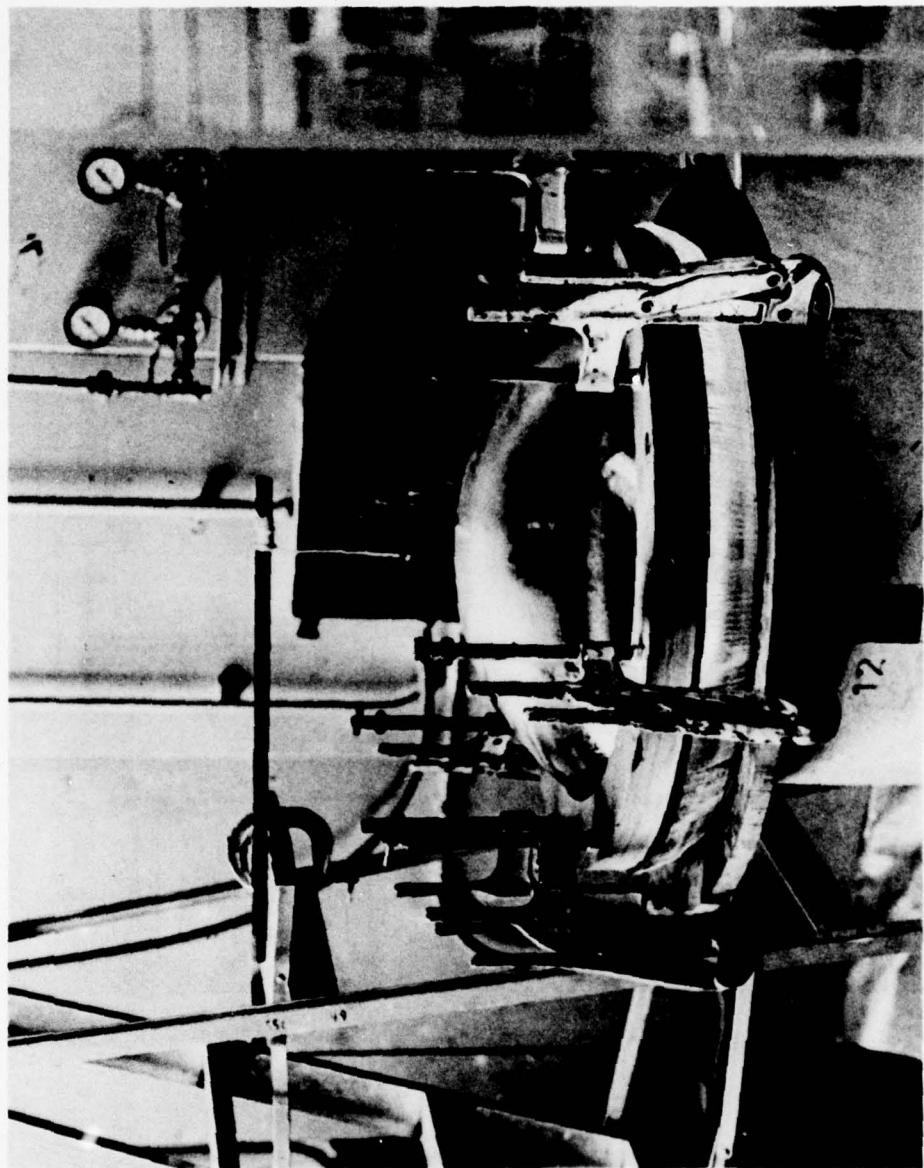
Figure 11.61. Typical setup for free-forming of spherical sectors with compressed gas. Acrylic discs are preheated to forming temperatures.

11-94
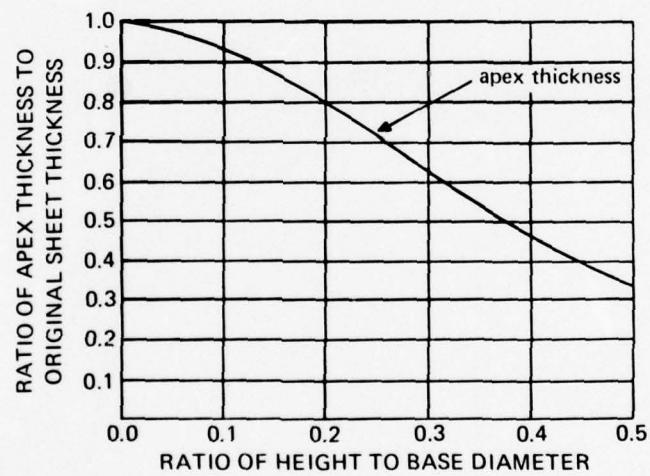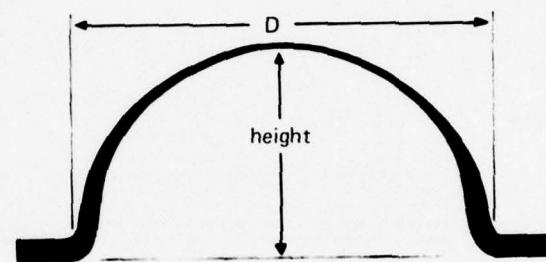
Figure 11.62. Typical thinning out of wall thickness in spherical sectors free-formed with compressed gas at temperatures from 270 to 350°F (132 to 177°C).
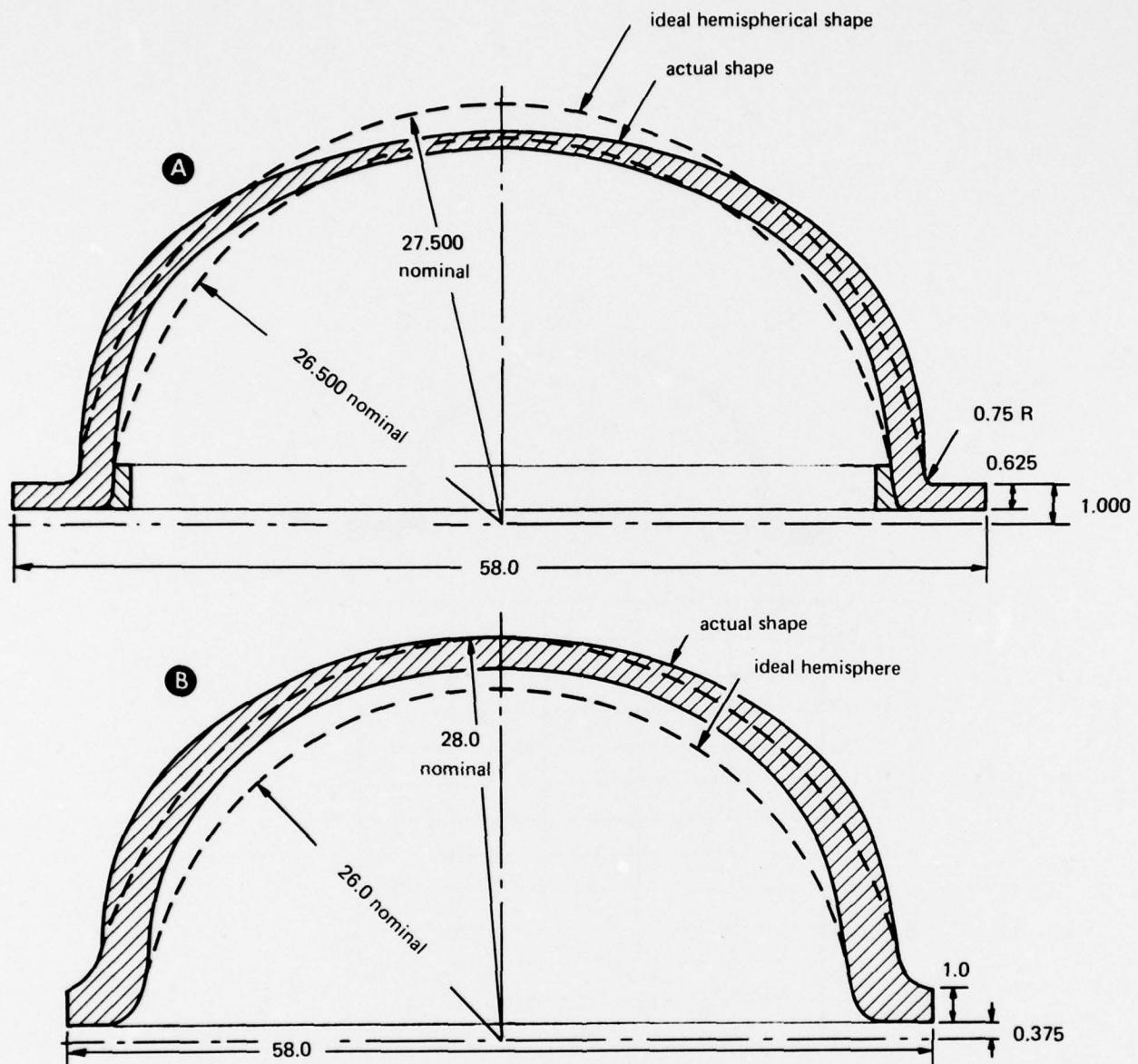
Figure 11.63. Typical deviations in sphericity found in spherical sectors free-formed with compressed gas at elevated temperature.

11-96
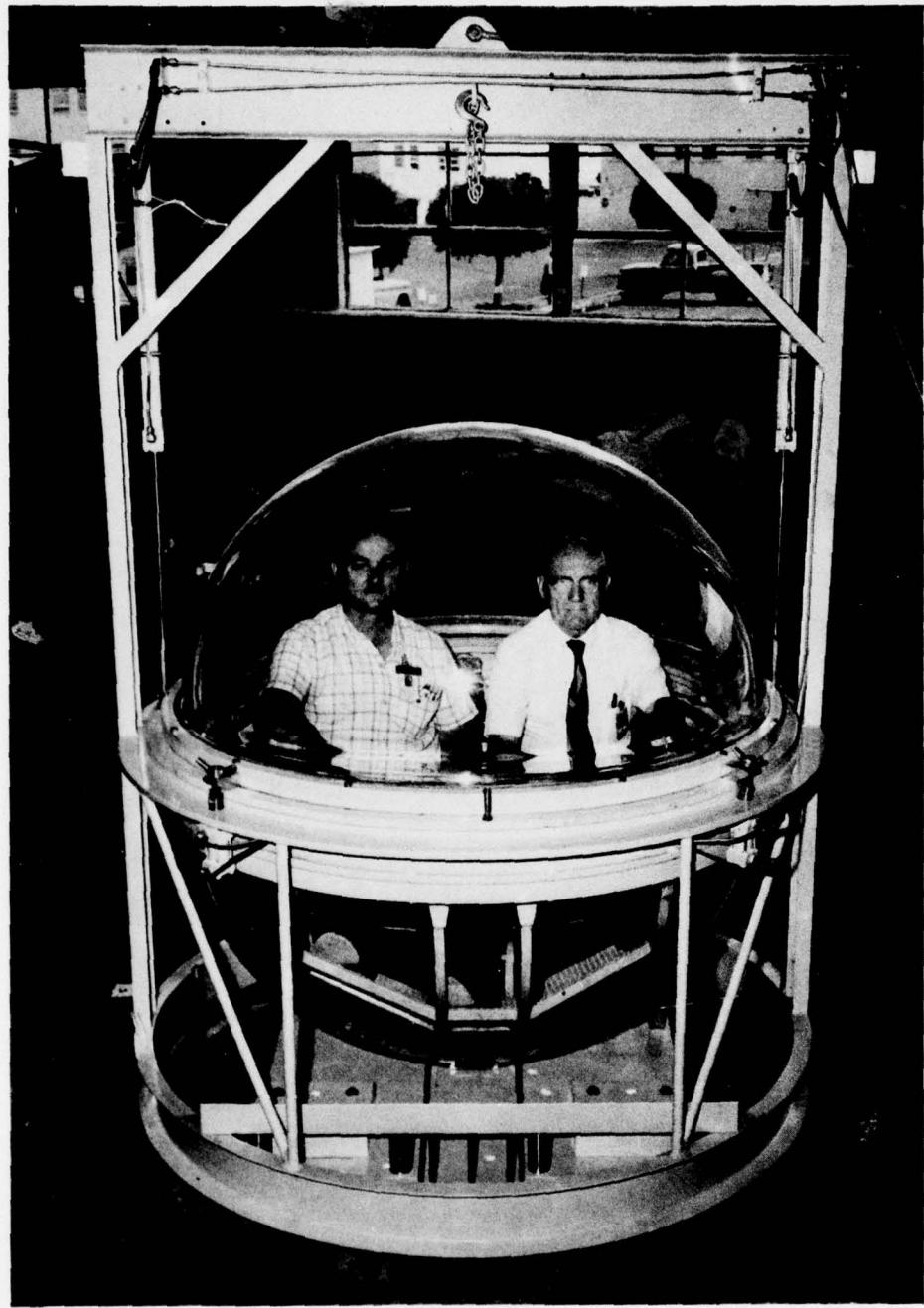
Figure 11.64. Typical application for spherical sectors free-formed with compressed gas. Underwater elevator with 60-foot (18 meters) depth capability built by the Naval Undersea Center for its offshore oceanographic tower.
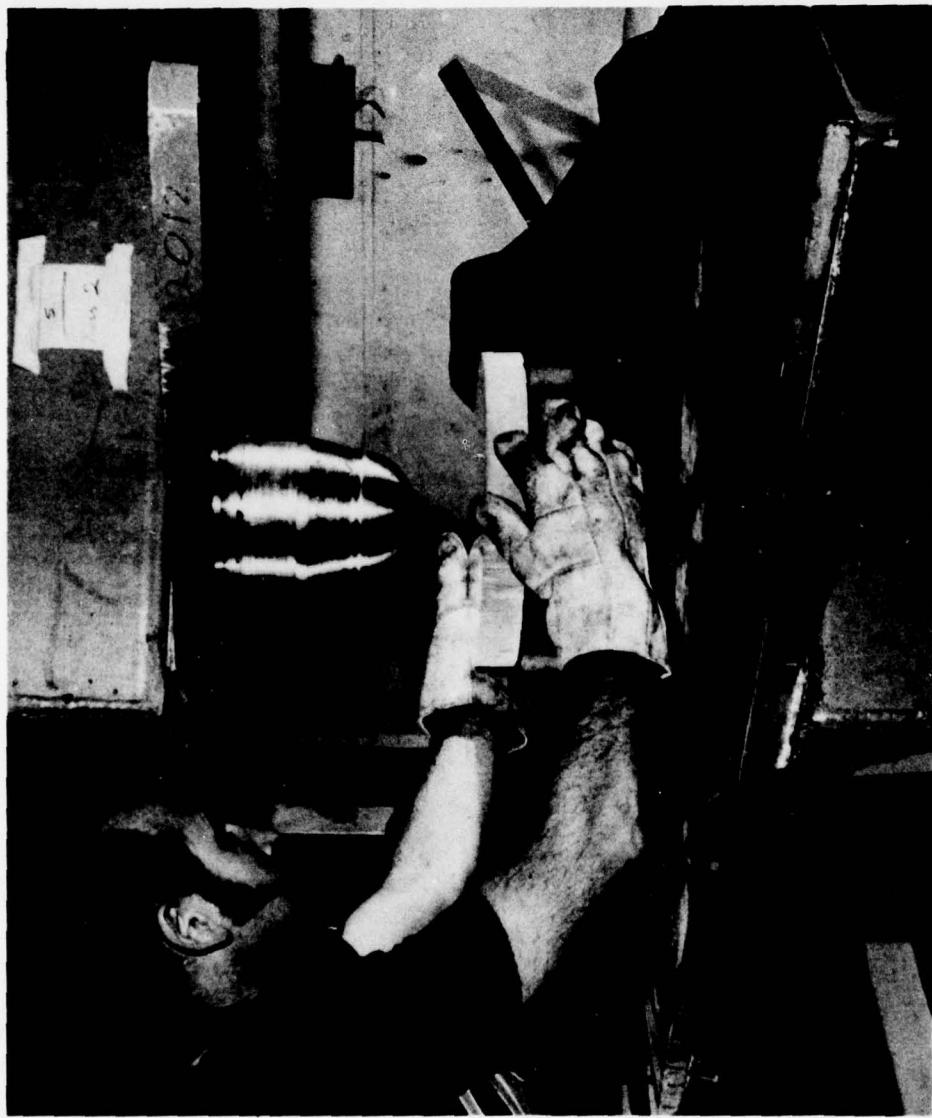
Figure 11.65. Typical setup for extrusion forming with male and female dies. An acrylic disc is preheated to thermoforming temperatures.
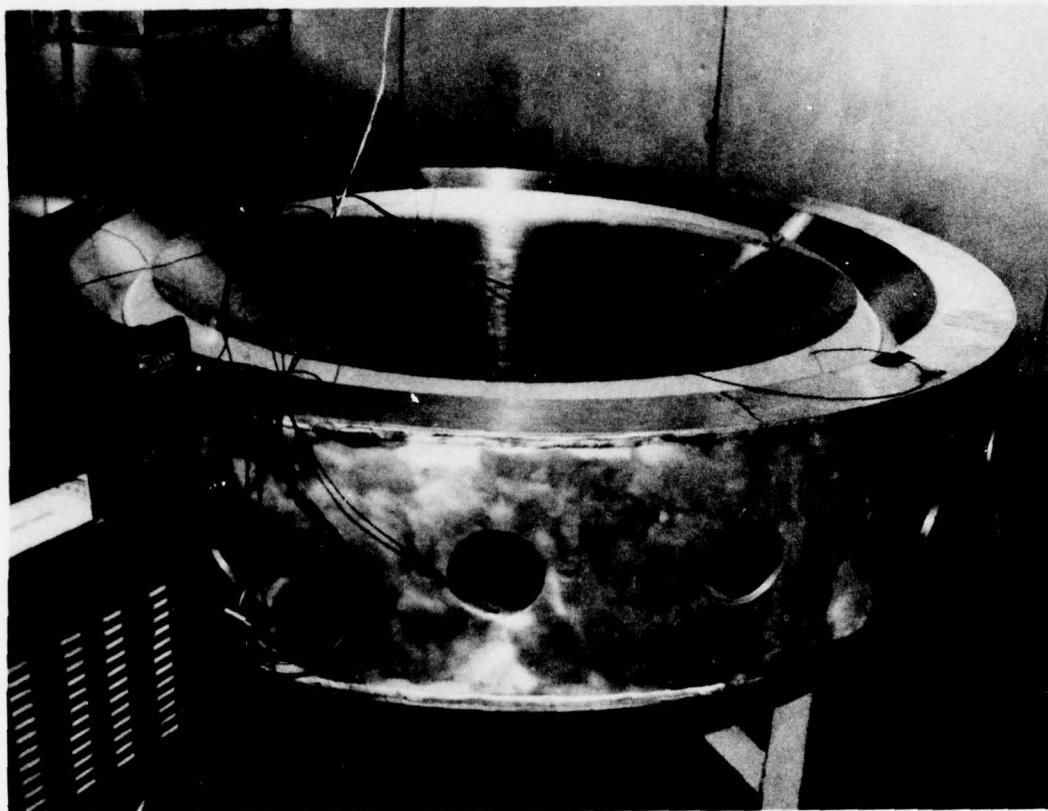
Figure 11.66. Vacuum forming in a female die using a disc and mold preheated to thermoforming temperatures.

Figure 11.67. The first, vacuum-formed, full-scale, spherical sector acrylic window for 3000-foot (914 meters) service. Window being inspected prior to hydrostatic testing by Dr. J.D. Stachiw, its designer.
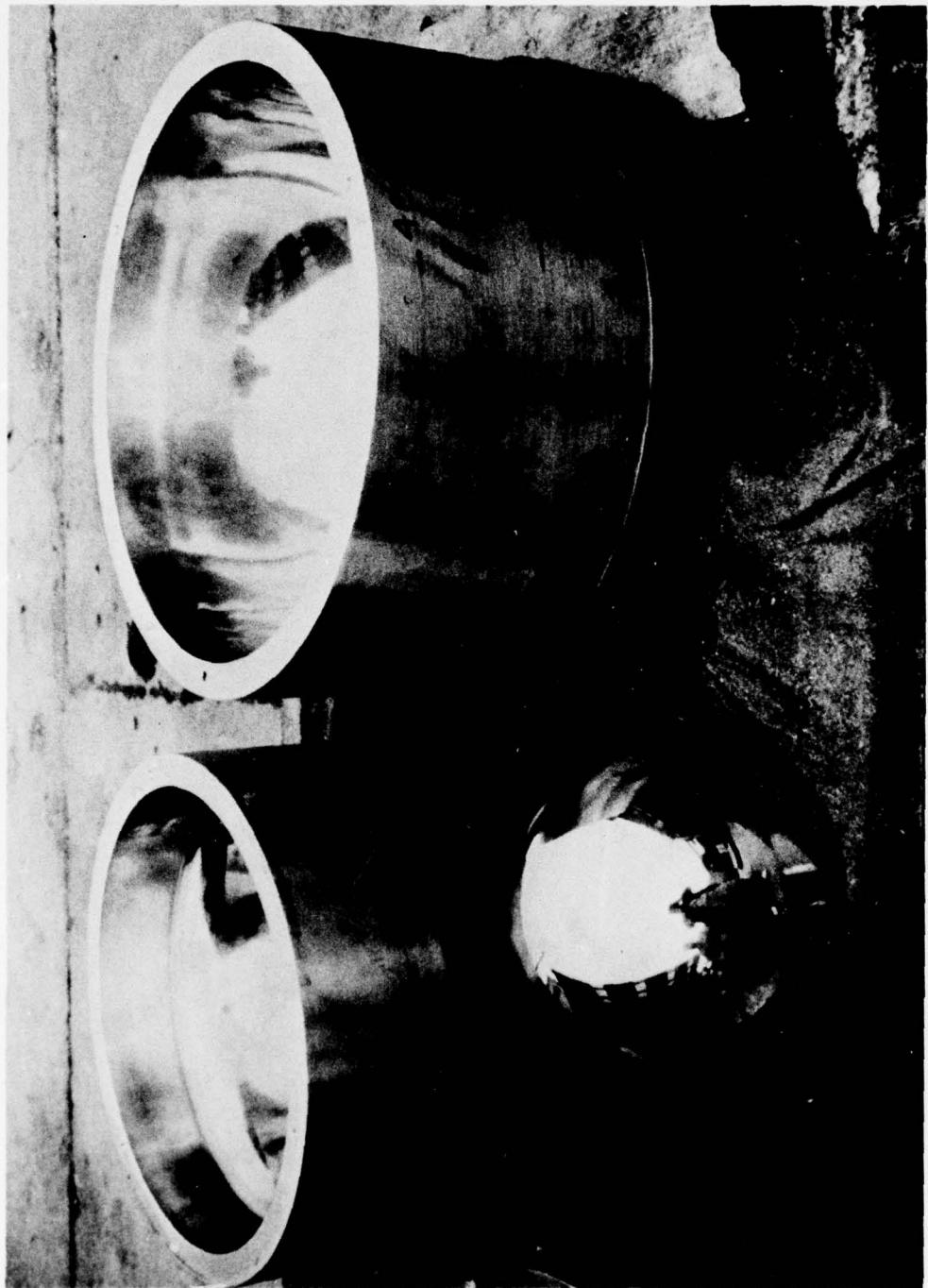
Figure 11.68. Typical mold assemblies for precision casting of spherical sectors. Sectors cast in such molds satisfy tight dimensional tolerances without further machining or sanding except on the bearing surface.

Figure 11.69. Precision-cast acrylic plastic hemisphere with D_i = 10 and t = 4 inches (10 centimeters) for 5000-pound-per-square-inch (34.4 megapascals) service.

Figure 11.70. Massive casting for an observation dome in the bow of the semisubmerged boat KAIMALINO of the Naval Undersea Center. $D_j = 65$ inches (165 centimeters); $t = 6.5$ inches (16.5 centimeters).
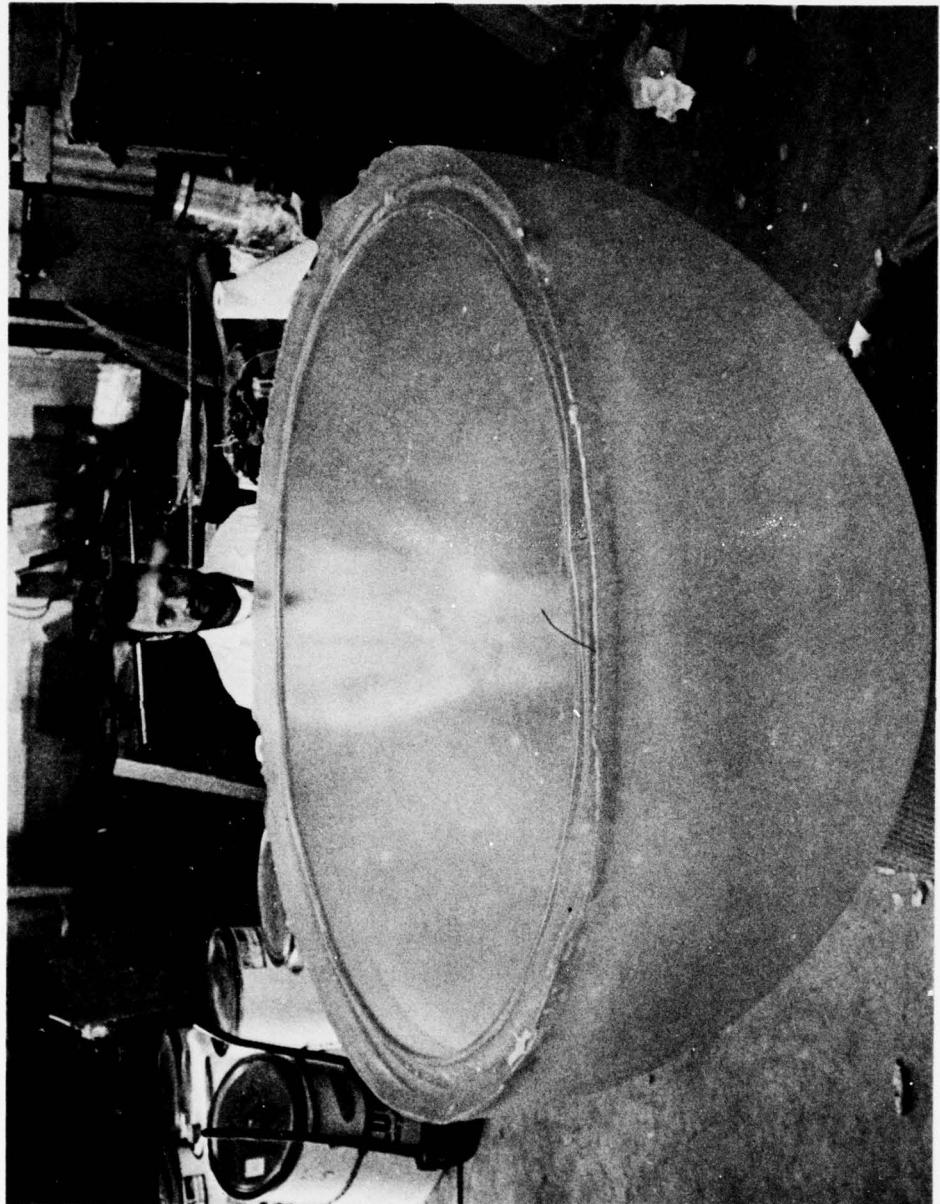
Figure 11.71. Massive castings for a pressure-resistant spherical hull. $D_i = 58$ inches (147 centimeters); $t = 4.25$ inches (10.8 centimeters).
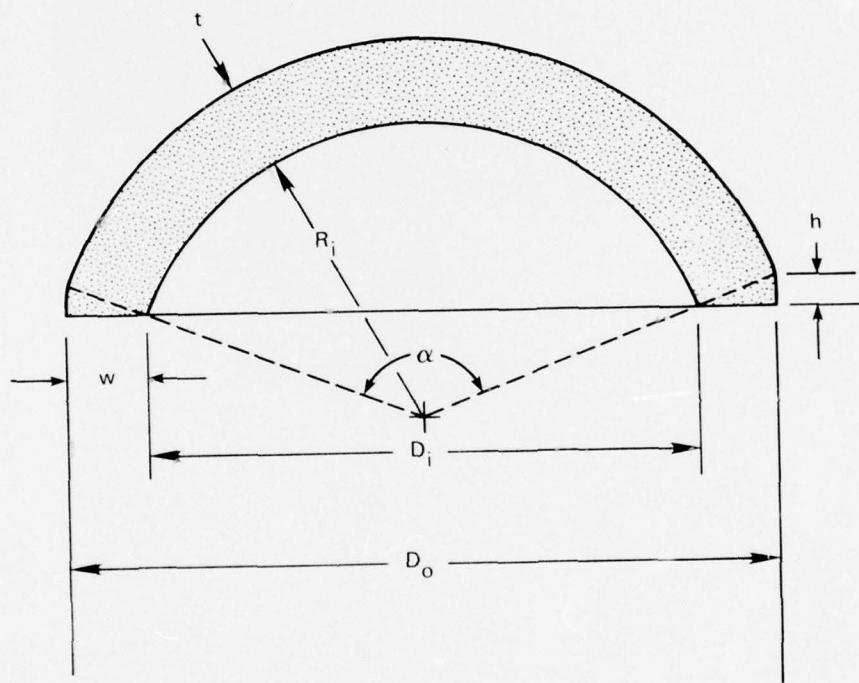
Figure 11.72. Definitions of terms for spherical sectors with square
edges. Note that this edge has two bearing surfaces. The plane
surface carries the vertical thrust while the cylindrical surface
carries the radial thrust.

Figure 11.73. Typical model-scale spherical sector with square edge and matching mounting flange used by Dr. J.D. Stachiw to establish structural performance criteria for these windows.
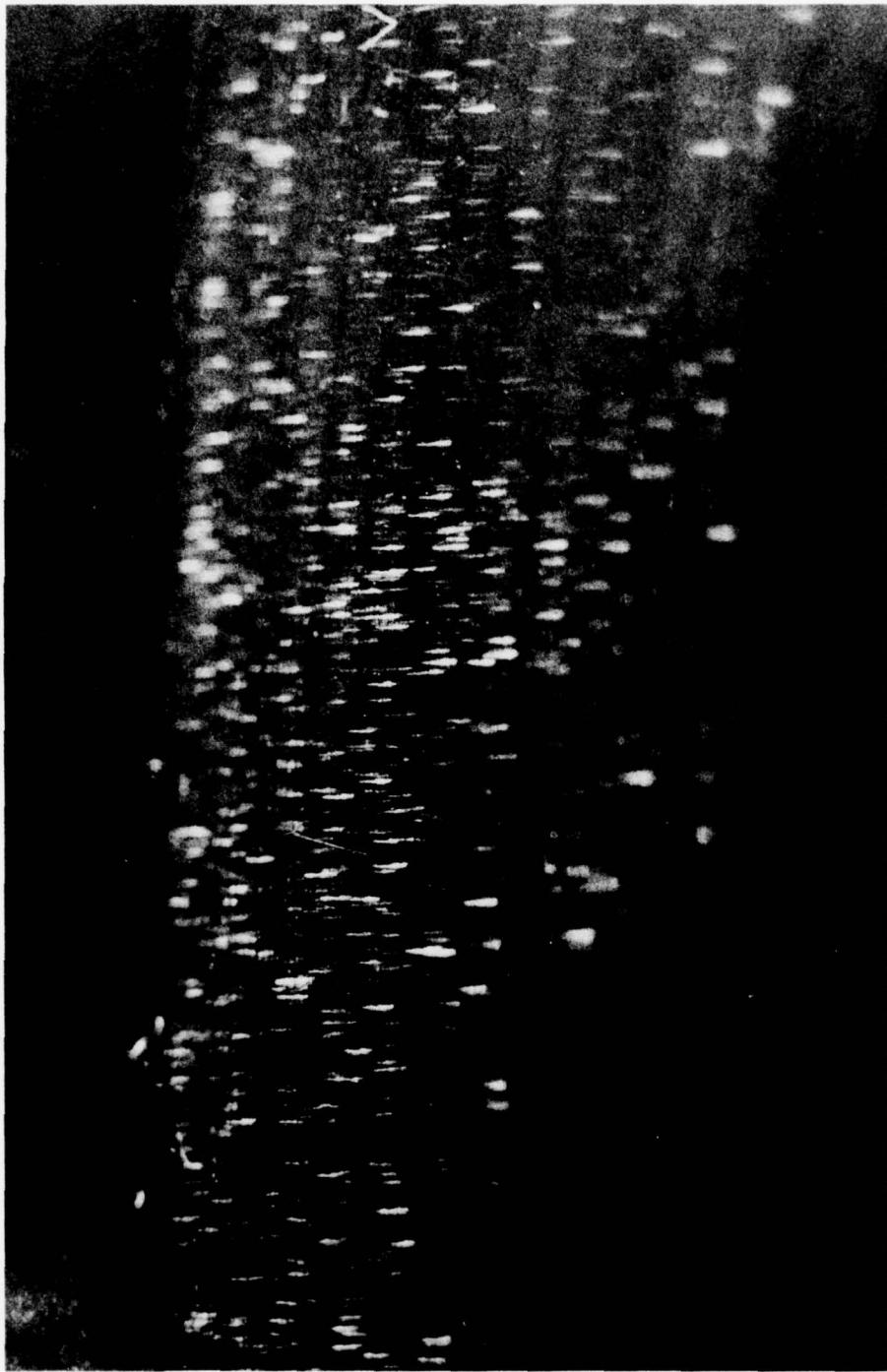
Figure 11.74. Conical seat on the mounting flange. The scratch marks are generated by the sliding of an acrylic plastic spherical sector with a conical bearing surface during repeated pressure cycling. $t/R_i = 0.16$; included angle = 120 degrees (2.09 radians); pressure = 1200 pounds per square inch (8.27 megapascals).

11-107

Figure 11.75. Square seat on the mounting flange. There are no scratch marks, although the acrylic plastic spherical sector with the square edge had the same dimensions and was subjected to the same pressure cycles as the spherical sector with conical bearing edge in figure 11.74.
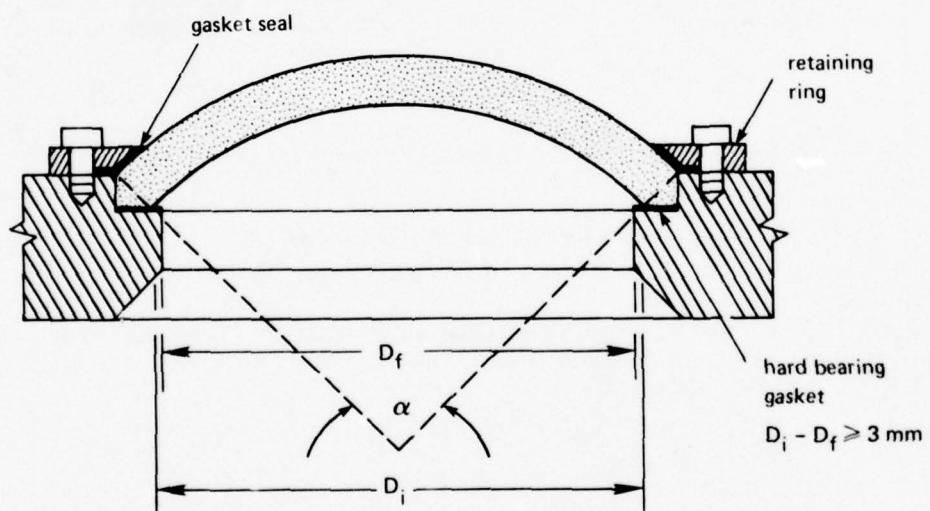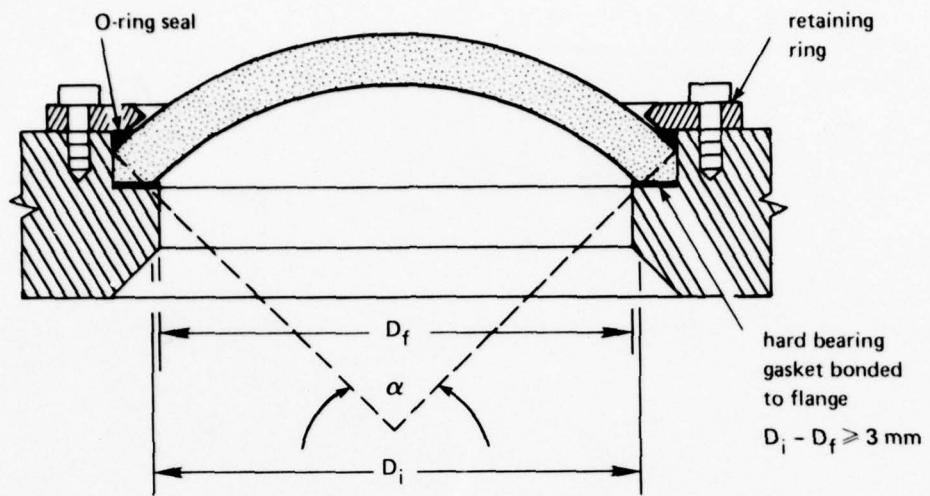
Figure 11.76. Sealing arrangements for spherical sectors with square edges (restrained edges).
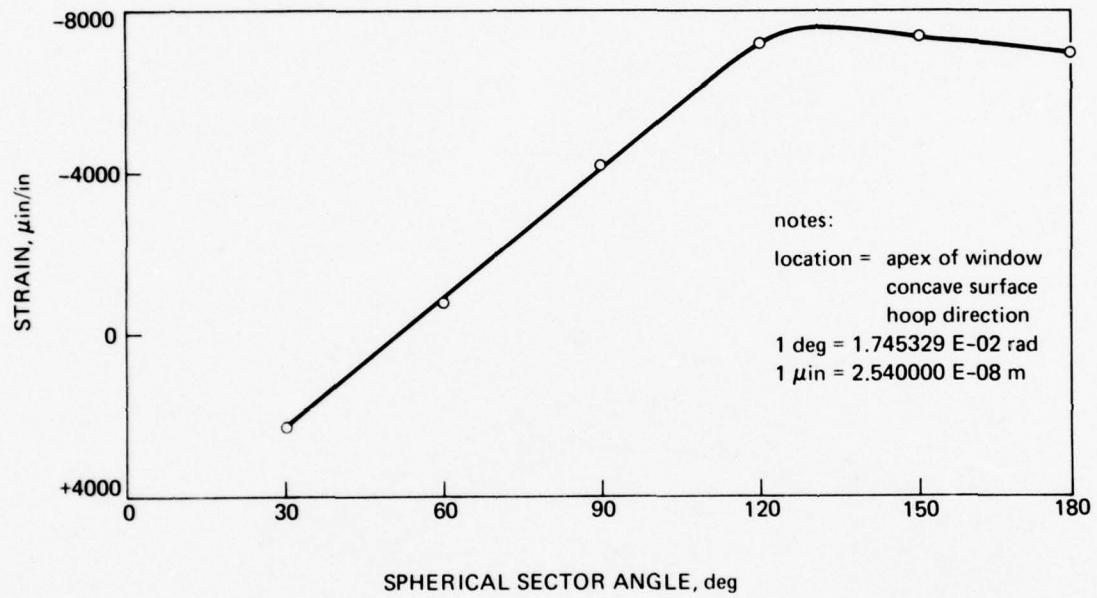
Figure 11.77. Hoop strain at the apex of concave surface for spherical sectors with square edges. Note that the magnitude of the strain is a function of the included angle. $t/R_i = 0.16$; $t = 70°F$ ($21°C$).

SPHERICAL SECTOR ANGLE, deg
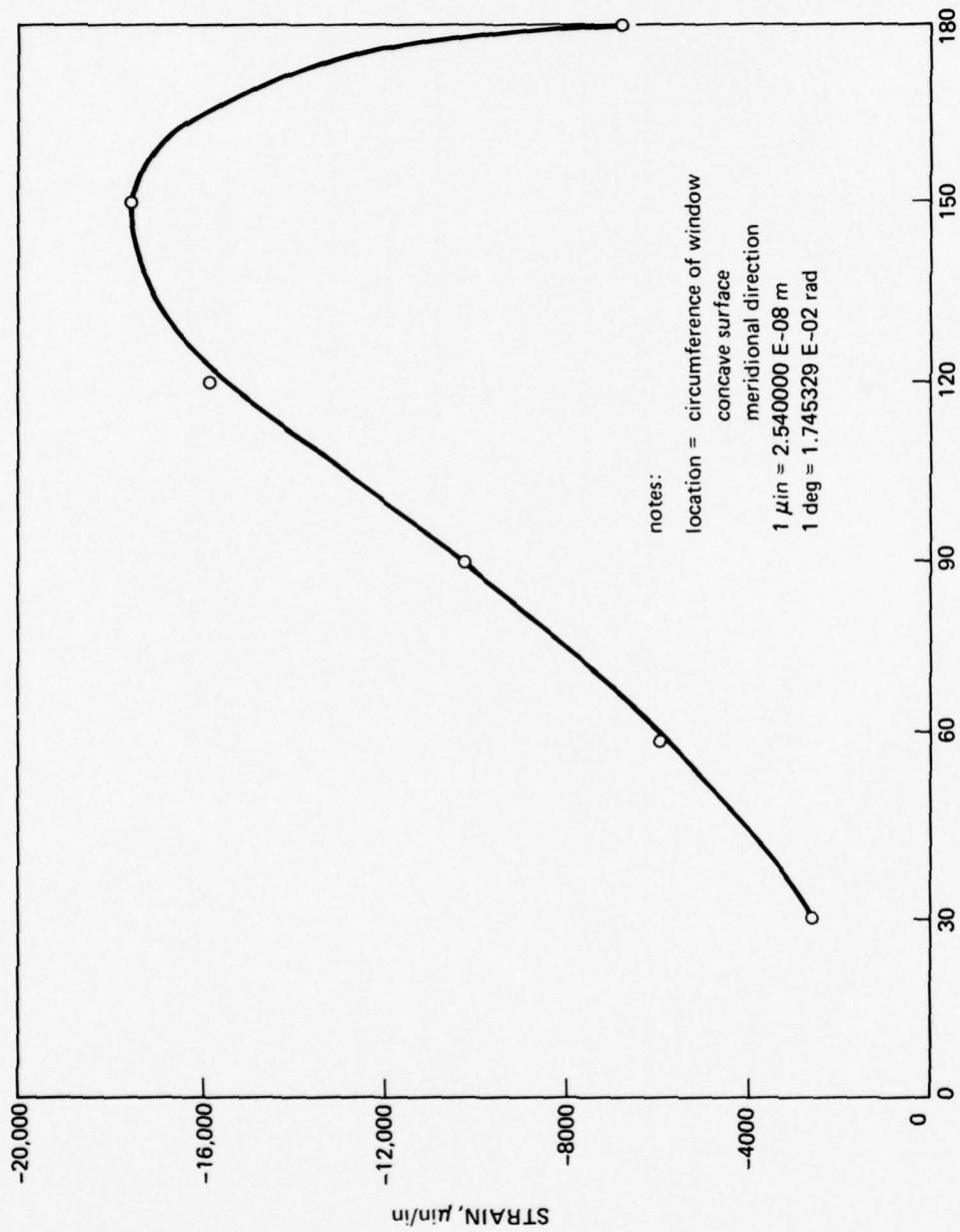
Figure 11.78. Meridional strain at the circumference of concave surface for spherical sectors with square edges. Note that the magnitude of the strain is a function of the included angle. $t/R_i = 0.16$; $t = 70° F (21°C)$.

notes:

location = circumference of window
concave surface
meridional direction

1 μin = 2.540000 E-08 m
1 deg = 1.745329 E-02 rad

STRAIN, μin/in
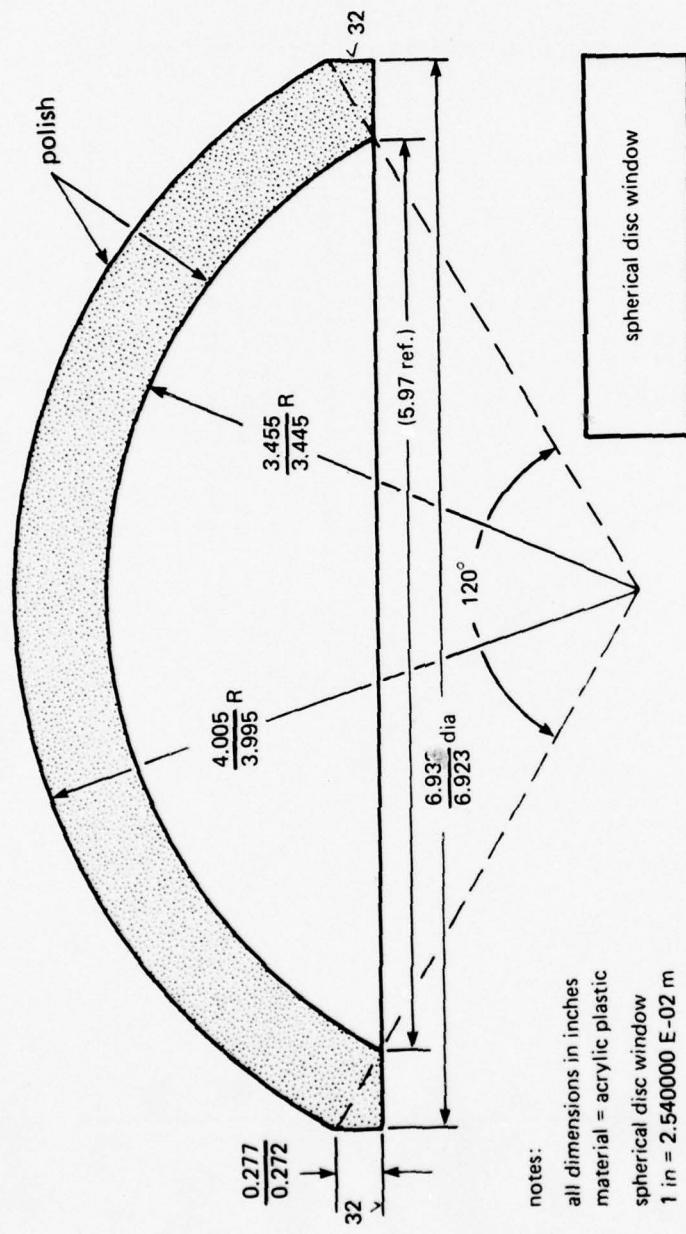
11-111

Figure 11.79. Dimensions of a typical model-scale window with square edges used in hydrostatic testing. $t/R_i = 0.16$; included angle = 120 degrees (2.09 radians).

polish

32

(5.97 ref.)

$\frac{3.455}{3.445}$ R

120°

$\frac{4.005}{3.995}$ R

$\frac{6.93}{6.923}$ dia

$\frac{0.277}{0.272}$

32

spherical disc window

notes:

all dimensions in inches

material = acrylic plastic

spherical disc window

1 in = 2.540000 E-02 m

notes:

all dimensions in inches
material = steel 80,000-psi (551 mPa) yield
spherical disc window flange
120-deg (2.09) configuration
1 in = 2.540000 E-02 m
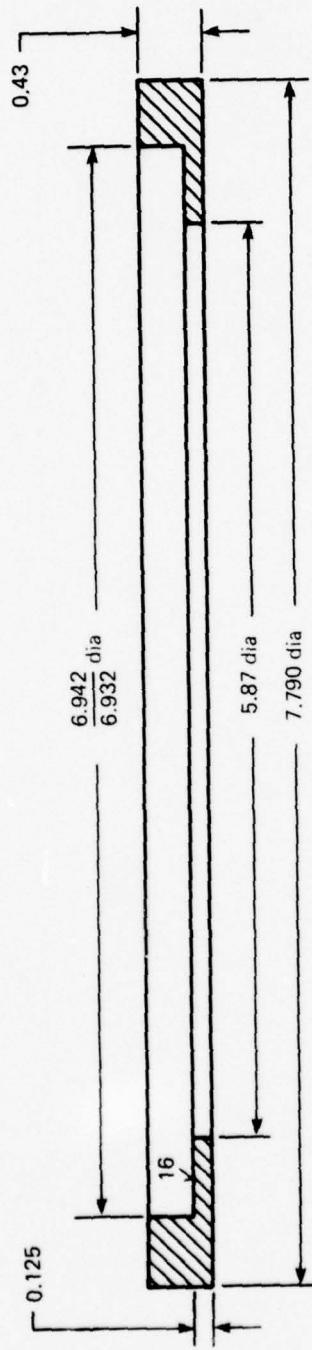
Figure 11.80. Dimensions of the mounting flange for the spherical window with square flange shown in figure 11.79.

11-113
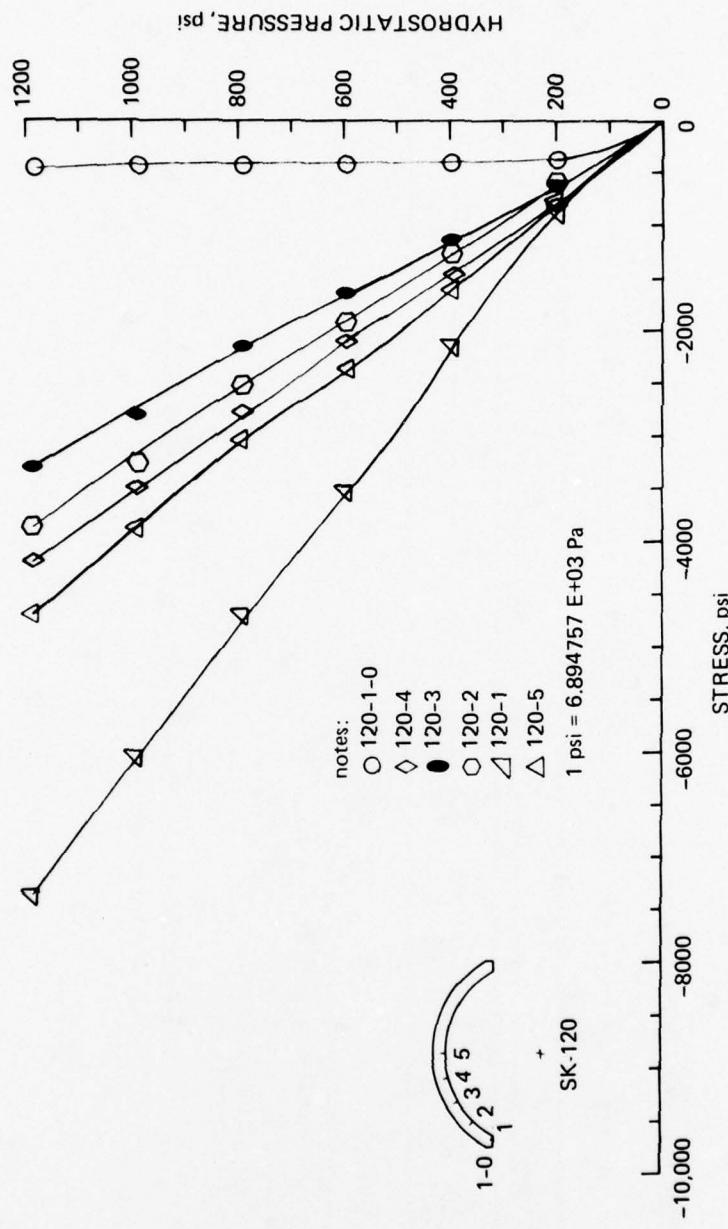
Figure 11.81. Distribution of meridional stresses on the spherical sector with square edge shown in figure 11.79.

11-114
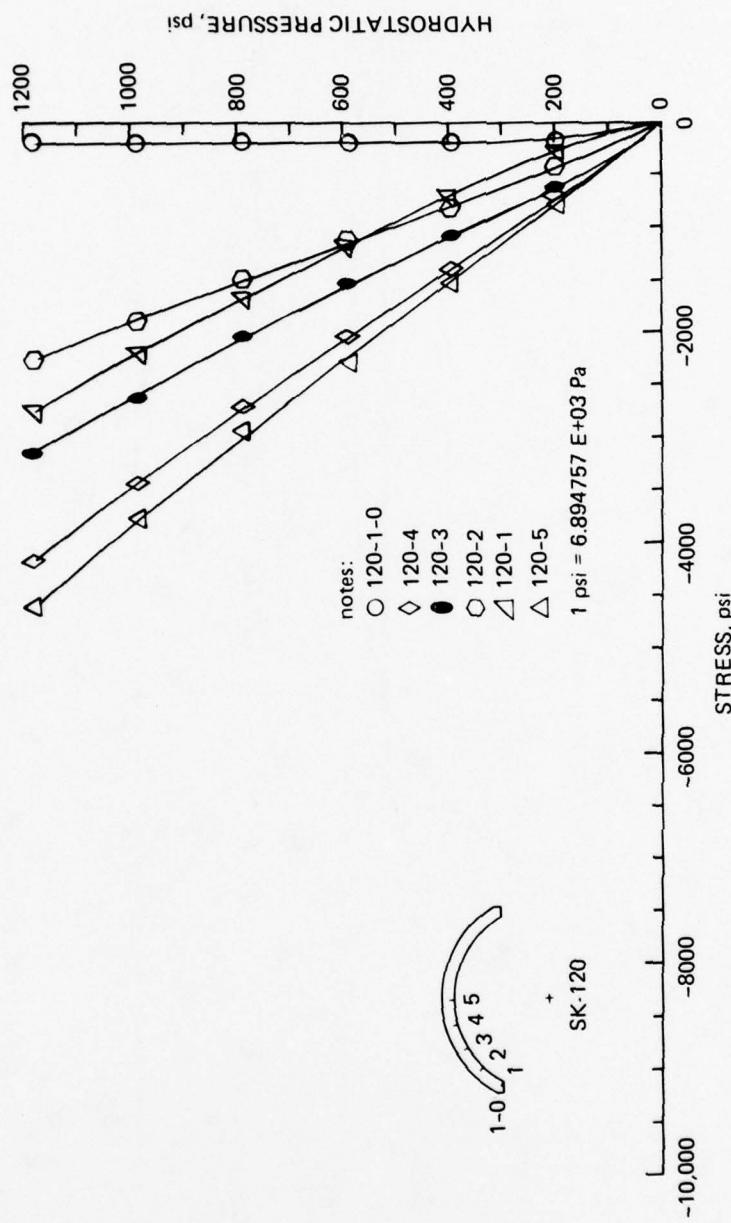
Figure 11.82. Distribution of hoop stresses on the spherical sector with square edge shown in figure 11.79.
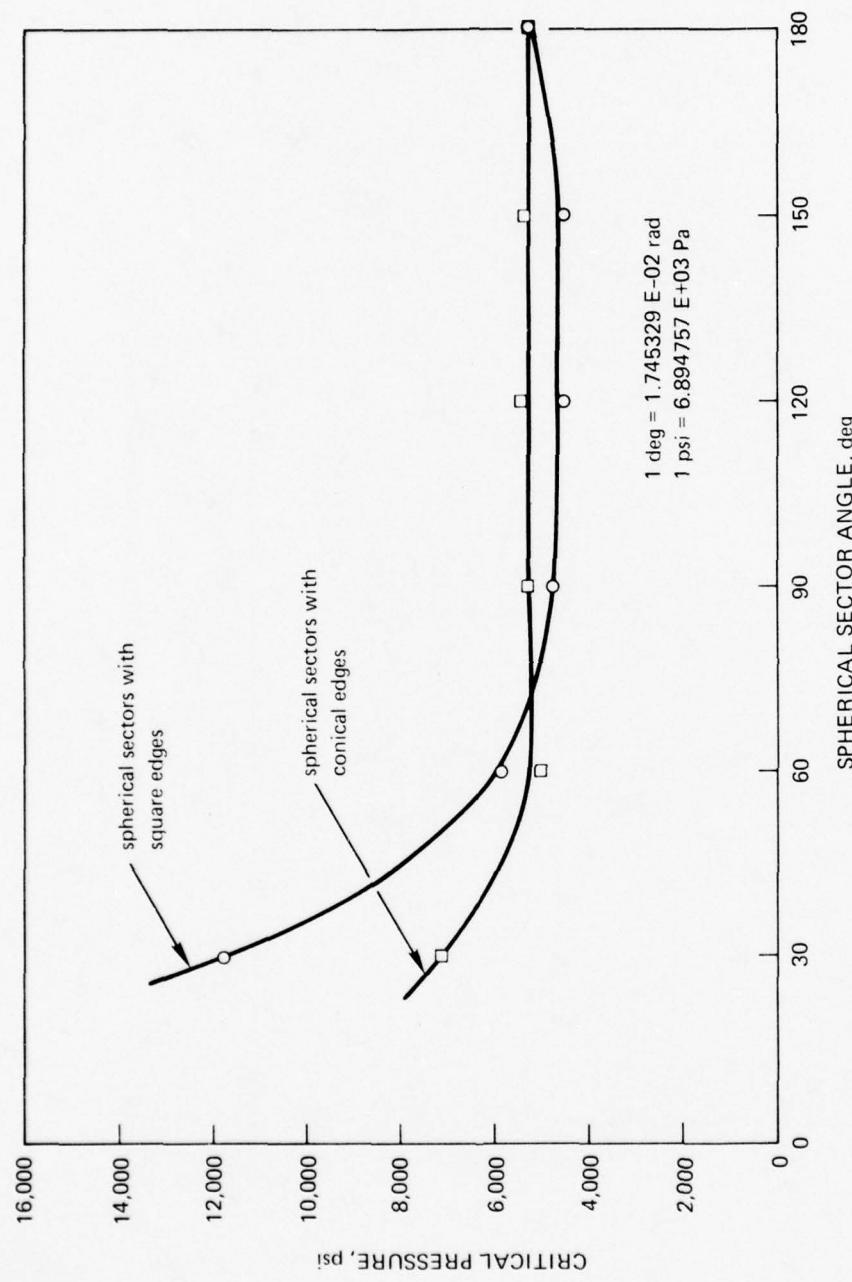
Figure 11.83. Comparison between the implosion pressures of sectors with conical bearing surfaces and sectors with square edges. $t/R_i = 0.16$; $T = 70°F$ ($21°C$).
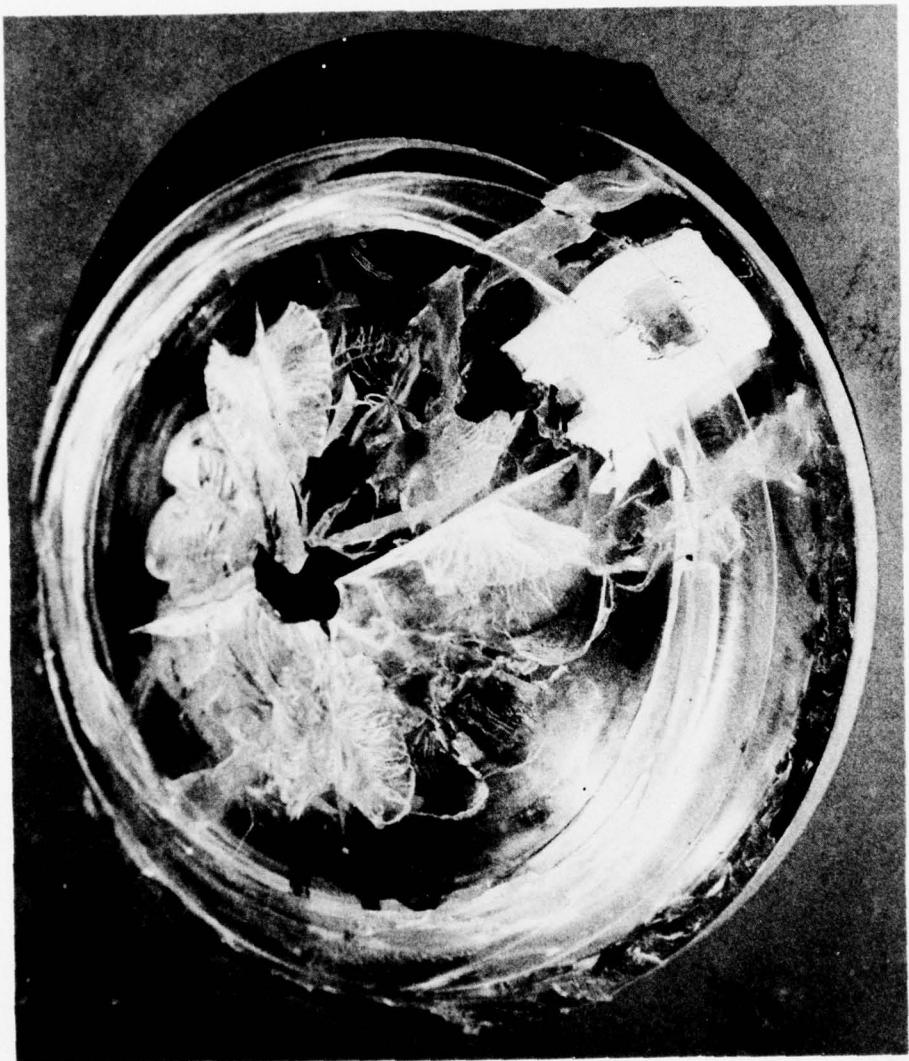
Figure 11.84. Typical plastic buckling failure observed on spherical sectors with square edges. $t/R_j = 0.16$; $T = 70°F$ ($21°C$); critical pressure = 4700 pounds per square inch (32.4 megapascals).

Figure 11.85. Typical model-scale test specimens with associated mounting flanges used for experimentally establishing the short-term critical pressure of spherical sectors with square edges.
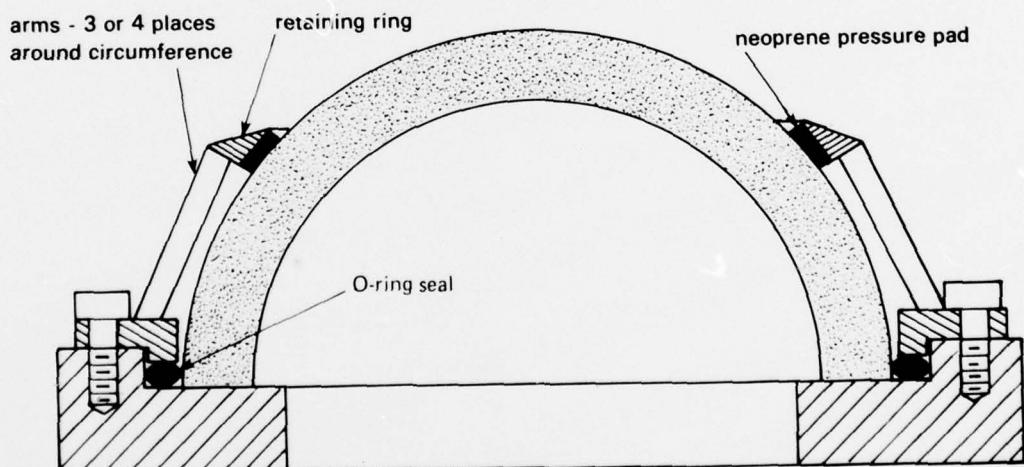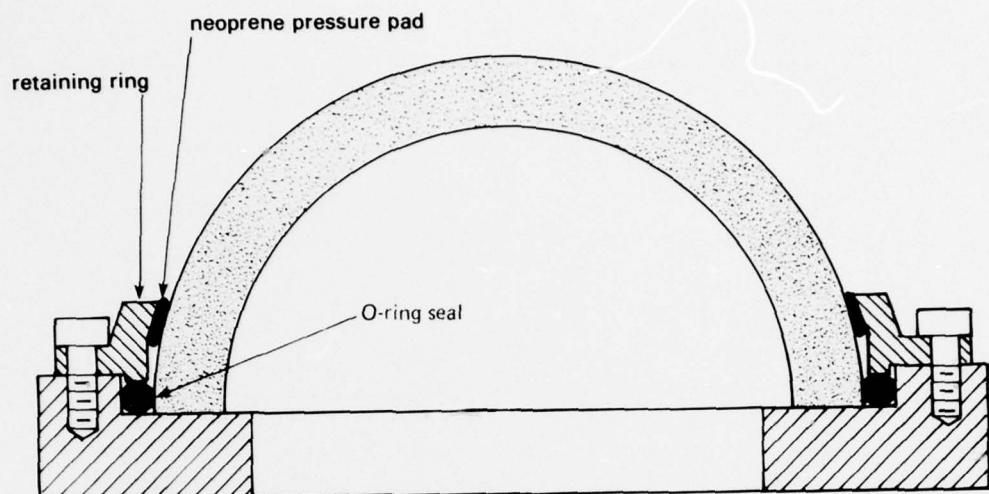
Figure 11.86. Attachment and sealing techniques for hemispheres.
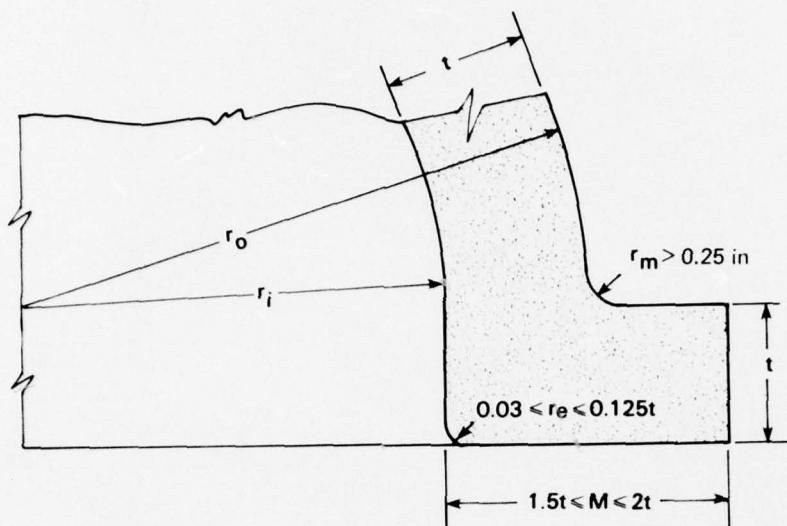
equatorial flange, type I

1 in = 2.540 000 E-02 m
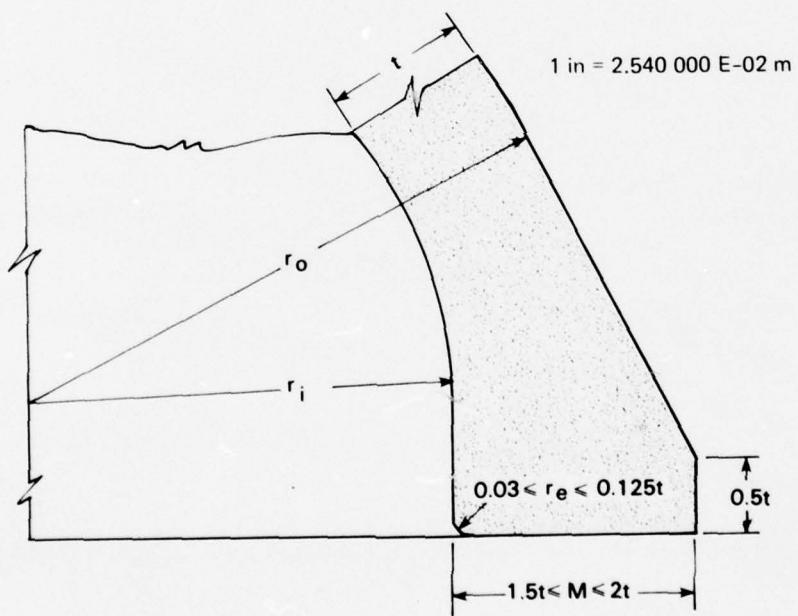
equatorial flange, type VI

Figure 11.87. Proper design for equatorial flanges on hemispheres.
Type VI flange is preferred for applications where internal pressures
may be encountered.

Figure 11.88. Results of fastening a flanged hemisphere to its mounting with screws passing through holes in the equatorial flange. Pressurization of the window causes the flange to separate from the window body.

11-121
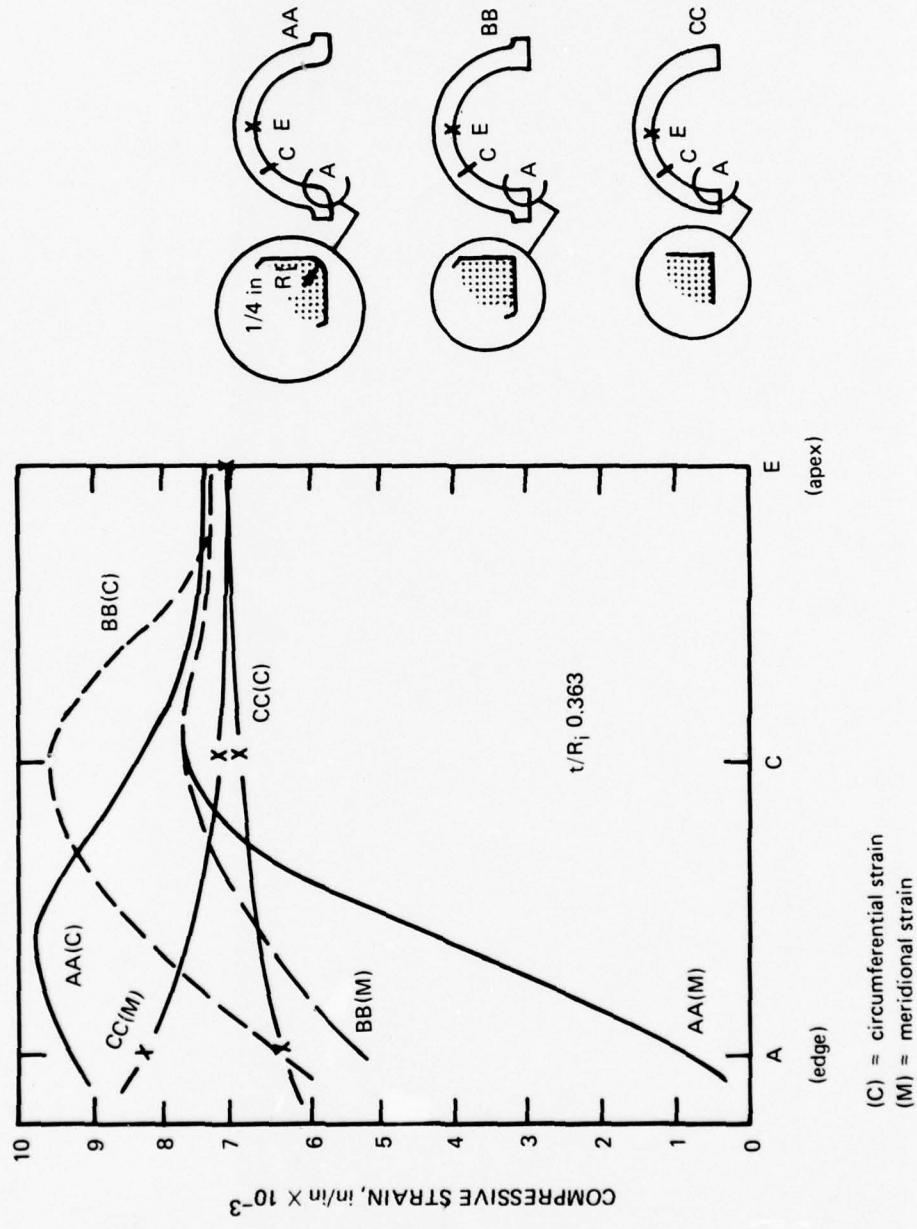
Figure 11.89. The effect of the equatorial-flange configuration on the distribution of strains on the concave surfaces of hemispheres with $t/R_i = 0.363$ under 2000-pounds per-square-inch (13.7 megapascals) hydrostatic loading at 75°F (24°C).

(C) = circumferential strain
(M) = meridional strain

11-122
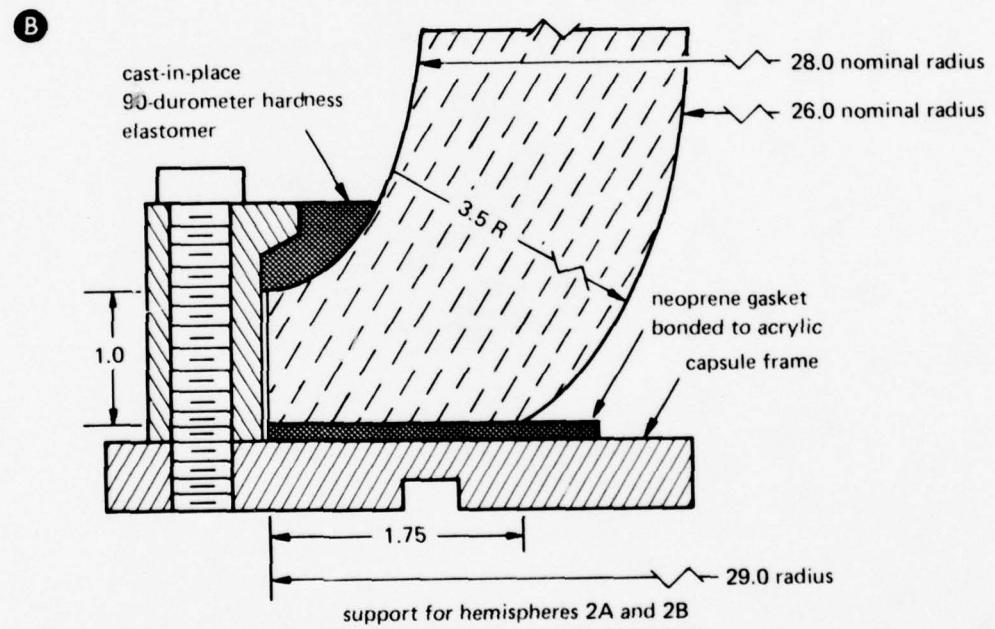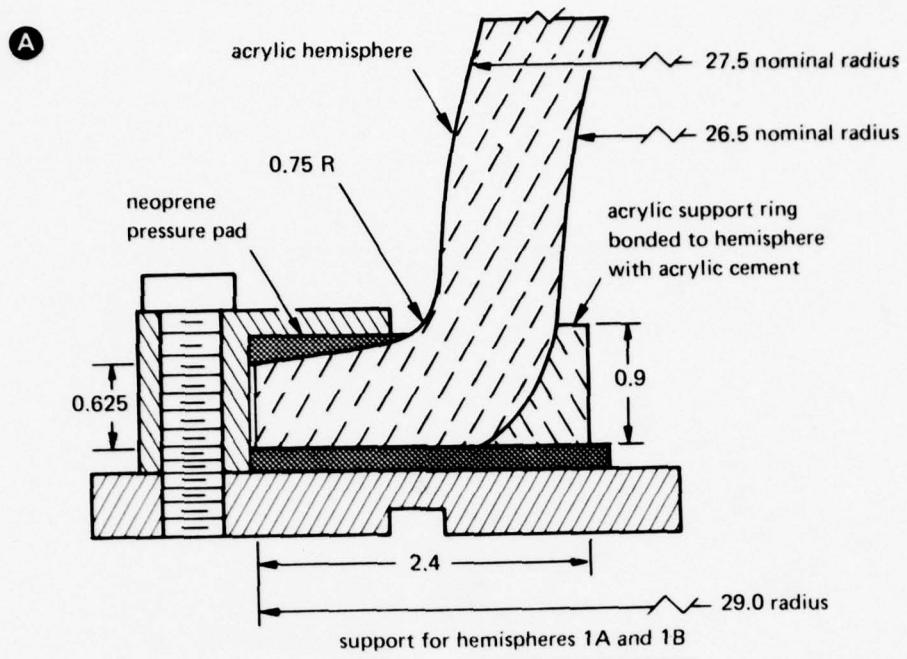
Figure 11.90. Proper and improper approaches to supporting the equatorial flange of a hemisphere thermoformed by free blowing of compressed gas. Hemisphere 2 has higher tensile stresses above the heel than does hemisphere 1 under the same pressure loading, even though it is 100 percent thicker. The acrylic heel back-up ring significantly decreases the bending moments in the transition zone between the heel and shell in hemisphere 1.

11-123

$$P_c = \sigma_y \frac{(1 + \alpha)(1 - \alpha^3)}{3\,\alpha^2} \,, \qquad \alpha = \frac{1}{1 + (t/R_i)}$$

$$Y_y = 18{,}000 \text{ psi}$$

P_c is the pressure at which complete plasticity of the wall occurs, assuming the simplified stress/strain diagram

$$t_C^{\circ} = (t_F^{\circ} - 32)/1.8$$

⊕ actual point

notes:

⊕ NUC TP410 test of flangeless window with sharp seat corner (single window, 70°F) held at 20,000 psi for 1 hr without implosion

⊡ Present test of flanged windows with rounded seat corner (average of five, 70-75°F)

△ NCEL R631 test of flangeless window with sharp seat corner (average of five, 69-70°F)

⊙ NUC TP355, test of flanged windows with sharp seat corner (average of three, 73-75°F)

HYDROSTATIC PRESSURE, psi × 10³

t/R$_i$

1 psi = 6.894757 E+03 Pa

$$t_C^{\circ} = (t_F^{\circ} - 32)/1.8$$

Figure 11.91. Comparison of critical pressures for flanged and flangeless hemispheres under short-term pressure loading. Lamé's equation can be used as a conservative lower boundary for $t/R_i > 0.1$.

11-124

Lamé's equation for hollow spheres:

$$\frac{\epsilon_t}{P} = \frac{\Delta R_i}{R_i P} = \frac{1-\mu}{E}\left\{\frac{1.5}{1-[1/(1+t/R_i)]^3}\right\} \qquad \begin{array}{l}\mu = 0.4 \\ E = 400{,}000 \text{ psi}\end{array}$$

ϵ_t = tangential strain on interior face, P = external pressure,
R_i = internal radius, ΔR_i = radial displacement on interior face

notes:

▣ ϵ_t/P measured at apex of type I and VI windows in 68-75°F temperature range (average of 18 tests)

⊠ $\Delta R_i/R_i$ measured at apex of window W at 72°F

△ ϵ_t/P measured at apex of windows without a flange; NUC TP410 (average of nine tests in 70-75°F temperature range)

⊙ $\Delta R_i/R_i$ measured at apex of windows without a flange; NCEL R-631 (average of five tests at 70°F temperature)

$$t_C^\circ = (t_F^\circ - 32)/1.8$$

1 psi = 6.894757 E+03 Pa

ΔR_i of apex

ϵ_t

detail of apex

R_i

R_i

type I flanged window

UNIT STRAIN, ϵ_t/P and $\Delta R_i/R_i P$, $in^2/16 \times 10^{-3}$

t/R_i

Figure 11.92. Comparison of measured and calculated strains for flanged and flangeless windows under short-term pressure loading. Strains measured at the apex of the interior surface in room temperature environment.

11-125
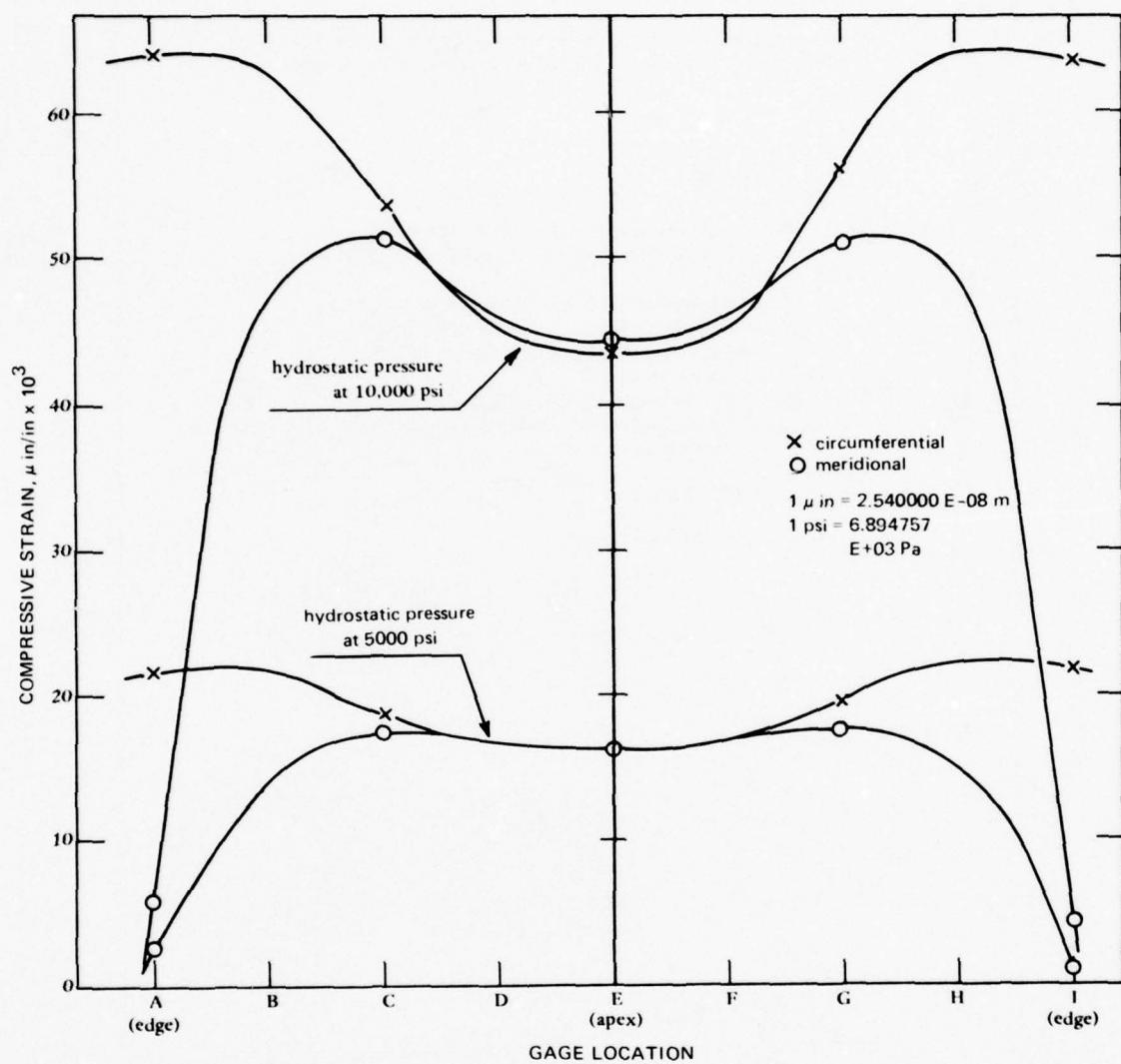
Figure 11.93. Distribution of strains on the interior face of a flanged hemisphere. Type I is under short-term hydrostatic loading. $t/R_i = 0.363$; $T = 75°F (24°C)$. Note that the effect of the flange on distribution of strains in the window increases with the magnitude of hydrostatic loading.
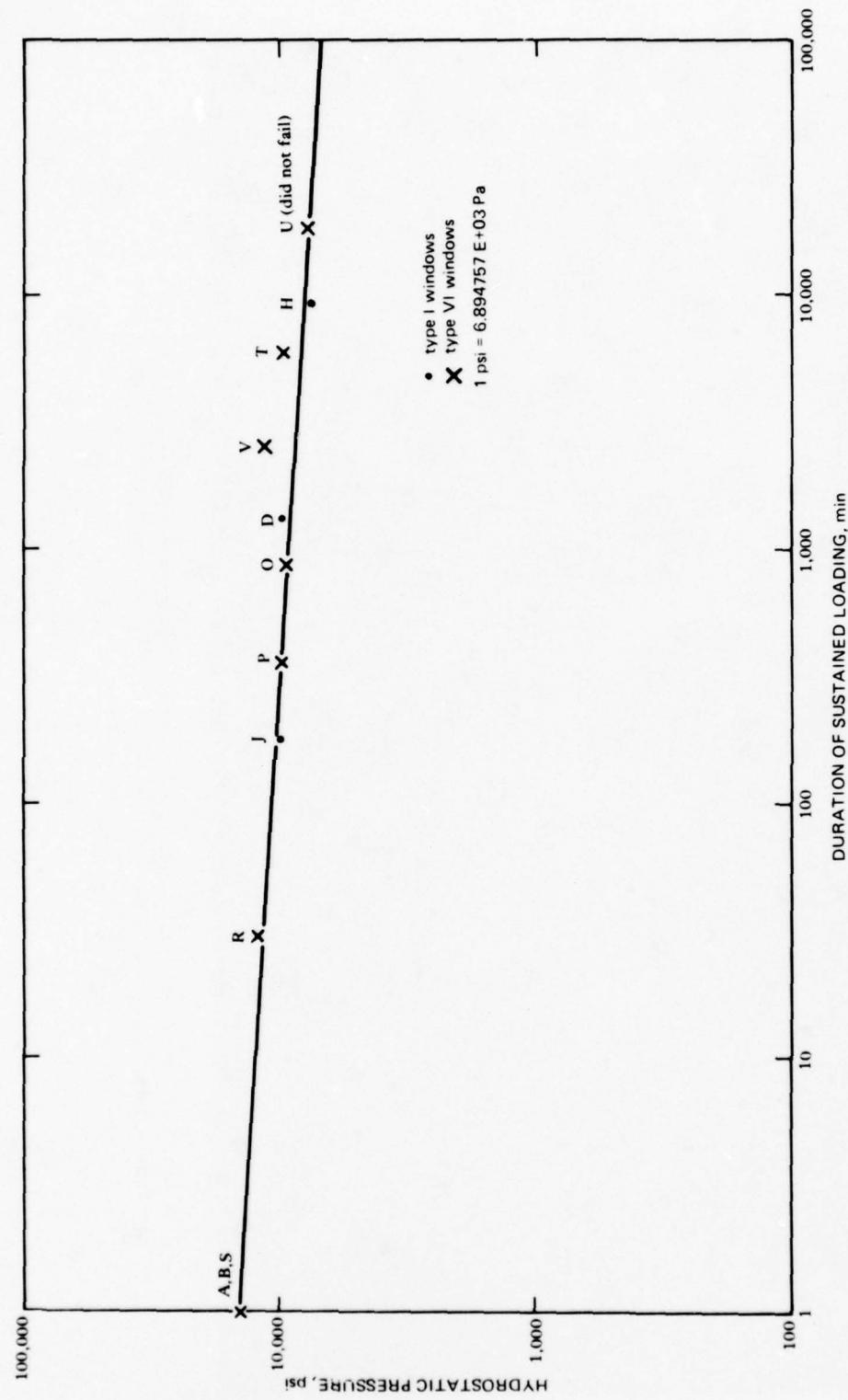
Figure 11.94. Static fatigue of flanged hemispheres types I and VI with $t/R_i = 0.363$ under long-term hydrostatic loading at room temperature. Note that the data fall on a straight line similar to points generated by flangeless spherical sectors in figure 11.31.

Figure 11.95. Separation of equatorial flange from the body of the window, a typical result of static or cyclic fatigue in flanged hemispheres. $t/R_i = 0.363$; $T = 70°F$ ($21°C$); pressure = 8000 pounds per square inch (55.1 megapascals); loading duration = 18,700 minutes.
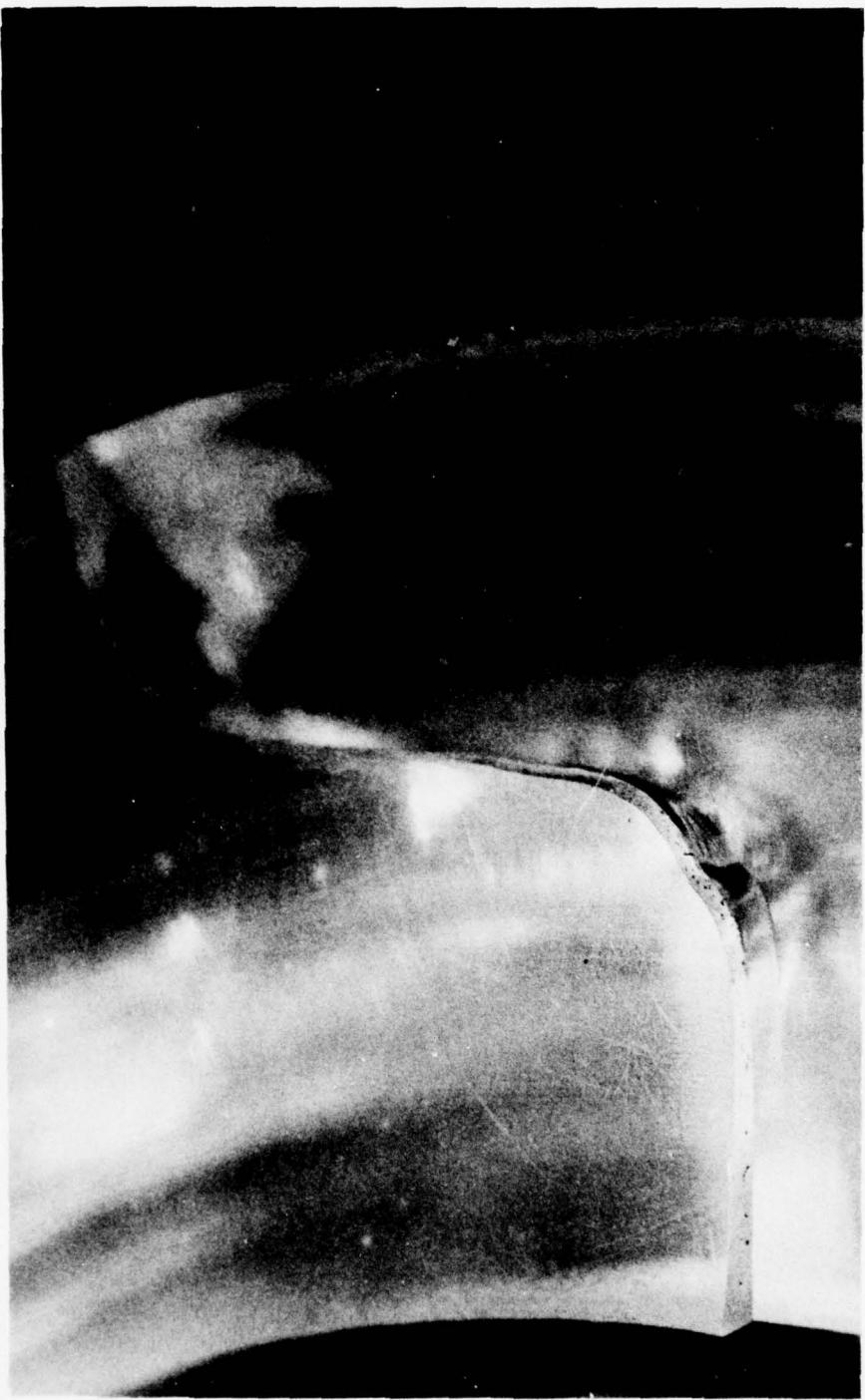
Figure 11.96. Typical crack in equatorial flange initiated on the concave surface of the flanged window by static or cyclic fatigue. $t/R_i = 0.363$, $T = 70°F$ (21°C).
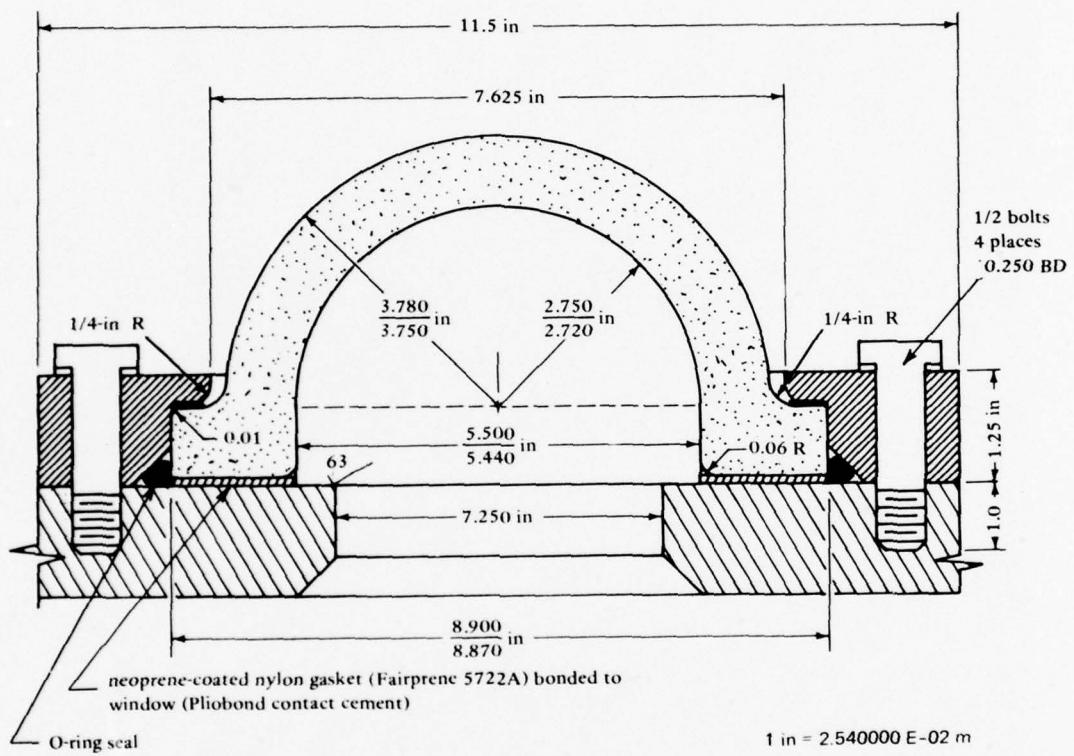
Figure 11.97. Mounting and sealing arrangement for a hemispherical
window with type I equatorial flange.

11-130
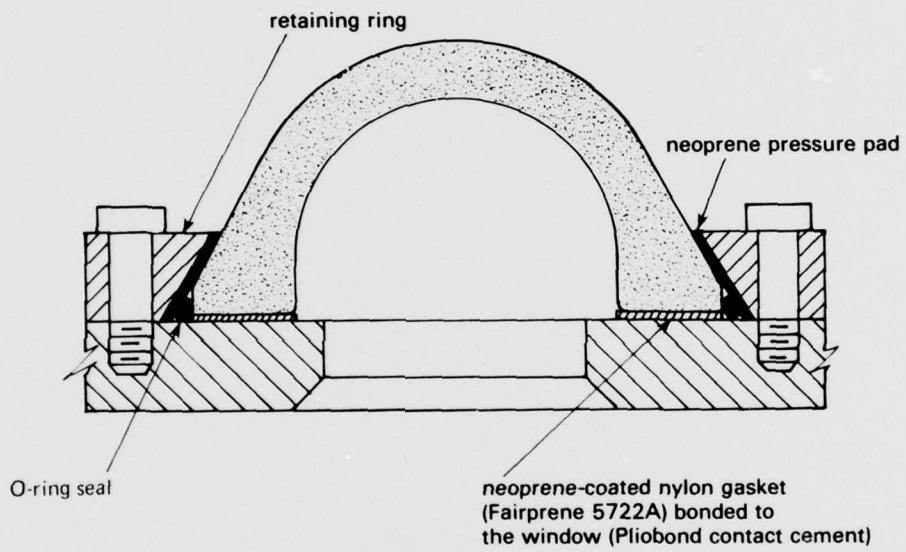
Figure 11.98. Mounting and sealing arrangement for a hemispherical window with type VI equatorial flange. This mounting and sealing arrangement is preferred for applications where some internal pressure may be encountered.
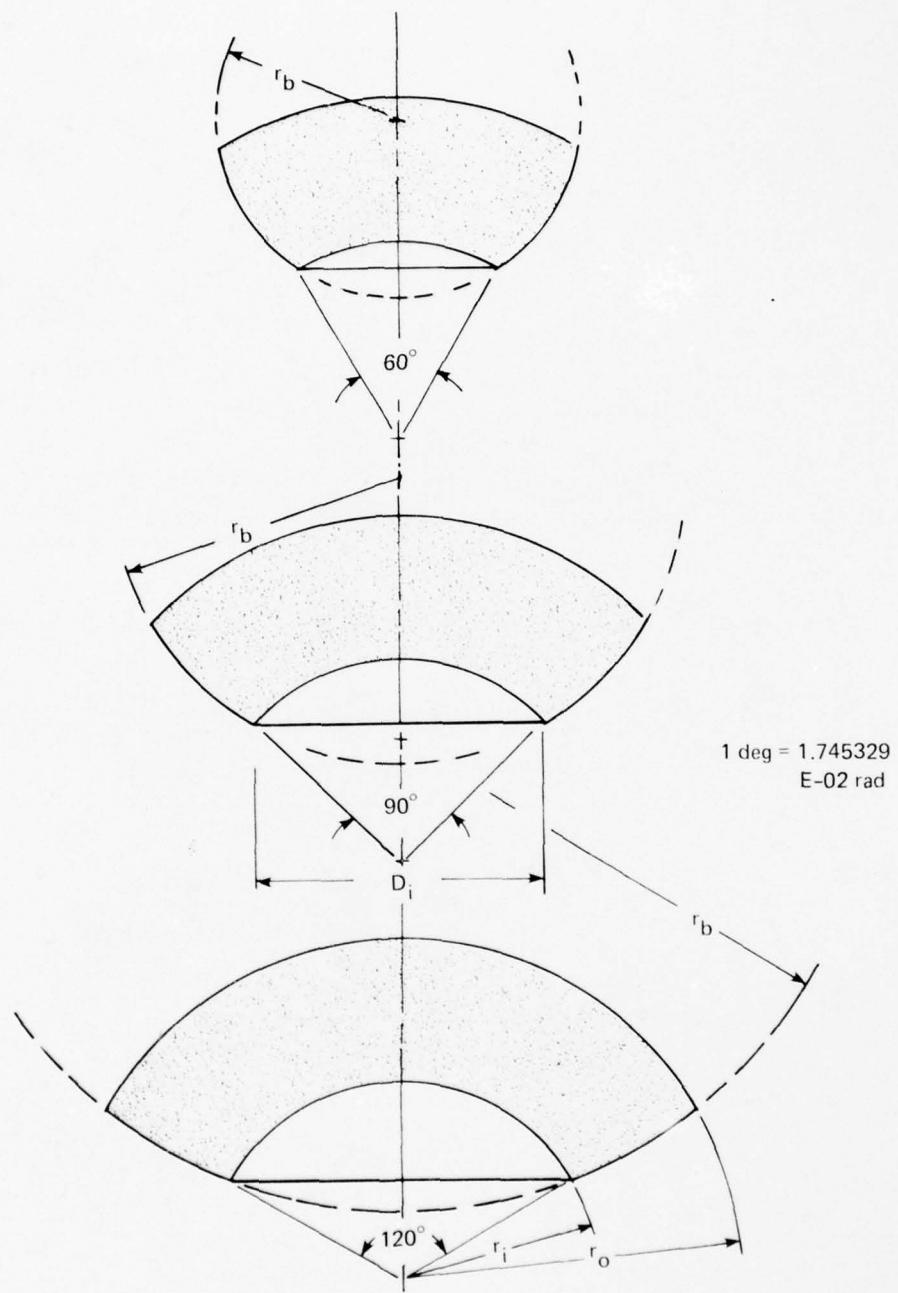
Figure 11.99. Spherical sectors with spherical bearing surfaces. Note that the size of this configuration can be also described with D_i, t, α, and R_i as in spherical sectors with conical bearing surfaces.

$1 \deg = 1.745329$ E–02 rad
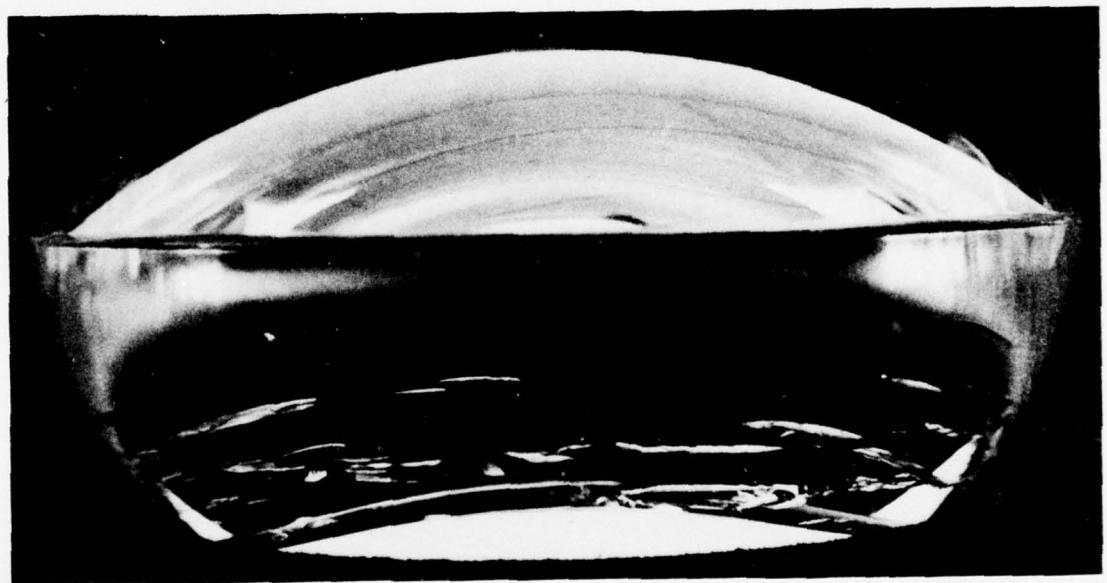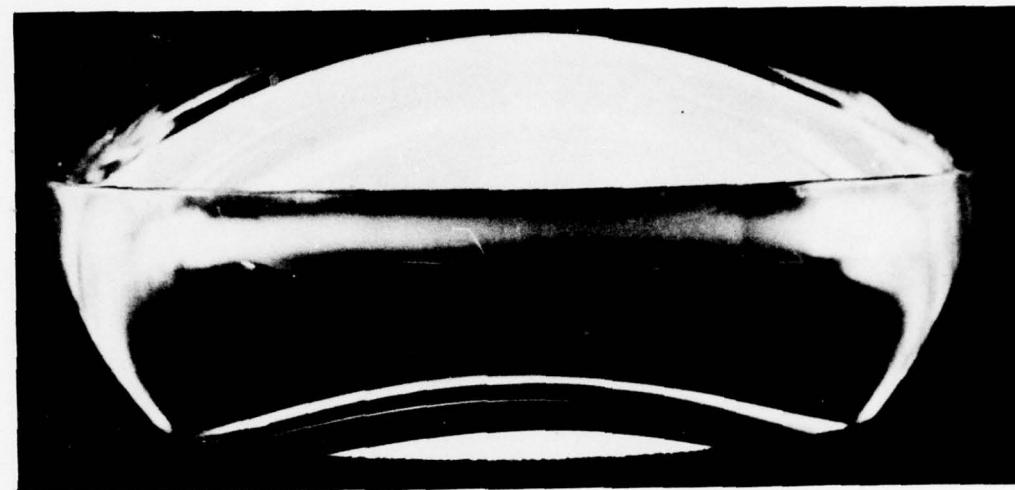
Figure 11.100. Cracks in the spherical bearing surface generated by cyclic fatigue under repeated pressurizations. Note that the appearance, distribution, and location of the cracks are similar to those found in spherical sectors with conical bearing surfaces.
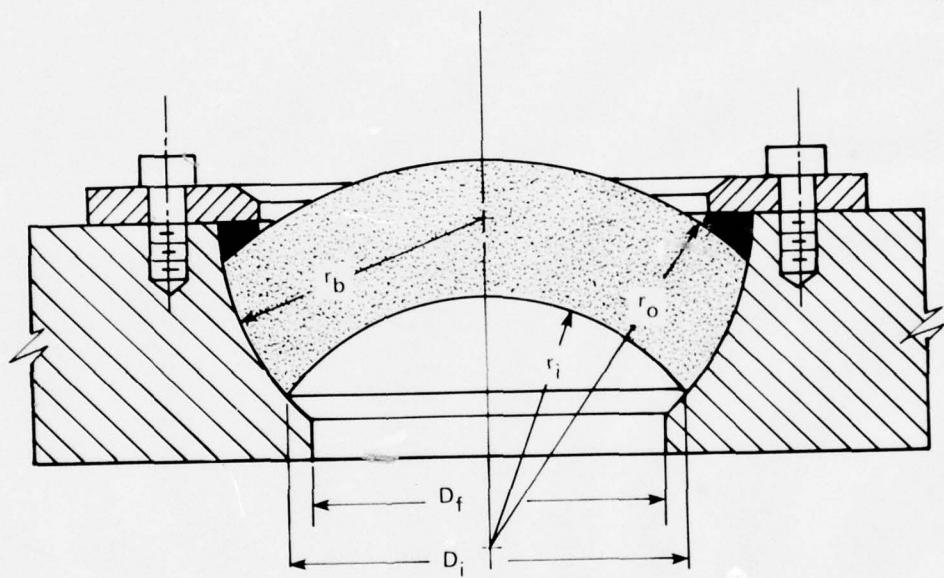
Figure 11.101. Mounting and sealing arrangement for a spherical
sector window with spherical bearing surface.
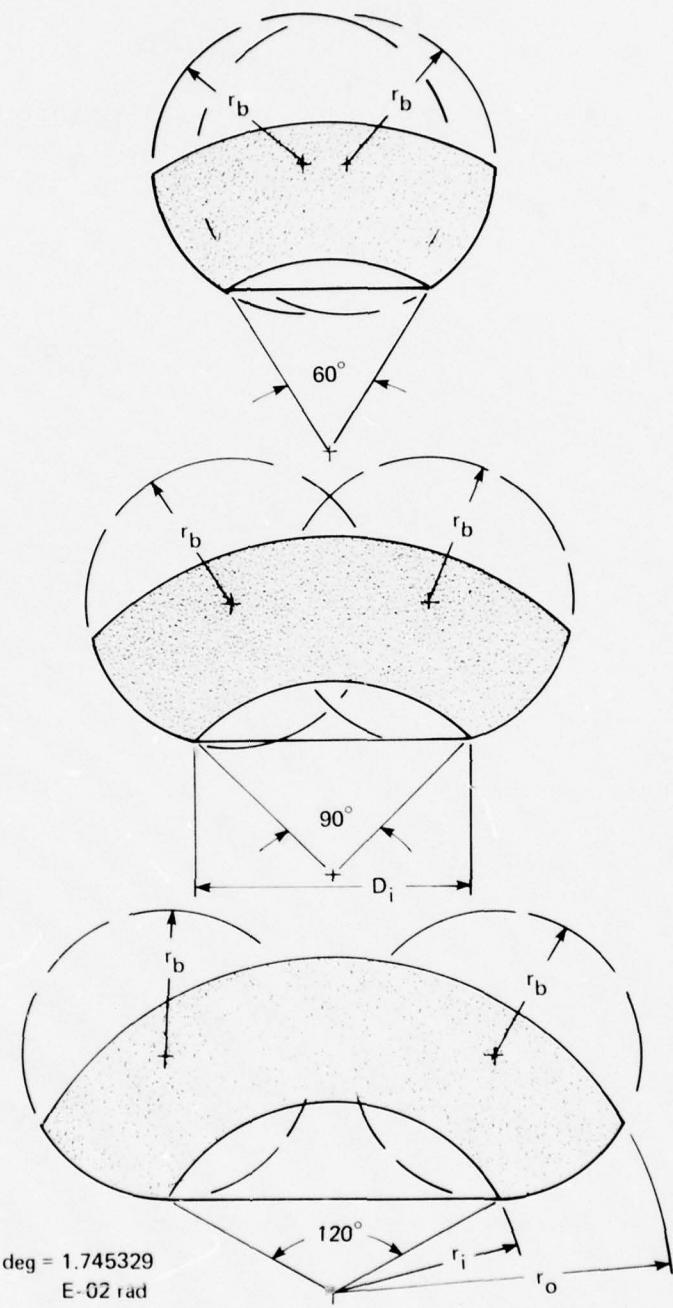
Figure 11.102. Spherical sector windows with toroidal bearing surfaces.

1 deg = 1.745329 E-02 rad

Figure 11.103. Hemispherical glass window with toroidal bearing surface mounted in a radially compliant titanium ring.
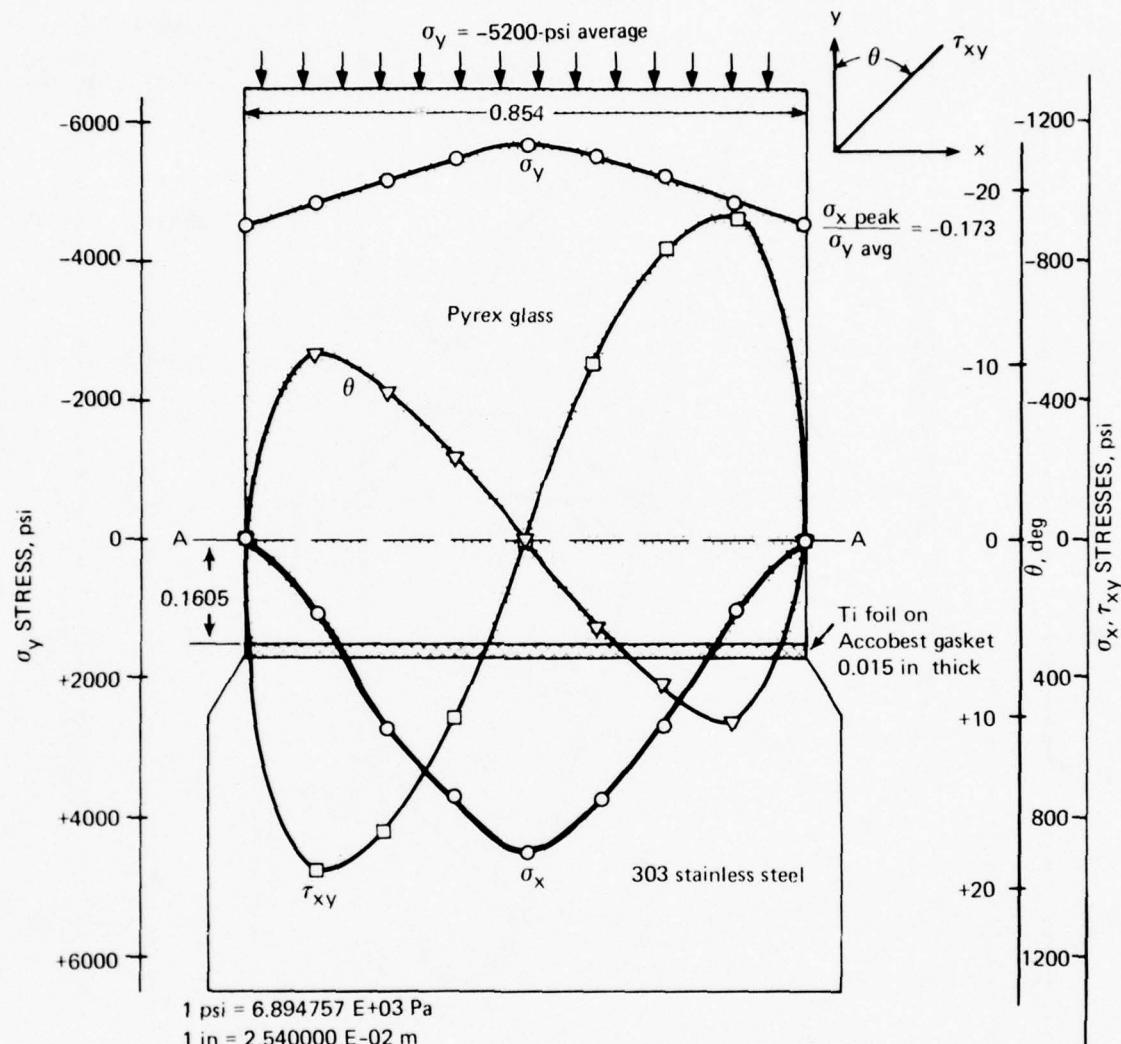
Figure 11.104. Simulated distribution of stresses across the wall of a hemisphere supported by a plane bearing surface under uniaxial compressive loading. Note that the σ_x stress is high and positive. Presence of this tensile transverse stress in the bearing surface will initiate cracks that are oriented parallel to the direction of load application.

11-137
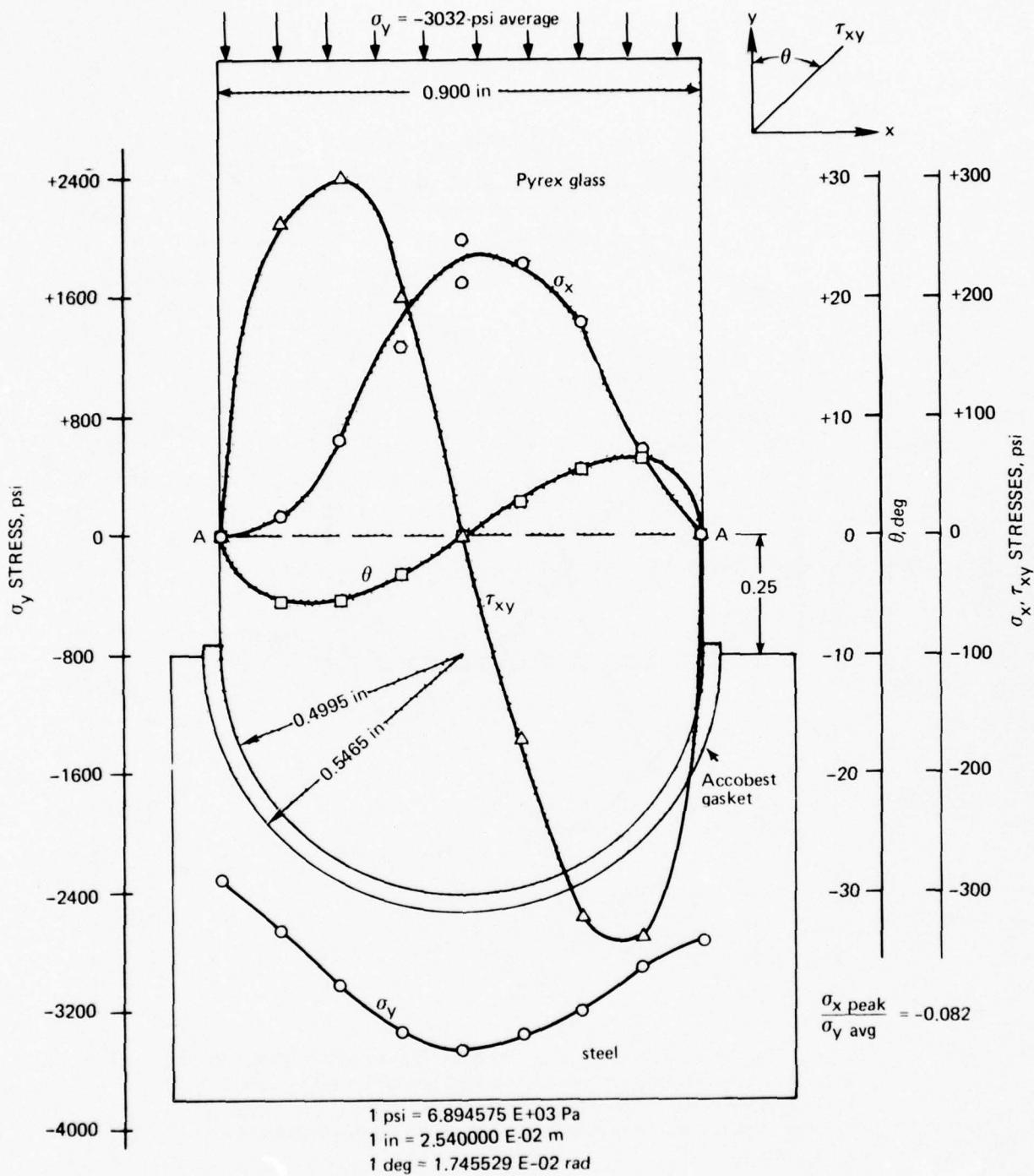
Figure 11.105. Simulated distribution of stresses across the wall of a hemisphere supported by a toroidal bearing surface with a radius equal to one-half of the thickness under uniaxial compressive loading. Note that in this configuration σ_x is low and positive. The substitution of a low tensile stress for high tensile transverse stress decreases the susceptibility of this bearing surface to initiation of cracks.

11-138
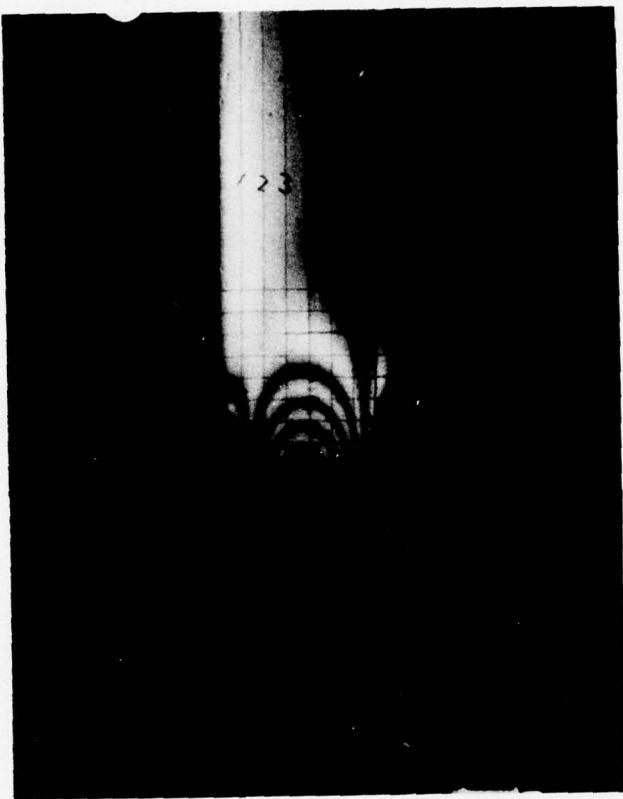
Figure 11.106. Photoelastic fringes in a glass specimen
with a toroidal bearing surface pressing against a steel
block with a matching seat. The radius of the torus
equals one-half of the shell thickness. Data from
this test were used for plotting stresses at the bear-
ing surface shown in figure 11.105.

$\sigma_y = -11,244$-psi average

Pyrex glass

0.900 in

$\dfrac{\sigma_x \text{ peak}}{\sigma_y \text{ avg}} = +0.250$

σ_y STRESS, psi

-6000

-7000

-11,000

-9000

-10,000

0.1687

-12,000

-13,000

θ

1.800

1.800

A

A

τ_{xy}

σ_y

σ_y

σ_x

Ti foil on Accobest gasket 0.015 in thick

7075 aluminum

θ, deg

τ_{xy}, σ_x STRESSES, psi

+15

+10

+5

0

-5

-10

-15

+3000

+2000

+1000

0

-1000

-2000

-3000

1 psi = 6.894575 E+03 Pa
1 deg = 1.745329 E-02 rad
1 in = 2.540000 E-02 m
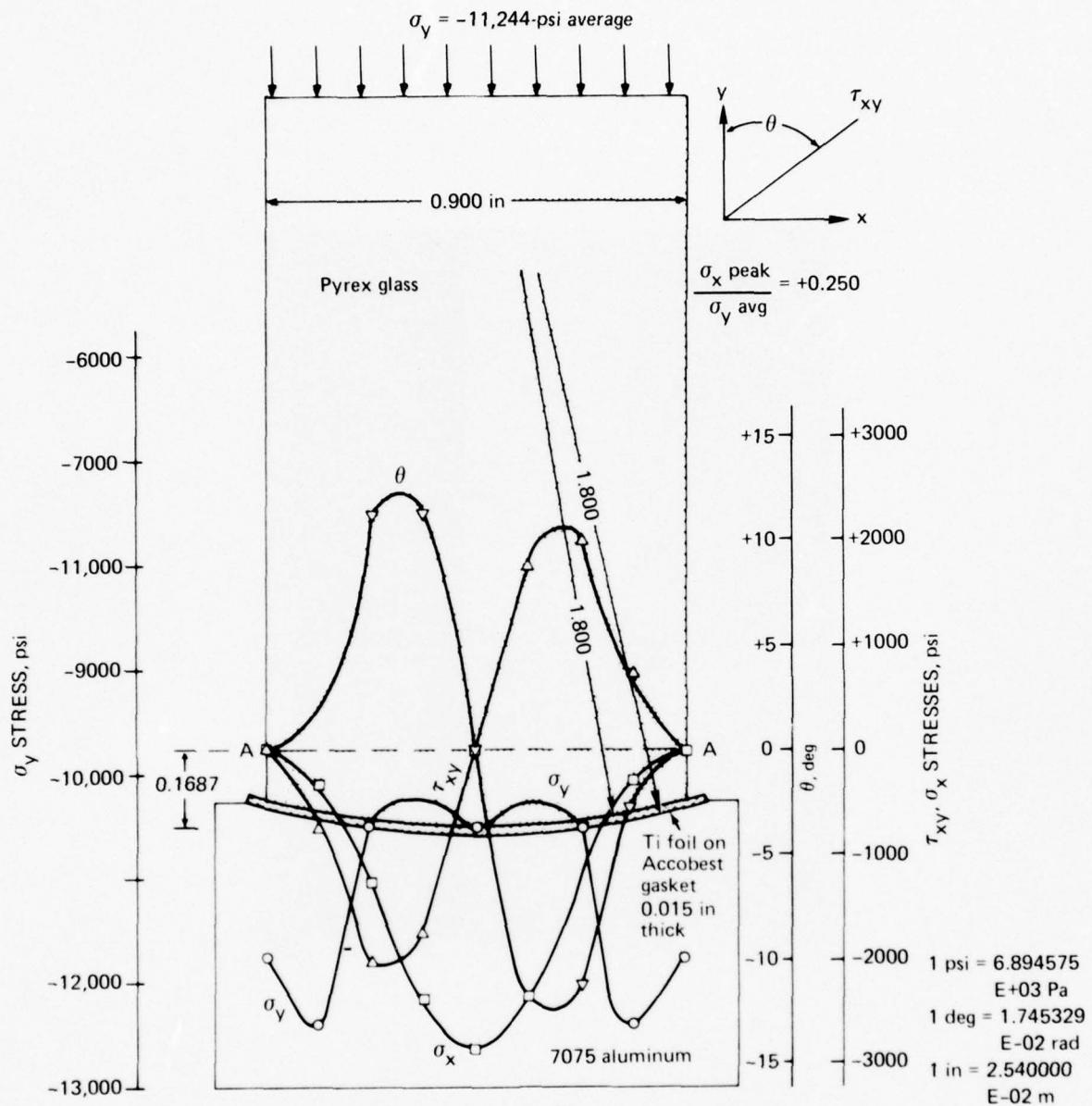
Figure 11.107. Simulated distribution of stresses across the wall of a hemisphere supported by a toroidal bearing surface with a radius equal to twice the thickness of the shell under uniaxial compressive loading. Note that in this configuration σ_x is high and negative. The high value of the compressive transverse stress makes the bearing surface on this joint even less susceptible to crack initiation than in the toroidal bearing surface with a radius equal to one-half of the shell thickness.
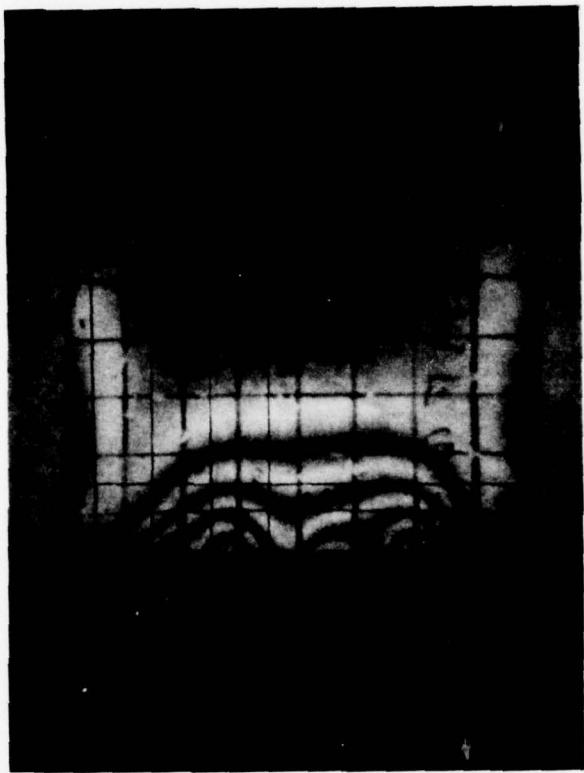
Figure 11.108. Photoelastic fringes in a glass specimen
with a toroidal bearing surface pressing against a steel
block with a matching seat. The radius of the torus
equals twice the shell thickness. Data from this test
were used for plotting stresses at the bearing
surface shown in figure 11.107.
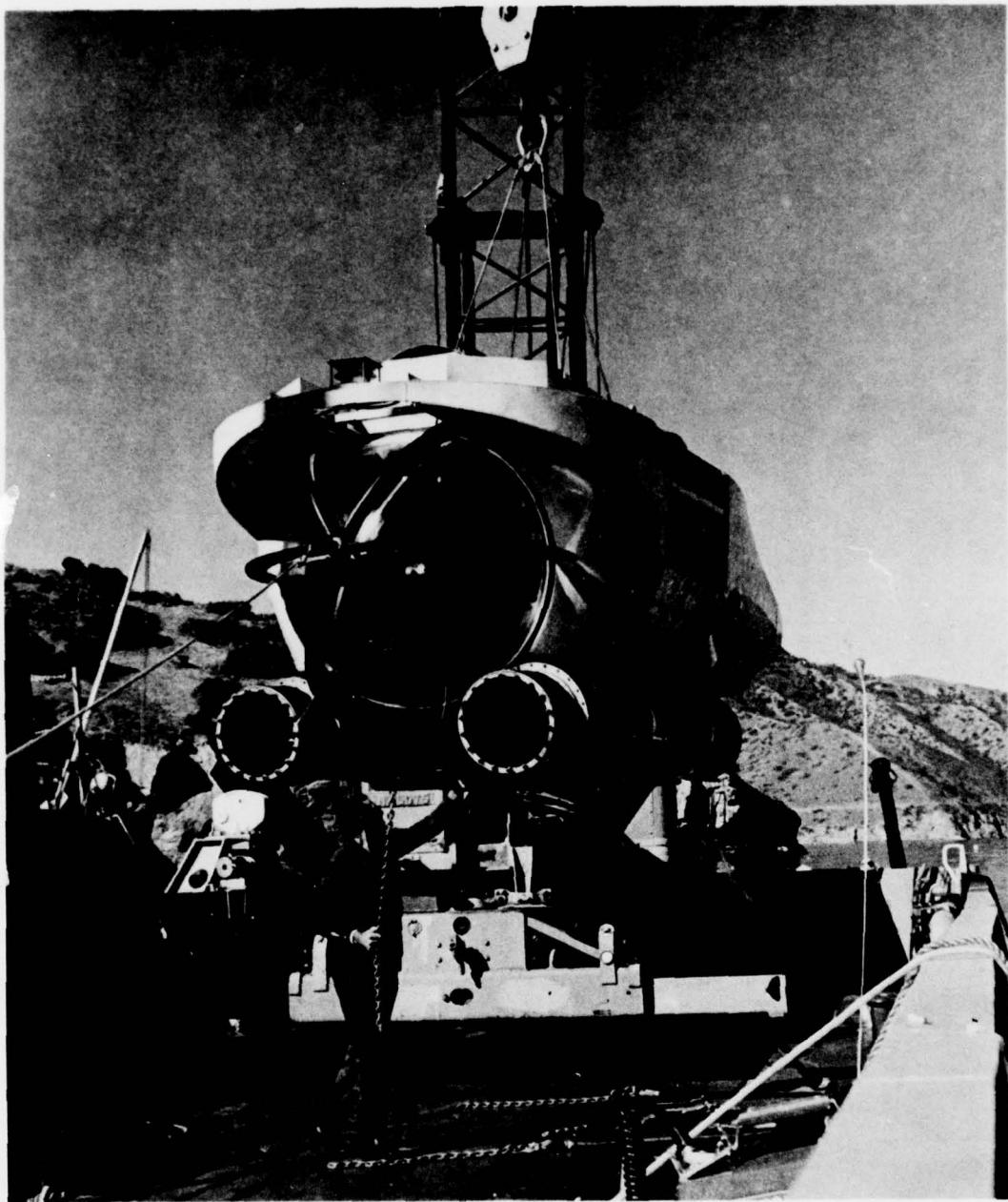
Figure 11.109. Submersible DEEPVIEW fitted with a glass bow dome whose toroidal bearing surface is mated to a compliant titanium ring with matching seat.
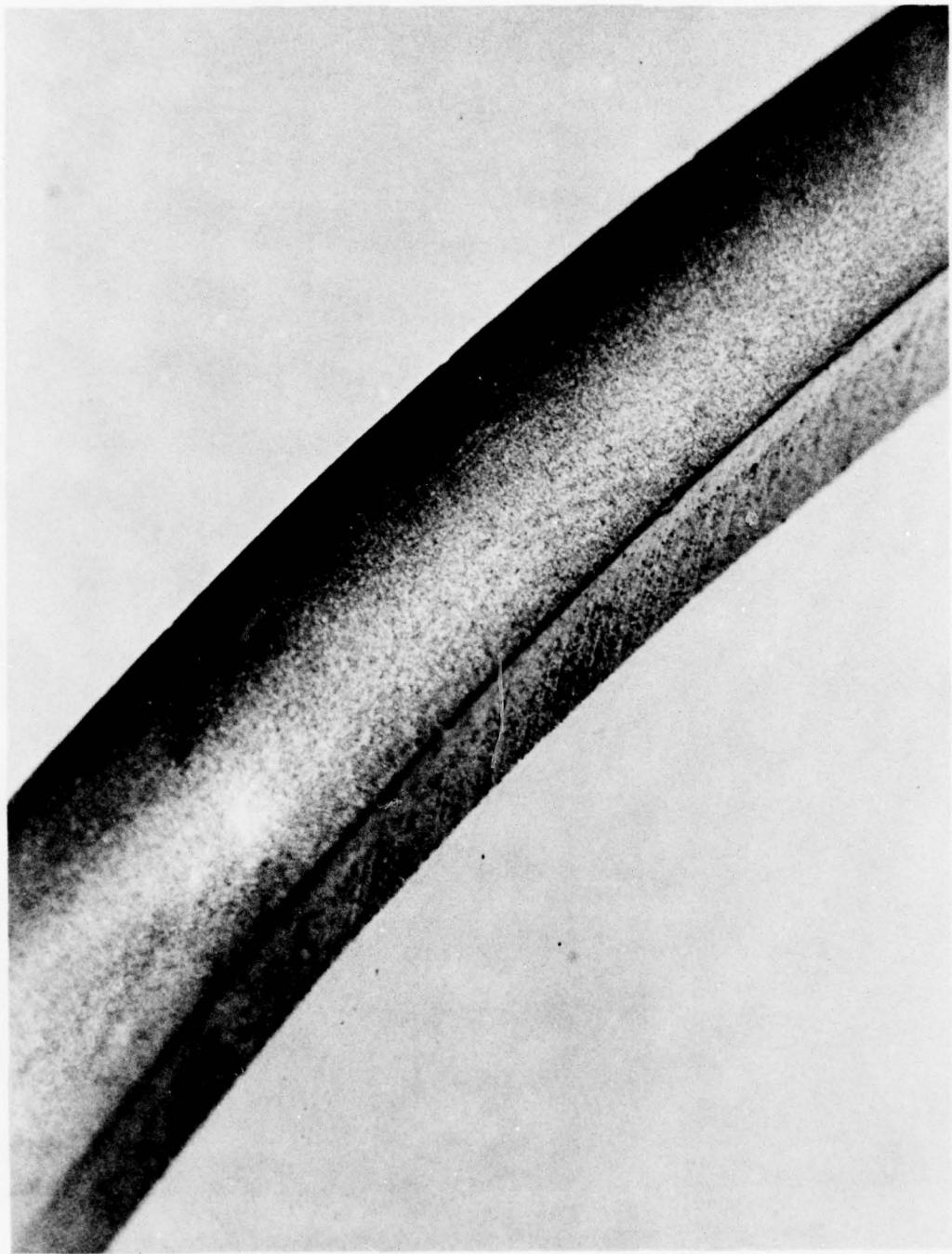
Figure 11.110. Close-up view of glass hemisphere with toroidal bearing
surface after extensive pressure cycling. Note absence of cracks.
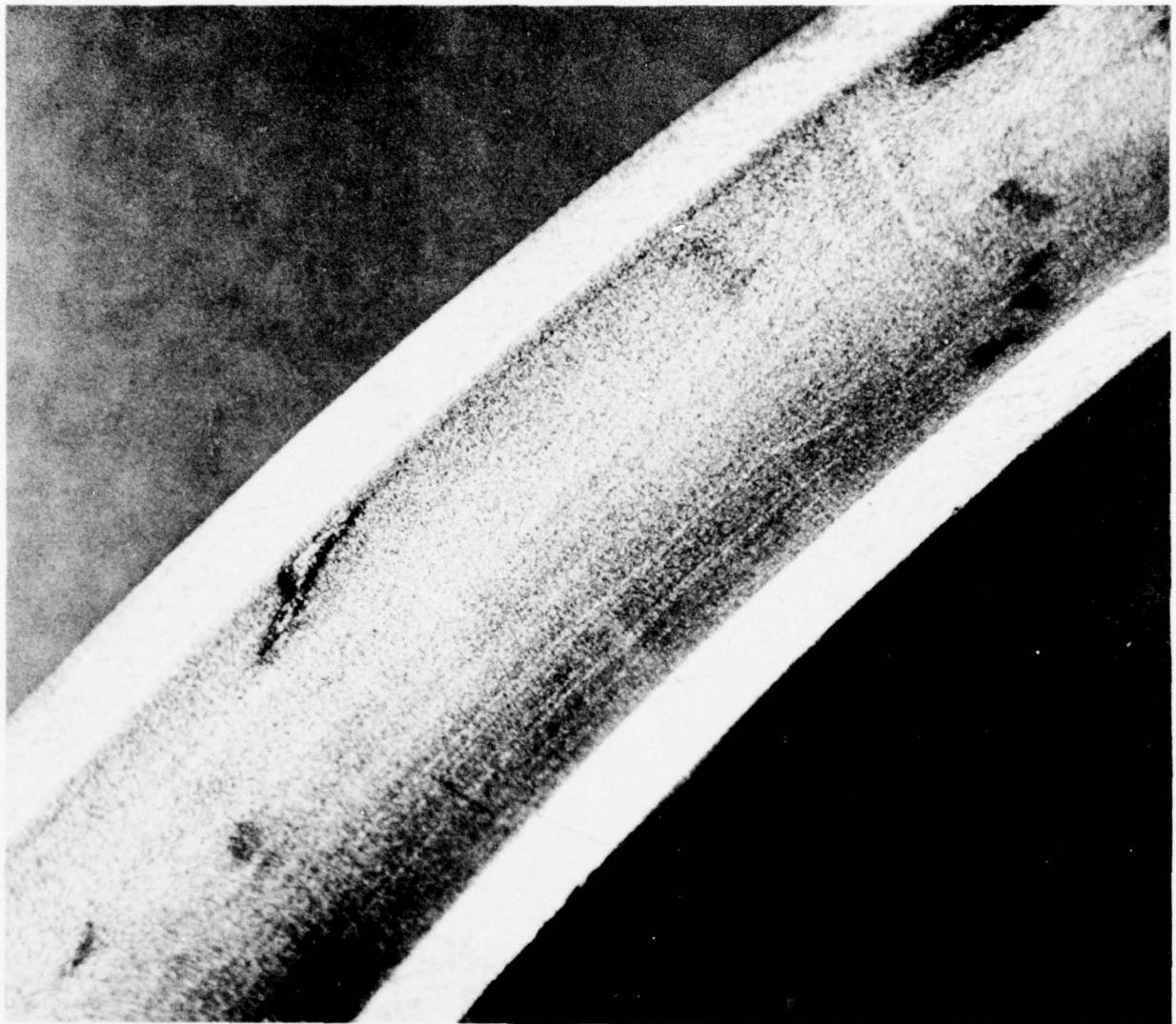
Figure 11.111. Close-up view of toroidal seat in compliant ring for hemisphere.
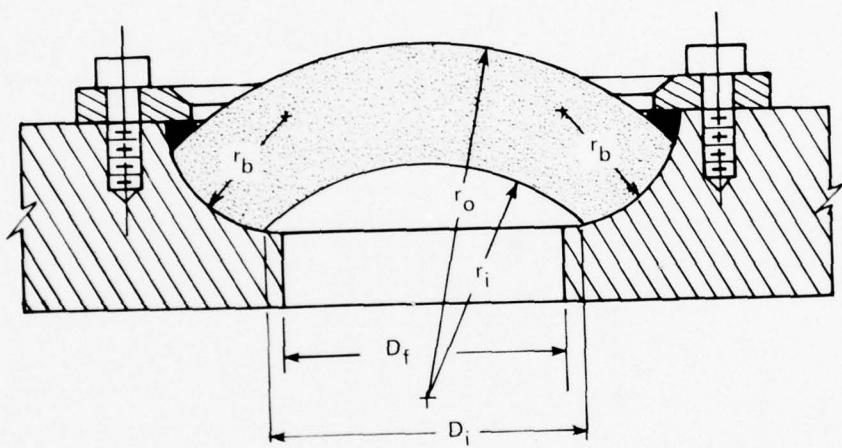
Figure 11.112. Typical mounting arrangement for spherical sectors under 180 degrees (3.14 radians) with toroidal bearing surfaces.

SECTION 12. SPHERICAL PRESSURE HULLS . . . 12-1

SECTION 12. SPHERICAL PRESSURE HULLS

12.1 INTRODUCTION

Although spherical shell sectors provide panoramic visibility as bow windows in submersibles, there are still many blind spots for the crew. The only way to eliminate them completely is to place the crew inside an acrylic sphere, where there is unlimited visibility in all directions.

The first to propose an all-acrylic spherical hull was Professor Auguste Piccard. His idea grew out of a frustration with the single small conical viewport which was at that time standard equipment on all bathyscaphs. Unfortunately, there was neither the engineering knowledge nor fabrication technology to support the proposal. It required an additional 30 years of ocean engineering development and the financial support of the U.S. Navy before acrylic spherical pressure hulls for submersibles became an operational reality (references 12.1 through 12.19).

Launching of NEMO (DSV 5), a spherical acrylic submersible, by the U.S. Navy in 1970 marked the beginning of the ultimate in underwater visibility. Since that time, three additional acrylic submersibles have been built and several more are in various stages of completion. The increase in numbers has been slow primarily because of the small seating capacity inside the spheres, i.e., two occupants — the pilot and the observer. However, as fabrication technology allows economical construction of spheres capable of seating three or four occupants in comfort, the number of acrylic plastic spherical submersibles in service will increase.

The ultimate reason for increasing the size of acrylic spheres is not to carry more occupants, but to carry two or three in comfort so that they can pursue scientific investigations unhampered by cramped quarters. An example of such an underwater observatory is the engineering feasibility design, completed in 1965, of a 120-inch-diameter (305 centimeters), tethered, 1-atmosphere habitat for long-term, *in situ* observation of benthic and pelagic sealife (figure 12.1). Since 1965, technology has advanced sufficiently to where spheres of such size can be built economically and within a short time without further research and development effort.

There has been also a concerted effort to decrease the cost of spheres that are capable of seating two persons for short-term underwater work assignments. If such spheres could be mass produced at a cost lower than that for metallic spheres of comparable size and depth capability, they would find extensive application as 1-atmosphere pilot compartments for a vast array of underwater construction equipment (figure 12.2).

Besides the cost and size factors which tend to limit the application of spherical pressure hulls, their limited operational depth capability also makes them less attractive than metallic hulls. The operational depth of acrylic spherical capsules was originally from 0 to 50 feet (0 to 15 meters), e.g., the HIKINO and NUC Offshore Tower Undersea Elevator. However, spherical acrylic hulls have since been built and certified for operation to 3000 feet (914 meters), a depth which is not yet the structural limitation of acrylic. There is no doubt that this depth will be reached, but it is doubtful whether it will be less than 6000

feet (1829 meters). Thus even the depth capability of spherical acrylic hulls is not a serious problem to their utilization, i.e., the 0- to 6000-foot (0 to 1829 meters) depth range includes future oil-drilling sites and the locations of ocean thermal energy conversion plants, kelp methane conversion plants, and ocean current power plants.

The limiting factor on the use of acrylic spherical pressure hulls in ocean engineering applications will ultimately be the imagination of the engineers and designers who develop such systems. It is hoped that this section will convince at least some of the designers that the performances of spherical pressure hulls fabricated from acrylic plastic can be predicted with as great a certainty as those of metallic hulls and that properly designed and built plastic spherical hulls for undersea applications surpass in safety and comfort those made from metal and steel.

12.2 STRUCTURAL PERFORMANCE

The structural performance of acrylic spherical pressure hulls depends not only on the physical properties of plastic but also on the type of construction and the design features, e.g., penetrations, attachments, and inserts. For this reason, it is worthwhile to separate the effects of construction and design features from those of the material properties.

12.2.1 Internal Pressure

Because of the lack of spherical internal pressure containers in service, there is almost a total absence of experimental data on their performance. This is surprising, as the spherical shape is an ideal configuration for the containment of internal pressure. There are many ocean engineering applications where a transparent sphere under internal pressure would be more advantageous than a metallic sphere with small transparent inserts, e.g., a personnel transfer capsule which is subjected to external pressure during some phases and internal pressure during other phases.

The reasons for lack of use as a container of internal pressure cannot be found in the physical properties of acrylic, as acrylic has served successfully under the tensile stresses in plane windows with plane bearing surfaces incorporated into diving bells and in cylindrical windows under internal pressure serving as one-person hyperbaric chambers in hospitals. Rather the reason is the lack of proven sphere designs with integral reinforcements around penetrations for hatches and feedthroughs. Users of personnel transfer capsules are thus reluctant to specify acrylic pressure hulls, as it would require the initiation of a major research and development effort to permit certification for human occupancy. As a result, there is little hope for development of internally pressurized, acrylic, personnel transfer capsules by the diving industry unless the government finances a pioneering effort in this area, similar to the Navy-sponsored development of acrylic spherical hulls for external pressure service.

In the absence of penetrations and joints with a short-term bond strength of less than 9000 pounds per square inch (62 megapascals), the magnitude of biaxial design stresses acceptable for cyclic pressurization service is as shown in table 12.1. In the presence of bonded joints with a minimum short-term tensile strength in the 5000- to 6000-pound-per-square-inch (34.5 to 41.4 megapascals) range, the magnitude of biaxial design

Table 12.1. Biaxial design stresses for cyclic pressurization service.

Maximum Temperature, $^\circ$F	Design Stress, psi
50	1500
75	1250
100	100
125	750
150	500

Notes:

$t^\circ_C = (t^\circ_F - 32)/1.8$

1 psi = 6.894757 E+03 Pa

must be discounted by at least 50 percent. Such bond strengths are easily obtained with PS-30 or PS-18 self-polymerizing cement.

The magnitudes of acceptable tensile design stresses have been experimentally established by the aircraft industry for internally pressurized, acrylic plastic canopies on fighter aircraft. Their reliable performance leads one to believe that these design stresses can be safely applied to spherical personnel transfer capsules or diving bells with lockout capability. Thus, what is lacking are experimentally proven designs for feedthroughs and hatches that would not generate excessive stress concentrations in acrylic spheres under internal pressure.

12.2.2 External Pressure

12.2.2.1 DEFINITION OF IDEAL SPHERES. To clarify the discussion on structural behavior of acrylic spheres under external pressure, an ideal sphere must be defined. As used in this section, the term describes the acrylic spheres fabricated for the U.S. Navy according to the specifications of J. D. Stachiw. These spheres were either fabricated by bonding spherical pentagons with PS-30 or PS-18 self-polymerizing cement in a special alignment fixture (figures 12.3 and 12.4) or by casting hemispheres in precision-machined metallic molds and subsequent bonding with PS-30 cement or the same resin mix used in casting the hemispheres (figures 12.3 and 12.5). In all cases the physical properties of the acrylic plastic met the requirements of ANSI/ASME PVHO-1 for acrylic plastic in manned hyperbaric chambers.

The diameter of the spheres varied from 15 to 66 inches (38 to 168 centimeters) and the t/R_0 ratio varied from 0.033 to 0.133. However, in all cases the deviation from sphericity at any one point on the sphere was less than $0.005 \times R_0$. The bonded joints were not of uniform thickness (figure 12.6), the PS-30 or PS-18 joint was softer than the parent material (figure 12.7), and the polymerized adhesive contained inclusions in the form of gas bubbles (figure 12.8). However, these imperfections had a negligible effect on the critical pressure or strain on the shell away from the joints, if the total cross-section of all imperfections in any one joint was less than 5 percent of the joint's cross-section.

Although these spheres were "ideal" from a conceptual viewpoint, they were "real" from the engineering viewpoint, i.e., they were made by plastic fabricators and not by research laboratories and thus represented structures one could expect from a typical plastic fabricator following good commercial practices. For this reason the data generated with these "ideal" spheres can be applied without any discount to the design of functional man-rated acrylic spheres, if they are "ideal," i.e., if they do not have any penetrations. (The effect of penetrations on the structural behavior of ideal spheres is discussed in section 12.2.3.)

12.2.2.2 SHORT-TERM PRESSURIZATION

<u>12.2.2.2.1 Critical Pressure</u>. Ideal acrylic plastic spheres are the optimum shape for resisting external hydrostatic pressure. Thus, for any given enclosed volume the spherical pressure hull provides the lowest ratio for structural weight to displaced volume for all known hull shapes, i.e., cylinder, spheroid, cube, pyramid, icosahedron, dodecahedron, etc. Hull shapes with plane surfaces pay a particularly high penalty in structural weight (figure 12.9).

The short-term critical pressure (STCP) of an acrylic sphere is a function of the t/R_o ratio, ambient test temperature, and physical properties of the acrylic plastic, i.e., increasing the t/R_o ratio increases the STCP, although not in a linear manner (figure 12.10), while increasing the ambient test temperature decreases the STCP (figure 12.11). Since the temperature of oceans and lakes only very rarely* exceeds 75°F (24°C) most experimental data were generated at that temperature. For most ocean engineering applications the experimentally generated STCP curve is very conservative, as the temperatures encountered at continental shelf depths are 40 to 50°F (4 to 10°C).

The STCP curves were generated with ideal spheres fabricated from acrylic plastic meeting the requirements of ANSI/ASME PVHO-1, tables A-1 and A-2 (section 15). Spheres fabricated from acrylic plastic whose physical properties do not meet these requirements will implode at a lower hydrostatic pressure. Since the relationship between the many time- and temperature-dependent physical properties of acrylic plastic and its structural performance under varying operational conditions is very complex, the use of acrylic plastic not meeting the ANSI/ASME-PVHO-1 criteria is not recommended unless the designer has the resources and time to generate experimentally validated performance curves for spheres made from that particular grade of acrylic plastic.

The short-term critical pressure of ideal acrylic spheres can also be approximated within acceptable accuracy by using the following equations:

$$S_1 = S_2 = -p \ \frac{3R_o^3}{2(R_o^3 - R_i^3)} \tag{12.1}$$

$$p_{cr} = \frac{-0.8 \sqrt{E_s E_t} \ (t/R_o)^2}{\sqrt{(1 - \mu^2)}} \ . \tag{12.2}$$

_____

*Temperatures exceeding 75°F (24°C) are only found in tropical seas near the surface and on the bottom where hot springs are present.

where

S_1 = meridional stress on internal surface, pounds per square inch

S_2 = hoop stress on internal surface, pounds per square inch

R_o = outside radius, inches

R_i = inside radius, inches

t = thickness, inches

μ = Poisson's ratio*

p = hydrostatic pressure, pounds per square inch

E_t = tangent modulus of elasticity, pounds per square inch*

p_{cr} = critical pressure at which implosion will take place, pounds per square inch

E_s = secant modulus of elasticity, pounds per square inch.*

Both equations are solved simultaneously for a given t/R_o ratio by substituting the proper S_1, μ, E_s, and E_t values until the p in equation 12.1 is equal to the p_{cr} in equation 12.2. When p = p_{cr}, both terms then represent the critical short-term hydrostatic pressure at which implosion of the ideal sphere will occur because of elastico-plastic general instability (figure 12.12).

If the sphere has significant local deviations from nominal thickness (> 1 percent) or radius of curvature (> 0.5 percent), the actual measured minimum thickness and maximum radius of external curvature must be utilized instead of nominal dimensions, as they will determine the critical pressure for local implosion.

The accuracy with which equations 12.1 and 12.2 predict general or local implosion varies with the t/R_o ratio. For thin shells the calculated p_{cr} will exceed the actual implosion pressure by several percent, while for thick shells the actual implosion pressure may exceed the calculated p_{cr} by 10 percent or more. In all cases the calculated p_{cr} value can be considered conservative for ambient temperatures $\leqslant 75°F$ (24°C). For higher ambient temperatures, the E_s, E_t, and μ values in figures 4.21, 4.22, and 4.25 provide p_{cr} values that are invariably higher than the actual implosion pressures. For this reason calculations of p_{cr} for ambient temperature $\geqslant 75°F$ (24°C) require a new set of experimentally generated curves that relate E_t, E_s, and μ to uniaxial compressive stress under short-term loading at the particular ambient temperature.

Although the short-term critical pressure of an ideal sphere is primarily a structural property used for comparing the structural properties of different shell designs, it is also of great value to the submersible or diving bell operator. To the operator it denotes the depth at which the hull will implode if it sinks out of control beyond its maximum operational depth. Thus, the ratio of the short-term critical pressure to design pressure (STCP/DP) serves as an overall indicator of sphere's structural adequacy for its stated design depth.

---

*μ, E_t, and E_s are functions of S_1 and S_2; their magnitudes at 75°F (24°C) are in figures 4.21, 4.22, and 4.25.

High ratios generally indicate a high safety margin that will allow the submersible to exceed for short periods its design depth by a large margin without permanent damage to the acrylic sphere. Thus a STCP/DP ratio of 4 allows the submersible in an emergency to exceed its design depth by 100 percent for the duration of a typical 240-minute dive, an STCP/DP ratio of 3 allows only a 50-percent emergency excursion beyond the design depth; and a very low STCP/DP ratio of 2 does not allow any emergency excursions beyond design depth.

Because of unforeseen circumstances, excursions beyond the design depth will occur in the life of every submersible. It is thus imperative to specify a STCP at 75°F (24°C) that exceeds the design depth by at least a factor of 3. Most of the diving system and ship classification societies, e.g., the American Bureau of Shipping and Det Norske Veritas, require a STCP/DP ratio in excess of 3. Others, among them the American Society of Mechanical Engineers, require at least an STCP/DP ratio of 4. Higher STCP/DP ratios than 4 are only of value if there are real possibilities that at design depth ambient temperatures will exceed 50°F (10°C). Such temperatures have been encountered only in isolated locations in the Red Sea and in the Abyssal Plain of the Atlantic near hot springs in the seafloor. The ANSI/ASME PVHO-1 Safety Standard (section 15) can serve here as a valuable guide to the designer who must specify STCP/DP ratios for acrylic pressure hulls slated to operate in the vicinity of hot springs on the seafloor or geothermally heated lakes.

12.2.2.2.2 Deformations. When externally pressurized, negative membrane strains are generated inside the spherical acrylic hull. Since the stresses, as predicted by equation 12.1, are highest on the interior surface, the strains are also highest at this location (figure 12.13). The strains increase linearly with an external pressure loading to an approximate level of 10,000 microinches per inch (1 percent), while at higher levels they become decidedly non-linear until just prior to implosion when they increase without any further increase in the external pressure.

Since the structural properties of acrylic plastic are dependent on the ambient temperature, the strains on the sphere vary with temperature, i.e., at low temperatures the strains are low and at high temperatures they are high (figure 12.14). In addition, the increase in temperature also raises the nonlinearity of the strain increase with external pressure.

Because of negative strains, the radius of the sphere decreases with external pressure until at the moment of implosion the internal volume of the sphere has decreased significantly. The value of volumetric contraction just prior to implosion remains surprisingly constant for any given t/R_o ratio over a wide range of ambient temperatures, although the E_s and E_t of acrylic plastic vary significantly with temperature. This indicates that the implosion of acrylic plastic shells by elastico-plastic instability is strain dependent rather than stress dependent. Thus, for example, the elastico-plastic failure of spheres with $t/R_o = 0.066$ will occur when the volumetric contraction of the sphere has reached approximately 6 percent (equivalent to approximately 2 percent of compressive membrane strain on the concave surface), regardless of the stress level and ambient temperature that produced this strain (figure 12.15). As a result, the maximum allowable membrane strain on the interior of an ideal sphere with $t/R_o = 0.066$ at design depth is about 0.4 percent. For other t/R_o ratios the magnitudes of volumetric contraction and compressive strain will differ, yet the principle will remain the same, i.e., for any given t/R_o ratio the sphere will implode only after a

certain compressive deformation has taken place. Thus for spheres with $t/R_o = 0.133$ implosion occurs only after a volumetric contraction of 12 percent (equivalent to about 3-percent compressive deformation) has occurred.

The radial displacement of an acrylic sphere under short-term hydrostatic loading is an important factor that must be taken care of during the design of external or internal attachments to the sphere. Local restraint imposed on the sphere by attachment to a rigid external or internal framework will cause uneven deformation of the sphere which will trigger premature sphere failure by elastic instability.

12.2.2.3 LONG-TERM PRESSURIZATION

12.2.2.3.1 Critical Pressure. Ideal acrylic plastic spheres implode under long-term external hydrostatic loading at pressures which are substantially lower than the short-term critical pressure for that particular t/R_o ratio, i.e., the longer the sphere is subjected to sustained hydrostatic pressure, the lower is its long-term critical pressure (LTCP). By the same logic, raising the ambient temperature will further lower the sphere's LTCP.

To date there is no proven analytical expression to calculate accurately the LTCP for any t/R_o ratio and ambient temperature. As a result the designer must totally depend on experimental data generated with model- and full-scale ideal spheres. These data exist only for a 0.033 to 0.133 range of t/R_o ratios at 75°F (24°C) ambient temperature (figure 12.16). On the basis of these data, it is feasible to predict the LTCP for a sphere whose t/R_o ratio is between 0.033 and 0.133 and whose maximum projected sustained loading will be less than 10,000 hours at 70°F (21°C) ambient temperature.

Although existing data do not cover sustained loading durations in excess of 10,000 hours, they still serve as the basis for extrapolation to 100,000 hours. Such extrapolation is accomplished by extending linearly the LTCP curves plotted on log-log coordinates from 10^4 to 10^5 hours. This technique has been proven valid for acrylic structures subjected to tensile, compressive, or flexure loadings. The extrapolation of existing data by a factor larger than 10 is not recommended, as there is insufficient data on the deterioration of acrylic plastic in the marine environment over periods in excess of 10 years.

Existing data also do not cover ambient temperatures that are higher or lower than 70°F (21°C). This is not a large problem for ambient temperatures less than 70°F (21°C), as it has been experimentally proven that decreasing the temperature increases the LTCP for the same duration of sustained pressurization, i.e., decreasing the temperature for a given LTCP increases the duration of loading required to cause implosion. Thus, basing the design for ambient temperatures less than 70°F (21°C) on LTCP graphs generated at 70°F (21°C) is conservative and acceptable. However, this is not true for temperatures greater than 70°F (21°C). Since higher temperatures decrease the LTCP for a given duration of loading, or decrease the required duration of loading to reach the same LTCP, a design based on LTCP graphs for 70°F (21°C) ambient temperature is unsafe and unacceptable. Thus for ambient temperatures above 70°F (21°C) it is necessary to generate a new set of LTCP curves based on higher ambient temperatures. Since the experimental data needed for the generation of an LTCP curve for a given t/R_o ratio and ambient temperature require at least three sphere specimens and 500 pressure vessel hours, the cost will generally exceed $25,000.

There is, however, a technique for obtaining fair approximations of LTCPs for ambient temperatures above or below 70°F (21°C). This technique is based on the experimentally proven premise that a change in ambient temperature is accompanied by a corresponding change in duration of loading to generate the same LTCP as at 70°F (21°C) ambient tempera- ture. Although the value of the ratio for the temperature difference to time conversion is not accurately known, it has been found that the temperature difference acts approximately like a time multiplier, i.e., for every 10°F (−12°C) of temperature difference from 70°F (21°C) the time to reach a given LTCP changes by a factor of 10. Thus, for example, the ambient temperature change from 70°F to 60°F (21 to 16°C) for a sphere with $t/R_o = 0.066$ would probably increase the required duration of loading from 2.2×10^4 to 2.2×10^5 minutes in order to fail at LTCP of 750 pounds per square inch (5.17 megapascals). Although this temperature- difference-to-time ratio is only an approximation, it is easy to see that the LTCP graphs plotted in figure 12.16 for 70°F (21°C) ambient temperature rapidly loose their validity with even a small change in ambient temperature. Still, if the ambient ocean temperature at design depth is $\leqslant 70°F$ (21°C), the design of the submersible based on LTCP graphs at 70°F (21°C) will be conservative and thus acceptable.

12.2.2.3.2 Mechanism of Implosion. Implosion under long-term sustained loading is generally of local, rather than general, nature. Thus under long-term loading the sphere fails locally by snap-through plastic buckling, while under short-term loading it fails by general elastico- plastic instability. Snap-through plastic buckling is always initiated by some small local deviation from sphericity or thickness, or both. Since at such local imperfections, because of the larger radius or lesser wall thickness, the compressive strains are larger than at locations where such imperfections do not exist, the local radius of sphericity will increase until an actual flat spot is formed (figure 12.17). Once the local radius approaches infinity, i.e., the surface changes from a curved to a plane shape, snap-through failure occurs.

Because of the formation of a flat spot, local snap-through failure is characterized by high tensile stresses on the interior surface at the center of the flat spot and on the exterior surface around the circumference of the flat spot. Crack formation occurs first on the in- terior surface at the apex, since these tensile stresses are higher than those on the exterior surface around the flat spot's circumference. As a result of the formation of a flat spot, a fracture forms on the interior surface of the spot at its center followed by ejection of frag- ments and leakage of water. The rapid filling of the sphere with water and the accompanying equalization of internal and external pressures cause the strains in the sphere to relax so that further penetration of the crack around the circumference of the flat spot on its exterior surface is arrested. The end results are a conical fracture surface penetrating the center and an incomplete crack around the circumference of the flat spot (figures 12.18 and 12.19) which has snapped back to its original sphericity because of the equalization of pressure on the exterior and interior of the sphere.

It is thus apparent that local deviations from sphericity and nominal thickness have a greater influence on LTCP than on STCP, where the rapid pressurization of the sphere does not allow sufficient time for the viscoelastic flow of acrylic plastic to convert local deviations into flat spots. Since the LTCP graphs of figure 12.16 were generated with ideal spheres, the design of any spherical pressure hull based on these graphs must specify the same sphericity and thickness tolerances. Deviations will make the data in figure 12.16 inapplicable, i.e., a sphere whose sphericity or thickness deviations exceed those of ideal spheres will implode sooner or at lower pressures than those in figure 12.16. Since the ideal spheres described

in this section were commercially built, there is no reason why spherical pressure hulls cannot meet the same dimensional tolerances. Invoking the ANSI/ASME PVHO Safety Standard on fabrication drawings for spherical hulls will insure the designer that the finished product will meet the criteria of ideal spheres (section 15).

12.2.2.3.3 Deformations. The deformation of ideal acrylic plastic spheres under long-term external hydrostatic loading, as measured by strains or volumetric change, is similar to that observed under short-term hydrostatic loading, except that for a given external pressure, temperature, and t/R_O ratio it is much larger. This difference at identical pressure is the result of the visoelastic nature of plastic. Thus, to predict the magnitude of strain or displacement for a given pressure loading, the duration of loading, as well as the temperature, must be considered.

Much data exist on the change in displacement under different magnitudes of long-term pressure loading at 70°F (21°C) ambient temperature for ideal spheres with t/R_O ratios of 0.066 and 0.122 (figures 12.20, 12.21, and 12.22). On the basis of these data, the following basic observations have been made: (1) At the moment of implosion under long-term pressurization the change in displacement for a given t/R_O ratio is approximately the same regardless of pressure level to which it was subjected; (2) this change in displacement is about the same as for short-term loading just prior to implosion; and (3) for every t/R_O ratio there is some long-term pressure level below which the change in displacement with time is negligible from the designer's viewpoint.

The first two observations indicate that the magnitude of displacement changes just prior to implosion under long-term pressurization is basically the same as under short-term pressurization. Comparison of graphs on figure 12.20 for long-term displacement with those on figure 12.15 for short-term displacement makes this apparent. These observations then confirm the statement previously made that under short-term loading the implosion of ideal acrylic spheres is primarily a function of strain and not of stress. For example, in both figures the change in displacement for spheres with t/R_O = 0.066 is approximately 6 percent prior to implosion while the pressure levels (and thus stresses) at the moment of implosion under short-term loading are 1500 to 1600 pounds per square inch (10.3 to 11.0 megapascals) as compared to long-term loading where they are 750 to 1500 pounds per square inch (5.17 to 10.3 megapascals), depending on the duration of loading.

The third observation indicates that for every t/R_O ratio and ambient temperature, there can be found long-term pressure levels below which time-dependent volumetric changes and strain increases become negligible after the initial creep phase lasting approximately 1 hour. Thus, for spheres with t/R_O = 0.066 at 70°F (21°C) ambient temperature, a long-term pressurization of approximately 750-pound-per-square-inch (5.17 megapascals) magnitude seems to generate after the initial 1-hour phase of deformation only a negligible time-dependent volumetric change and strain increase. This means that the creep of the material is so low that it will require more than 1 year before the magnitude of volumetric change that triggers the elastico-plastic instability of the sphere is reached. Since typical applications for acrylic pressure hulls are small submersibles and portable habitats, a projected static fatigue life of 1 year provides a more-than-adequate margin of safety. This may not be the case for applications in permanent habitats with a life expectancy of at least 50 years. In this instance, the definition of negligible creep is different, i.e., creep would be considered negligible for design purposes if the critical magnitude of volumetric change was reached

after 100 years or more. In the case of spheres with $t/R_O = 0.066$ at 70°F (21°C) the pressure load satisfying this definition would probably be 450 pounds per square inch (3.1 megapascals).

For other t/R_O ratios and ambient temperatures, the magnitudes of maximum long-term pressure levels producing only negligible creep would differ substantially from those established for $t/R_O = 0.066$ at 70°F (21°C) (figure 12.23). The experimental approach to establishing the safe, maximum, long-term pressure levels would be the same as the one used for spheres with $t/R_O = 0.066$ at 70°F (21°C). In all cases the use of structural scale models is admissible, since it has been experimentally proven that the structural performance of scale models is identical to that of full-scale spheres of the same t/R_O ratio built from material with the same physical properties, i.e., there is no material thickness scaling effect for acrylic plastic, unlike glass, concrete, or other brittle materials.

The practical conclusion is that in both analytical calculations and experimental evaluations of acrylic sphere designs the emphasis should be placed on strains rather than stresses, as the former are the more reliable nondestructive predictors of implosion and indicators of safe operational pressures.

12.2.2.4 CYCLIC PRESSURIZATION. The discussions on short- and long-term loadings have conclusively shown that the deformation of a sphere under external hydro-static loading is a function not only of pressure but also of ambient temperature and duration of loading. With the aid of data presented in those sections it is possible to select a t/R_O ratio so that implosion will not occur during the short-term or sustained pressurization at design pressure, duration of loading, and temperature. There still remains, however, the problem of cyclic pressurization, where the acrylic sphere is repeatedly subjected to its design pressure. In such a case it is important to know whether the magnitude of strains grows with each pressure cycle or whether its magnitude remains constant.

No basic data have yet been generated on the intrinsic fatigue life of a cyclic plastic material under uniaxial or multiaxial compression. Thus, the designer is left to his own devices on this matter. The best that can be done is to generate design data or to rely on the empirical design rules developed by the U.S. Navy during its acrylic submersible research-and-development program.

Although experimental data do not exist on the implosion of ideal acrylic spheres under cyclic pressurization, it can be postulated with reasonable confidence that implosion occurs in the same manner as it does under long-term loading, except that the deformation leading to local implosion increases in intervals defined by characteristics of each pressure cycle. In other words the local formation of a flat spot proceeds only during the loading phase of each pressure cycle. During the relaxation phase of each pressure cycle, the flat spot returns partially, or completely, to its original spherical shape.

Thus the number of pressure cycles required to implode an ideal sphere depends on the magnitude of flat-spot growth rate, the duration of the loading phase, the magnitude of curvature regeneration rate, and the duration of the relaxation phase in each cycle. Implosion will occur in few cycles if the flat-spot growth rate is high and the duration of the loading phase long, while the curvature regeneration rate is low and the duration of relaxation phase short. Operationally this is accomplished by pressurizing the sphere during each cycle to the

proximity of its short-term critical pressure, maintaining the pressure for a long period of time at a high ambient temperature, and subsequently allowing the sphere to relax at 0 pressure for only a brief period during each cycle. Conversely, the implosion can be avoided for thousands of pressure cycles by keeping the ratio of design pressure to STCP low, duration of the sustained pressure periods short, ambient temperature low, and the relaxation periods long.

Because of the many parameters influencing the fatigue life of an acrylic sphere, it is prohibitively expensive to generate sufficient experimental data to formulate design curves for all ambient temperatures, t/R_O ratios, magnitudes of pressure, durations of sustained loading periods, and durations of relaxation periods. Because of the complexity of test parameters, design curves do not exist that consider all these individual factors. Instead only sufficient experimental data have been generated to validate a set of simple design rules which allow the designer to select the proper t/R_O ratio for the projected operational scenario.

The only existing experimental data are the result of pressure cycling acrylic spheres with $t/R_O = 0.066$ and 0.133 ratios at $70°F$ ($21°C$) ambient temperature at the Naval Civil Engineering Laboratory and Naval Undersea Center. The experimental variables in the testing program were the pressure and the duration of sustained loading phases. The objective of the testing program, conducted with several scale model and full-size acrylic spheres, was to establish the pressure level which generates such high strains that the subsequent relaxation phase is not capable of reducing them again to zero. In all cycles the duration of the relaxation phase was kept equal to the sustained loading phase. The rationale for keeping the lengths of both phases equal was that in typical operational scenarios for diving systems the length of the relaxation phase is either equal to or exceeds the sustained loading phase, i.e., the diving system spends more time on deck than submerged.

The findings indicate that, if the sustained pressure during the loading phase of the cycle does not exceed 30 percent of STCP, the strains generated by the loading phase will return to zero during the relaxation phase whose duration equals that of the sustained loading phase (figures 12.24 and 12.25). This was true regardless of the sustained loading duration, if the duration of the relaxation phase equaled the length of the sustained loading phase (figure 12.26). In addition, it was found that during each individual pressure cycle the magnitude of strains at a given location was essentially the same (figure 12.27). Since these findings are based on data from spheres with $0.066 \leqslant t/R_O \leqslant 0.133$ at $70°F$ ($21°C$) ambient temperature, cycled 4000 times, with the sustained loading phases varying from 1 to 7200 minutes, their application is generally restricted to acrylic spheres whose t/R_O ratios, operational pressures, ambient temperature, duration of pressurization, and projected operational life fall in the range of those parameters.

The extrapolations of findings, based on the above range of parameters, that have proven acceptable are $0.033 \leqslant t/R_O \leqslant 0.133$, ambient temperatures $28 \leqslant °F \leqslant 70$ ($-2 \leqslant °C \leqslant 21$), and number of cycles $4000 \leqslant N \leqslant 10,000$. Extra caution must be exercised when applying the findings to t/R_O ratios in excess of 0.133, since it is not known at what t/R_O ratio tensile strains will begin to grow on the interior surface during the relaxation phase of each pressure cycle. Such tensile strains have been observed in ideal spheres with $t/R_O = 0.266$, where they initiated tensile cracks on the interior surface at pressures equal to 30 percent of STCP (see discussion in section 11). Thus, if a designer exceeds the $t/R_O = 0.133$

limit in order to attain a design pressure in excess of 1350 pounds per square inch (9.3 megapascals), he must insure experimentally that if the chosen t/R_O ratio generates tensile strains on the interior of the sphere during relaxation periods they will not initiate fracture of the sphere in a number of cycles that is smaller than the specified fatigue life, i.e., the sphere should not fracture after 100 pressure cycles if the design specifications call for a fatigue life of 2000 cycles.

In summary, it can be stated that for ideal acrylic plastic spheres with $t/R_O \leqslant 0.133$ operating at ambient temperatures $< 75°F (24°C)$, the design pressure must be $\leqslant 30$ percent of STCP at $75°F (24°C)$ if the initiation of cracks and implosion are not to occur in less than 1000 and 10,000 cycles, respectively. This finding, appropriately modified to consider stress risers in the form of penetrations, forms the basis of depth ratings for all man-rated acrylic plastic spheres by the U.S. Navy, American Bureau of Shipping, Det Norske Veritas, and American Society of Mechanical Engineers.

12.2.3 Spheres With Penetrations Under External Pressure

12.2.3.1 DEFINITION OF SPHERES WITH PENETRATIONS. The basic structural difference between the ideal acrylic plastic spheres described in section 12.2.2.1 and the acrylic plastic spheres with penetrations is the presence of openings in the spherical shell. The penetrations may be small or large and closed with permanently installed or removable plugs made of plastic or metal. The functions that the penetrations perform vary. The large ones accommodate hatches for ingress or egress of personnel, while the smaller ones usually contain bulkheads for hydraulic or electrical penetrators or mechanical attachments. The number and locations of the penetrations may also vary, depending on the function for which the sphere is intended. There is, however, one common design feature, i.e., a central spherical angle subtended by the bearing surface of the acrylic shell at the edge of penetration. The magnitude of the spherical angle will vary with the ratio of the external penetration diameter to the external spherical radius of the sphere. The end result is a design, where independent of the spherical radius or penetration diameter, the bearing surface of the acrylic shell at the penetration is always at right angles to the external and internal surfaces of the sphere (figure 12.28).

The reasons for this commonality in design of penetrations are both historical and structural. Historically, this is the design developed for penetrations in the acrylic plastic submersible NEMO (figure 12.29) by its inventor, J.D. Stachiw. Because of its proven performance, it has been utilized since 1965. From the structural viewpoint, the spherical cone angle of the shell's edge provides good bearing support to the closure and is also instrumental in developing a good seal between the closure and the spherical shell.

Other types of bearing surfaces have been proposed for the edges of penetrations, but none has been sufficiently proven to provide serious competition to the bearing surface with a spherical cone angle. The spherical cone angle minimizes shear stresses at the interface between the closure and the shell. Furthermore, it provides good contact between the closure and the shell, even if there is some mismatch because of dimensional tolerances between the diameters of the closure and of the penetration. As a result, it is the only type of penetration design that is recognized by all major classification societies and design standards for acrylic pressure hulls in manned submersibles and habitats.

12.2.3.2 DESIGN CHARACTERISTICS OF SPHERICAL CONE PENETRATIONS WITH REMOVABLE CLOSURES. The basic design characteristics of spherical cone penetrations with demountable closures are as follows.

a. The apex of the cone angle lies at the center of the acrylic sphere.

b. The conical angle of the removable closure matches that of the penetration within ±0.50 degree.

c. The major diameter of the closure exceeds the major diameter of the penetration by about 1 percent to provide positive bearing support to the outer surface of the shell at all times, even when some differential movement occurs between the closure and the shell.

d. The minor diameter of the closure is less than the minor diameter of the penetration by about 0.5 percent to provide positive bearing support to the inner surface of the shell at all times, even when some differential movement occurs between the closure and the shell.

e. The closure is retained in place by a split flange bolted to the interior surface of the closure.

f. An elastomeric gasket compressed between the split flange and the interior surface of the shell evenly distributes the load generated by tightening of screws and insures positive pressure between the mating conical surfaces of the closure and of the shell.

g. Sealing between the closure and the acrylic shell is accomplished by a radially compressed O-ring in the bearing surface of the closure or by a potting compound adhering to both the exteriors of the shell and the closure.

h. The demountable closures are generally fabricated from material with a much higher modulus of elasticity and crack propagation resistance than acrylic.

i. The closures are made as thin as it is structurally feasible to give the closures maximum compliance with the deformation of the acrylic shell.

Typical examples of demountable closures are the hatch and penetration bulkhead utilized in the acrylic submersible NEMO (figure 12.30). Fabricated from cadmium-plated 4430 alloy steel, they provided an economical solution to penetration closures in an acrylic hull. The hatch was of ample size for ingress and egress of occupants, while the penetration bulkhead provided an adequate number of threaded openings for electric and hydraulic penetrators. A metallic hatch ring was interposed between the hatch and the acrylic hull to protect the acrylic bearing surface from scratches generated by sand particles trapped between the hatch and its seat during repeated opening and closing. The hatch ring was sealed with a radially compressed O-ring against the acrylic bearing surface.

12.2.3.3 STRUCTURAL PERFORMANCE OF IDEAL SPHERES WITH PENETRATIONS

<u>12.2.3.3.1 Short-Term Pressurization.</u> Implosions of spheres with penetrations plugged by metallic closures occur under short-term pressurization by general elasticoplastic instability as in ideal spheres without penetrations (figures 12.31 through 12.37). The magnitude of

the critical pressure is the same as for ideal spheres without any penetrations, if the acrylic sphere with penetrations meets the following design parameters.

    a.   The spherical cone angle of the penetration is less than 50 degrees (0.8 radian).

    b.   The edges of two identical adjacent penetrations are separated by a distance which exceeds one-half of the penetration cone angle. If the two adjacent penetrations are dissimilar in size, then the distance separating the edges must exceed one-half of the larger penetration cone angle.

    c.   The radial rigidity of the closure exceeds the radial rigidity of the acrylic sector, which it replaces, by a factor less than 40.

    d.   The critical pressure of the closure exceeds the STCP of the ideal sphere by at least 25 percent.

Experimental data generated by implosions of model-scale acrylic spheres without any and with one, two, three, and four penetrations confirm this finding. On the basis of this finding the experimentally proven STCP curves for ideal spheres (figures 12.10 and 12.11) can be used without any modifications for design of spheres with multiple penetrations.

    Strains in spheres with penetrations plugged by metallic closures differ substantially from those in spheres without penetrations. Not only are they larger, but their distribution is not uniform. On spheres without penetrations they are uniform on any one given spherical surface, while on a sphere with penetrations their magnitude varies inversely with the distance from the edge of penetration. The maximum strain is measured along the meridional orientation on the concave surface at the very edge of penetration. Its value has been extrapolated from experimental strain measurements near the penetration to be 5 times higher than at a location far from the penetration (figure 12.38). The hoop strains on the concave surface at the edge of penetration have been extrapolated to be substantially lower than the meridional stresses at the same location, but still higher than hoop stresses at locations far from the penetration (figure 12.39). The maximum strain values at the very edge of penetration are extrapolated values because the electrical resistance straingages cannot be located at the very edge, but only in the proximity of the edge. For this reason the measured value of strain concentration is only 2 while the extrapolated value is about 5.

    In spheres with penetrations plugged by acrylic or polycarbonate plastic closures, there are no stress concentrations near edges of penetrations because of the identical physical properties of both the shell and closure materials (figure 12.40). Thus, if a design objective is to avoid stress risers, the closure should be made from a plastic that has the same physical properties as does acrylic plastic. Plastic closures are not exclusively used because of their low scratch resistance, low heat transfer, and ease with which the threaded holes required for attaching the hatch hardware, e.g., hinges, handles and locks, cause crack initiation. Because of these drawbacks, plastic closures are limited to small inserts for electric and hyraulic penetrators.

12.2.3.3.2 Long-Term Pressurization. Spheres with penetrations plugged by removable metallic closures implode under long-term pressurization by local plastic instability in the same manner as do ideal spheres without penetrations, if the penetrations and closures meet the criteria in section 12.2.3.3.1. Thus, the experimentally proven LTCP curve for ideal spheres (figure 12.16) can be applied without modification to the design of spheres with multiple penetrations.

Strains in spheres with penetrations plugged by removable metallic closures are identical to those in ideal spheres without penetrations at all locations, except within 0.1 radian of the penetration edge. The maximum strain is on the concave surface at the very edge of penetration oriented in a meridional direction (figure 12.41). Its maximum value at the very edge of penetration, extrapolated from measurements taken in proximity of penetration, appears to be approximately 5, the same as under short-term pressurization (figures 12.41 and 12.42). The measured value is only 2, similar to the value measured under short-term pressurization.

Measurement of strains in the vicinity of penetrations during and after long-term pressurization shows that if the magnitude of measured strains near the penetration is below 3 percent they return to zero during relaxation at zero pressure, providing the duration of the relaxation period is equal to or exceeds the duration of the sustained pressurization phase (figures 12.41 and 12.42). This finding has also been substantiated by measuring volume changes in spheres with multiple penetrations under long-term pressurization.

Cracks form on the conical surfaces of penetration edges due to viscoelastic flow of acrylic plastic subjected to high bearing stresses by the metallic bearing surfaces on the closures. These shear cracks originate on the conical bearing surface of the acrylic hull that is in contact with the metallic closures and propagate radially in parallel to the external surface of the sphere. Their depth is a function of external pressure, ambient temperature, and duration of sustained loading (figure 12.43). The presence of an O-ring groove on the bearing surface of the closure that is in physical contact with the acrylic bearing surface makes the crack appear at a much lower external pressure and duration of sustained loading than if the O-ring groove was not in contact with the acrylic.

Thus, if the appearance of shear cracks on the edge of the penetration is to be avoided or delayed, O-ring grooves in metallic closures should be either eliminated or kept from contacting the acrylic bearing surface. This is accomplished by totally eliminating the radial O-ring seal from the bearing surface of the metallic closure or by interposing a crack-resistant but rigid gasket material between the acrylic bearing suface of the penetration and the bearing surface of the metallic closure in which the radial O-ring is located (figure 12.44). The preferred gasket material is polycarbonate plastic, as it is extremely crack-resistant and yet possesses the same physical properties as acrylic plastic.

Regardless of which design is used to minimize the occurrence of these shear cracks, sealing can be accomplished by squirting room-temperature-vulcanizing (RTV) silicone rubber into the annular space between the convex surface of the sphere and the flange on the closure or its bearing gasket (figure 12.45). Because the salicylic acid in RTV silicone rubber slightly dissolves both plastics, its adhesion to these materials is excellent. Extreme care must be exercised, however, in the placement of RTV silicone rubber in the annular space. If it enters the space between the bearing surfaces of the acrylic and the closure or its gasket, the solvent contained in RTV silicone rubber will sensitize the plastic bearing surfaces, causing them to develop shear cracks at very low external pressure loading. This can be avoided by first securing the closure in place with an internal split retaining ring and screws and then squirting the rubber into the annular space. After potting, the acrylic hull should not be pressurized externally for at least 100 hours so that the RTV silicone rubber cures completely. Failure to take this precaution will cause the external pressure to force some of the uncured material into the space between mating bearing surfaces, causing them to develop stress corrosion cracks.

An alternate approach to sealing the closures against the acrylic sphere is to replace RTV silicone rubber with an axially compressed O-ring. This is a somewhat more expensive seal, as it requires closer dimensional tolerances in the closures, gasket, and penetration. There are two advantages to this technique: (1) There is no danger in spilling the RTV silicone rubber on the plastic bearing surfaces and (2) the assembly can be pressurized immediately after placement of the ring. O-rings seals have not been used as extensively as the potted RTV silicone rubber seals, mostly because of the expense of accurately machining large penetrations and the associated gaskets and closures (figures 12.46 and 12.47).

Although experimental data on initiation of shear cracks in the bearing surfaces of penetrations on acrylic spheres under long-term pressurization are not extensive, they are adequate to substantiate the following observations for a single pressurization of 4000-hour duration:

a. Shear cracks appear at sustained pressures whose magnitudes are greater than 20 percent of STCP, if the metallic closures with an O-ring groove bear directly against the acrylic conical surface.

b. Shear cracks appear at sustained pressures greater than 25 percent of STCP, if the metallic closure without an O-ring groove bears directly against the acrylic conical surface.

c. Shear cracks appear at sustained pressures greater than 30 percent of STCP, if a polycarbonate gasket is interposed between the metallic closure (with or without O-ring grooves) and the acrylic conical surface (figure 12.48).

d. Shear cracks do not appear in acrylic plastic bearing surfaces of penetrations only if the closure is a perfectly fitted spherical sector of acrylic or polycarbonate plastic with the same thickness as the acrylic sphere.

12.2.3.3.3 Cyclic Pressurization. Implosion occurs in acrylic spheres with multiple penetrations plugged by demountable closures in the same manner and after the same cyclic pressurization history (magnitude of pressure, duration of loading phase, duration of relaxation phase, ambient temperature, and number of pressure cycles) as it does in ideal spheres without penetrations, if the characteristics of penetrations and closures meet the requirements of sections 12.2.3.2 and 12.2.3.3.1.

Cracking caused by cyclic fatigue, however, first appears on the acrylic bearing surfaces at edges of penetrations rather than where the spherical curvature is maximum and the shell thickness is minimum. These cracks are generated by local shear stresses at the interface between the bearing surfaces of the metallic closure and acrylic sphere (figure 12.49). These fatigue cracks appear only after the sphere has been subjected to a certain number of pressure cycles. After they appear, they then increase in length and depth with each pressure cycle. These cracks propagate radially from the edges of penetration in parallel to the curved surfaces of the sphere. Because the shear fatigue cracks on the acrylic bearing suface do not penetrate the spherical surfaces of the sphere, they do not cause leakage around penetrations. However, if allowed to continue they will ultimately weaken the acrylic shell around the penetration so that the local structural weakness becomes the source of instability and produces local implosion.

The same measures described for prevention of shear cracks at penetrations under long-term pressurization (section 12.2.3.3.2) can be taken to prevent shear crack initiation under cyclic pressurizations. The best and most expensive prevention against crack initiation is a polycarbonate gasket interposed between the closure and the acrylic shell. The least expensive, but still fairly effective, approach is to eliminate O-ring grooves in the metallic surface bearing against the acrylic conical surface at the edge of the opening. For short cyclic fatigue life applications even the direct contact between the O-ring groove in the closure and acrylic hull is acceptable.

Experimental data on generation of cyclic fatigue shear cracks at interfaces between closures and edges of penetrations are quite limited (nine model- and one full-scale acrylic spheres in the $0.066 < t/R_O < 0.013$ range). The following findings have been made on their basis and successfully applied to the design of manned acrylic submersibles which have amassed to date an excellent structural performance record:

a. The cyclic fatigue shear cracks at edges of penetrations appear only after some finite number of pressurizations. High pressure, long cycle duration, and high ambient temperature make the cracks appear sooner than low pressure, short cycle duration, and low ambient temperature.

b. The cumulative duration of sustained pressure phases appears to play a greater role in crack generation than does the total number of pressure cycles, providing the magnitude of pressure is the same in both cases. For example, 100 pressure cycles with 100-hour pressure phases appear to decrease the fatigue life of the closure-sphere interface to the same degree as do 1000 pressure cycles with only 6-hour pressure phases (figure 4.50).

c. The fatigue life appears to be inversely related to the external pressure during a given pressure cycle. It is a conservative postulate, for example, that two pressurization cycles to 100 pounds per square inch (0.69 megapascal) decrease the cyclic fatigue life of the acrylic bearing surface as does a single pressurization to 200 pounds per square inch (1.4 megapascals), providing ambient temperatures and duration of loadings are the same in both cycles.

d. The cyclic fatigue cracks at the closure-sphere interface appear only after approximately 4000 cycle hours under the following test parameters:

1. The ambient temperature is less than or equal to 75°F (24°C).

2. The duration of the relaxation phase is equal to the loading phase in each cycle.

3. For metallic closures with the O-ring in direct contact with the acrylic sphere, the external pressure is equal to 0.15 STCP at 75°F (24°C).

4. For metallic closures without the O-ring groove in direct contact with the acrylic sphere, the external pressure is equal to 0.25 STCP at 75°F (24°C).

5. For metallic closures with a polycarbonate gasket interposed between the metallic closure and the acrylic hull, the external pressure is equal to 0.35 STCP at 75°F (24°C).

Because shear cracks at the closure-hull interface must become very large before they trigger implosion, it is very easy to notice them several hundreds of pressure cycles prior to implosion. Thus the closures do not have to be periodically removed to detect the presence of incipient cracks. It is simply sufficient for the crew to observe the external surface of the sphere near penetrations. Only when the shear cracks exceed 1 inch (2.54 centimeters) in depth is corrective action needed, e.g., enlarging the penetration with a lathe or a mill until all cracks have been machined out. In this instance, the annular space between the edge of the enlarged opening and the old closure is then filled with a custom-made polycarbonate gasket whose increased thickness compensates for the increased diameter of the penetration.

12.2.3.3.4 Dynamic Pressurization. Acrylic spheres in manned diving systems are often sub-jected to dynamic overpressures generated by underwater explosions or implosions. In either case, rapidly traveling wave fronts impinge upon the submerged sphere and generate in it stress fields whose character rapidly changes with time. Because the wave front travels very quickly, the deformation of the sphere is not uniform as it is under static pressure load-ing. As a result, the stresses and fracturing in a sphere under dynamic loading differ sub-stantially from those found in a sphere under static loading.

Fracture formation generally occurs at two locations on the sphere: (1) the concave surface closest to the source of explosion and (2) the concave surface farthest from the source of explosion. The star-shaped fractures (figure 4.51) are very similar to those previously observed on spherical windows after they impacted a submerged obstacle with a plane surface. Their shape indicates that they are the result of a local membrane flexure generating tensile stresses on the interior suface of the sphere. Depending on the severity of explosion, the flexure cracks originating on the interior surface may penetrate partially or totally the full thickness of the spherical shell. Only if the cracks penetrate the shell completely will leakage take place, resulting in loss of the diving system.

If the sphere is oriented with the penetration facing the source of explosion, the fracture will take the form of spokes radiating from the edge of penetration (figure 12.52). The radial cracks radiating from the penetration are for a given magnitude of dynamic over-pressure generally more severe than the star-shaped cracks originating at a location far from the penetration, i.e., instead of partially penetrating the shell thickness the radial cracks penetrate the shell completely.

The presence of static pressure significantly decreases the extent and depth of fractures generated by dynamic overpressure. This effect is explained by superposition of static compressive membrane strains on the dynamic tensile strains generated by momentary overpressure. Since the magnitude of static compressive strains increases linearly with external pressure, the resistance to formation of fractures generated by dynamic overpressure also increases linearly. The favorable relationship between static pressure and resistance to cracking has been experimentally observed in the 0 to 0.3 STCP static pressure range.

It is not known how far this favorable relationship continues, since at static pressures close to STCP even a very slight dynamic loading will cause the sphere to implode violently, i.e., at static pressures close to STCP even a small dynamic overpressure will deform the sphere sufficiently to have it fail by elastic instability. At low static pressures, however, this is

not possible as even a very high dynamic overpressure cannot sufficiently deform the sphere to help the low static pressure collapse the sphere by general instability. Thus, the local deformation of the sphere, instead of triggering collapse by elastic instability, causes flexure fractures to appear. It can be stated with a high degree of assurance that the beneficial effect of static pressure on the performance of acrylic spheres under dynamic loading exists to at least 0.5 STCP. A similar relationship also exists between static pressure and resistance of the acrylic sphere to point impact.

These relationships make acrylic submersibles more resistant to underwater explosions and impact at design depth than when floating on the ocean's surface. Acrylic spheres are thus well suited for work submersibles and bottom-crawling construction equipment that routinely utilize explosive charges for cutting pipes and lines near or on the ocean bottom. Since acrylic plastic also serves as an effective sound and vibration barrier, the detrimental effects of underwater explosion on the crew and sensitive electronic equipment are significantly mitigated.

Sufficient experimental data have been generated to permit the establishment of safe standoff distances for spheres with $t/R_o = 0.133$ against explosive charges of different magnitudes (figure 12.53). For acrylic spheres with other t/R_o ratios this relationship has not been yet experimentally established. There exists, however, enough knowledge about the effect of dynamic overpressure on the structural response of acrylic spheres to permit the establishment of a conservative dynamic pressure threshold below which the acrylic sphere will not incur any structural damage. Thus, it is postulated that if the magnitude of dynamic pressure at a point on the sphere closest to the explosive charge is ≤ 0.25 STCP implosion or fracture will not take place providing the ambient static pressure is in the 0 to 0.5 STCP range.

12.2.3.4 DESIGN OF SPHERICAL ACRYLIC PRESSURE VESSELS FOR HUMAN OCCUPANCY

12.2.3.4.1 Structural Design. Although there are many approaches for designing acrylic spheres for manned pressure service, only a limited number has been accepted as reliable by the ocean engineering community and societies for the classification and certification of diving systems.

The characteristics of an acceptable design for an acrylic sphere with penetrations are summarized in ANSI/ASME PVHO-1 Safety Standard for Pressure Vessels for Human Occupancy (section 15 of this report). To be readily acceptable, it must utilize (1) penetrations whose edges form spherical cones with included angles less than or equal to 50 degrees (0.9 radian); (2) closures whose radial rigidity does not exceed the modulus of elasticity of acrylic plastic by a factor larger than 40; (3) spacing between adjacent penetrations that is larger than the radius of the larger penetration; (4) external, potted-in-place seals between the closures and the acrylic hull; (5) a shell thickness based on the experimentally derived STCP curve and conversion factors described in ANSI/ASME PVHO-1; (6) acrylic plastic whose properties meet the requirements of ANSI/ASME PVHO-1; and (7) a fabrication process capable of producing acrylic spheres with the dimensional tolerances required in ANSI/ASME PVHO-1. Utilizing these design criteria, pressure hulls for up to 3000-foot (914 meters) depth service have been built, certified, and operated successfully for many years (figure 12.54).

It is necessary to point out that the design criteria for acrylic spheres in manned diving systems are very conservative to prevent loss of life. For spheres serving as instrument housings for a one-time application these criteria are too restrictive and unnecessarily conservative. For such applications the conversion factors in ANSI/ASME PVHO-1 and section 15 can be decreased from 4 ($<50°$F ($10°$C)), 6 ($<75°$F ($24°$C)), 8 ($<100°$F ($38°$C)), 10 ($<120°$F ($49°$C)), and 16 ($<150°$F ($66°$C)) to 2, 3, 4, 5, and 8, respectively. Because of this the spheres will carry a significantly higher payload, although a penalty in terms of decreased dynamic overpressure resistance, short-term critical pressure, long-term critical pressure, and acrylic fatigue life will be paid. However, the decreased fatigue life can be tolerated, as after a single or at most several dives the sphere will be discarded.

12.2.3.4.2 Attachments. *External attachments* pose no problems for securely attaching steel pressure hulls to the framework of a diving system. Traditional attachment techniques are bolting and welding, which secure the hull to the external framework against static forces generated by gravity and buoyancy or dynamic forces generated by underwater explosions and surface waves. However, these attachment techniques are inapplicable for acrylic spheres, as neither welding nor bolting to the acrylic hull is permissible.

There are three major factors to be considered when designing attachments for acrylic spheres: (1) The acrylic sphere shrinks significantly under external pressure (approximately 2-percent diameter decrease at design depth) and any attachment to the sphere must allow for radial contraction and expansion of the sphere; (2) closures for acrylic spheres are designed to resist primarily external pressure and not forces tending to pull them out of the sphere; and (3) joints in the plastic hull are not capable of withstanding high tensile stresses.

Thus, a typical design for lifting a steel diving bell by attaching lift lines to padeyes welded to the hull near the hatch is not acceptable for an acrylic plastic diving bell, as it would place the joints in the acrylic hull in tension and tend to pull the closures out of the hull (figure 12.55). The introduction of internal spring-loaded tie rods, however, makes such a design acceptable, as the tie rods now carry all tensile loads applied externally to the closure, while under external hydrostatic loading the tie rods simply shorten by contraction of the springs (figure 12.56). This design has not been widely utilized, as the tie rods clutter up the interior of the sphere and the springs require fine adjustment to exert adequate, but not excessive, tensile forces.

The simplest and most reliable attachment design uses an external metallic cage which not only safely retains the sphere but also transmits all the forces from the lifting sling to the ballast below (figure 12.57). This was the design used in the NEMO (DSV #5) submersible. The sphere is retained by vertical guide pins that are located around the circumference of the end closures. These pins slide freely inside holes provided for this purpose in the upper cage flange. Because of these pins, the acrylic sphere cannot displace horizontally to strike the cage while its vertical movement is limited by the spacing between the upper and lower cage flanges. A neoprene gasket placed between the external surfaces of the closures and the cage flanges eliminates banging of the sphere against the cage flanges during launch or retrieval of the submersible.

Still another attachment design relies on tapered polycarbonate plastic pins fastened radially to the equator of the sphere. The pins seal against the acrylic shell by fitting into tapered holes machined in the acrylic sphere around its circumference. The tight fit between the tapered pin and its tapered hole is generated and maintained by a plastic nut screwed on the threaded tip of the pin. The vertical loads on the sphere are transferred by the horizontal pins to an equatorial ring with oversize radial holes into which the pins fit loosely. A structural scale model of this attachment arrangement has been built and found to perform satisfactorily under hydrostatic and gravity loadings (figure 12.58).

For applications where the diving system is lifted out of the water by lifting lines fastened directly to the service module below the sphere, a different attachment may be utilized. In this case the attachment needs to resist only the vertical buoyancy force and lateral hydrodynamic drag. The sphere is held against a contoured seat in the framework by a bolt or cable fastened to the bottom of the lower closure and the frame of the submersible (figure 12.59). By severing the cable with a hydraulic or explosive-actuated cutter it is possible to release the sphere from a disabled diving system and thus save its occupants. One further advantage of this attachment is that it does not block the view from the interior of the acrylic sphere.

Special attachments must be used if the sphere is routinely subjected to dynamic pressures generated by underwater explosions. The attachment must provide restraint for lateral forces of large magnitude without generating stress concentrations at the points of attachment. This is generally accomplished by distributing the lateral reaction force over a large surface of the sphere near the end closures. To decrease further the dynamic stresses in the hull, hydraulic shock absorbers are interposed between the bearing pads pushing against the sphere and the external frame (figure 12.60).

Internal Attachments pose no problems for fastening furniture and equipment to the interior surface of spherical steel pressure hulls. Attachment is generally done by bolting to lugs welded to the interior surface of the hull. The small radial displacement of the steel sphere makes it feasible to neglect this radial displacement in location and attachment of internal equipment. This is not feasible with acrylic spheres where the radial changes at design pressure are in the 1 to 2 percent range. For this reason direct attachment of internal components to the surface of the acrylic sphere is not recommended. In addition, attaching massive components to the acrylic hull is structurally cumbersome, as bonded lugs or threaded polycarbonate pins penetrating the hull would have to be employed.

There are several approaches to fastening equipment to an acrylic hull so that radial contraction of the hull does not apply compressive forces to the equipment and that does not require bonding of lugs or fastening of pins to the hull. The least desirable approach is to fasten all equipment to an internal cage which is separated from the acrylic hull by elastomeric spacers. This approach is cumbersome and expensive, as it requires piecemeal assembly of the cage inside the hull from prefabricated components brought into the interior through a hatch. Furthermore, the structure of the internal cage obstructs panoramic vision for the crew (figure 12.61).

An acceptable solution is to mount all internal components to a floor which is suspended from vertical, spring-loaded tie rods that are attached to polar closures (figure

12.62). The internal tie rods take up less space than the internal cage and are easier to install. There is, however, still some obstruction to the panoramic view, and crowding of the interior is also a problem.

A better solution is to place the floor on a foamed-in-place plastic cushion. The approach is inexpensive, does not add significant weight, and helps to dampen equipment-induced vibration (figure 12.63). The major problems are that the foam soaks up hydraulic oil, poses a fire hazard, and makes repair of electric or hydraulic lines imbedded in the plastic impossible. For this reason, foamed-in-place plastic has not been used.

The best solution is to mount the internal equipment on a floor which, in turn, is fastened to the bottom penetration (figure 12.64). This attachment does not obstruct the view from the interior, allows access through a trapdoor to the conduits below the floor, and provides total separation between the hull and the equipment. This is the arrangement that with some minor modifications has been used in most submersibles and diving bells with acrylic plastic spheres.

12.2.3.5 FABRICATION OF ACRYLIC SPHERES.

Acrylic spheres may be fabricated in many ways, depending on the design depth, optical requirements, specified weight-to-displacement ratio, size of production lots, and production cost limitation. Although there is a significant difference in optical quality between spheres fabricated by different techniques, they all produce structurally sound spheres acceptable for manned service.

12.2.3.5.1 Thermoforming. The thermoforming process relies on forming heated sheets of acrylic plastic into hemispheres. After machining the equatorial joint surfaces, the hemispheres are joined together by bonding with PS-30 adhesive. This process is rapid, proven, utilizes inexpensive fixtures, and the resulting hemispheres are free of optically objectionable inclusions or bonded joints. The finished spheres have only one joint at the equator, and experience has shown that it can be made so thin that it is hardly noticeable.

The thermoforming fixture is generally a highly polished thin metallic mold that provides uniform curvature for the vacuum or pressure-formed acrylic hemispheres. Hemispheres can be also formed without any mold by free forming with compressed air. However, because of the large variations in spherical curvature on the finished product this approach is used only to build spheres not slated for manned service.

Although this process is reliable and inexpensive, it has some serious drawbacks and limitations that have precluded its wide application. The major drawback is wide variation in shell thickness at various points on the formed hemisphere, and the major limitation is the inability to form hemispheres with $t/R_o \geq 0.08$ without utilization of expensive matching of male and female mold assemblies and presses capable of generating very large forming pressures. Because the variation in thickness across a given hemisphere may easily reach 50 percent, the depth rating of thermoformed hemispheres is determined by the thinnest spot on the hemisphere, which is always found at the apex. Thus, both the low t/R_o ratio and the thinness of the shell at the apex keep the depth ratings of spheres assembled from thermoformed hemispheres at less than 100 feet (30 meters).

To circumvent these problems, a modification to the basic thermoforming process has been developed by which spheres with a $t/R_o \leqslant 0.12$, a thickness variation less than 5 percent, and sphericity deviation less than 0.5 percent have been successfully formed for depth service to 3000 feet (914 meters). This modification consists of substituting the forming of small structural modules with spherical curvature for forming of complete hemispheres. Because these modules subtend only small spherical angles they can be formed in great thicknesses without significant thinning at the center of the module. Only two shapes of structural modules have been widely used in the fabrication of acrylic spheres: spherical pentagons and spherical triangles in the form of orange peels.

The major difficulties in using thermoformed modules for assembly of spheres are precision alignment and inclusion free bonding of individual structural modules. Both problems have been solved by employing sophisticated alignment fixtures and bonding techniques. The acrylic spherical hulls for NEMO, MAKAKAI, and JOHNSON-SEA-LINK 1 and 2 were built using these forming and bonding techniques. Because this process is one of the standard approaches to the construction of large acrylic spheres, it is discussed in appendix A.

12.2.3.5.2 Casting. Although the construction of spheres by the assembly and bonding of thermoformed modules continues to be the most inexpensive and reliable fabrication technique, another fabrication process has been recently developed. The reason for developing this new technique was dissatisfaction with the presence of many noticeable bonded joints in the field of vision and the inability of the thermoforming process to produce thick spheres for depths in excess of 3000 feet (914 meters).

This fabrication technique utilizes a casting process in precision-machined female and male mold assemblies that produce within tight dimensional tolerances acrylic plastic hemispheres of any diameter and thickness. Because only a single equatorial joint is required for bonding the two hemispheres, the optical performance of the sphere has been significantly enhanced. Furthermore, uniform thickness and sphericity have eliminated the presence of local optical distortions so common in spheres assembled from many structural modules with slightly varying thicknesses and sphericities.

The primary difficulty that had to be overcome in the development of this technique was the prevention of meridional fractures and cavities caused by the shrinkage of the resin mixture during its polymerization. After appropriate modification of the resin polymerization process, these problems were eliminated. The acrylic spheres produced by this process are decidedly superior both optically and structurally to those assembled from thermoformed modules. Their acceptance by users, however, has been somewhat less than enthusiastic because of the large investment required for precision-machined steel male and female molds. Because of its great potential for the future, however, the casting process is briefly described in appendix A.

12.2.3.6 REPAIR OF DAMAGED ACRYLIC SPHERES. After several years of service, an acrylic plastic sphere will show signs of wear, i.e., surface crazing, scratches, and cracks. The presence of crazing, scratches, or cracks on the spherical surfaces of the sphere does not decrease its operational depth rating, since the material in the sphere is in membrane compression when subjected to external pressure and thus the surface discontinuities do not act as stress risers. Still, their presence reduces the optical performance of the sphere and

contributes significantly to the anxiety of the crew. Thus, after the crazing, scratches, and cracks reach a certain density on the spherical surface of the sphere, measures must be taken to eliminate them.

Crazing presents the greatest problem, as it is easily induced and generally covers a large area (figure 12.65). Factors which induce crazing are

a. Residual stresses in the material that are introduced during fabrication and are not removed because the annealing temperature is too low ($<175°F$ ($79°C$)) or the annealing process is too short.

b. Sensitization of the surface to stress-induced crazing by cleaning the surface with improper cleaning fluids, e.g., MEK, acetone, alcohols, etc.

c. Weathering, particularly sunlight and ozone.

Once crazing appears on the surface of the sphere it will not disappear, but will grow in depth and area coverage. The only known approach to this problem is to tolerate it as long as it is optically possible and then to remove it by deep sanding or machining of the whole surface. Since after deep sanding or machining the whole surface must be again polished and the sphere annealed, this operation is expensive, averaging 20 percent of the original sphere acquisition cost.

Scratches do not present a problem, as they do not grow in depth, width, or length with each external pressure cycle. Thus, there is no need to remove them by local sanding and polishing unless they become truly objectionable from the optical viewpoint. If the sanding and polishing are localized, annealing with a heat lamp may suffice to prevent buildup of localized residual stresses that may generate surface crazing in a short period of time.

Fractures present a serious problem, as they will probably grow in depth with each external pressurization and subsequent relaxation phase. Fractures on the spherical surfaces are usually initiated by point impact or dynamic pressure loading in the form of an underwater explosion. If the depth of the fracture exceeds 12 percent of the wall thickness, the sphere should be immediately repaired. There are three proven approaches for repairing these fractures.

The oldest approach is to drill or rout out the fracture and fill in the cavity with PS-30 self-polymerizing cement. Since PS-30 cement is softer than the cast acrylic plastic material of the sphere, only small fractures can be repaired in this manner without weakening the sphere (figure 12.66). If, after removal of the fractured material, the maximum width of the cavity exceeds 0.187 inch (0.5 centimeter) it should not be filled with PS-30 cement. A casting slurry (mix of monomer resin and polymethyl-methacrylate powder) should be used and the whole sphere should then be subjected to the elevated temperature and pressure required for polymerization of the slurry (figure 12.67). Since the elevated temperature in the polymerization process requires removal of the end closures and equipment from the sphere and placing the sphere in a heated and pressurized autoclave, it is rarely undertaken. The costs associated with this process are high, and length of time the diving system is out of commission is very long. Still, if properly planed, the local casting repair restores the sphere to its original condition without noticeable optical discontinuities (figure 12.68).

A somewhat less expensive approach is based on machining out a spherical sector containing the fractured material and plugging the opening with a bonded-in-place spherical acrylic sector with dimensions identical to those of the one removed (figure 12.69). PS-30 adhesive is used to bond the new spherical sector. To prevent crazing of the bonded surfaces, the sphere and the sector are annealed prior to and after bonding. There is no size limitation for this kind of repair.

The least expensive approach is to machine out the spherical sector containing the fractured material and to plug the opening with a polycarbonate plastic insert held in place by bolts and a retaining ring. The plug is sealed in place with RTV silicone rubber applied to the exterior surfaces of the sphere and plug (figure 12.40). This repair is limited to small fractures, as the polycarbonate plastic plug, being less transparent than the acrylic sphere, will block the view from the interior of the sphere. This repair technique is particularly attractive for quick repair of small fractures in the field, as it demands no special skills or tools and requires only local annealing with a heat lamp of the machined conical bearing surface in the acrylic sphere. At a later time the polycarbonate plug can be removed and replaced with a bonded-in-place acrylic plug with superior optical properties.

Shear cracks on the conical bearing surfaces of penetrations present a special problem as they are a sign of fatigue age and thus unavoidable. Their elimination requires the removal of closures and remachining of conical bearing surfaces. Following the machining operation, the sphere must then be annealed and the closure provided with a polycarbonate spacer than also serves as a bearing gasket. After the refinishing of the conical bearing surfaces and placement of the bearing gaskets, the acrylic sphere can be returned to service without any decrease in depth rating. The alternative to refinishing the conical bearing surfaces at penetrations is to reduce the depth rating of the sphere. Since the costs of refinishing two conical bearing surfaces and procuring polycarbonate bearing gaskets are generally less than 40 percent of the acquisition costs of a new sphere, this is a more economical solution than discarding the sphere by drastically derating its depth.

Based on this discussion, it appears that by applying these procedures the safe operational life of acrylic spheres can be extended to at least 10,000 pressure cycles, if age and weathering do not degrade the physical properties of the acrylic to the extent that the operational depth of the sphere must be substantially derated or the sphere discarded. Since long-term weathering data for thick acrylic plastic ($\geqslant$ 2 inches (5 centimeters)) are not now available, the age limitation on thick acrylic spheres must be based on the weathering data of very thin acrylic plastic ($\leqslant$ 0.25 inch (0.6 centimeter)). Until weathering data for thick acrylic shells become available, the current 10-year life limitation of depth ratings for spheres based on weathering of thin acrylic plastic must suffice.

12.3 REFERENCES

12.1   Moldenhauer, J. G., et al., "The Design, Fabrication and Testing of Acrylic Pressure Hulls for Manned Vehicles," ASME Paper No. 65-WA/UNT-10, Chicago, November 1965.

12.2   Naval Civil Engineering Laboratory, Report R-676, "Development of a Spherical Acrylic Plastic Pressure Hull for Hydrospace Application," by J. D. Stachiw, April 1970.

12.3   Naval Civil Engineering Laboratory, Technical Note N-1113, "The Spherical Acrylic Pressure Hull for Hydrospace Application; Part II — Experimental Stress Evaluation of Prototype NEMO Capsule," by J. D. Stachiw, October 1970.

12.4   Naval Civil Engineering Laboratory, Technical Note N-1134, "The Spherical Acrylic Pressure Hull for Hydrospace Application; Part IV — Cyclic Fatigue of NEMO Capsule #3," by J. D. Stachiw, October 1970.

12.5   Naval Civil Engineering Laboratory, Technical Note N-1094, "The Spherical Acrylic Pressure Hull for Hydrospace Application; Part III — Comparison of Experimental and Analytical Stress Evaluations for Prototype NEMO Capsule," by H. Ottsen, March 1970.

12.6   Naval Undersea Center, Technical Publication 383, "Cast Acrylic Dome for Undersea Applications," by J. D. Stachiw, January 1974.

12.7   Naval Undersea Center, Technical Publication 410, "Development of Precision Casting Process for Acrylic Plastic Spherical Shell Windows Applicable to High Pressure Service," by J. D. Stachiw, June 1974.

12.8   Naval Undersea Center, Technical Publication 451, "NEMO Model 2000 Acrylic Plastic Spherical Hull for Manned Submersible Operation at Depths to 3000 Feet," by J. D. Stachiw, December 1974.

12.9   Naval Undersea Center, Technical Publication 493, "Improved Fabrication Process for Spherical Acrylic Plastic Submersible Hulls," by J. D. Stachiw, December 1975.

12.10 Naval Undersea Center, Technical Publication 505, "Spherical Acrylic Plastic Hulls Under External Explosive Loading," by J. D. Stachiw, March 1976.

12.11 Stachiw, J. L., and Stachiw, J. D., "Effect of Weathering and Submersion in Seawater on the Mechanical Properties of Acrylic Plastic," ASME Paper No. 77-WA/OCE-5, Atlanta, November 1977.

12.12 Stachiw, J. D., and Dolan, R. B., "Spherical Acrylic Pressure Hulls with Multiple Penetrations," ASME Paper No. 77-WA/OCE-2, Atlanta, November 1977.

12.13 Stachiw, J. D., "Spherical Acrylic Pressure Hulls for Undersea Exploration," *Journal of Engineering for Industry*, Trans. ASME, Series B, Vol. 93, No. 2, May 1971.

12.14 Tsuji, K., and Bates, R., "Fabrication of NEMO Type Submersible," ASME Paper No. 70-WA/UNT-4, New York City, November 1970.

12.15 Maison, J. R., and Ottsen, H., "Stress Analysis of NEMO Type Submersible," ASME Paper No. 70-WA/UNT-8, New York City, November 1970.

12.16   Snoey, M. R., and Katona, M. G., "Stress Analysis of a Spherical Acrylic Pressure Hull," ASME Paper No. 70-UNT-B, December 1970.

12.17   Stachiw, J. D., *Failure Modes of Spherical Acrylic Shells Under External Hydraulic Loading*, edited by R. Szilard, The University Press of Hawaii, 1973.

12.18   Trowbridge, T., "Optical Properties of a Spherical Plastic Underwater Observatory NEMO," ASME Paper No. 70-UNT-A, December 1970.

12.19   Stachiw, J. D., and Maison, J., "Acrylic Pressure Hull for JOHNSON-SEA-LINK Submersible," ASME Paper No. 71-WA/UNT-6, Washington, November 1971.
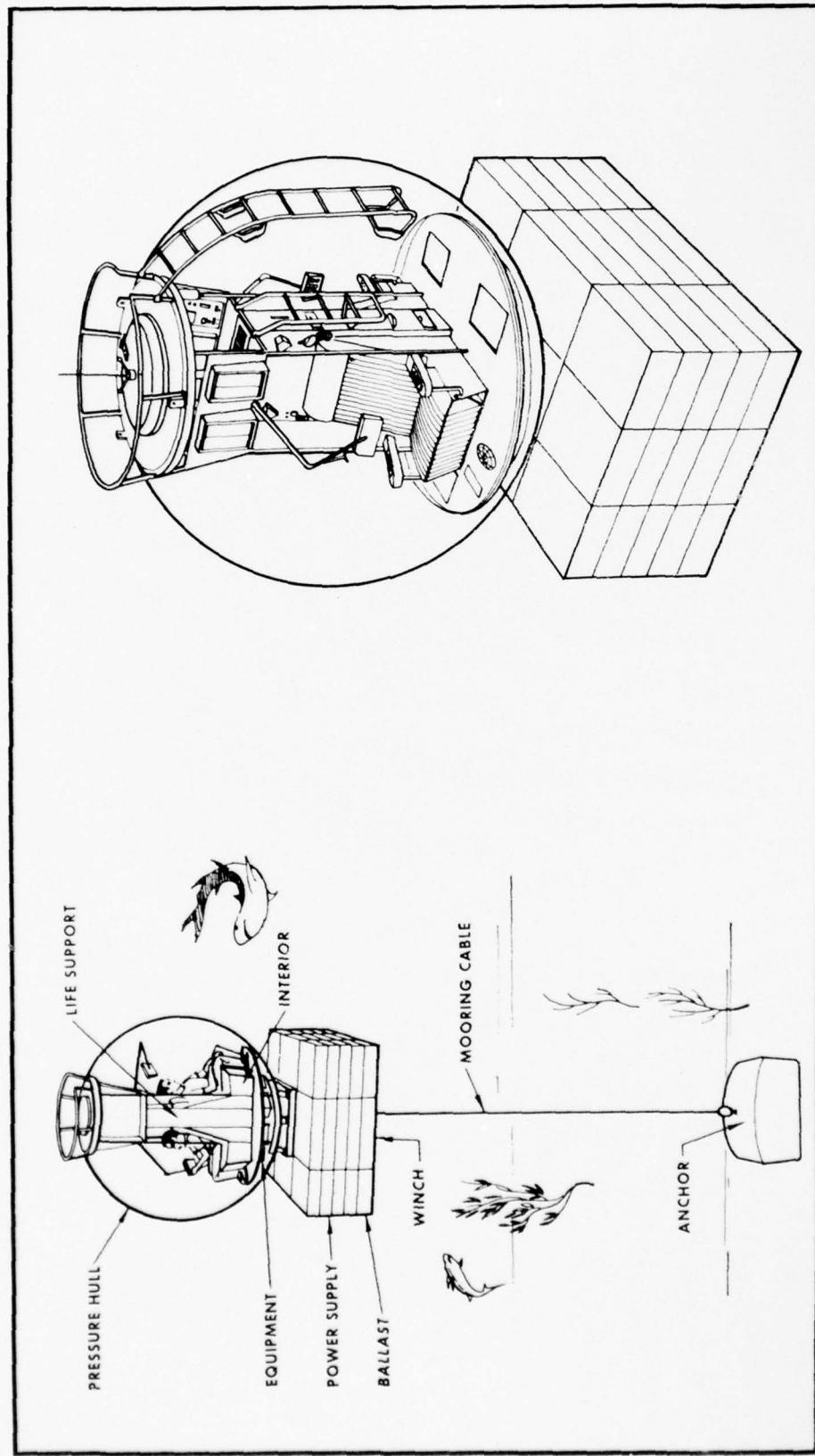
Figure 12.1. Engineering concept of a 10-foot-diameter (3 meters) underwater observatory which, depending on mission requirements, can operate in either a tethered or free-floating mode for many days at a time.

Labels in figure: LIFE SUPPORT, INTERIOR, PRESSURE HULL, EQUIPMENT, POWER SUPPLY, BALLAST, WINCH, MOORING CABLE, ANCHOR
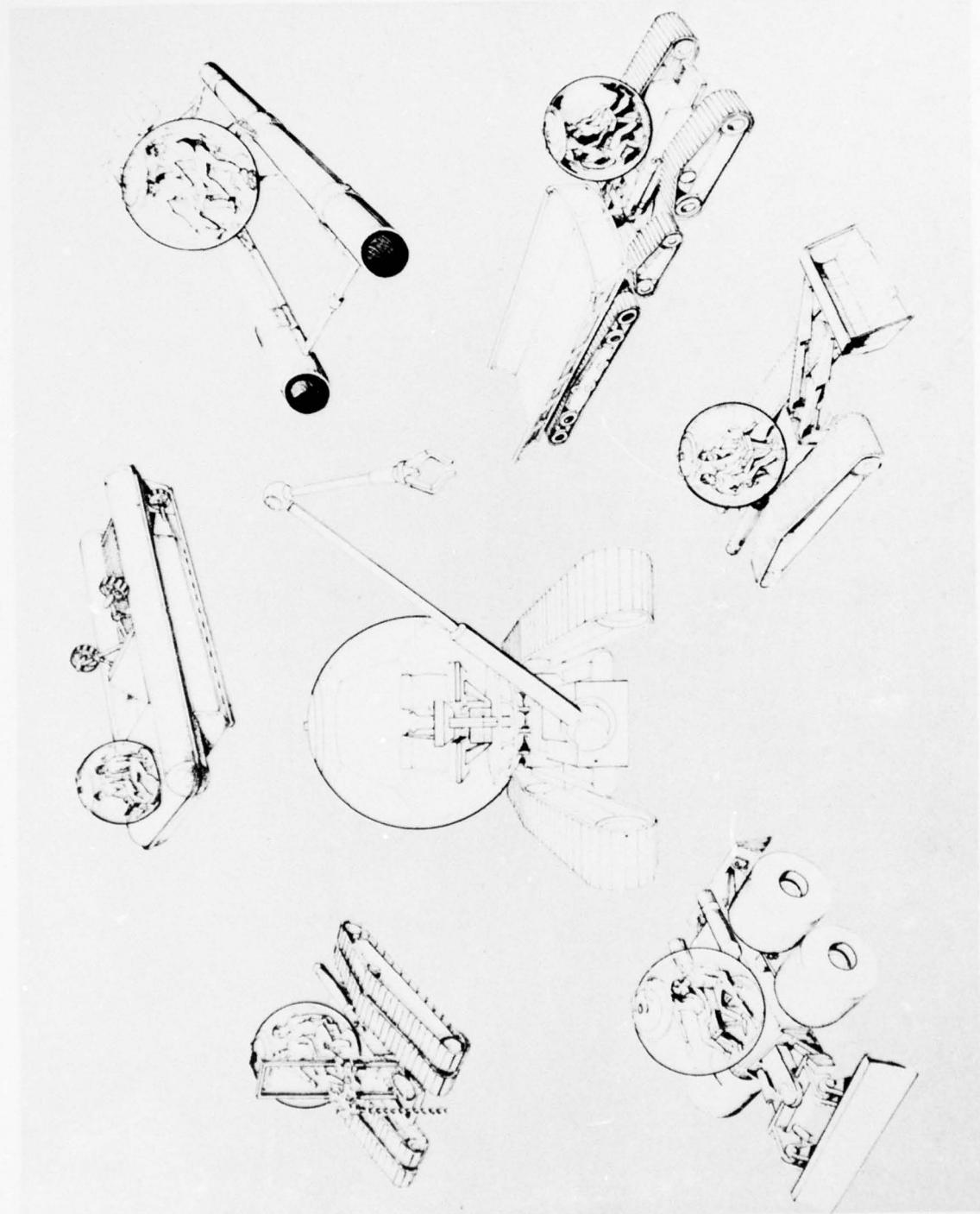
Figure 12.2. Engineering concept of standardized acrylic spherical pressure hulls that can function as interchangeable crew compartments on underwater construction equipment.

plan view

plan view

elevation view

elevation view

assembly of spherical pentagons

assembly of 2 hemispheres
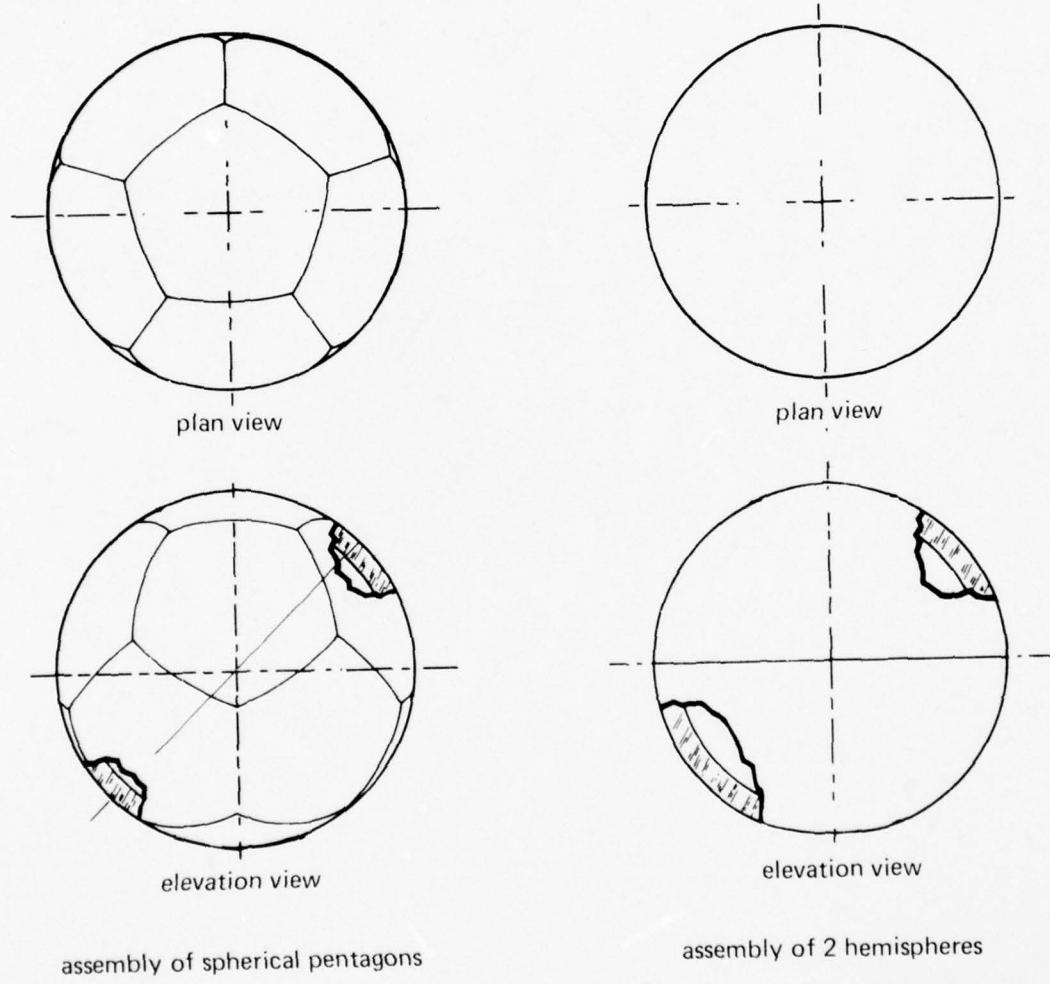
Figure 12.3. Proven construction techniques for spherical acrylic pressure hulls.
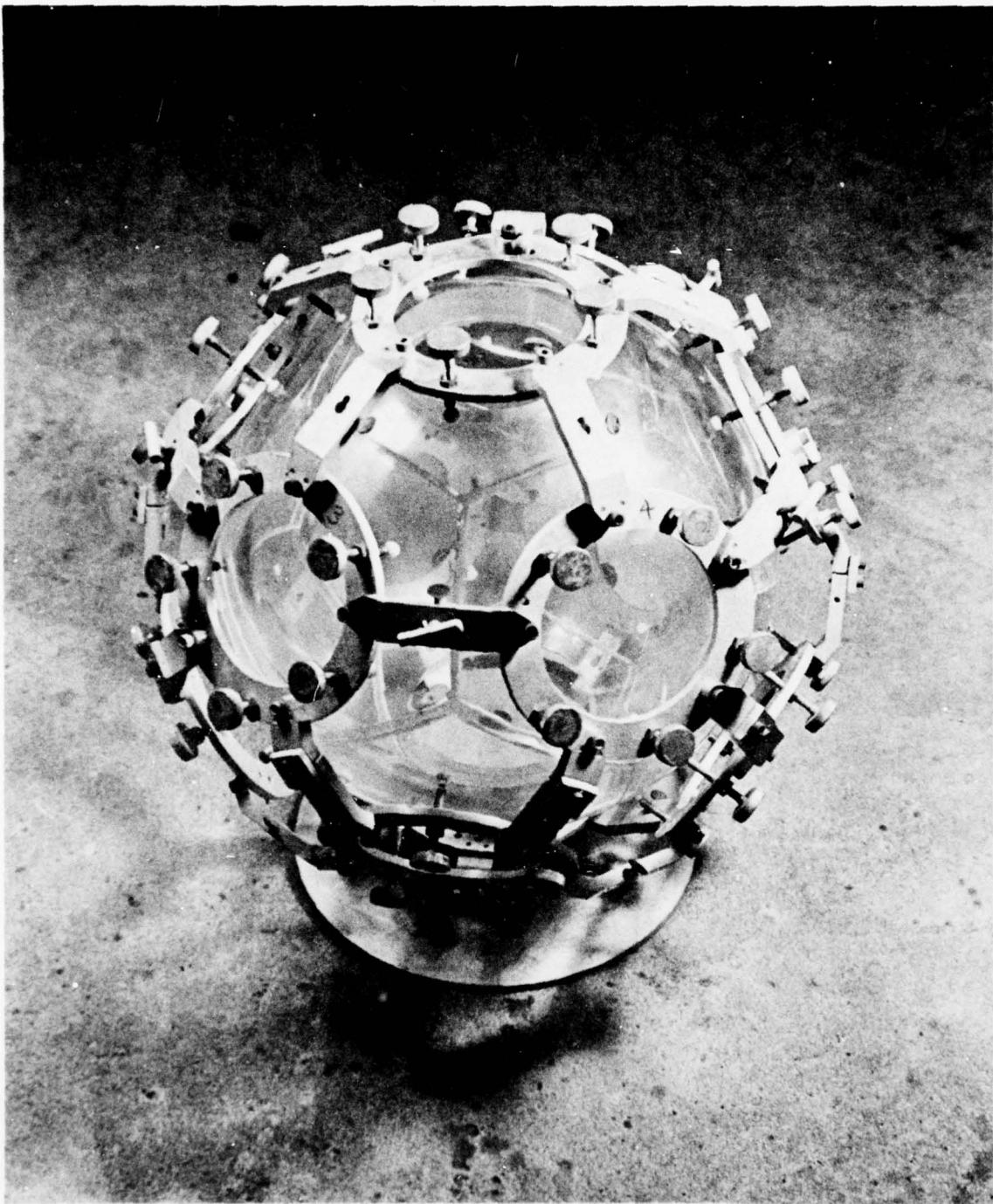
Figure 12.4. Fixture for aligning 12 spherical pentagons prior to bonding them together to form a model-scale spherical acrylic pressure hull with $R_0 = 7.5$ inches (19 centimeters).
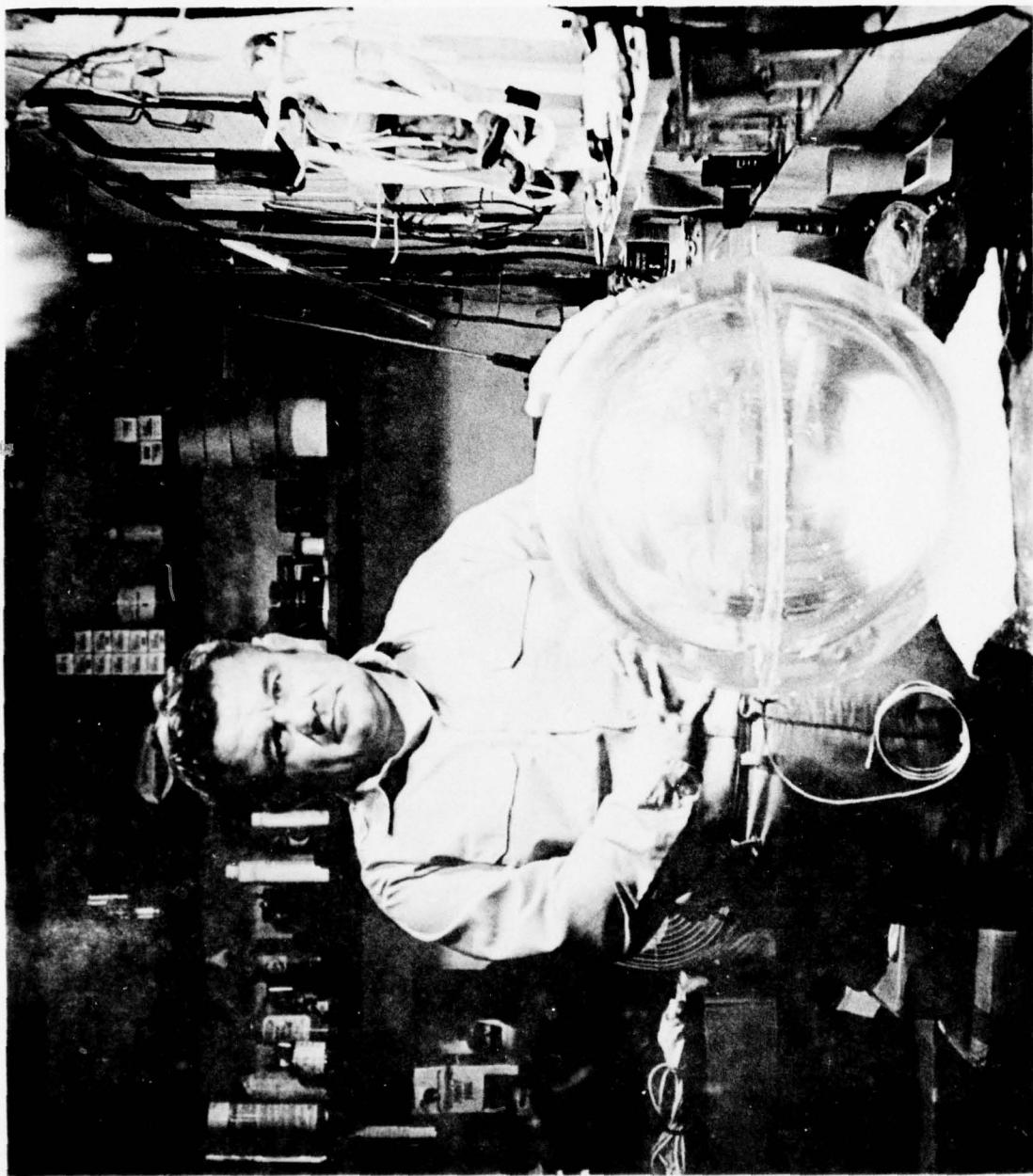
Figure 12.5. Alignment of two precision-cast hemispheres for bonding together into a spherical pressure hull.

0.125 in (0.3 cm)

Figure 12.6. Typical variations in the width of bonded joints in acrylic spherical pressure hull assembled from 12 spherical pentagons.
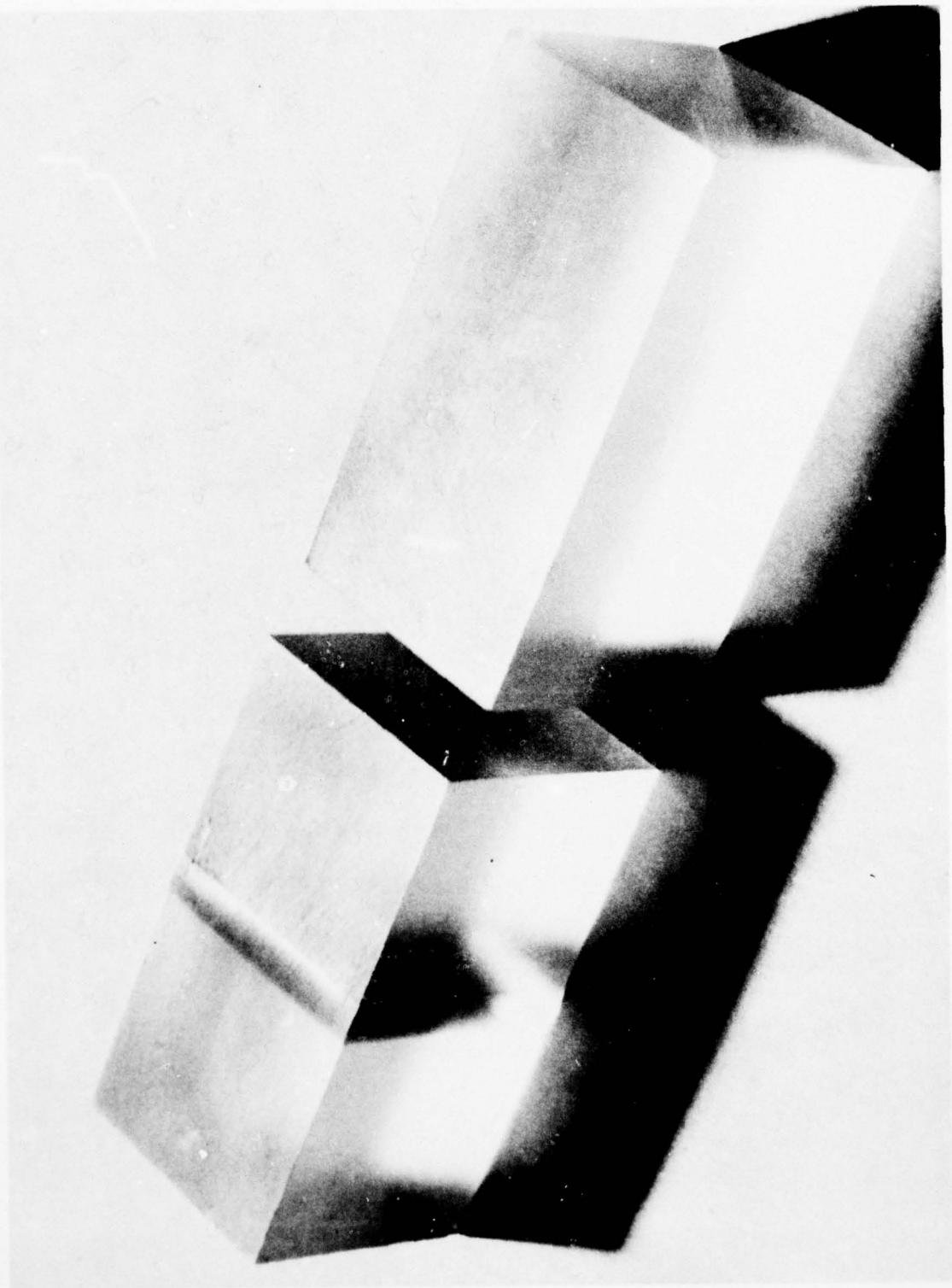
Figure 12.7. Two acrylic plastic test specimens after uniaxial compression testing to 15,000 pounds per square inch (103.4 megapascals). Note that the PS-18 adhesive in the joint has permanently deformed, while the parent material has not.
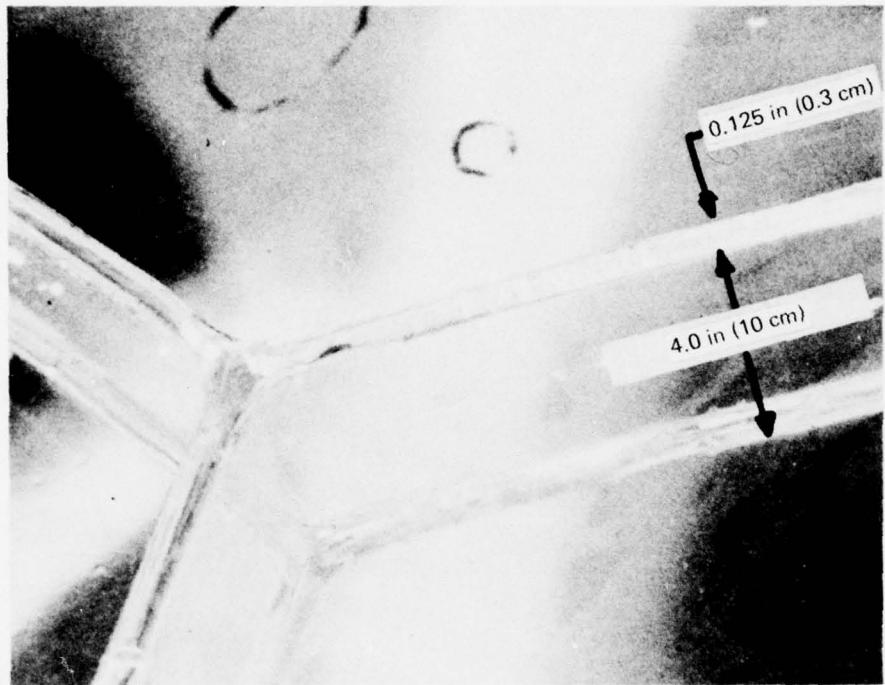
Figure 12.8. Typical inclusions in the bonded joint of an acrylic spherical hull assembled from 12 spherical pentagons.
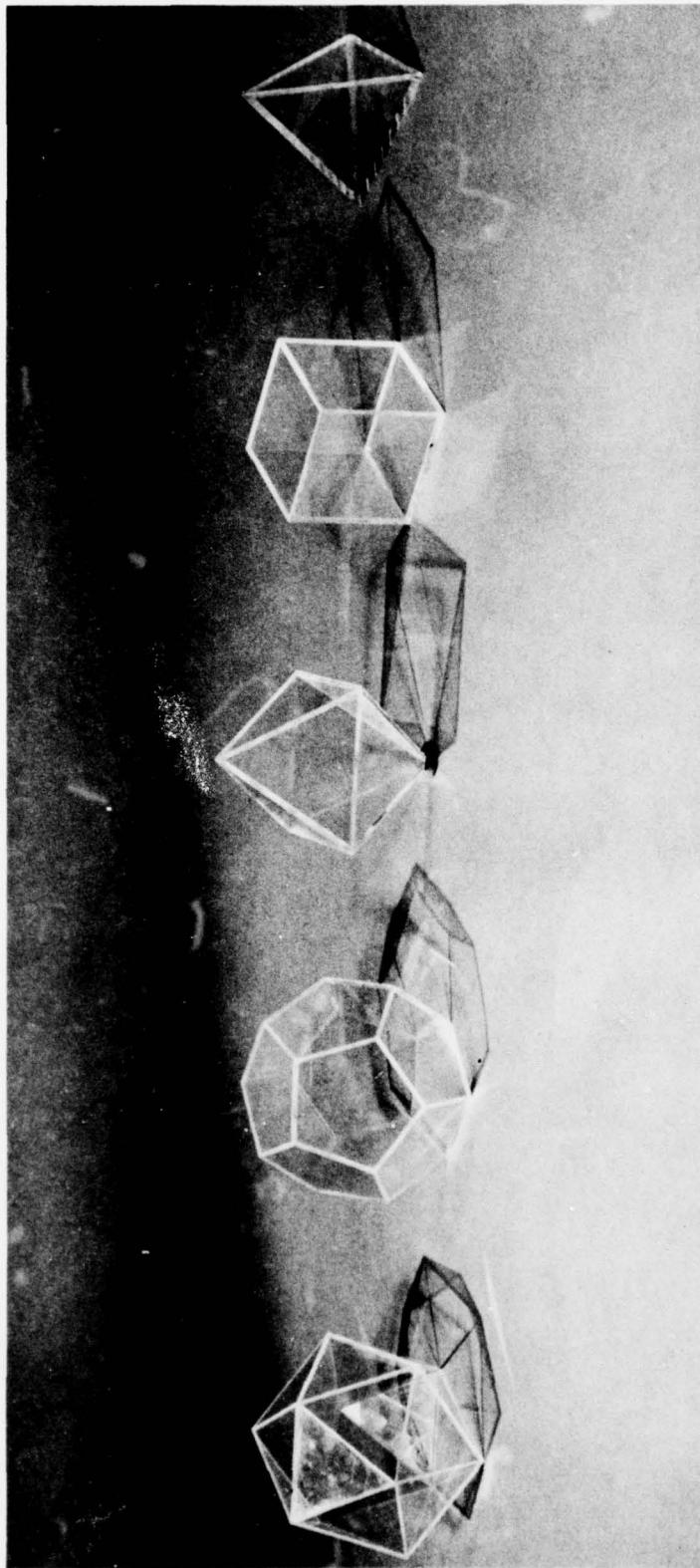
Figure 12.9. Acrylic pressure hulls with plane surfaces can be used in place of spherical hulls only in very shallow waters, as the critical pressure of such shapes is very low. All the shapes in this figure have a 0.25 inch (0.6 centimeter) wall thickness and are proportioned to fit inside a circumscribed 10-inch-diameter (25 centimeters) sphere. The short-term critical pressures of these shapes are shown below:

Shape	$\dfrac{\text{STCP Shape}}{\text{STCP Sphere}}$	STCP Shape, psi	Volume, in^3	Weight, lb	STCP $\times$ volume/weight
Tetrahedron	0.15	170	64	1.2	9.05×10^3
Hexahedron	0.09	100	192	2.1	9.15×10^3
Octahedron	0.16	180	166	1.8	1.67×10^4
Dodecahedron	0.14	160	348	2.3	2.42×10^4
Icosahedron	0.33	380	317	2.6	4.64×10^4
Ideal sphere 10 inch outside diameter	1.0	1130	523	3.4	1.74×10^5

Notes: 1 psi = 6.894757 E+03 Pa; 1 lb = 0.04536 kg; 1 in = 2.540000 E–2 m

12-36
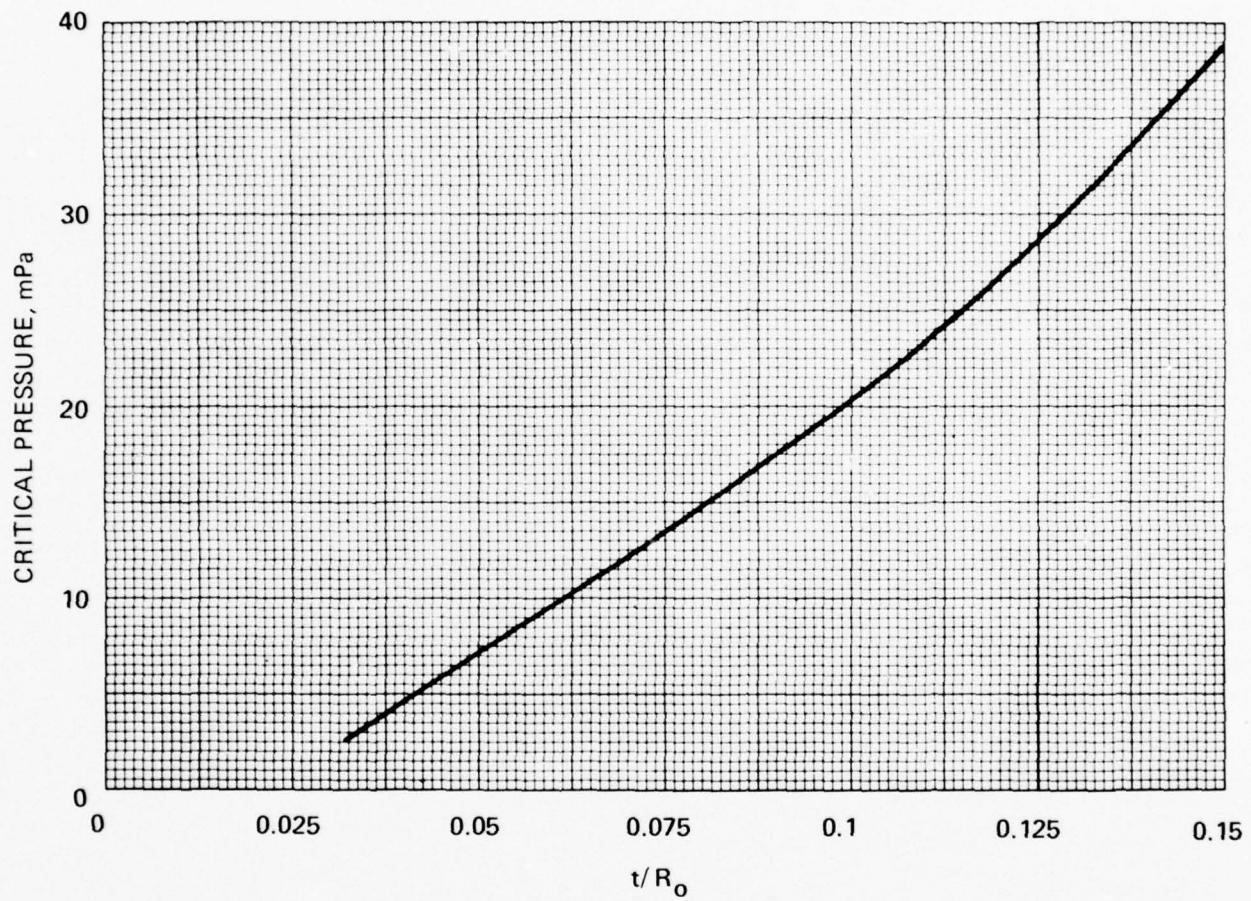
Figure 12.10. Short-term critical pressure of ideal acrylic spheres under external pressure loading at 75°F (24°C) ambient temperature as a function of t/R_O ratio.
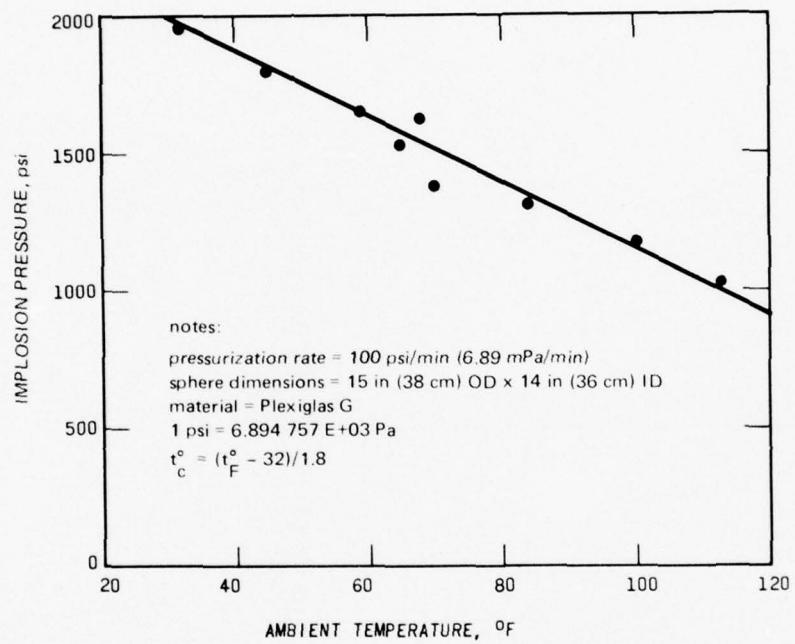
Figure 12.11. Effect of ambient temperature on the short-term critical pressure of ideal acrylic spheres with $t/R_O = 0.066$ under external pressure loading.

12-38
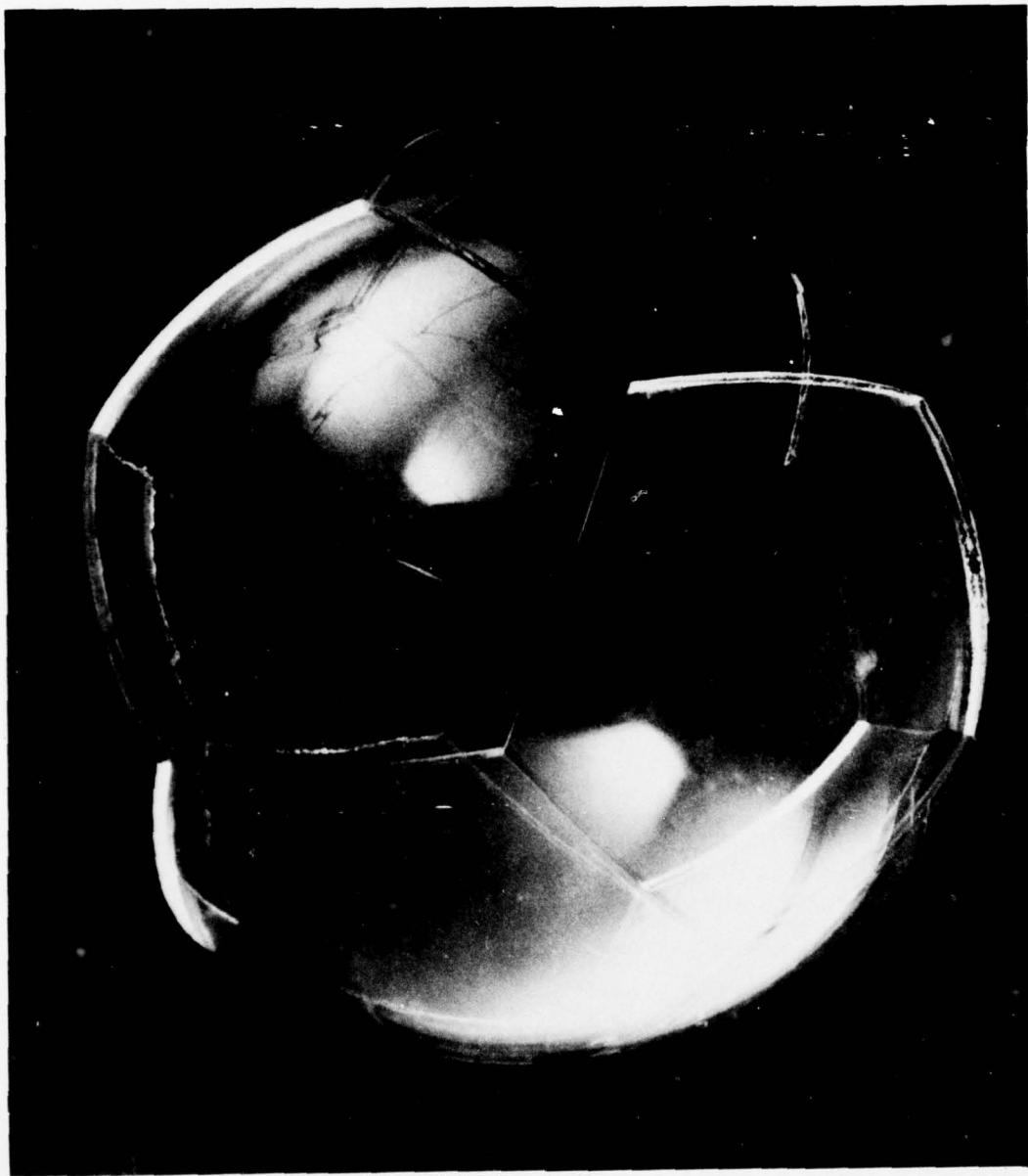
Part A. Ideal sphere before implosion.

Figure 12.12. Typical general implosion of an ideal sphere with $t/R_O = 0.066$ under short-term external hydrostatic pressurization at ambient room temperature.

Part B. Ideal sphere after general implosion at 1500 pounds per square inch (10.3 megapascals) under short-term pressurization.

Figure 12.12. Continued.
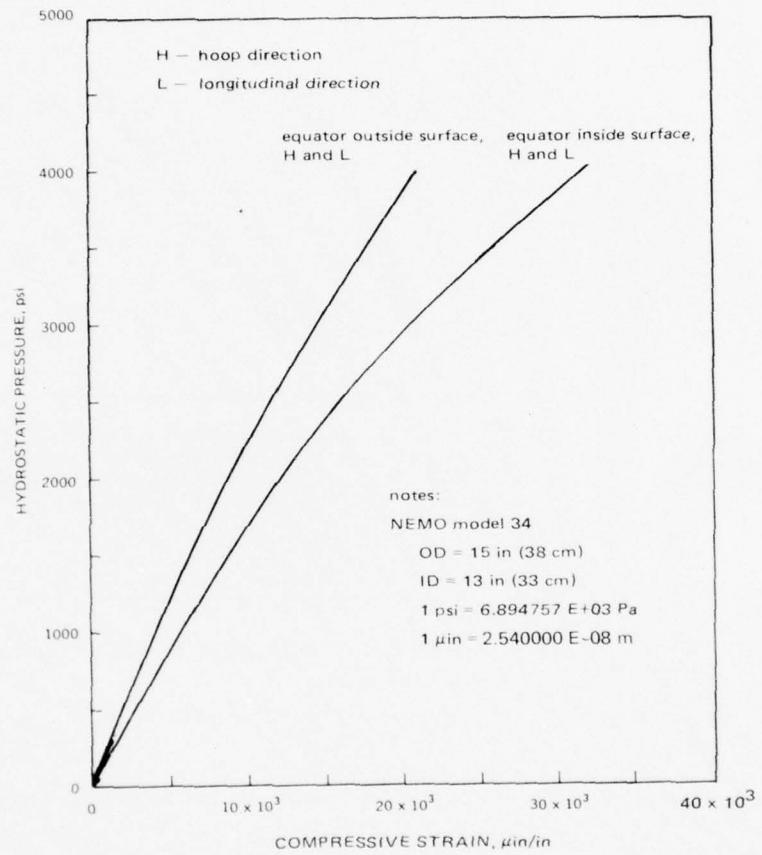
Figure 12.13. Typical strains in an ideal acrylic sphere with
$t/R_O = 0.133$ under short-term external pressurization at
an ambient room temperature of $75°F$ ($24°C$).
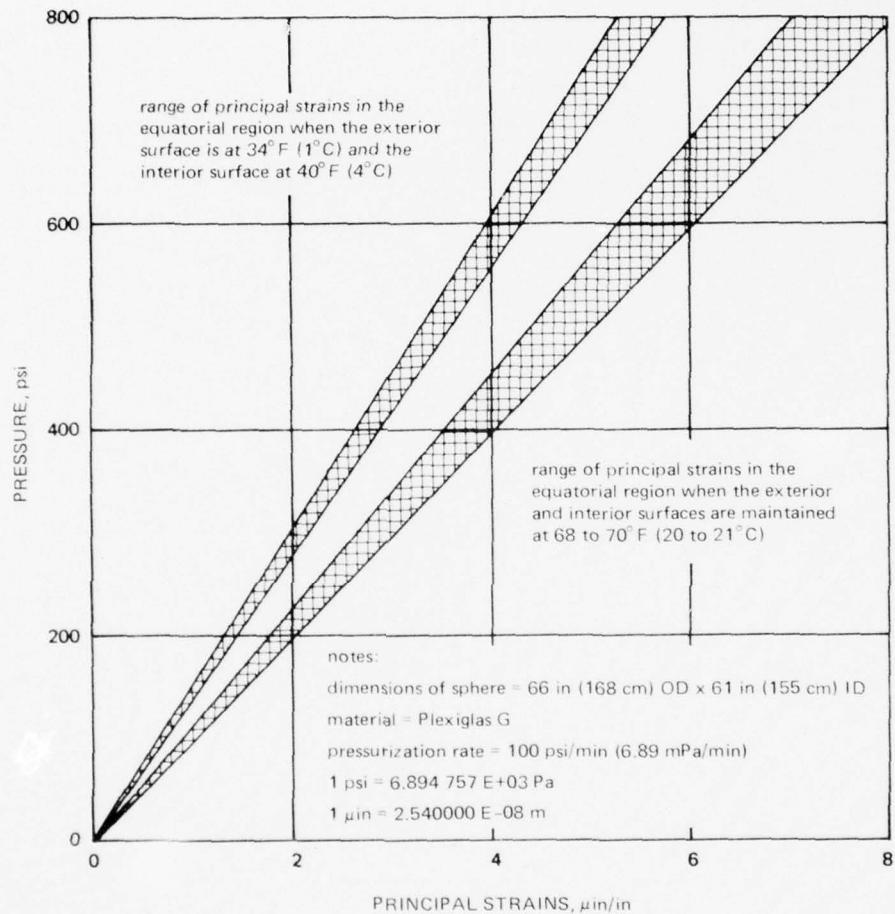
Figure 12.14. Effect of temperature on the magnitude of strains on the interior of an ideal acrylic sphere with $t/R_o = 0.075$ under short-term external hydrostatic pressurization.

12-42
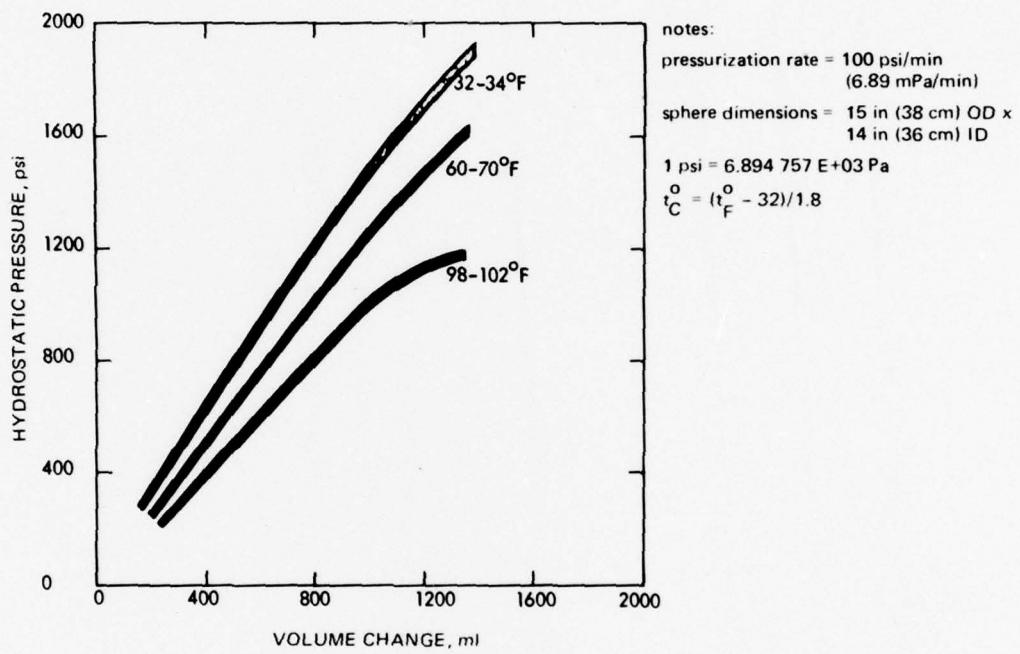
Figure 12.15. Effect of temperature on the volumetric decrease of ideal acrylic spheres with $t/R_O = 0.066$ under short-term external pressurization.
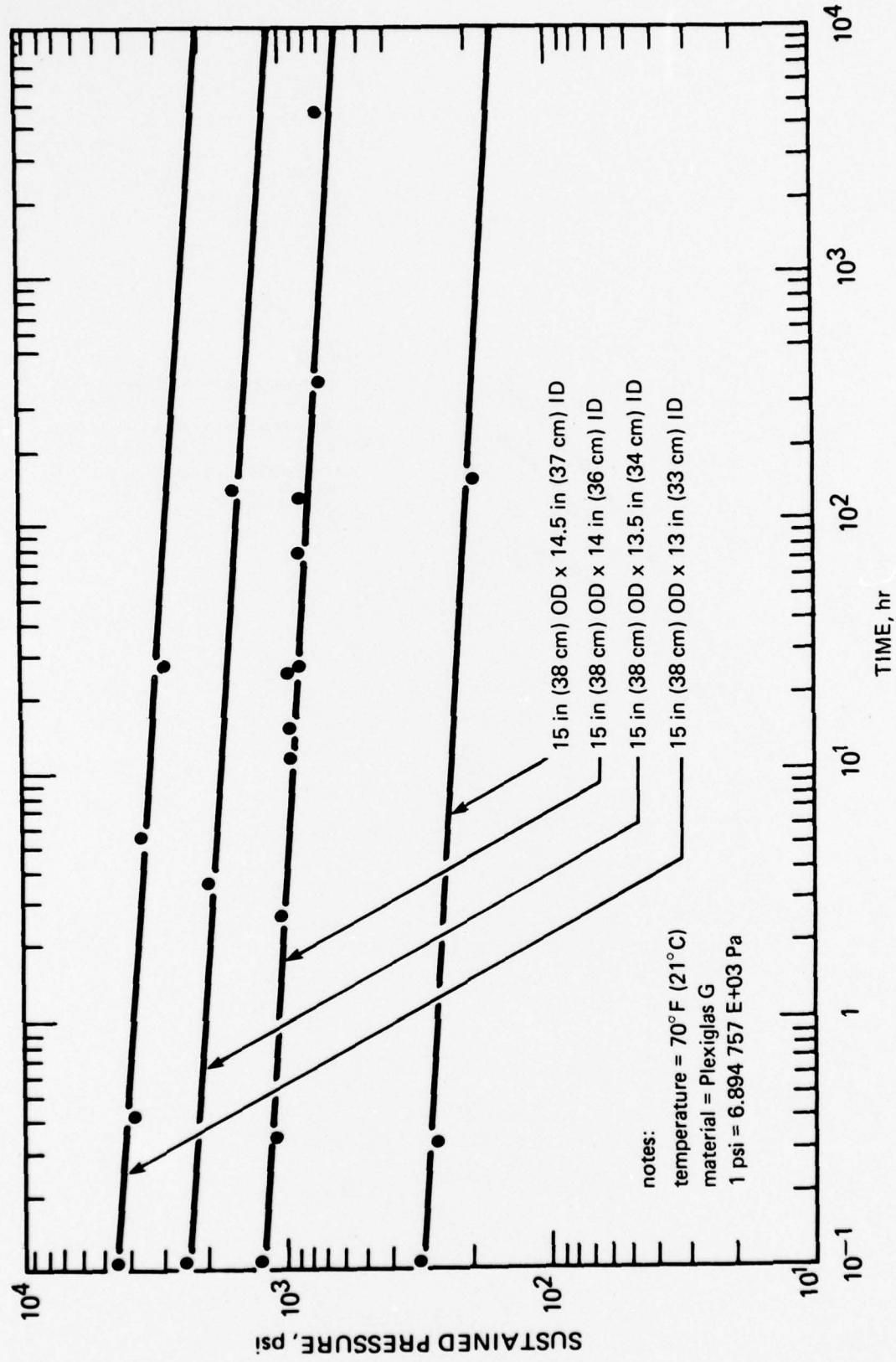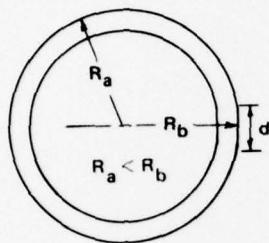
Figure 12.16. Effect of loading duration on the critical pressure of ideal acrylic spheres under sustained external pressure at ambient room temperature of 70°F (21°C).

15 in (38 cm) OD x 14.5 in (37 cm) ID
15 in (38 cm) OD x 14 in (36 cm) ID
15 in (38 cm) OD x 13.5 in (34 cm) ID
15 in (38 cm) OD x 13 in (33 cm) ID

notes:
temperature = 70°F (21°C)
material = Plexiglas G
1 psi = 6.894 757 E+03 Pa

TIME, hr

SUSTAINED PRESSURE, psi

d = diameter of area with a larger
radius of curvature than R_a
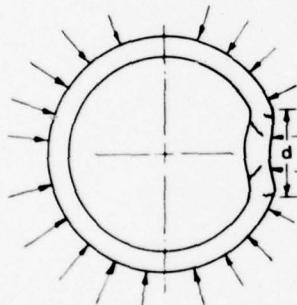

R_a

R_b

$R_a < R_b$

d

Phase 1 — small area with
larger radius resulting from
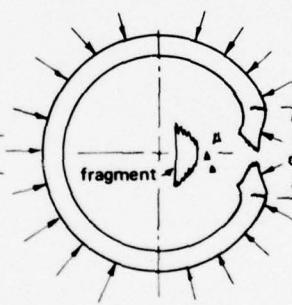imperfect fabrication
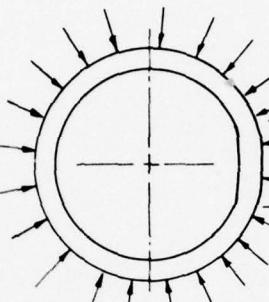
Phase 2 — under hydrostatic
loading both the area and
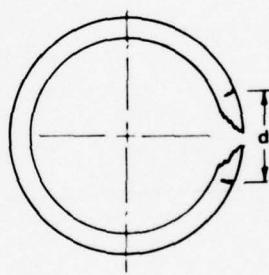the radius of curvature
increase at the imperfection
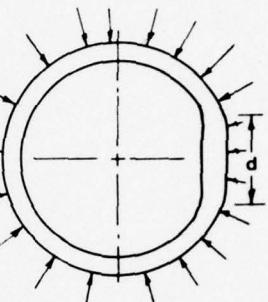
Phase 3 — the area of imperfection
does not increase any more, only
the radius of curvature increases

fragment

Phase 4 — area of imperfection
remains constant, the direction
of the radius of curvature
reverses itself, fractures appear

Phase 5 — local penetration of
pressure hull takes place

Phase 6 — surface of the hull
returns to its original sphericity
at zero pressure

Figure 12.17. Mechanism of local viscoelastic buckling in an
ideal acrylic plastic hull under long-term sustained external
pressurization.

12-45

Figure 12.18. Local failure of an acrylic sphere with $t/R_o = 0.066$ caused by local viscoelastic buckling after 22,300 hours of sustained pressurization at $70°F$ $(21°C)$ average temperature.
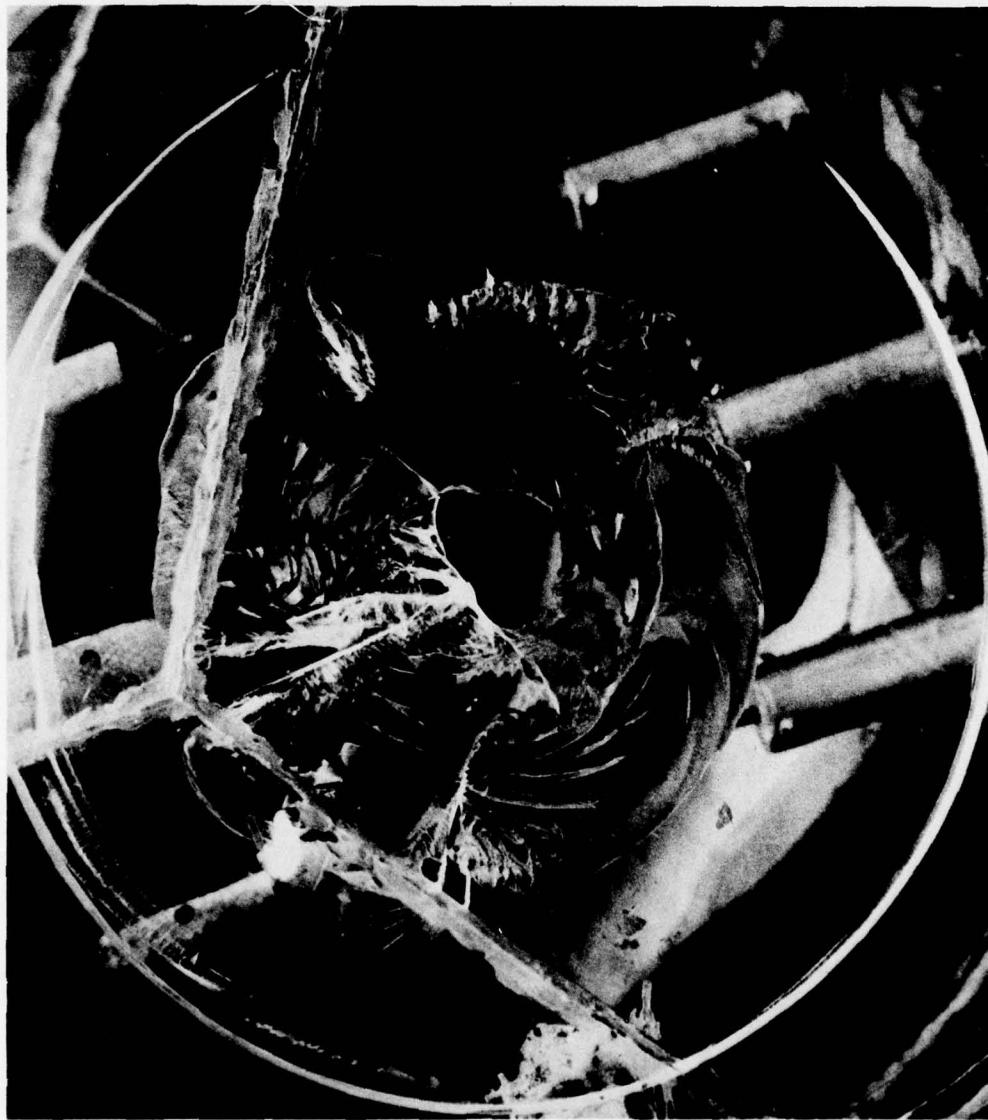
Figure 12.19. Closeup of local failure of figure 12.18. Note the cone-shaped fracture surface with its apex penetrating the external surface and the circular crack originating on the external surface penetrating to the midplane of the wall thickness. Both the conical fracture surface and the circular crack cross the bonded joints, indicating that these joints do not serve as planes of weakness in the hull.
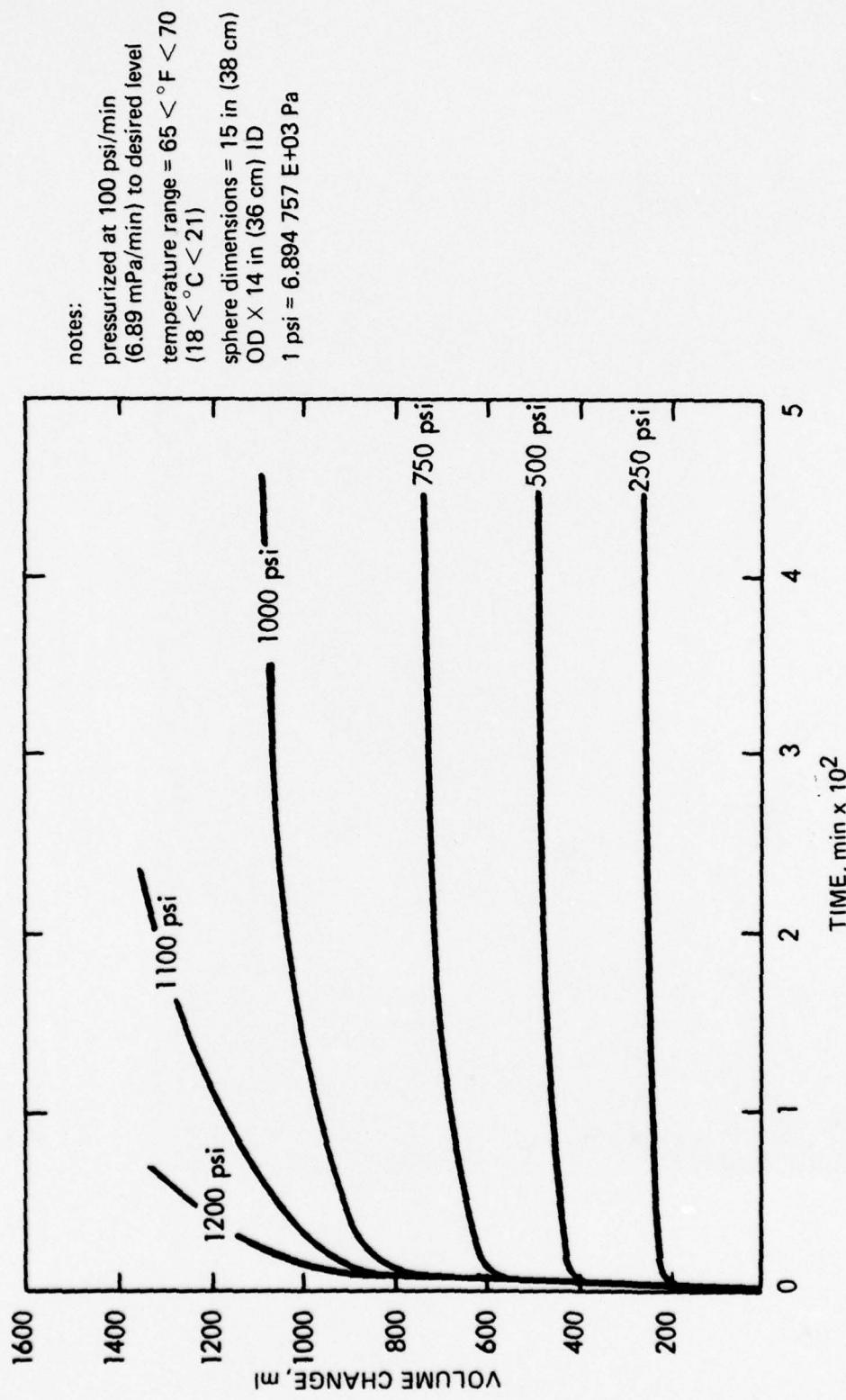
Figure 12.20. Effect of sustained external pressure level and duration of loading on the magnitude of volumetric decrease of ideal spheres with t/R_o = 0.066 and R_o = 7.5 inches (19 centimeters).

notes:

pressurized at 100 psi/min (6.89 mPa/min) to desired level

temperature range = 65 < °F < 70 (18 < °C < 21)

sphere dimensions = 15 in (38 cm) OD × 14 in (36 cm) ID

1 psi = 6.894 757 E+03 Pa

TIME, min x 10^2

VOLUME CHANGE, ml

notes:

pressurized at 16 psi/min (0.1 mPa/min)
to desired pressure level

temperature = 68°F (20°C)

sphere dimensions = 66 in (168 cm) OD
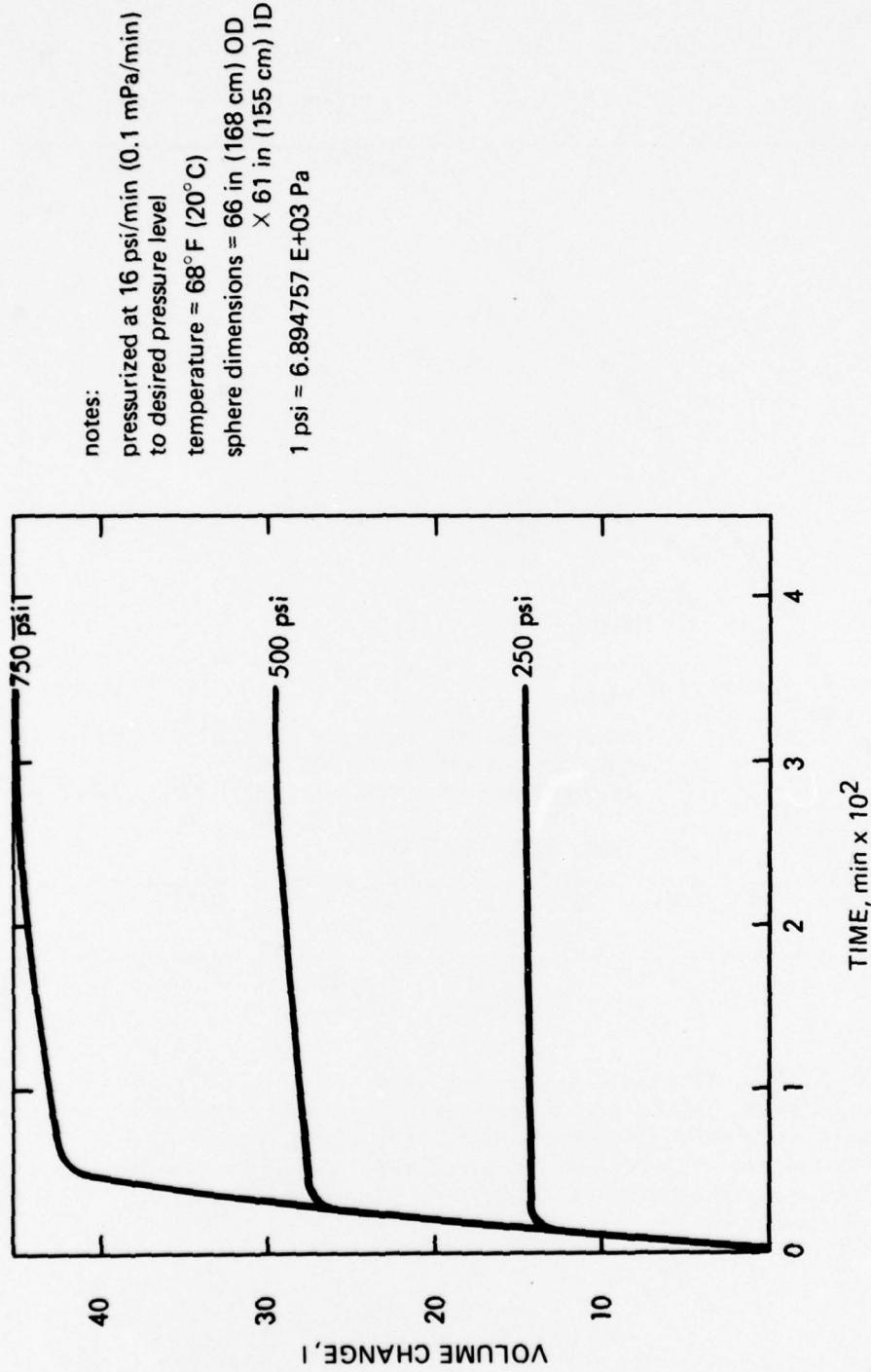 X 61 in (155 cm) ID

1 psi = 6.894757 E+03 Pa

Figure 12.21. Effect of sustained external pressure level and duration of loading on the magnitude of volumetric decrease of ideal spheres with $t/R_o = 0.075$ and $R_o = 33$ inches (84 centimeters). The volumetric decrease of large spheres represents the same fraction of the original sphere volume as of small spheres with identical t/R_o ratios.
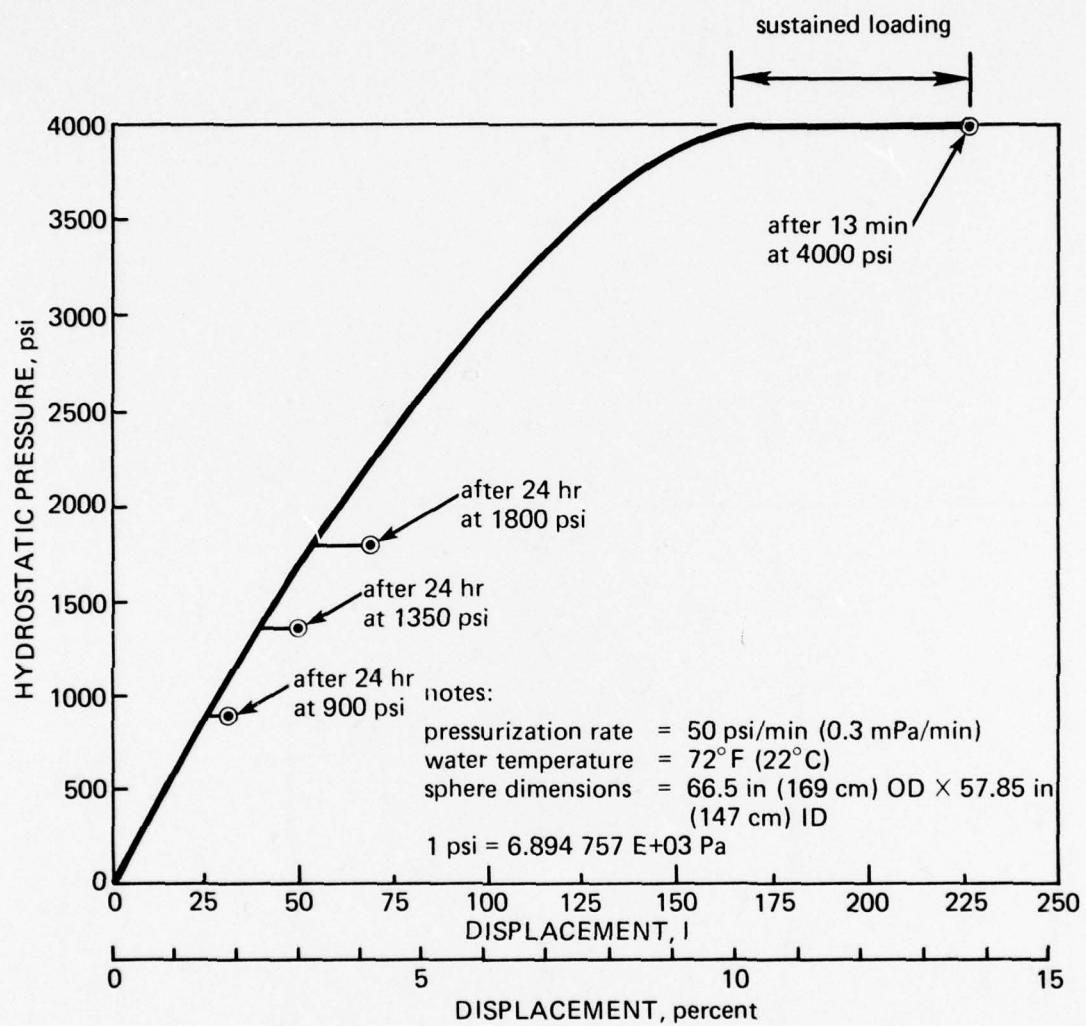
12-49

Figure 12.22. Effect of pressure on the volumetric decrease of an acrylic sphere with t/R_o = 0.130 and R_o = 33.25 inches (84.5 centimeters). The sphere was depressurized and allowed to relax for 24 hours between individual sustained pressurizations. Note that at 4000 pounds per square inch (27.5 megapascals) (0.842 STCP), the volumetric decrease was so large that it resulted in a general implosion after 13 minutes of sustained pressurization.
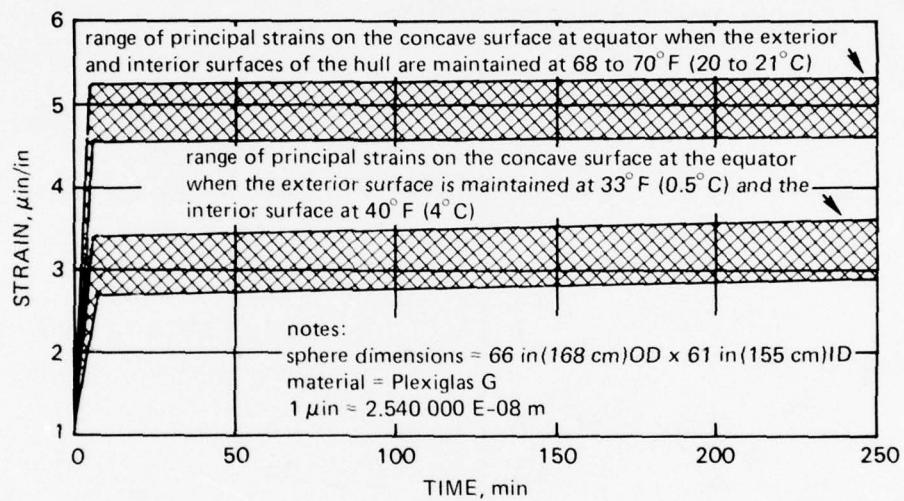
Figure 12.23. Effect of temperature on the magnitude of long-term strains on the interior of an ideal acrylic sphere with $t/R_o = 0.075$ under sustained external pressure loading.

Figure 12.24. Compressive membrane strains on the exterior of an ideal acrylic sphere with $t/R_O = 0.075$ during external pressure cycling at room temperature environment. The lengths of the sustained loading and relaxation phases of the pressure cycle correspond to typical deployment at sea.
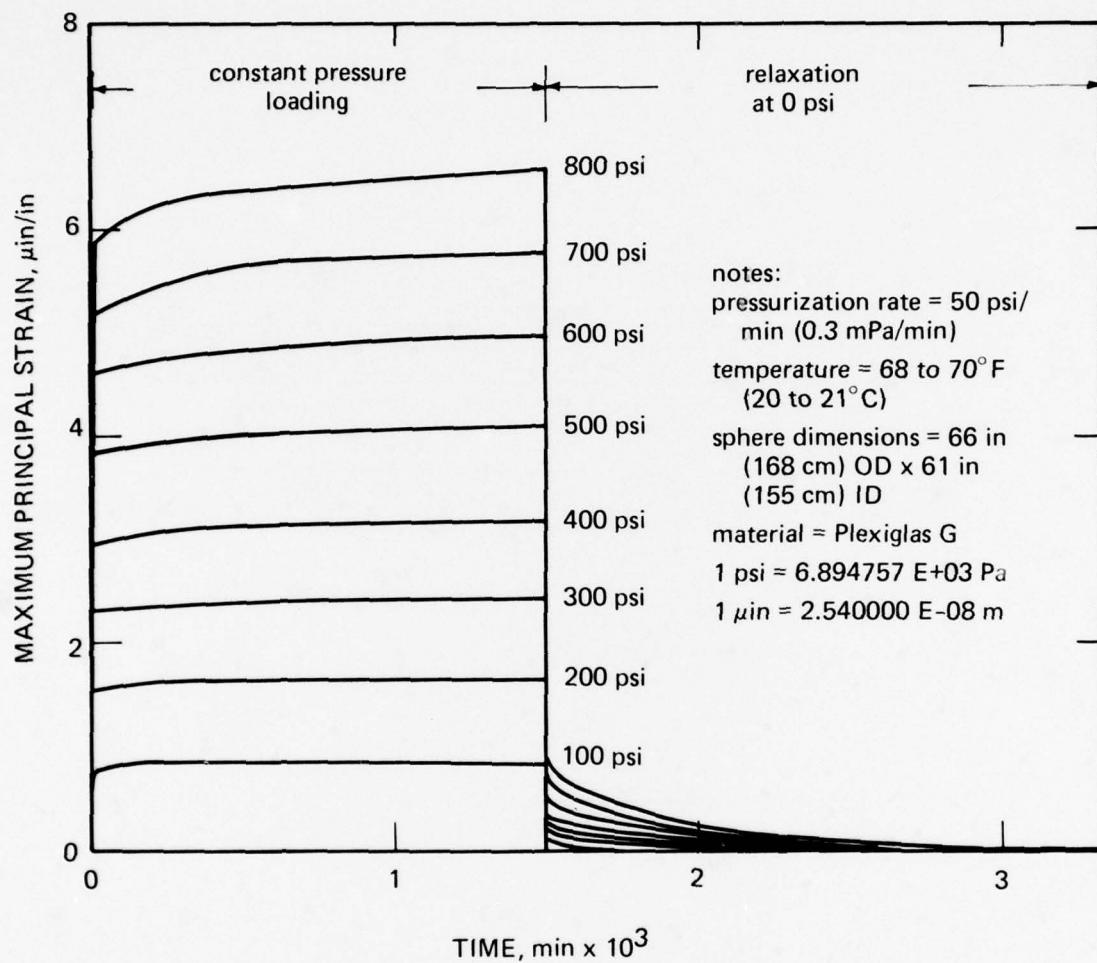
Figure 12.25. Compressive membrane strains on the interior of an ideal acrylic sphere with $t/R_o = 0.075$ during external pressure cycling at room temperature environment. The lengths of the sustained loading and relaxation phases of the pressure cyc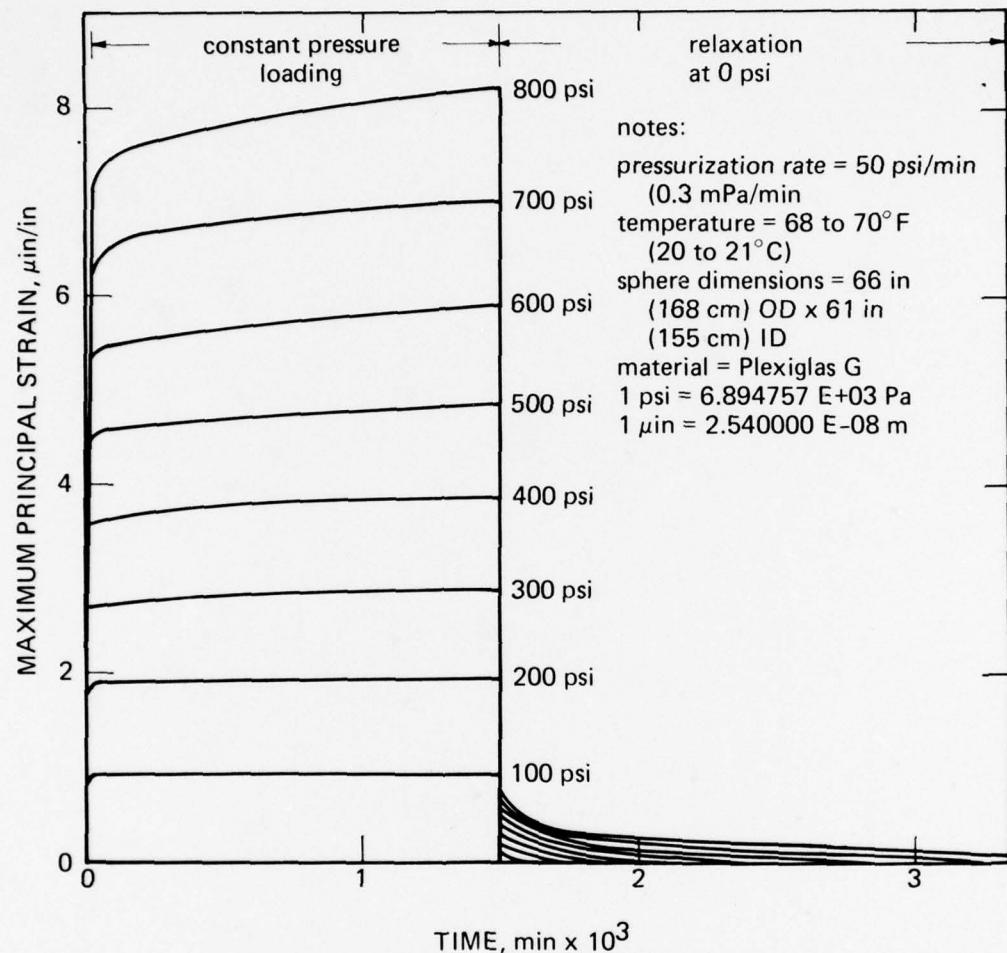les correspond to typical deployment at sea. Note that the duration of the relaxation phase required to drop strains to zero increases with the pressure to which the sphere is subjected during the loading phase.
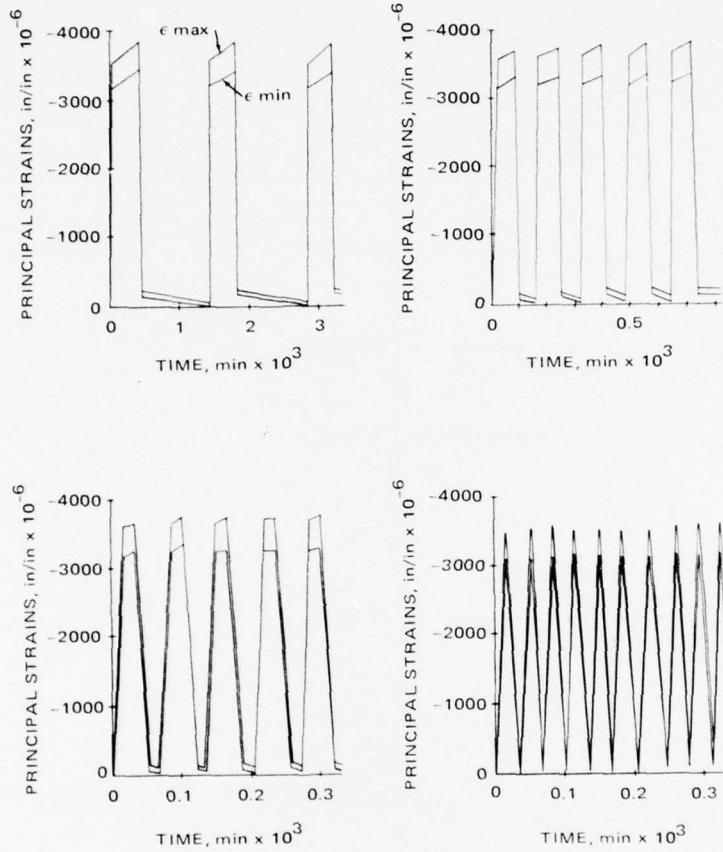
12-53

Figure 12.26. Strains on the exterior surface of an ideal acrylic sphere with $t/R_o = 0.075$ at ambient room temperature while being subjected to 500-pound-per-square-inch (3.44 megapascals) external pressure cycles of different durations.
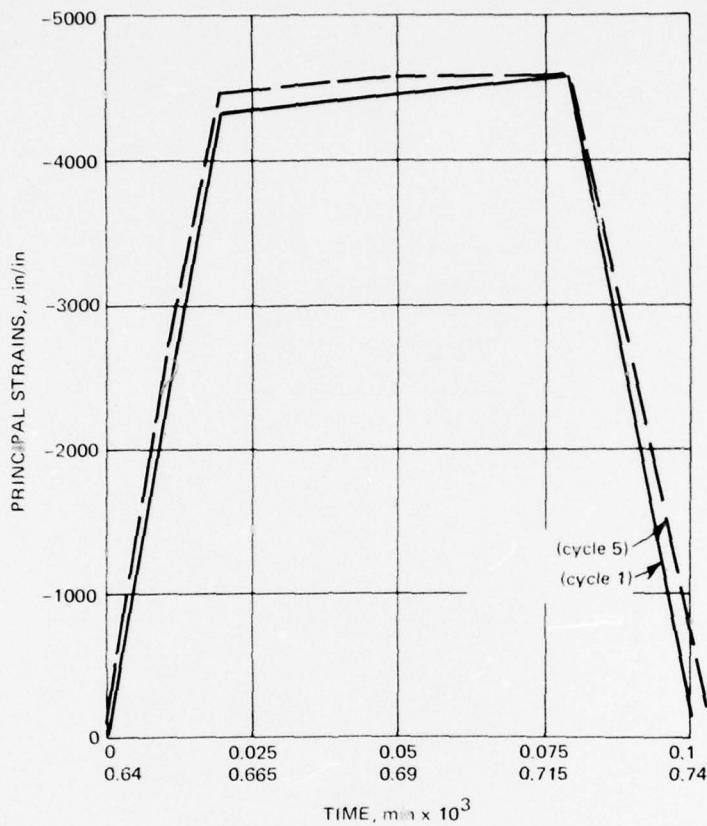
Figure 12.27. Comparison of strains recorded during the loading phases of first and fifth pressure cycles on the interior of the ideal acrylic sphere with $t/R_O = 0.075$ at ambient room temperature while subjected to pressure cycling at 500 pounds per square inch (3.4 megapascals). Note that there has been no significant change in strain magnitude between cycles 1 and 5, indicating that total relaxation of material takes place between individual cycles.
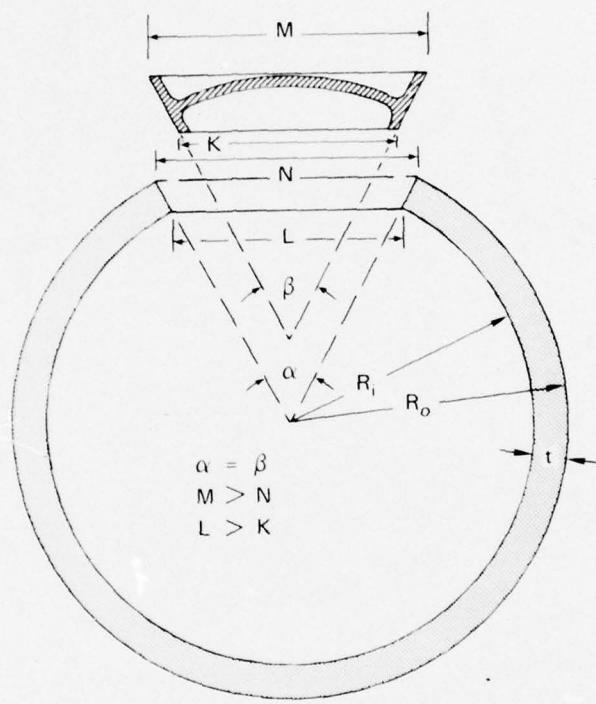
Figure 12.28. Typical penetration and closure
design criteria for spherical acrylic hulls.

Figure 12.29. Model- and full-scale acrylic hulls for NEMO program with polar penetrations containing metallic closures in the form of hatches and feed-through bulkheads.
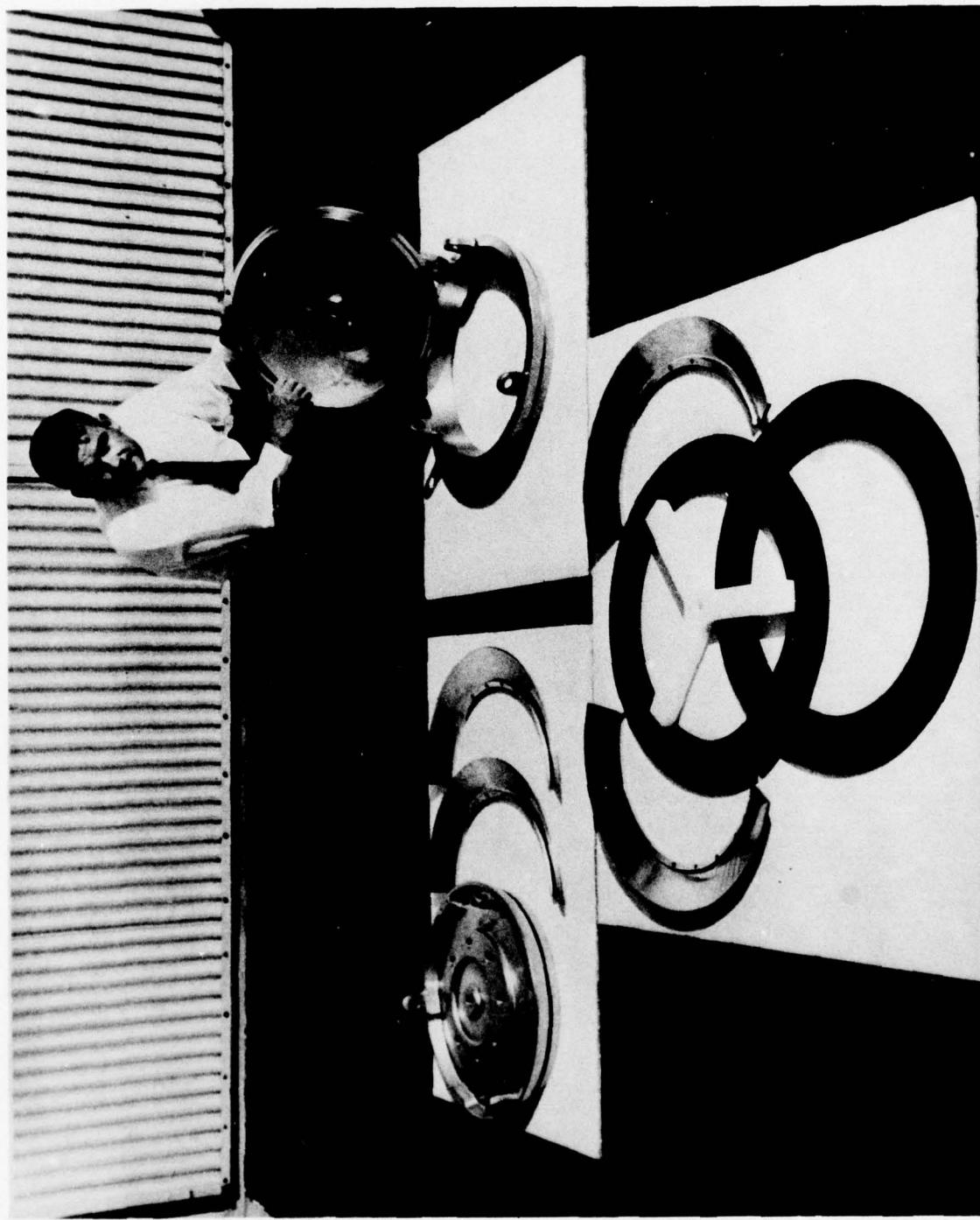
Figure 12.30. Typical metallic closures for penetrations in spherical acrylic hulls. This set of steel closures was used on the acrylic submersibles NEMO and MAKAKAI.

Figure 12.31. Scale model of a spherical acrylic hull with $t/R_o = 0.066$ and two 40-degree (0.7 radian) conical penetrations located 180 degrees (3.14 radians) center-to-center apart. Its short-term critical pressure of 1460 pounds per square inch (10 megapascals) does not differ significantly from the short-term critical pressure of the ideal hull with the same t/R_o ratio but without any penetrations (figure 12.12).

Figure 12.32. Fragments of a full-size NEMO hull with twin penetrations 180 degrees (3.14 radians) center-to-center apart after external short-term pressurization to destruction at ambient room temperature. Note that fragments are irregular and that the fracture surfaces cut across bonded joints indicating that both the joints and the penetrations do not act as planes of structural weakness. The 1850-pound-per-square-inch (12.7 megapascals) short-term critical pressure of the full-scale hull with $t/R_o = 0.075$ has been predicted by extrapolating (equations 12.1 and 12.2) the 1500-pound-per-square-inch (10.3 megapascals) short-term critical pressure of a model-scale hull with $t/R_o = 0.066$. This finding confirms that data from testing of inexpensive scale models can be used with confidence to predict the behavior of full-scale hulls without further tests.

Figure 12.33. Scale model of a spherical acrylic hull with t/R_o = 0.066 and two 40-degree (0.7 radian) conical penetrations located 117 degrees (2.04 radians) center-to-center apart. Its short-term critical pressure of 1450 pounds per square inch (9.99 megapascals) does not differ significantly from the short-term critical pressure of a hull with the same t/R_o ratio, but without any penetrations (figure 12.12).

Figure 12.34. Scale model of a spherical acrylic hull with $t/R_o = 0.066$ and three 40-degree (0.7 radian) conical penetrations located 90 (1.57), 90 (1.57), and 180 degrees (3.14 radians) center-to-center apart. Its short-term critical pressure of 1500 pounds per square inch (10.3 megapascals) does not differ significantly from the short-term critical pressure of a hull with the same t/R_o ratio, but without any penetration (figure 12.12).
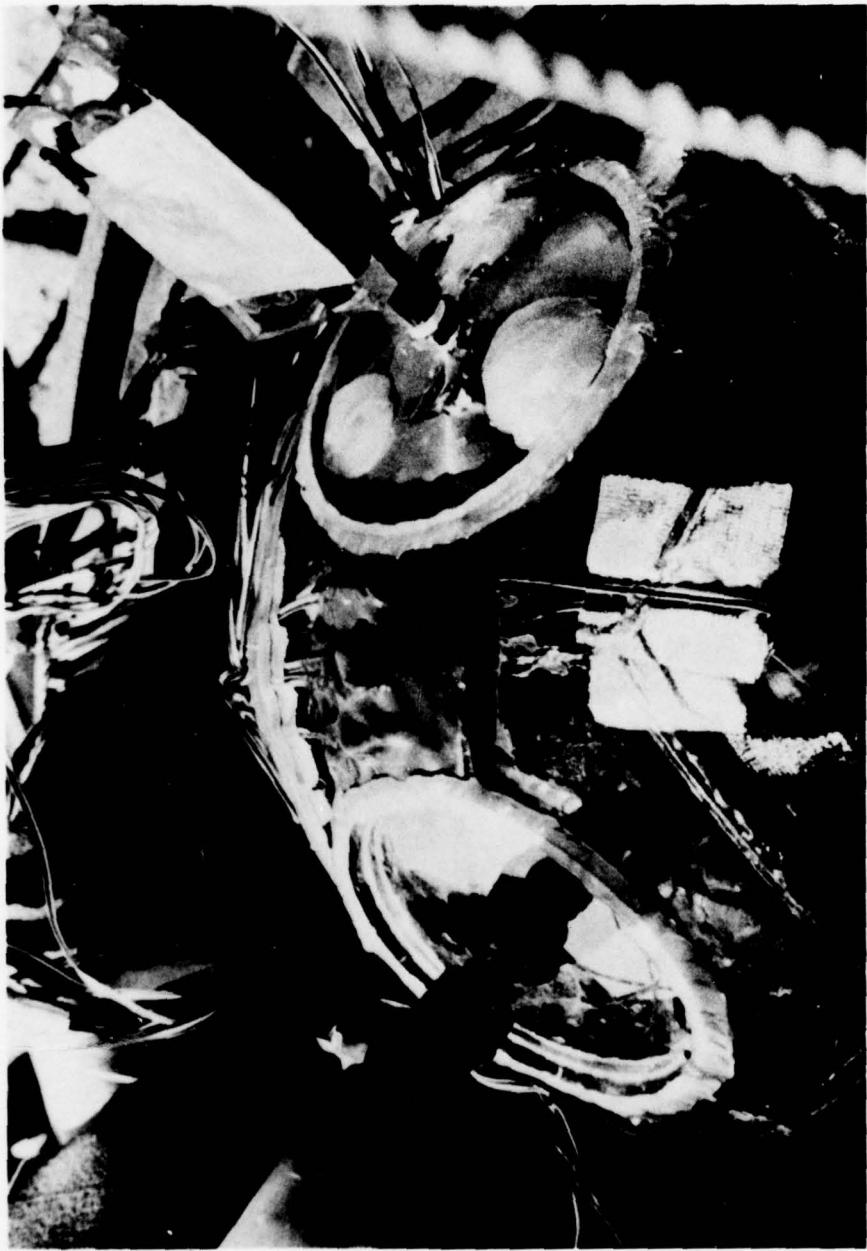
Figure 12.35. Scale model of a spherical acrylic hull with $t/R_o = 0.066$ and two 40-degree (0.7 radian) conical penetrations located 63 degrees (1.09 radians) center-to-center apart. Its short-term critical pressure of 1400 pounds per square inch (9.6 megapascals) does not differ significantly from the short-term critical pressure of a hull with the same t/R_o ratio, but without any penetrations (figure 12.12).
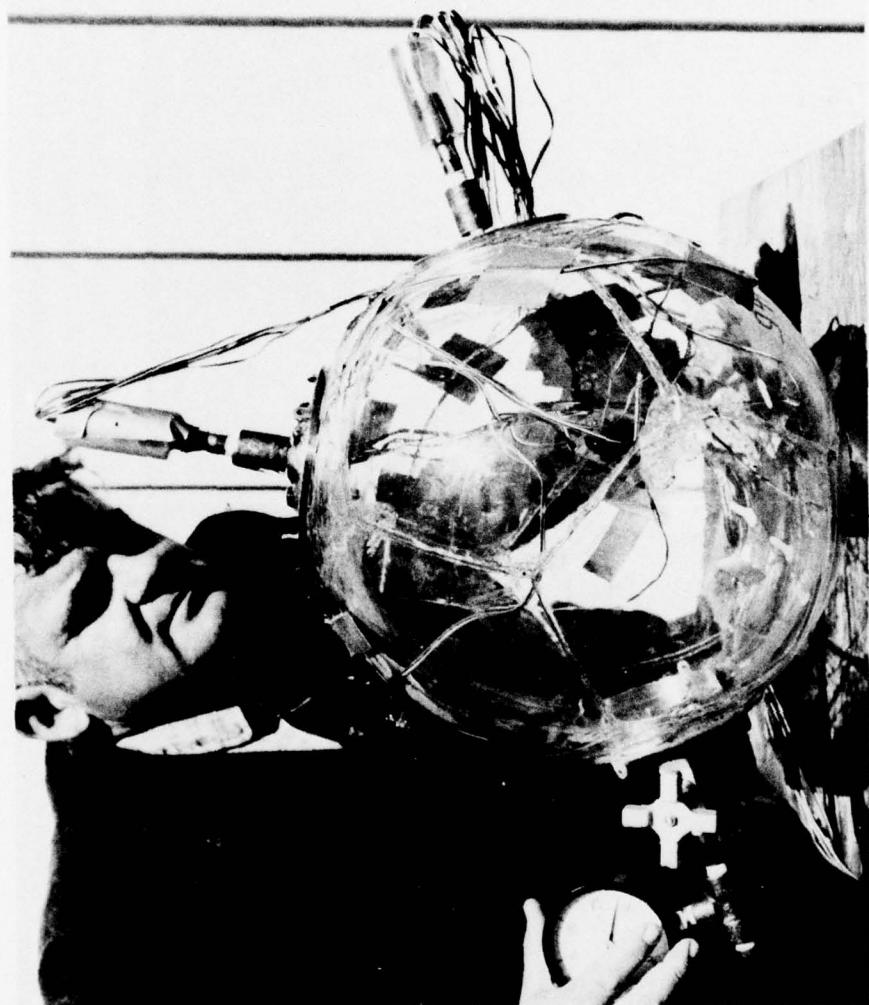
Figure 12.36. Scale model of a spherical acrylic hull with $t/R_o = 0.066$ and three 40-degree (0.7 radian) conical penetrations located 63 (1.09), 117 (2.04), and 180 degrees (3.14 radians) center-to-center apart. Its short-term critical pressure of 1500 pounds per square inch (10.3 megapascals) does not differ significantly from the short-term critical pressure of a hull with the same t/R_o ratio, but without any penetrations (figure 12.12).

Figure 12.37. Scale model of a spherical acrylic hull with $t/R_o \approx 0.066$ and four 40-degree (0.7 radian) conical penetrations located 63 degrees (1.09 radians) center-to-center apart. Its short-term critical pressure of 1500 pounds per square inch (10.3 megapascals) does not differ significantly from the short-term critical pressure of a hull with the same t/R_o ratio, but without any penetrations (figure 12.12).

Figure 12.38. Distribution of meridional (longitudinal) stresses around a 40-degree (0.7 radian) penetration in an acrylic hull with $t/R_O = 0.066$ under 100-pound-per-square-inch (0.68 megapascal), external, short-term hydrostatic pressure at ambient room temperature. Note that in the elastic range of acrylic plastic the stress concentration in the meridional direction at the very edge of penetration closed with a steel hatch appears to be 5. The dashed line indicates extrapolated values, i.e., because of the physical size limitations of straingages they cannot be placed on the edge itself. The highest measured value of stress concentration is only 1.7 at a location 0.017 radian from the edge of penetration.
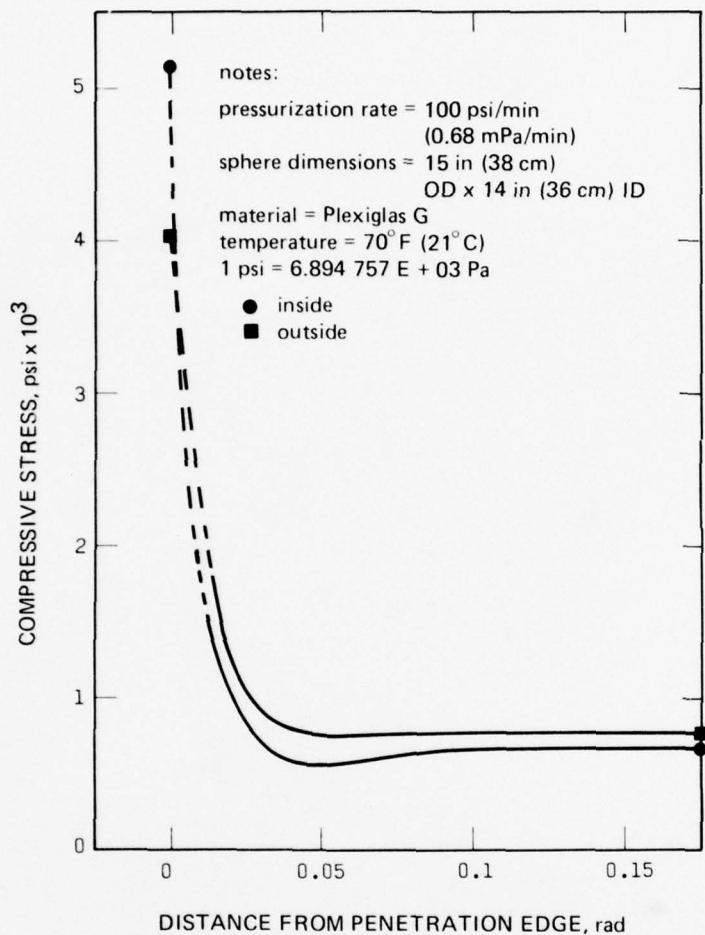
12-66
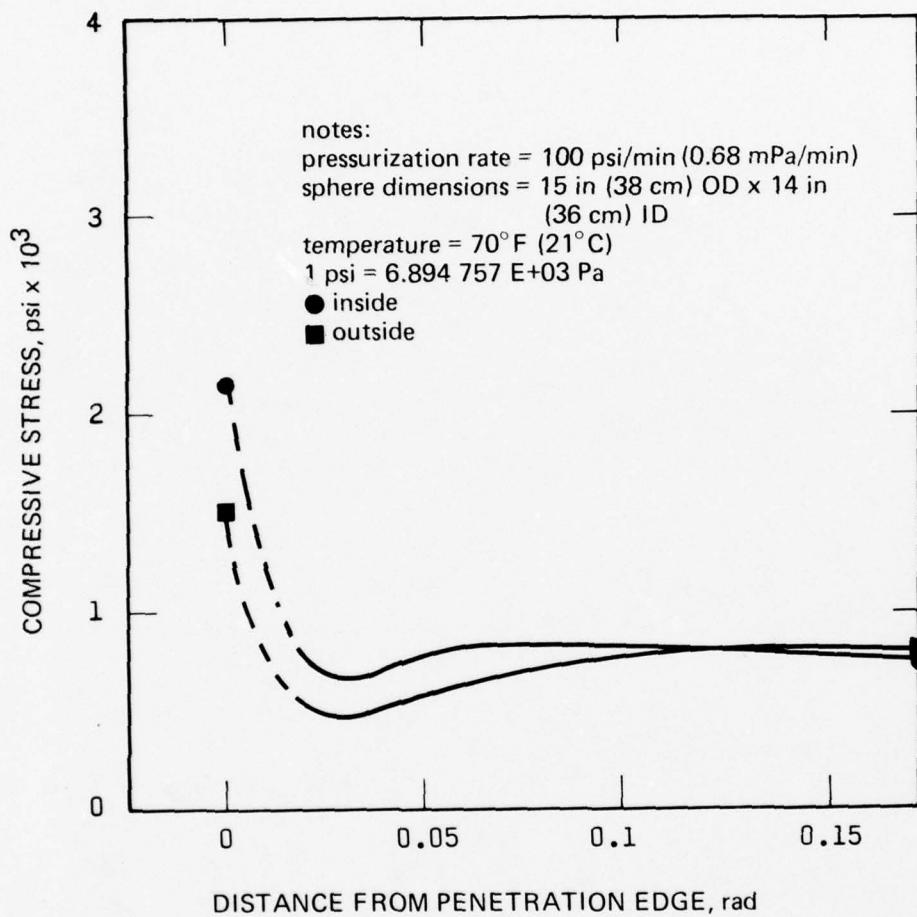
Figure 12.39. Distribution of circumferential stresses around a 40-degree (0.7 radian) penetration in an acrylic hull with $t/R_0 = 0.066$ under 100-pound-per-square-inch (0.69 megapascal), external, short-term hydrostatic pressure at ambient room temperature. Note that in the elastic range of acrylic plastic the stress concentration in circumferential direction at the edge of penetration closed with a steel hatch appears to be 2. The dashed line, similar to figure 12.38, indicates extrapolated values. The highest measured value of stress concentration is only 0.6 at a location 0.017 radian from the edge of penetration.
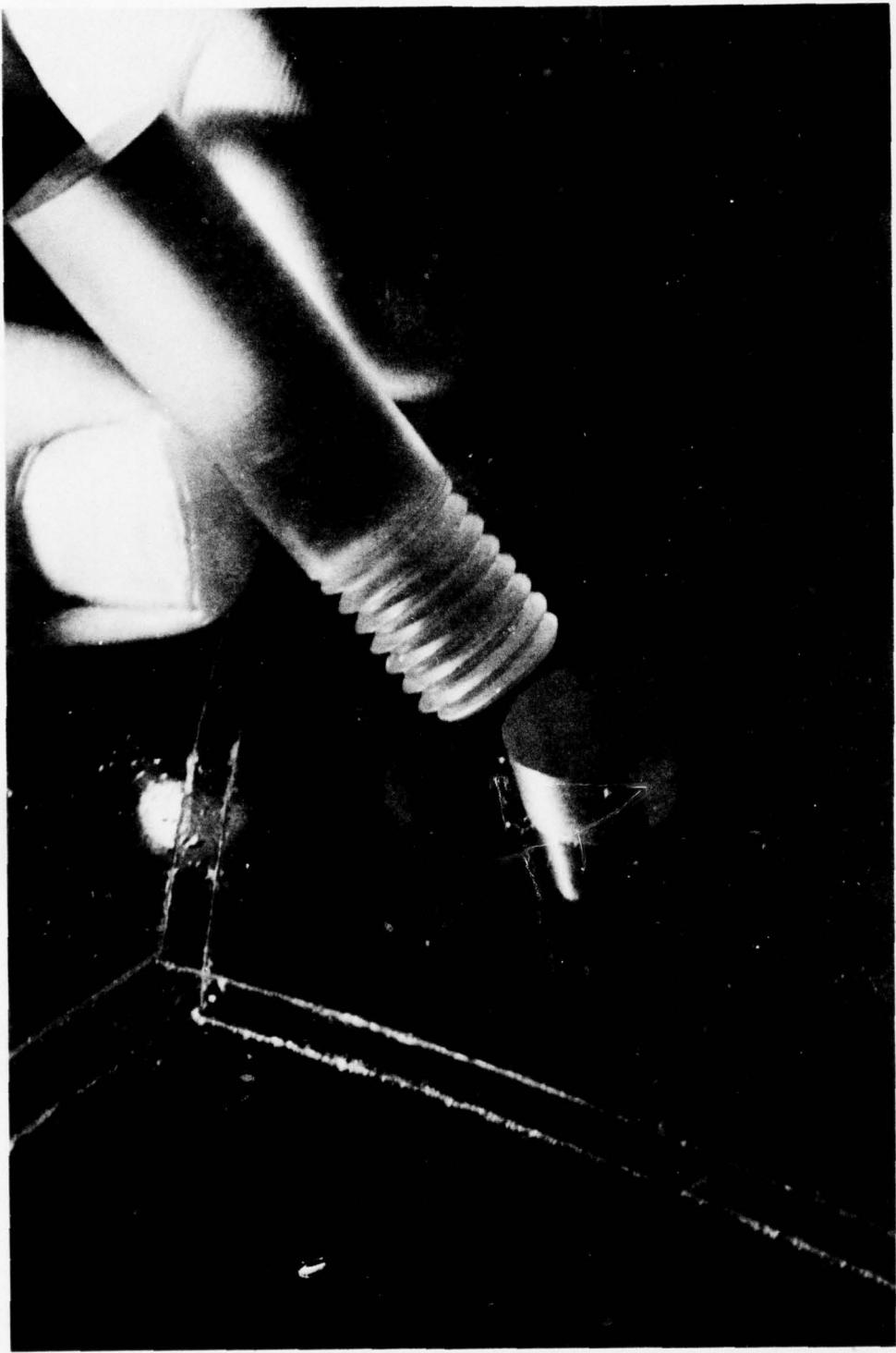
Part A. Threaded conical polycarbonate insert used in acrylic hulls for attachment of external or internal fixtures to the hull without generation of stress concentrations.

Figure 12.40. Threaded polycarbonate inserts used in acrylic hulls.

Part B. Model-scale acrylic hull with external mounting ring attached to the hull with threaded conical poly-carbonate inserts. The holes in the mounting ring are oversized, allowing the pins to slide freely during contraction of the hull under external hydrostatic pressure. A plastic washer bearing on an elastomeric gasket is used under every plastic nut placed on the threaded end of the conical polycarbonate insert. Tightening of the nut seats the conical insert firmly in its seat preventing any leakage around the insert.

Figure 12.40. Continued.

polycarbonate plastic penetrator
for
15 in (38 cm) OD X 13 in (33 cm) ID NEMO model

26°41'

polycarbonate
plastic insert

RTV
potting

4.30 dia

0.125

acrylic
hull

0.0625

1.3125

0.960

1/16

0.125 neoprene gasket

3.000 dia
2.990

aluminum retainer ring

4.0 dia

cross-section

0.3125 bolts on
2.0 dia circle

notes:
all dimensions
are in inches
1 inch = 2.540 000 E–02 m
1 deg = 1.745 329 E–02 rad
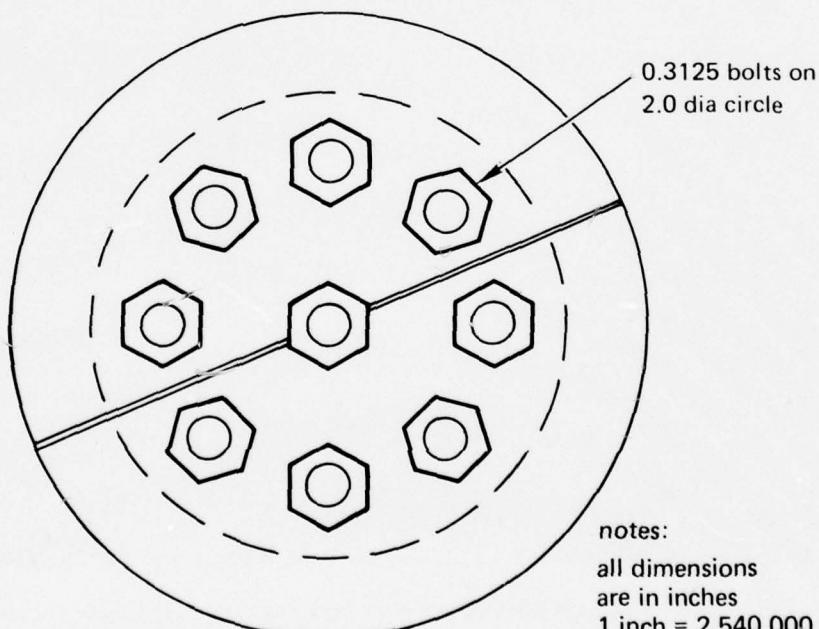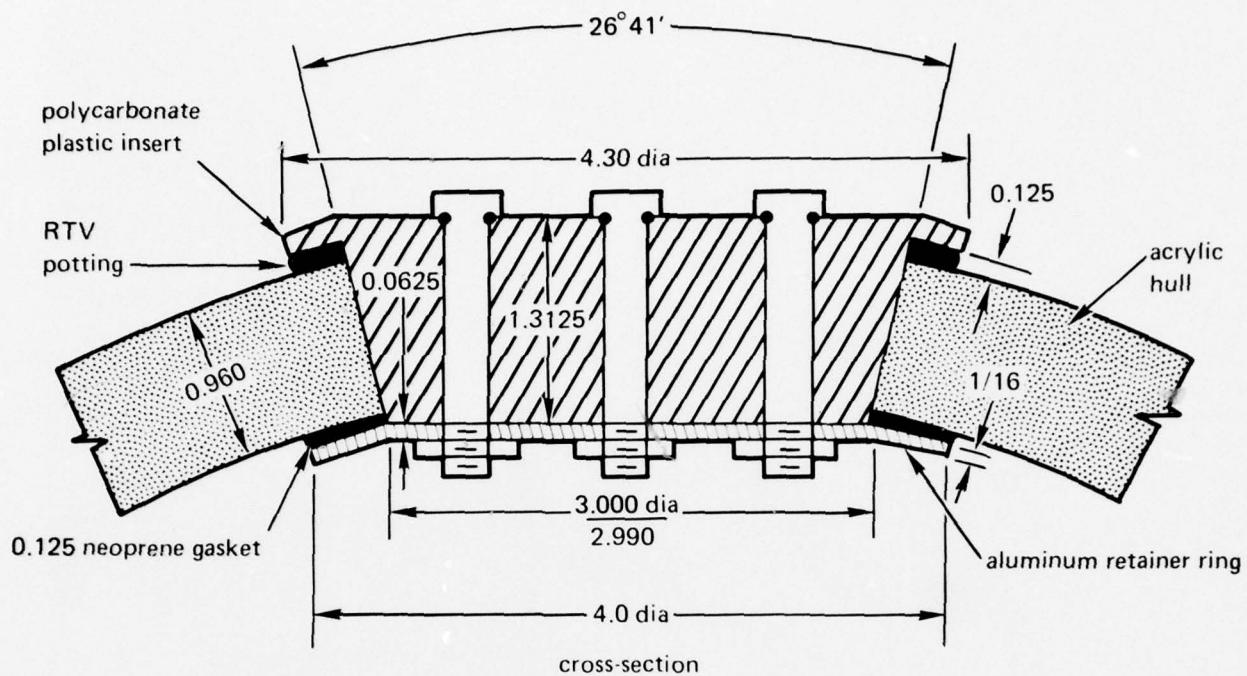
bottom view

Part C. When used as bulkheads for electric and hydraulic feedthroughs, large conical polycarbonate inserts do not introduce stress concentrations in the acrylic hull. In this test, the bolts simulated the presence of feedthroughs in the insert.

Figure 12.40. Continued.

Part D. Placement of the polycarbonate insert into a model-scale acrylic hull with $t/R_o = 0.133$. This model imploded at 4500 pounds per square inch (31 megapascals), the same short-term critical pressure as for an ideal sphere without polycarbonate inserts.

Figure 12.40. Continued.
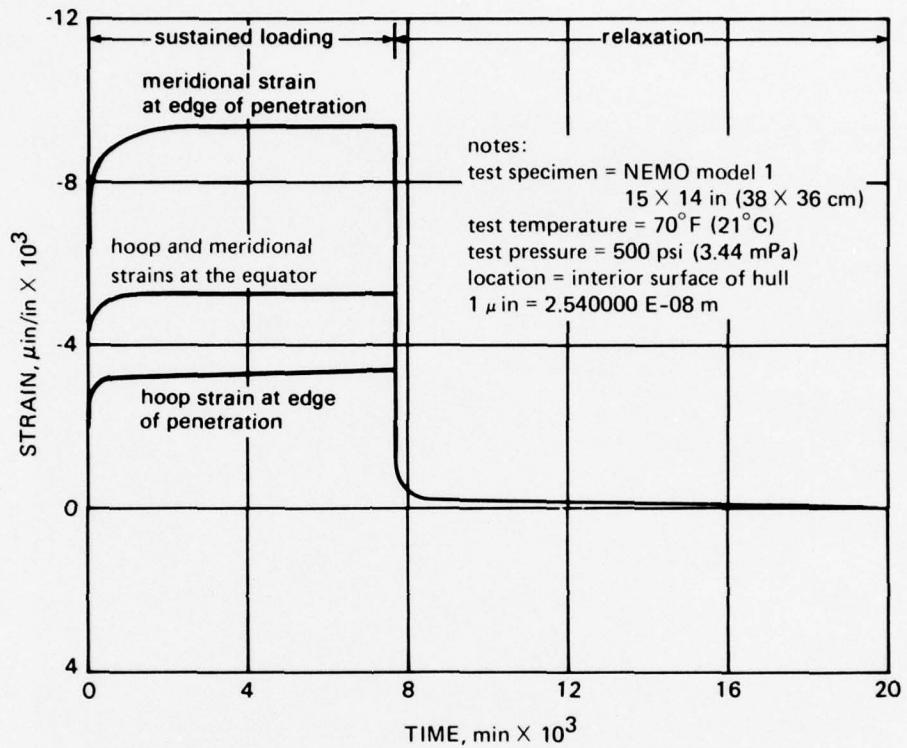
Figure 12.41. Distribution of strains on the interior surface of a model-scale acrylic sphere with $t/R_o = 0.066$ under long-term, 500-pound-per-square-inch (3.44 megapascals), hydrostatic loading at room temperature. The 40-degree (0.7 radian) conical penetration is closed with a steel hatch bearing directly against the acrylic hull. The measured strain concentration in the meridional direction at the hatch is a factor of 1.8, while the concentration factor in hoop direction is 0.6. Compare this with solid lines on figures 12.38 and 12.39 where stress concentration factors of 1.7 and 0.6 under short-term loading are shown. The close agreement between measured stress concentrations under short- and long-term pressurizations indicates that the metallic hatch generates stress concentrations of approximately the same magnitude under short- or long-term loading, if the plastic is in the elastic range.
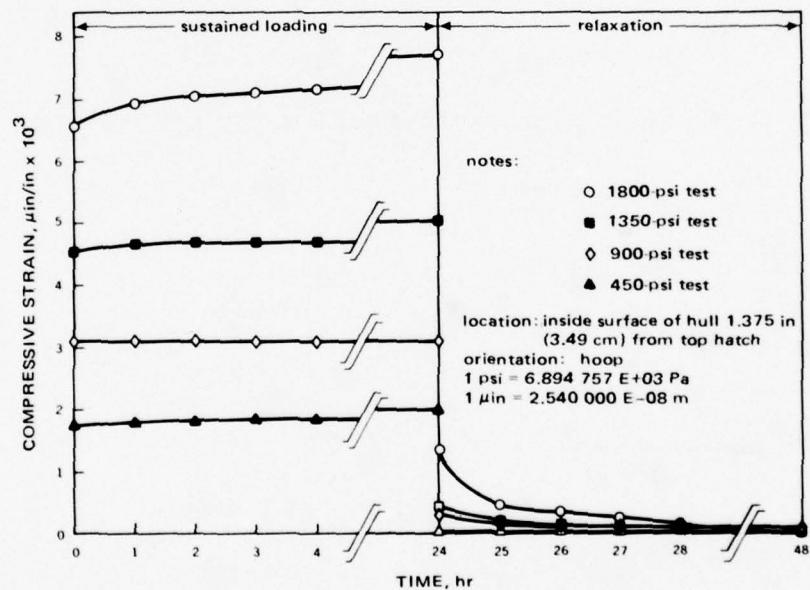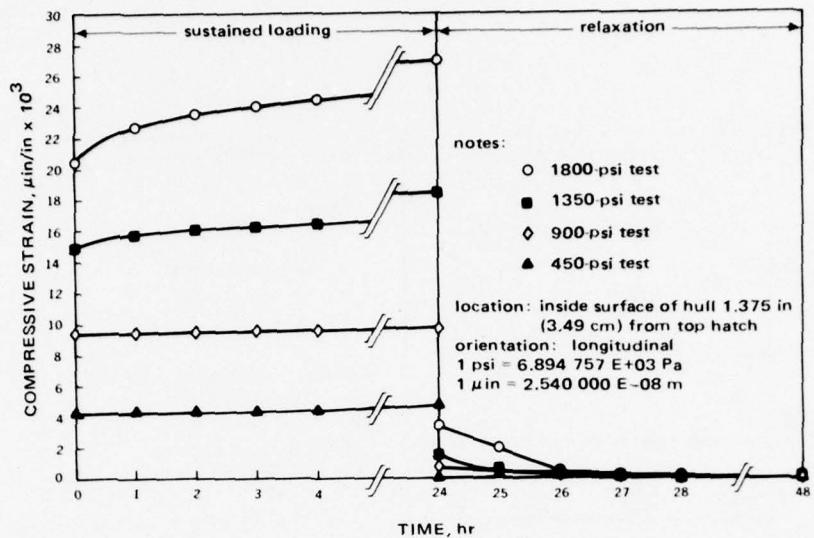
Figure 12.42. Distribution of strains on the surfaces of a full-scale acrylic sphere with $t/R_o = 0.121$ under different levels of sustained external hydrostatic pressure at room temperature. The 48-degree (0.8 radian) conical penetrations are closed in this sphere with aluminum hatches. Due to test constraints the measurement of strains near the hatches was at locations 0.04 radian from the edge of penetration. The magnitude of the stress concentration factor, i.e., longitudinal strain at penetration/longitudinal strain at equator and hoop strain at penetration/hoop strain at equator, changes very little between the different levels of sustained pressurization.
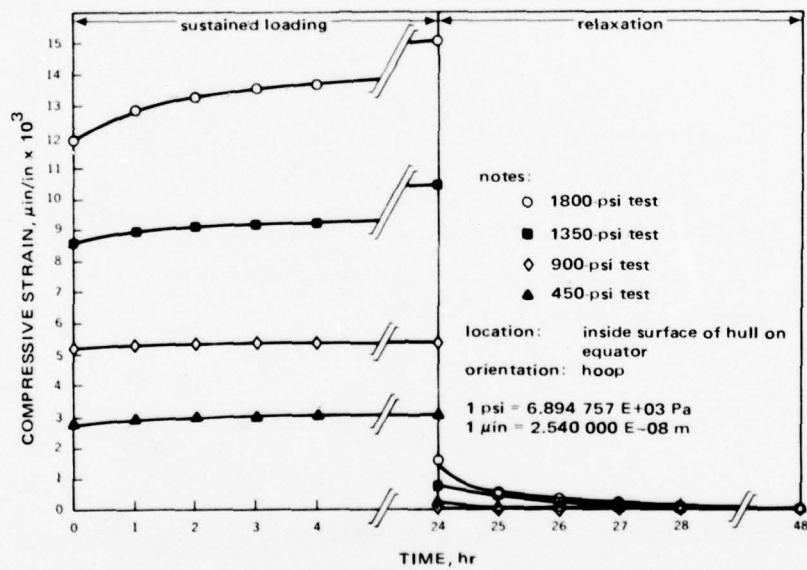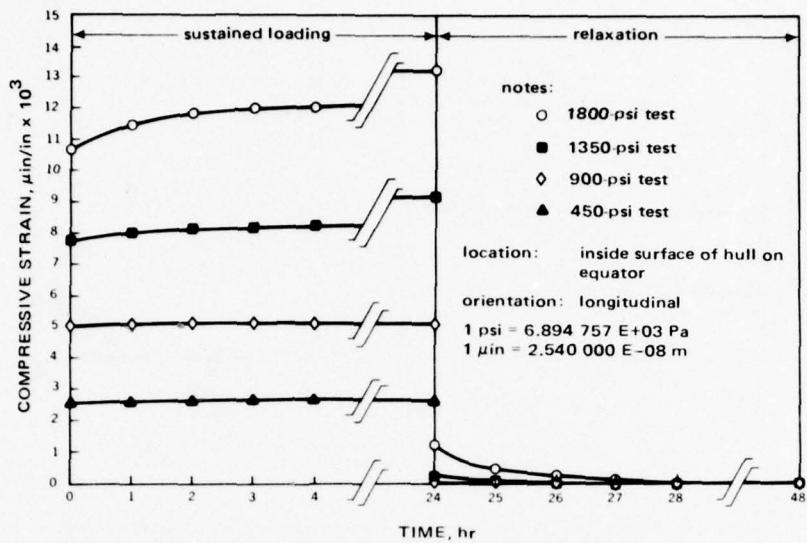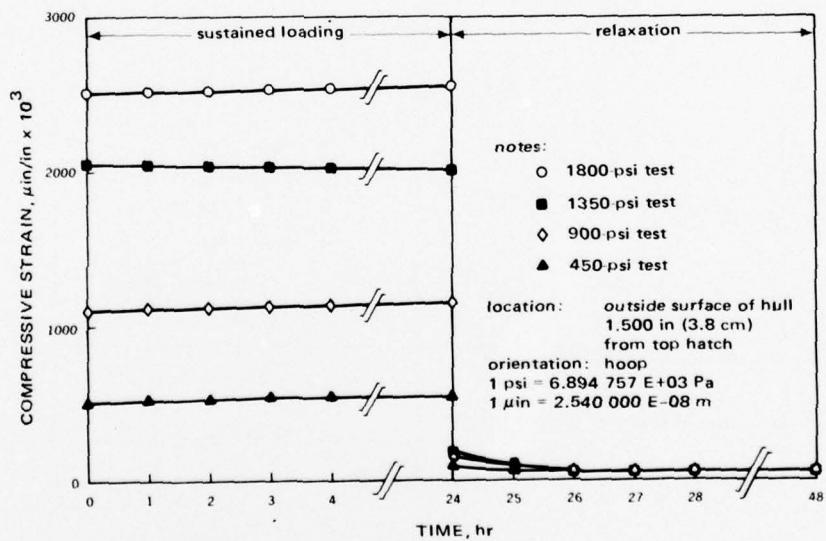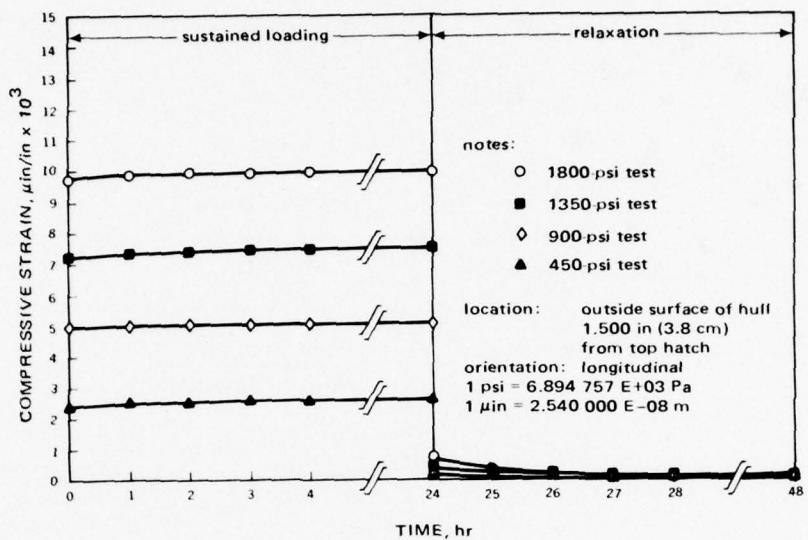
Figure 12.42. Continued.

Figure 12.42. Continued.

12-75
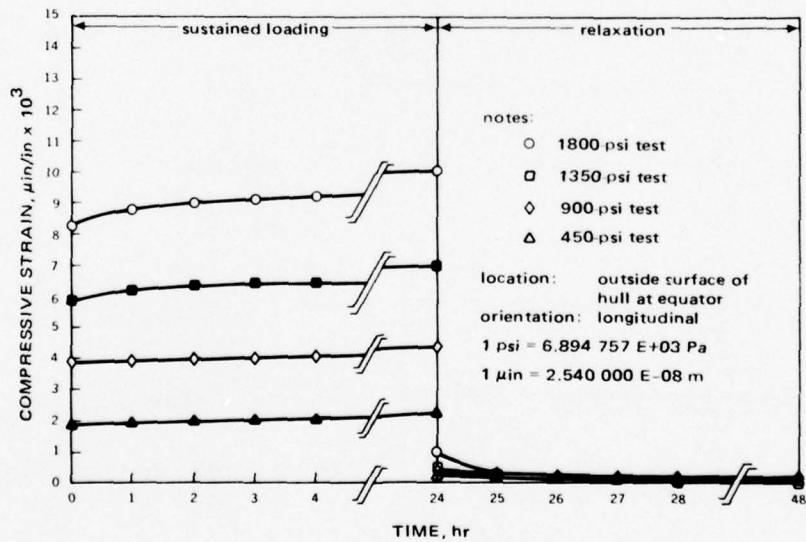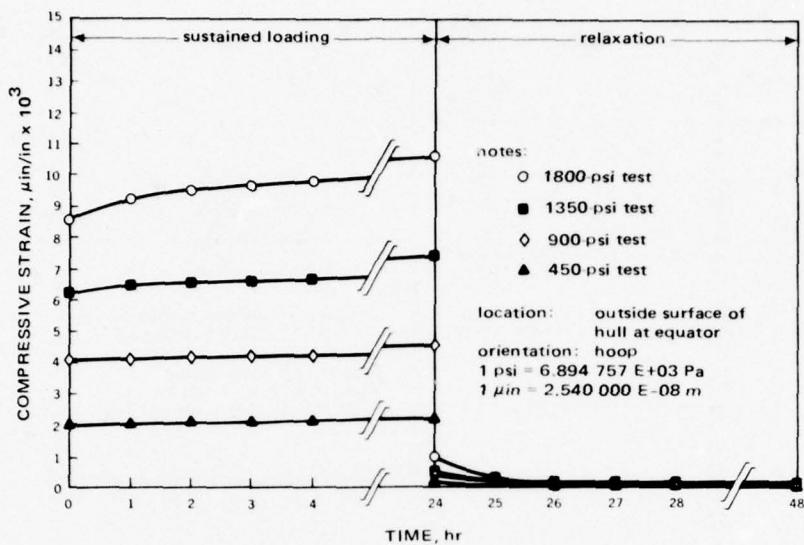
Figure 12.42. Continued.
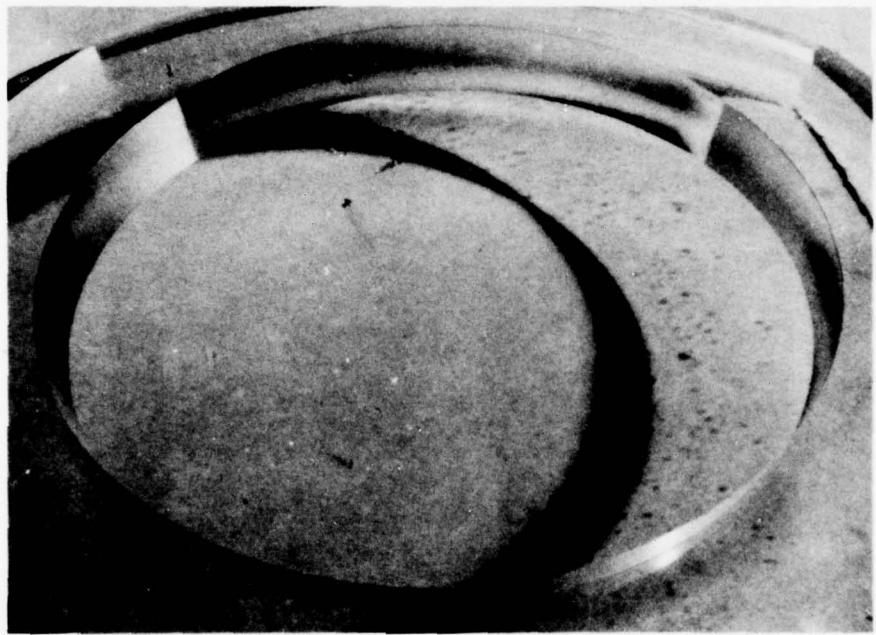
Part A. Appearance of acrylic bearing surface at penetration for metallic closure in an acrylic hull with $t/R_o = 0.066$ prior to long-term pressurization.

Figure 12.43. Cracks on conical surfaces during long-term pressurization.

Part B. The same conical bearing surface after long-term pressuri-
zation of 1530-minute duration at 900 pounds per square inch
(6.2 megapascals) in room temperature environment. Note that
the cracks extend radially from the edge of penetration into
the body of the hull.

Figure 12.43. Continued.
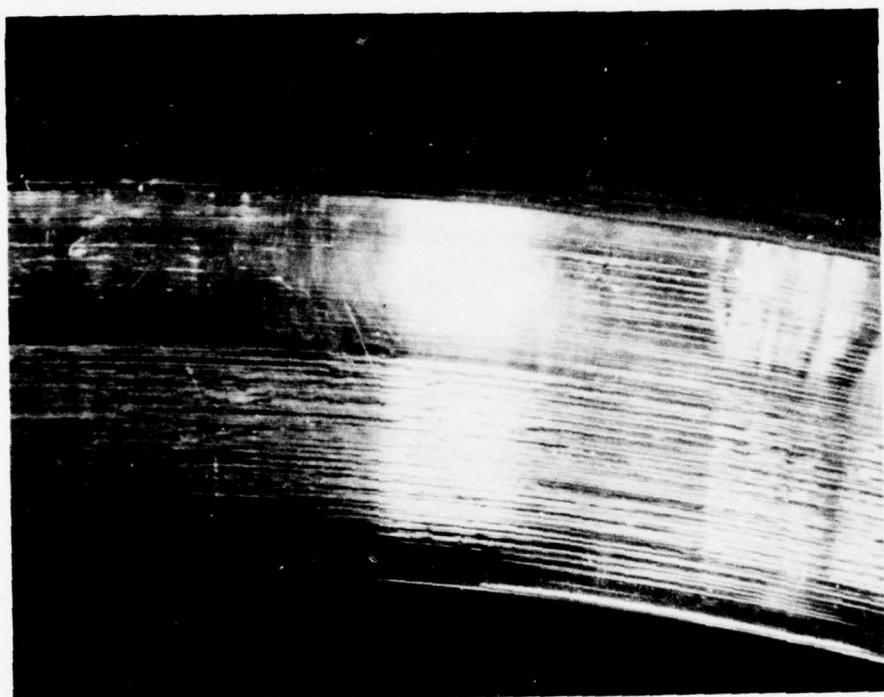
Part C. *The same conical bearing surface viewed at right angles.*

Figure 12.43. Continued.
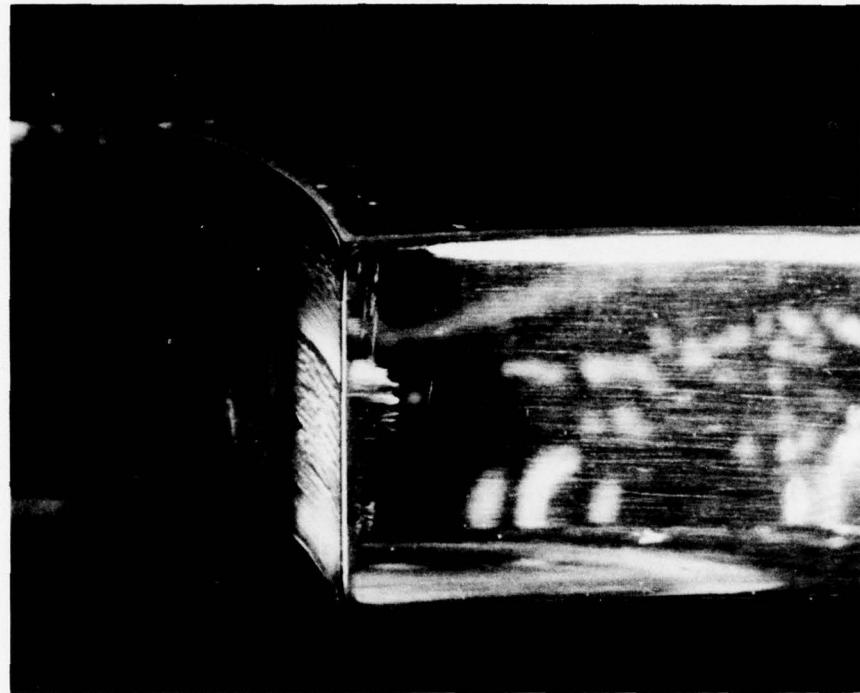
Part D. Section through the same conical bearing surface. Note that the magnitude of shear cracks is maximum at the center of the wall thickness where the O-ring groove on the closure contacts the bearing surface. The balance of shear cracks is distributed from the middle of the wall thickness to the interior hull surface.

Figure 12.43. Continued.
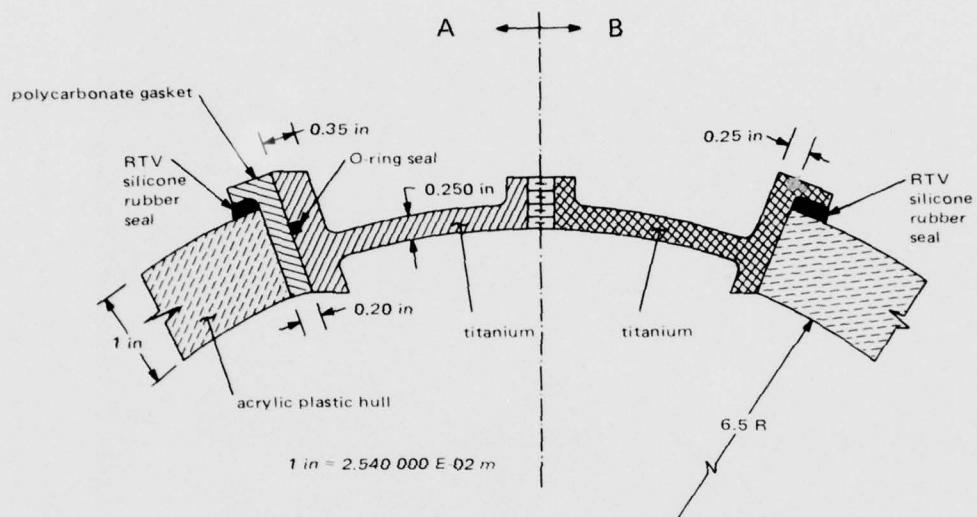
Figure 12.44. Alternate design approaches for elimination of shear cracks in the acrylic bearing surface at the penetration of a sphere with $t/R_O = 0.133$. In design A a polycarbonate gasket is interposed between the O-ring groove in the metallic closure and acrylic hull, while in design B the metallic closure bears directly against the hull but the O-ring groove has been eliminated from the metallic closure.
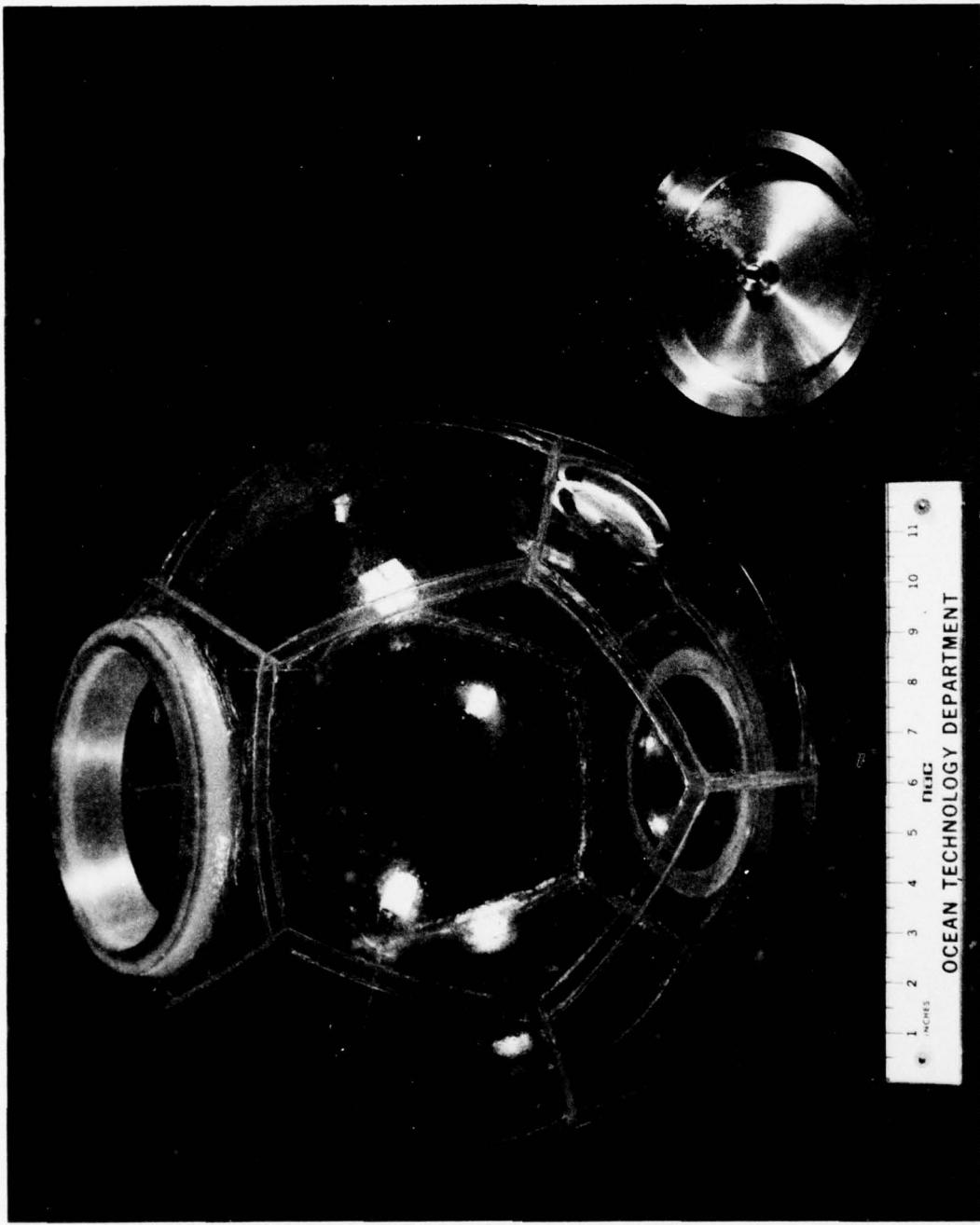
Figure 12.45. Model-scale acrylic sphere with $t/R_O = 0.133$. Sphere was equipped with closure plates of design A at the top and design B at the bottom. Shear cracks were not observed in the acrylic bearing surfaces at the penetrations after 4000 hours of loading phases in 1000 cyclic pressurizations to 1350 pounds per square inch (9.3 megapascals).
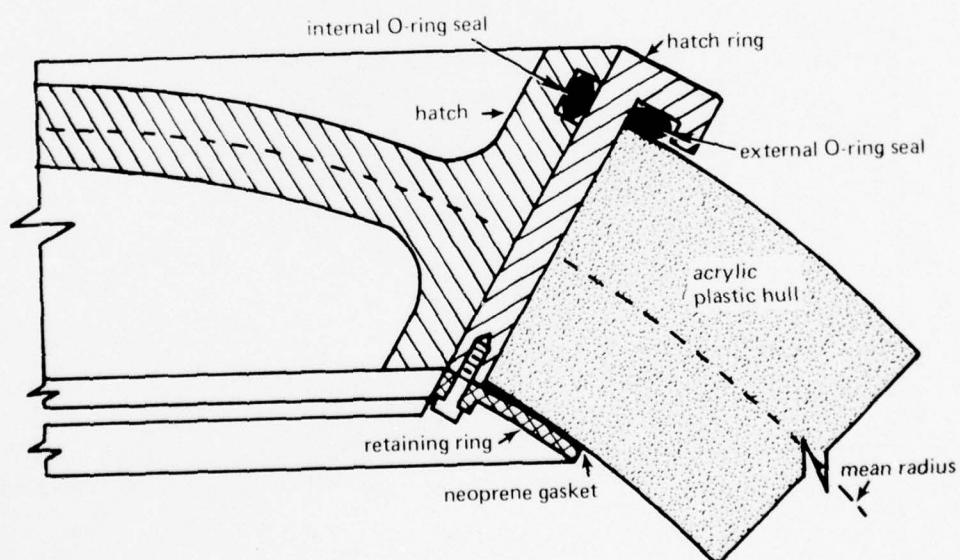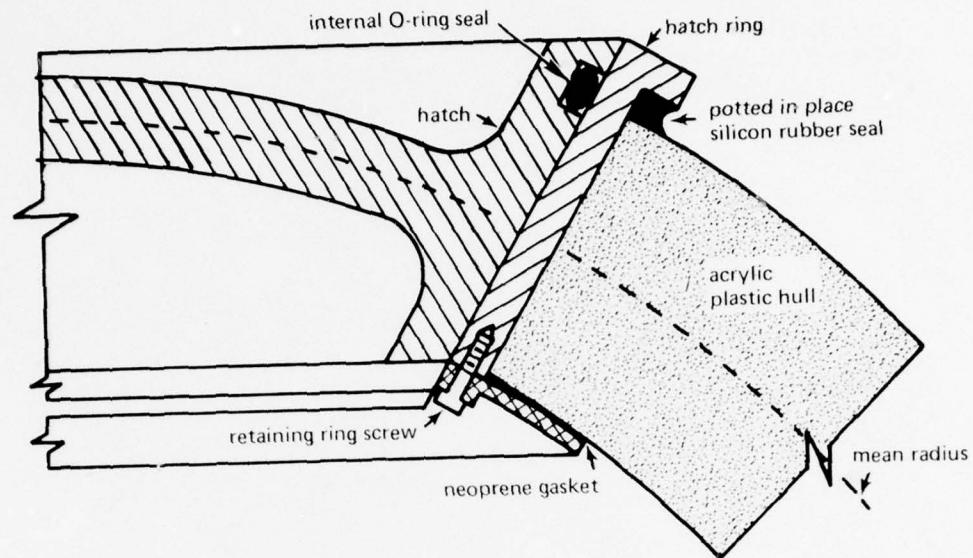
Figure 12.46. Two alternate sealing arrangements for removable metallic hatches. The designs incorporate the same approach to eliminate shear cracks as does design B for closure plates (figure 12.44). The metallic hatch ring is interposed between the metallic hatch and the hull to protect the acrylic bearing surface from scratches generated by repeated opening and closing of the hatch.
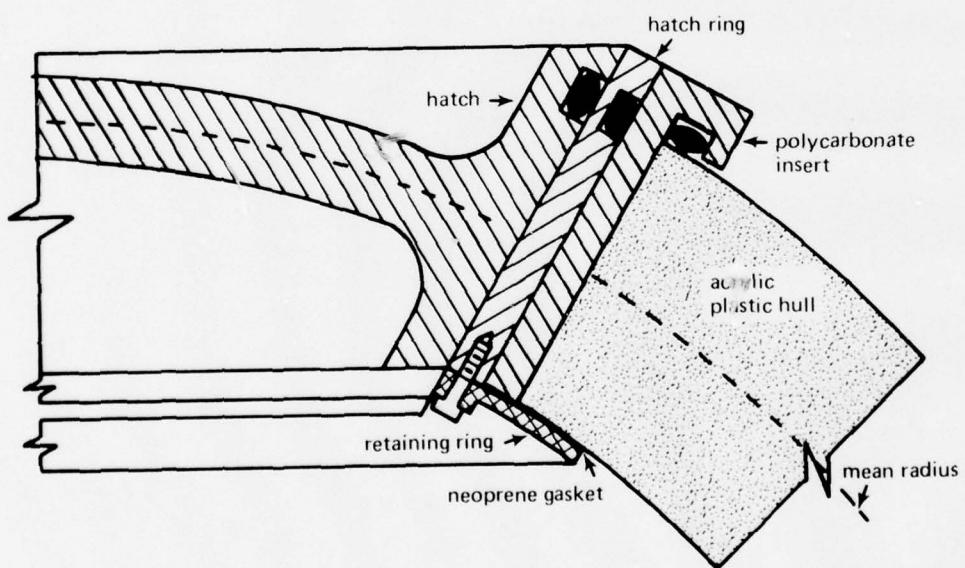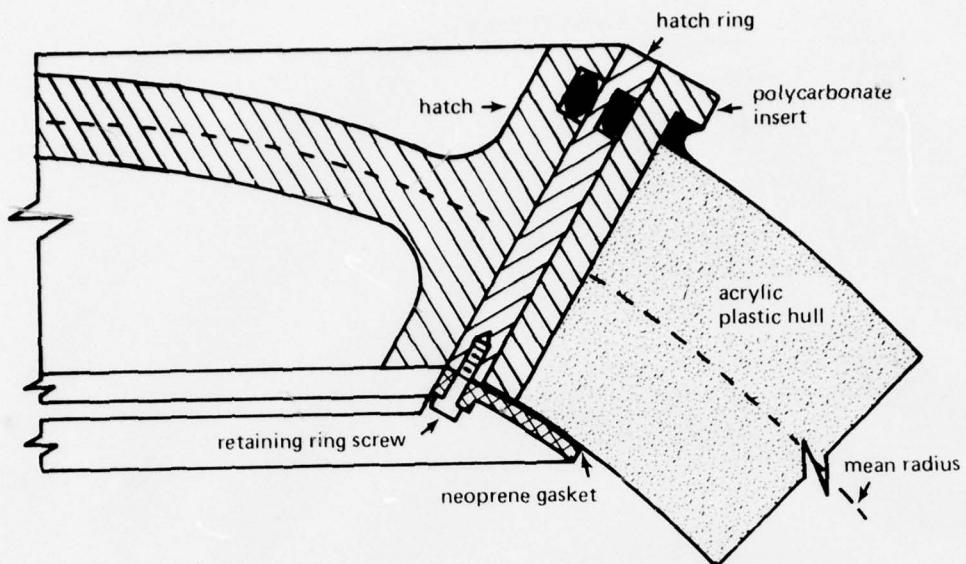
Figure 12.47. Two alternate sealing arrangements for removable metallic hatches. The designs incorporate the same approach to eliminate shear cracks as does design A for permanently mounted closure plates (figure 12.44). The metallic hatch ring is interposed between the metallic hatch and the polycarbonate gasket to protect the plastic bearing surface from scratches generated by repeated opening and closing of the hatch.
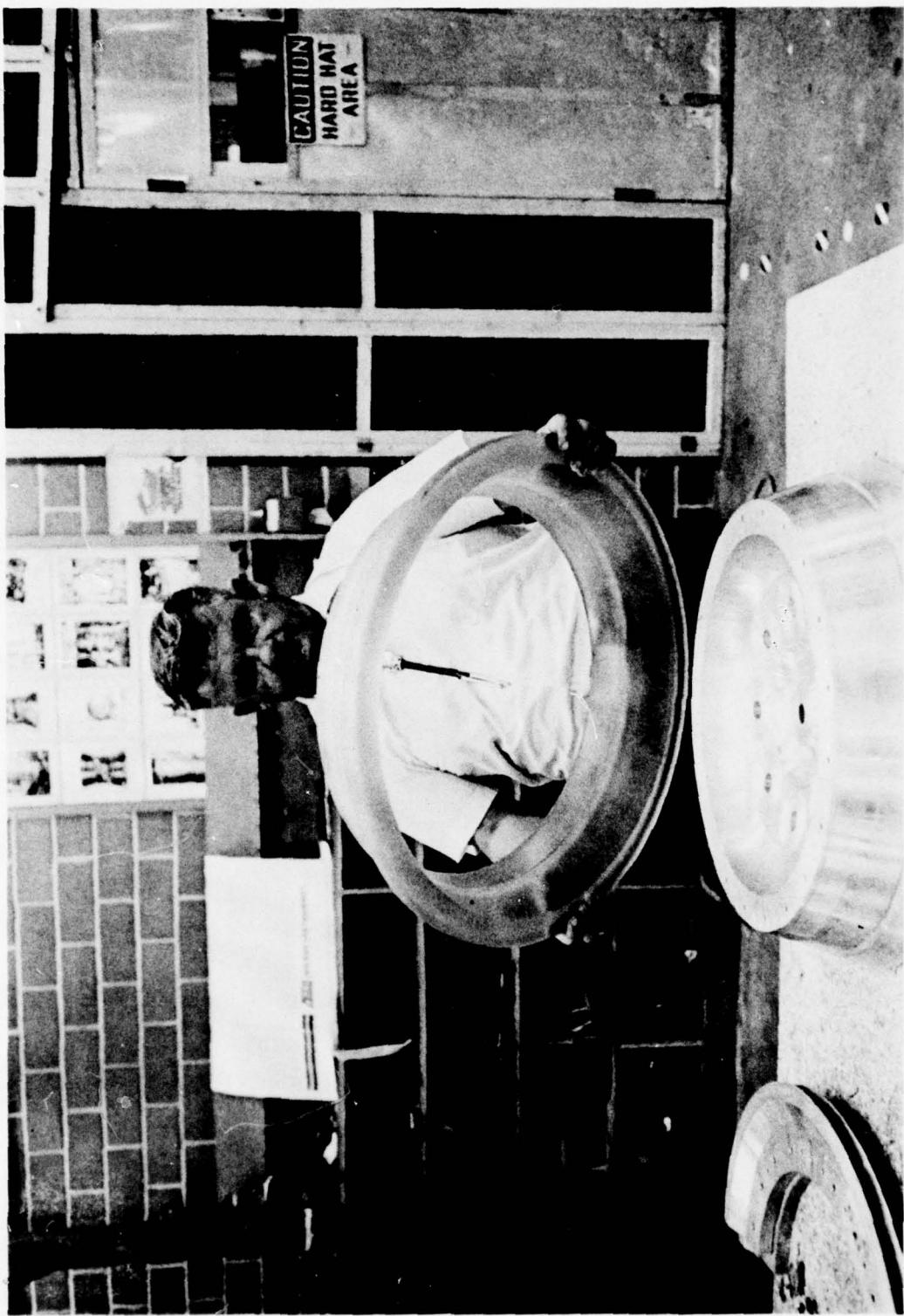
Figure 12.48. Polycarbonate gasket for penetrations in the full-scale acrylic hull NEMO Mod 2000 with $t/R_o = 0.121$ for 3000 feet (914 meters) operational depth capability.
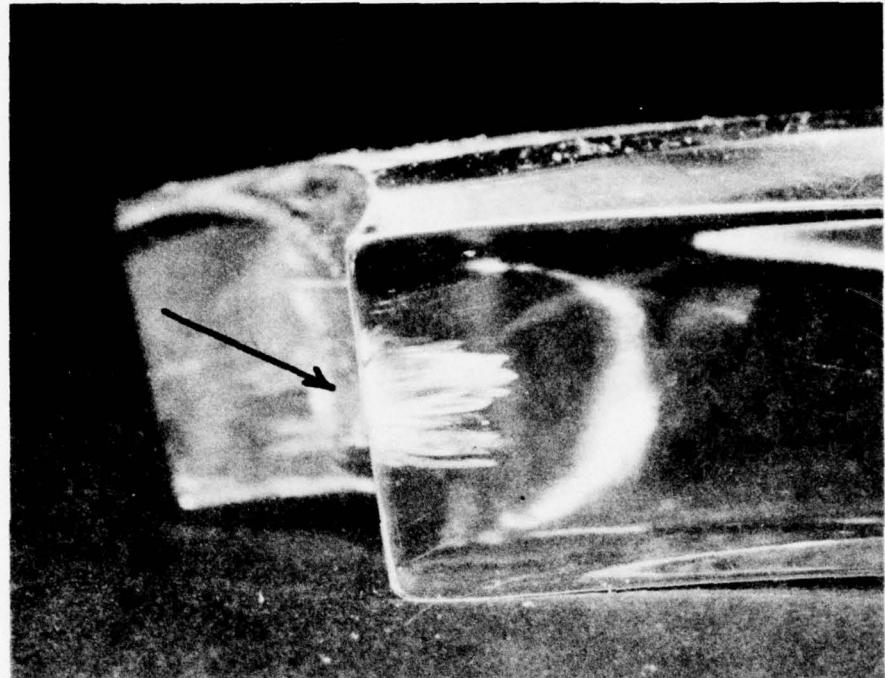
Figure 12.49. Section through a conical bearing surface in a penetration where the metallic closure with an O-ring groove was in direct contact with the acrylic during 300 pressure cycles to 500 pounds per square inch (3.44 megapascals) at ambient temperature. The durations of loading and relaxation phases in each cycle were 24 hours each. Note that the cyclic fatigue shear cracks in the model-scale sphere with $t/R_O = 0.066$ are similar to the static fatigue cracks of figure 12.43. They are again deepest at the location where the O-ring on the metal closure contacted the acrylic bearing surface.
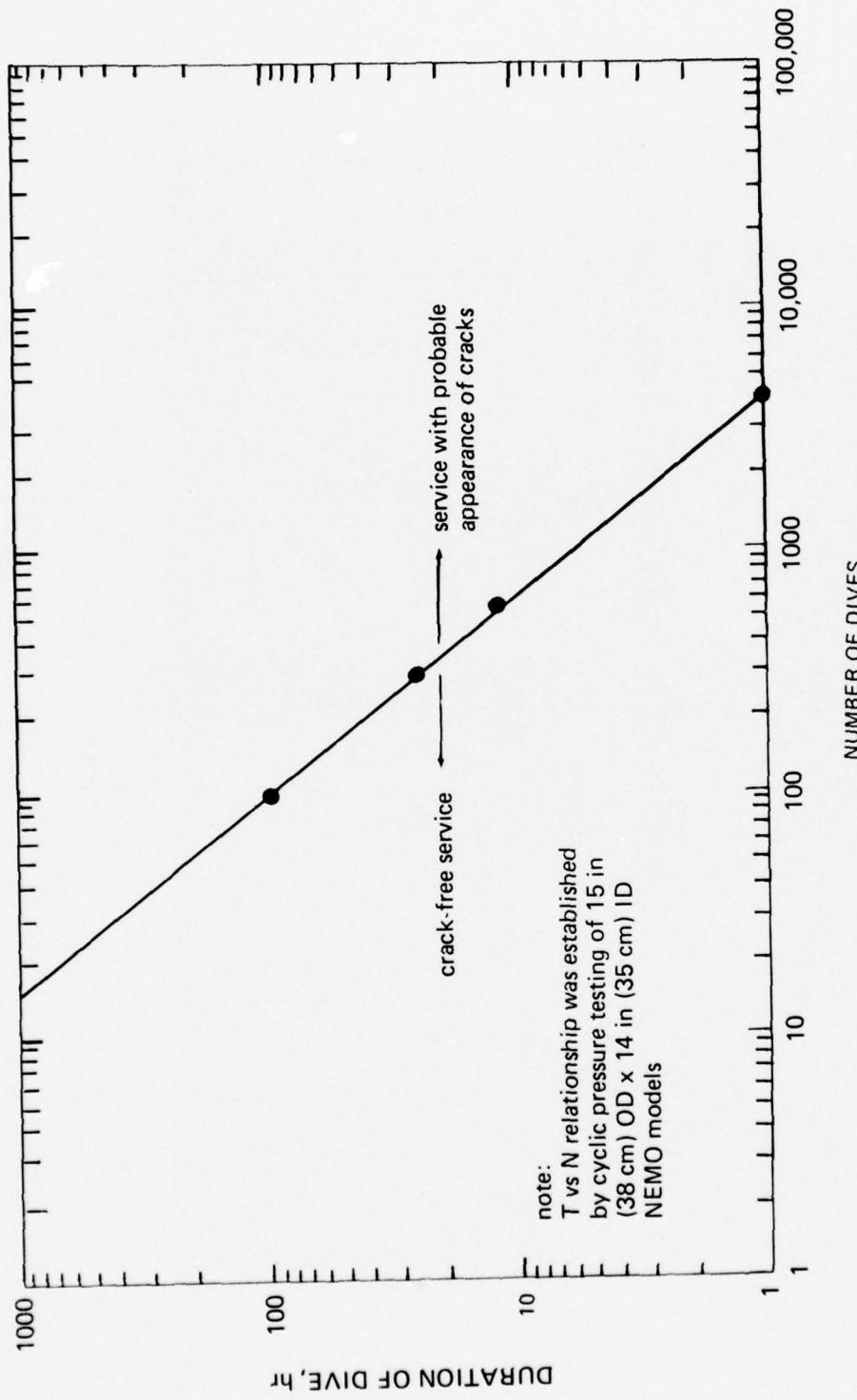
Figure 12.50. Experimentally established cyclic pressurization fatigue life of acrylic spheres with $t/R_o = 0.066$ and penetration closures according to designs A or B (figure 12.45) under an external pressure of 450 pounds per square inch (3.1 megapascals).

Figure 12.51. Star-shaped fracture in acrylic hull initiated by dynamic overpressure resulting from underwater explosion. The fracture was initiated on the interior surface of a spherical hull with $t/R_o = 0.066$ by a dynamic overpressure of 1035 pounds per square inch (7.1 megapascals) at a depth of 5 feet (1.5 meters). This fracture did not penetrate the full thickness of the hull.
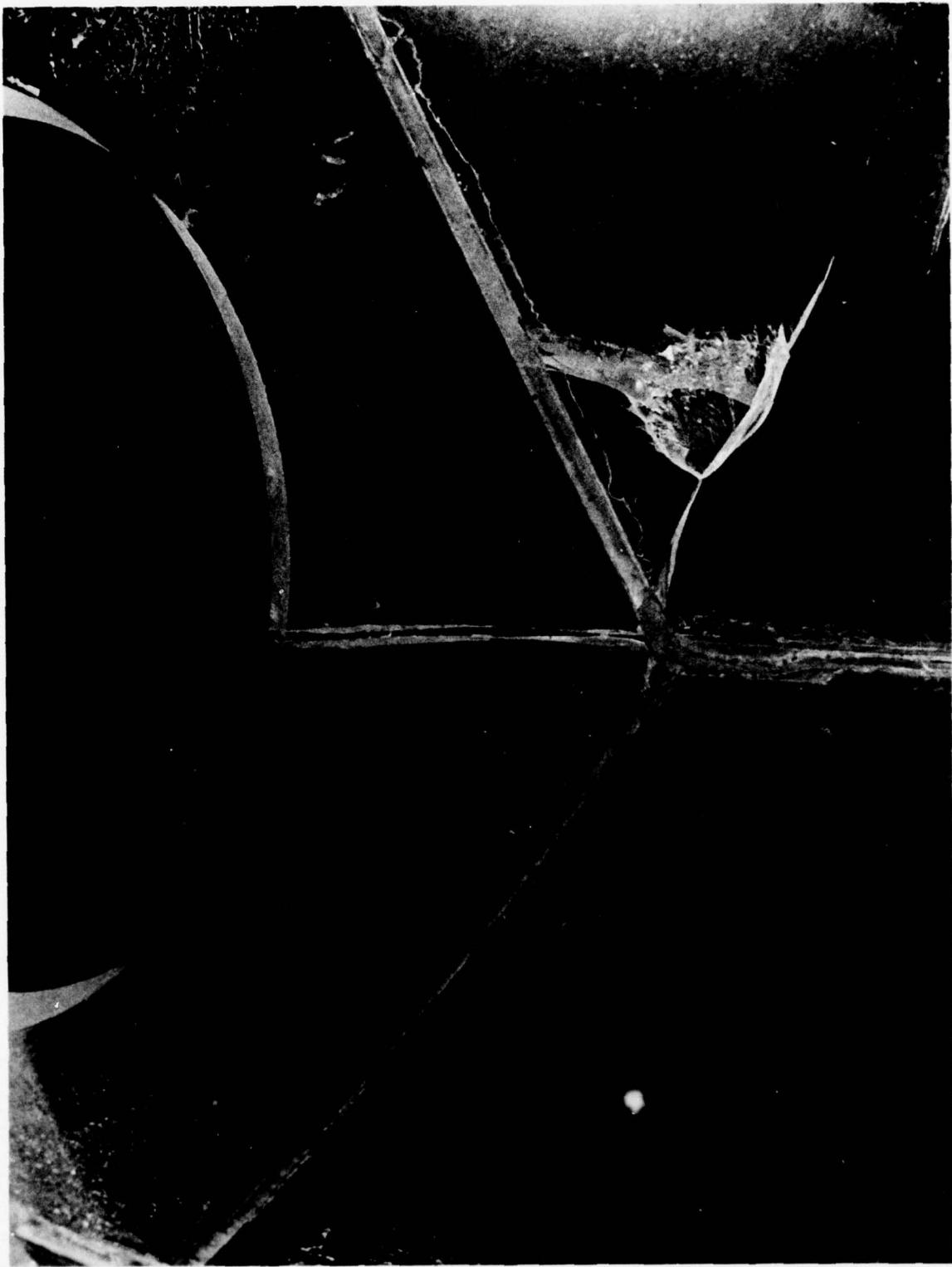
Figure 12.52. Radial cracks radiating from a penetration in an acrylic hull with $t/R_0 = 0.066$ after being subjected to a dynamic overpressure of 1035 pounds per square inch (7.1 megapascals) at a depth of 5 feet (1.5 meters). Note that these cracks penetrate the full thickness of the hull causing it to leak.
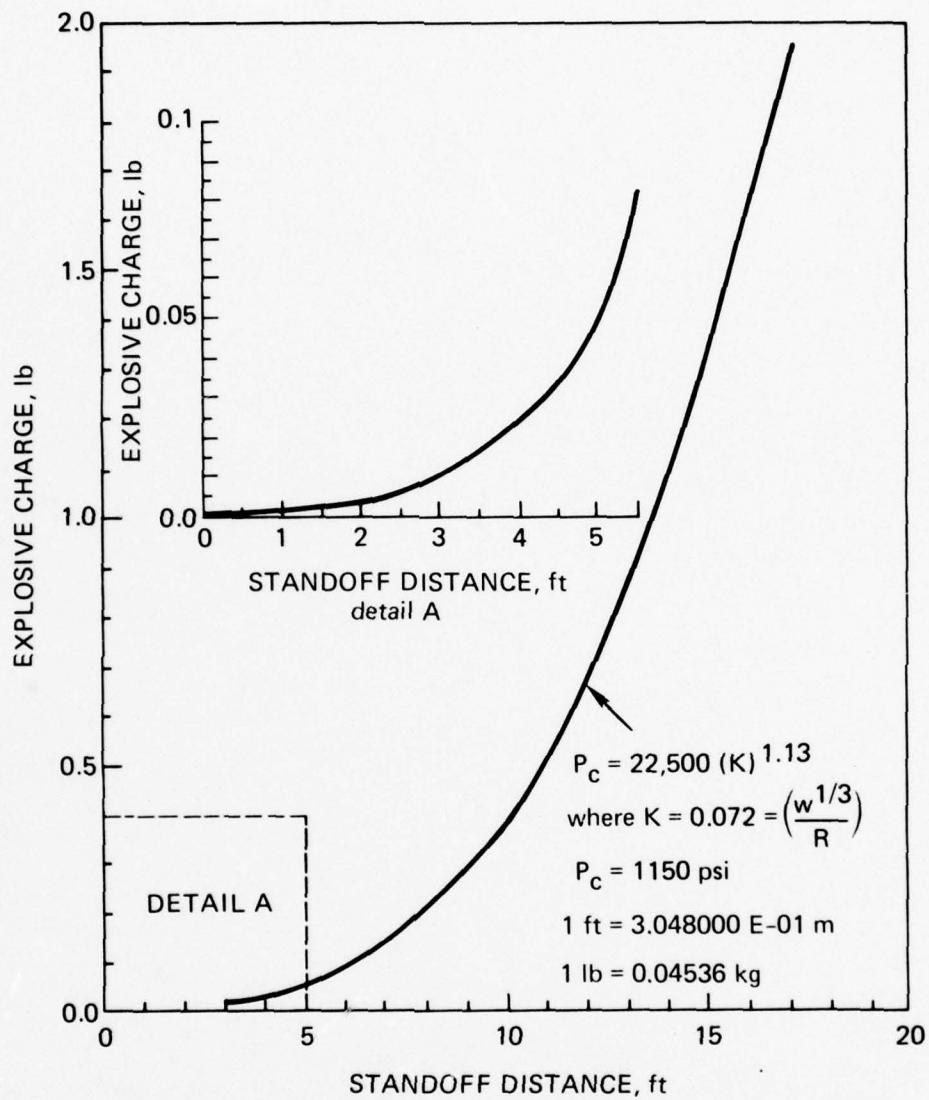
Figure 12.53. Experimentally established safe standoff distances between a spherical acrylic hull with $t/R_O = 0.121$ and sources of underwater explosions. For thicker hulls the safe standoff distances would be less, while for thinner hulls the distances would be greater. At these standoff distances, the explosives can be set off repeatedly without any damage to the hull in the depth range of 0 to 3000 feet (0 to 914 meters).
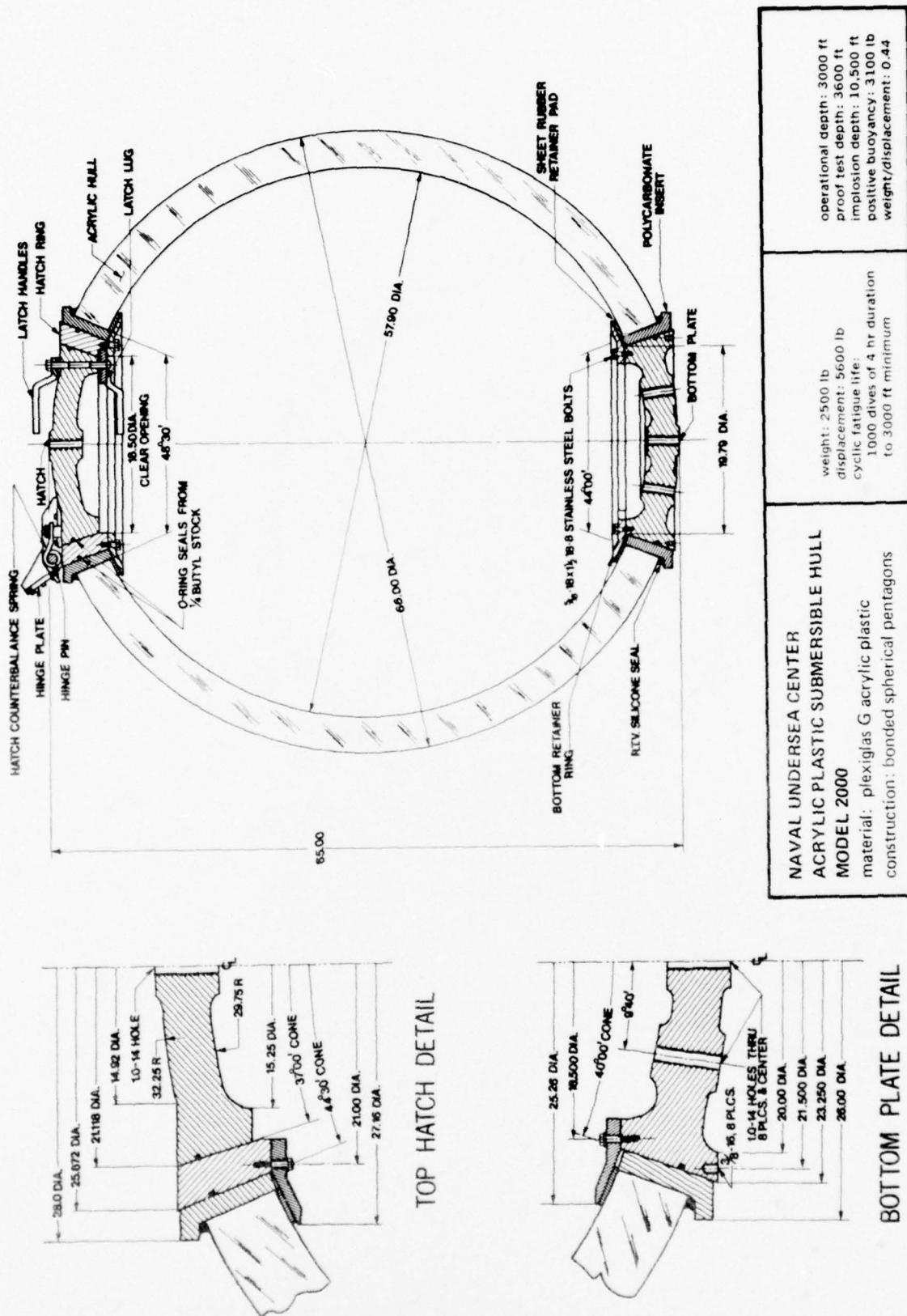
Figure 12.54. Typical design of an acrylic hull with multiple penetrations for manned submersibles with 3000-foot (914 meters) operational depth capability. This design, developed for the U.S. Navy by the Naval Undersea Center, has been incorporated by the Harbor Branch Foundation in their Johnson-Sea-Link 2 and 3 submersibles.
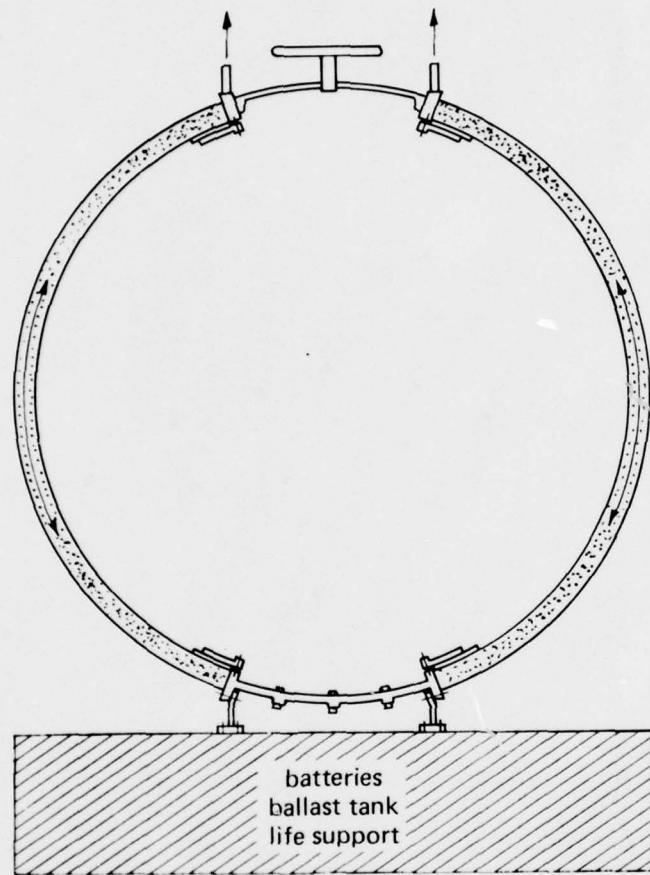
Figure 12.55. Undesirable approach to lifting an acrylic diving bell by attaching lines to the lifting eyes in the hatch ring. This approach creates tensile stresses in the hull and shear stresses at the edges of both penetrations. When afloat, the service module generates shear stresses at the edge of bottom penetration.
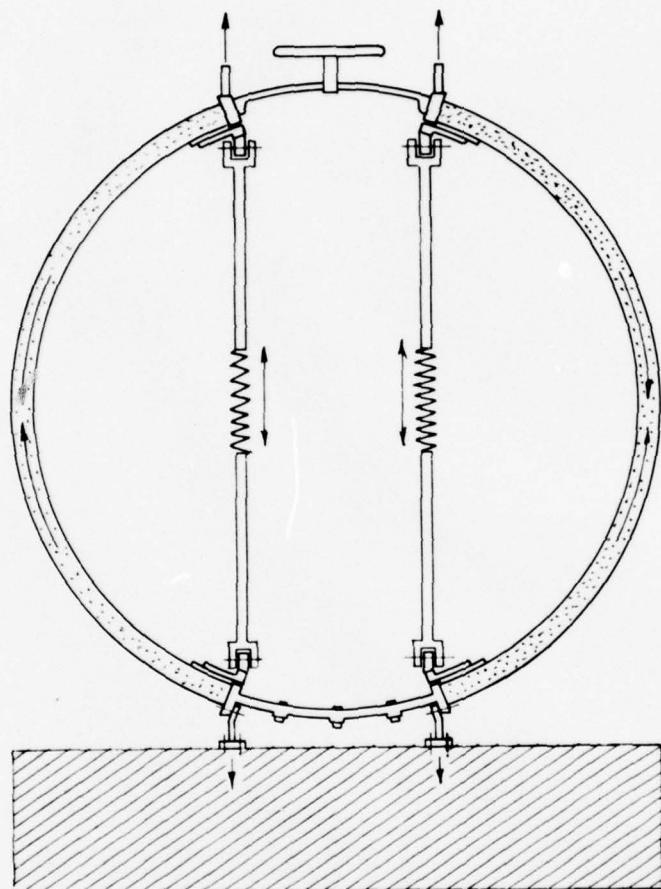
Figure 12.56. Same type of lifting attachment as in figure 12.55, except that spring-loaded tie rods have been added to decrease, or totally eliminate, tensile stresses in the hull and shear stresses at the edges of penetrations during lifting. During a dive the springs contract to prevent buckling of the rods.

lifting sling

sliding fit between pin and opening in cage ring

rigid cage rib

rubber gasket

cage ring bolted onto the cage ribs

ring with guide pins bolted onto the hatch ring

acrylic plastic hull

detail

lifting slings

service module (power pack and winch)
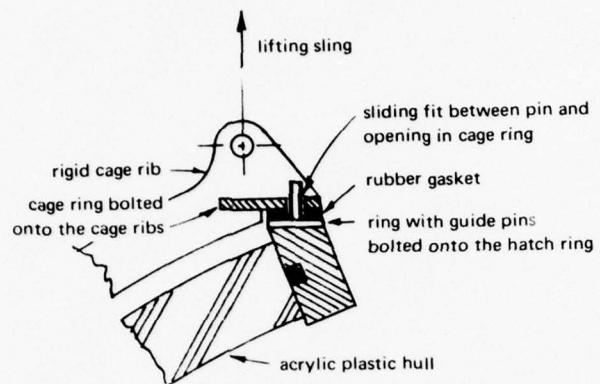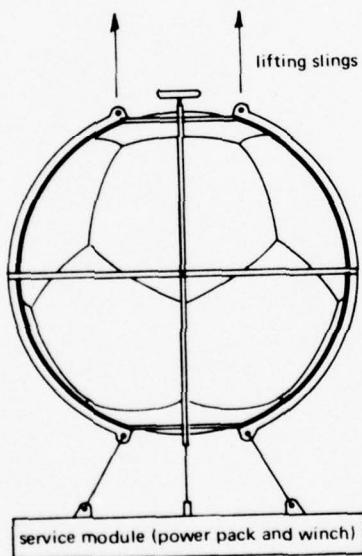
Figure 12.57. Lifting arrangement used in NEMO submersible. In this arrangement, tensile stresses are generated during lifting only in the external cage, while the hull is totally unstressed. When submerged, the hull floats inside the cage until the hatch ring presses against the interior of the cage ring.
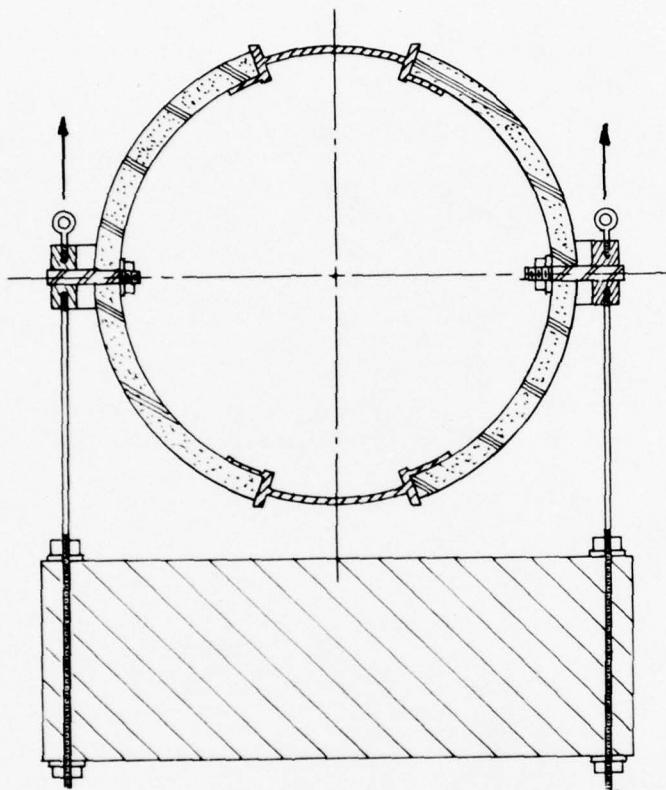
Figure 12.58. Lifting and hold-down arrangement for a sphere that utilizes an equatorial ring attached to the hull by tapered polycarbonate pins (see figure 12.40B). During lifting of the diving bell only the dead weight of the sphere imposes a shear force on the tapered pins. When submerged, only the buoyancy of the hull imposes a shear force upon the pins.
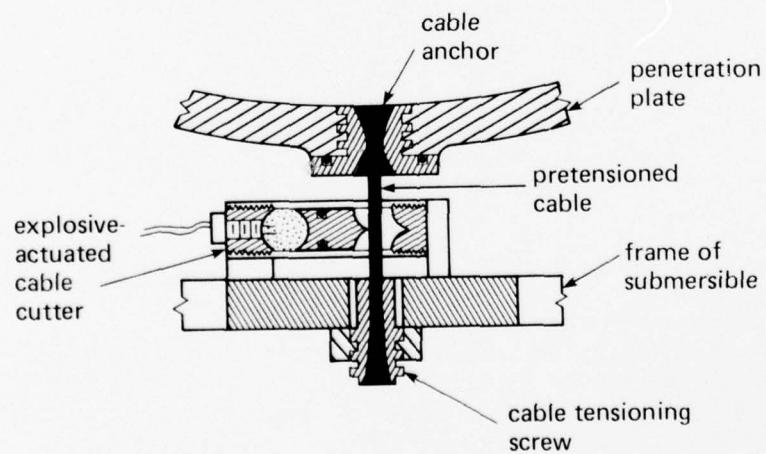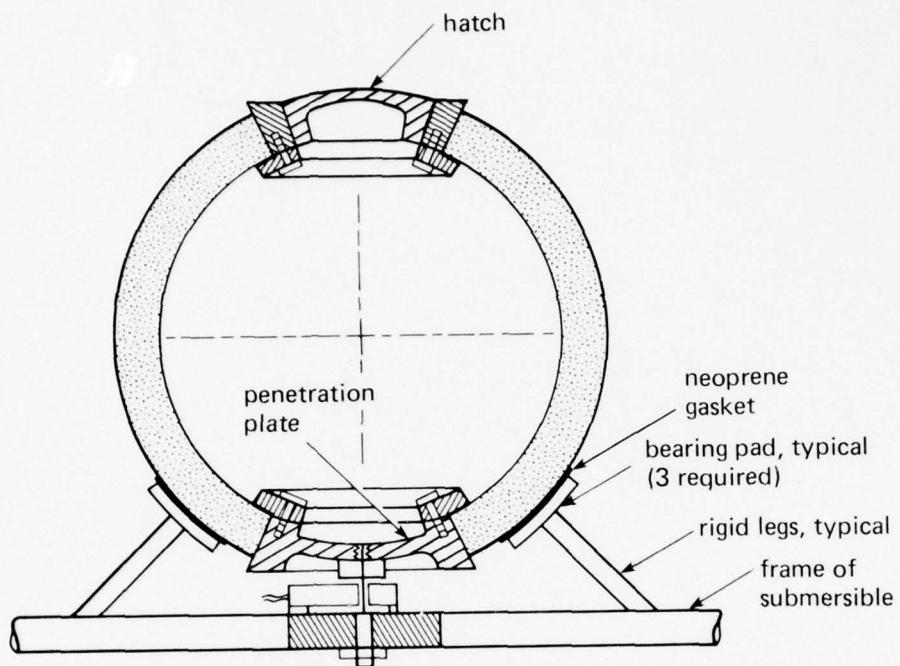
Figure 12.59. Attachment of the sphere to the service module by a single cable fastened to the center of the bottom closure. When submerged the upward buoyancy of the sphere generates shear forces in the hull near the penetration. This type of attachment was utilized for the acrylic hull in the U.S. Navy's submersible MAKAKAI.

shock
absorbers

frame of
submersible

soft elastomeric
bearing gasket

GRP bearing pad

compressed spring

to common ambient-
pressure-compensated
oil accumulator
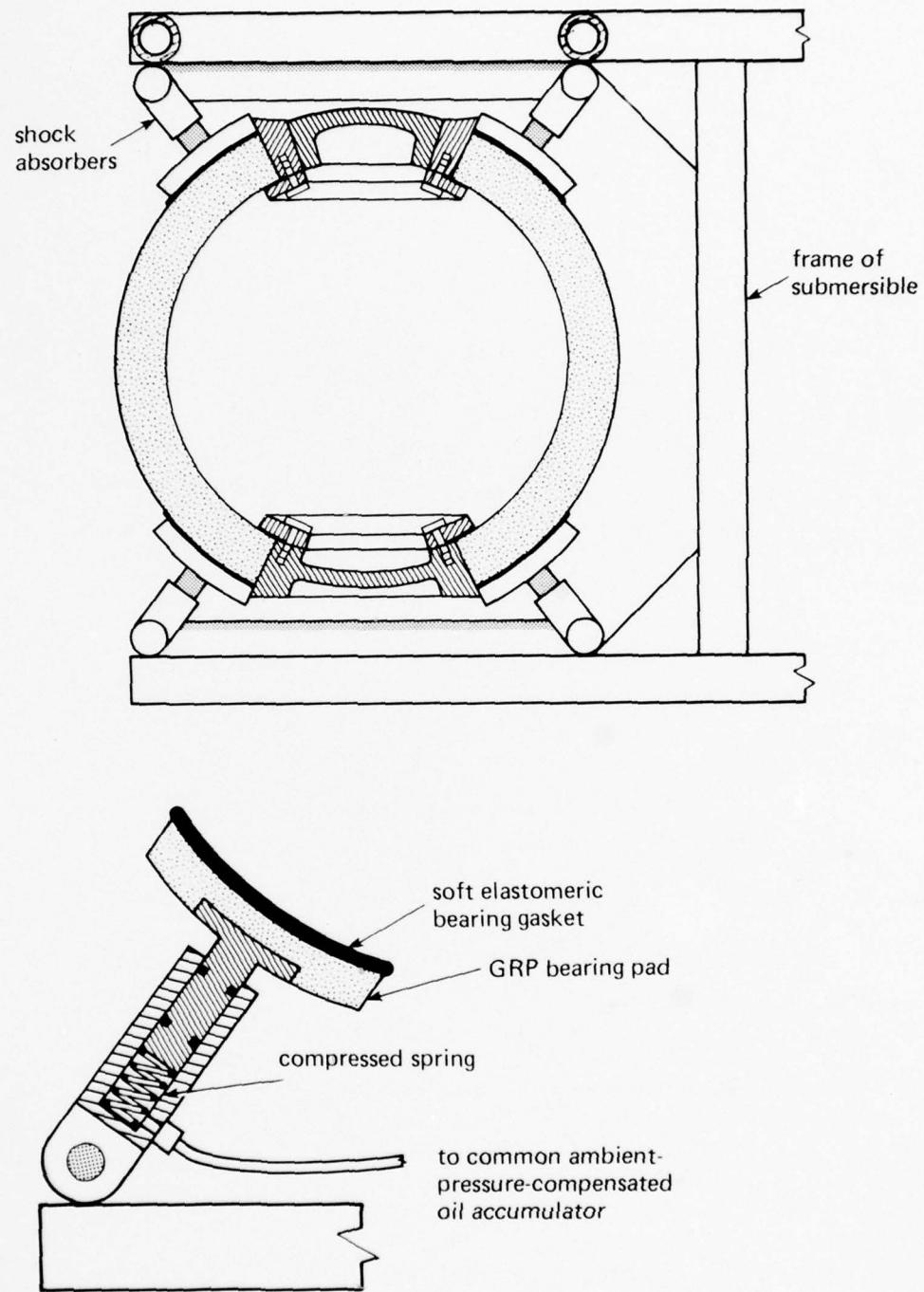
Figure 12.60. Mounting for acrylic sphere which incorporates several oil-filled shock absorbers for mitigation of shock loading on the sphere when it is subjected to an underwater pressure wave front.
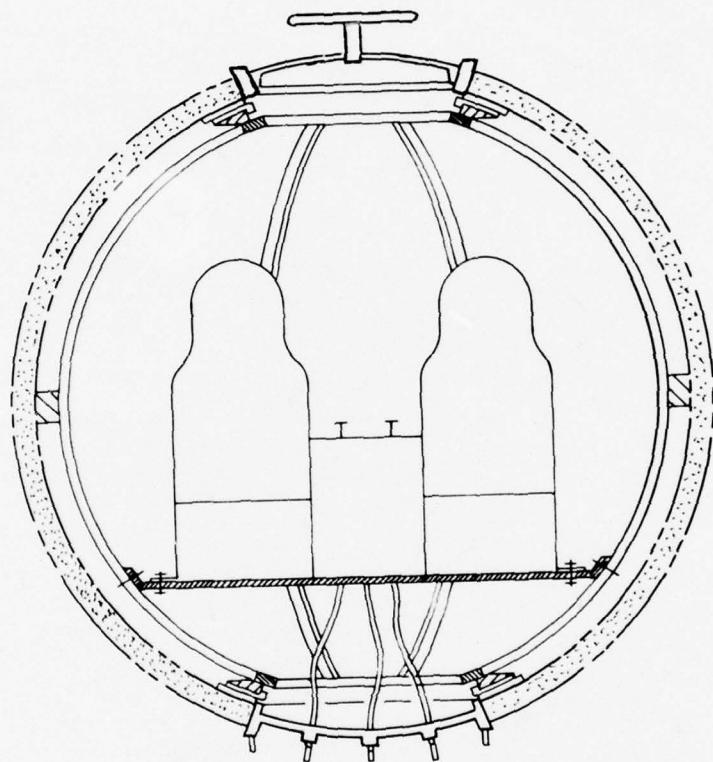
Figure 12.61. Internal cage for attachment of equipment inside the sphere. Elastomeric spacers between the cage and the hull allow for contraction of the sphere under external pressurization without compressing the cage.
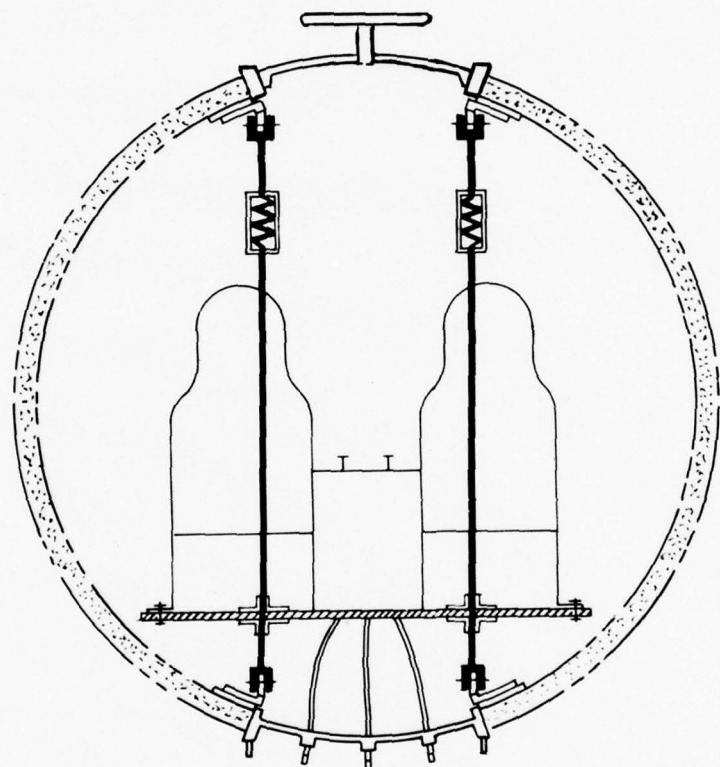
Figure 12.62. Attachment of all interior equipment to a floor which, in turn, is suspended from spring-loaded tie rods.
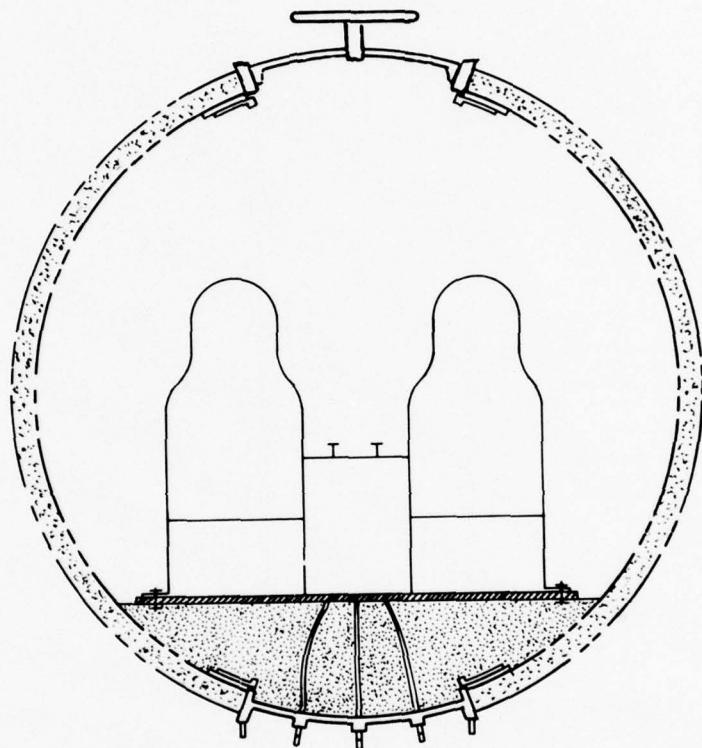
Figure 12.63. Attachment of interior equipment to a floor which rests on a styrofoam foundation. Contraction of the sphere is absorbed by the foam so that the floor always remains in its original location.
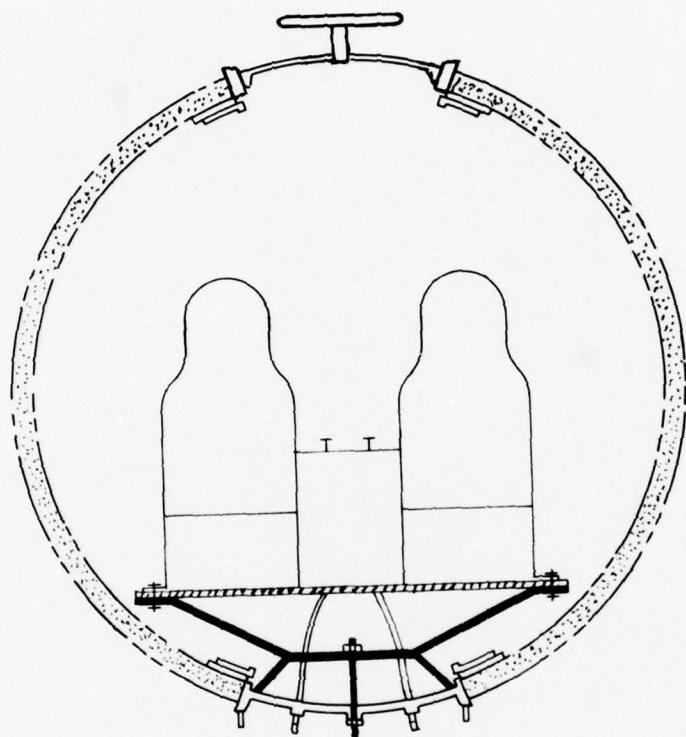
Figure 12.64. Attachment of interior equipment to a floor which is firmly attached to the bottom closure. Radial contraction of the sphere does not displace the floor from its original location.

Figure 12.65. Typical crazing that may be found after years of service and weathering on the exterior surface of an acrylic sphere that was not properly annealed. The presence of crazing does not decrease the structural strength of the sphere under external pressure loading, since the stresses on the concave and convex surfaces of the sphere are compressive.

Part A. Surface gouge prior to routing.

Figure 12.66. Repair of fractures on spherical surface of acrylic sphere.

Part B. Local routing for removal of gouge.

Figure 12.66. Continued.

CEL TESTS

In the tests cond... y the Civil Engineering

Laborat... both ... method and a core ... method were use... ...ement (Type II) con- crete slabs. A tota... ...d six cores were made at each ... ...robes in stronger and stronger c... ...e conducted with two slabs of conc... a Moh's hardness ... ...ive aggregate with limestone aggregate ... ...slab containing ...rdness of 3.5.

WMC Model PRS-... ...re used because this is the type used ... ...ly testing concrete incorporating natural a... ...would, there- fore, be the probe used i... ...ormal weight concrete. The PRS-01 pro... ...o be used in with o... testing concrete containing ma...racture lightweight ggregates; this is done by pushing the probe and

half. Each
has a care...
point. .

RESULTS

The
accuracy
coring
method
encount
an epox
compou
Cost

Part C. Routed cavity after backfill with PS-30 adhesive.

Figure 12.66. Continued.

GENERAL INFORMATION

SERVICING

A. It is the user's responsibility to see that this unit is operating at all times in accordance with the F.C.C. Citizens Radio Service regulations.

If you install your own transceiver, do not attempt to make any transmitter tuning adjustments. Adjustments are prohibited by the F.C.C. unless you hold or are in the presence and under the supervision of a first or second class radio telephone licensed person. A Citizen Band or Amateur License is not sufficient.

B. Only crystals, tubes or other components that will not cause violations of the technical regulations of Part 95 and type acceptance requirements of Part 2, Chapter 1 of the F.C.C. Rules and Regulation can be used for substitution o replacement of parts.

Part D. Repaired spot after sanding and polishing.

Figure 12.66. Continued.
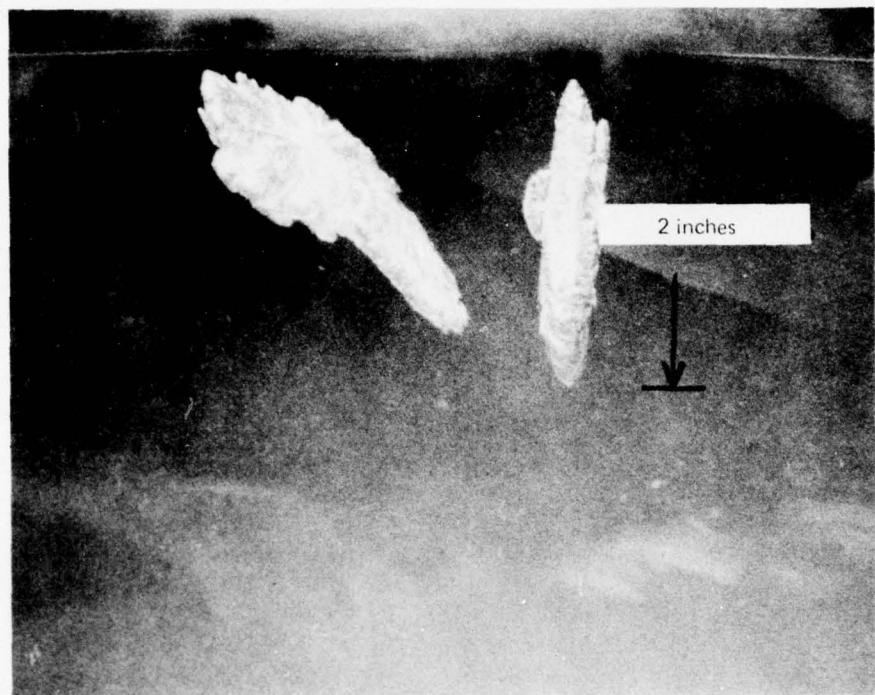
Figure 12.67A. Typical inclusions sometimes found in custom-cast acrylic hemispheres or in the bonded joint between thermoformed structural components of the sphere. The inclusion shown here was found inside the hemispherical casting for the NEMO Mod 2000 B pressure hull with a 4.125-inch (10.4 centimeters) wall thickness.
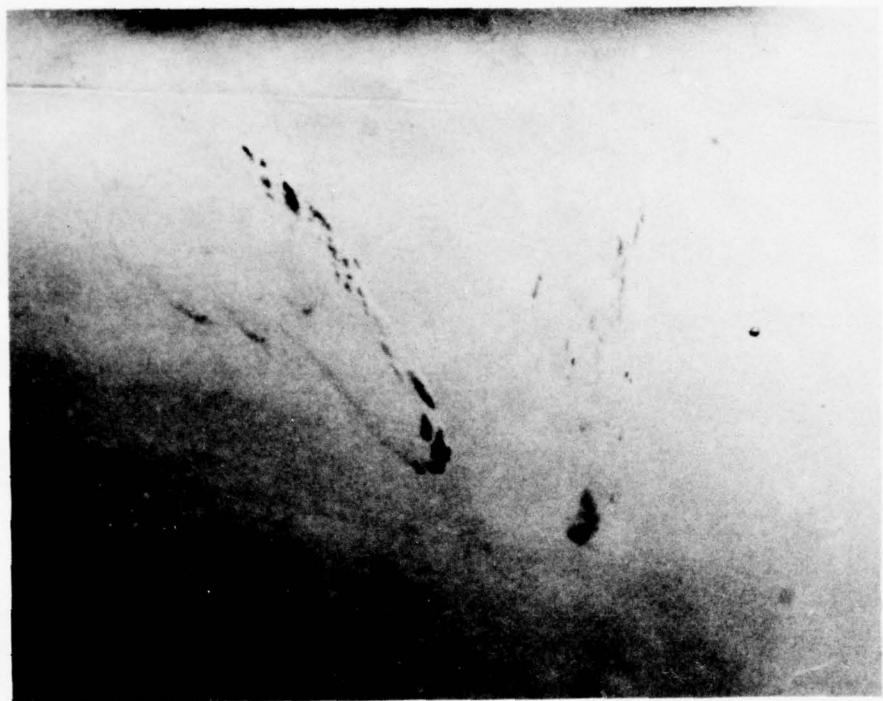
Figure 12.67B. Inclusions shown in figure 12.67A after partial drilling, filling with acrylic casting slurry, and polymerization in a pressurized autoclave. After such a repair the inclusion ceases to be the source of structural weakness.
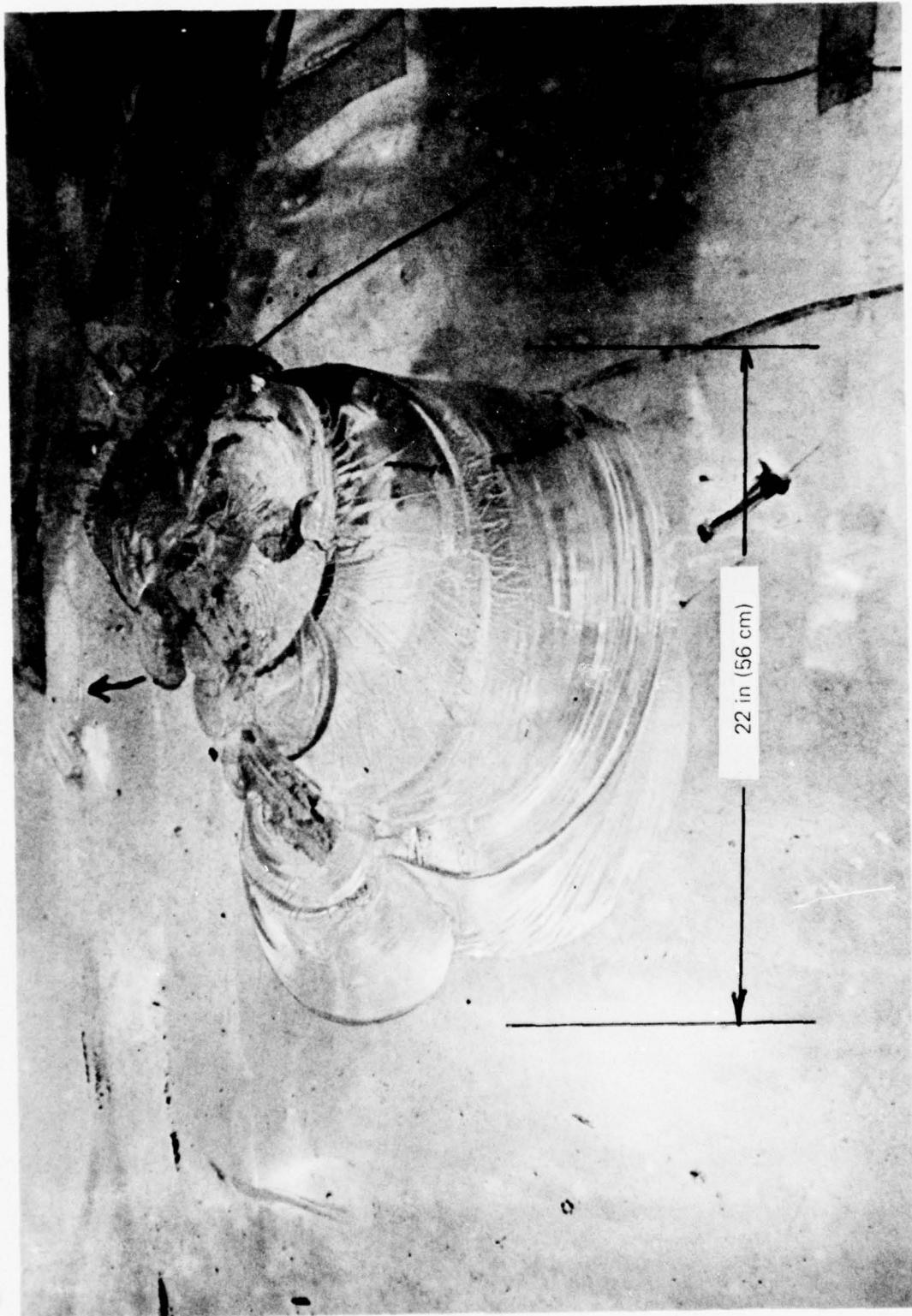
Figure 12.68A. Typical conchoidal fracture surface resulting from point-impact loading on a full-scale NEMO Mod 2000 acrylic hull with a 4-inch (10.1 centimeters) wall thickness. The fracture was approximately 1 inch (2.54 centimeters) deep.

22 in (56 cm)

Figure 12.68B. The same hull after grinding out the conchoidal fracture, building up the wall thickness with a cast-in-place patch, fairing the patch surface to the convex curvature of the hull, and polishing it to optical transparency. When viewed at right angles to the surface of the sphere the patch cannot be visually detected.
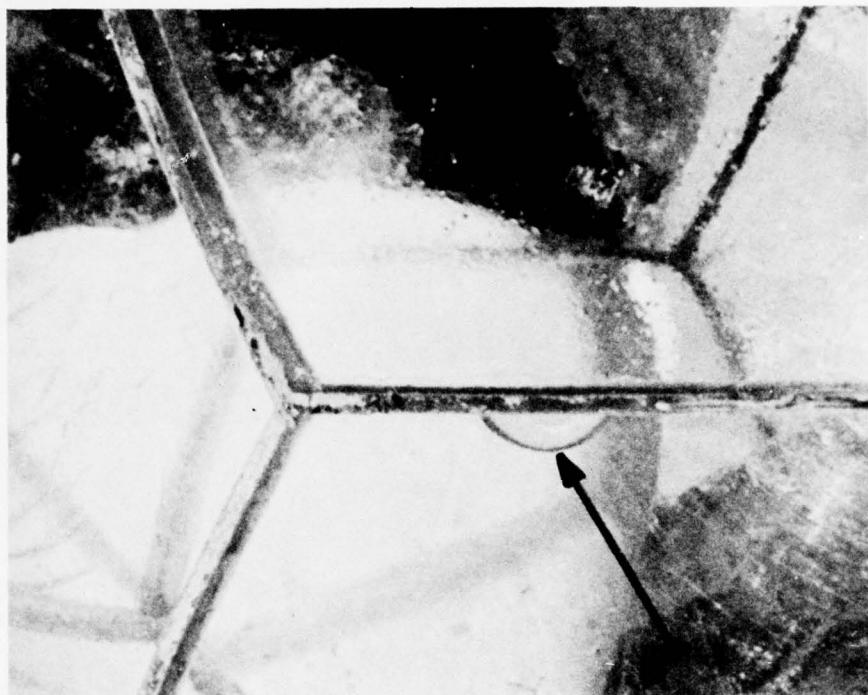
Part A. Typical fractures inside a model-scale sphere with $t/R_o = 0.133$. Fractures were initiated by a dynamic overpressure of 6170 pounds per square inch (42.5 megapascals).

Figure 12.69. Repair of a fracture with acrylic plugs.
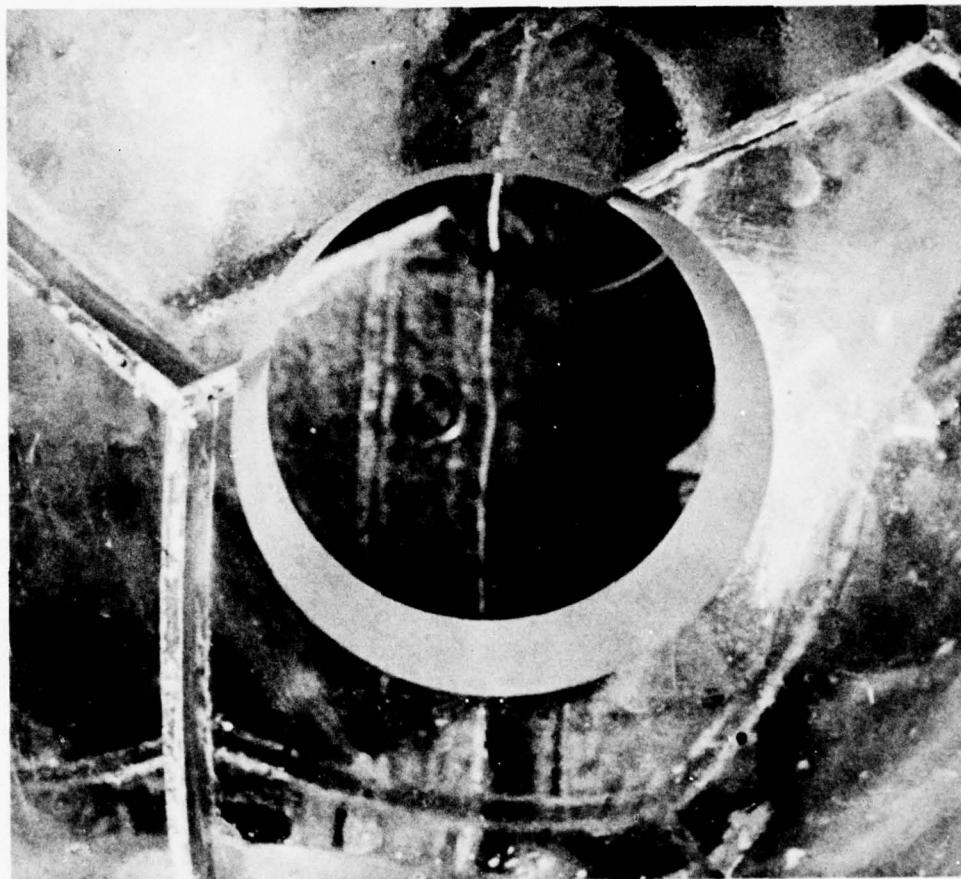
Part B. Same sphere after removal of fractured material at both locations. The conical bearing surface of the penetration forms a spherical angle of 26 degrees 41 minutes (0.46 radian).

Figure 12.69. Continued.

Part C. Plugging the penetration with an acrylic spherical sector whose spherical angle matches that of the penetration and whose outside and inside radii of curvature match those of the hull.

Figure 12.69. Continued

12-113

Part D. Spherical sector after bonding in place with PS-30 cement. Note the presence of some air bubbles in the bonded joint which cuts across existing bonded joints between individual structural modules of the sphere.

Figure 12.69. Continued.

acrylic plug

edge of plug
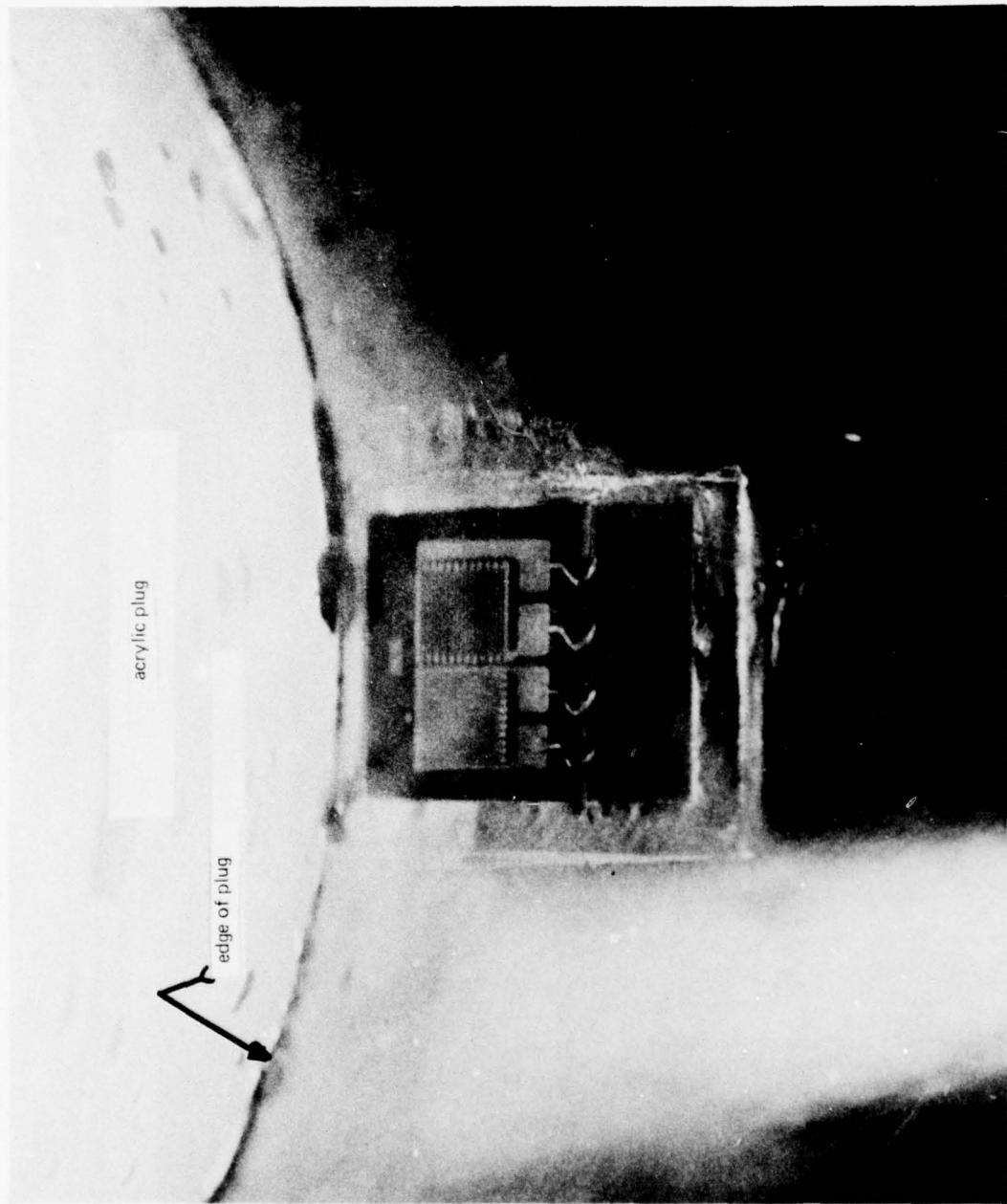
Part E. Repaired area after it has been instrumented with electric straingages prior to external pressure testing. The strains measured at this location were identical to those found at locations far from the repaired area.

Figure 12.69. Continued.

Part F. Acrylic sphere after short-term pressurization at 4500 pounds per square inch (31 megapascals). The repaired areas did not serve as initiators of buckling, since the short-term critical pressure of the repaired sphere was the same as that for an identical sphere without repairs previously tested.

Figure 12.69. Continued.
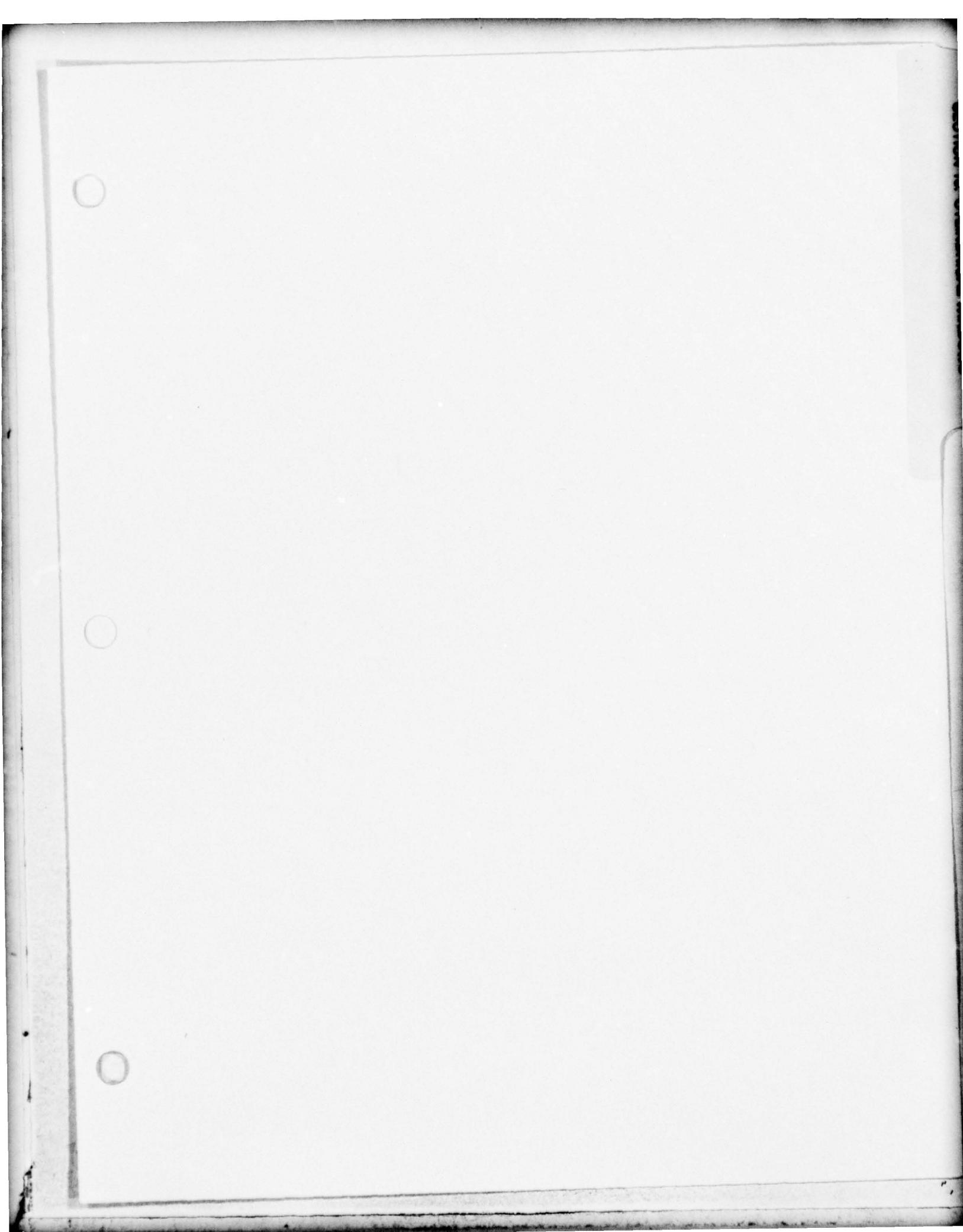
SECTION 13. CYLINDRICAL WINDOWS

13.1 INTRODUCTION

Although spherical pressure hulls are the optimum structural shape for resisting external or internal pressures, there are many applications where it would be more advantageous from fabrication or operational viewpoints to use a cylindrical shape. A cylindrical shape, for example, would lend itself better for incorporation into a streamlined submersible whose length is five to six times greater than its diameter.

Utilizing a cylindrical shape, a streamlined submersible to transport many people comfortably could be designed. To accomplish the same with a spherical hull would require a very large sphere that would not only be expensive to build but also difficult to maneuver underwater. There would be some drawbacks to the cylindrical construction, but they would be minor compared to the advantages gained.

The major drawback would be optical, as the cylindrical hull would act like an asymmetric lens distorting the shape of images perceived by the passengers and crew. As the radius of the cylinder increased, however, the magnitude of distortion would decrease. Thus, for cylindrical hulls in submersibles carrying many passengers the optical distortion would be tolerable, as the radius of such a hull would probably exceed 5 feet (1.5 meters).

Submersibles have not yet been built with cylindrical acrylic pressure hulls, although many leading ocean engineers have seriously proposed such designs (figure 13.1). Instead, many submersibles have been, and are being, built with cylindrical windows located in the conning towers (figure 13.2). In this location, the cylindrical shape of the window perfectly matches the cylindrical shape of the conning tower. Utilization of plane disc, conical frustum, or spherical shell sector windows would be quite inappropriate from structural and cost-effectiveness viewpoints. The major variation in cylindrical windows located in conning towers is the extent of the cylindrical shape. In some designs the cylindrical windows are installed around the circumference of the conning tower as cylindrical sectors, while in others they form continuous rings. In either case they are an appropriate solution to a difficult design problem.

Complete acrylic plastic cylindrical pressure hulls for ocean engineering applications have been built to date only in small sizes to protect electronic packages from the effects of pressure and salt water in a nonmetallic, transparent, corrosion-proof enclosure (figure 13.3). For short-term dives from 0 to 3000 feet (0 to 914 meters), the weight-to-displacement ratio of cylindrical pressure-resistant housings for electronic packages compares favorably with cylindrical housings made of corrosion-resistant steel or aluminum alloys at a fraction of their cost.

Cylindrical pressure hulls are also desirable for containing internal pressure. Because hatches can be easily incorporated into the metallic end closures of cylindrical hulls, they are very cost-effective solutions to the design of pressurized aquaria or hyperbaric chambers for medical research. Thus, acrylic hyperbaric chambers are found in hospitals for treating patients with pressurized oxygen, which has been found to provide many beneficial results, particularly in treatment of burns and septicemia (figure 13.4).

It thus appears that cylindrical pressure hulls of acrylic plastic satisfy many operational requirements of transparent structures for internal or external pressure applications. For this reason it is necessary to discuss cylindrical windows, i.e., they are not scientific curiosities but proven engineering solutions to many operational requirements posed by submersibles and hyperbaric chambers.

13.2 INTERNAL PRESSURE

13.2.1 Structural Response

The structural response of cylinders to internal pressure depends to a large degree on the support given to the cylinder by end closures or ring stiffeners. The simplest structural condition is represented by a monocoque (smooth wall) cylinder whose ends are free to slide on flat bulkheads held together by metallic longitudinal structural members, e.g., tie rods (figure 13.5). In such a cylinder, there are only hoop and radial stresses whose maximum values can be readily calculated on the inner surface with Lamé's equation for thick cylinders (reference 13.1):

$$S_{radial\ maximum} = -p \quad (at\ inner\ surface)$$

$$S_{hoop\ maximum} = \frac{R_O^2 + R_i^2}{R_O^2 - R_i^2}\ p \quad (at\ inner\ surface), \qquad (13.1)$$

where

R_O = external radius, inches (meters)

R_i = internal radius, inches (meters)

p = internal pressure, pounds per square inch (pascals).

If the ends of the cylinder are restrained from expanding by means of a metallic bulkhead with a restraining edge or ring (figure 13.5), longitudinal bending and shear stresses will be introduced into the cylinder near its end. The magnitude of these stresses can readily exceed the maximum hoop stress found in the cylinder, if the t/R_i ratio and length are of certain magnitudes:

maximum longitudinal bending stress at edges of end rings or bulkheads $\geq L_f$ apart

$$\sigma_f = (-6\ M_0)/t^2 . \qquad (13.2)*$$

maximum shear stress at edges of end rings or bulkheads

$$\sigma_s = V_0/t . \qquad (13.3)*$$

where

maximum transverse shear load at edges of acrylic rings with A cross-section $\geq L_f$ apart

$$V_0 = 2\ M_0\ \lambda .$$

---

*Equations 13.2 and 13.3 from references 13.2 and 13.3

maximum transverse shear load at edges of steel rings or bulkheads $\geq L_f$ apart

$$V_0 = p/\lambda \ .$$

maximum bending moment at edges of acrylic rings

$$M_0 = \frac{p}{2\lambda^2} \left(\frac{A}{A + tc + 2t/\lambda} \right) .$$

maximum bending moment at edges of steel rings or bulkheads

$$M_0 = p/2\lambda^2$$

$$\lambda = \sqrt[4]{\frac{3(1 - \mu^2)}{R^2 t^2}} \ .$$

M_0 = bending moment, inch-pound per linear inch (Newton-meter per meter) of circumference,

p = hydrostatic pressure, pounds per square inch (pascals),

C = width of ring, inches (meters),

A = cross-section of ring, inches (meters),

t = shell thickness, inches (meters),

R = mean radius of shell, inches (meters),

$L_f \geq 4/\lambda$, inches (meters),

V_0 = transverse shear normal to wall, pounds per linear inch (kilograms per meter),

μ = Poisson's ratio.

In addition, if there are significant temperature changes in the ambient environment the acrylic tube will attempt to expand significantly, contributing more bending stresses to the location near the end restraint. For this reason, metallic end closures with radial restraints are not recommended for acrylic cylinders under internal pressure, unless a very thorough analysis has been made of the stresses introduced by their presence.

If the design requirements call for end stiffeners in the hoop direction, they are best provided by acrylic plastic ring stiffeners bonded to the cylinder. These generate smaller longitudinal bending stresses in the cylinder because their modulus of elasticity and coefficient of thermal expansion match those in the acrylic cylinder. However, even with acrylic stiffeners, the bending stresses in the cylinder must be repeatedly calculated while the spacing of stiffeners and the shell thicknesses are varied so that the optimum stiffener spacing is determined.

There are generally only two reasons for designing a cylinder with circumferential end stiffeners for internal pressure service. The major reason is the inability to fabricate a thick enough monocoque cylinder for withstanding a specified internal pressure. The other is to provide a means to attach the cylinder to some other structure. In some cases rings are bonded to the ends of the cylinders, not to serve as stiffeners, but to function as

retainers for a self-energizing seal ring. In such a case the bonded ring should have the smallest feasible cross-section so that its presence will not generate significant tensile bending stresses in the tube.

In general it can be stated that no weight or cost savings accrue from the use of acrylic ring stiffeners on a thin cylinder in lieu of a thicker monocoque cylinder. In fact, ring-stiffened cylinders for internal pressure are generally more expensive than monocoque tubes. The design is more expensive because of the extensive stress calculations required, and the fabrication is costlier because of the additional machining required for the stiffeners and tube to insure proper fit. Thus there is no doubt that wherever feasible the design of cylinders for internal pressure should use monocoque shells closed off with bulkheads that allow the edge of the shell to displace radially with a minimum of restraint.

Attachment of end closures to the cylinder by means of integral or bonded-on acrylic end flanges and bolts should be avoided, as this arrangement invariably becomes the weak point of the structure because of the stress risers associated with such construction. To maximize the pressure rating of the cylinder, internal or external metallic tie rods running the full length of the cylinder should be used. This method not only eliminates most of the stress risers in the ends of the cylinder but it also eliminates longitudinal bending and axial tensile stresses in the shell which, when combined with hoop stresses, create a biaxial stress field and thus decrease the ultimate tensile strength of the acrylic plastic.

13.2.2 Mode of Failure

Monocoque cylinders fail catastrophically by fragmentation when the maximum tensile stress in the cylinder reaches the ultimate tensile strength of the acrylic plastic. For cylinders free to slide on the end closures, the maximum stress is represented by the hoop stress calculated with Lamé's equation for the interior surface. For cylinders restrained at the ends, the maximum tensile stress may not be the hoop stress, but rather the bending stress generated by the end restraint.

Ring-stiffened cylinders also fail catastrophically by fragmentation when the maximum resultant tensile stress in the cylinder or stiffener reaches the ultimate tensile strength of the acrylic plastic. The maximum resultant tensile stress may occur on the exterior of the shell midway between stiffeners or on the interior surface adjacent to the stiffener. If the stiffeners are inside the cylinder, failure may be triggered by separation of the shell from the stiffener.

The ultimate tensile strength of the material will vary with the operational scenario. The highest tensile strength will be found under short-term pressurization at low ambient temperature; the lowest value will be encountered during sustained long-term pressurization while exposed to the effects of weather. The effects of cyclic loading fall between those of short-term and sustained long-term loading.

The ultimate tensile strength of the material is further lowered by surface discontinuities such as crazing, scratches, or exposure to harmful chemicals, e.g., ether, alcohol, acetone, MEK, etc., particularly when the material is in stressed condition. Because the failure of a cylinder under internal pressure is catastrophic, and in most cases without warning, steps must be taken to inspect the surfaces of the cylinder for signs of surface deterioration before

each pressurization. The presence of scratches or crazing should serve as immediate cause for declaring the pressure vessel unsafe until the surface stress riser has been removed.

The ultimate tensile strength for different loading conditions has been established for acrylic plastic by testing tensile and flexural specimens under short-term, long-term, and acrylic loading regimes. The actual ultimate tensile strength value of acrylic plastic is discussed in section 4.

13.2.3 Design

In the design of cylinders under internal pressure, there are two important guidelines: (1) to avoid the creation of tensile stress concentrations and (2) to keep design stresses below the ultimate tensile strength of the material under the projected operational conditions.

Tensile stress concentrations can be readily avoided by selecting a monocoque shell design, allowing the ends of the shell to displace radially under internal pressurization and/or temperature changes, and avoiding the use of O-ring grooves in the sealing surfaces of the shell.

Choosing the right design stress level is a more difficult matter, since only a few operational scenarios can predict with certainty the actual service conditions to which a marine pressure vessel will be subjected during its life. If the actual service conditions are not known, then it is almost impossible to state with any degree of certainty what the value of ultimate tensile strength will be in actual service. Faced with this problem, the designer must select *working stress values* by basic rules which are conservative enough to cover most operational situations which may occur during the specified service life (not to exceed 10 years) of the pressure vessel. These basic rules are shown in table 13.1. It should be noted that these values are functions of the maximum ambient temperature that will be encountered by the cylinder in a pressurized state during its operational life. As a result, it is imperative that

Table 13.1. Maximum recommended tensile design stresses for internal pressure vessels made of acrylic plastic.*

Design Temperature, °F (°C)**	Design Tensile Stress, psi (mPa)†
50 (10)	1800 (12.4)
77 (25)	1500 (10.3)
104 (40)	1200 (8.3)
126 (52)	1100 (7.6)
140 (60)	1000 (6.9)
158 (70)	800 (5.5)
176 (80)	600 (4.1)
194 (90)	300 (2.1)

*Acrylic plastic which satisfies the physical and chemical properties of ANSI/ASME PVHO-1 (appendix A, tables A1 and A1).

**Maximum ambient temperature during pressurization of pressure vessel.

†Maximum working stress in acrylic tube at design pressure.

the designer select the maximum temperature which is predicted to occur during pressurization of the cylinder. If there is no reliable way to predict this value, 122°F (50°C) should be chosen. This will insure that the tensile stresses used in the design will provide an ample safety margin for most conceivable operational conditions involving human occupancy, even in the tropics.

13.2.4 Mounting and Sealing

The mounting of internally pressurized cylinders must allow unrestrained expansion of the cylinder's ends under the action of internal pressure and temperature, otherwise the mounting will act as a restraint that will initiate fracture near the end of the cylinder because of bending or shear stresses (equations 13.2 and 13.3). Free radial expansion and contraction of the cylinder's ends are facilitated by a ≤ 63-rms finish on the end closure and a ≤ 32-rms finish on the cylinder's ends. Sliding is enhanced by extension of the rods and axial contraction of the cylinder during its internal pressurization. As a result, the friction between the end closures and the cylinder is inversely proportional to the internal pressure. This effect is very beneficial, as it decreases the friction to its minimum value at the maximum internal pressure, i.e., when the potential for high tensile bending stresses at the end closures is the greatest.

Crucial items in the design of the mounting are selection of proper tie rod size and specification of the proper torque. Excessive tightening during assembly may induce in the acrylic excessively high compressive axial stresses, which may be further aggravated by an increase in ambient temperature. The end result may be either ruptured tie rods or a permanently deformed cylinder. This situation can be alleviated by using thick neoprene gaskets under the ends of the cylinder. Because of the gasket's compressibility, compensation for changes in the lengths of the cylinder or tie rods can be easily made without unduly raising the compressive stresses in the cylinder or tensile stresses in the tie rods.

The sealing of a cylinder with unrestrained ends under internal pressure requires careful attention to design details. The seal must perform reliably, although the ends displace radially because of changes in internal pressure or temperature. Although many designs have been experimented with over the years, only two provide reliable sealing when there are large-magnitude radial displacements and a lack of axial compression at the maximum internal operating pressure (figure 13.6).

Seal design A is particularly well suited for applications where the cost of the seal and mounting is to be minimized and thermal expansion of the cylinder in service is expected to be only of minor magnitude, i.e., the variation in ambient temperature will be less than 50°F (10°C). The cost of this seal is low because it does not require either an extra-fine surface finish on the mating end closure surface or elaborate seal components in excess of a molded neoprene channel gasket. In addition, the thick gasket allows the cylinder to expand freely in the axial and radial directions while at the same time protecting the end of the cylinder from scuffing against the end closure.

Seal design B is particularly well suited for applications where very large radial and axial displacements are expected and the presence of a gasket cannot be tolerated under the

13-6

edge of the cylinder. This seal is of the self-energizing type, i.e., the higher the internal pressure the more positive the sealing action. Because the axial and radial O-rings are contained in a plastic seal ring, a gap between the edge of the cylinder and the bearing surface on the end closure can be safely bridged without loss of sealing ability.

To insure proper working of the self-energizing seal, the plastic seal ring must be of tough plastic material (polycarbonate, polyethylene, nylon, or Delrin) and the thickness must be less than that of the cylinder, insuring that the ring will have a larger radial displacement under pressure than will the acrylic plastic cylinder. Metals do not make good seal rings for acrylic cylinders as their high modulus of elasticity makes them less radially compliant than the acrylic cylinder. Acrylic plastic should not be used for seal rings, as the crack sensitivity of the acrylic plastic may lead to initiation of cracks at the roots of O-ring grooves.

13.2.5 Impact Protection

Acrylic cylinders under internal pressure are very sensitive to the initiation of fracture by point-impact loading or contact with corrosive chemicals. Since propagation of fracture in a pressurized cylinder results in an instantaneous catastrophic failure, steps must be taken to protect it. This can be done by placing the pressure vessel inside another acrylic cylinder whose sole function is to serve as a protective barrier against external impacts and contacts with chemicals. Similar protection can be achieved by laminating to the exterior of the cylinder a transparent elastomeric layer that serves as a cushion and as a protective barrier against contact with chemicals. A still different approach is to coat both surfaces of the cylinder with a hard, impervious transparent coating which will protect both surfaces against scratches and contact with chemicals. The latter technique must be implemented with an external wire screen cage to provide impact protection.

13.3 EXTERNAL PRESSURE

13.3.1 Structural Response

Similar to cylinders under internal pressure, the structural response of cylinders to external pressure depends to a large degree on the support given to the cylinder by end closures or ring stiffeners (figure 13.7). The basic difference between the stress values and stress fields in monocoque cylinders under internal pressure and those under external pressure is that in the former the basic membrane stress is positive while in the latter it is negative. In both cases the presence of end restraints and stiffeners generates flexure moments that superimpose axial bending stresses upon the membrane stresses. For cylinders under internal pressure the superposition of the positive bending stress component on the positive axial membrane stress (present in cylinders with end flanges bolted to bulkheads) can lead to the initiation of catastrophic failure. However, for cylinders under external pressure the superposition of the negative bending stress component on the negative axial membrane stress (present in all cylinders regardless of end conditions) leads only to local yielding and redistribution of stresses. It is only after the yielding point of acrylic plastic in compression has been exceeded by a significant amount that a catastrophic failure is initiated. The magnitude of axial bending and shear stresses at end restraints, i.e., rings or bulkheads with

13-7

ledges, can be calculated by using equations 13.2 and 13.3 and the magnitude of axial membrane stress:

$$\sigma_{ac} = \frac{-p\, D_O^2}{D_O^2 - D_i^2} \tag{13.4}$$

The basic reason for providing a cylinder with rigid end supports or stiffeners distributed along the length of the cylinder is to prevent the cylinder from collapsing because of elastic or plastic instability. Since implosion by elastic or plastic instability requires less energy than an implosion caused by hoop membrane stress yielding, the former will occur at a lower hydrostatic loading than the latter. Because elastic instability is only a function of the cylinder's dimensions and the material's modulus of elasticity, the implosion can occur at pressures which are only a small fraction of the critical pressure that is dependent on the yield strength of acrylic plastic.

It is worthwhile to note here that the elastic stability of a cylinder with given dimensions is the same regardless of whether the cylinder is of monolithic or segmented construction, if all joints are oriented axially and the bearing surfaces of the joints are flat and at right angles to the curved surfaces of the cylinder (figure 13.8). This allows, if necessary, a very large cylinder to be assembled from many narrow longitudinal segments, providing the joints have external elastomeric gasket seals bonded to acrylic with waterproof adhesive. The segmented approach can be also used with rib-stiffened cylinders without any loss of elastic stability. The instrumentation capsule in figure 13.3 is a good example of construction where both the cylinder and stiffeners are assembled from segments, in this case two segments.

For some t/D_O and E_t, the critical pressures resulting from elastic instability or yielding of material are the same while for others they differ substantially. Unsupported long acrylic plastic cylinders designed to yield at low pressures generally buckle prior to reaching the yield point of the material. If such a long cylinder is stiffened with many circumferential stiffeners or if it is shortened and supported at the ends, its elastic stability is increased to the point where the cylinder fails first by yielding. However, long acrylic plastic cylinders that are designed to yield at high pressures generally have such a high elastic stability that they yield prior to elastic buckling. For such cylinders, there is no need to increase their stability with circumferential stiffeners, as this will not raise their collapse pressure.

13.3.2 Modes of Failure

One of the most important characteristics that must be determined for an acrylic cylinder under design is whether the elastic instability will occur prior to, at the same time, or after the yielding of the material. Only if the instability occurs before the material yields is it worthwhile to provide the cylinder with circumferential supports. The yielding of unsupported cylinders in the circumferential orientation can be calculated by equating the maximum hoop stress on the interior of a cylinder, obtained with Lamé's equation (equation 13.1), to the short-term yield strength of the acrylic plastic. The resulting relationship,

13-8

$$p = -S_{max} \frac{R_o^2 - R_i^2}{R_o^2 + R_i^2} , \qquad S_{radial\ maximum} = p, \text{ at inner surface,} \qquad (13.5)$$

gives a conservative value of the pressure at which yielding will be initiated under short-term loading, if a value of 15,000 pounds per square inch (103.4 megapascals) (the minimum value allowed by ASME/ANSI PVHO-1) is used as the short-term yield strength of the material at 65 to 75°F (18 to 24°C).

The critical pressure at which elasticoplastic instability will occur in an unsupported cylinder under short-term loading can be conservatively predicted with reasonable accuracy by using the following expression:

$$p_{cr} = \frac{2\sqrt{E_t E_s}}{(1 - \mu^2)} \left(\frac{t}{D_o}\right)^3 . \qquad (13.6)$$

providing the proper values of E_s and E_t are used. Since E_s and E_t are functions of membrane hoop stresses, equation 13.6 cannot be directly solved, as both the critical pressure and the moduli of elasticity at given hoop stress levels are unknown. Because of these unknown values, the equation must be solved by successive iteration with equation 13.5.

The actual computation procedure is identical to the one described for equations 11.1 and 11.2. A value for p_1 in equation 13.5 is assumed, and the corresponding maximum hoop stress is calculated. Utilizing figures 4.21, 4.22, and 4.25, E_s, E_t, and μ corresponding to the calculated maximum hoop stress at ambient room temperature are found. By inserting the calculated values into equation 13.6, a tentative p_{cr_1} is obtained. If $p_{cr_1} > p_1$, then the assumed value of p_1 is too low and a new higher value for p_2 must be chosen. The process of calculating S_{max}, i.e., finding values for E_s, E_t, and μ and computing p_{cr_2}, must be now repeated. If the computed $p_{cr_2} = p_2$, then p_{cr_2} is the critical pressure at which elasticoplastic instability will occur under short-term loading conditions. For ambient temperatures above or below 75°F (24°C), the designer must develop relationships for E_s, E_t, and μ as functions of temperature, as they are not available in the published literature.

To predict elasticoplastic creep instability under long-term loading conditions, the same equations and reiterative calculations must be used, except that E_{ef} and μ must correspond both to the ambient temperature and magnitude of hoop stresses in the cylinder and also the duration of loading. E_{ef}, the effective modulus of elasticity, is used in place of E_s and E_t, as these physical properties are associated only with short-term loadings.

Since experimentally derived curves relating E_{ef} and μ to the maximum compressive stress, ambient temperature, and duration of loading are not available, elasticoplastic creep instability under long-term loading cannot be accurately calculated unless E_{ef} is first experimentally established for the desired temperature, stress, and duration of loading. However, if the maximum compressive hoop stresses do not exceed the values shown in table 13.1, the effective moduli of elasticity, E_{ef}, in table 13.2 can be substituted for both E_s and E_t in equation 13.6 to determine if the long-term critical pressure exceeds the design pressure.

Table 13.2. Maximum recommended effective moduli of elasticity E_{ef}[*] for acrylic tubes under long-term internal or external pressure loading.[**]

Design Temperature °F (°C)	Duration of Sustained Pressurization			
	1 day	10 days	100 days	1000 days
50 (10)	390,000	340,000	300,000	270,000
77 (25)	360,000	310,000	272,000	237,000
104 (40)	325,000	270,000	222,000	182,000
126 (52)	315,000	250,000	200,000	160,000
140 (60)	290,000	220,000	169,000	128,000
158 (70)	270,000	200,000	145,000	107,000
176 (80)	240,000	165,000	110,000	77,000
194 (90)	198,000	110,000	60,000	33,000

[*]The effective moduli of elasticity apply only to acrylic plastic structures where the maximum compressive or tensile stress does not exceed the values shown in table 13.1. For higher stress values, the effective moduli of elasticity are significantly lower.

[**]Effective moduli of elasticity for durations of loading different from those shown can be obtained by extra- and interpolation of log-log scale.

13.3.3 Design

If, as a result of computations with equations 13.5 and 13.6, it is found that a monocoque cylinder will fail by elasticoplastic instability at a much lower short-term pressure than is required by design criteria, there are two courses of action available to the designer. The wall can be made thicker, increasing both the critical pressures for instability and hoop yield until the critical pressure for elasticoplastic instability surpasses the specified minimum value for short-term pressure. This design approach is simple, reliable, and produces an inexpensive cylindrical structure for a specified short-term critical pressure. The only drawback is that the unsupported cylinder is heavier than necessary, and for applications in submersibles this is a serious disadvantage. Another approach is to provide the cylinder with circumferential supports which substantially raise the elastic stability with very little added weight. Whenever feasible, this is accomplished by supporting the ends of the cylinder with a machined ledge in the bulkheads (figure 13.7). In many cases this will increase the elastic stability to the point that the cylinder will yield before implosion by elastic instability. There are many cases, however, where this arrangement does not raise the elastic stability sufficiently. If this is the case, the elastic stability can be further increased by placement of intermediate circumferential stiffeners between the bulkheads. Since the addition of stiffeners is costly it is desirable to determine beforehand the potential weight savings. The potential savings, if any, are readily calculated by plotting the results of equations 13.5 and 13.6 on the same figure (figure 13.9). Depending on the

magnitude of desired short-term critical pressure the potential savings may be substantial or negligible. In either case, pictorial representations of these equations will aid the designer in the decision-making process. The elastic instability of a cylinder supported circumferentially by end closures or intermediate circumferential stiffeners is usually calculated by R. vonMises' equation (reference 13.4):

$$ y = \frac{1 - \sigma^2}{n^2 + \frac{\alpha^2}{2} - 1} \left(\frac{\alpha^2}{\alpha^2 + n^2} \right)^2 + \frac{X}{n^2 + \frac{\alpha^2}{2} - 1} \left[(n^2 + \alpha^2)^2 - 2\mu_1 n^2 + \mu_2 \right] \dots , $$

(13.7)

where

$$ \mu_1 = 1/2 \left[1 + (1+\sigma)\rho \right] \left[2 + (1-\sigma)\rho \right] $$

$$ \mu_2 = (1 - \sigma\rho) \left[1 + (1+2\sigma)\rho - (1-\sigma^2) \left(1 + \frac{1+\sigma}{1-\sigma}\rho \right) \rho^2 \right] $$

$$ X = t^2/3\,D^2 $$

$$ y = p \frac{D}{2t} \frac{1 - \sigma^2}{E} $$

$$ \rho = \alpha^2/n^2 + \alpha^2 $$

$$ \alpha = \pi D/2L $$

σ = Poisson's ratio

p = short-term critical pressure, psi

D = $D_o + D_i/2$, inches

t = wall thickness, inches

L = spacing between stiffeners, inches

n = number of buckling lobes around the circumference of the tube

E = $\sqrt{E_s \times E_t}$.

To calculate the elastic instability of a cylinder supported by bulkheads or ring stiffeners spaced L apart, a number n which minimizes p for a given D, t, L, E, and Poisson's ratio is selected. The number of buckling lobes will usually exceed n = 2, as only unsupported long tubes fail by a two-lobe buckling mechanism.

Since equation 13.7 requires reiterative calculations for its solution, it is seldom used by the designer. Therefore, to help the designer, the equation has been solved for many L/D and t/D ratios and the results presented in graphical form (figure 13.10). By using these data, it is relatively easy to determine the effect of spacing between supports on the critical pressure, i.e., decreasing the spacing between the end closures by 50 percent generally doubles the critical pressure, while decreasing it by 90 percent generally increases the critical pressure tenfold. If the spacing between bulkheads is decreased to such an extent that there is very little useful space left inside the cylinder for a payload, circumferential stiffeners are substituted for rigid end supports (figure 13.11).

13-11

Stiffeners for cylinders can take many shapes, depending on the cylinder's intended use. If the shapes were to be rated on structural efficiency (measured by elastic-stability-to-weight ratios) the rectangular shape (B) is considered to be least efficient and the cellular sandwich* (F) the most efficient. This finding has been experimentally substantiated by imploding a series of acrylic plastic cylinders with the same outside diameters, lengths, weights, and inside clear diameters but with different shaped stiffeners (figures 13.12 through 13.18). However, from the viewpoints of cost, ease of fabrication, and visibility through the hull, the most cost-effective approach is that which uses simple ring stiffeners with a rectangular cross section (figure 13.11, shape B). These stiffeners are easy to machine and bond in place, while their narrow width provides a maximum viewing area between stiffeners.

The spacing of stiffeners depends on many factors. First, it must be close enough to prevent elastic instability of the shell at pressures below the specified short-term critical pressure. The spacing of stiffeners is calculated by using equation 13.7. (It is assumed that the stiffeners will not fail prior to buckling of the shell between stiffeners.) Second, the maximum compressive principal stress found on the inner surface of the cylinder at the edge of the stiffener cannot exceed the compressive yield strength of the material at pressures below the specified short-term critical pressure. Third, the maximum axial tensile principal stress on the outer surface of the cylinder on the center of the stiffener cannot exceed the ultimate tensile strength of the material at pressures below the specified short-term critical pressure. Fourth, the maximum transverse shear stress in the cylinder at the edge of the stiffener cannot exceed the shear strength of the material at pressures below the specified short-term critical pressure. Fifth, the elastic instability of the ring stiffener must not occur at pressures below the specified short-term critical pressure. Sixth, the compressive hoop stress in the stiffener must not exceed the yield strength of the material at pressures below the specified short-term critical pressure.

Since the equations relating external pressure, stiffener size, and stiffener spacing to the maximum compressive tensile and shear stresses in the cylinder assembly are complex, they will not be derived here. Rather a simplified semigraphical approach, developed by Krenzke and Short (reference 13.5) for the calculation of nominal stresses at critical locations in a rib-stiffened shell (figures 3.19 through 3.22), is shown. The following definitions apply:

A_f = the area of the stiffener, assumed to be concentrated at the median surface of the shell

h = shell thickness

L_f = center-to-center spacing of stiffeners

b = the effective width of a stiffener in contact with the shell

L = $L_f - b$

R = radius to the median surface of the shell

ν = Poisson's ratio

E = Young's modulus

P = external pressure

---

*A type of design where the flanges of T-shaped stiffeners are joined around their circumferences to form a double-walled cylinder.

and

$$\alpha = A_f/hL_f$$

$$\beta = b/L_f$$

$$\theta = \frac{\sqrt[4]{3(1 - \nu^2)}}{\sqrt{Rh}} L$$

$$\gamma = \frac{P}{2E} \left(\frac{R}{h}\right)^2 \sqrt{3(1 - \nu^2)} \ .$$

The equations describing stress distribution in a ring-stiffened cylinder can be worked rapidly by utilizing graphical solutions for F_1, F_2, F_3, and F_4 (plotted in figures 13.19 through 13.22). These equations can be written as:

$$1 - \frac{\sigma_{\phi mf}}{\sigma_u} = \frac{\left(1 - \frac{\nu}{2}\right)\alpha}{\alpha + \beta + F_1(1 - \beta)} \tag{13.8}$$

$$1 - \frac{\sigma_{\phi mm}}{\sigma_u} = \left(1 - \frac{\sigma_{\phi mf}}{\sigma_u}\right) F_2 \tag{13.9}$$

$$\sqrt{\frac{1 - \nu^2}{0.91}} \frac{\sigma_{xbf}}{\sigma_u} = \left(1 - \frac{\sigma_{\phi mf}}{\sigma_u}\right) F_3 \tag{13.10}$$

$$\sqrt{\frac{1 - \nu^2}{0.91}} \frac{\sigma_{xbm}}{\sigma_u} = \left(1 - \frac{\sigma_{\phi mf}}{\sigma_u}\right) F_4 \tag{13.11}$$

and

$\sigma_u = -PR/h$ = the circumferential stress in an infinite unstiffened cylinder

$\sigma_{\phi mf}$ = the circumferential membrane stress in the shell at a stiffener

$\sigma_{\phi mm}$ = the circumferential membrane stress at midbay

σ_{xbf} = the longitudinal bending stress in the shell at a stiffener

σ_{xbm} = the longitudinal bending stress at midbay.

The circumferential stress $\sigma_{\phi_i^o m}$ and the longitudinal stress $\sigma_{x_i^o m}$ on the shell surface at midbay can be obtained by the following relationships

$$\sigma_{\phi_i^o m} = \sigma_{\phi mm} \pm \nu \sigma_{xbm} \tag{13.12}$$

$$\sigma_{x_i^o m} = \frac{1}{2} \sigma_u \pm \sigma_{xbm} \ . \tag{13.13}$$

while the circumferential stresses ${}^{\sigma}\phi_i^o f$ and the longitudinal stresses ${}^{\sigma}x_i^o f$ on the shell surface at the stiffener are given by

$$\sigma_{\phi_i^o} f = \sigma_{\phi m f} \pm \nu \sigma_{xbf} \tag{13.14}$$

$$\sigma_{x_i^o} f = \frac{1}{2}\sigma_u \pm \sigma_{xbf} \; , \tag{13.15}$$

where the subscripts o and i represent the outside and inside surfaces of the shell, respectively. The circumferential stress $\sigma_{\phi f}$ in a stiffener can be obtained from

$$\sigma_{\phi f} = \sigma_{\phi m f} - \frac{\nu}{2}\sigma_u \; . \tag{13.16}$$

Although these equations were originally derived for nominal stresses in perfectly elastic materials, they also apply with acceptable accuracy to acrylic plastic cylinders under the following conditions:

    1.   Under short-term loading, i.e., the pressure is raised at a rate greater than or equal to 100 pounds per square inch per minute (0.7 megapascal per minute), the calculated stresses are accurate from 0 to 9000 pounds per square inch (0 to 62 megapascals) in tension and 0 to 15,000 pounds per square inch (0 to 103.4 megapascals) in compression.

    2.   Under long term-loading conditions, i.e., the pressure is held for at least 1 hour, the calculated stresses are accurate only from 0 to 4500 pounds per square inch (31 megapascals).

    3.   The ambient temperature is less than or equal to 75°F (24°C).

Since equations 13.8 through 13.16 do not consider the effect of stress risers, the calculated values of stresses in the shell at the stiffeners represent nominal, and not peak, stresses. To arrive at the value of peak stresses in the shell near the stiffeners, it is necessary to multiply the values of calculated nominal stresses at that location by a stress concentration factor whose magnitude is a function of fillet radius, shell thickness, and stiffener width (figures 13.23 and 13.24).

For certain geometries of stiffener-shell-fillet configurations, the experimentally measured peak bending stress in the shell at the stiffener is 100 percent greater than is the calculated nominal bending stress at the same location. For this reason, the effect of stress risers must be considered in the design of the ring-stiffened shell and such stiffener-shell-fillet configurations chosen where the resulting stress concentration factor is less than or equal to 1.25.

It is also necessary to size the stiffeners so that they do not buckle or yield under the stresses generated in them by the radial displacement of the shell that they support. To determine the proper depth and width of the acrylic plastic stiffener required to prevent elasticoplastic buckling is rather difficult, as the stiffener acts in unison with that section of the shell that it supports. The actual stability of the stiffener-shell assembly lies between two values

which are relatively easy to calculate. The conservative approach for sizing the acrylic plastic stiffener is to assume that the shell does not contribute anything to the stability of the cylinder so that each stiffener must withstand all loading imposed by hydrostatic pressure acting on the shell section equal in length to the frame spacing, i.e., center-to-center distance between adjacent frames:

$$p_{cr} = \frac{24\sqrt{E_t\,E_s}\,I_r}{D_f^3\,L_f} ,$$

(13.17)*

where

E_s = secant modulus of elasticity, pounds per square inch

E_t = tangent modulus of elasticity, pounds per square inch

I_r = moment of inertia of the ring cross-section about a neutral axis parallel to the axis of the ring, inches[4]

$D_f = 2R_f$ = diameter to the neutral axis of the ring, inches

L_f = frame spacing, center-to-center, inches.

The liberal approach is to assume that the stiffener and shell of length L_f together form a structural unit whose critical pressure is significantly higher than that of the stiffener alone. The critical pressure of this compound structural element is also calculated by using equation 13.17 except that the moment of inertia I_k is based on the sum of the ring and shell cross-sections about their common neutral axis parallel to the axis of the cylinder.

The actual buckling failure of the rib-stiffened acrylic plastic cylinder will generally be closer to the critical pressure calculated with the liberal assumption — the stiffener and shell of length L_f act as a compound structure — than it will be to the critical pressure calculated with the conservative assumption — the shell itself does not contribute any stability to the cylinder. Analytical expressions do exist, however, that allow the designer to predict general elastic instability with great accuracy. The designer requiring their use should consult the references at the end of this section.

When using equation 13.17 to determine the adequacy of the stiffener's size, special attention must be paid to the values of E_s and E_t. If the objective is to calculate the general elastic instability under short-term loading at ambient room temperature, the values of E_s and E_t shown on figures 4.21 and 4.22 can be utilized with confidence. For the calculation of general instability under long-term loading conditions, E_{ef} is used in place of E_s and E_t as the latter values represent only physical properties under short-term loading. Unfortunately, published data are not available to relate E_{ef} to the stress level duration of loading and temperature. As a result, the critical pressure at which general elasticoplastic instability occurs under long-term loading cannot be accurately calculated at the present time.

The best that can be accomplished is to estimate whether the stiffeners in the cylinder are adequately sized for the desired design pressure under long-term loading conditions.

*From reference 13.6.

13-15

This can be easily accomplished because the values of E_{ef} under long-term loading at different ambient temperatures are known (table 13.2), providing the maximum stress in the ring stiffeners does not exceed the recommended design values (table 13.2). The elastic stability of the acrylic plastic stiffeners, like that of the cylinder between the stiffeners, is considered adequate if the critical pressure of the stiffeners calculated with equation 13.17 and the E_{ef} values from table 13.2 exceed the design pressure by at least 100 percent. The maximum stress in rectangular stiffeners can be readily calculated with the aid of Lamé's equation for thick cylinders (equation 13.5), providing that the stiffener spacing and width of stiffener are taken into account.

This discussion of equations for calculating the elastic instability of the shell and stiffeners, as well as the distribution of stresses at design pressure in a rib-stiffened cylinder under long-term loading, has shown that this is a long and complicated procedure that produces results with less than satisfactory accuracy. This lack of accuracy is the direct result of the lack of published data on the deformation of acrylic plastic in a complex stress field over a long period of time under different ambient temperatures. However, even with this shortcoming, the analytical approach to the design of acrylic plastic cylinders is satisfactory, providing high safety factors are applied to the calculated values of elastic instability.

There exists, however, an alternate approach to the design of acrylic plastic cylinders. This approach is empirical and is based on the same assumptions as are the empirical design approaches discussed in previous sections for other acrylic structures. In this approach, one or several scale models of cylinders are imploded under short-term loading at ambient room temperatures. The implosion pressure, when divided by an appropriate conversion factor (table 13.3), becomes the design pressure at which the cylinder can be safety operated under long-term and/or cyclic loading.

Table 13.3. Conversion factors for short-term implosion
pressures* of acrylic plastic cylinders.

Temperature Range				
50°F ($\leqslant 10°C$)	75°F ($\leqslant 24°C$)	100°F ($\leqslant 38°C$)	126°F ($\leqslant 52°C$)	151°F ($\leqslant 66°C$)
6	7	9	11	17

*The implosion pressure must be the result of pressurization at 100 pounds per square inch (0.7 megapascal) per minute in a 75°F (24°C) ambient environment.

By utilizing this empirical approach the designer, if desired, can base the design of test models on engineering experience alone without any calculations. However, to minimize the number of models tested, the designer will usually size the structural components of the cylinder to withstand the required short-term pressure and use the short-term hydrostatic pressurization only to confirm and/or complement calculations. The empirical approach has the further advantage that the experimental test results are more convincing and acceptable to classification societies and certifying authorities than are calculations based on insufficient material data.

13.3.4 Mounting

Considerable care must be exercised by the engineer in designing the mounting and seals for a cylinder under external pressure. In some respects this is a more difficult task than designing the mounting and seals for a cylinder under internal pressure, i.e., higher magnitude compressive strains are allowed by ANSI/ASME PVHO-1 in the cylinder at design pressure. If the design-pressure/short-term implosion pressure ratios are compared for internal and external pressure service, they are found to be approximately 100 percent larger for external pressure service. As a result, the resulting strains are also approximately 100 percent higher.

Similar to acrylic plastic cylinders under internal pressure, the ends of the cylinders can be radially restrained or allowed to move freely. Mountings that provide radial restraint are generally used with simple cylinders, while those that allow the ends of the cylinder to contract are used with ring-stiffened or sandwich cylinders. However, there is no valid structural reason why the designer should not choose the rigid restraint or free-sliding mounting, regardless of whether the acrylic plastic cylinder is of monocoque, ring-stiffened, or sandwich construction.

For proper performance, rigid restraint mountings require that the following criteria be considered during the design process:

a. The width of the ledge providing radial restraint to the end of the cylinder must be adequate so that the radial bearing stresses do not exceed the yield point of the plastic. To prevent stress concentrations caused by out-of-roundness of the cylinder and line contact between the edge of the ledge and the interior of the cylinder during pressurization, a hard, 0.063-inch-thick (0.16 centimeter), bearing gasket bonded to the circumference of the ledge is recommended. The need for the gasket can be eliminated by machining the interior surface of the cylinder at the end and providing the edge of the ledge with a generous radius.

b. The diameter of the ledge must be based on the ambient design temperature at which the cylinder will be pressurized. If a gasket is utilized on the ledge, its thickness must be considered.

c. The bearing surface of the mounting that provides axial support to the cylinder must be flat and smooth to avoid line or point contact with the end of the cylinder. Some unevenness and roughness are allowed on the plane bearing surface, if a hard bearing gasket is bonded to that surface.

Free-sliding mountings are much easier to design, as their performance is independent of ambient temperature. The only requirement is that the plane bearing surface on the mounting be flat, possess a ≤ 32-rms finish, and have a liberal coating of grease. Thin, hard bearing gaskets may be used if they are securely bonded to the ends of the cylinder.

13.3.5 Sealing

Sealing of cylinders under external pressure can be achieved with O-rings or U-seals (figures 13.25 and 13.26). For rigid end restraint, the most reliable and structurally acceptable design is C. For a free-sliding mounting seal, designs D and E are equally reliable; however, design D is somewhat more structurally desirable.

13.3.6 Attachment

In attaching the mountings to the cylinder for external pressure service, the designer has more options available than when designing for cylinders under internal pressure. For internal pressure the designer is limited to continuous external or internal rods that tie together the end closures; however, either continuous or interrupted tie rods can be used for external service. This is possible because the external pressure itself pushes the mountings against the cylinder and the attachments are only used to hold the cylinder in place when the cylinder is at zero pressure.

The interrupted tie rods are generally fastened to a continuous flange or several lugs bonded to the ends of the cylinder. Because the interrupted tie rods do not obstruct visibility from the interior of the cylinder, they are more popular than the continuous rods. The important points to consider when designing interrupted tie rods are changes in the length and diameter of the tube caused by variations in ambient temperature and application of hydrostatic loading. Linear expansion and contraction of the tube are generally compensated for by the addition of an elastomeric gasket securely bonded to the retaining ring and compressed against the flange on the cylinder. Radial changes are allowed to occur freely by providing sufficient radial clearance between the cylinder and the retainer ring and polishing the flange surface for ease of sliding.

13.4 FABRICATION

13.4.1 Monocoque Cylinders

Several proven techniques exist for fabricating monocoque cylinders: extrusion, thermoforming of cast sheets and bonding of joints, static casting, and centrifugal casting.

The extrusion process is generally limited to small diameters and thin walls. In addition, the physical properties of the extruded acrylic plastic are inferior to those of cast acrylic. Thus, extrusions are softer, have a lower compressive yield point, lower deformation temperature, lower resistance to crazing, and higher creep rate under sustained loading. This makes extruded cylinders unacceptable for manned service, as defined by ANSI/ASME PVHO-1 (see section 15). However, their low cost makes them acceptable and cost-effective for throwaway instrumentation packages.

The thermoforming of cast acrylic sheets into cylindrical segments and the subsequent bonding of these sectors with acrylic cement produce cylinders with walls up to 4 inches (10 centimeters) thick and unlimited in length and diameter. The drawbacks of this technique are usually lack of circularity and lesser tensile strength in the joints because of inclusions, undercuts, and incomplete bonding. As a result the tensile strength of the cylinder is reduced by about 40 percent, decreasing by the same amount the internal pressure rating of the cylinder. This is not a drawback, however, for external pressure service, as the bonded joint is under compression and thus its lower tensile strength does not decrease the pressure rating of the cylinder. Because of their disadvantages, cylinders fabricated by bonding of thermoformed segments have not found wide application in pressure vessels for manned service, although substantial numbers of one-man hyperbaric chambers have been built by Vickers Ltd. and are currently in operation with satisfactory performance records.

Static casting is the process that can produce flawless cylinders of any length, diameter, or thickness. The practical limit of this process is the availability of autoclaves with required dimensions. However, diameters up to 10 feet (3 meters), lengths to 20 feet (6 meters), and wall thicknesses up to 1 foot (0.3 meter) do not currently pose any problems (figure 13.27). By building a special autoclave, cylinders with diameters to 20 feet (6 meters), lengths to 50 feet (15 meters), and thicknesses to 5 feet (1.5 meters) could be built by utilizing the current state of technology; even larger cylinders could be assembled from longitudinal segments.

Since the physical and optical properties of custom castings can vary significantly with fabricators and castings, it is important to check cast cylinders for physical and optical properties. Properly cast cylinders have presently encountered no difficulties in meeting the requirements of ANSI/ASME PVHO-1 for manned pressure vessels.

The major drawback of this process is the presence of inclusions in the cast acrylic. Perfect cylinders have been cast in the past, and there is no doubt that large perfect cylinders can be cast in the future. Some inclusions which can decrease the tensile and compressive strengths of the plastic are generally present. However, if the number and size of the inclusions do not exceed certain limits, the cylinder will still satisfy the requirements of ANSI/ASME PVHO-1.

Centrifugal casting is a process in which the generation of large inclusions is overcome by the imposition of centrifugal forces that compress the acrylic resin during the polymerization process so that gas bubbles do not grow. Furthermore, because centrifugal casting is accomplished in a rotating cylindrical mold, the resulting castings have no measurable deviation from circularity. The physical and chemical properties of centrifugal castings equal or exceed those of statically cast cylinders.

Cylinders with diameters to 30 inches (76 centimeters), lengths to 8 feet (2.4 meters), and thicknesses to 1 inch (2.5 centimeters) have been cast using this technique. Many of them have been incorporated into one-man hyperbaric chambers for medical use by Sechrist Industries. The service record of centrifugally cast cylinders under internal and external pressure service has been excellent.

The major drawback of this process is the high investment in rotary molds and autoclaves. Because of the high investment required for tooling, centrifugal casting is used only when many high-grade cylinders of the same diameter and length are required. When the requirement is only for a single cylinder, the cost-effective method is static casting.

13.4.2 Stiffened Cylinders

Rib-stiffened cylinders are made either by casting a heavy monocoque cylinder from which subsequently excess material between the stiffeners is removed by machining or by bonding internal stiffeners, machined from sheets or plates, to a thin monocoque shell. The first technique provides a superior product, as fillets at the roots of stiffeners can be machined to any desired radius, thus avoiding any significant stress concentration at that location. Also, the appearance of the finished product is more pleasing since all

surfaces can be polished to make all parts of the ring-stiffened cylinder optically transparent. Because of its high cost, this process is used only for cylinders of small diameter. Bonding internal stiffeners machined from cast sheets to the interior surface of cylinders is the prevalent approach for making ring-stiffened or sandwich cylinders because of the low cost and ease of fabrication. This is the technique that will be utilized when man-sized cylindrical submersibles are built in the future, except that the ring stiffeners will be machined from ring castings instead of cast sheets.

13.5 CONCLUSION

Cylindrical windows, although not as popular or free of optical distortion as spherical or plane windows, meet many operational requirements that are hard to satisfy using other window shapes. Cylindrical windows have been basically used as internal pressure vessels for medical hyperbaric chambers and viewports on the conning towers of small submersibles. There is no doubt, however, that at some future date large portions of cylindrical hulls on submersibles will be built of acrylic plastic so that passengers can be provided with the same visibility now available to pilots.

13.6 REFERENCES

13.1   Lamé, G., "Lecons sur la Théorie Mathématique de l'Élasticité des Corps Solides," Paris, France, 1852.

13.2   Schorer, H., "Design of Large Pipe Lines," *Transactions of the American Society of Civil Engineers*, vol. 98, pp. 101, 1933.

13.3   Maulbetsch, J. L., Hetenyj, M., "Stresses in Pressure Vessels," American Society of Mechanical Engineers, *Journal of Applied Mathematics*, vol. 3, no. 3, pp. A-107, 1936.

13.4   United States Experimental Model Basin, Report 366, "The Critical External Pressure of Cylindrical Tubes Under Uniform Radial and Axial Load," by R. Von Mises, August 1933.

13.5   David Taylor Model Basin, Report 1393, "Graphical Method for Determining Maximum Stresses in Ring-Stiffened Cylinders Under External Hydrostatic Pressure," by M. A. Krenzke and R. D. Short, October 1959.

13.6   David Taylor Model Basin, Report 396, "The Influence of Stiffening Rings on the Strength of Thin Cylindrical Shells Under External Pressure," by C. Trilling, February 1935.

13.7 BIBLIOGRAPHY

13.1   Bijlaard, P. P., "Theory and Tests on the Plastic Stability of Plates and Shells," *Journal of Aeronautical Sciences*, vol. 16, no. 9, pp. 529-541, 1949.
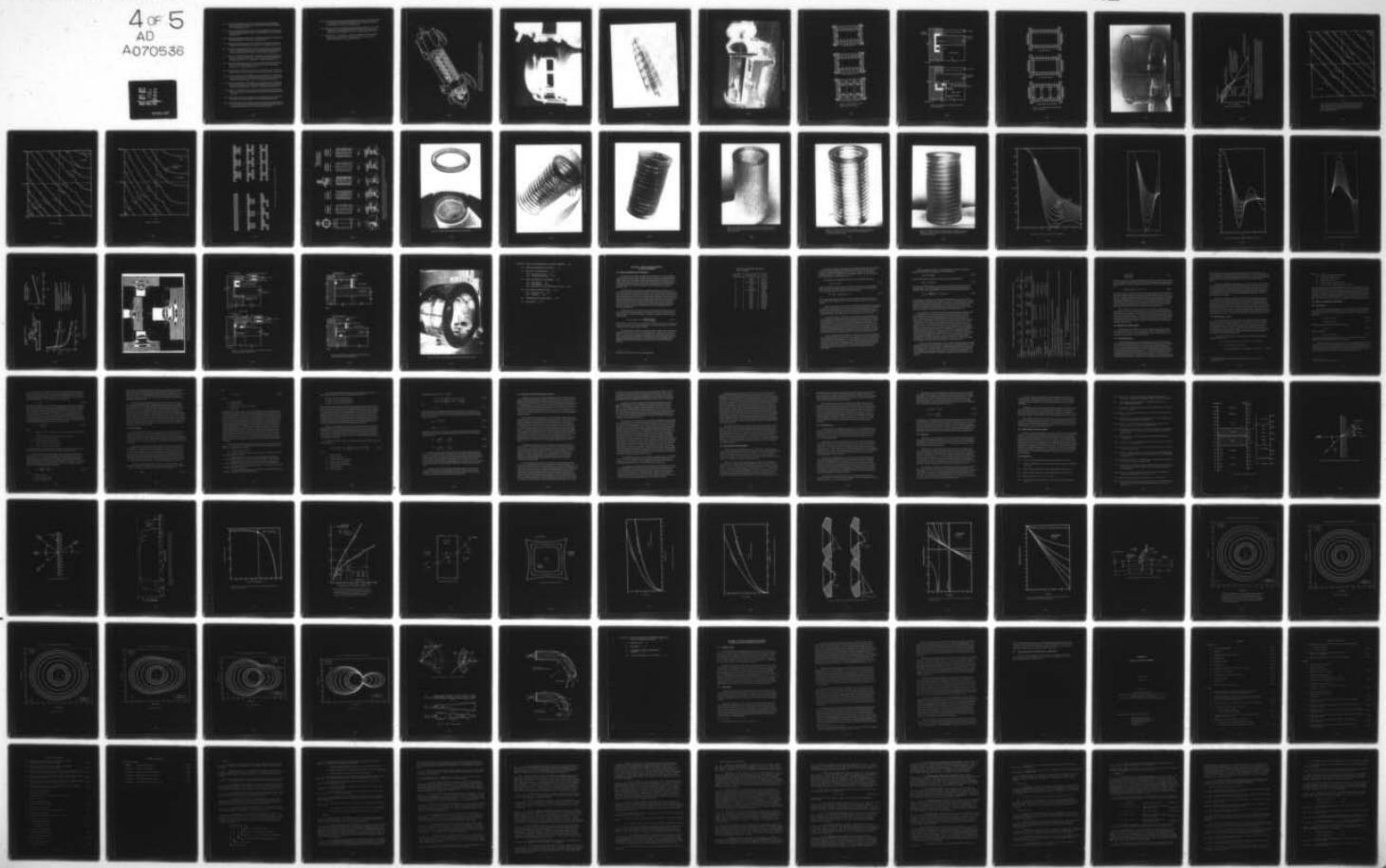
13.2   David Taylor Model Basin, Report 855, "General Instability of Ring-Stiffened Cylinders with Clamped Ends Under External Pressure by Kendrick's Method," by E. L. Kaminsky, July 1954.

13.3   David Taylor Model Basin, Report 1106, "A Graphical Method for Determining the General Instability Strength of Stiffened Cylindrical Shells," by T. E. Reynolds, September 1957.

13.4   David Taylor Model Basin, Report 1291, "Yield Failure of Stiffened Cylinders Under Hydrostatic Pressure," by M. E. Lunchick, January 1959.

13.5   David Taylor Model Basin, Report 1392, "Inelastic Lobar Buckling of Cylindrical Shells Under External Hydrostatic Loading," by T. E. Reynolds, August 1960.

13.6   David Taylor Model Basin, Report 1393, "Plastic Axisymmetric Buckling of Ring-Stiffened Cylindrical Shells Fabricated from Strain-Hardening Materials and Subjected to External Hydrostatic Pressure," by M. E. Lunchick, January 1961.

13.7   David Taylor Model Basin, Report 1497, "Axisymmetric Elastic Deformations and Stresses in a Ring-Stiffened, Perfectly Circular Cylindrical Shell Under External Hydrostatic Pressure," by J. G. Pulos and V. L. Salerno, September 1959.

13.8   David Taylor Model Basin, Report 1543, "Axisymmetric Elastic Deformations and Stresses in a Web-Stiffened Sandwich Cylinder Under External Hydrostatic Pressure," by J. G. Pulos, September 1961.

13.9   National Advisory Committee for Aeronautics, Technical Note 2561, "A Study of Poisson's Ratio in the Yield Region," by G. Gerard and S. Wildhor, January 1952.

13.10   Naval Construction Research Establishment, Report NCRE/R.211, "The Buckling Under External Pressure of Circular Cylindrical Shells with Evenly Spaced Equal Strength Circular Ring Frames – Part I," by S. Kendrick, February 1953.

13.11   Naval Construction Research Establishment, Report NCRE/R.244, "The Buckling Under External Pressure of Circular Cylindrical Shells with Evenly Spaced Equal Strength Circular Ring Frames – Part III," by S. Kendrick, September 1953.

13.12   Oppel, G. V., and Mehta, P. K., "Stress Analysis of Ring-Stiffened Sandwich Shells Subjected to Uniform External Pressure," *Internal Journal of Mechanical Sciences*, vol. 5, 1963.

13.13   Pennsylvania State University, Ordnance Research Laboratory, Report NOrd 16597-89, "Shells for Underwater Vehicles," by J. D. Stachiw, September 1962.

13.14   Pennsylvania State University, Ordnance Research Laboratory, Report NOrd 16597-91, "General Instability of Circumferentially Stiffened Sandwich Shells Subjected to Uniform External Pressure," by J. D. Stachiw, December 1962.

13.15 Pennsylvania State University, Ordnance Research Laboratory, Report NOrd 16597-97, "The Effects of Shell Joints and Bonding on the Stability of Acrylic Resin Cellular Shells," by J. D. Stachiw, September 1963.

13.16 Polytechnic Institute of Brooklyn Aeronautical Laboratory, Report 171-A, "Stress Distribution in a Cylindrical Shell Under Hydrostatic Pressure Supported by Equally Spaced Circular Ring Frames," by V. L. Salerno and J. G. Pulos, 1951.

13.17 Windenburg, D. F., and Trilling, C., "Collapse by Instability of Thin Cylindrical Shells Under External Pressure," *Transactions of the American Society of Mechanical Engineers*, vol. 56, pp. 819-825, 1934.
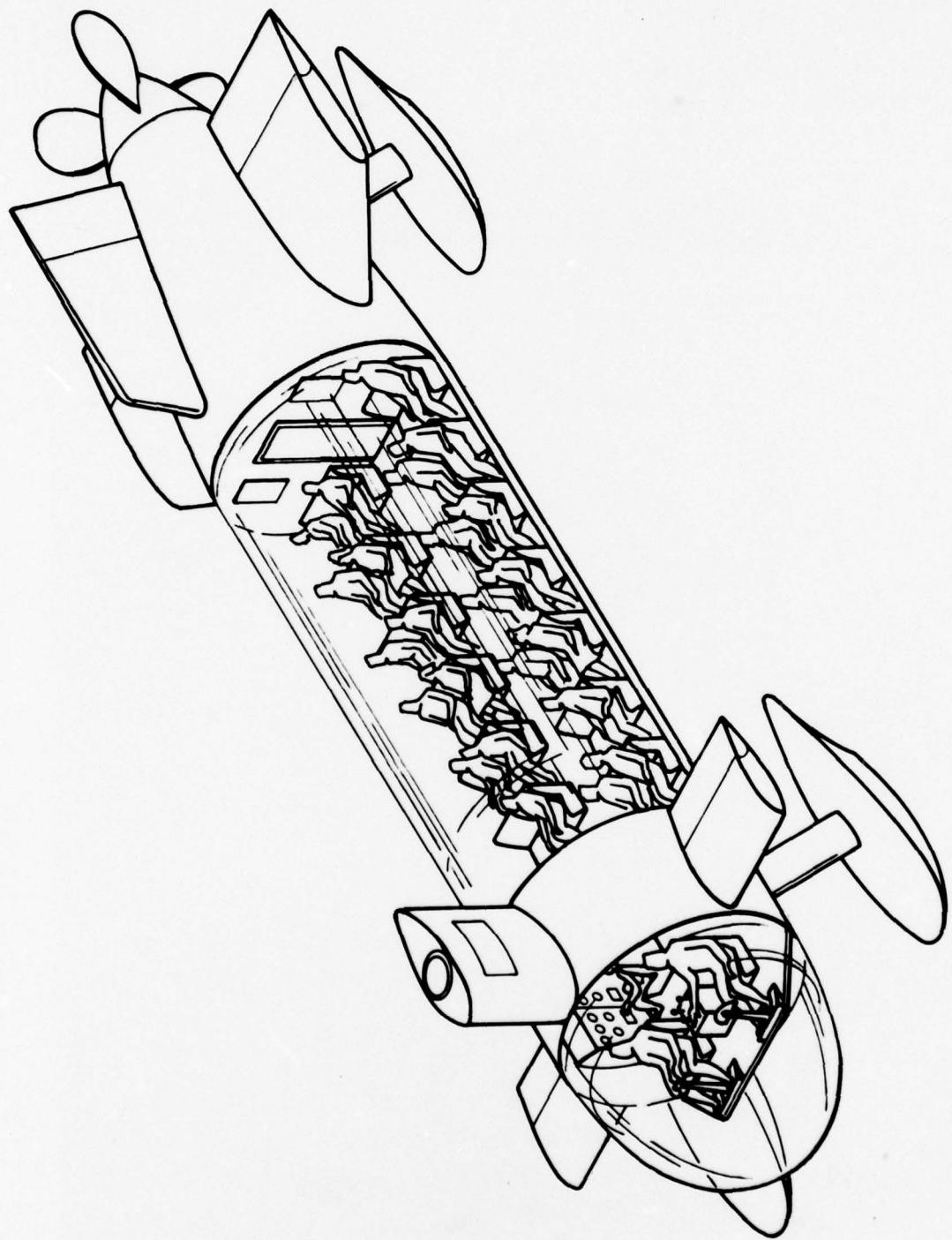
Figure 13.1. Artist's concept of a submersible for underwater sightseeing. Note that in addition to the acrylic bow window, the submersible is also equipped with a cylindrical acrylic hull which provides unsurpassed visibility for all passengers.
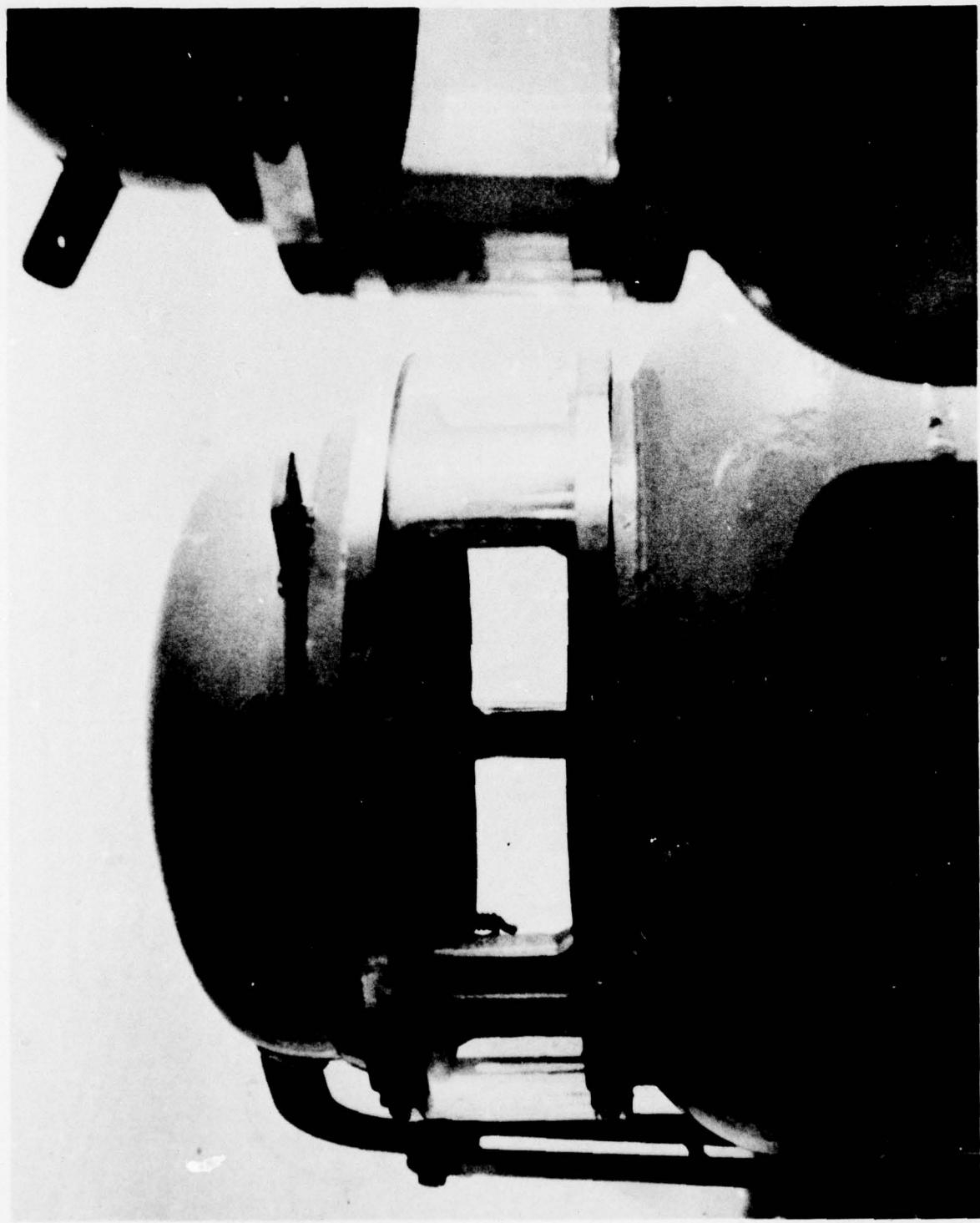
Figure 13.2. Cylindrical windows on the twin conning towers of a small submersible.
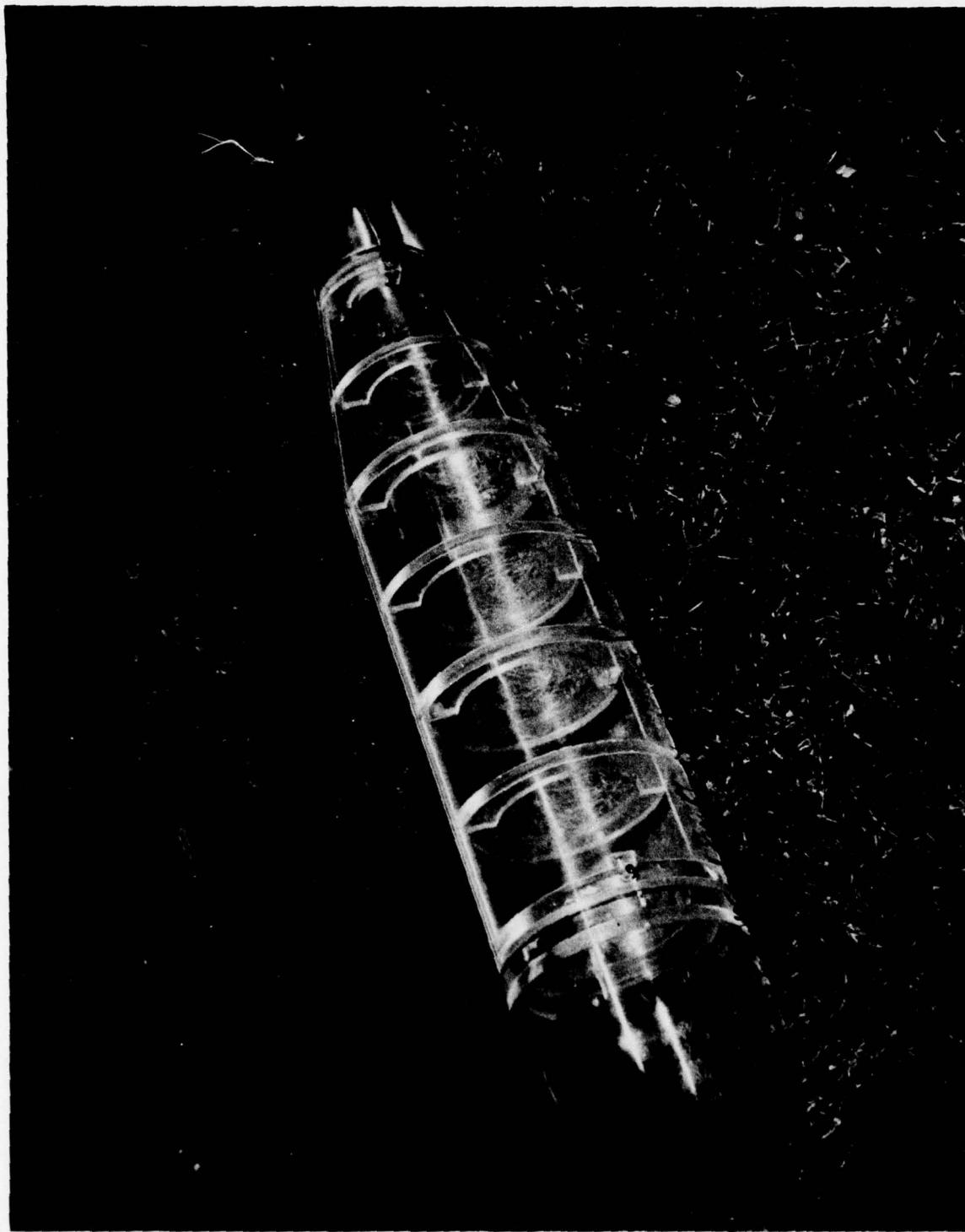
Figure 13.3. Ring-stiffened acrylic capsule with 8 inch (20 centimeters) outside diameter and 47 inch (119 centimeters) overall length for 500-pound-per-square inch (3.44 megapascals) service.
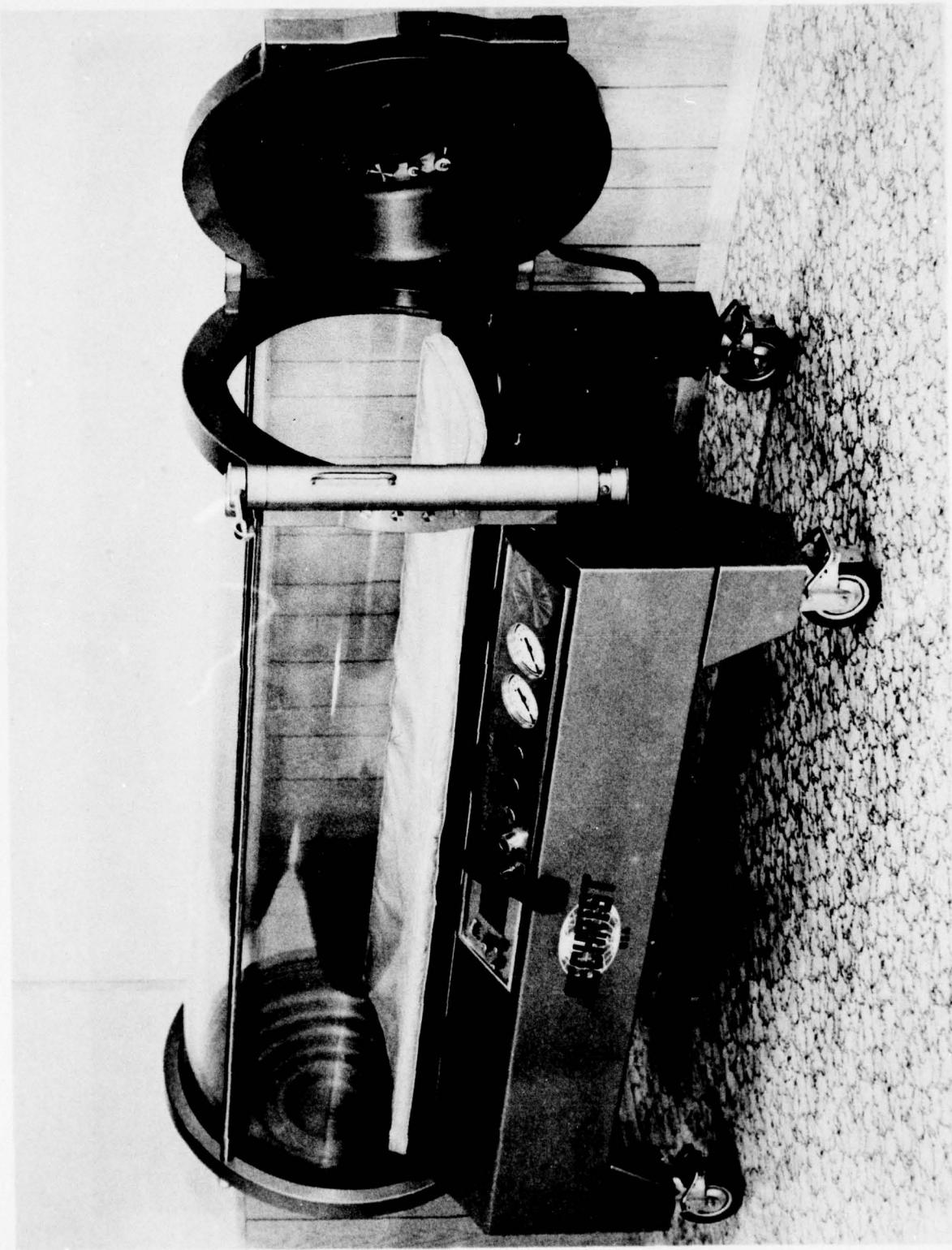
Figure 13.4. One-man hyperbaric chamber for 30-pound-per-square-inch (0.2 megapascal) oxygen service in hospitals.

unsupported cylinder

cylinder supported at the ends

cylinder supported by ring stiffeners
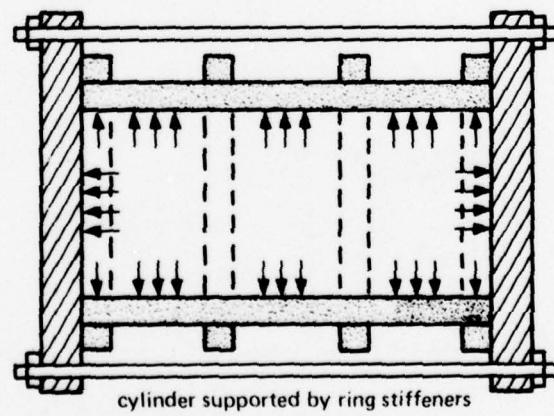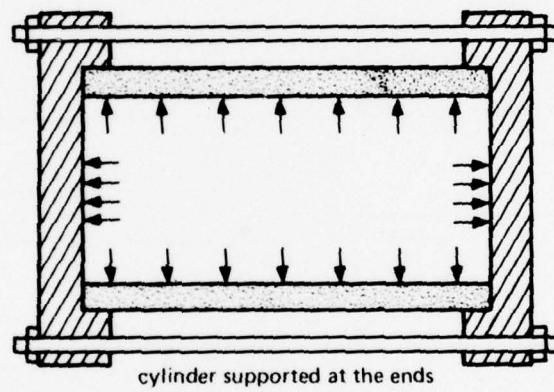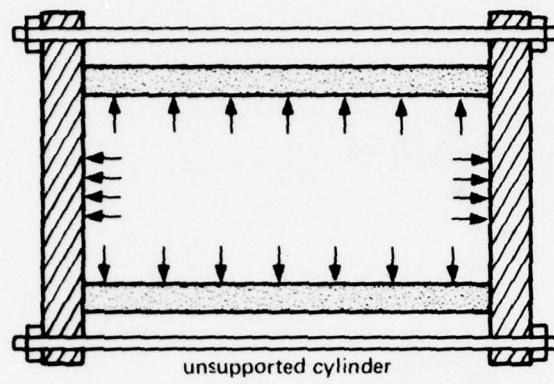
Figure 13.5. Types of support for acrylic
cylinders under internal pressure.
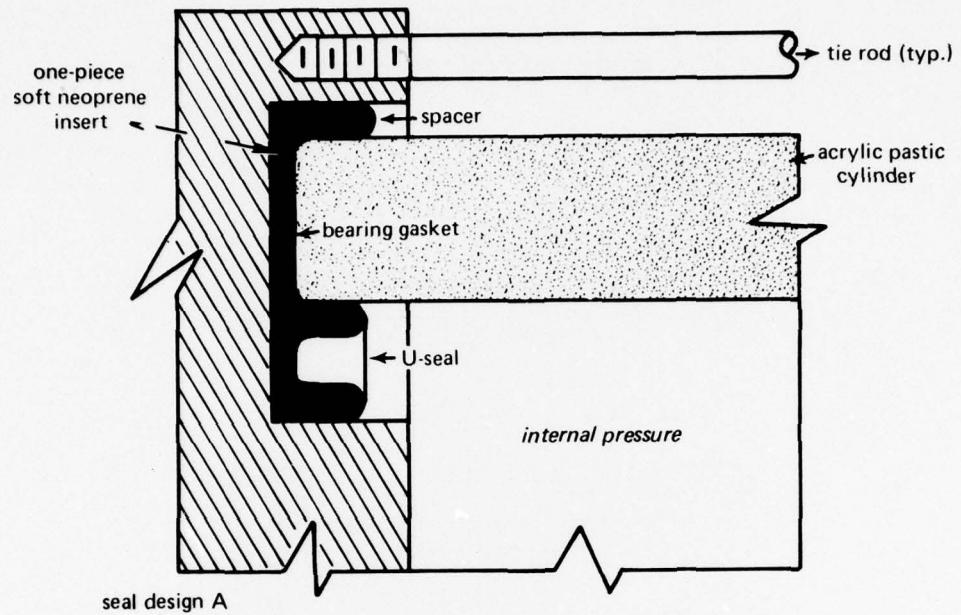
seal design A

seal design B
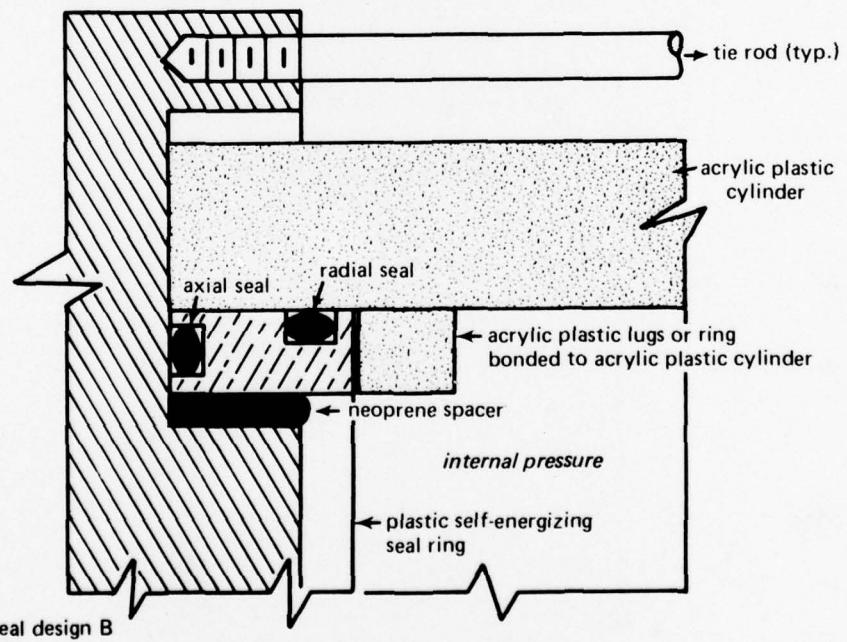
Figure 13.6. Typical seals for unstiffened acrylic cylinders under internal pressure.

unsupported cylinder

cylinder supported at ends

cylinder supported by ring stiffeners
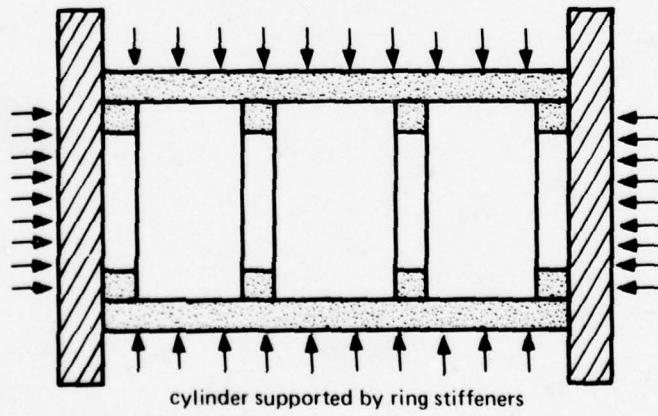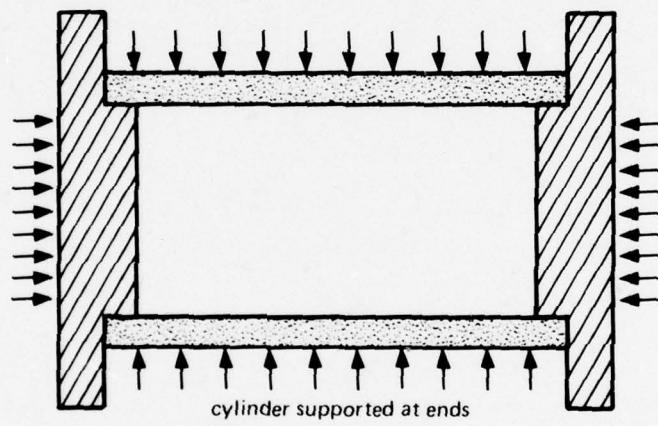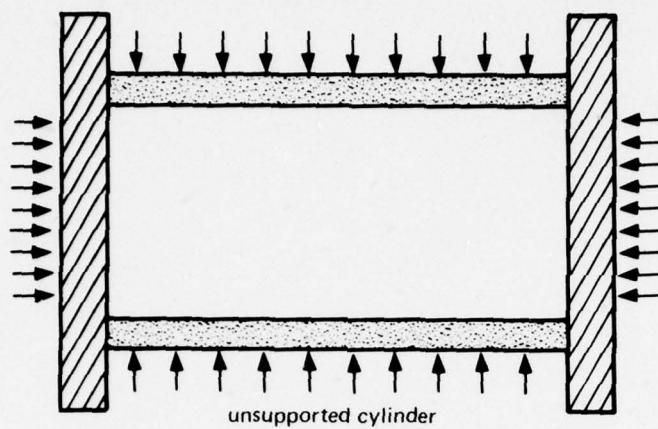
Figure 13.7. Types of supports for acrylic cylinders under external pressure.
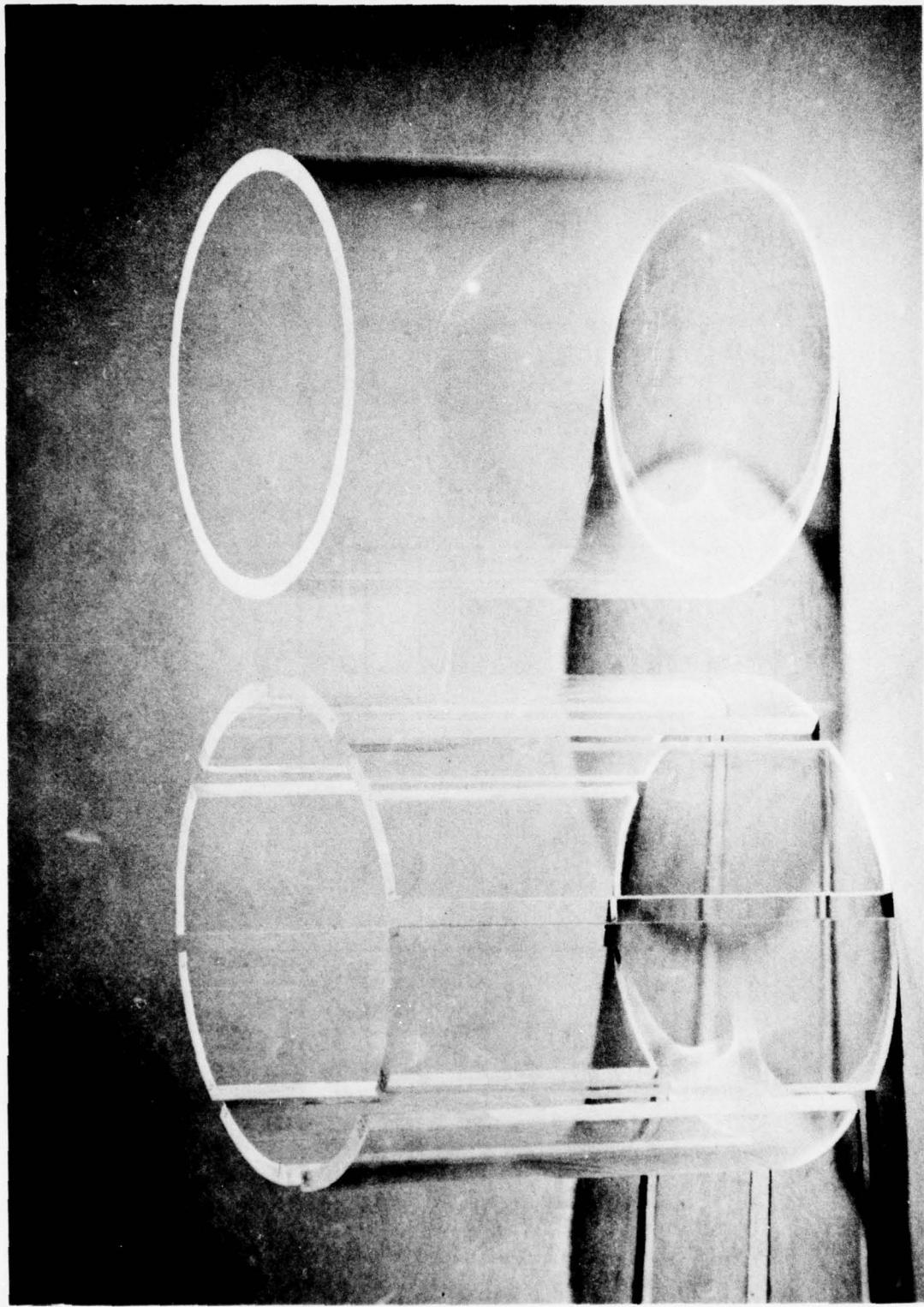
Figure 13.8. Elastic stabilities of monolithic and segmented cylinders with identical dimensions and end supports. The critical pressures of the 12-inch-long (30 centimeters) cylinders (11 inch (28 centimeters) outside diameter and 10 inch (25 centimeters) inside diameter) supported at the ends by metallic bulkheads were 790 pounds per square inch (5.45 megapascals).
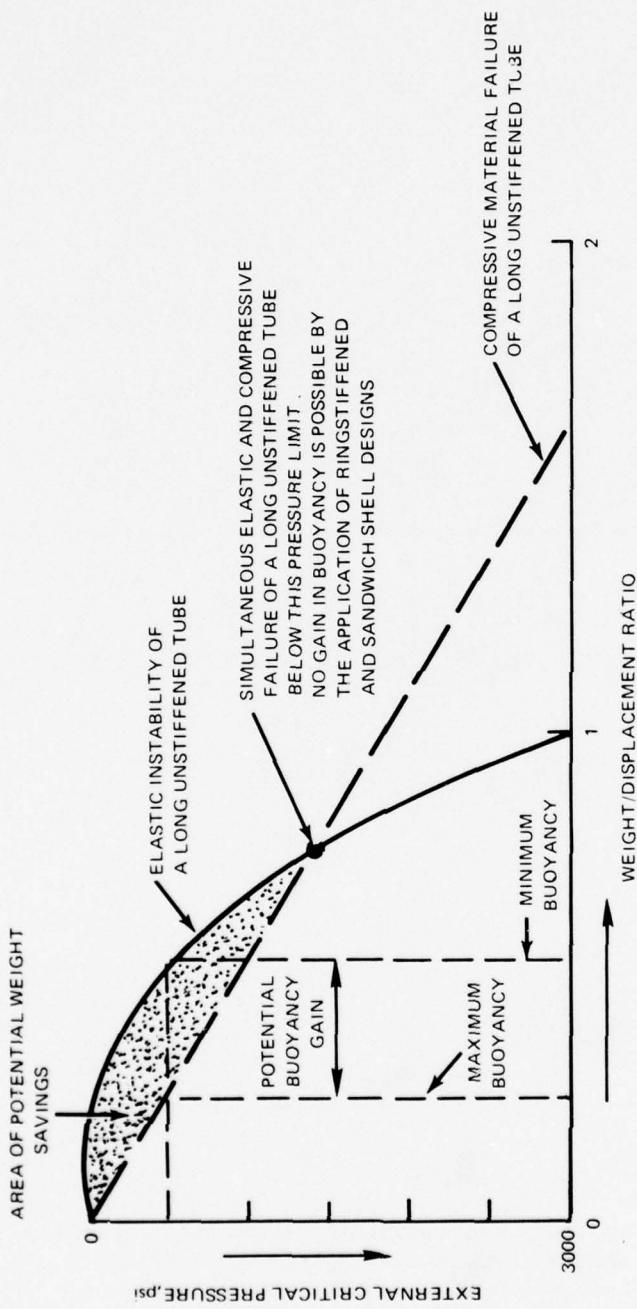
Figure 13.9. Typical curves for predicting whether the implosion of long unstiffened cylinders from a given material will occur by elastic instability or compressive material failure. The area of potential weight savings is enclosed by the elastic-instability and material-failure curves of an infinitely long cylinder. The dotted lines show the potential savings that would result from using ring stiffeners in a smooth cylinder designed for some selected pressure in the pressure range where potential weight savings are theoretically feasible.

13-31
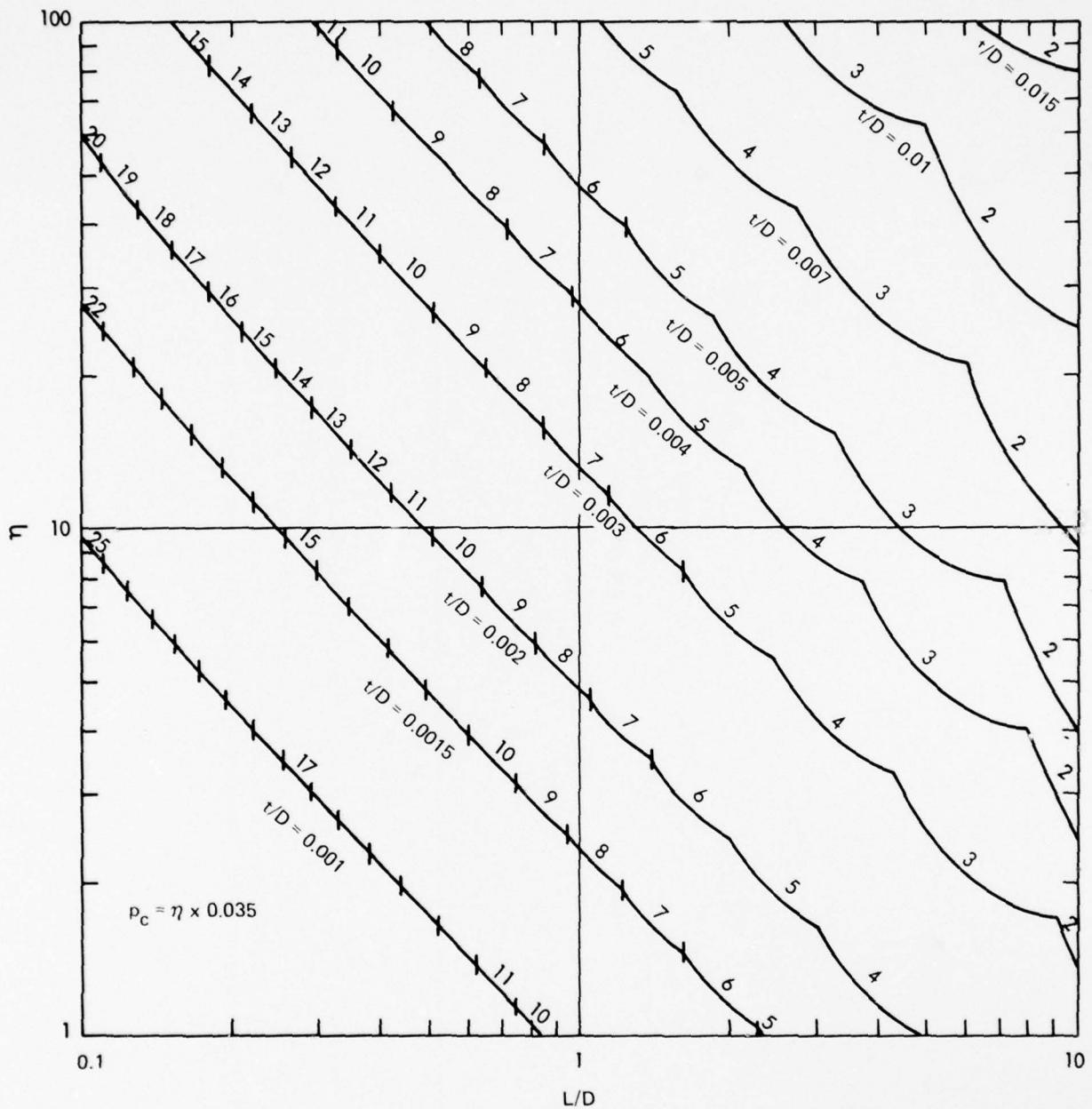
Figure 13.10. Elastic instability of tubes supported by bulkheads or stiffeners L distance apart under short-term loading at ambient temperatures less than or equal to 75°F (24°C). The curves are based on $\sqrt{E_s E_t} = 350,000$ pounds per square inch (2413 megapascals). For higher ambient temperatures, lower values of $\sqrt{E_s E_t}$ should be used.

13-32
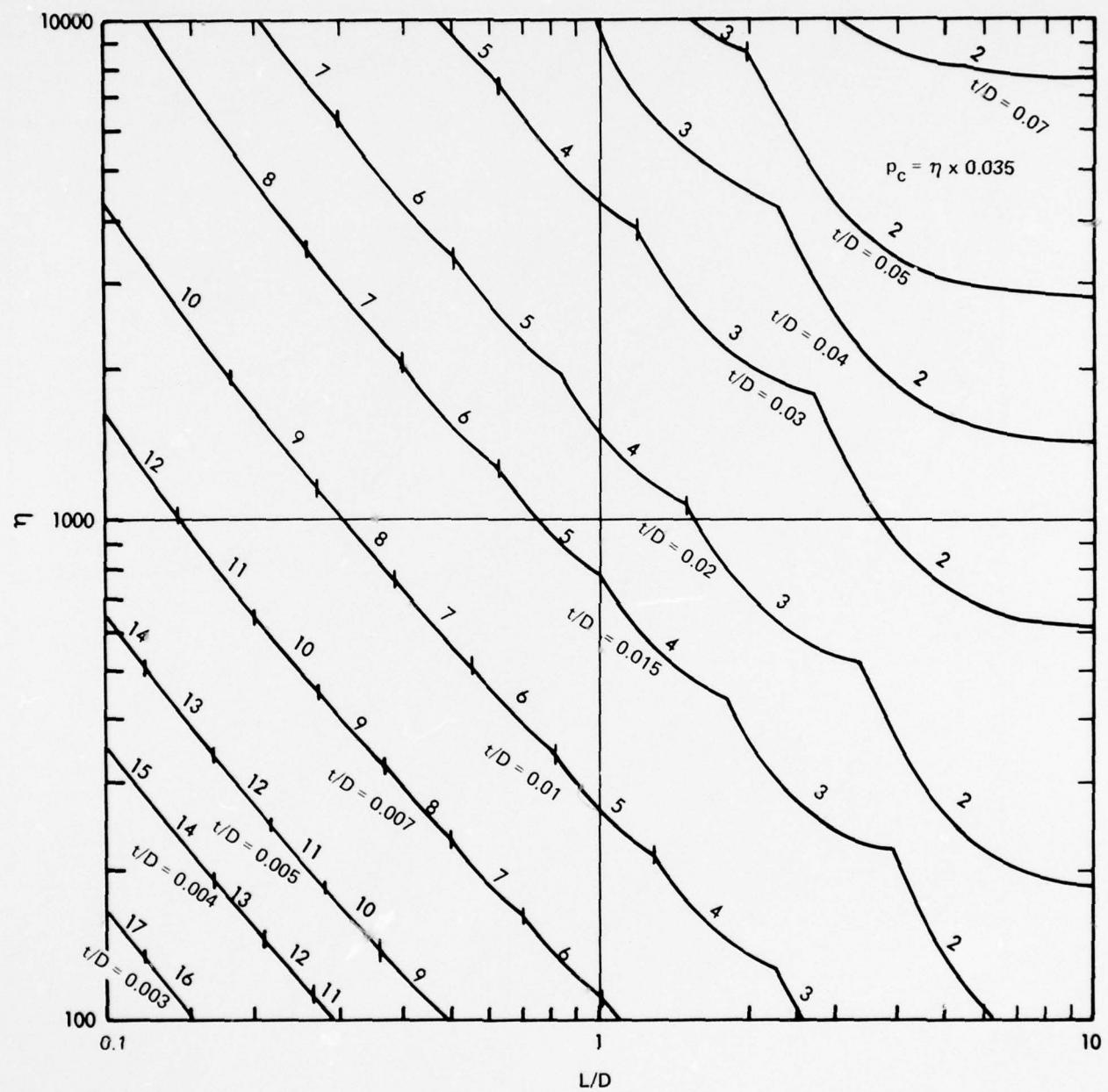
Figure 13.10. Continued.
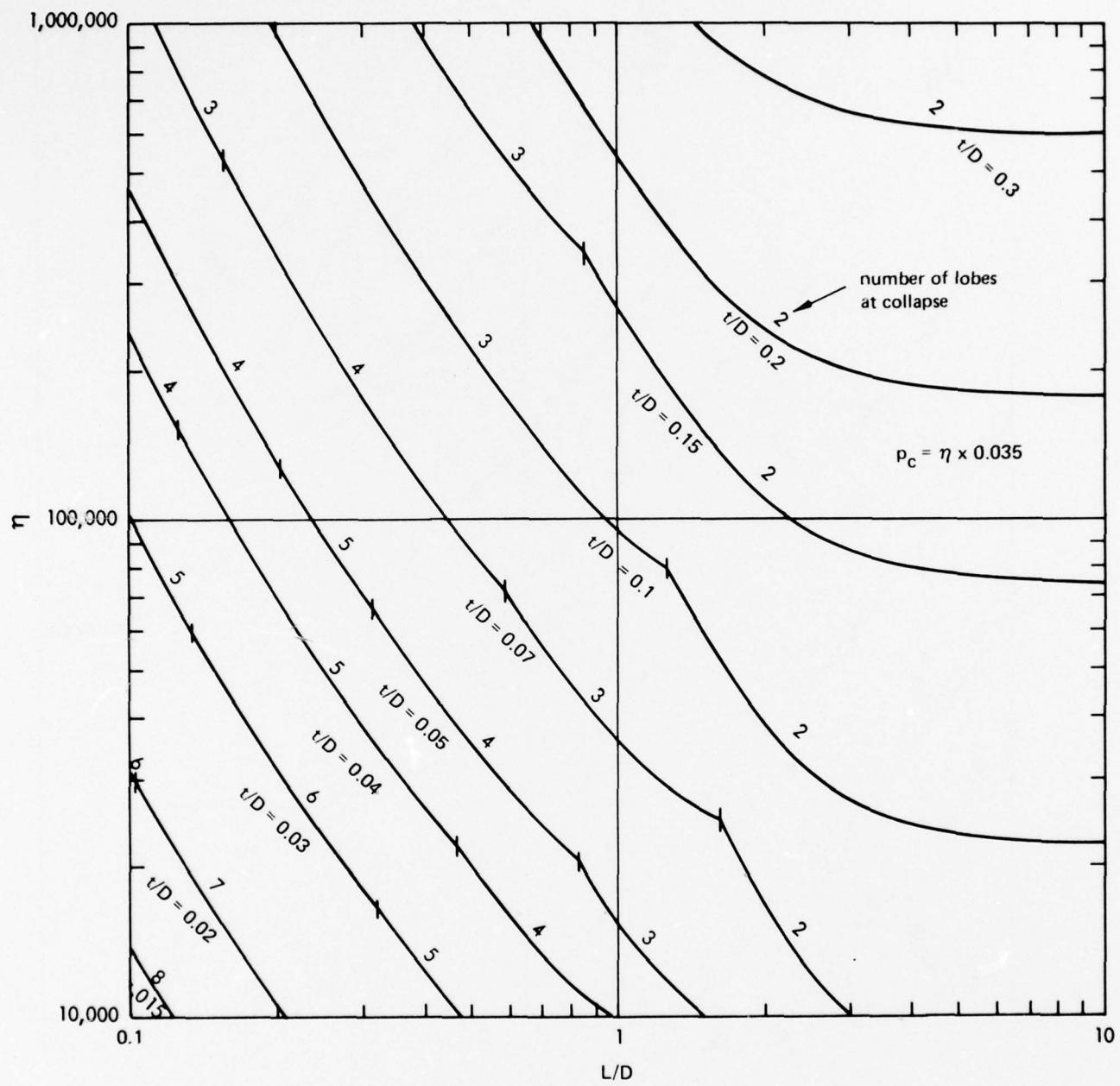
Figure 13.10. Continued.
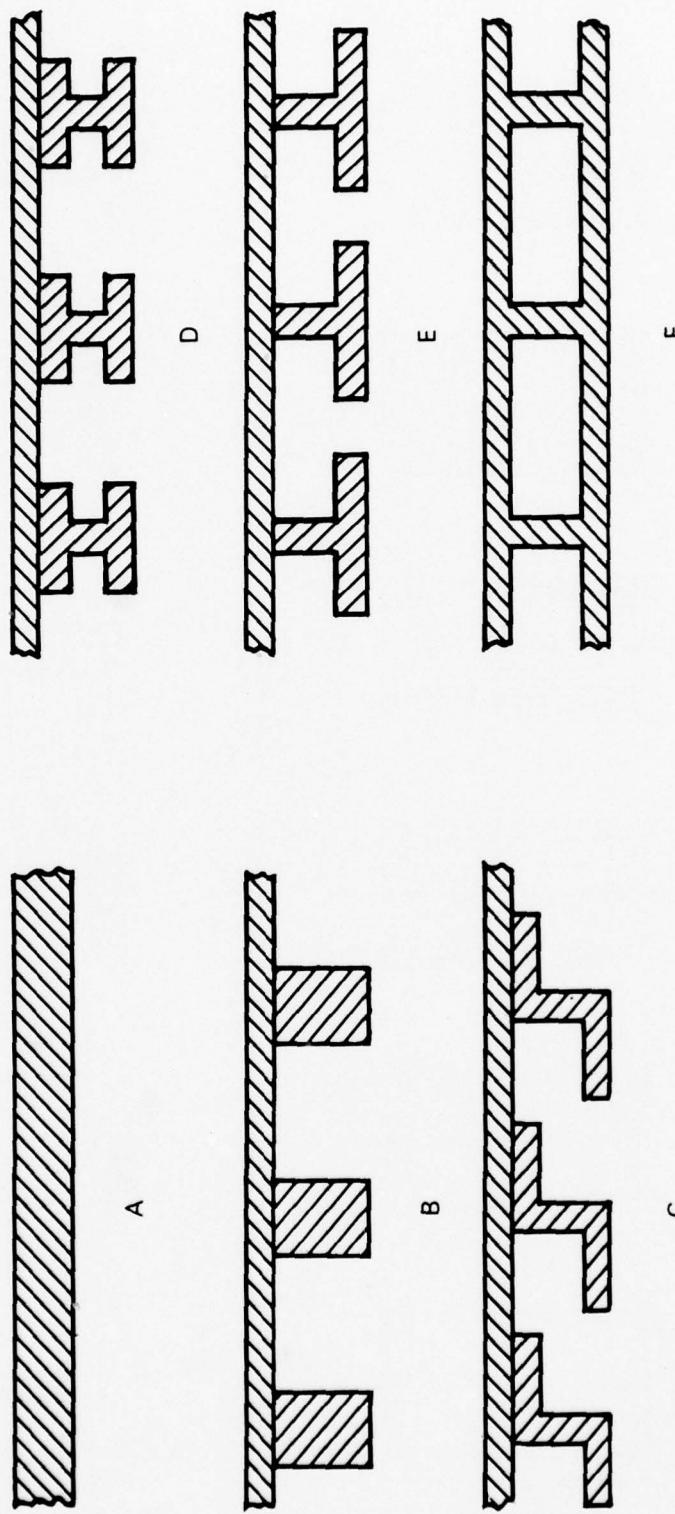
Figure 13.11. Typical shapes of circumferential stiffeners for cylinders.
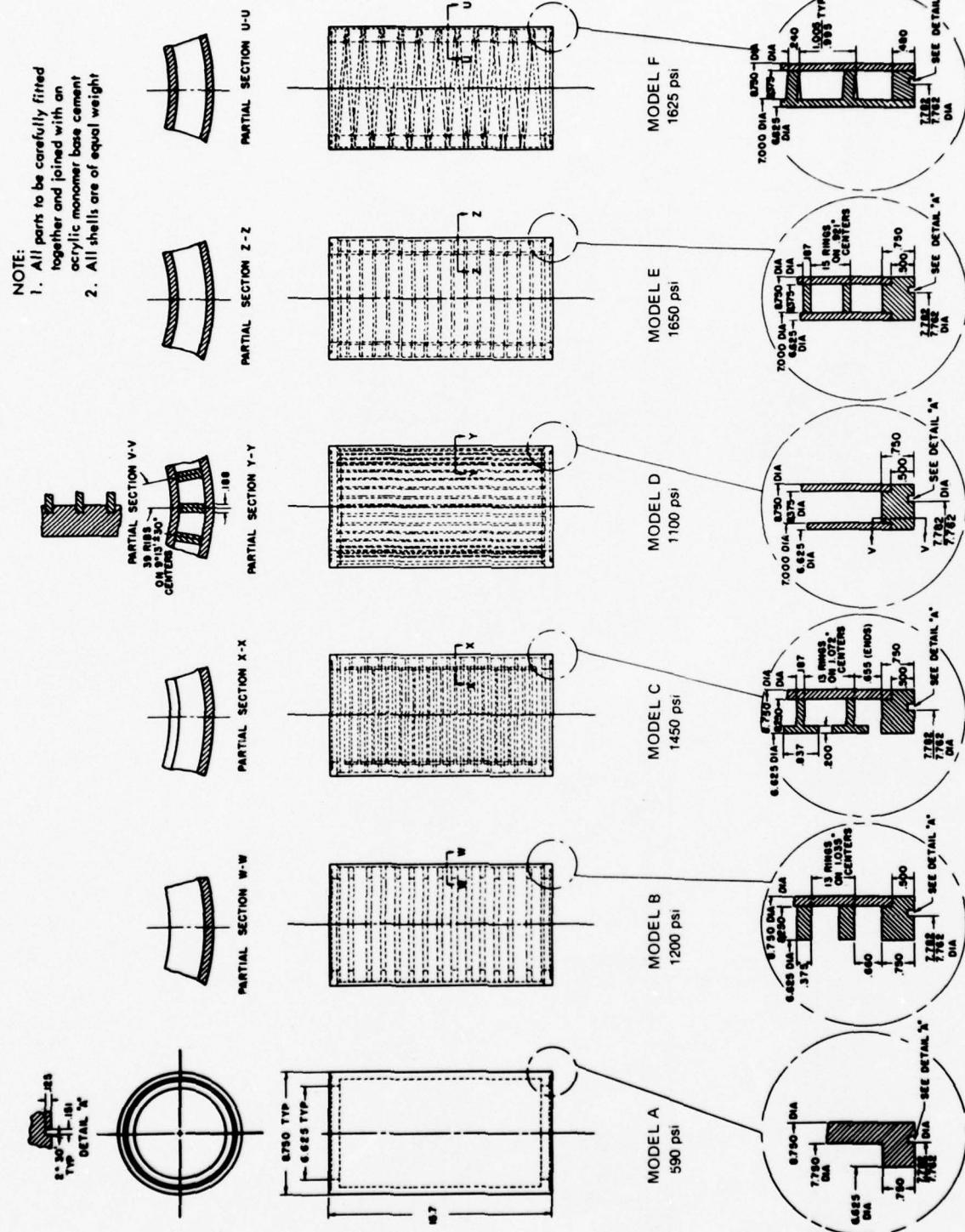
Figure 13.12. Dimensions of acrylic plastic cylinders used in the experimental evaluation of stiffener effectiveness. All cylinders have identical outside and inside diameters, lengths, and weights. Note that the smooth cylinder (model A) supported only at the ends has the lowest critical pressure.

13-36
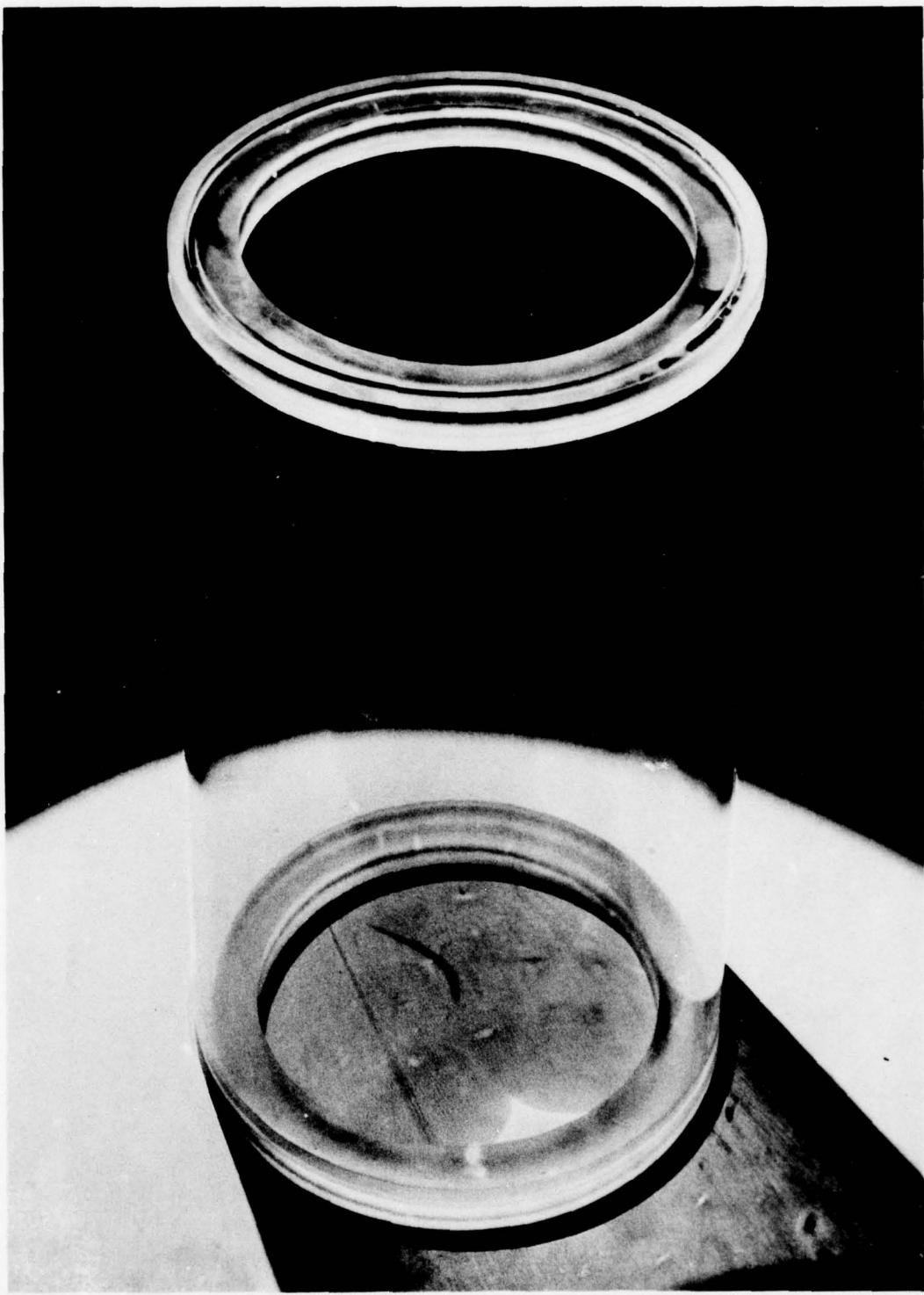
Figure 13.13. Smooth cylinder supported only at the ends (model A).
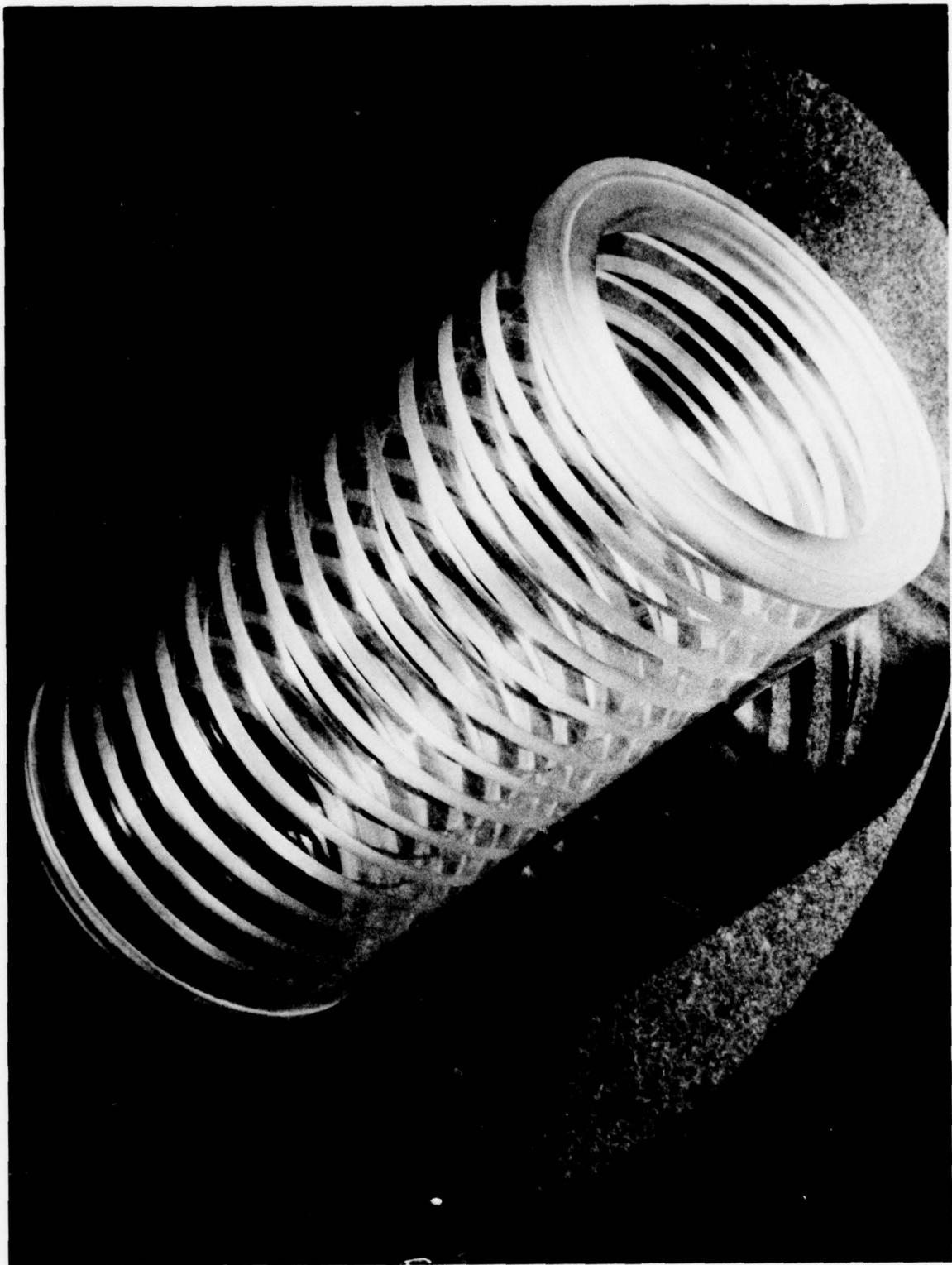
Figure 13.14. Smooth cylinder supported by rectangular ring stiffeners (model B).
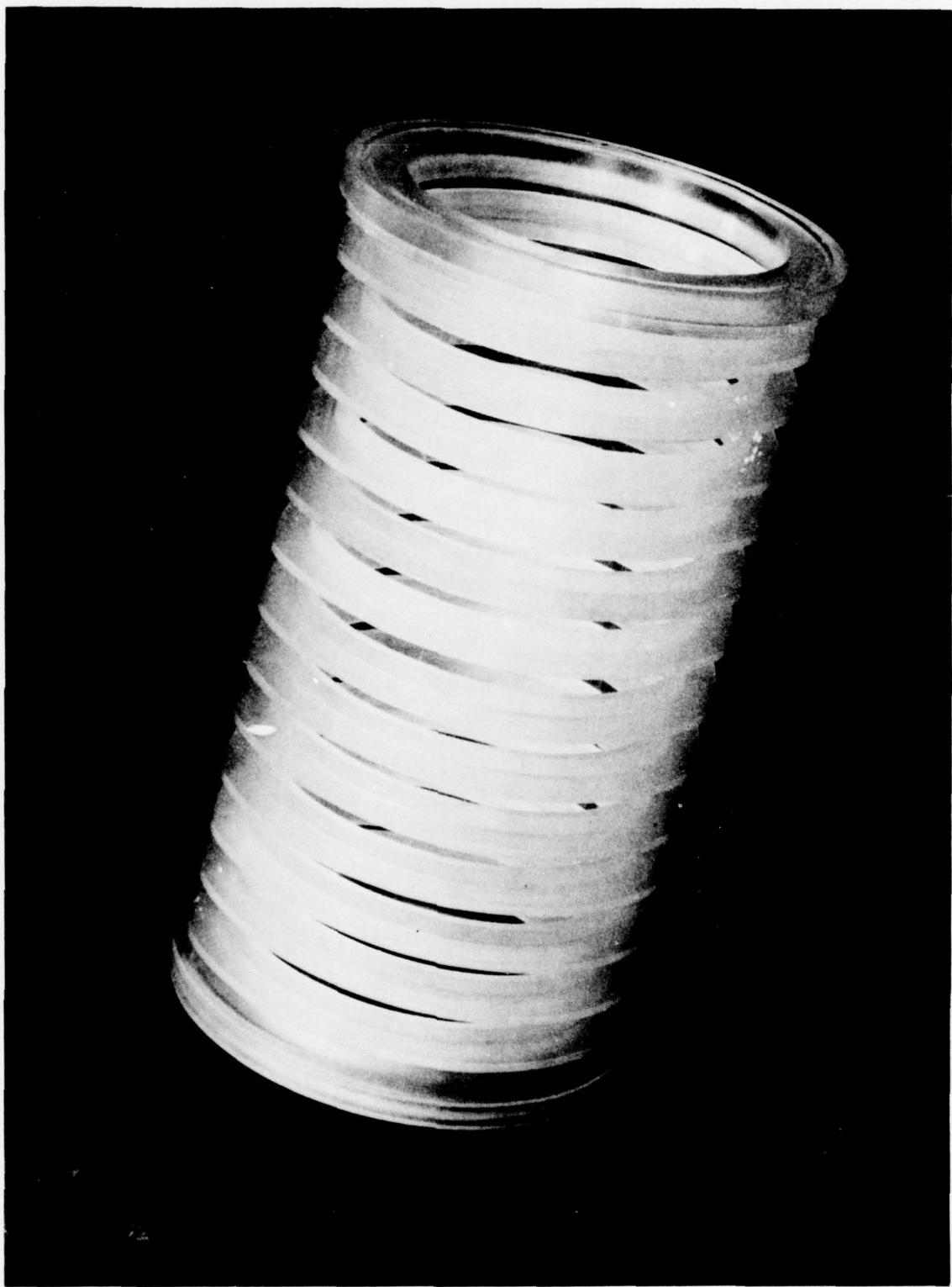
Figure 13.15. Smooth cylinder supported by T-shaped ring stiffeners (model C).
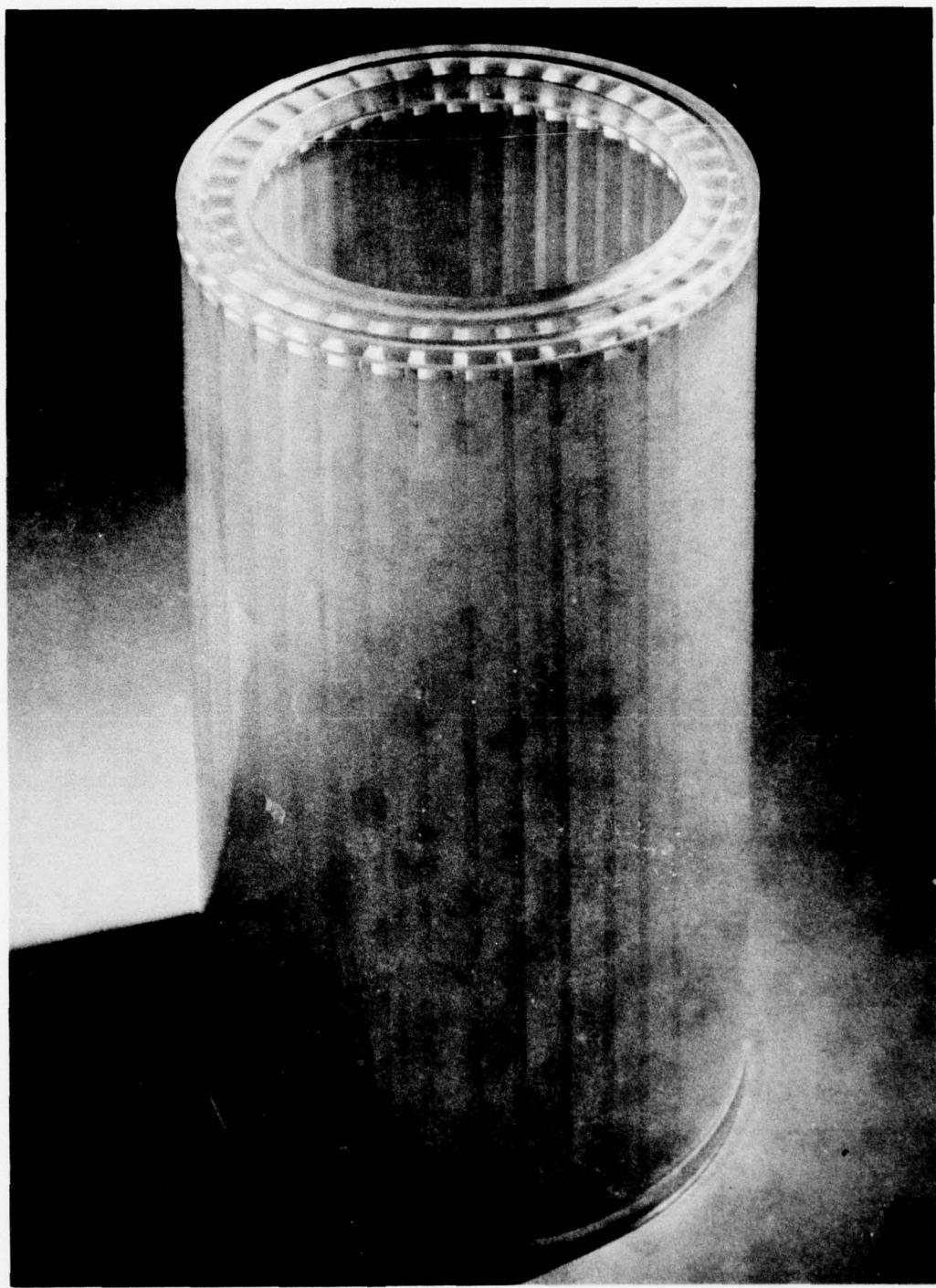
Figure 13.16. Cylinder which derives its elastic stability from sandwich construction. The thin outer and inner cylinders are tied together into a structural entity by axial stiffeners (model D).
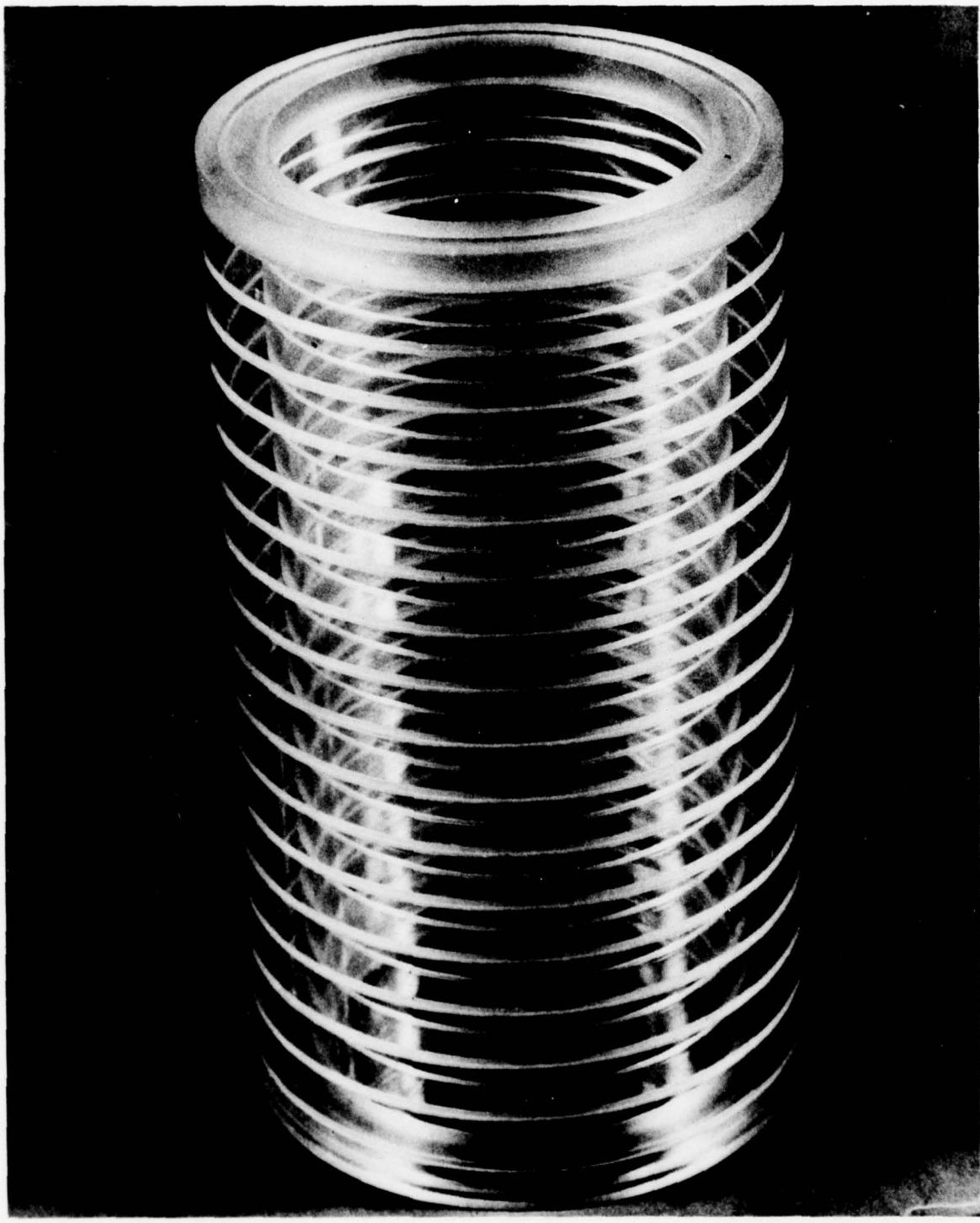
Figure 13.17. Cylinder which derives its elastic stability from sandwich construction. The thin outer and inner cylinders are tied together into a structural entity by circumferential stiffeners (model E).

13-41
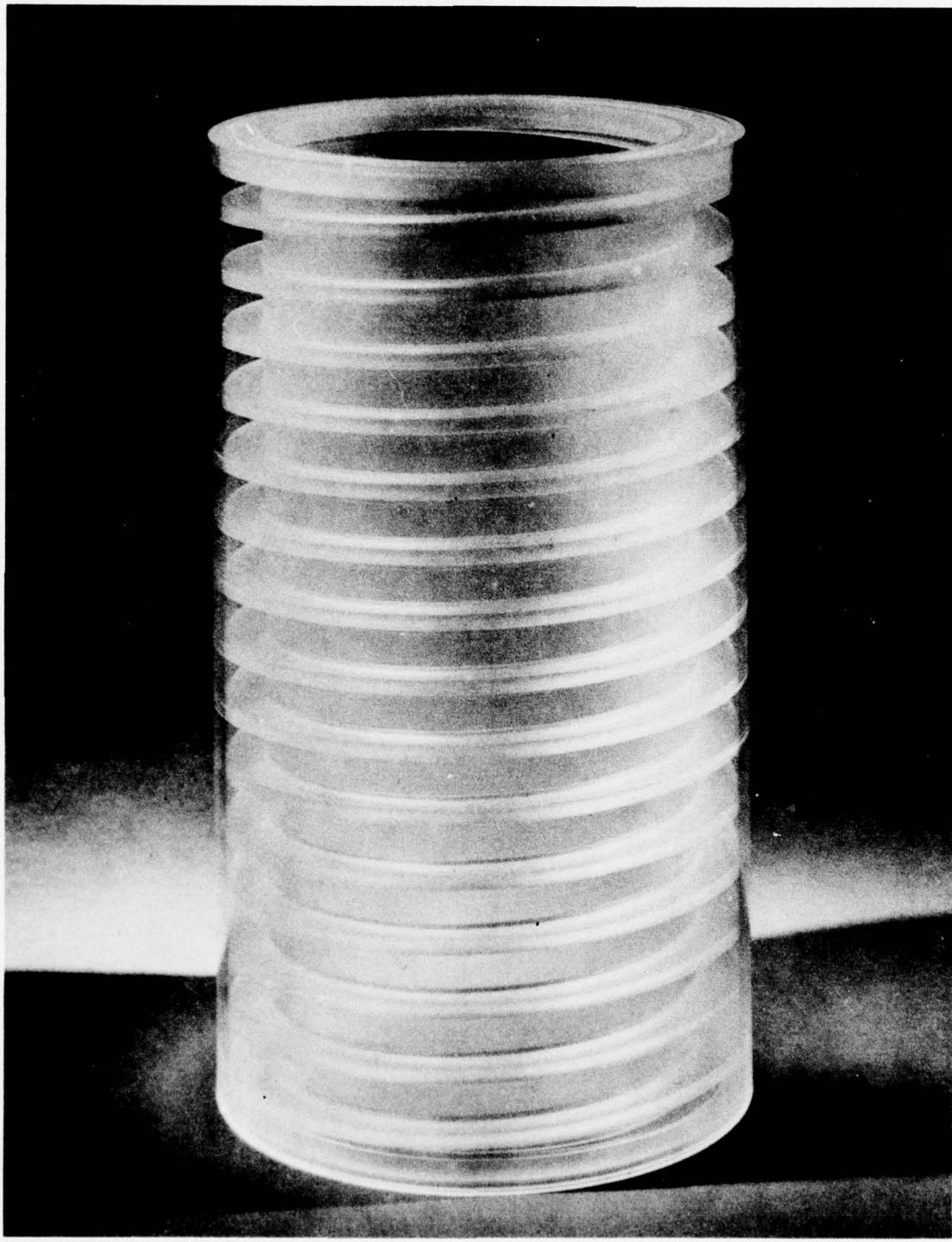
Figure 13.18. Cylinder which derives its elastic stability from sandwich construction. The thin outer and inner cylinders are tied together into a structural entity by a helicoid stiffener (model F).
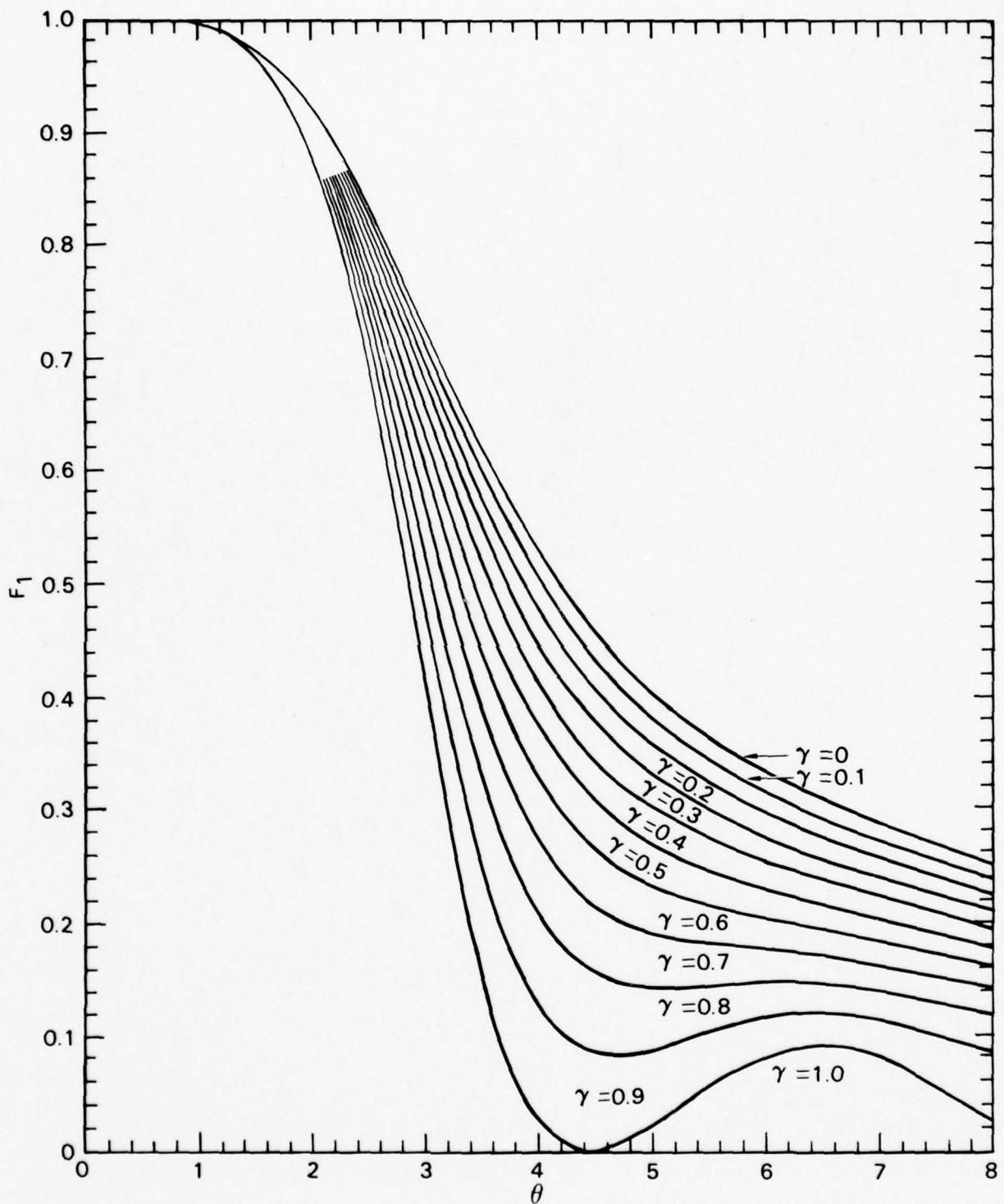
Figure 13.19. Plot of F_1 as a function of θ for equation 13.8.
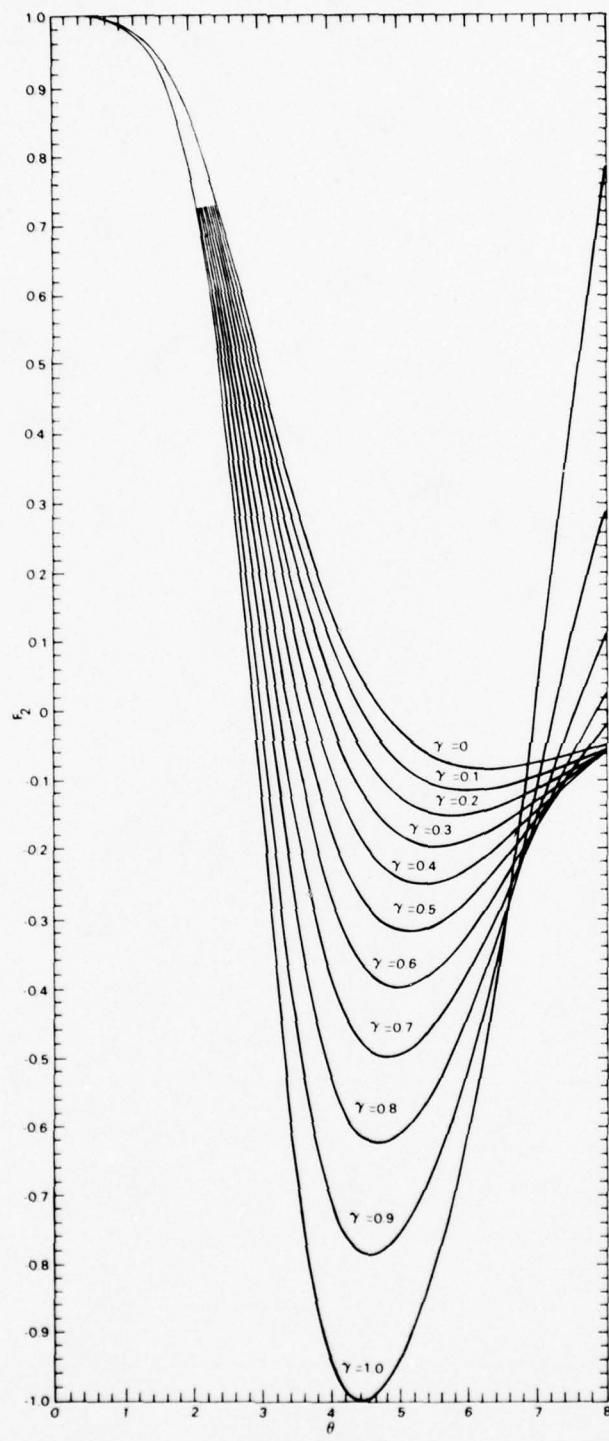
Figure 13.20. Plot of F_2 as a function of θ for equation 13.9.

13-44
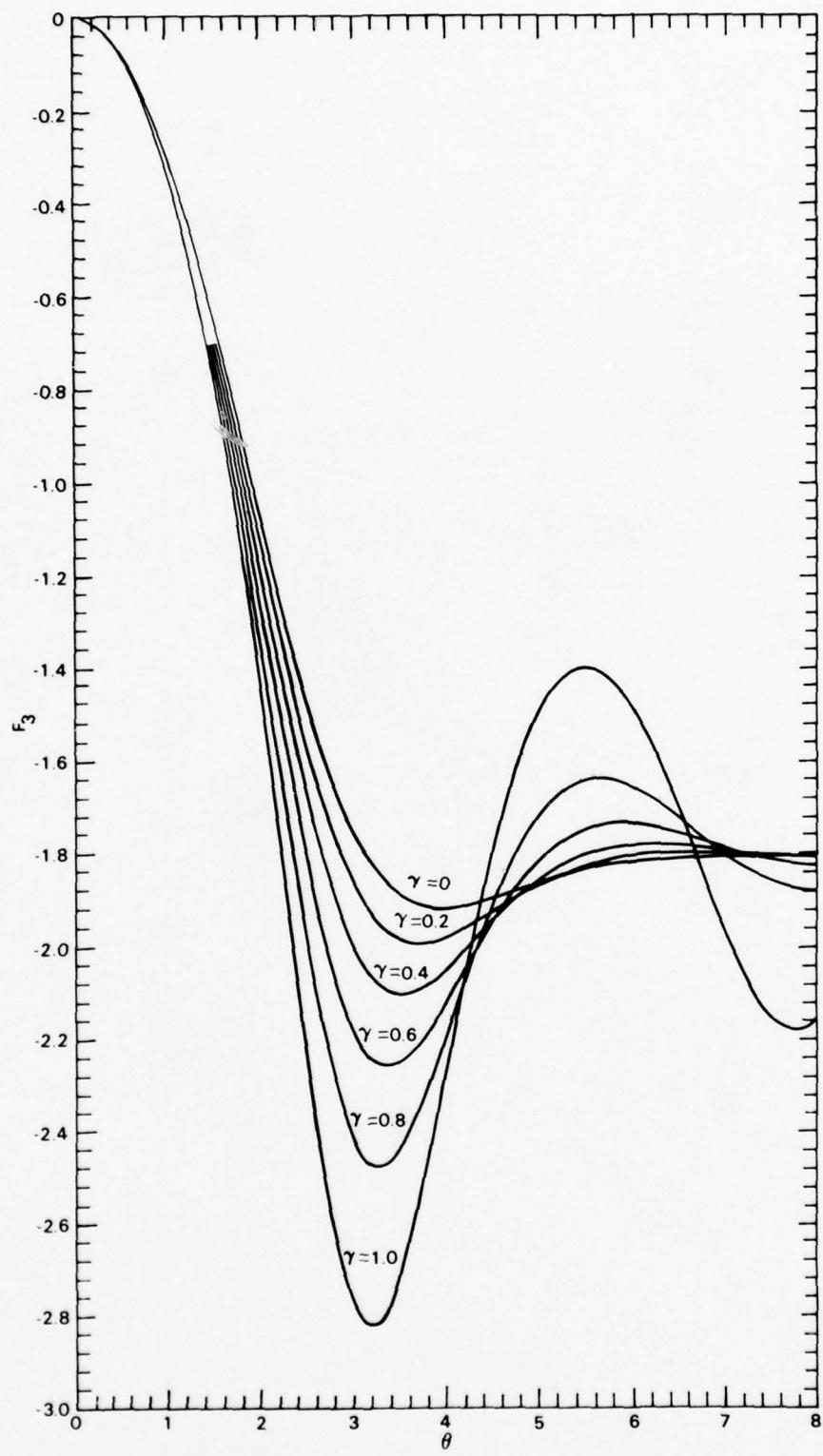
Figure 13.21. Plot of F_3 as a function of θ for equation 13.10.

13-45
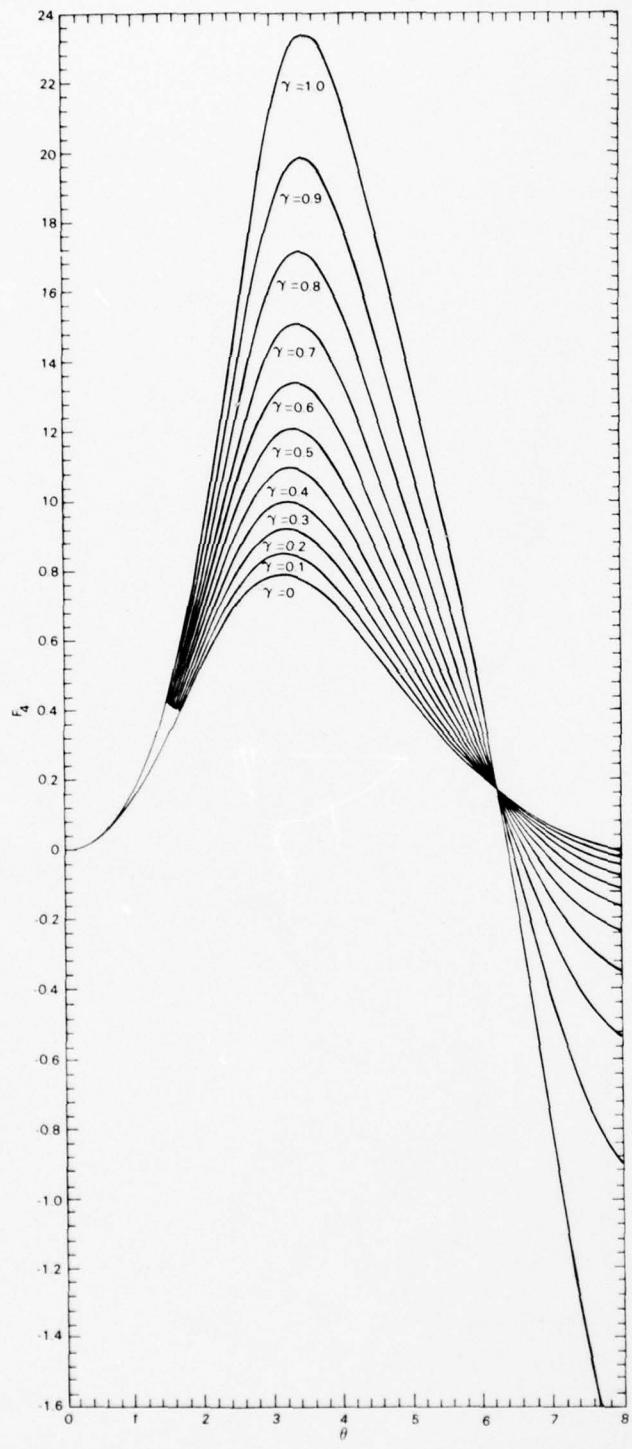
Figure 13.22. Plot of F_4 as a function of θ for equation 13.11.
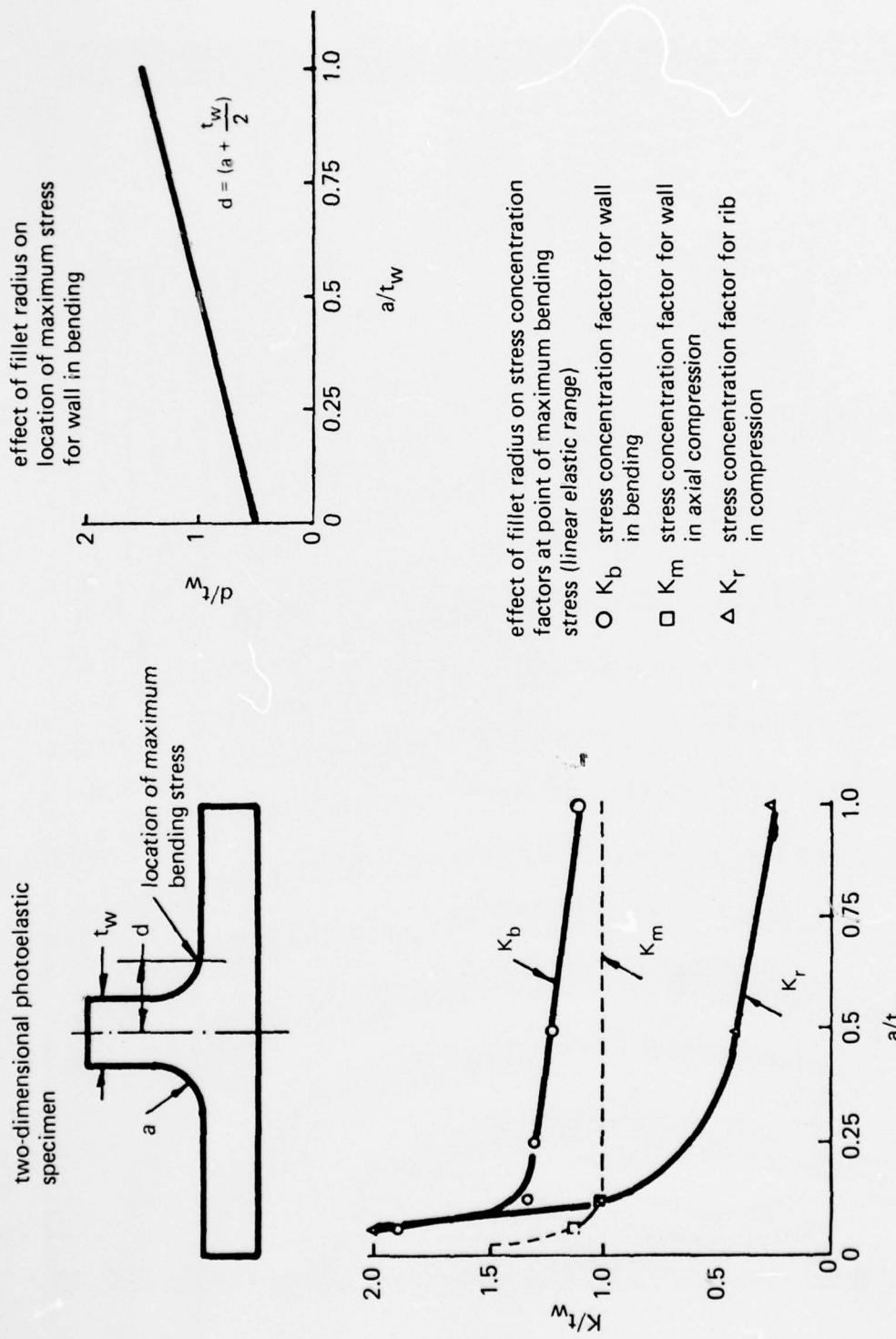
Figure 13.23. Stress concentrations at wall and internal stiffener junctures in cylinders under external pressure. Data based on results of a two-dimensional photoelastic study.
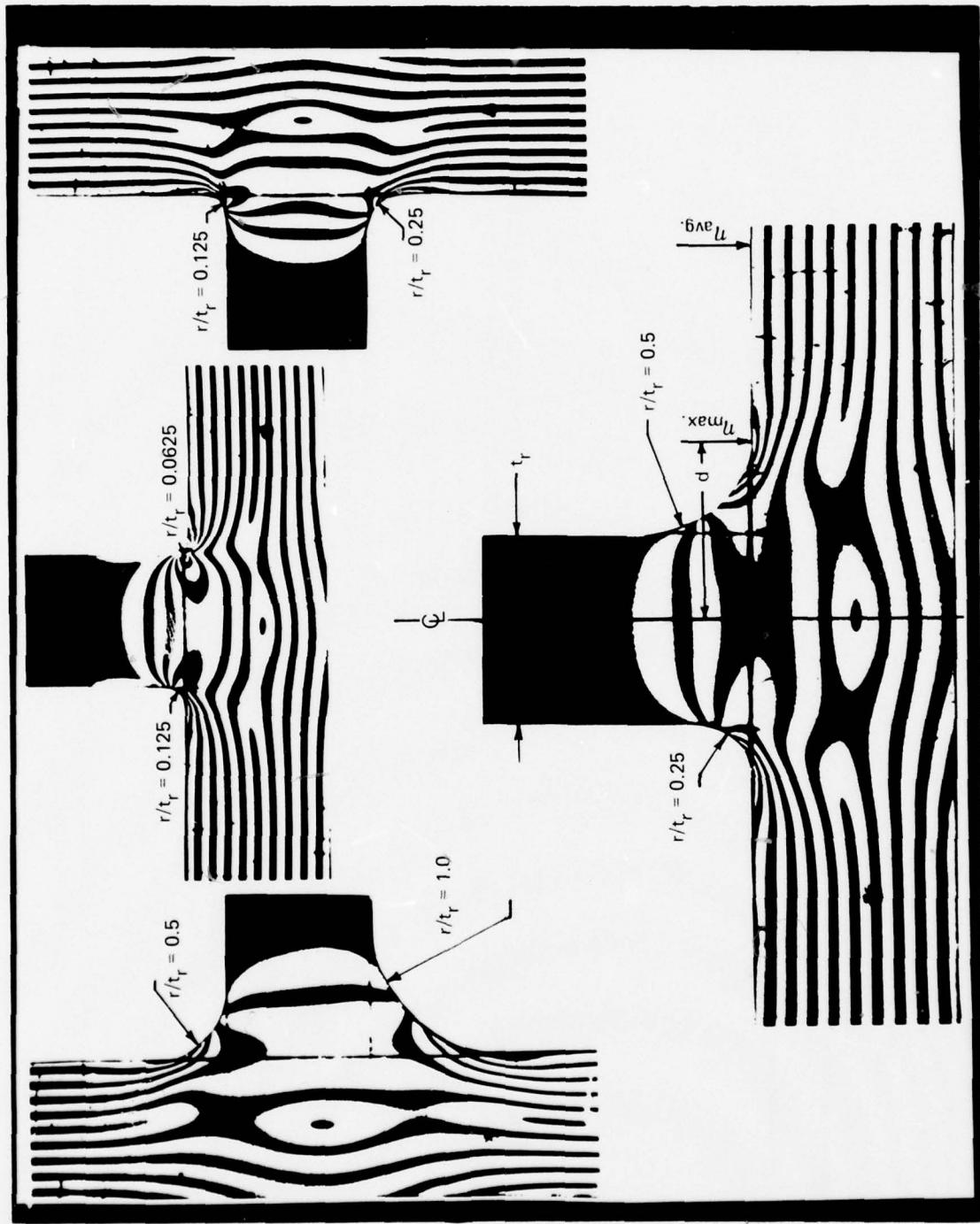
Figure 13.24. Photoelastic fringes in two-dimensional specimens simulating the junctures between internal stiffeners and the wall of a cylinder under external pressure.

external pressure

axial contraction compensator

tie rod (typ.)

neoprene washer

neoprene U-seal bonded to
the cylinder and flange

acrylic plastic
cylinder

hard neoprene or cork
bearing gasket bonded
to the flange

seal design C

external pressure

plastic
self-energizing
seal ring

nut

tie rod (typ.)

neoprene washer

retaining ring

hard neoprene or cork
bearing gasket

acrylic plastic
cylinder

seal design d

Figure 13.25. Typical sealing arrangements with continuous tie rods for
acrylic cylinders under external pressure.

13-49
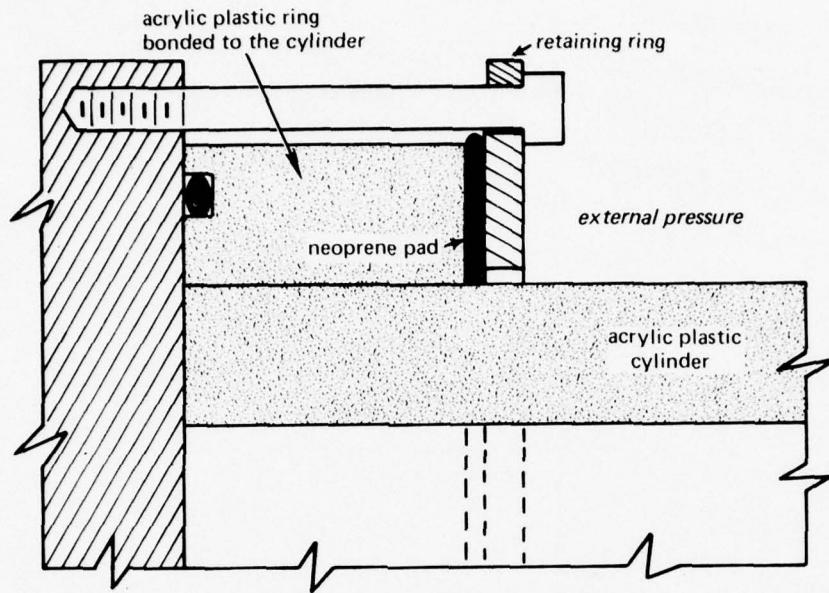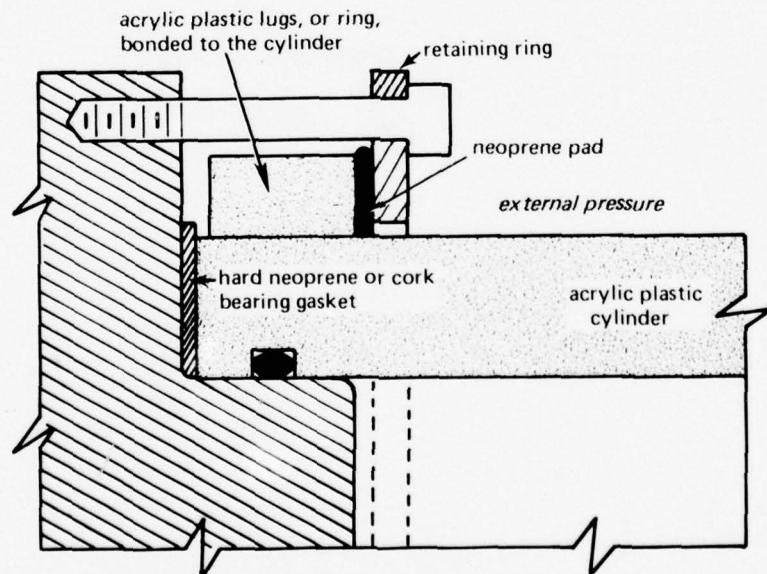
Figure 13.26. Typical sealing arrangements with interrupted tie rods for acrylic cylinders under external pressure.
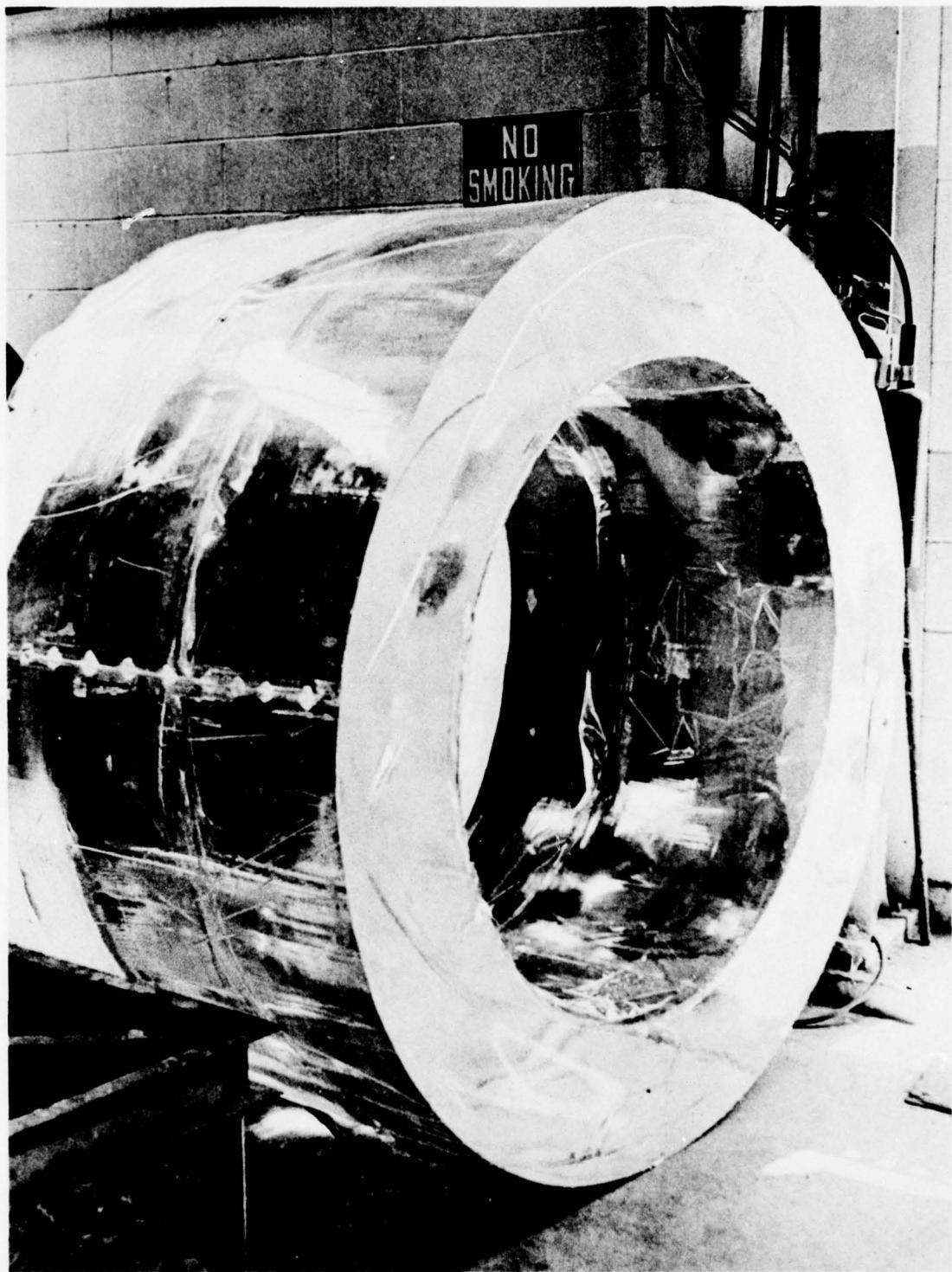
Figure 13.27. Massive acrylic cylinder cast by Cadillac Plastic and Chemical Company.

SECTION 14. OPTICAL CHARACTERISTICS OF ACRYLIC WINDOWS . . . 14-1

SECTION 14. OPTICAL CHARACTERISTICS
OF ACRYLIC WINDOWS

14.1 OPTICAL PROPERTIES OF MATERIALS

In 1887, Hertz succeeded in propagating electromagnetic waves with wavelengths of approximately 10 meters. Since that time, much of the progress in experimental physics has been the discovery of methods of producing electromagnetic waves at different wavelengths. Although some properties of these waves depend upon their wavelengths, they are all propagated with the same velocity in free space, approximately 3×10^{10} centimeters per second. Figure 14.1 shows them arranged in order of wavelength and frequency (reference 14.1).

In certain regions of the spectrum, it is still very difficult to excite the waves. Although these regions are not completely explored, they do not really present gaps in the spectrum. The limits of the spectrum at the two ends are not perfectly defined. At the long wavelength end, methods of producing and detecting radiation gradually become less efficient as the wavelength increases. At the short wavelength end, an enormous concentration of energy is needed to produce vibrations of extremely high frequency. The range of wavelengths to which the eye is sensitive and to which we give the name "light" is thus seen as part of a much wider spectrum. The electromagnetic theory brings visible light into relation with the other types of electromagnetic radiation and also with the fundamental theories of electricity and magnetism.

In media other than a vacuum, the velocity of the propagation of light is decreased, and in glass the velocity is approximately two thirds that in free space. The ratio of the velocity of light in a vacuum to its velocity in a medium is known as the index of refraction of that medium:

$$\text{index of refraction: } N = \frac{\text{velocity in vacuum}}{\text{velocity in medium}} \quad . \tag{14.1}$$

Since the index of refraction of air is approximately 1.0003 and since most optical work is performed in air, the index of refraction commonly used in engineering is related to air, which is assumed to have a refractive index of 1.0000.

When white light is spread into its component colors, the light is said to be dispersed. Refracting white light from air into a denser medium produces a spectrum as indicated in figure 14.2. The colors are actually in a continuous spectrum giving rise to the fact that N' must vary with the color or wavelength of the light being refracted. In specifying the exact index of refraction of particular colors, it is customary to use certain dark lines at wavelengths of elements in the emission spectra of the sun (reference 14.2) as indicated in table 14.1.

---

*This section was contributed by J. J. Lones of Adroit Engineering.

Table 14.1. Spectrum lines for specifying
index of refraction.

Designation	Wavelength, nm	Element
t	1014.0	mercury
s	852.1	cesium
A′	769.9 and 766.5	potassium
r	706.5	helium
C	656.3	hydrogen
C′	643.8	cadmium
D	589.6 and 589.0	sodium
d	587.6	helium
e	546.1	mercury
F	486.1	hydrogen
F′	480.0	cadmium
g	435.8	mercury
G′	434.1	hydrogen
h	404.7	mercury
H	396.8	calcium
K	393.4	calcium
i	365.0	mercury

The index of refraction at any particular wavelength is generally said to be proportional to the density of the material, whereby increasing the density increases the index of refraction. This analog is qualitative as there are certain exceptions, e.g., the index of refraction for ether is 1.36 and the index of refraction for water is 1.33, but ether with its lower density floats on water (reference 14.3).

The deviation of any particular ray in figure 14.2 is expressed by Snell's law,

$$N \sin I \approx N' \sin I' \qquad\qquad (14.2)$$

(figure 14.3). When the angle of incidence I is fairly small, equation 14.2 shows that the angle of refraction I' will also be small. Under these circumstances, a very good approximation is obtained by setting sine equal to the angle in radians,

$$\frac{I}{I'} \approx \frac{N'}{N} \quad ; \text{ small angles only } . \qquad\qquad (14.3)$$

To keep Snell's law in proper perspective, it can generally be stated that a refracted ray passes closer to the normal in the denser medium as compared to the ray in the less dense medium.

Figure 14.3 also shows how reflected rays always make an angle with the normal that is equal to the angle of incidence. This basic law is readily explained when it is remembered that medium of the reflected ray has the same refractive index as the incident ray, but opposite in sign, thereby creating a slope reversal on application of Snell's law. Although somewhat elementary, the negative refractive index concept is useful in ray tracing.

The refractive index of a yellow line is used to describe the optical properties of most materials. In the United States, this principal index N_D is taken at the wavelength of 589.3 nanometers, which is the mean wavelength between the sodium D lines of 589.6 and 589.0 nanometers. Elsewhere in the world, the principal index N_d is taken at the wavelength of 587.6 nanometers, the helium d line (reference 14.3). In figure 14.2, the angular divergence between the red and blue refracted lines for wavelengths C and F is a measure of the dispersion produced by the material in which the refraction is occurring. This dispersion angle has been greatly exaggerated in the figure in relation to the average deviation of the spectrum, which is measured by the angle by which ray D is deviated.

It may be generalized that the higher the refractive index of a material, the higher will be its dispersion; however, in nature there are exceptions to this rule. Diamond, a very dense material with a specific gravity of 3.52, has a high refractive index that varies from 2.4100 at the C line to 2.4354 at the F line. The difference in these values, which is the dispersion of the material, is only 0.0254; however, a dense flint glass with a lower refractive index may have a value of 0.0500 for the same dispersion value (reference 14.3). The refractive indices for acrylic (table 14.2) are N_F=1.49776, N_D=1.49168, and N_C=1.48919.

Based on data from equation 14.3, where the angle of incidence is small, the dispersion of C and F rays ($I'_C - I'_F$) (figure 14.2) is proportional to

$$N_F - N_C = 0.00857 \qquad (14.4)$$

and in the same manner the deviation of the D ray ($I - I'_D$) is proportional to

$$N_D - 1 = 0.49168 . \qquad (14.5)$$

The measure of dispersion $\Delta N = N_F - N_C$ and its ratio with the basic refracting power of the material $N_D - 1$ give the dispersion relative to the amount of bending that a light ray undergoes. This is known as the dispersive power of the material and is designated by ω:

$$\frac{1}{\omega} = V_D = \frac{N_D - 1}{N_F - N_C} = 57.4 \text{ for acrylic.} \qquad (14.6)$$

The reciprocal of the dispersive power V_D (sometimes designated by ν) is known as the reciprocal relative dispersion, Abbe V-number, or V-value. The subscript D of the V-number matches the subscript of the principal index of refraction used in calculating the V-number. Outside the United States the principal index is the d spectral line of 587.6 nanometers with the corresponding V-number designated as V_d. When other than the F and C lines are used for the V-number, an appropriately designated alternate subscript is used.

Optical materials are commonly classified by their principal index of refraction and the corresponding V-number. Numbers describing optical glass types take the form of a six-digit number with the first three digits representing the principal index minus one ($N_D - 1$) and the last three digits representing the V-number to one decimal place. In both cases the decimal points are omitted, and the two groups of numbers may or may not be separated by a space or colon. For example, an N_D of 1.491 and a V of 57.4 would be expressed as 491:574. Although optical properties are readily available for glasses, it is somewhat difficult to find the same characteristics for the plastics used in optical systems. However, recent increases in the use of plastic optics have resulted in the users essentially defining the properties of their materials, as this information is not generally available from the plastics manufacturing sources. The data in table 14.2 are supplied from technical references and are in agreement with available sources; however, it should be expected that the compounds will slightly vary. Data for acrylic in this section have been accurate for general engineering. Any exacting uses or extremes of temperature should be further investigated, e.g., Smith has indicated that the index of refraction of acrylic varies strongly with temperature (typically ΔN is about −0.00013 per $^{\circ}C$) (reference 14.1).

Transmission of light through acrylic will vary with wavelength and angle of incidence. Transmission as a function of wavelength at normal incidence is plotted in figure 14.4. These data are for the two basic grades of acrylic — ultraviolet absorbing (UVA) and ultraviolet transmitting (UVT) — at a thickness of 0.125 inch (3.2 millimeters) (reference 14.6). However, when light is incident on an optical surface in air then the amount transmitted is a function of the angle of incidence. At 0-degree (0 radian) incidence the reflectance of the surface is

Table 14.2. Properties of optical plastics which can be injection-molded (references 14.3 and 14.4).

Index	N_t	N_C	N_D	N_d	N_F	N_h	N_i	V_D
Wavelength, nm	1014.0	656.3	589.3	587.6	486.1	404.7	365.0	
materials								
1. acrylic	1.48312	1.48919	1.49168	1.49165*	1.49776	1.50663	1.51359	57.4
2. polystyrene	1.5500	1.5849	1.5903		1.6040	1.6254		30.9
3. SAN	1.5500	1.5627	1.5673		1.5790	1.5791		34.9

compound	specific gravities	coefficient of expansion	refractive index change
1. polymethyl methacrylate	1.17 to 1.20	5.0 to 9.0 ($\times 10^{-5}$/°C)	-11 to -13 ($\times 10^{-5}$/°C increase)
2. polystyrene	1.04 to 1.09	6.0 to 8.0 ($\times 10^{-5}$/°C)	-11 to -13 ($\times 10^{-5}$/°C increase)
3. Styrene-acrylonitrile copolymer	1.075 to 1.100	3.6 to 3.8 ($\times 10^{-5}$/°C)	-11 to -13 ($\times 10^{-5}$/°C increase)

trade names

1. *Plexiglas*, Rohm and Hass Co.; *Lucite*, Du Pont Co.; *Acrylite*, American Cyanamid Co.

2. *Dylene*, Koppers Co.; *Lustrex*, Monsanto Chemical Co.

3. *Lustran*, Monsanto Chemical Co.; *Bakelite C-11*, Union Carbide Plastics Co.

optical glass equivalents (similar V-number)

1. K-10   501   564   (source: Schott Optical Glass, Inc.
2. TiF-6   617   310   Duryea, Pennsylvania, and Mainz, West Germany)
3. SF-7   640   346

*index of refraction N_d calculated from Hertzberger approximation formula (reference 14.5):

$$N_d = N_t (-0.045919) + N_C (0.744598) + N_F (0.326272) + N_i (-0.024952)$$

$$r = \left(\frac{N' - N}{N' + N}\right)^2 , \qquad (14.7)$$

where N is the index for the incident medium and N′ is the index for the refracted medium. This is the result of the polarization of the incident light which gradually increases with the increasing angle of incidence to the polarizing angle, known as Brewster's angle (reference 14.3):

$$\text{Brewster's angle: } \bar{I} = \tan^{-1} N . \qquad (14.8)$$

For acrylic at $N_D = 1.491, \bar{I} = 56.15$ degrees (0.98 radian). Figure 14.5 shows that beyond the polarizing angle, transmission decreases rapidly with increasing incidence until at 90 degrees (1.57 radians) all light is reflected with none transmitted (reference 14.6). Incidence up to the polarizing angle results in decreasing the plane-polarized component of reflected light which is parallel to the plane of incidence. At the polarizing angle only the slowly increasing polarized component which is perpendicular to the plane of incidence remains; however, further increasing the incidence rapidly increases the reflection of both of the plane-polarized components, which accounts for the rapid transmission loss.

The plot in figure 14.5 is for one surface of air and acrylic or acrylic and air. If more than one surface exists, then each surface will have its own transmission losses affecting the light path. At 0-degree (0 radian) incidence, the reflectance of an air-acrylic interface is 3.9 percent (equation 14.7). The water-acrylic interface of an underwater viewport has at 0-degree (0 radian) incidence a reflectance of only 0.3 percent. These observations suggest that coating the water interface of an underwater viewport would mainly benefit scratch resistance and that coating the air interface would both improve scratch resistance and reduce reflection losses.

14.2 IMAGERY IN VIEWING MEDIA

The existence of any window in a hyperbaric chamber implies that there will be viewing through this interface. The sensor or photo receptor for viewing can be one of many forms, e.g., an observer's eyes, a photographic camera, or a television camera. All are related when the subject to be detected is in water.

14.2.1 Photographic Sensing

Practical considerations in constructing a photographic system for use in water often dictate that the illumination source be attached to the camera assembly. This results in some or all of the path between the subject and the camera being illuminated by the source. It is well known that if the lamp is separated from the camera and placed near the subject then the photographic range is increased considerably because of the reduction of scattered light in the water path (reference 4.7). A set of curves that depicts exposure approximations for an electronic flash light source is in figure 14.6 (reference 4.8). It should be noted that these curves are for a system in which the camera and the light are the same distance from the subject. Although they can be separated by some distance laterally

off the sighting line, the maximum predicted range is still quite short in relation to the maximum range for image detection in the ocean (reference 4.7). This is a good example of a system limited by the practical considerations of film sensitivity, exposure time, illumination power, and numerous mechanical constraints imposed by remote operation at great depths.

Edgerton also suggests that the light output of an electronic flash is not well defined by the watt-second rating, as this is an electrical quantity that describes the power source of the lamp and that does not consider the efficiency of the lamp or the reflector (reference 4.9). It follows that one of the most important factors in underwater photography (or any viewing/detection system) is the design of an efficient illuminator assembly, regardless of the type of light source involved. Few underwater lighting assemblies now in use fully utilize the source flux output.

Temperature and salinity gradients in ocean water do not appreciably attenuate the spatial frequency transmitted by the image; however, absorption of the light energy level by the water path does degrade the power of image-forming light. Image-forming light is that which maintains an electromagnetic phase relationship as it travels through a medium. Biological masses produce little or no absorption of the light energy level, but they do retard the electromagnetic phase so that some of the image-forming light no longer contributes to the image at the sensor's location. This light of retarded phase, even through it originated at the subject, reduces the sensor's image-recording ability because it has the effect of increasing the background or "noise" signal relative to the image-forming signal (reference 4.7).*

14.2.2 Refractive Index of Water

The refractive index of water is useful for certain design application of viewports. Usually the principal index N_D is estimated at 1.33 for freshwater and 1.34 for seawater; however, when work is conducted requiring considerable accuracy it is important to be aware of index variations in the actual environment. Austin and Halikas (reference 4.11) have published an extensive volume on the refractive index of seawater with respect to wavelength, pressure, temperature, and salinity. It is impossible to cover their contribution here except to say that the data agree with earlier reference work and that it discusses the subject from the baseline of distilled water.

An empirical expression for the refractive index of water has been developed by McNeil (reference 4.12):

$$N_\lambda = 1.3247 + 3.3 \times 10^3 \lambda^{-2} - 3.2 \times 10^7 \lambda^{-4} - 2.5 \times 10^{-6}T^2$$

$$+ (5 - 2 \times 10^{-2}T)(4 \times 10^{-5}S)$$

$$+ (1.45 \times 10^{-5}P)(1.021 - 6 \times 10^{-4}S)(1 - 4.5 \times 10^{-3}T) . \qquad (14.9)$$

---

*If additional information in the field of underwater photography is required, a good reference is the text by Mertens (reference 14.10).

where

N_λ = refractive index of water at wavelength

λ = wavelength of light, nanometers

T = temperature of water, °C

S = salinity of water, parts per thousand

P = pressure of water, kilograms per square centimeter.

Since this expression agrees with the Austin/Halikas data to three decimal places, which is the practical accuracy of the index for optical materials,* this is an accurate expression for seawater's refractive index. A practical example is the calculation of a change in focus for one specific lens system because of pressure-related changes in seawater's refractive index. In this case, the maximum permissible depth variation is ±2640 meters for the underwater lens system to maintain a resolution limit of 50 cycles per millimeter on a low-contrast target. This is a change in focus of ±0.05mm for a 40mm focal length lens (reference 4.12).

14.3 OPTICAL GEOMETRY OF VIEWPORTS

14.3.1 Plane Window

When a plane window with parallel faces is in contact with two media of different refractive indices, any ray passing through the window at other than normal to the faces is deviated as shown in figure 14.7. At the interfaces, the deviation in accordance with Snell's law is

$$N_1 \sin I_1 = N_2 \sin I_2 \tag{14.10}$$

$$N_2 \sin I_3 = N_3 \sin I_4. \tag{14.11}$$

Neglecting curvature from pressure acting on the window

$$I_2 = I_3. \tag{14.12}$$

Then by substitution

$$N_1 \sin I_1 = N_3 \sin I_4, \tag{14.13}$$

which shows that the angular deviation from water to air through the flat window is *independent of the window thickness or refractive index.*

For an observer in the air with a 75-degree (1.3 radians) half-angle field-of-view, the angular half-field is 46.12 degrees (0.8 radian) in seawater. If these angles represent cones of view, then the observer's cone of 4.66Ω in air is reduced to 1.93Ω in water. (Ω is in units of steradians, a measure of solid angle.) The ratio of these solid angles indicates that the observer's effective field-of-view in the water is well under half of that in air.

---

*The acrylic index will seldom be known to this accuracy.

The reduction in the angular field at the air-water interface produces an apparent magnification of objects in the water, which results in the apparent distance to the object being less than its actual distance from the window. With small objects on or near a viewing axis perpendicular to the window surface, i.e., with small incidence angles in water, the virtual image distance S′ is related to the actual object distance S by

$$S' = \frac{S}{N},\qquad\qquad (14.14)$$

if the window's thickness is small relative to the actual distance of the object. Contrary to what is assumed in numerous texts, at large viewing angles from the normal to the window surface the virtual image does not follow the perpendicular distance expressed in equation 14.14. This can be readily observed by looking at the surface of an aquarium at an air angle of refraction of approximately 70 to 80 degrees (1.2 to 1.4 radians) that intersects the glass surface close to a corner near the observer. Upon moving along the line-of-sight toward the corner, the virtual images in the aquarium go out of focus at the same time as does a finger held near the fixation point on the glass surface. If the in-water virtual images were substantially behind the surface, they would not go out of focus along with the finger. An approximation of the virtual image distance (reference 14.13) is

$$S' = \frac{N_2 \cos^2 I'}{N_1 \cos^2 I}\, S,\qquad\qquad (14.15)$$

where

S'	=	distance of in-water virtual image from surface interface along path-of-sight in air
S	=	actual water path distance to object from surface interface
N_1	=	refractive index of object medium
N_2	=	refractive index of observer medium
I	=	angle of incidence in object medium
I'	=	angle of refraction in observer medium.

This expression also assumes negligible window thickness. Although off-normal viewing imparts considerable aberration to the image, it sometimes cannot be avoided.

Images recorded by a sensor in air behind a flat window are distorted when the object is in water. Again considering a sighting axis that is normal to the window, the distortion occurs as a result of the lateral magnification (image height) changing as the image position moves radially away from the sighting centerline. With a flat window in water, the distortion is considered positive and is designated as "pincushion." Figure 14.8 shows how it appears in a recorded image. Figures 14.9 and 14.10 provide plots of the numerical values of distortion from the relationship

$$P = \left(\frac{\cos I}{\cos I'} - 1\right)\,100,\qquad\qquad 14.16)$$

where

P	=	distortion, percent
I	=	angle of incidence in water
I'	=	angle of refraction in air

(reference 4.14). The distortion is plotted for both the water-incidence and air-refraction angles. When utilized for photography, these angles become the half-angles for the field-of-view in the corresponding medium. If the half-angle of a camera system is under 12 degrees (0.2 radian), i.e., when the full field-of-view in air is less than 24 degrees (0.4 radian), then the distortion is less than 1 percent, and the chromatic aberration caused by dispersion is usually acceptable.

Despite the limitations of the flat acrylic window, it has been in use for many years as a viewport in submersibles. Attempts have been made to improve the angle of view through these ports by optically coupling supplementary devices to the air surface. Figure 14.11 shows some configurations used in research submersibles (reference 14.15). In this example, a, c, and d are prisms of acrylic coupled to the window with glycerol. The prisms of a and d, disks with flat viewing faces at various angles, are more practical than the double-prism arrangement in c. The bellows type device in b is attached to a thin faceplate, and water or a suitable oil is optically coupled with the viewport. The bellows device works quite well, and it has the added capability of accepting various optical elements directly or in place of the bellows faceplate. An optical system that can be attached to the bellows is the Ivanoff corrector (references 14.16 and 14.10). It consists of a negative lens element in contact with the fluid medium, then an air-spaced positive element, the com- bination correcting flat port aberrations.

14.3.2 Dome Window

From the standpoint of stress, it is easy to recognize the advantage of a spherical viewport over a flat one. If the viewport is hemispherical, it is then in its basic form, i.e., half of a spherical pressure vessel. When the supporting edge is properly seated there is a minimum of distortion of the dome surfaces, thus it becomes a very practical optical element in a pressure environment. A basic understanding of the optical dome is best accomplished by studying its use in an optical system with rays converging or passing through the center of curvature.

Optical rays that are confined to small enough angles for the sine and tangent to be considered equal are said to be in the paraxial region, an infinitely narrow bundle on the optical axis. In comparison to ray traces at large angles, this theory allows the images to be analyzed with simple expressions. It must always be remembered that these first- order (or Gaussian) formulae produce image relationships for the perfect optical system. In practice, there is always some departure from the first-order layout; however, a valu- able insight is gained into the nature of the relationship between the object and the image. (The reader should note that expressions for first-order theory show the refractive indices as n as opposed to N for actual ray traces. This is common practice in optical texts.)

To begin investigating dome imagery, consider a dome whose thickness is small enough to produce little optical effect and yet large enough to maintain curvature between the media — water and air. This interface forms a lens with focal lengths of

$$f = -\frac{nr}{n-1} \tag{14.17}$$

14-10

and

$$f' = -\frac{r}{n-1} \ .$$

(14.18)

where

f = first focal length

f′ = second focal length

n = refractive index for object space (water)

r = dome radius .

If the object's space refractive index is 4/3, an approximation for water, then the second focal length f′ is negative and equal to three times the dome radius. This expression for f′ is the virtual image distance for an object at a principal distance D′ of infinity in water and a sensor or observer in air. A virtual image is one that has an apparent position from some vantage point but that does not occupy a real position in space, i.e., no aerial image exists which can be recorded on film at that location. In this instance, the image appears to be located a distance of 3r toward the object from the dome apex or air-water interface. This is known as the principal image distance d′. Object-image positions for this hypothetical case are plotted in figure 14.12. Dome radius is positive when the center of curvature is in the air medium and negative when in the water medium. Virtual images occur at the negative principal image distances. For the dome viewports described herein, the dome's positive radius portion is enlarged in figure 14.13. In both figures the distances of the principal object and image are in terms of unit measures (reference 4.14). Any desired units can be applied to the curves; however, it is of value to consider a dome of one-unit radius as in figure 14.13. This indicates that all images will fall between the dome-water interface and −3r from that interface for conjugate objects located between the interface and infinity.

The foregoing hypothetical representation helps form a mental impression of dome imagery. To complete the exact paraxial analysis of any existing dome viewport, the following conventions must be established:

a. Light travels from left to right.

b. All radii are positive when the center of curvature is to the right of the surface and negative when it is to the left.

c. All object distances are positive when they are measured to the left of a reference point and negative when they are measured to the right of a reference point.

d. All image distances are positive when they are measured to the right of a reference point and negative when they are measured to the left of a reference point.

e. The first and second focal lengths are positive for a converging lens system and negative for a diverging lens system.

f. All object and image dimensions are positive when measured upward from the optical axis and negative when measured downward.

A lens system or single-lens component can be described by the location of six points along the optical axis. These are the cardinal points of the lens:

F_1 and F_2, first and second focal points

P_1 and P_2, first and second principal points

N_1 and N_2, first and second nodal points.

The first and second designations are related to parallel rays on the right and left sides of the lens, respectively. Focal points are located where parallel rays are focused or crossing the axis of positive lenses and where the rays appear to diverge from the axis of negative or diverging lenses. Parallel rays refracted through the system can be described as having been deviated at their intersection with the refracted ray. The intersections of all such parallel rays on one side of the lens with their refracted rays form a surface that is perpendicular to the optical axis at the principal point. In this first-order optics region near the axis, the surface is a plane tangent to the actual extended principal surface. Each set of parallel rays thus has its corresponding principal and focal points designated first or second in accordance with the side where the parallel rays are focused.

When a ray is not parallel to the axis, does not pass through the focal point, and emerges parallel to itself on both sides of the lens, it is said to cross the axis through the nodal point. If a lens has the same medium on both sides, then each principal point coincides with its corresponding nodal point. Separation of these points occurs with the dome viewport, as the media are water and air. Figure 14.14 depicts the cardinal points F_1F_2, P_1P_2, and N_1N_2 of the dome port. They are the first and second focal, principal, and nodal points, respectively.

The general formula for a thick lens in first-order optics can be applied to the dome viewport to obtain

$$\frac{n}{f} = \frac{n''}{f'} = \frac{n'-n}{r_1} + \frac{n''-n'}{r_2} - \left[\frac{n'-n}{r_1} \cdot \frac{n''-n'}{r_2} \cdot \frac{r_1-r_2}{n'} \right] \quad . \tag{4.19}$$

where

f = first focal length

f' = second focal length

n = refractive index for object space

n' = refractive index for the dome

n'' = refractive index for image space

r_1 = dome outer radius

r_2 = dome inner radius.

Letting the image space be air ($n'' = 1.0$), then

$$f' = \frac{1}{\frac{n'-n}{r_1} - \frac{n'-1}{r_2} + \left[\frac{n'-n}{r_1} \cdot \frac{n'-1}{r_2} \cdot \frac{r_1-r_2}{n'}\right]} \qquad (4.20)$$

and

$$f = nf'. \qquad (4.21)$$

These first and second focal lengths are negative for the dome in water, and as shown in figure 14.14 they are measured from the first and second nodal points at the dome's center of curvature. The location of the first and second principal points to the left of the nodal points is expressed by

$$N_1 P_1 = \frac{f(n-1)}{n} \qquad (4.22)$$

$$N_2 P_2 = f'(n-1). \qquad (4.23)$$

Negative values indicate P is to the left of N, and positive values place P to the right of N. First-order object and image nodal distances (D and d, respectively) are specified relative to the nodal points:

$$d = \frac{nDf}{nD - f} = \frac{nDf'}{D - f'} \qquad (4.24)$$

$$D = \frac{df}{n(d-f)} = \frac{df'}{d - nf'}. \qquad (4.25)$$

The sign convention used herein produces positive numbers for objects that are a distance D to the left of the dome as in figure 14.14. Since positive numbers for distance d are also by convention located to the right of the lens and give inverted images, the image's negative distance d places the upright virtual images to the left of the dome. This results from the negative sign of the dome's focal lengths f and f' in equations 4.20 and 4.21. These first-order object and image nodal relationships are very useful, but it must be remembered that they apply only to the very thin bundle of rays near the optical axis (reference 4.14).

Evaluation of the dome's port imagery shows that all objects in water are seen relatively close to the dome. If the images are observed from the center of the dome, then there is no distortion and only a minimum of image aberration, since all rays from the object are at or near normal to the dome's refracting surface.

14.3.3 Binocular Viewing with a Single-Dome Viewport

Stereopsis is the process of combining physiological actions of binocular viewing with psychological interpretations of the brain to produce steroscopic vision. To be more specific, stereopsis is the perception of relative depth which arises from the presence of disparities in the retinal images. It is perhaps the single most important advantage of having two, frontally placed eyes. Stereopsis is not synonomous with binocular vision: Despite the continuous presence of double images, which can be seen if things are observed closely, we generally have a single perception of visual space, i.e., we perceive only one of all objects when in reality two images in double vision actually exist. A complete description of the process of stereopsis is beyond the scope of this report; however, basic information should be discussed.

When images are not in proper register on the two retinas, double images are seen. Convergence of the eyes is the adjustment for variations in distance to objects. With proper fusion (convergence and focusing) the brain provides single vision. Certain disparity, or displacement variations of the image from the fixation point on the retinas, produces stereopsis, but excessive disparity can cause either double vision or a monoscopic effect, i.e., the brain recognizes one or the other of the two images. In some cases this "monoscopic" effect actually produces sufficient depth perception to be considered stereopsis. In such cases the image rapidly varies between single and double vision as effort is applied to maintain fusion. In actuality double vision exists for all objects outside the fusional areas of the retina; however, the brain tends to ignore images that are not in focus. (This is the two images in double vision referenced in the preceding paragraph.) It is the physiological process of fusion of the two focused images that permits the psychological factor of attention to take place in the brain and provide depth perception (reference 14.17).

Instrument designers know how much disparity can occur in images for stereoscopic vision, e.g., the old parlor stereopticons. In binocular viewing the fusion process permits errors to exist in image rotation and displacement and even allows disruption of the accommodation-convergence relationship (reference 14.18). When these tolerances are excessive, the observer's performance varies from discomfort to double vision (diplopia). Tolerance to image disparity increases with distance to the fixation point. Therefore, it is understandable that the abnormal distances to the virtual image encountered when viewing through a single underwater dome viewport can produce problems for binocular viewing.

The virtual optical images seen from a dome port become the objects observed by sensors in air behind the dome. Because of their short virtual image distances, small domes with an inside radius of 50 to 200 millimeters produce abnormal combinations of convergence and focus for human eyes, normally separated approximately 50 to 70 millimeters. If the underwater scene is sufficiently detailed, the fusion problem is reduced; however, if the observer is watching a single distinct object on a clear, smooth sandy bottom in shallow water with sufficient sunlight, then the chances of double vision through a small dome are excellent. The distance separating the observer's eyes precludes both eyes from having a vantage point at the dome's center or along the same dome radius at any one time, i.e., only one eye can look down one dome radial line-of-sight. If the dome's inner radius

is small enough, then the port aperture D_i may even preclude image acquisition by both eyes; therefore, the smaller dome ports have limited use for binocular viewing. They are used mainly for monoscopic sensing in photography or instrumentation. Stereoscopic perception via binocular viewing through a single-dome viewport requires the inner radius (dome-air interface) to be relatively large in comparison to the observer's eye separation.

One undersea vehicle which is good for minimizing the limitations of spherical window viewing is the U.S. Navy's NEMO (Naval Experimental Manned Observatory DSV #5). The NEMO is essentially two large hemispherical dome windows joined together to create a transparent spherical hull large enough to transport two occupants. Observers inside the acrylic hull have an almost unlimited view of the undersea environment. Metal hatches at the two poles of the sphere present the only obstructions to vision. Since the inception of NEMO, the Johnson-Sea-Link and MAKAKAI submersibles have been built with acrylic spherical hulls similar in size to that of the NEMO, approximately 30 inches (76 centimeters) inside radius.

Navy studies of the virtual images seen from within the NEMO provide good insight into the optical imagery of a dome air-water interface (reference 14.19). For image evaluation data, the hull is considered to be a perfect sphere without any obstructions to vision, e.g., hatches or cement joints in the acrylic. The data in figure 14.15 represent two-dimensional cross-sections of the observer's image domain for all planes passing through the eye position x and center of the sphere C. To help visualize what these plots represent, consider drawing them full size on the floor of a large room. The scale for this hypothetical layout is measured in feet and the sphere's center is the origin of the plot coordinates. The ordinate and abcissa are not drawn through the origin, but are placed at the edge to maintain clarity. Now let an observer lie on the "floor layout" so that a point midway between his eyes occupies a position at x so that a rope laid on the floor in the shape of any one of the image's locus lines can be seen. By moving about inside the limit of the acrylic sphere's radius, it is assumed that with both eyes an observer at x can see any point on the selected image's "locus rope" on the floor. The real object's location in water for this image point can be found by moving along a radial line from the sphere's center through the rope's image point, a distance from the sphere's center that is equal to the R_{co} number on the particular image's locus plot used to place the rope on the floor. The locus of the actual object in water could thus be represented by another rope placed in a true circle on the floor at a radius of R_{co} from the sphere's center.

If the NEMO's image plots are rotated about the coordinate abcissa, a line through the eye's position and sphere's center, a three-dimensional plot of the spatial virtual image's locus surfaces is generated. The coordinate scales can also be used to measure straight-line distances from the eyes to any image point on the locus lines.

It is important to understand the true representation of the image lines. Less confusion will result if the reader disregards the fact that the virtual image's locus lines seem to be plotted in water and treats the entire plot as if it exists in the air space of the observer. The basic premise of a virtual image is that it appears to exist in the medium and spatial domain of the observer. The acrylic sphere in figure 14.15 can thus be considered as the limit of observer's movement in the air medium and the only reference to water space is the object's radial distance R_{co} on each image's locus line.

Reference is made in figure 14.15 to "best" and "worst" eye orientations. The definition of the terms refers to the orientation of a line between the observer's eyes. Relating again to the hypothetical full-size floor plot, an observer is in the best orientation when lying on the floor with his eyes at x so that the line between them is perpendicular to the floor, i.e., the observer is lying on his side. If the observer stands in a pit in the floor with his eyes straddling the x, then the line between his eyes is theoretically in the floor plane of the plot, which is considered the worst orientation. In either orientation, the observer must maintain the correct position of the line between his eyes and rotate his body in a manner to allow viewing of all image points on the image's locus. The second implication in the connotations of best and worst orientations relates to the distorted perceptual distance to the object in water which is created by the close proximity of the virtual image. Ray traces in the Navy studies show that the best orientation has a slightly greater virtual image distance than does the worst orientation. However, the difference in these comparative distances is so small in relation to the actual distance of the object in water that the orientations might be more accurately described as having least and most range deceptions, respectively. In both cases the actual deception in the virtual distance of the image is quite large.

The NEMO viewing study gives additional merit to the dome viewport, for the ray trace data also show little distortion, even off the optical axis where first-order optical analysis is invalid. Figure 14.15F helps understand the image distance relationship of the flat window in equation 14.15 if the sphere's radius is considered large enough to represent a flat window tangent to the sphere at the inside surface where the image line-of-sight is refracted by the acrylic-air interface. Equation 14.15 shows that the image's distance from the air interface approaches zero as the angle of refraction in air approaches 90 degrees (1.57 radians). The image's locus lines in figure 14.15F all fall noticeably close to the sphere, where the NEMO's refraction angle is high because of the eye's position close to the inside surface.

14.4 RAY TRACING AND LIGHT PIPES

Analysis of light for engineering purposes is usually conducted with ray theory related to the wave propagation of light. In an isotropic medium (a uniform refractive index in all directions), light waves from a point source travel in an ever increasing spherical radius. If the distance of travel is far enough, the radius can be considered infinite and the wave is a plane. If one point on any wave is followed through an isotropic medium, it will travel a straight line. This line is called an optical ray.

When rays of a wave cross from one medium to another of differing refractive index, the velocity is altered along with the possibility of changes in wavefront radius and direction of travel. If the interface between the media is accurately shaped to a specific curve — spherical, aspherical, or plane — then the wave behaves in a very predictable manner. Any ray will have a slope that produces an angle of incidence at the media interface. Snell's law can be applied at the interface to calculate ray refraction angles. In optical systems having numerous elements of varying curvature and separation, the geometry of the ray path becomes somewhat complex. However, desk-top calculators with

reasonable program and memory capacities can easily compute and store ray trace information. This type of ray analysis is not normally required for basic dome viewport design. A good set of ray trace equations can be found in reference 4.1 (Smith), and there are other optics publications that discuss analytical ray tracing. In any case, the user is cautioned to observe sign conventions of the particular source.

When evaluating the basic behavior of optical rays through a window, it is often convenient to plot the rays directly on a scale drawing of the window. Ray slope and location can then be calculated and transferred to the drawing. There are numerous graphical ray-trace techniques which produce satisfactory accuracy for this level of design. As early as 1926, J.H. Dowell used graphical ray tracing in London. His work is difficult to locate, but John Strong has published some of Dowell's work (reference 14.20). Chan Street has expanded the Dowell technique in a valuable volume published by the Society of Photo-Optical Instrumentation Engineers (reference 14.21). It should be mentioned here that a graphical ray analysis of complex optical systems often produces clear indications of performance with much less effort than is possible using computer analysis techniques.

14.4.1 Dowell Ray Trace

The data in figure 14.16 depict the steps required to execute a graphical ray trace through a dome viewport by using Dowell's technique. Ray 1 enters the dome at a known point with a known slope and is traced from the water through the acrylic into air. The convenience of this procedure is that all construction lines can be in another area of the dome drawing or on an overlay sheet. The basic tool is a drafting machine or a similar device for making parallel lines.

Construction begins with drawing three arcs to any scale on an auxiliary diagram near the dome layout. Each arc's radius represents a scale value of the refractive index of one medium. The three arcs in figure 14.16 represent air, water, and acrylic refractive indices. Ray 1 is in water; thus it is drawn in the index diagram parallel to the same ray 1 in the dome layout. It goes from the center of the index diagram to the arc representing the medium of the ray — water. This is the first rule of the procedure: A ray in any medium of the layout is always parallel to a ray slope line from the index diagram's center to the corresponding index arc of that medium.

The slope is next established for line 2 in the scale layout. It goes from the ray intercept at the refracting surface to the center of curvature of that surface. This slope is transferred (in parallel fashion) for drawing line 2 from the end of line 1 at the index arc of water. From where line 2 intersects the index arc of the next medium, acrylic, a line to the center of the index diagram represents the slope of the refracted ray in the next medium. This is the second rule of the procedure for ray refraction at a surface: In the index diagram, ray slope lines of corresponding incident and refracted rays are connected at the index arcs of the two media by a construction line drawn parallel to a radial of the optical refracting surface at the point of refraction.

Having obtained the slope of the refracted ray 3, the procedure is repeated to provide ray 5 in air. The construction lines are numbered in the index diagram in sequence with the parallel lines or rays of the dome scale layout.

It is of interest to note what happens to the refraction of a ray between air and a denser medium when the angle of incidence in air approaches 90 degrees (1.57 radians), a physical limit. Corresponding to the 90-degree (1.57 radians) incident angle is an angle of refraction known as the critical angle of the medium in contact with the air. The critical angle will always be an angle of incidence less than 90 degrees (1.57 radians). Snell's law is applied to compute the critical angle by using an incident angle of 90 degrees (1.57 radians) with an index of refraction of 1.00 for air:

$$N_{air} \sin 90° = N' \sin I_c \tag{14.26}$$

$$I_c = \sin^{-1} \left(\frac{1}{N'} \right) \tag{14.27}$$

The significance of the critical angle lies in the fact that light may travel in either direction along a refracted ray. If the light moves from the dense medium into air, it is quite possible to have the angle of incidence in the dense medium exceed the critical angle. In such a case all rays with incidence beyond the critical angle of a material will be totally reflected, provided air is the adjacent refracting space. The total internal reflection condition is sometimes used to achieve specific results, e.g., in prisms for internal beam deflection and in light piping to stop the random rays from traveling through the optical piping medium.

14.4.2 Light Pipes

A knowledge of ray tracing and of the effects of the critical angle forms the basis for understanding applications of light piping. Because acrylic is an excellent medium for light piping, it is in common use for directional control of light rays to transmit illumination through pressure hulls (reference 14.22). The rays in a large light pipe take random paths that do not form or transmit images.

When light flux is to enter a light pipe from a single source, the distance of the source from the surface determines the relative amount of energy entering the piping, assuming the entrance area to be constant. If a hot source is positioned too near an acrylic light pipe, softening may occur. With tolerable heating, the light will enter a light pipe and react as shown in figure 14.17. Contrary to popular speculation, the convergent cone does not "funnel" the light to the exit end. Some light escapes from the side of the convergent pipe because rays do not remain beyond the critical angle and are transmitted through the light pipe surfaces. Although some of the rays do arrive at the exit of a convergent pipe by total internal reflection or by straight-line transmission, they are few.

Since light rays can travel in either direction reversing ray travel in the convergent pipe must be considered. In this case, the pipe becomes a divergent pipe similar to the one in figure 14.17, except that it can now accept light input at specific points and incidence angles to allow the rays to be retained by total internal reflection and piped to the exit end. What is accomplished by the additional lighting of the divergent pipe at the correct side angle is an effective increase in the input acceptance area of the pipe, which now produces more flux at the exit than is possible with end lighting only.

The surface quality of a light pipe is of prime importance for the occurrence of internal reflections. Irregularities will absorb the light, transmit it out of the medium, or reflect it back in the wrong direction. However, these surface effects are not always undesirable, as they are often used to achieve desired control of all or part of the light in the piping.

If the light pipe is curved to fit a particular design, the radius of curvature can cause an excessive light loss. Figure 14.18 depicts the results of bending a rectangular cross-section. The minimum radius of twice the thickness for rectangular sections must be increased for round sections. In general, bends should be avoided since some light is always lost in any bend radius. If bends must be used, the radius must be kept at the maximum.

When the light arrives at the end of a light pipe or is extracted anywhere along the path, its exit is also dependent on surface quality. A rough or frosted surface at an exit end produces diffuse emission on the surface area. If a rough surface is placed on the pipe's wall prior to the exit, light will be emitted at that point and the remaining light piped to the end will be reduced accordingly (reference 4.6).

14.5 COMPARISONS AND CONCLUSIONS

Selecting a window configuration for any undersea application requires compromise, regardless of the final solution. Flat windows limit the field-of-view and cause considerable aberrations, and dome windows form images abnormally close to the port. Both types have curvature in the virtual image as seen from the air medium. The flat window offers slightly better stereoscopic perception when used as a single port, and the limited viewing angle can be overcome. The dome window seems a natural choice in monoscopic sensing through smaller viewports as in photography, since it offers low distortion and good optical characteristics when properly matched to the sensor optics. Acrylic hull penetrations for the purpose of transmitting illumination can use either type of window blended with light pipe theory and diffusers. Considering the successful mechanical history of flat and dome acrylic windows, it is certain that both concepts will continue to see wide use in hydro-scope equipment.

14.6 REFERENCES

14.1   Smith, W. J., *Modern Optical Engineering*, McGraw-Hill: New York, 1966.

14.2   Thomas, W., *SPSE Handbook of Photographic Science and Engineering*, John Wiley. New York.

14.3   Jenkins and White, *Fundamentals of Optics*, McGraw-Hill: New York, 1957.

14.4   Agranoff, J., *Modern Plastics Encyclopedia*, McGraw-Hill: New York, 1966.

14.5   Hertzberger, M., *Opt. Acta*, vol. 6, pg. 197, 1962.

14.6   E. I. du Pont de Nemours and Company, *Lucite Acrylic Resins Design Handbook*, 1968.

14.7 Duntley, S. Q., "Underwater Visibility and Photography," *Optical Aspects of Oceanography*, edited by Jerlov and Nielson, Academic Press: New York, 1974.

14.8 E.G.&G. International, Manual B-3405A, "204B Underwater Camera," by H. E. Edgerton, December 1968.

14.9 Edgerton, H. E., "Underwater Photography with Strobe Lighting," *Optical Spectra*, pg. 3-17, January 1967.

14.10 Martens, L. E., *In-Water Photography and Theory and Practice*, Wiley-Interscience: New York, 1970.

14.11 Scripps Institution of Oceanography, SIO Reference 76-1, "Index of Refraction of Sea Water," by R. W. Austin and G. Halikas, 1976.

14.12 McNeil, G. T., "Metrical Fundamentals of Underwater Lens System," *Optical Engineering*, vol. 16:2, pg. 128–139, March-April 1977.

14.13 North American Aviation, "Principles of Underwater Viewing," by F. J. Hetlinger and D. H. Pickrell in *Optimum Manipulator Systems for Manned Submersibles*, 31 March 1966.

14.14 Photogrammetry, Inc., "Optical Fundamentals of Underwater Photography," by G. T. McNeil, 1972.

14.15 Van Sciver, W. J., "A Correcting Prism for Underwater Viewports," *Ocean Engineering*, vol. 2, pg. 228, November 1973.

14.16 Ivanoff, A., et al., *Optical System for Distortionless Underwater Vision*, U.S. patent 2,730,014, 10 January 1956.

14.17 Corliss, D. A., "Binocular Vision, I. The Law of Identical Visual Direction and the Geometry of Retinal Disparity," *Optical Engineering*, vol. 16:2, pg. SR47–SR48, March–April 1977.

14.18 Boeing Aerospace Company, "Design Handbook for Imagery Interpretation Equipment," by R. J. Farrell and J. M. Booth, 1975.

14.19 American Society of Mechanical Engineers, ASME Publication Number 70-UnT-A, "Optical Properties of a Spherical Plastic Underwater Observatory NEMO," by T. Trowbridge, 1971.

14.20 Dowell, J. H., "Graphical Methods Applied to the Design of Optical Systems," London Optical Convention, *Proceedings*, 1929.

14.21 SPIE, "Graphical Ray Tracing, An Advanced Text," by C. Street, 1974.

14.22 Naval Civil Engineering Laboratory, Technical Note N-1469, "Externally Generated Light (EGL) System for Hyperbaric/Hypobaric Chambers," by K. O. Gray, January 1977.
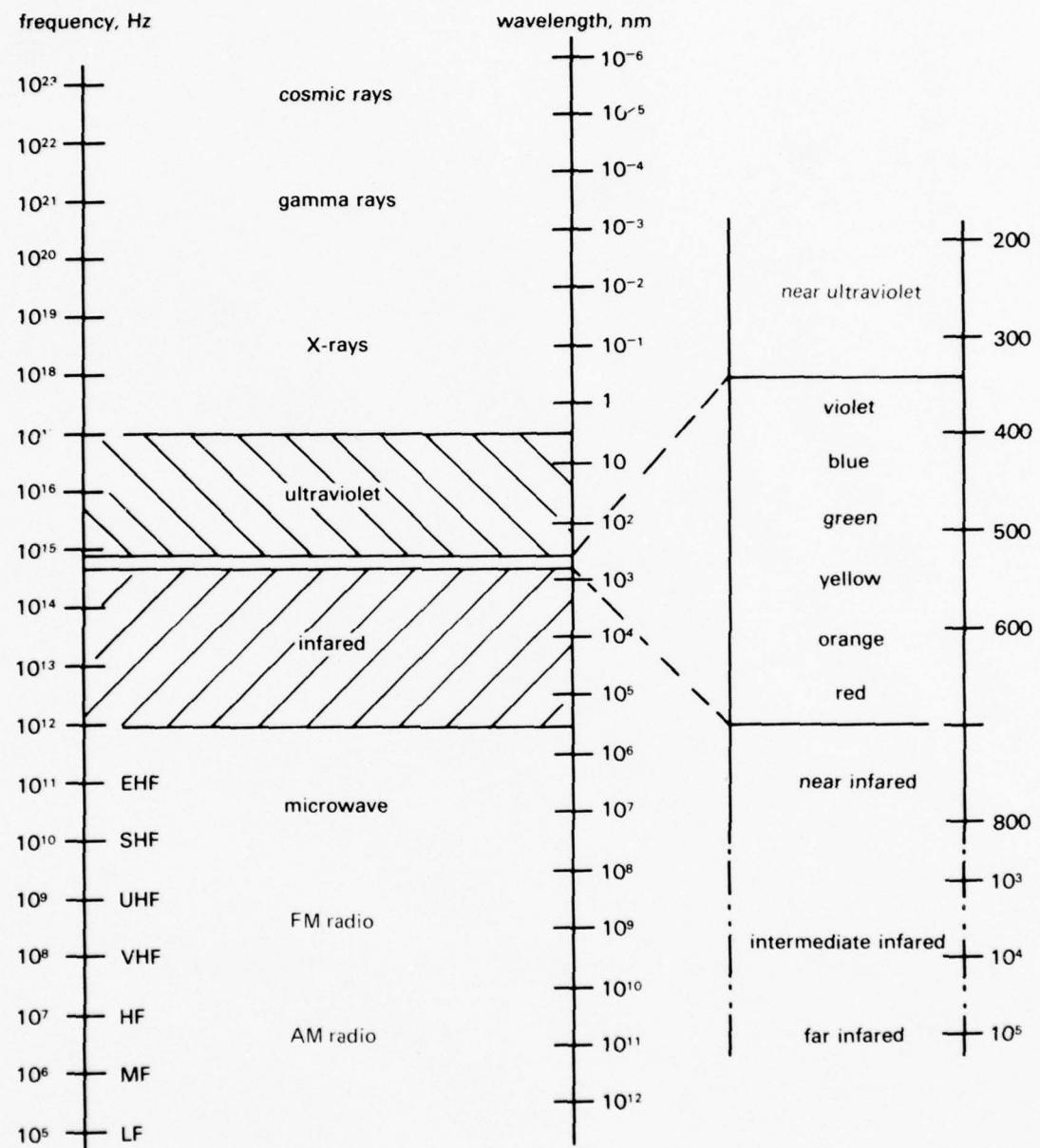
Figure 14.1. The electromagnetic spectrum.
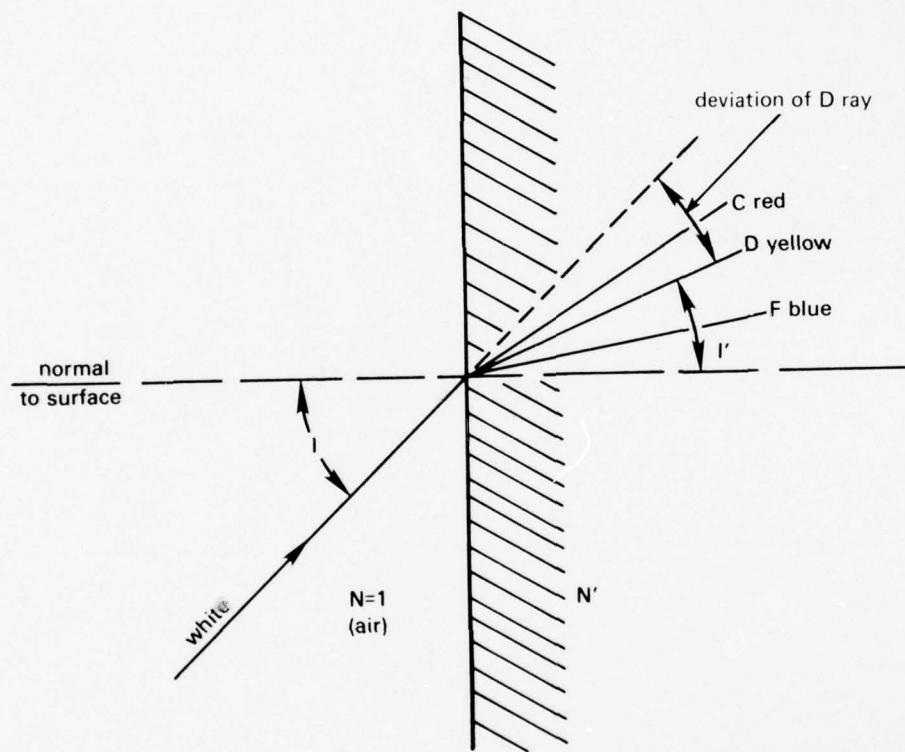
Figure 14.2. Dispersion of white light after refraction into a dense medium.
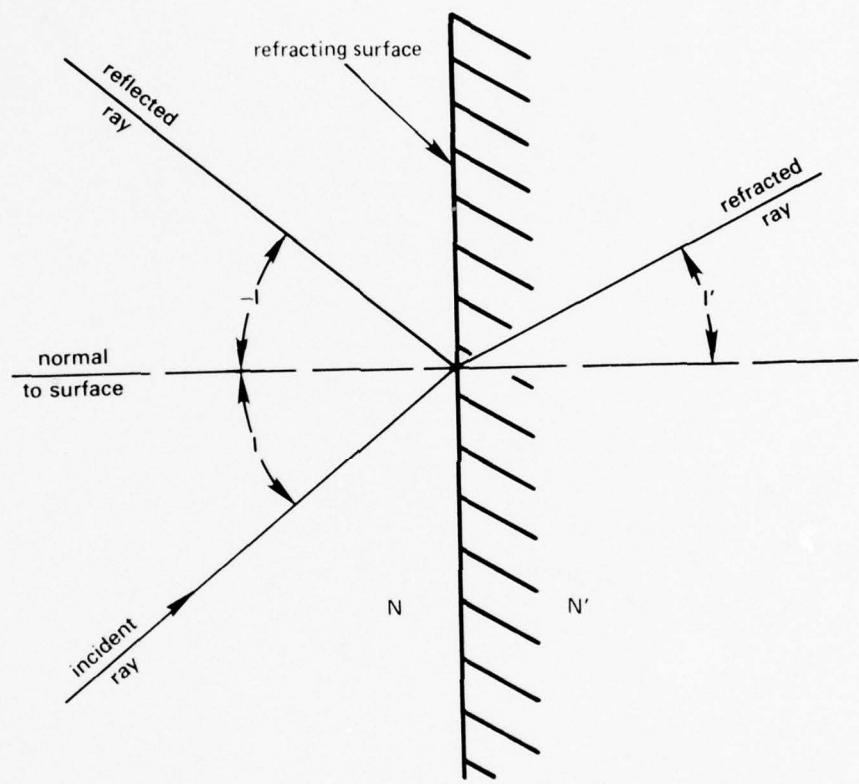
Figure 14.3. Refraction and reflection.
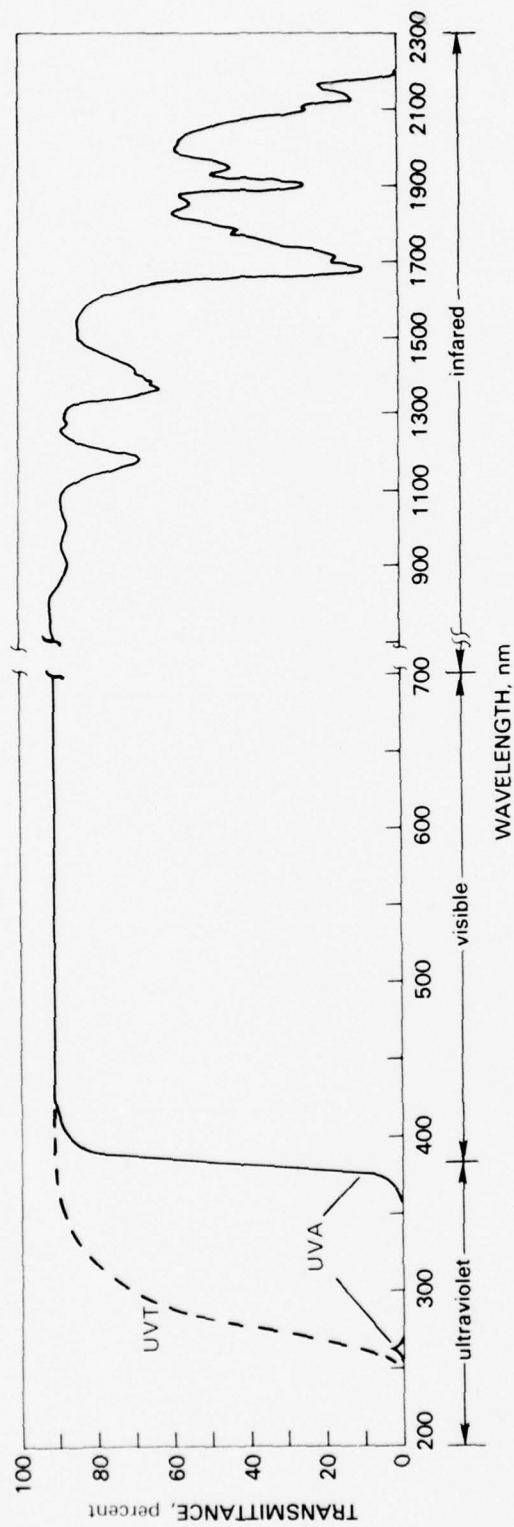
Figure 14.4. Light transmission properties of polymethyl methacrylate (acrylic) for 0.125 inch (3.2 millimeters) thickness. UVA is ultraviolet absorbing grade, and UVT is ultraviolet transmitting grade.

14-24
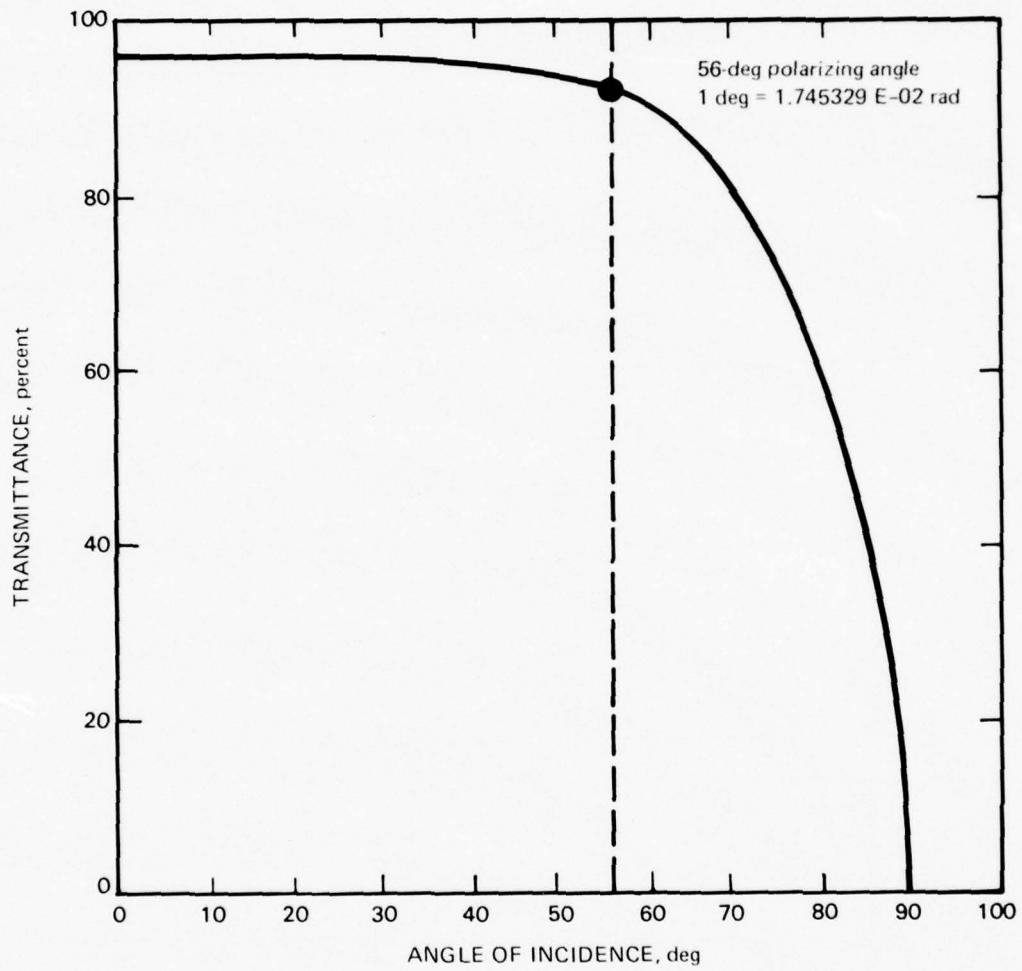
Figure 14.5. Light transmission and angle of incidence for polymethyl methacrylate (acrylic) in contact with air.

$$*N = \frac{1.61 \sqrt{ASA \times WS}}{F}$$

ASA = film speed
WS = light watt second
F = lens opening

example   ASA   WS   F
A   200   100   11
B   200   400   4
C   800   1000 2

1 ft = 3.048000 E-01 m

CAMERA AND LIGHT DISTANCE FROM SUBJECT, ft
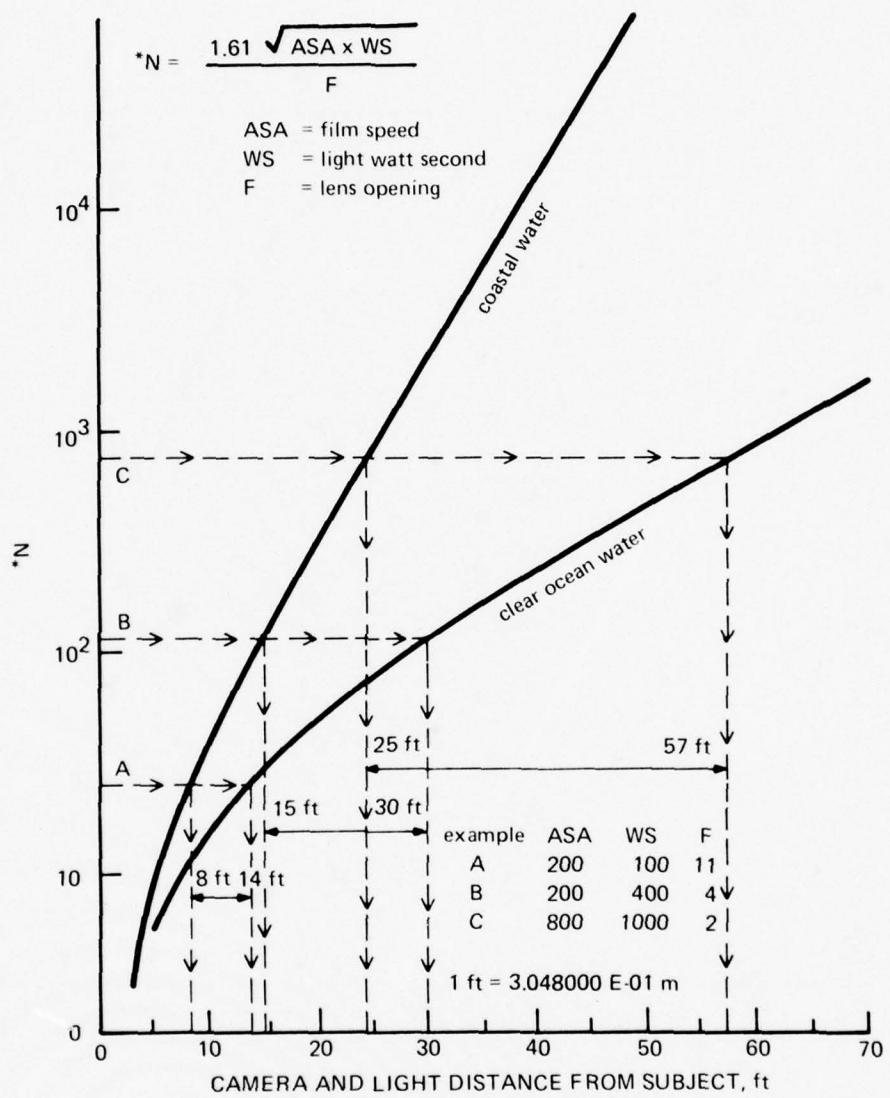
Figure 14.6. Deep-ocean photo guide for correct film exposure. The many variables involved in obtaining high quality deep-sea photographs indicate the necessity of a certain amount of experimentation by the user. The above guide, which is based on accumulated experience, provides a beginning point for such experiments.
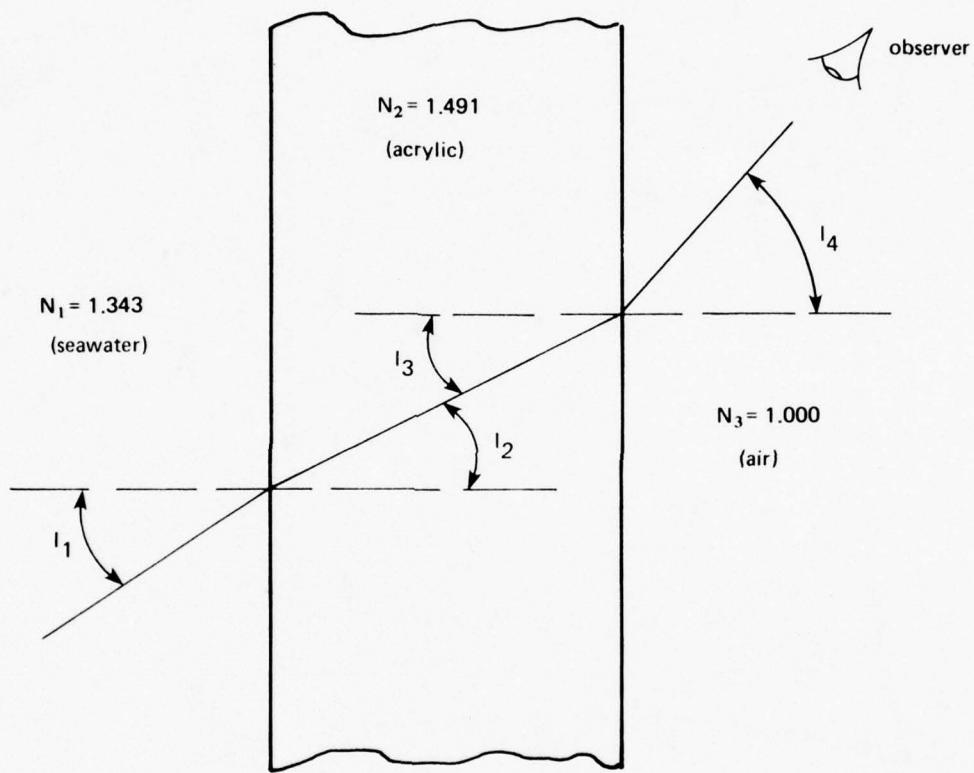
Figure 14.7. Flat port ray deviation.
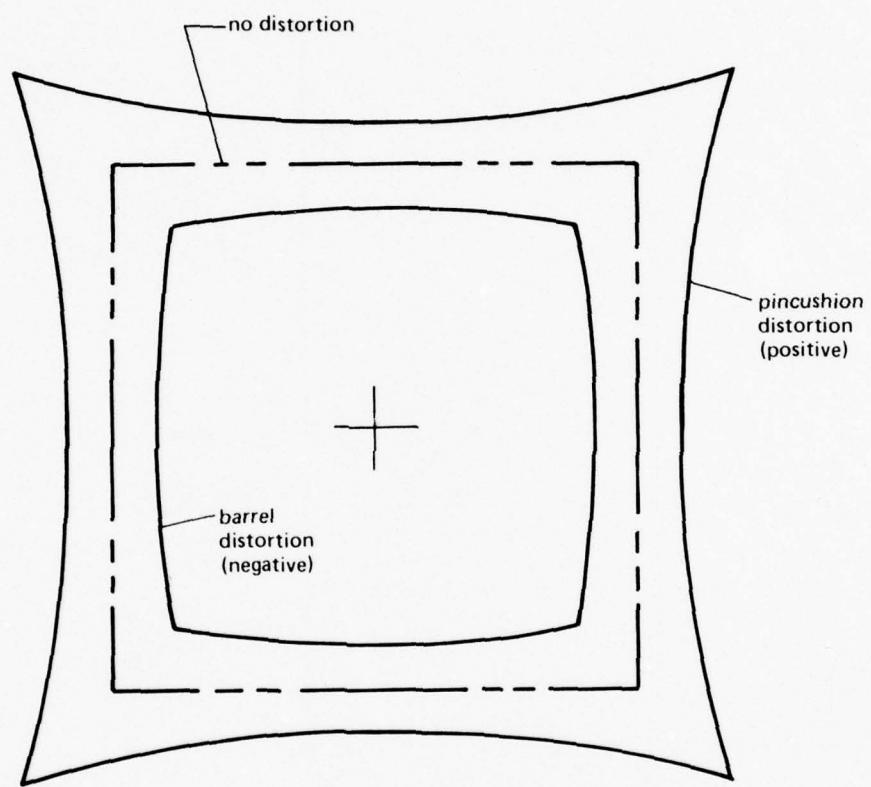
Figure 14.8. Camera image distortions.
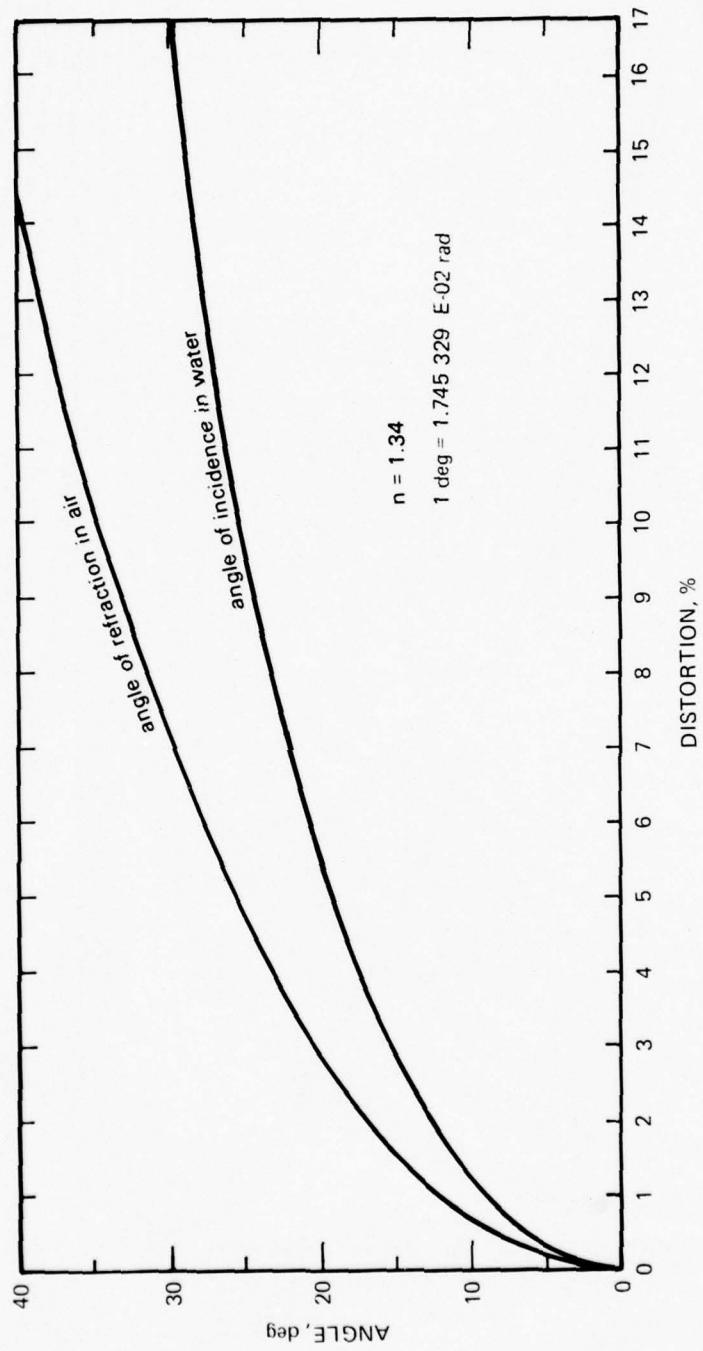
Figure 14.9. Distortion of a thin flat window.

14-29
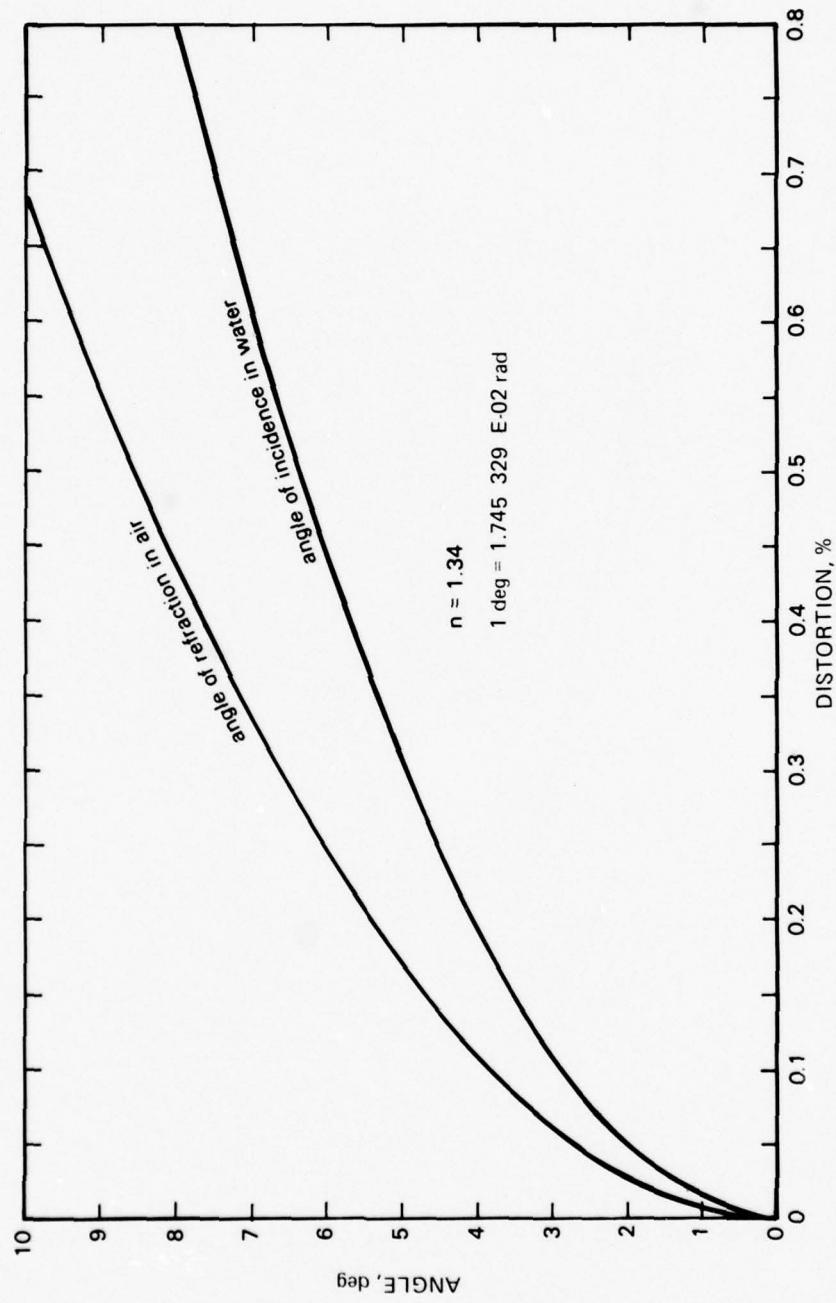
Figure 14.10. Distortion of a thin flat window near normal incidence and refraction.

14-30
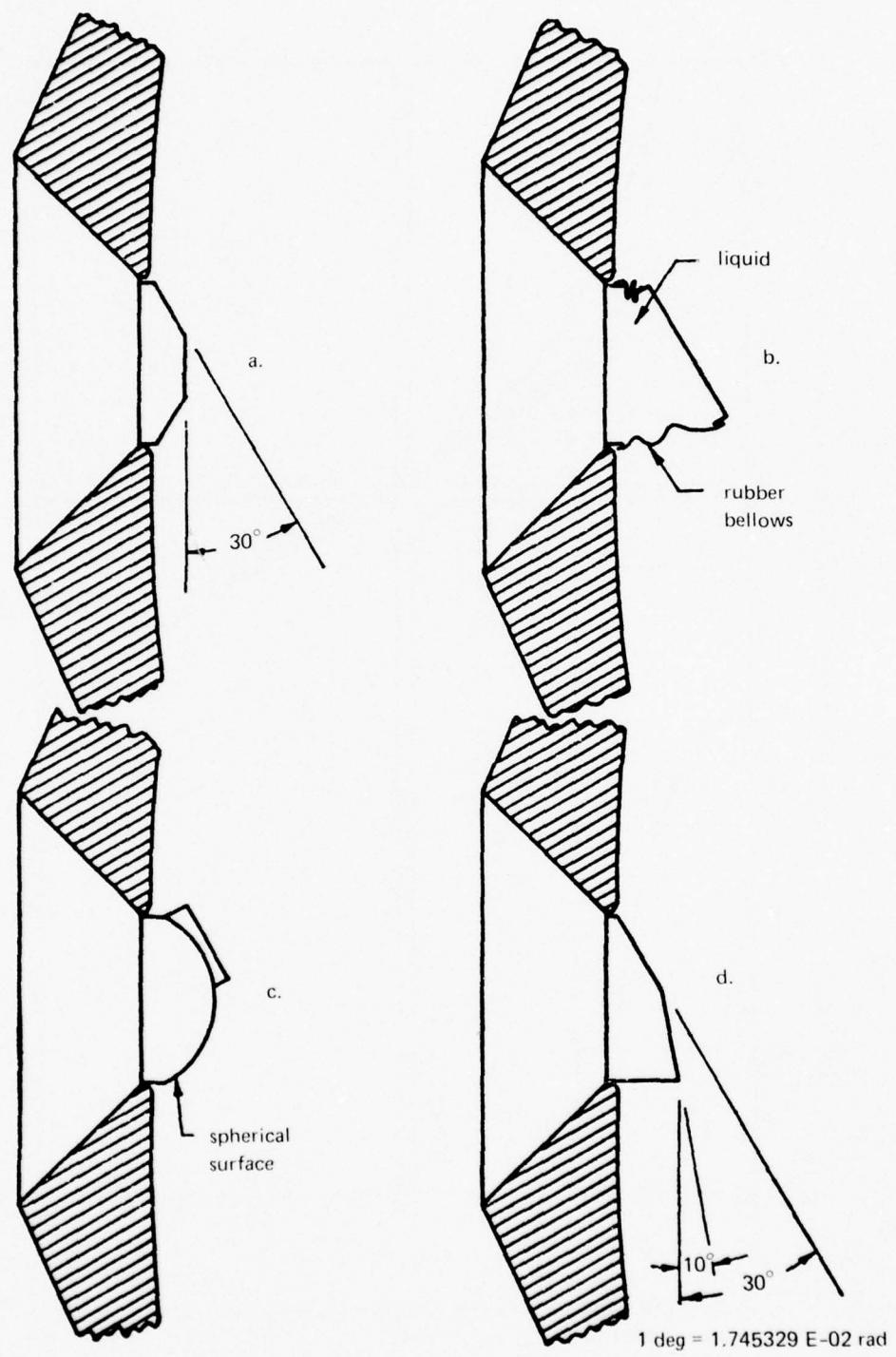
Figure 14.11. Optical devices to increase a flat window's field-of-view.
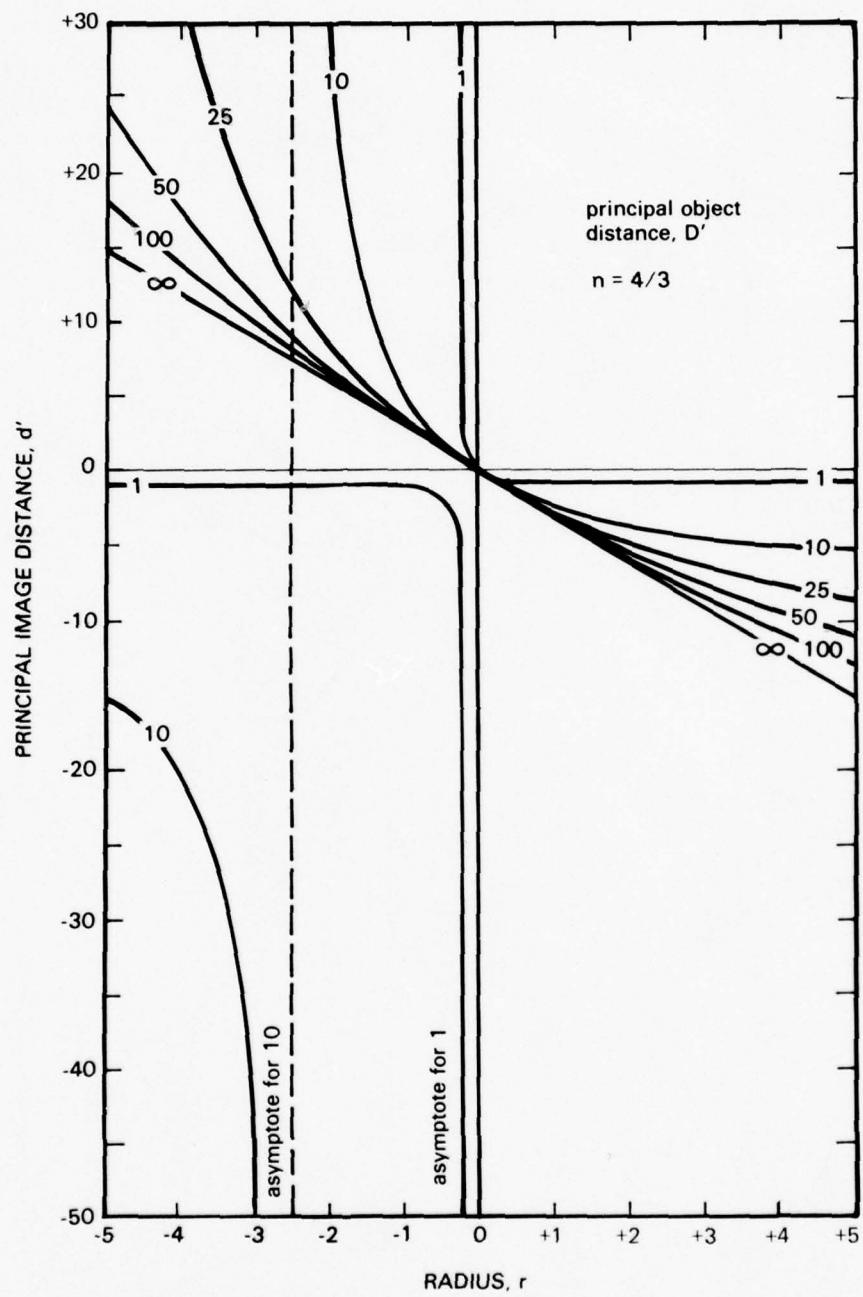
Figure 14.12. Distances of a thin dome window object and an image from the air-water interface.
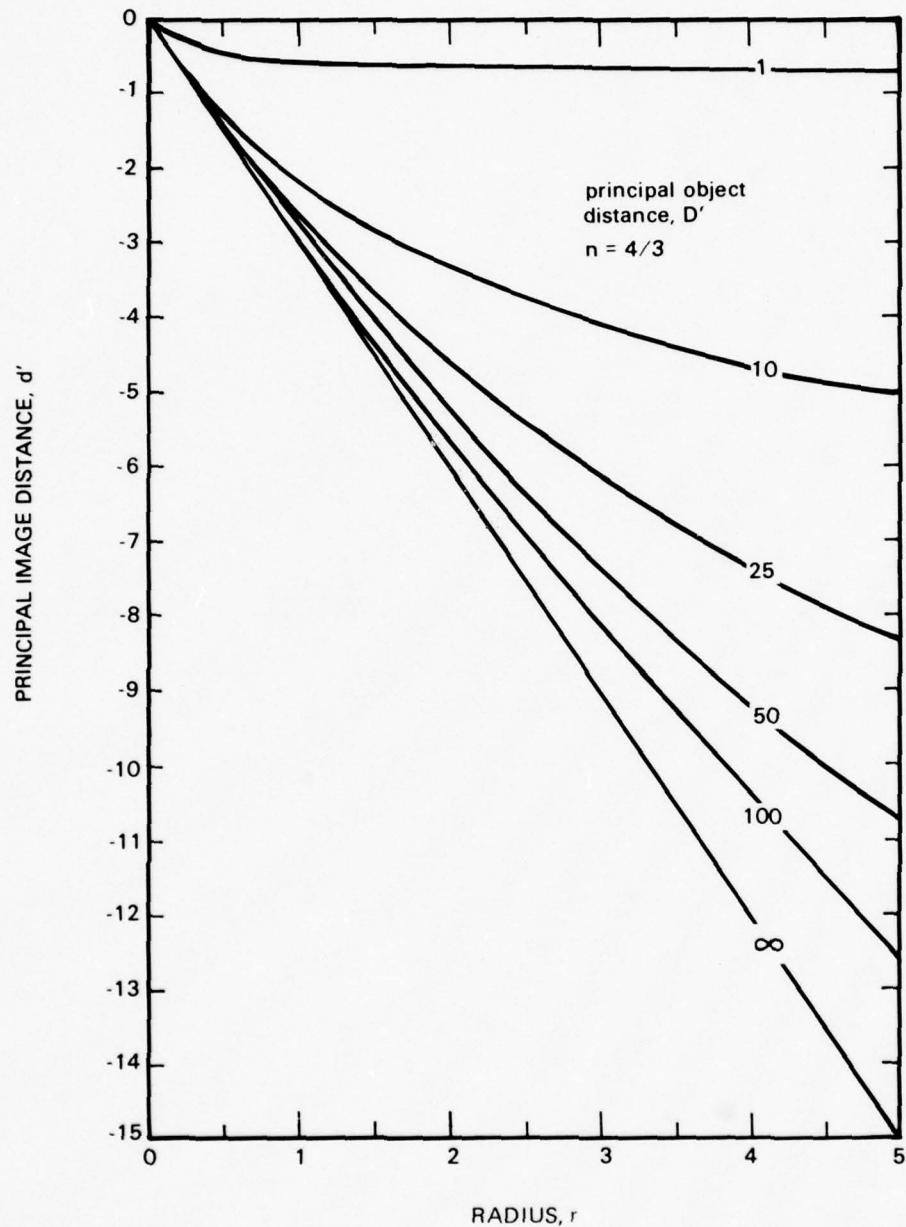
Figure 14.13. Distances of a thin dome viewport object and an image from air-water interface (positive portion of radius).
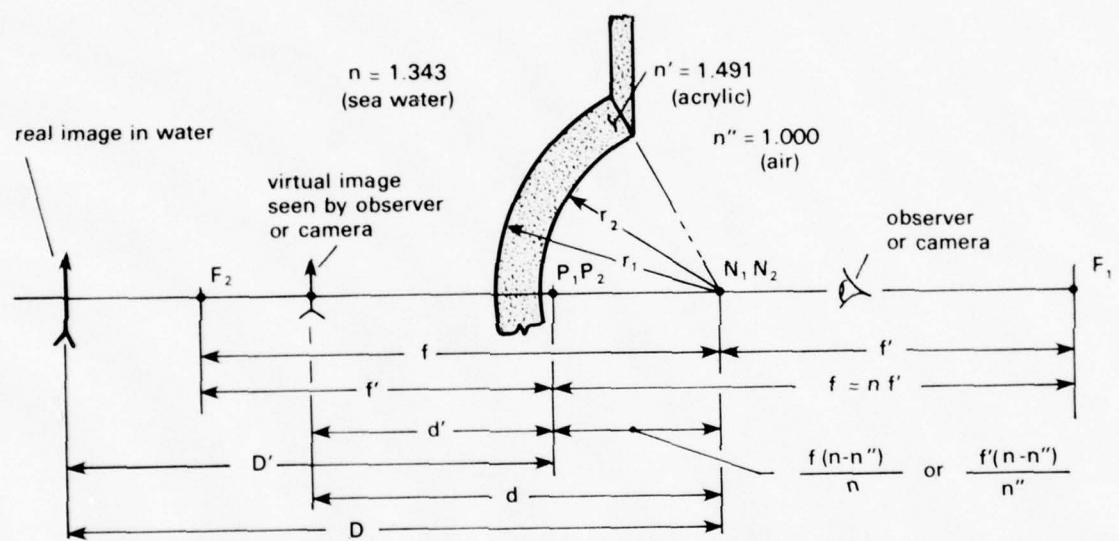
Figure 14.14. Relationships of dome paraxial object and image.

Part A. R_{ce} = 0.5 foot (0.2 meter); best eye orientation.
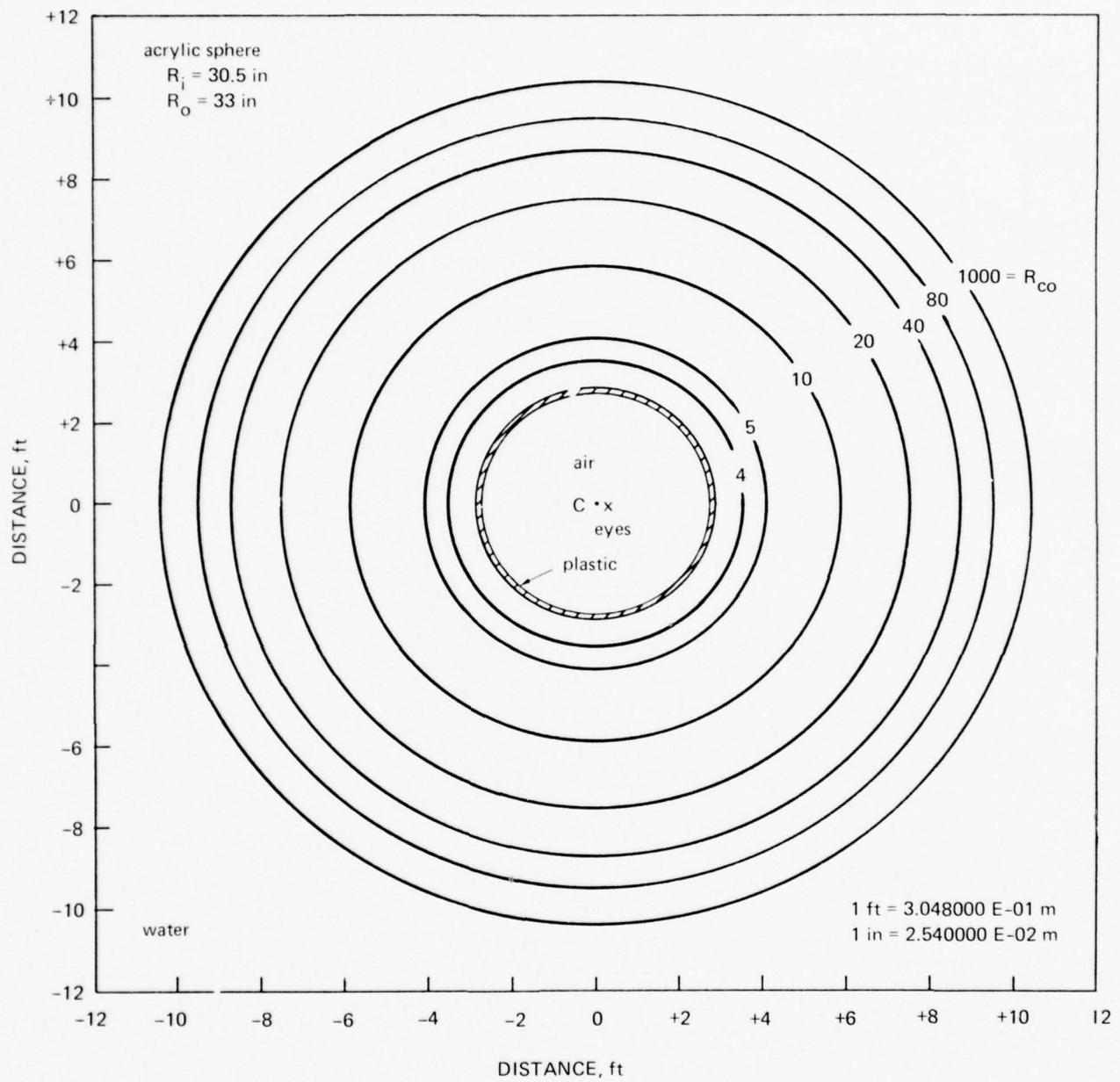
Figure 14.15. Virtual images of circles with radius R_{co} in water. Images are concentric with the center of the acrylic sphere in which the observer is located. The head of the observer, denoted by x, is positioned in the same plane as the circles, but at a distance of R_{ce} from the center of the sphere. (The outer and inner radii of the spheres are 33.0 and 30.5 inches (84 and 77 centimeters), respectively.)

14-35

Part B. R_{ce} = 0.5 foot (0.2 meter); worst eye orientation.

Figure 14.15. Continued.

14-36
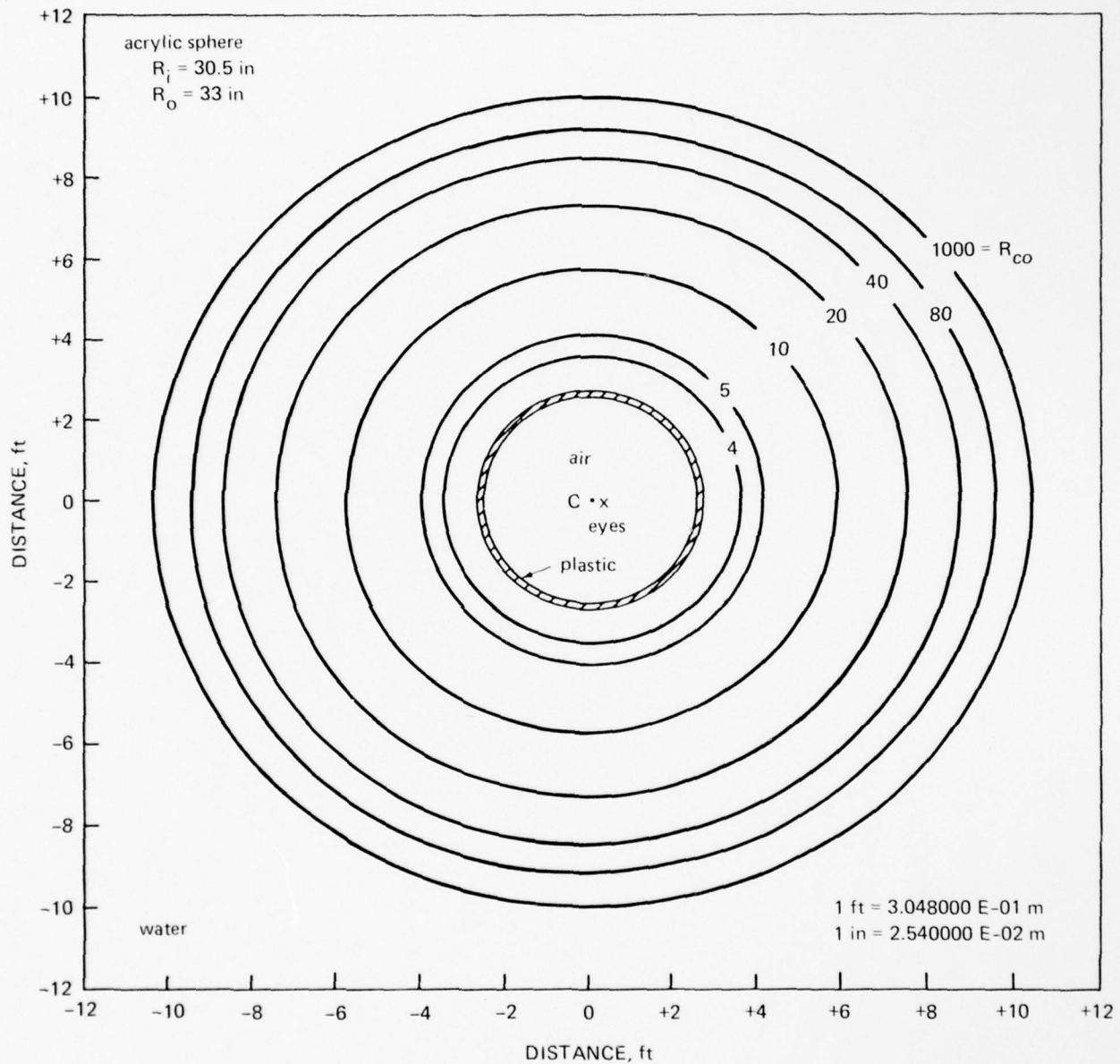
Part C. R_{ce} = 1.5 feet (0.5 meter); best eye orientation.
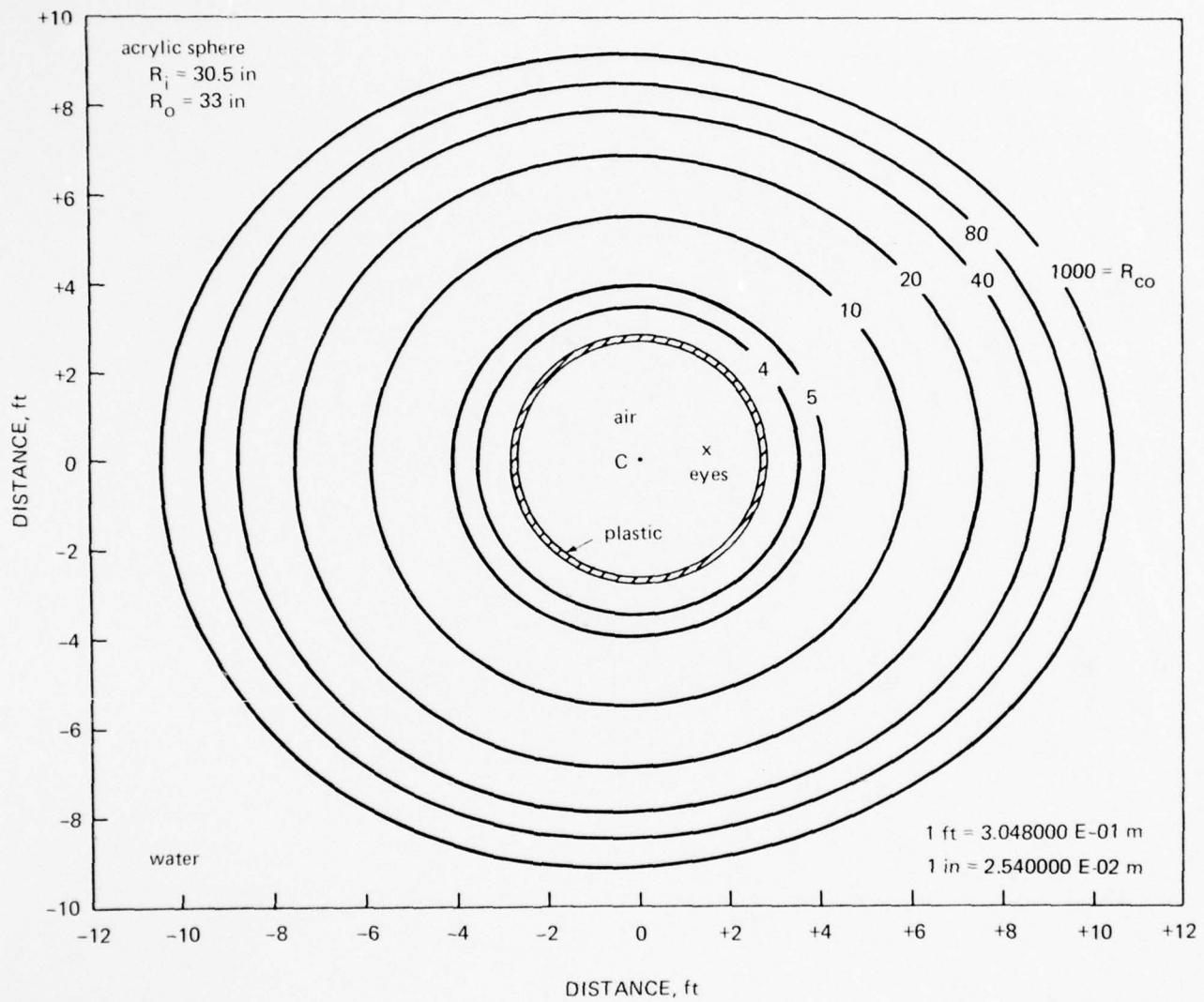
Figure 14.15. Continued.

Part D. R_{ce} = 1.5 feet (0.5 meter); worst eye orientation.
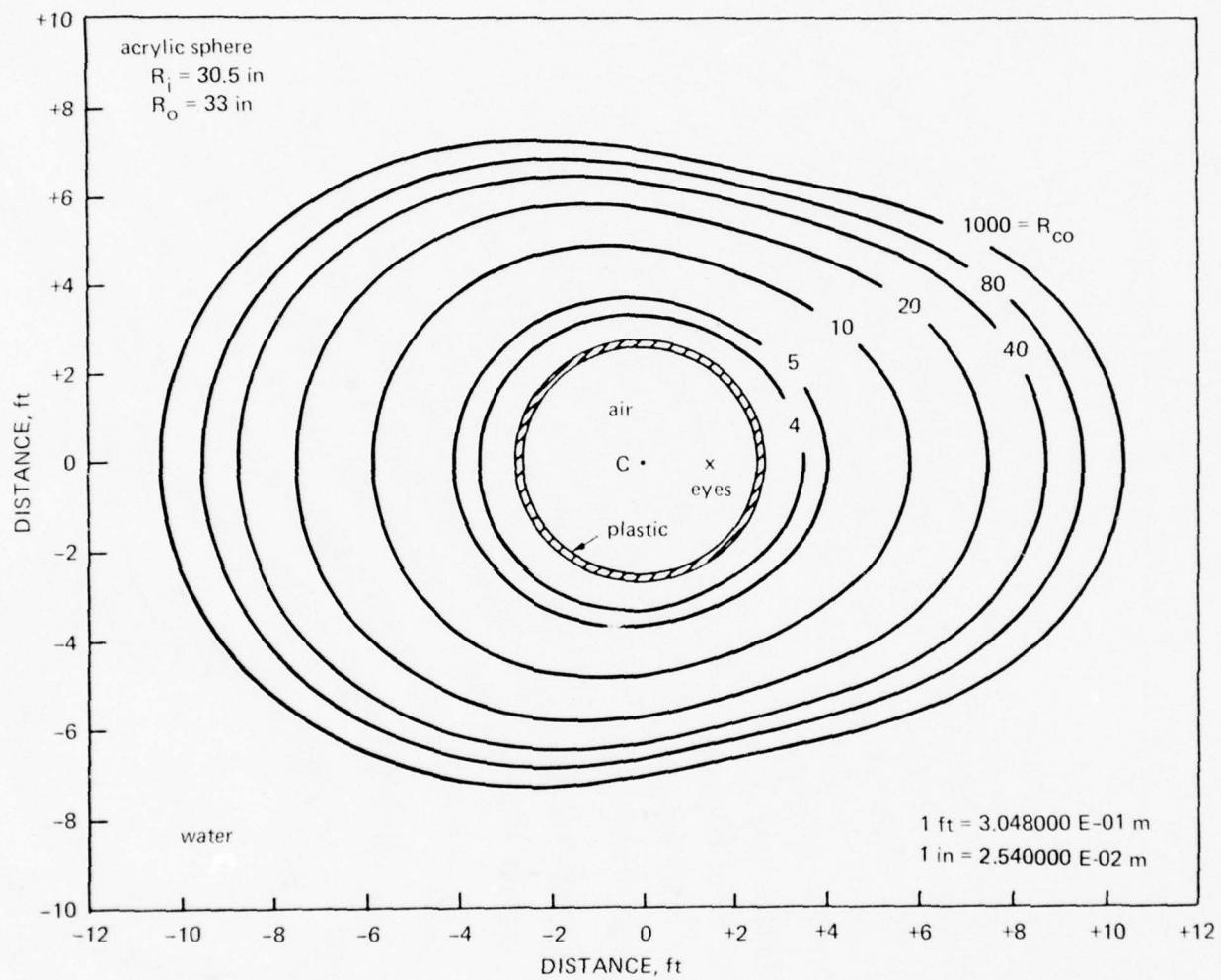
Figure 14.15. Continued.

Part E. R_{ce} = 2.5 feet (0.8 meter); best eye orientation.
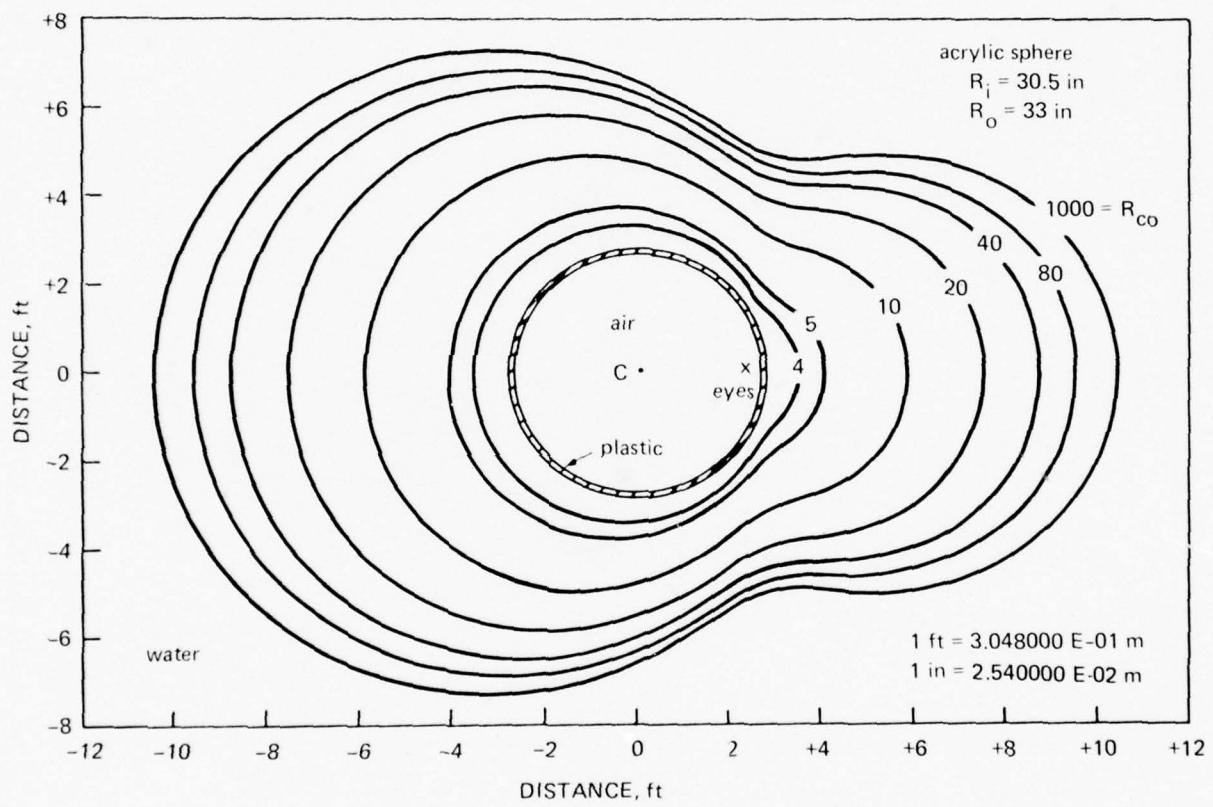
Figure 14.15. Continued.

Part F. $R_{ce} \approx 2.5$ feet (0.8 meter); worst eye orientation.
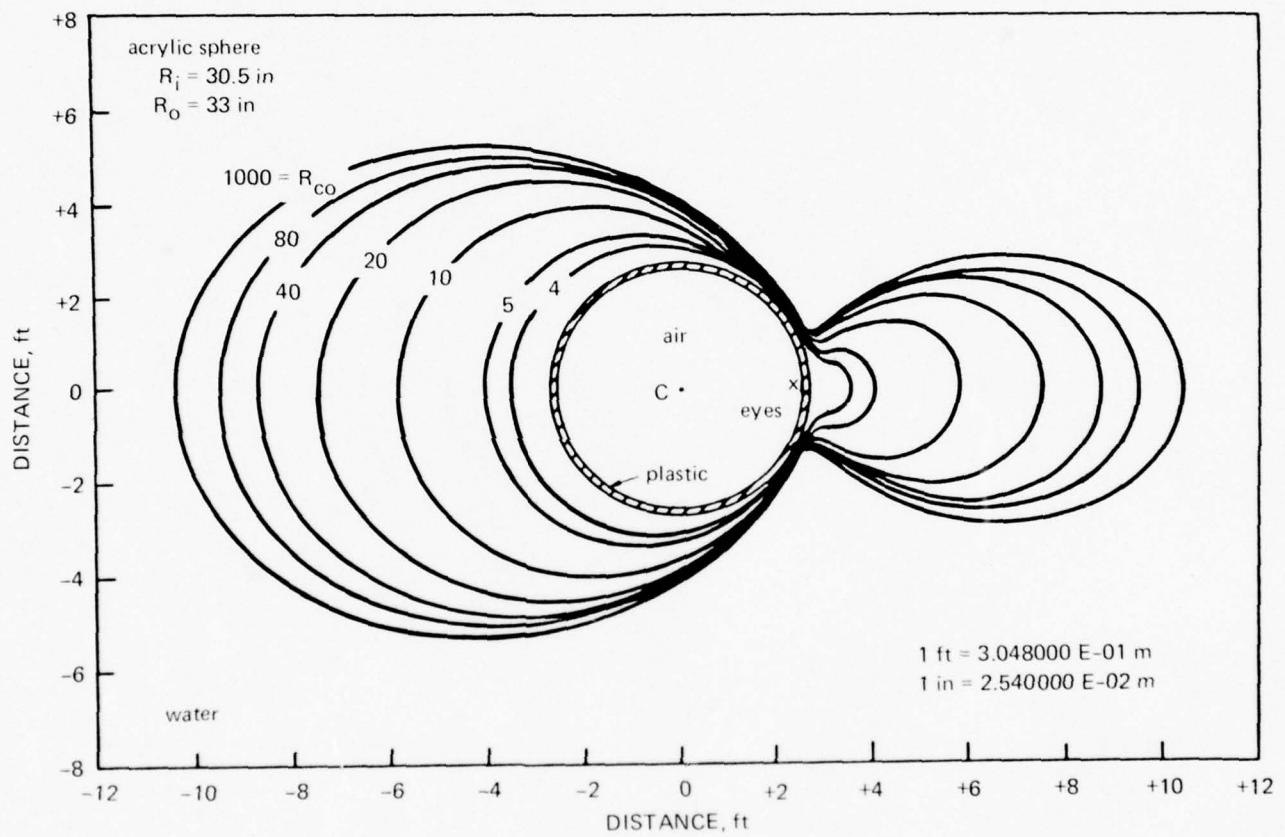
Figure 14.15. Continued.
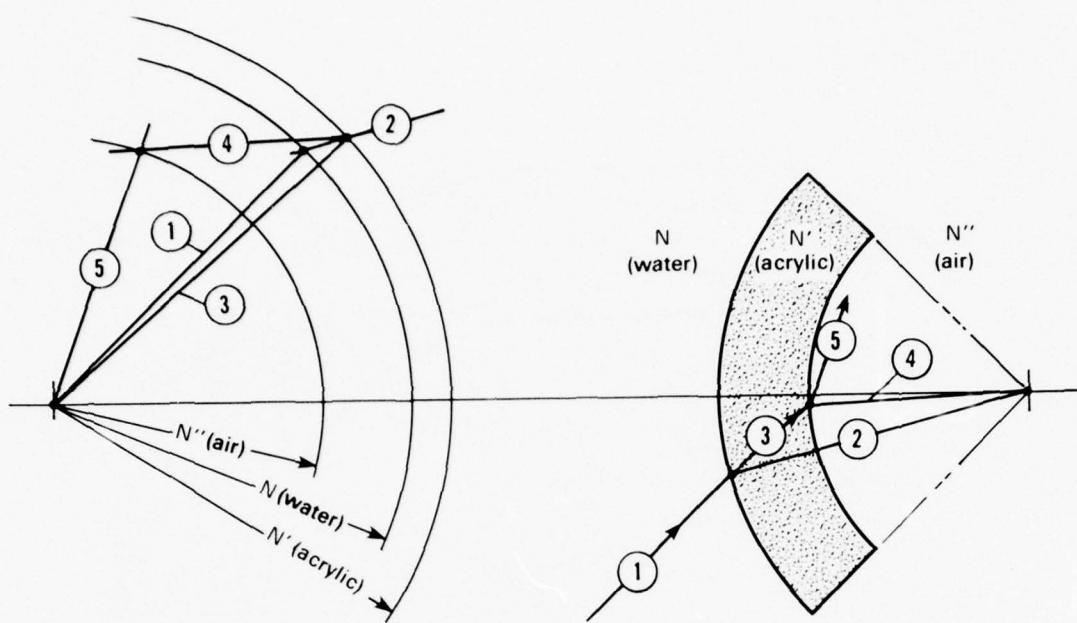
Figure 14.16. Graphical ray trace through a dome window.
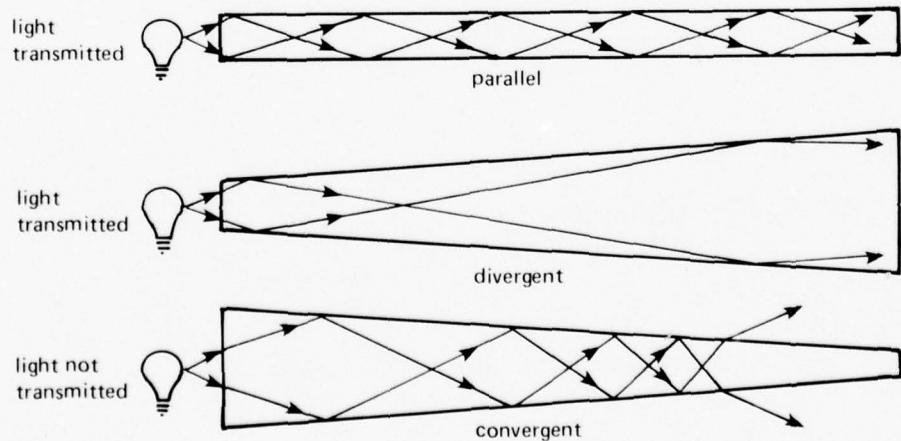
Figure 14.17. Taper reactions in light pipes.

inside radius equal to
or greater than twice the thickness

T

2T

all light "piped"

inside radius less than
twice the thickness

T

T

some light
"escapes"
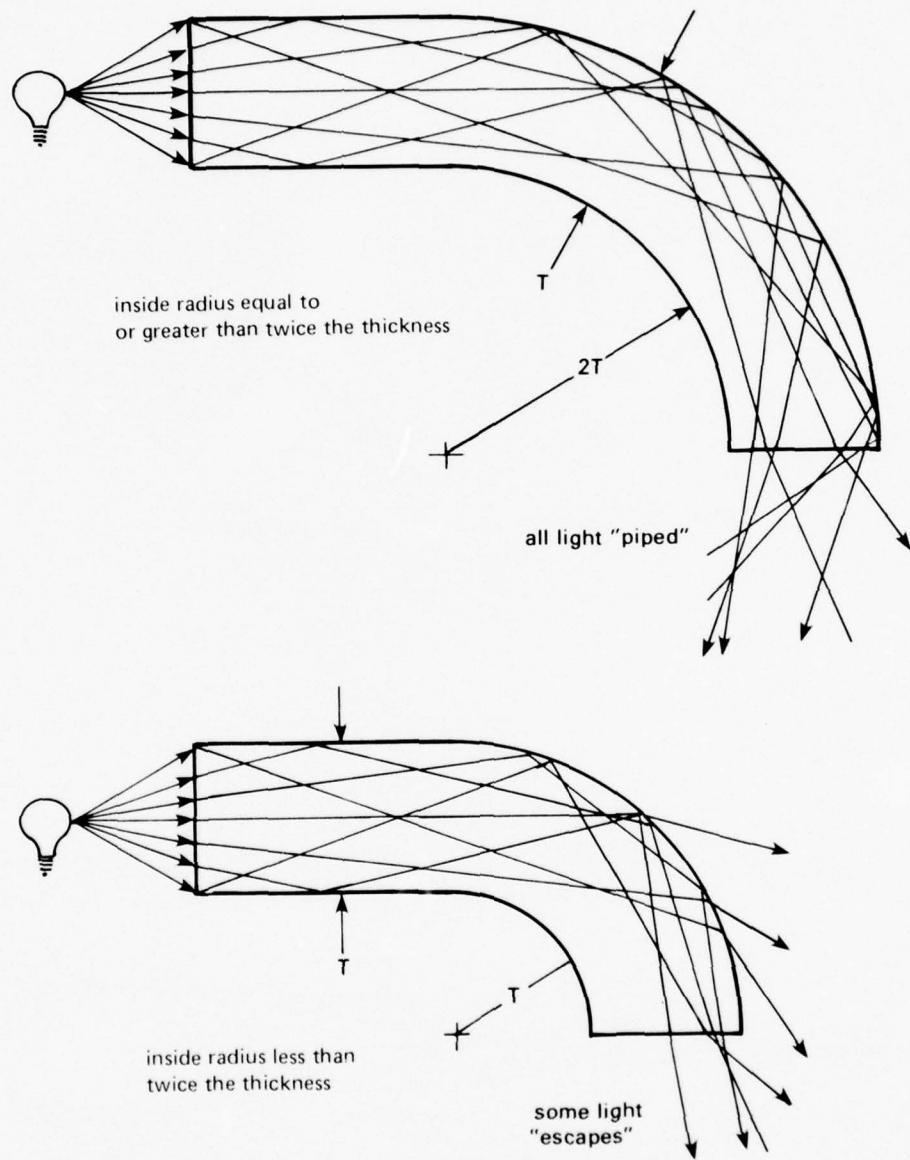
Figure 14.18. Effects of bending a rectangular light pipe.

SECTION 15. SAFETY STANDARD FOR VIEWPORTS
IN PRESSURE VESSELS FOR HUMAN OCCUPANCY

15.1   INTRODUCTION

A safety standard for acrylic plastic viewports in pressure vessels for human occupancy has been developed by the ANSI/ASME* Safety Codes Committee on pressure vessels for Human Occupancy. Appendix A of this standard, the section on designed viewports, was authored by the Subcommittee on Viewports, chaired since its inception in 1971 by Dr. J. D. Stachiw of the Naval Ocean Systems Center, San Diego, California. To date 16 drafts of this appendix have been prepared and all have been approved by the ASME Safety Codes Committee on Pressure Vessels for Human Occupancy.

Although the work of the subcommittee is far from complete, the tentative safety standard has filled a need in the ocean-engineering community. Its presence has allayed the fears of designers concerning the use of acrylic plastic as pressure-resistant structural members in pressure vessels for human occupancy. With the data presented in ANSI/ASME PVHO-1, Appendix A, the user can specify with confidence viewports for pressures from −15 to +20,000 pounds per square inch (−0.1 to 138 megapascals) at 0 to 150°F (−18 to +66°C) without any restrictions on their diameters, if a shape that is similar to one of the nine standard viewport shapes in the safety standard is used. For viewport shapes or operational conditions differing from those in the safety standard, the user must develop safe design criteria based on a design validation program that follows the guidelines specified in ANSI/ASME PVHO-1 and yet also closely conforms to specific operational requirements.

15.2   DISCUSSION

Viewports are an integral part of all pressure vessels for human occupancy. Well designed viewports maintain the structural integrity of the vessel, allow occupants to observe the exterior space around the vessel, and make it possible for the pressure-vessel attendants to keep the occupants under visual surveillance. To perform safely, the viewports must be designed by knowledgable engineers and constructed by competent personnel from quality materials.

Thousands of viewports in service around the world on submersibles, diving bells, deck chambers, hospital chambers, wet pots, and personnel-transfer capsules attest to the confidence placed in them by the users of such equipment. In fact, the incidence of disabling accidents caused by the structural failure of viewports is less than that caused by the failure of any other component. This safety record has been possible because of adequate safety factors in design and meticulous attention to quality control during fabrication. As long as this practice is continued, pressure-resistant viewports will retain their excellent reputation in the ocean-engineering industry.

---

* *American National Standard Institute/American Society of Mechanical Engineers.*

The safety record of pressure-resistant viewports is the result of efforts by many engineers, fabricators, divers, engineering societies, classification societies, and government agencies. Most credit belongs to the U. S. Navy which has generously supported research at the Naval Civil Engineering Laboratory (now Civil Engineering Laboratory), Naval Undersea Center, and David Taylor Model Basin (now Naval Ship Research and Development Center) into the structural performance of acrylic plastic viewports and pressure hulls of different shapes under hydrostatic/hydrodynamic loadings. Substantial credit must also be given to the American Society of Mechanical Engineers, Ocean Technology Division (now Ocean Engineering Division), which, under the chairmanship of Dr. J. D. Stachiw, initiated and continues to sponsor work on the standardization of design approaches and fabrication techniques. Credit must also be given to the U. S. Coast Guard for defraying the expenses associated with the writing and preparation of illustrations for the ANSI/ASME PVHO-1 safety code.

Although the effort to standardize the design and fabrication of viewports was initiated by the Navy in 1964 and by ASME in 1971, the work has not yet been completed. Although there are many reasons for this, the two major ones are (1) the great diversity of technical and economic interests that must be considered prior to arriving at a concensus opinion and (2) the dynamic growth of the technical field with accompanying changes in design philosophies. Still, the 16 drafts of the proposed standard have served a very useful purpose by providing a focal point for dialogues between the designers, fabricators, users, and certifying authorities. By being first in the field, the drafts also functioned as the basis for the construction rules of Det Norske Veritas, the American Bureau of Shipping, and the U. S. Coast Guard.

Because the work of the safety codes committee reflects the consensus of diverse interests in the ocean-engineering field, the codification of the safety standard for viewports, even when officially accepted, will not be a rigid document, but will be one which will continue to change and reflect progress in viewport design and fabrication technology. The sixteenth draft of appendix A to ANSI/ASME PVHO-1* reflects only contemporary views on this subject; future advances in stress analysis techniques, fabrication processes, and material sciences will drastically change its content. For this reason, the prospective user of the pressure vessel should become acquainted with the contents of the most recent version of the safety standard before specifying it for the viewports for the pressure vessel under design.**

To understand the safety standard, the philosophy underlying its formulation must be understood. The philosophy, which is rather simple, is based on the premise that safe windows can be routinely obtained only when all elements in the procurement process adhere to established and proven procedures. These elements are design, material, fabrication, and acceptance testing. Because of their importance, they require extensive documentation which sebsequently becomes the technical pedigree of the given viewport. Thus, if one invokes ANSI/ASME Safety Standard PVHO-1, Appendix A, in the procurement of a window for a manned pressure vessel, one is assured that the finished window will be properly designed and fabricated from approved material, using acceptable fabrication procedures.

---

* Appendix A is reproduced on pages 15-5 through 15-18

** Copies of the ANSI/ASME PVHO-1 Safety Standard can be obtained for $10 from the American Society of Mechanical Engineers, United Engineering Center, 345 E. 47th Street, New York, N. Y. 10017

There is no claim being made that the safety standard represents the sole approach to arriving at a safe product. To the contrary, there are many other valid approaches for procuring a safe window. What differentiates the approach in ANSI/ASME PVHO-1, Appendix A, from the others is its brevity and the absence of requirements for experimental validation of designs chosen on the basis of data in appendix A. Experimental design validation is not required because of satisfactory experience with the appendix's conversion factors which relate the critical and operational pressures of windows at different ambient temperatures.

Since the data in appendix A address only the minimum acceptable level of reliability and safety, the designer is encouraged to use conversion factors and quality assurance procedures in excess of those stipulated. However, even when the designer goes beyond the safety standard, the values for window thickness and the quality-control procedures in the standard will provide useful guidelines for comparison. To help designers continue beyond the standard, extensive lists of pertinent references have been included in all sections of this report. Careful analysis of the data and findings in these publications will give the designer not only a better understanding of technical guidelines used in establishing ANSI/ASME PVHO-1, Appendix A, but it will also allow the development of original designs that are based on past research.

Although the ANSI/ASME PVHO-1 Safety Standard does not address itself to in-service inspection of windows, some technical criteria have to be made available for the personnel performing inspection for classification societies. Such criteria have been developed by the Viewport Committee of the ASME Ocean Engineering Division. These criteria fall short of their objective. However, in the absence of any other better defined criteria they perform a valuable service for personnel involved in the inspection process, i.e., they focus attention on the essentials of the inspection. These inspection criteria can be found at the end of this section under "In-service Inspection of Viewports." At the present time, the in-service inspection of viewports is not a part of ANSI/ASME PVHO-1 Safety Standard; however, there are good indications that it may become a part in the future.

For technical and administrative reasons, ANSI/ASME Safety Standard PVHO-1, Appendix A, does not address itself to glass windows. The technical reasons are that acrylic plastic is more economical, has better impact resistance, and there is more documentation on which to base reliable design and fabrication procedures. The administrative reason is that the ANSI/ASME Safety Code Committee on Pressure Vessels for Human Occupancy did not possess adequate resources to address itself to both materials simultaneously. Because acrylic plastic windows are more prevalent in service than are glass ones, they were chosen first for investigation. As the proposed safety standard becomes accepted and the amount of associated administrative effort decreases, the committee will, if sufficient interest is shown by the ocean-engineering community, address itself to windows fabricated from other transparent materials, including glass.

At the present time, utilization of windows made from materials other than acrylic plastic is not recommended in pressure vessels for human occupancy, unless the designer is willing to conduct an extensive experimental validation program. Such a program will generally require approximately 1 year and $100,000. As a result of the high cost associated

with experimental validation programs for individual designs in nonacrylic materials, it will require either generous government support or a cooperative effort of the ocean-engineering community to prosecute a well coordinated test program at ASME to serve as the basis of acceptance for windows made of materials other than acrylic plastic.

15.3   ANSI/ASME SAFETY STANDARD PVHO-1, APPENDIX A

Because of its unique position in the field of viewport technology, the sixteenth draft of the tentative safety standard, dated May 16, 1978, is reporduced in this report for the benefit and comment of readers and users.

APPENDIX A

DESIGN OF ACRYLIC VIEWPORTS

Draft No. 16

12 May 1978

Prepared by

Subcommittee on Viewports
ASME Safety Code Committee on Pressure Vessels for Human Occupancy
Committee on Windows for Hydrospace
Ocean Engineering Division, American Society of Mechanical Engineers

Address inquires and comments on viewports to:

Dr. J. D. Stachiw, Chairman
ASME Subcommittee on Viewports
Naval Ocean Systems Center
San Diego, CA 92152
(714) 225-7811

CONTENTS

CONTENTS (continued)

FIGURES

CONTENTS (continued)

CONTENTS (continued)

CERTIFICATION FORMS

A.   General

A.1   Viewports in pressure vessels for human occupancy require careful design, installation, and maintenance of the window, flange, retaining rings and seals.

A.2   The design engineer of the chamber must assure himself that the viewport is adequate for the design conditions of the chamber, particularly the design pressure, temperature at design pressure, and cyclic life at design pressure.

A.3   Each viewport window shall be individually certified by the window supplier. The window supplier's certification shall include the following:

a.   A material certification of each lot of acrylic plastic which shall certify the minimum values of physical properties called out in Table A-1 for each lot and verify for each casting or lot, as defined in Chapter B, the minimum values specified in Table A-2 that have been experimentally verified.

b.   A fabrication certification for each window which shall identify all forming, machining, polishing, heat treatment and inspection processes to which the window was subjected by the window fabricator.

c.   A design certification for each window which shall include engineering calculations and/or a description of the experimental method and data used to verify compliance of the window design with the requirements of ASME Safety Standard for Pressure Vessels for Human Occupancy.

d.   A pressure testing certification for each window which shall describe the pressure, temperature, pressurization rate, duration of sustained loading and viewport flange used during the pressure test.

e.   Identification of each window with the window supplier's certifications. The identification shall be located on the window's seating surface. It shall consist of 3.2 mm (0.125 inch) letters and numbers made by the window fabricator with an indelible black felt marker through a paper stencil. The identification shall contain the following information as per example shown below:

50-100-PVHO- RT-21-75

Year of window fabrication

Fabricator's serial number of window

Window fabricator's name or identification symbol

Initials for "Pressure Vessel Human Occupancy"

Maximum temperature, °F

Design pressure, psi
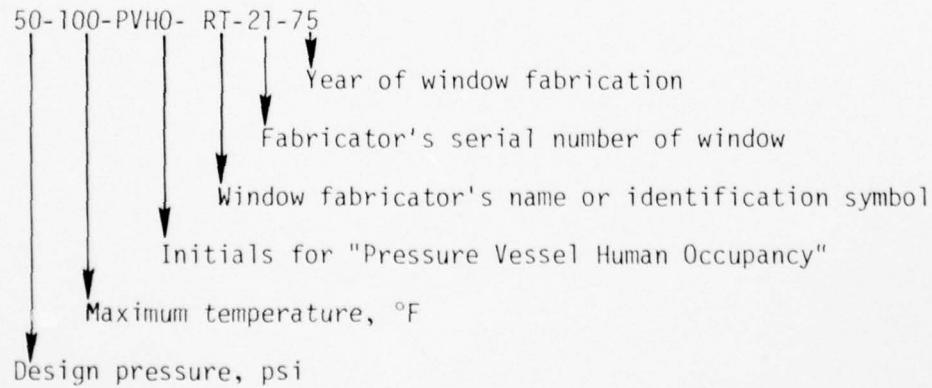
A.4   The windows covered by this Standard are intended for use only in chambers with window service conditions defined by:

    a.   _maximum allowable working pressure_, equal to design pressure,

    b.   _maximum temperature at design pressure_, equal to design temperature,

    c.   _pressure cycles_ at design pressure and temperature.

A.5   The windows covered by this Standard _are not intended_ for applications where any of the following restrictions on design parameters are exceeded:

    a.   The operating temperature shall be within the $-18°C$ $(0°F)$ to $+66°C$ $(+151°F)$ temperature range.

    b.   The pressurization or depressurization rate shall be less than 1 megapascal (145 psi) per second.

    c.   The contained fluids (external or internal) shall be only water, air or gases used in life support systems.

    d.   The number, or the total duration of pressure cycles during the operational life of the window shall not be more than 10,000 cycles or 40,000 hours, respectively.

    e.   The maximum operational pressure shall not exceed 138 megapascals (20,000 psi).

    f.   The exposure to nuclear radiation shall be less than 4 megarads.

    g.   The design life of the windows shall be less than 10 years.

B.   Material

B.1   Windows shall be fabricated only from cast polymethyl methacrylate plastic, hereafter referred to as acrylic plastic. The acrylic plastic used for fabrication of windows must satisfy two general requirements:

    a.   The casting process used in production of acrylic plastic shall be capable of producing material with the minimum physical properties shown in Table A-1. The manufacturer of material shall certify that the _typical physical properties_ of the material satisfy the criteria of Table A-1 and shall identify the material by lot number as required by Chapter A. If the manufacturer is not willing to certify that the typical physical properties of his castings meet the requirements of Table A-1, experimental verification of all properties shown on Table A-1 becomes mandatory.

    b.   The acrylic plastic castings from which the windows are produced _must possess the minimum physical properties_ specified in Table A-2. The acceptance tests of castings shall be conducted for the window fabricator by the manufacturer of acrylic plastic or by an independent materials testing laboratory.

The certified results of acceptance tests (specified in Table A-2) for sheet or custom castings shall be furnished together with the manufacturer of plastic lot or product certificate (specified in Table A-1) to the chamber fabricator/user.

B.2   Acrylic plastic castings shall be suppied in sheet form or as custom castings. All acrylic plastic sheet castings shall have a nominal thickness of 12.5 mm (1/2") or greater.

For purposes of this Standard, acrylic plastics in the form of custom castings are classified as either Type 1 or Type 2 castings.

a.   Type 1 custom castings are defined as being of such thickness, and configuration and produced by such a process as to meet the requirements of Table A-1 without experimental verification. To be considered Type 1 custom casting the manufacturer of plastic must certify that he has produced castings of similar shape and thickness and of the same material in the past and that such castings have met the requirements of Table A-1.

b.   Type 2 custom castings are defined as being produced in such a thickness or configuration, or by such a process that the manufacturer of acrylic plastic must experimentally verify that the acrylic plastic castings posses the minimum physical properties specified in Table A-1. All custom castings failing to meet requirements of Type 1 are classified as Type 2 custom casting.

B.3   Acceptance tests performed according to B-1.b on a single casting can be used not only to certify the particular casting, but also under special circumstances, an entire lot of castings. The cases listed below define the conditions under which acceptance testing of a single casting according to B-1.a and B-1.b can certify the entire lot:

a.   Acceptance tests performed according to B-1.b on one sheet casting chosen at random from a lot of acrylic plastic cast sheets (defined in Chapter K), shall serve to certify all sheets of that lot providing that the manufacturer of plastics shall positively and permanently identify each sheet so certified with a lot number and ASME Safety Standard number PVHO-1.

b.   The manufacturer of acrylic sheet castings may certify that a product of a given thickness meets the typical physical properties specified in Table A-1 without identification of lot number. Each casting so certified must have acceptance tests performed on it according to B-1.b and at that time is assigned to it an inventory control identification which shall be utilized in lieu of a lot identification in all PVHO-1 documentation.

c.   Acceptance tests performed according to B-1.b on specimens cut from one Type 1 custom casting, taken at random from a lot of custom castings, shall serve to certify all castings of that lot. The manufacturer shall positively and permanently identify each certified casting with lot number and ASME Safety Standard number PVHO-1.

d.   Single Type 1 custom castings shall have acceptance tests performed according to B-1.b on specimens cut from each casting.

e.   Type 2 custom castings shall have tests performed according to
B-1.a and B-1.b on specimens cut from each casting to experimentally verify
that the acrylic plastic possesses the physical properties specified both in
Tables A-1 and A-2. Tests for experimental verification of properties in
Table A-1 shall serve also to certify the properties in Table A-2.

B.4   Testing of acrylic plastic castings for the physical and optical
properties specified in Tables A-1 and A-2 shall follow ASTM methods where
applicable. Where possible, samples for testing shall be taken from an inte-
gral part of the casting. A test coupon casting may be used to supply material
for testing provided the test coupon and window castings meet the lot require-
ments in Chapter K. Samples for testing are to be cut so that no surface of
the test sample is closer to an unfinished cast surface than the normal trim
line. Where possible, test samples shall be cut from the central portion of
the original casting, e.g., large casting cut into several windows. The test
methods for physical properties specified in Table A-2 shall be as follows:

a.   Tests for tensile properties shall be performed per ASTM D638,
using testing speed "B". If feasible, specimens shall have an as-cast surface
(if it is smooth enough) as one of the faces.

b.   Tests for compressive properties shall be per ASTM 695 using a
specimen which is one solid piece, the dimensions of which are 25 mm x 12.5 mm
x thickness (1" x 1/2" x thickness) of casting. When the thickness exceeds
12.5 mm (1/2") samples are to be 25 mm x 12.5 mm x 12.5 mm (1" x 1/2" x 1/2")
in dimension.

c.   Test for compressive deformation shall be performed per ASTM 621
Method a, using specimens loaded to 27.58 MPa (4,000 psi based on original cross
section), and tested at 50°C (122°F). The sample size is a 12.5 mm (1/2") cube.
To test nominal 12.5 mm (1/2") thick material machine the specimen in such a
manner that the as-cast surfaces serve as the load-bearing surfaces. Do not
stack samples to reach 12.5 mm (1/2") height, instead test a sample, 12.5 mm x
12.5 mm x nominal thickness. Nominal thickness over 12.5 mm (1/2") yield standard
test specimens. These sampling procedures override those called out in D-621.

d.   Test for the presence of an ultraviolet absorber (ultraviolet
transmittance) shall be made using a monochromator having a bandwidth of 10 nm
or less, a photometer having reproducibility of ±1% of full scale, and the
practices of ATSM-E-308 to measure the spectral transmittance in the 290 to
330 nanometer (nm) wavelength band. Report value of one specimen of nominal
12.5 mm (1/2") thickness. Measurements can be made on the casting or on the
monomer mix from which the plastic is to be cast. Solid samples shall have two
polished faces through which the light passes.

e.   Since ASTM standard method is not available for measurement of
residual acrylic monomer the B-5 procedure is recommended.

f.   The clarity of one casting shall be visually rated per ASTM-D702-
68, paragraph 7.1.15. Clear print of size 7 lines per column inch (25 mm) and 16
characteristics to the linear inch (25 mm) shall be clearly visible when viewed
from a distance of 500 mm (20") through the thickness of the casting with the
opposite faces polished.

B.5   A sample of suitable size shall be obtained and analyzed for unpolymerized methyl methacrylate and unpolymerized ethyl acrylate *monomers using gas liquid chromatographic techniques* (described in Snell and Otto "Encyclopedia of Industrial Chemical Analysis," Interscience Publisher, 1972, Vol. 4, pp. 211-217, and Vol. 16, p. 99, or one giving equivalent results). Samples for testing are to be cut so that the center point of the analyzed piece is no closer to the original edge or surface of the casting than the thickness divided by 2. The following (after Cober and Samsel, SPE transactions "Gas Chromatograph, A New Tool for Analysis of Plastics," April 1962, pp. 145-151) is a suitable procedure:

        a.   The instrument shall be a Beckman GC-2A gas chromatograph with a hydrogen flame detector and a 1828 mm (6 foot) column of 6.3 mm (1/4") stainless tubing operated at 100°C (212°F).   Pack the column with 25% dithylene glycol adipate polyester (LAC-2-R-446, Cambridge Industries Company) and 2% phophoric acid on a 80-100 mesh Celite filter aid. The acrylic plastic to be analyzed shall weigh approximately 2.0 grams and shall be dissolved in exactly 50 milliliters of methylene chloride. Inject a 3 microliter/aliquot of the plastic/ solvent solution into the gas chromatographic apparatus. Compare the areas of the resulting peaks with the areas produced by the injection of a standard solution. Prepare the standard solution by dissolving 20-30 milligrams of pure monomers in 50 milliliters of methylene chloride.

        b.   Acrylic plastics which do not dissolve shall be analyzed by swelling the plastic and extracting the soluble portion. Place a solid piece of unsoluble acrylic plastic weighing about 1 gram and 20 milliliters of methylene chloride in a glass bottle, and place on a shaker for 24 hours. After 24 hours the fluid portion shall be analyzed for monomeric methyl acrylate and monomeric ethyl acrylate as per B.5.a.

    B.6   Laminating several sheets of acrylic plastic to arrive at the desired window thickness is not permitted.

    B.7   Joining of acrylic plastic castings by bonding is permitted providing that:

        a.   The joint shall see in service only membrane compressive stresses.

        b.   The tensile strength of the bond shall be at least 50 percent of the parent material strength as established by ASTM-D-638 test on 5 tensile coupons cut from a bond quality control specimen that was bonded at the same time and in the same manner as the acrylic castings intended for actual service.

        c.   The significant and critical dimensions of inclusions, as well as the critical spacing between adjacent inclusions shall not exceed those called out in Paragraph G16 for a given window shape. The critical size of inclusion population shall not exceed the cross-section area of the bonded joint in square centimeters divided by 100. The critical density of population shall not exceed 2 inclusions per square centimeter of contiguous joint cross-section area.

        d.   The joint shall be pressure-tight during hydrostatic testing of the window.

C.   Window Geometry and Thickness

    C.1   The acrylic plastic windows in pressure vessels for human occupancy
must have one of the standard geometries shown in Figures A-1, A-2, A-3, and
A-4. Minimum acceptable thickness and slenderness ratios shall comply with the
requirements of Figures A-1, A-2, A-3, and A-4 for the specific window geometry.

    C.2   Windows of (a) other geometries, or (b) standard geometries, but with
lower conversion factors (CF), may be proposed for use in chambers for human
occupancy providing that the experimental and analytical data substantiating
the new window design parameters are submitted for review and are accepted by
the ASME Safety Code Committee on Pressure Vessels for Human Occupancy. Window
designs with non-standard geometries need not be submitted for review and approval
by the Committee if the design has been experimentally verified according to
Chapter L and the design and its experimental verification certified by a regis-
tered professional engineer.

    C.3   The dimensions of a standard window in the 0 to 69 megapascal (0 -
10,000 psi) design pressure range shall be based solely on the basis of the
window's short term critical pressure (STCP) and the approved conversion factor
(CF) for the given maximum ambient temperature. Minimum STCP values of some
standard window geometries (based on tests conducted by the U. S. Navy, refer-
ences 1 through 20) are given in Figures B-1 through B-12. CF values for the
standard window geometries are given in Tables B-1 through B-5. Calculations of
STCP on the basis of these figures satisfy the requirements of this Standard
under paragraph A.3.c. However, it is also acceptable to have the designer
establish the STCP with his own destructive tests of full scale, or model scale
windows performed according to procedure C.5. providing such tests are witnessed
by and are acceptable to the Authorized Inspector.

    C.4   The dimensions of windows in the 69 to 138 megapascal (10,000 to
20,000 psi) design pressure range, shall be based solely on nondestructive tests
in the form of long term and cyclic pressurizations. Dimensions of approved
windows for this design pressure range (based on tests conducted by the U. S.
Navy, references 1 through 20) are given in Table C-1. Only conical frustum
windows with included angle of 90 degrees, or larger, are qualified for this
pressure range.

    C.5   STCP of an acrylic plastic window is, for the purposes of this Stan-
dard, defined as the pressure at which catastrophic failure of the window takes
place (window disintegrates releasing pressurized fluid into, or from the chamber)
when subjected to hydrostatic pressure increasing at a constant rate of approxi-
mately 4.5 megapascals (650 psi) per minute. The pressurization must take place
at ambient temperature range of 21 to 25°C (70 to 77°F) in a flange that satis-
fies the requirements of Chapters D, E, and F.

        a.   The evaluation of a design is to be conducted on a minimum of
five full scale windows and the results are considered representative only if
the lowest critical pressure is at least 75 percent of the mean critical pressure
of the other four windows. In such a case, the STCP value of the window design

is to be taken as the lowest critical pressure among the five tests. In case the lowest critical pressure does not meet this criterion, the STCP value of the window design is to be equal to the single lowest critical pressure among the five tests multiplied by a factor of 0.75.

    b. Model scale windows may be substituted for full scale windows in C.5.a. tests, if in addition to the five model scale windows, at least one full scale window is tested. The test data (STCP calculated according to C.5.a.) generated by testing of model scale windows is considered acceptable only if the critical pressure of the full scale window is equal to, or above the single lowest critical pressure among the five tests. In case that the critical pressure of the single full scale window does not meet this criterion, four more full scale windows shall be tested and the STCP value of the window design shall be calculated according to C.5.a. on the basis of full scale windows alone.

    C.6   The STCP of a window accepted for service in pressure vessels for human occupancy shall not be less than

$$STCP = (CF \times P) \hspace{2cm} \text{(Equation 1)}$$

where CF and P are the conversion factor and design pressure (megapascals), respectively.

    a.   For flat disc windows, shown in Figure A-1, use conversion factors from Table B-1 and short term critical pressures from Figures B-1 and B-2. Figure B-1 shall be utilized for determination of critical pressures in the 0 to 50 MPa range, while Figure B-2 shall be used for 50 to 300 MPa range. Short term critical pressures may be also experimentally determined according to procedure C.5.

    b.   For conical frustum windows, shown in Figure A-1, use conversion factors from Table B-2 and short term critical pressures from Figures B-3 and B-4. Figure B-3 shall be utilized for determination of critical pressures in the 0 to 50 MPa range, while Figure B-4 shall be used for the 50 to 300 MPa range. Short term critical pressures may be also experimentally determined according to procedure C.5.

    c.   For double bevelled disc windows, shown in Figure A-1, use conversion factors from Table B-2 and short term critical pressures from Figures B-3 and B-4. Figure B-3 shall be utilized for determination of critical pressures in the 0 to 50 MPa range, while Figure B-4 shall be used for the 50 to 300 MPa range. Short term critical pressures may be also experimentally determined according to procedure C.5.

    d.   For spherical sector windows with conical edge, shown in Figure A-2, use conversion factors from Table B-3 and short term critical pressures from Figures B-5 and B-6. Figure B-5 shall be utilized for determination of critical pressures in the 0 to 50 MPa range, while Figure B-6 shall be used for the 50 to 300 MPa range. Short term critical pressures may be also experimentally determined according to procedure C.5. These windows are accepted only for service where the hydrostatic pressure is applied to the convex face.

e. For spherical sector windows with square edge, shown in Figure A-2, use conversion factors from Table B-4 and short term critical pressures from Figures B-5 and B-6. Figure B-5 shall be utilized for determination of critical pressures in the 0 to 50 MPa range, while Figure B-6 shall be used for the 50 to 300 MPa range. Short term critical pressures may be also experimentally determined according to procedure C.5. The windows are accepted only for service where the hydrostatic pressure is applied to the convex surface.

f. For hemispherical windows with equatorial flange, shown in Figure A-3, use conversion factors from Table B-4 and short term critical pressure from Figures B-5 and B-6. Figure B-5 shall be utilized for determination of critical pressures in the 0 to 50 MPa range, while Figure B-6 shall be used for the 50 to 300 MPa range. Short term critical pressures may be also experimentally determined according to procedure C.5. The windows are accepted only for service where the hydrostatic pressure is applied to the convex surface.

g. For cylindrical windows, shown in Figure A-3, use conversion factors from Table B-5 and short term critical pressures from Figure B-7 through B-11. Table B-5-A and Figure B-7 shall be utilized only in determination of conversion factors and critical pressures for internal pressure service. Table B-5-B and Figures B-8 through B-11 shall be utilized only in determination of conversion factors and critical pressures for external pressure service.

h. For hyperhemispherical windows, shown in Figure A-4, use conversion factors from Table B-3 and short term critical pressures from Figure B-12. Short term critical pressures may be also experimentally determined according to procedure C-5. The windows are accepted for service where (a) the hydrostatic pressure is applied only to the convex surface, or (b) the hydrostatic pressures are applied to either surface but the magnitude of internal design pressure does not exceed 5 percent of the external design pressure.

i. For NEMO windows, shown in Figure A-4, use conversion factors from Table B-3 and short term critical pressures from Figure B-12. Short term critical pressures may be also experimentally determined according to procedure C-5. The windows are accepted for service where (a) the hydrostatic pressure is applied only to the convex surface, or (b) the hydrostatic pressures are applied to either surface but the magnitude of internal design pressure does not exceed 5% of the external design pressure.

C.7 When selecting the conversion factors from Tables B-1, B-2, B-3, B-4, and B-5, temperature ranges must be chosen on the basis of highest ambient sustained temperature expected during operation of the chamber at the design pressure. If the interior of the chamber is illuminated by externally mounted incandescent lights shining through the windows, the 66°C (151°F) temperature range shall be mandatory in selection of conversion factors for all windows. For chambers not illuminated with externally mounted lights, the temperature ranges shall be chosen on the basis of environment temperature where the chambers reach design pressure. If the design pressure is reached when:

a. only submerged in water, use ambient temperature of water at that depth;

15-17

b. only in air, use the average of maximum ambient external and internal air temperatures;

c. either in air or water, use the average of maximum ambient external and internal air temperatures.

C.8   When a viewport is subjected to pressurization from both sides, the thickness of the window must be selected on the basis of the highest design pressure, regardless of whether this pressure is external or internal to the chamber.

D.   Window Seats

D.1   The window seat cavity in the viewport flange must be dimensioned to provide the window bearing surface with support during hydrostatic testing and subsequent operation at maximum design pressure.   The dimensions of window seat cavities for standard window geometries are shown in Figures C-1, C-2, C-3, C-4, C-5, C-6 and C-7.

D.2   The surface finish on the window seat cavity must be ≤ 64 rms.

D.3   The surface of the window seat cavity must be protected against corrosion preferably by a weld overlay of corrosion resistant material prior to final machining.   Painting of seat cavity surface, anodizing it, or plating it with electroless nickel is also an acceptable means of preventing surface corrosion.

E.   Viewport Flanges

E.1   Because of the large mismatch between the moduli of elasticity in the plastic window and the matellic flange, it must be assumed in stress calculations that the window does not provide any reinforcement for the hull material around the penetrations.

E.2   Any of the analytical, or empirical, methods for stress and displacement calculations acceptable to the applicable ASME Code may be used for dimensioning the thickness, width, and location of the flange around the viewport penetration.

E.3   Reinforcements for penetrations of chambers must meet the requirements of Paragraph 3.5.2 of this Standard and the requirements of ASME Section VIII, Division 1 or Division 2, Boiler and Pressure Vessel Code as applicable.

E.4   The following minimum requirements shall be met by viewport flanges shown on Figures C-1, C-2, C-3, and C-4 with a finished diameter opening in excess of 63.5 cm (24 inches).

a.   Radial deformation of the window seat at maximum internal, or external design pressure must be less than $0.002 \times D_i$.

b. Angular deformation of the window seat at maximum internal or external design pressure must be less than 0.5 degrees.

Viewport flanges shown on Figures C-5, C-6 and C-7 do not have to meet the radial and angular deformation limits stated in E-4.a and E-4.b.

F.   Window Seals

F.1   As primary seals for standard window geometries shown in Figures A-1, A-2, A-3 and A-4, a soft elastomer compressed between the high pressure face of the window and retainer ring will be acceptable. The soft elastomeric seal may take the form of a flat gasket, or a seal ring with O, U or X cross section. The gasket or seal ring must be of sufficient thickness to permit adequate compression without permanent set. Double bevelled disc and cylindrical windows shall utilize as primary seal a seal ring radially compressed between the cylindrical surface of the window facing the pressure and the cylindrical window seat in the flange. Hyperhemispherical and NEMO type windows may also utilize as a primary seal, an elastomeric potting compound that adheres to both the external spherical surface of the window and the lip of the mounting flange.

F.2   Retainer rings must provide the following minimum initial compression of the gasket in millimeters (for values of N, see Tables B-1, B-2, B-3 and B-4).

a. $N \times \dfrac{(0.015 \, D_i)}{\mathrm{Tan} \; \alpha/2}$ - conical frustum windows   (Equation 2)

b. $N \times (0.01 \, R_i \sin \alpha/2)$ - spherical shell sector windows
with conical edge   (Equation 3)

c. $(0.01t + 0.25)$ - flat disc windows   (Equation 4)

d. $(0.01t + 0.25)$ - spherical shell sector windows
with square edges   (Equation 5)

e. $(0.01t + 0.25)$ - hemispherical windows with
equatorial flange   (Equation 6)

F.3   The minimum compression of seal rings shall be governed by specifications of seal ring manufacturers for the given seal ring size and service.

F.4   A secondary seal is required between the window and the steel cavity seat for flat discs, spherical sectors with square edge and hemispheres with equatorial flange. The secondary seal also serves as a bearing gasket for the window. This gasket must be bonded with contact cement to the metal flange seat. Thickness of the gasket must not exceed 3.2 millimeters (0.125 inches). Neoprene impregnated nylon cloth, neoprene of 90 durometer hardness, and cork gaskets have been found to be acceptable for such application.

F.5   Seal ring grooves are not permitted in the bearing surface of any window shape, or the bearing surface of the seat in the metal flange unless

experimental data, showing the cyclic fatigue life of such a viewport assembly at design pressure and temperature to be in excess of 10^4 standard pressure cycles (four hours under pressure followed by four hours of relaxation), is submitted to and accepted by the Committee on PVHO. Seal ring grooves are allowed in any window shape or its seat in the metal flange, providing that the groove is located in the non-bearing surface. Seal ring grooves in windows shall have $\geq$0.5 mm (0.020 inch) radii at the bottom of the groove to prevent the groove from acting as a crack initiator.

F.6   The configurations of window mountings and seal arrangements shown on Figures B-1 through B-12 represent designs acceptable under this Safety Standard, and are shown there only for guidance of designers.

G.   Dimensional Tolerances and Surface Finish

G.1   Thickness of the window shall be everywhere equal to or greater than the nominal value determined by procedure of C-6.

G.2   The major diameter of the conical bearing surface on a window, shall be machined within +0.000/-0.002 D_0 of nominal value.

G.3   The included conical angle of the window must be within +0.25/-0.000 degrees of nominal value.

G.4   The included conical angle of the window seat in the flange must be within +0.000/-0.025 degrees of the nominal value.

G.5   The major diameter of the conical seat cavity in the flange must be within +0.002 D_0/-0.000 of nominal value.

G.6   The concave, or convex surface of a window shall not differ from an ideal spherical sector more than ±0.5 percent of the specified nominal external spherical radius for standard CF values (Tables B-3 and B-4, Figures B-5, B-6 and B-12).

G.7   The external diameter of the flat disc window shall be within +0.000/-0.25 mm, or +0.000/-0.75 mm of the nominal value depending on whether the window will be sealed with an O-ring, or a flat gasket seal, respectively.

G.8   The diameter of the seat cavity for a flat disc window shall be within +0.25/-0.00 mm, or +0.75/-0.000 mm of the nominal value depending on whether the window will be sealed with an O-ring, or flat gasket seal, respectively.

G.9   The external diameter of the spherical window with square seat shall be within +0.000/-0.0005 D_0 of nominal value.

G.10   The diameter of the seat cavity for a spherical window with square seat shall be within +0.0005 D_0/-0.000 of the nominal value.

G.11   The roundness of cylindrical windows shall not differ from an ideal cylinder more than ±0.5 percent of the specified nominal external radius for standard CF values (Table B-5).

G.12 The bearing surface of the window shall have at least 32 rms finish.

G.13 Viewing surfaces shall be polished to satisfy ASTM D702-68 optical clarity requirement.

G.14 All other surfaces shall be machined, or sanded to attain a 63 rms finish. Saw cut finish is not acceptable on any window surface.

G.15 Scratches (or machining marks) on the surfaces of and inclusions in the body of the window shall not be acceptable if they exceed the specified critical dimension, critical spacing, critical size of population, critical density of population, or are found in a critical location.

G.16 The critical dimension of inclusions, critical spacing, critical size of inclusion population, critical location and critical density of inclusion population depend on the shape of the window. Only inclusions whose diameter or length exceed the specified significant dimension will be considered during a visual inspection, all others will be disregarded.

a. Spherical sectors with conical edge, hyperhemispheres, NEMO windows, conical frustums with $t/D_i \geq 0.5$, double beveled discs with $t/D_i \geq 0.5$, and cylinders under external pressure loading:

significant dimension: 0.4 mm

critical dimension: 0.05t

critical size of population: total volume of window in cubic centimeters divided by 10,000;

critical density of population: 1 inclusion per 16 cubic centimeters of contiguous volume;

critical spacing between adjacent inclusions: select the larger of the two adjacent inclusions and multiply its diameter by a factor of 2;

critical locations: no inclusions are permitted on, or within critical spacing to all of the bearing and sealing surfaces.

b. Spherical sectors with square edge, hemispheres with equatorial flange, cylinders under internal pressure, conical frustums with $t/D_i < 0.5$, double beveled discs with $t/D_i < 0.5$ and discs:

significant dimension: 0.4 mm

critical dimension: 0.8 mm

critical size of population: total volume of window is cubic centimeters divided by 10,000;

critical density of population: 1 inclusion per 16 cubic centimeters of contiguous volume;

END
DATE
FILMED

8 -79

DDC

<u>critical spacing between adjacent inclusions</u>: 6 mm

<u>critical location</u>:   no inclusions are permitted on, or within critical spacing to all of the surfaces.

G.17 Critical dimensions of scratches (or machining marks), critical spacing, critical sizes of scratch population, critical locations and critical densities of scratch population depend on the shape of the window. Only scratches whose depth exceeds the significant dimension will be considered during a visual inspection, all others will be disregarded.

a. Spherical sectors with conical edge, hyperhemispheres, *NEMO* windows, conical frustums with $t/D_i \geq 0.5$, double beveled discs with $t/D_i \geq 0.5$ and cylinders under external pressure loading:

<u>significant dimension</u>:   0.25 mm

<u>critical dimension</u>:   1.5 mm

<u>critical size of population</u>: total length of all scratches in centimeters equals total surface area divided by 1000

<u>critical density of population</u>: none specified

<u>critical spacing between scratches</u>: none specified

<u>critical locations</u>:   no scratches are permitted on the bearing and sealing surfaces.

b. Conical frustums with $t/D_i < 0.5$, double beveled discs with $t/D_i < 0.5$, discs, and cylinders under internal pressure.

<u>significant dimension</u>:   0.08 mm

<u>critical dimension</u>:   1.5 mm

<u>critical size of population</u>: total length of all scratches in centimeters equal total surface area divided by 1000

<u>critical density of population</u>: none specified;

<u>critical spacing between scratches</u>: none specified

<u>critical locations</u>:   no scratches are allowed on the bearing and sealing surfaces, on any faces of double beveled discs and cylinders, and on low pressure faces of conical frustums and discs.

c. Spherical sectors with square edge, and hemispheres with equatorial flange:

<u>significant dimension</u>:   0.08 mm

critical dimension: 0.25 mm

critical size of population: total length of all scratches in centimeters equals total surface area divided by 1000;

critical density of population: none specified

critical spacing between scratches: none specified

critical locations: no scratches are permitted on bearing and sealing surfaces, on low pressure face of spherical sector with square edge, and in the heel and instep areas of flanged hemisphere.

H.   Fabrication of Windows

H.1   Windows shall be fabricated only from acrylic plastic casting satisfying the requirements of Sections A and B.

H.2   No fabrication process, solvent, cleaner, or coolant shall be used during the fabrication that degrades the original physical properties of the acrylic casting.

H.3   During the fabrication process, each window shall be identified with identification and fabrication verification documents containing pertinent material and fabrication data.

H.4   The windows shall be annealed at least once during the fabrication process. The mandatory annealing shall take place prior to final installation after all forming, machining, and machine polishing operations have been already completed by the fabricator. Annealing schedule shown in Table D-1 shall be followed. Handlapping and hand polishing after annealing is allowed.

H.5   After mandatory annealing at the conclusion of fabrication process each finished window shall be subjected to a quality control inspection.

H.6   The quality control inspection shall consist of dimensional and visual checks whose objective is to determine whether the finished window meets the dimensional tolerances, material quality, and surface finish requirements called out in Sections A, B and G. Only windows that satisfy the requirements of Sections A, B, C and G shall be accepted.

H.7   New windows with spherical surfaces, whose dimensional tolerances, surface finish, or inclusions exceed the limits called out in Paragraphs G.1 through G.17 may be repaired by spot-casting, providing that the following conditions are satisfied:

a.   The repaired spot shall see in service only compressive stresses.

b.   The casting mix used for spot repairs shall have the same chemical composition and shall be polymerized in the same manner as the casting mix in the massive window casting.

c. For repaired spots located in (1) areas within 2 degrees of the window's edge circumference, or (2) areas not visible from the interior of the pressure vessel by an observer in a typical position required for operation of the vessel the following limitations apply:

(i) The volume of a single repaired spot shall not exceed 10 percent, and cumulative volume of all repaired spots 20 percent of the total window volume, respectively.

(ii) There is no limit on the number of repaired spots.

d. For repaired spots located in areas outside 2 degrees of the window's edge circumference and visible from the interior of the pressure vessel by an observer in a typical position required for operation of the vessel the following limitations apply:

(1) The area of any repaired spot shall not exceed 0.025 percent of the total window area.

(2) Only two repaired spots are permitted.

e. After completion of machining and polishing operations the window is to be annealed as per H.4.

f. Location and extent of spot casting repairs are to be noted on a sketch attached to the window certification.

I. Installation of Windows in Chambers

I.1 The window cavity seat in the flange must be thoroughly cleaned. Aliphatic naphtha and hexane are suitable for cleaning.

I.2 The window cavity seats for all window shapes possessing conical bearing surfaces shall be thoroughly coated with grease prior to placement of window inside the window cavity so that the greased surfaces will act as secondary seals. Silicone greases are suitable for this purpose. Other greases must be checked for chemical compatibility with acrylic plastic.

I.3 After placement of window inside the window cavity, the primary elastomeric seal will be placed on the high pressure face of the window, and the retainer tightened until the seal compression reaches the minimum value specified in Section F.

J. Pressure Testing

J.1 Each window shall be pressure tested at least once prior to being accepted for service.

J.2 The pressure test shall take place with the window installed in the chamber, or a test fixture whose window seat dimensions, retaining ring, and seals are identical to that of the chamber.

15-24

J.3   The window shall be pressurized with gas or water until design pressure is reached. The design pressure shall be maintained for a minimum of one, but not more than four hours, followed by depressurization at a maximum rate not to exceed 4.5 megapascals (652 psi) per minute.

J.4   The temperature of the pressurizing medium during the test shall be the design temperature for which the window is rated with a tolerance of +0/-2.5°C (0/-5°F). Brief deviations from above temperature tolerances are allowed, providing that the deviation does not exceed ±5.5°C (10°F) and lasts less than 10 minutes.

J.5   Window that leaks during the pressure tests shall be removed, fitted out with new seals and retested. If, during the retest, the leakage continues, efforts will be made to complete the test by stopping the leak with a temporary seal. The inability of seals to operate properly during the test shall be noted in the test report, submitted at the conclusion of the pressure test to the chamber manufacturer/user.

J.6   At conclusion of the pressure test, the windows shall be visually inspected for presence of crazing cracks or permanent deformation. This examination may be performed without removal of the window from the chamber.

J.7   Presence of crazing, cracks or permanent deformation visible with unaided eye (except for that necessary to correct for 20/20 vision) shall be the cause of rejection of the windows and shall be so noted on the test report.

J.8   A hydrostatic or pneumatic test in excess of design pressure, may be substituted for the mandatory tests of J.3 and J.4. During the hydrostatic or pneumatic test the pressure shall be maintained for a minimum of one, but not more than 4 hours. The test pressure shall not exceed 1.6 x design pressure or 20,000 psi, whichever is the lesser value. The temperature of the pressurizing medium during the test shall be at least 14°C (25°F) lower than the design temperature (except for 10°C design temperature, where the temperature during the test shall be in the 0 to 4°C range) to prevent permanent deformation of windows tested above design pressure. All the other requirements of the mandatory pressure test spelled out in J.5 and through J.7 shall be retained.

K.   Definitions

1.   Acrylic   Methyl methacrylate plastic possessing physical and mechanical properties shown in Tables A-1 and A-2.

2.   Conversion factor   An empirical ratio of short term critical pressure to design pressure specified on the basis of past experience as the safe relationship between these parameters for a given temperature.

3.   Critical pressure   Hydrostatic pressure that, acting on one side of the window, causes it to lose structural integrity and ability to remain impermeable to water.

4.	Cylindrical window	Window consisting of a tube with circular cross-section.
5.	Custom casting	Casting of any shape that is not carried as a standard production item in a manufacturer's sales catalog.
6.	Fabricator of windows	Fabricates finished acrylic plastic windows from plastic castings, marks them with identification and provides fabrication certification.
7.	Full scale window	Window, whose all dimensions are identical to the window in actual service.
8.	Inventory control identification	Identification assigned to a single sheet or custom casting by the fabricator of windows when lot identification is not provided by the manufacturer or plastic. The inventory control identification shall consist of a number, ICI, followed by initials of window fabricator and date (i.e., 3-ICI-RT-5/5/76) made with black felt marker on a minimum of four locations on the casting. On a sheet casting protected with masking paper the markings shall be made on the paper at four corners of the sheet approximately 2 inches from the edges.
9.	Lot identification	Identification affixed by the manufacturer of plastic to all castings constituting a lot of material.
10.	Lot of material	Unit of manufacture consisting of a single production run of 2000 lbs., or less, poured from the same mix of monomeric material and made at the same time, undergoing identical processing from monomer to polymer.
11.	Manufacturer of plastic	Converts methyl methacrylate resin into acrylic plastic castings; provides Material Certification Part I, may also provide Material Certification Part 2.
12.	Material testing laboratory	Tests material specimens cut from acrylic plastic castings; provides Material certification, Part 2.
13.	Megapascal	Metric unit of pressure, equal to 10 bars, or 145 psi.

14.	Model scale window	Window, whose all dimensions are scaled down linearly from the window in actual service.
15.	Pressure testing laboratory	Pressure tests windows installed in viewport flanges; provides pressure testing certification.
16.	Sheet castings	Sheets of acrylic plastic cast on production line basis and carried as a standard production item in a manufacturer's sales catalog.
17.	Supplier of windows	Supplies finished windows with all required certifications to the chamber manufacturer (original equipment), or user (replacement). There is nothing in this Safety Standard prohibiting the supplier from performing the functions of plastic manufacturer, material testing laboratory, window designer, window fabricator and pressure testing laboratory providing that these functions generate the required certifications.
18.	Viewport	Penetration in the pressure vessel equipped with an impermeable and pressure-resistant transparent window that is seated in a flange and held in place by a bolted-on, or screwed-on, retaining ring.
19.	Window	Transparent, impermeable and pressure-resistant insert in the viewport.
20.	Inclusion	A foreign substance in the body of acrylic plastic; an inclusion may take the form of a void, a grain of sand, a pebble, or chunk of plaster, or a piece of silicone rubber that flaked off from the mold.
21.	Scratch	A mark on the smooth surface of the window; its origin may be a deep cut by machining tool, or contact with a sharp object during handling.
22.	Critical Dimension	Dimension of inclusion or scratch that cannot be exceeded; for inclusions it is diameter or length, whichever is largest; for scratches it is the maximum depth measured from the smooth surface to the bottom of the scratch.
23.	Significant Dimension	Inclusions and scratches whose dimensions exceed the significant dimension must be considered during quality control inspection; for inclusions it is either the diameter or length that

must be measured, depending on which one is the largest; for scratches one must measure only the depth.

24.	Critical size of population	Total number of inclusions or total length of scratches with significant dimensions that cannot be exceeded in a finished window.
25.	Critical density of population	Number of inclusions or scratches per specified contiguous area or volume of window that cannot be exceeded in a finished window.
26.	Critical spacing	Minimum allowable spacing between peripheries of inclusions or scratches in a finished window.
27.	Critical location	Location where inclusions or scratches whose size exceeds the significant dimension cannot be tolerated.
28.	Standard window geometry	Proven window geometry that because of its safe service record has been incorporated in this Standard. Windows with standard geometries may be used in pressure vessels for human occupancy without having to undergo experimental design qualification.
29.	Non-standard window geometry	Unproven window geometry that must be first experimentally qualified for the intended design pressure and temperatures.
30.	Design qualification	Experimental procedure for verifying the conformance of a non-standard window design to mandatory structural requirements of the standard.
31.	Short term critical pressure (STCP)	Pressure required to catastrophically fail a window at 650 psi/minute pressurization rate in 70-77°F (21 to 25 PC) ambient temperature environment.
32.	Short term proof pressure (STPP)	Pressure that a window must withstand without catastrophic failure under short term pressurization at 650 psi/minute (45 MPa) rate in design temperature ambient environment. The Standard defines short term proof pressure as equal to 4 x design pressure.
33.	Long term proof pressure (LTPP)	Pressure that a window must withstand without catastrophic failure under sustained pressurization of 80,000 hours duration in design temperature ambient environment. The Standard defines long term proof pressure as equal to design pressure.

34.	Cyclic proof pressure (CPP)	Pressure that a window must withstand without cracking under intermittent pressurization in the form of 1000 standard pressure cycles (4 hour long pressure phase followed by 4 hour long relaxation phase) in design temperature environment. The Standard defines cyclic proof pressure as equal to design pressure.
35.	Cyclic fatigue life	Number of pressure cycles that a window can withstand prior to catastrophic failure when pressure cycled to design pressure in design temperature environment. The Standard defines the cyclic fatigue life as 10^4 standard pressure cycles.

L.   Non-Standard Window Geometries

L.1   Acrylic plastic windows with non-standard geometries may be incorporated into chambers for human occupancy providing that their material properties and structural performance satisfy the mandatory short term, long term, and cyclic proof pressure requirements of the Standard.

L.2   The window with non-standard geometry must meet the following mandatory requirements:

a.   short term proof pressure = 4 x design pressure, sustained without catastrophic failure at design temperature environment under short term pressurization.

b.   long term proof pressure = design pressure sustained continuously for 80,000 hours in design temperature environment without catastrophic failure;

c.   crack-free cyclic proof pressure = design pressure sustained intermittently during 1000 pressure cycles of 8 hours each duration in design temperature environment without cracking.

L.3   The short term proof pressure (STPP) of the window with non-standard geometry shall be experimentally verified with a minimum of 5 model scale, or full scale windows.

a.   The windows shall be individually pressurized at 650 psi/minute rate in design temperature environment until catastrophic failure takes place;

b.   The critical pressures of all five windows must exceed the short term proof pressure.

L.4   The long term proof pressure (LTPP) of the window with non-standard geometry shall be experimentally verified with a minimum of five model scale, or full scale windows.

a.   The windows shall be individually subjected to sustained pressure loading at design temperature;

b. Each window shall be subjected to a different hydrostatic pressure and the duration of sustained pressure preceding the catastrophic failure recorded;

c. The pressures to which the individual windows shall be subjected are 0.9, 0.8, 0.75, 0.7 and 0.65 times the average critical pressure established experimentally in L.3.

d. The experimental data points of L.4.c shall be plotted on log-log coordinates and the relationship between critical pressures and duration of loading represented empirically by a straight line. The experimental points generated in L.3 with zero sustained loading duration shall be also plotted on the same graph. The testing of any window specimen that has not failed in 10,000 hours of sustained loading may be terminated at that time and its data point omitted from the graph.

e. Extension of the plotted line to 80,000 hours shall be accepted by this Standard as valid prediction of critical pressures in this time range.

f. The predicted critical pressure at 80,000 hours of sustained loading must exceed the long-term proof pressure.

L.5   The crack-free cyclic proof pressure (CPP) of the window with non-standard geometry shall be experimentally verified on a minimum of two model scale, or a single full scale window.

a. The window shall be pressure-cycled 1000 times form 0 to design pressure in design temperature environment;

b. The length of the individual pressure cycles may vary, form one cycle to another but the average length of the sustained loading and relaxation phases in all of the pressure cycles must equal, or exceed 4 hours;

c. At the completion of 1000 pressure cycles the window shall be visually inspected with unaided eye (except for that necessary to correct for 20/20 vision) for the presence of cracks;

d. Absence of visible cracks shall be considered proof that the window design meets the crack-free cyclic proof pressure requirement of the Standard.

L.6   The temperature of tap water serving as pressurizing medium during the performance of proof tests is allowed to deviate from the specified design temperature by the following margin:

a. Short term pressurization of L.3:   +10°F (5.5°C);

b. Long term pressurization of L.4:   +10°F (5.5°C);

c. Cyclic pressurization of L.5:   +25°F (14°C).

L.7   The successful qualification of a window design with non-standard geometry for a chosen design pressure and temperature under the procedures of L.1 through L.5 does not qualify automatically other windows with same geometry but different t/D_i ratios.

Table A-1 Specified Values of Physical Properties For Each Lot
(To be certified by the manufacturer of material)

Test Procedures ASTM	Physical Property	Minimum Values	
		Engineering Units	Metric Units
D256*	Izod notched impact strength	$\geq$ 0.25 ft-lb/in.-min.	$\geq$ 13.3 J/m
D542*	Refractive index	1.49 ± 0.01	1.49 ± 0.01
D570*	Water absorption, 24 hr.	$\leq$ 0.25%	$\leq$ 0.25%
D621	Compressive deformation, 4000 psi, 122 F	$\leq$ 0.85%	$\leq$ 0.85%
D638*	Tensile:		
	(a) Ultimate strength	$\geq$ 9000 psi	$\geq$ 62 MPa
	(b) Elongation at break	$\geq$ 2%	$\geq$ 2%
	(c) Modulus	$\geq$ 400,000 psi	$\geq$ 2760 MPa
D695*	Compressive, yield strength	$\geq$ 15,000 psi	$\geq$ 103 Mpa
	Modulus	$\geq$ 400,000 psi	$\geq$ 2760 MPa
D732*	Shear, ultimate strength	$\geq$ 8,000 psi	$\geq$ 55 MPa
D785*	Rockwell hardness	$\geq$ M scale 90	$\geq$ M scale 90
D790*	Flexural, ultimate strength	$\geq$ 14,000 psi	$\geq$ 97 MPa
D792*	Specific gravity	1.19 ± 0.01	1.19 ± 0.01
E308	Ultraviolet (290-330 nm) light transmittance	$\leq$ 5%	$\leq$ 5%
D702	Clarity, visually rated	Must have readibility	
D696	Coefficient of linear thermal expansion at	10^{-5} (in./in. · F)	10^{-3} (mm/mm · C)
	+60	4.0	1.83
	+80	4.3	1.96
	+100	4.7	2.15
D648	Deflection temperature of plastics under flexure	$\geq$ 200°F	$\geq$ 93°C
Method B.5	Residual monomer:		
	(a) methyl methacrylate	$\leq$ 1.5%	$\leq$ 1.5%
	(b) ethyl acrylate	$\leq$ 0.01%	$\leq$ 0.01%

Note 1.   Tests marked with an asterisk (*) require testing of a minimum of two specimens. For others, test a minimum of one specimen. Where applicable use the sampling procedures described in B.4. For other tests use the sampling procedures described in the appropriate ASTM test methods.

2.   Where two specimens are required in the test procedure, the average of the test values will be used to meet the requirements of the minimum physical properties of Table A-1.

Table A-2 Specified Values of Physical Properties For Each Casting
(To be verified by testing of specimen from each casting or lot as defined in Chapter B.2).

Test Procedures ASTM	Physical Property	Specified Values	
		Metric Units	Engineering Units
D638*	Tensile ultimate strength	≥62 MPa	≥9,000 psi
	elongation at break	≥2%	≥2%
	modulus of elasticity	≥2760 MPa	≥400,000 psi
D695*	Compressive yield strength	≥103 MPa	≥15,000 psi
	modulus of elasticity	≥2760 MPa	≥400,000 psi
D621*	Compressive deformation at 4000 psi and 122° F	≤1 percent	≤1 percent
E308	Ultraviolet transmittance (for 0.5 inch thickness)	≤5 percent	≤5 percent
D702	Visual Clarity	Must pass Readability test	Must pass Readability test
Method B.5	Residual methyl methacrylate monomer	≤1.5 percent	≤1.5 percent
Method B.5	Residual ethyl acrylate monomer	≤0.01 percent	≤0.01 percent

Note 1. Tests marked with an asterisk (*) require testing of a minimum of two specimens. For others, test a minimum of one specimen. Where applicable use the sampling procedures described in B.4.

2. Where two specimens are required in the test procedure, the average of the test values will be used to meet the requirements of the minimum physical properties of Table A.2.

TABLE B-1

CONVERSION FACTORS FOR ACRYLIC PLASTIC
FLAT DISC WINDOWS

Operational Pressure Ranges	Temperature ranges				
	(50°F) ≤ 10°C	(75°F) ≤ 24°C	(100°F) ≤ 38°C	(126°F) ≤ 52°C	(151°F) ≤ 66°C
N = 1	CF = 5	CF = 6	CF = 8	CF = 10	CF = 16
(2500 psi) 17.2 MPa N = 2	CF = 5	CF = 6	CF = 8	CF = 10	(4000 psi) - - - - - 27.6 MPa
(5000 psi) 34.5 MPa N = 3	CF = 5	CF = 6	- - - - - 48.3 MPa (7000 psi)		
(7500 psi) 51.7 MPa					

Note: The conversion factors (CF) shown in Table B-1 apply only to short term critical pressures (STCP) plotted in Figures B-1 and B-2.

TABLE B-2

CONVERSION FACTORS FOR ACRYLIC PLASTIC
1. CONICAL FRUSTUM WINDOWS
2. DOUBLE BEVELED DISC WINDOWS

Operational Pressure Ranges	Temperature Ranges				
	(50°F) ≤ 10°C	(75°F) ≤ 24°C	(100°F) ≤ 38°C	(126°F) ≤ 52°C	(151°F) ≤ 66°C
↑ N = 1 ↑ (2500 psi) 17.2 MPa	CF = 5	CF = 6	CF = 8	CF = 10	CF = 16
N = 2 ↕ (5000 psi) 34.5 MPa	Conversion factors for these pressures must be interpolated between the upper and lower values shown — CF = 4	CF = 5	CF = 7	CF = 9	(4500 psi) 31.0 MPa
N = 3 (7500 psi) 51.7 MPa	CF = 4	CF = 5			
N = 4 (10,000 psi) 69.0 MPa	CF = 4	CF = 5	55.2 MPa (8000 psi)		

Note: The conversion factors (CF) in Table B-2 apply only to short term critical pressures (STCP) plotted in Figures B-3 and B-4.

TABLE B-3

CONVERSION FACTORS FOR ACRYLIC PLASTIC
1. SPHERICAL SECTOR WINDOWS WITH CONICAL EDGE
2. HYPERHEMISPHERICAL WINDOWS WITH CONICAL EDGE
3. NEMO TYPE WINDOWS WITH CONICAL PENETRATIONS

Operational Pressure Ranges	Temperature Ranges				
	(50°F) ≤ 10°C	(75°F) ≤ 24°C	(100°F) ≤ 38°C	(126°F) ≤ 52°C	(151°F) ≤ 66°C
N = 1 — (2500 psi) 17.2 MPa	CF = 4	CF = 6	CF = 8	CF = 10	CF = 16 / 10.3 MPa – – – (1500 psi)
N = 2	CF = 4	CF = 6	CF = 8 ⌐ 24.1 MPa (3500 psi)	CF = 10 ⌐ / CF = 8	20.7 MPa (3000 psi)
N = 3 — (5000 psi) 34.5 MPa	CF = 4				
(7500 psi) 51.7 MPa					

Note: The conversion factors (CF) in Table B-3 apply only to short term critical pressures (STCP) plotted in Figures B-5, B-6 (for spherical sector windows with conical edge) and B-7 (for hyperhemispherical windows with conical edge and NEMO type windows with conical penetrations).

TABLE B-4

CONVERSION FACTORS FOR ACRYLIC PLASTIC
1. SPHERICAL SECTOR WINDOWS WITH SQUARE EDGE
2. HEMISPHERICAL WINDOWS WITH EQUATORIAL FLANGE

Operational Pressure Ranges	Temperature Ranges				
	$(50^{\circ}F)$ $\leq 10^{\circ}C$	$(75^{\circ}F)$ $\leq 24^{\circ}C$	$(100^{\circ}F)$ $\leq 38^{\circ}C$	$(126^{\circ}F)$ $\leq 52^{\circ}C$	$(151^{\circ}F)$ $\leq 66^{\circ}C$
N = 1 ↑	CF = 5	CF = 7	CF = 9	CF = 11	CF = 17 10.3 MPa (1500 psi)
(2500 psi) 17.2 MPa					
N = 2	CF = 5	CF = 7	CF = 9 20.6 MPa (3000 psi)		
(5000 psi) 34.5 MPa					
N = 3	CF = 5				
(7500 psi) 51.7 MPa					

Note: The conversion factors (CF) in Table B-4 apply only to short term
critical pressures (STCP) plotted in Figures B-5 and B-6.

15-37

TABLE B-5

CONVERSION FACTORS FOR ACRYLIC PLASTIC
CYLINDRICAL WINDOWS

A. Internal Pressure

Operational Pressure Ranges	Temperature Ranges				
	(50°F) ≤ 10°C	(75°F) ≤ 24°C	(100°F) ≤ 38°C	(126°F) ≤ 52°C	(151°F) ≤ 66°C
(250 psi) 1.72 MPa $\uparrow$ A = 1 $\downarrow$	13	14	15	20	25

The conversion factors (CF) in Table B-5A apply only to short term critical pressures (STCP) plotted in Figure B-7.

B. External Pressure

Operational Pressure Ranges	Temperature Ranges				
	(50°F) ≤ 10°C	(75°F) ≤ 24°C	(100°F) ≤ 38°C	(126°F) ≤ 52°C	(151°F) ≤ 66°C
(2500 psi) 17.2 MPa $\uparrow$ N = 1 $\downarrow$	6	7	9	11	17

The conversion factors (CF) in Table B-5B apply only to short term critical pressures (STCP) plotted in Figures B-8, B-9, B-10, B-11. Since the tube may fail due to yielding of material (Figure B-8), or elastic buckling (Figures B-9, B-10, B-11) both modes of failure must be considered in selection of t/D ratio. Which of the modes of failure is chosen as the design criterion depends on which of the failure modes requires a higher t/D$_i$ ratio for the desired short term critical pressure. The mode of failure requiring a higher t/D$_L$ ratio is chosen as the design criterion.

TABLE C-1   Conical Frustum Windows for Design
Pressures in Excess of 69 MPa
(10,000 psi)

Design Pressure		TEMPERATURE RANGES								
		≤ 10°C (50°F)					≤ 24°C (75°F)			
			D_i/D_f					D_i/D_f		
		t/D_i	60°,	90°,	120°,	150°,	t/D_i	60°,	90°,	120°,	150°
MPa	PSI										
75.86	(11,000)	1.0	↑	↑	↑	↑	1.1	↑	↑	↑	↑
82.76	(12,000)	1.1					1.2				
89.66	(13,000)	1.2					1.3				
96.55	(14,000)	1.3					1.4				
103.45	(15,000)	1.4	1.13	1.17	1.23	1.69	1.5	1.13	1.17	1.23	1.69
110.34	(16,000)	1.5	↑	↑	↑	↑	1.6	↑	↑	↑	↑
117.24	(17,000)	1.6					1.7				
124.14	(18,000)	1.7					1.8				
131.03	(19,000)	1.8					1.9				
137.93	(20,000)	1.9	1.20	1.26	1.53	2.48	2.0	1.20	1.26	1.53	2.48

NOTE: D_i/D_f ratio refers to conical Frustum seat specifications shown in
Figure C-1

TABLE D-1   Annealing Schedule for Acrylic Plastic Windows

A.   Recommended Heating Times for Elevated
     Temperature Annealing of Acrylic

| Thickness (inches)	Heating Time* in Hours for Acrylic Placed in a forced-Circulation Air Oven Maintained at the Indicated Temperature			
	212F (100C)	195F (90C)	185F (85C)	175F (79C)
0.500 to 0.750 inc.	4	6	8	11
0.875 to 1.125 inc.	4-1/2	6-1/2	8-1/2	11-1/2
1.250 to 1.500 inc.	5	7	9	12
1.750	5	7	9	12
2.000	6	8	10	13
2.250	7	9	11	14
2.500	9	11	13	15
3.000	11	12	14	17
3.250	13	14	16	17
3.500	13	14	16	19
3.750	14	16	18	20
4.000	17	18	20	22
5.000	23	24	26	28

*Includes period of time required to bring part up to annealing temperature, but not cooling time.

B. Recommended Cooling Rates for Acrylic Subjected
   to Elevated Annealing Temperatures

Thickness (inches)	Maximum Cooling Rate	Time in Hours to Cool Acrylic from the Indicated Annealing Temperature at the Maximum Permissible Rate to the Removal Temperature of 160°F.			
	°F/hr °C/hr	212F (100C)	195F (90C)	185F (85C)	175F (79C)
0.500 to 0.750 inc.	14 (25)	2	1-1/4	1	1/2
0.875 to 1.125 inc.	10 (18)	3	2	1-3/4	3/4
1.250 to 1.500 inc.	7.2(13)	4	2-1/2	2	1
1.750	6.1(11)	4-1/2	2-3/4	2	1
2.000	5.5(10)	5-1/4	3-1/2	2-1/2	1
2.250	5 (9)	6	4	3	1-1/4
2.500	4.5(8)	6-1/2	4-1/4	3-1/4	1-1/4
3.000	4 (7)	7-1/4	4-3/4	3-1/2	1-1/2
3.250	3.5(6)	8	5-1/4	4	1-3/4
3.500	3.5(6)	8-3/4	5-3/4	4-1/4	1-3/4
3.750	3.5(6)	9-1/4	6-1/4	4-1/2	1-3/4
4.000	3 (5)	10-1/2	6-3/4	5	2
5.000	2 (3)	18	10	8	3-1/2

NOTE: Both the recommended heating times and cooling times may be exceeded by
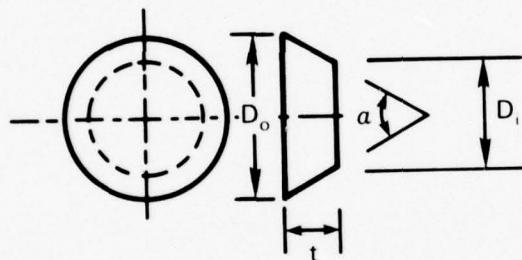   the fabricator upon his discretion.

FLAT DISC WINDOW
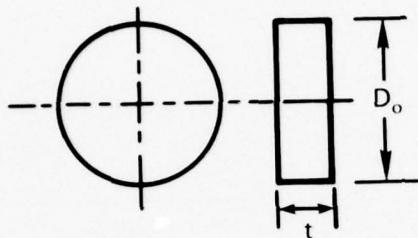
$t \geqslant 12.5$ mm (0.5 in.)
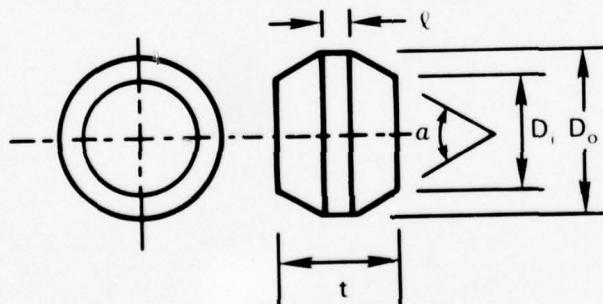
$t/D_o \geqslant 0.125$

CONICAL FRUSTUM WINDOW

$t \geqslant 12.5$ mm (0.5 in.)

$t/D_i \geqslant 0.125$

$a \geqslant 60°$

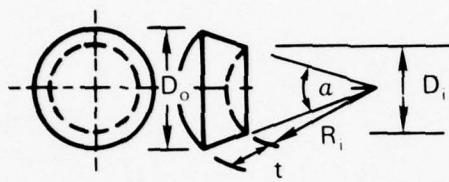DOUBLE BEVELED DISC WINDOW

$t \geqslant 25$ mm (1.0 in.)

$t/D_i \geqslant 0.250$

$a \geqslant 60°$

$\ell \leqslant 0.25t$
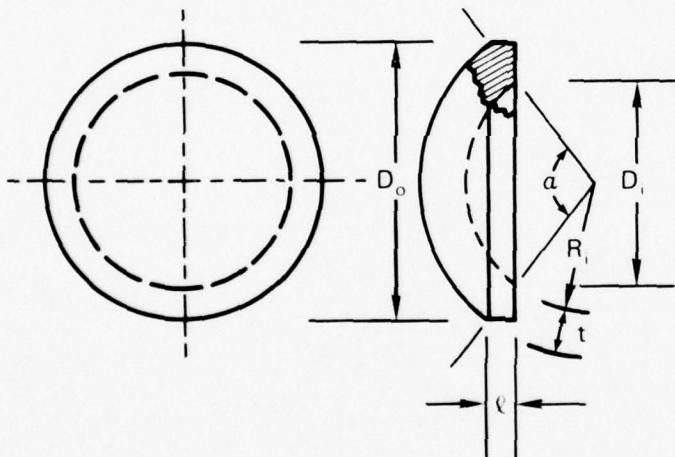
Figure A-1. Standard window geometries.

SPHERICAL SECTOR WINDOW WITH CONICAL EDGE

$t \geqslant 12.5$ mm (0.5 in.)
$a \geqslant 60°$
$t/R_i \geqslant 0.09$ FOR $a \geqslant 60°$
$t/R_i \geqslant 0.06$ FOR $a \geqslant 90°$
$t/R_i \geqslant 0.03$ FOR $a = 180°$

SPHERICAL SECTOR WINDOW WITH SQUARE EDGE

$t \geqslant 12.5$ mm (0.5 in.)
$30° \leqslant a \leqslant 150°$
$t/R_i \geqslant 0.03$
$D_i = 2R_i \sin a/2$
$D_o = 2R_o \sin a/2$
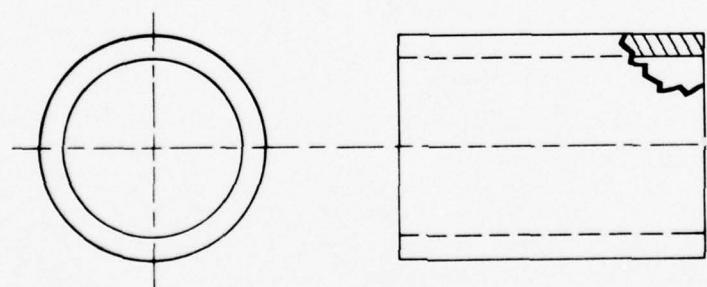$R_o = R_i + t$
$\ell = t \sin (90° - a/2)$

Figure A-2. Standard window geometries.

HEMISPHERICAL WINDOW WITH EQUATORIAL FLANGE
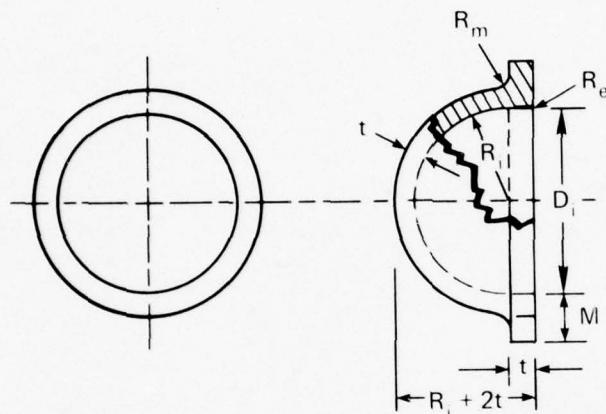
$t \geq 12.5$ mm (0.5 inches)

$t/R_i > 0.03$

$D_o = (D_i + 4t)$

$R_m \geq 3$ mm (0.125 inches)

0.5 mm $\leq R_e \leq 0.125\,t$

$1.5\,t \leq M \leq 2.0\,t$

CYLINDRICAL WINDOW

$t \geq 12.5$ mm (0.5 inches)

Figure A-3. Standard window geometries.

HYPERHEMISPHERICAL WINDOW

$t \geq 12.5$ mm(0.5 inches)

$0.03 \leq t/R_i \leq 0.15$

$a \leq 100°$

NEMO WINDOW

$t \geq 12.5$ mm(0.5 inches)

$0.03 \leq t/R_i \leq 0.15$

$a \leq 50°$

$\beta \leq 50°$

$\gamma \leq 50°$

$\theta \geq 25°$
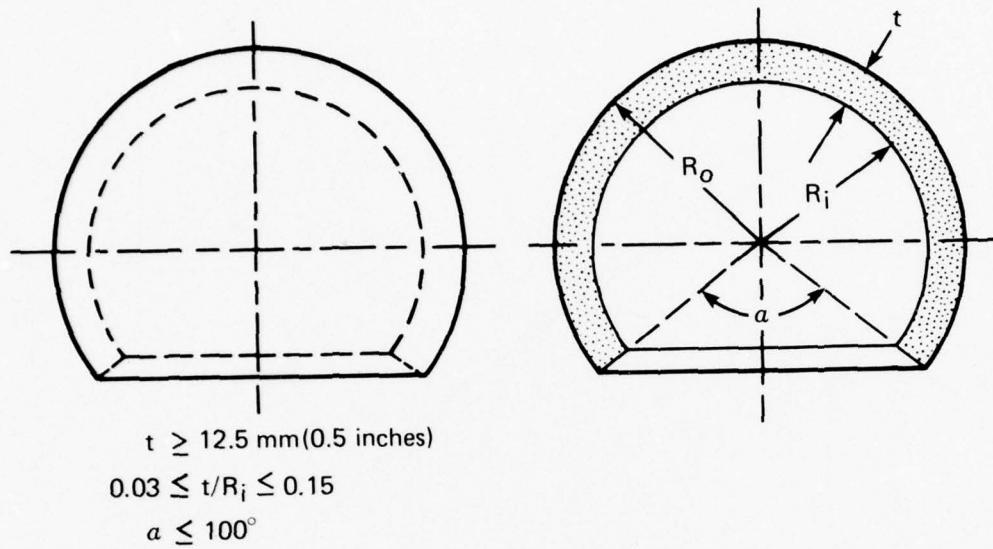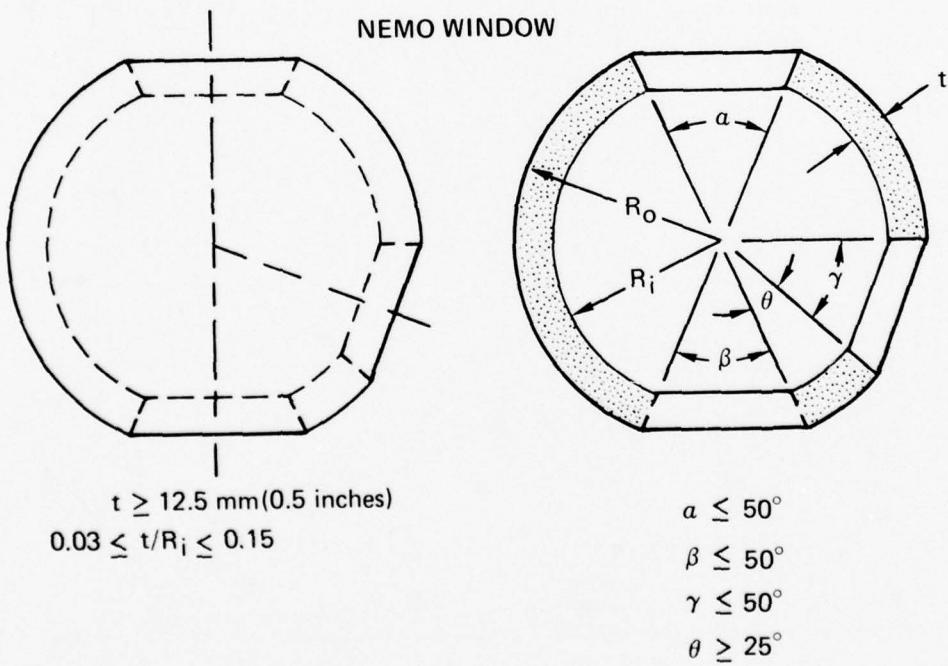
Figure A-4. Standard window geometries.
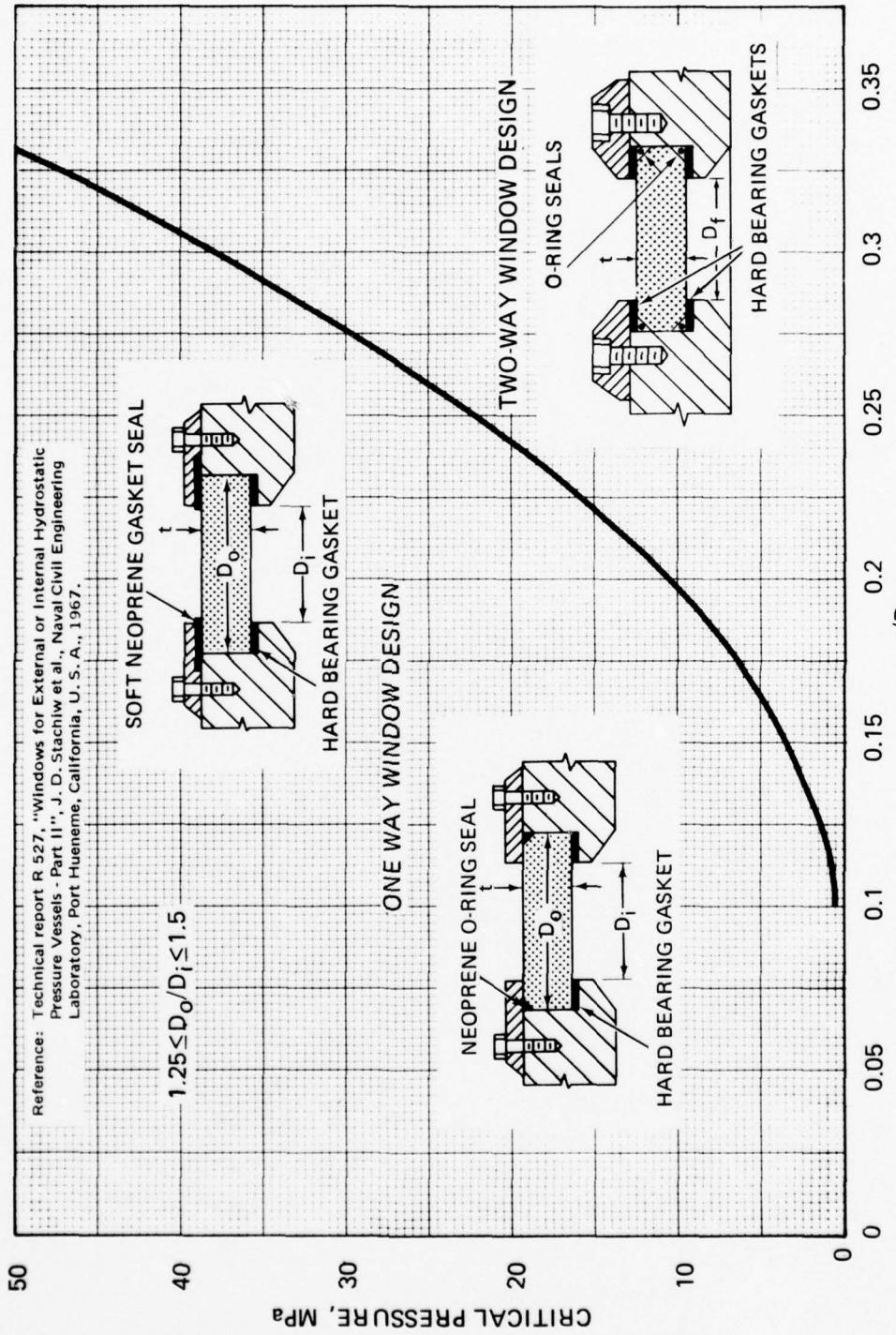
Figure B-1. Short term critical pressure of flat disc acrylic windows.
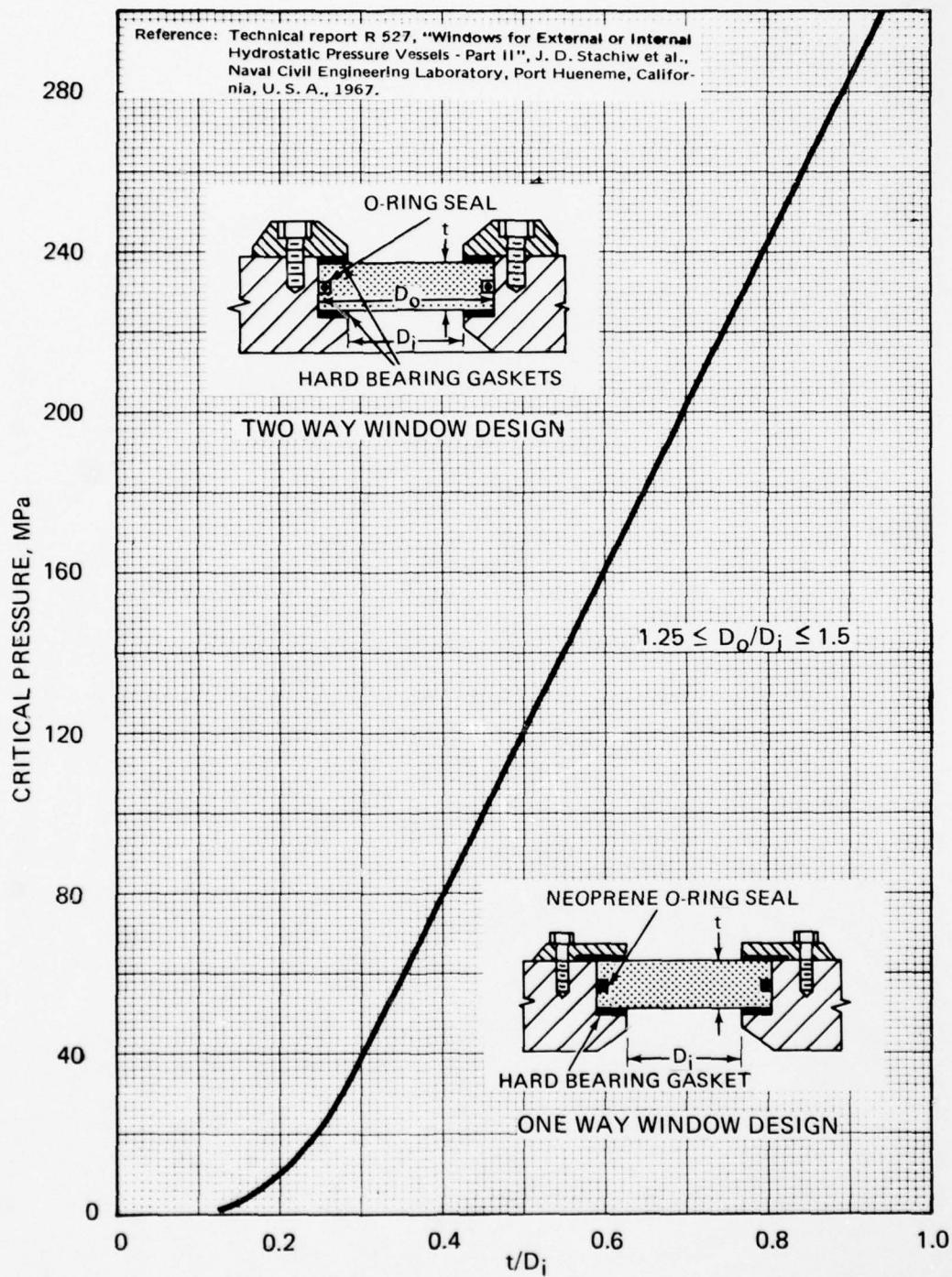
Figure B-2. Short term critical pressure of flat disc acrylic windows.
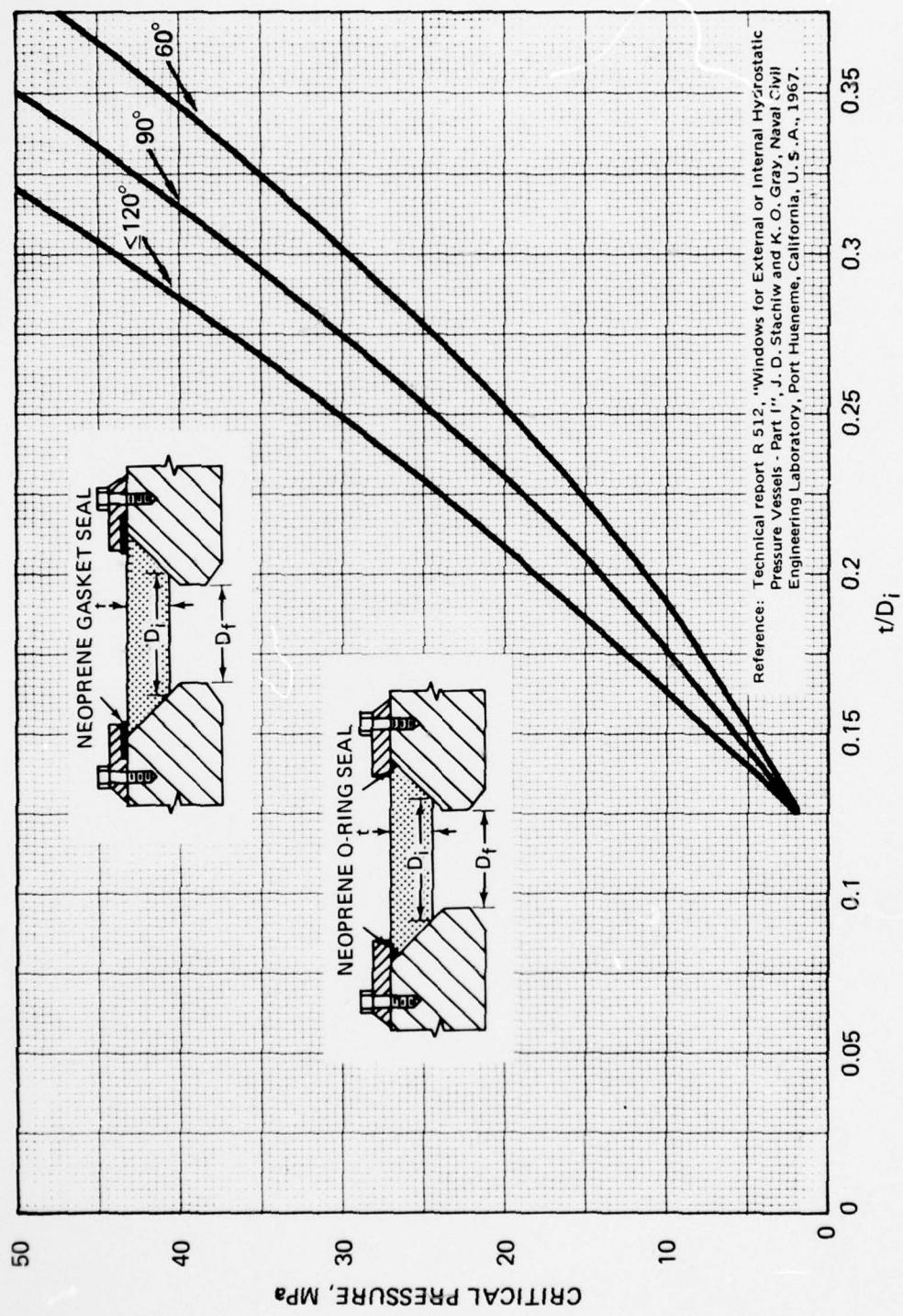
Figure B-3. Short term critical pressure of conical frustum acrylic windows.
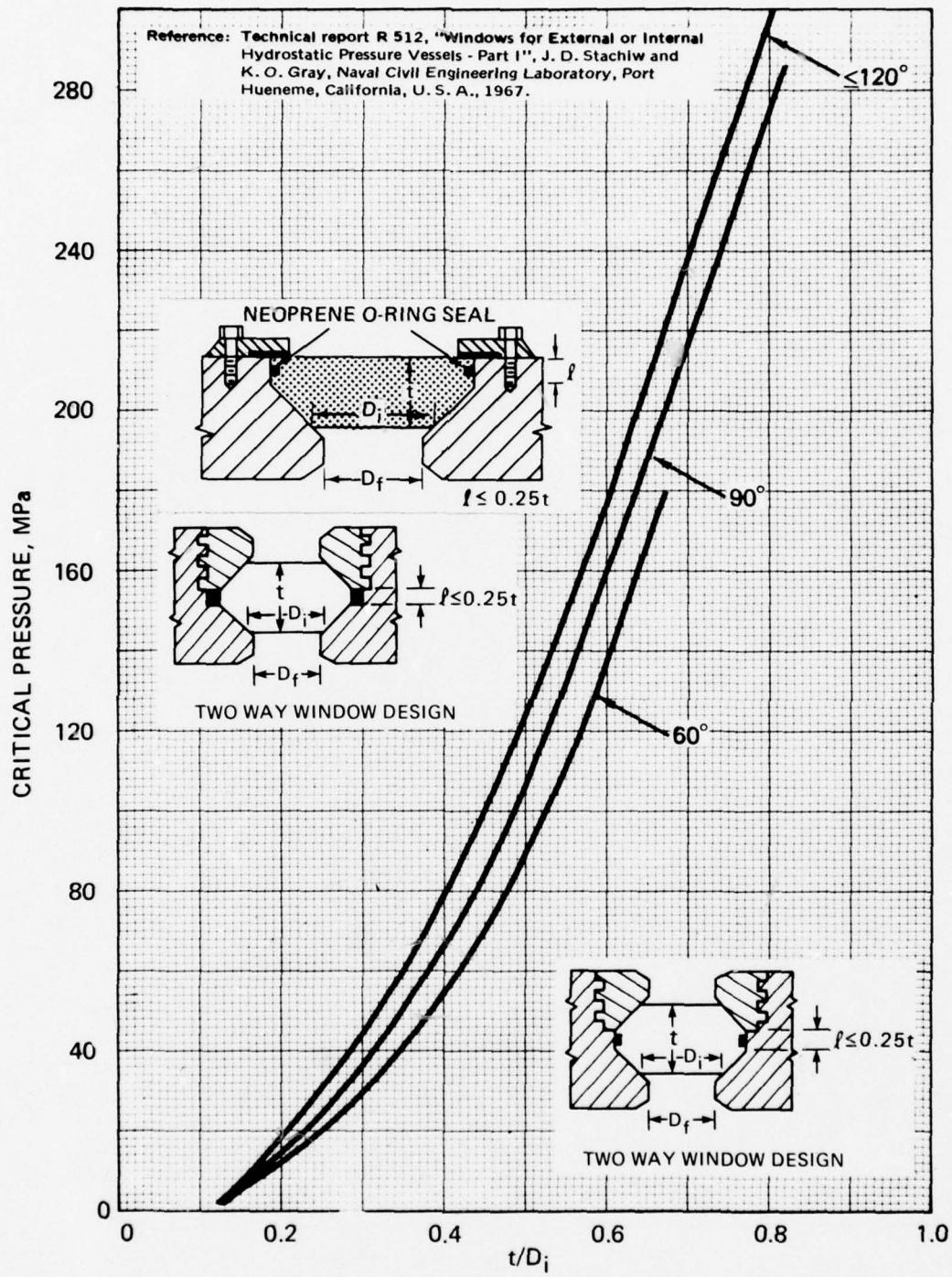
Figure B-4. Short term critical pressure of conical frustum acrylic windows.
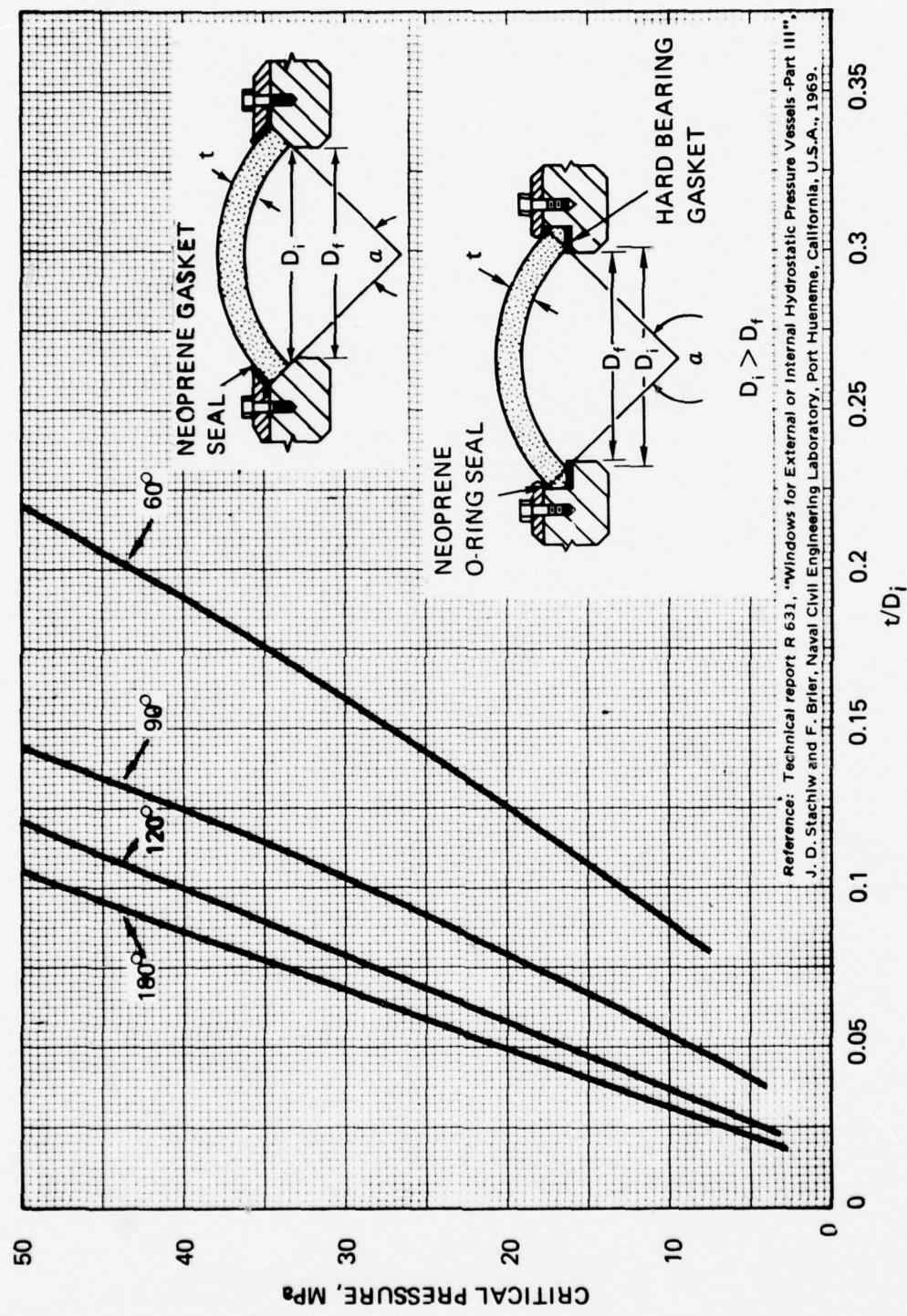
Figure B-5. Short term critical pressure of sherical shell windows.

Reference: Technical report R 631, "Windows for External or Internal Hydrostatic Pressure Vessels -Part III", J. D. Stachiw and F. Brier, Naval Civil Engineering Laboratory, Port Hueneme, California, U.S.A., 1969.
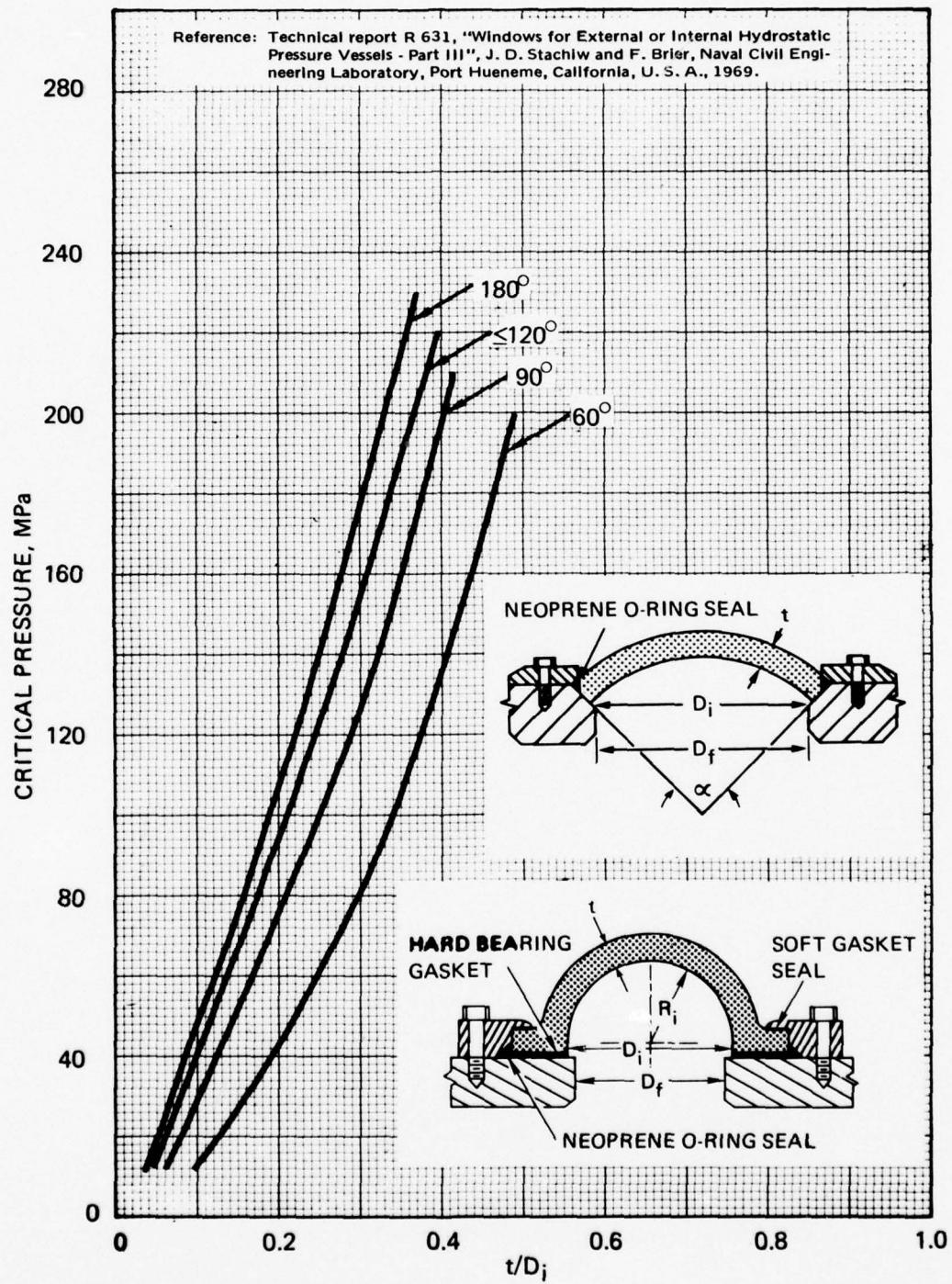
Figure B-6. Short term critical pressure of spherical shell windows.
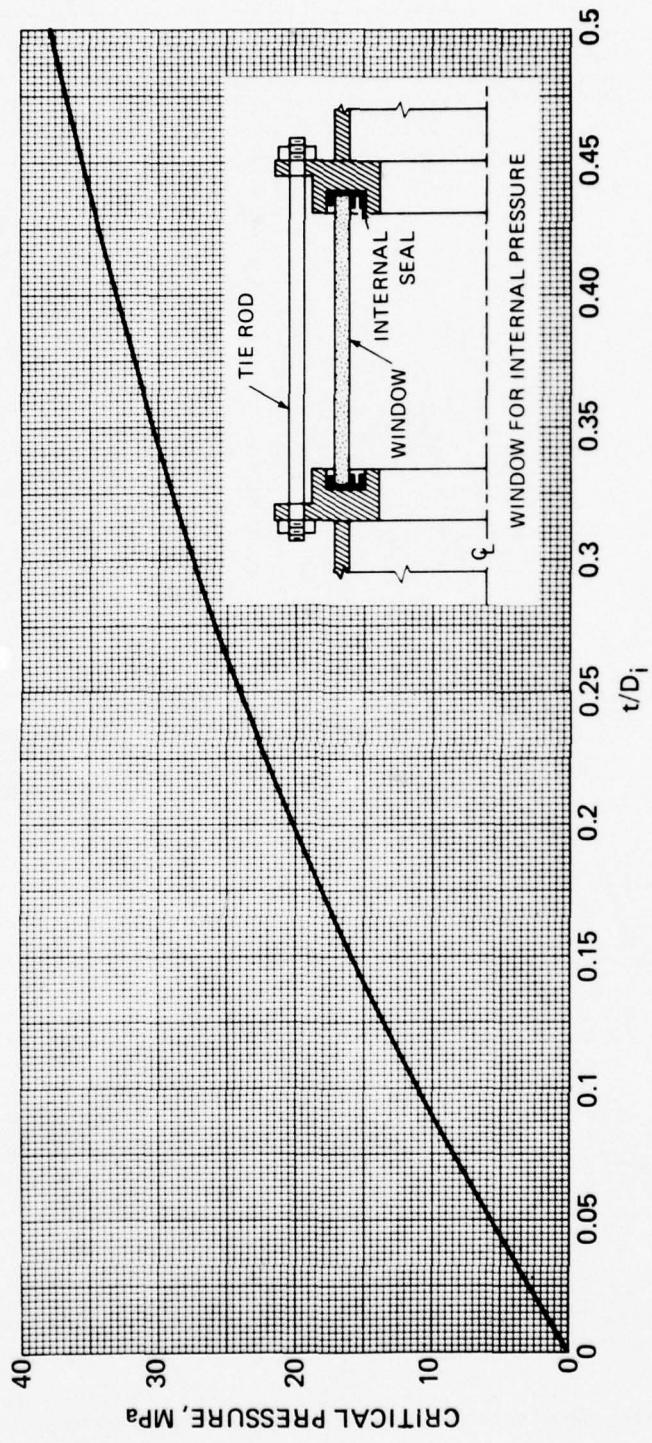
Figure B-7. Short-term critical pressure of cylindrical windows pressurized internally.
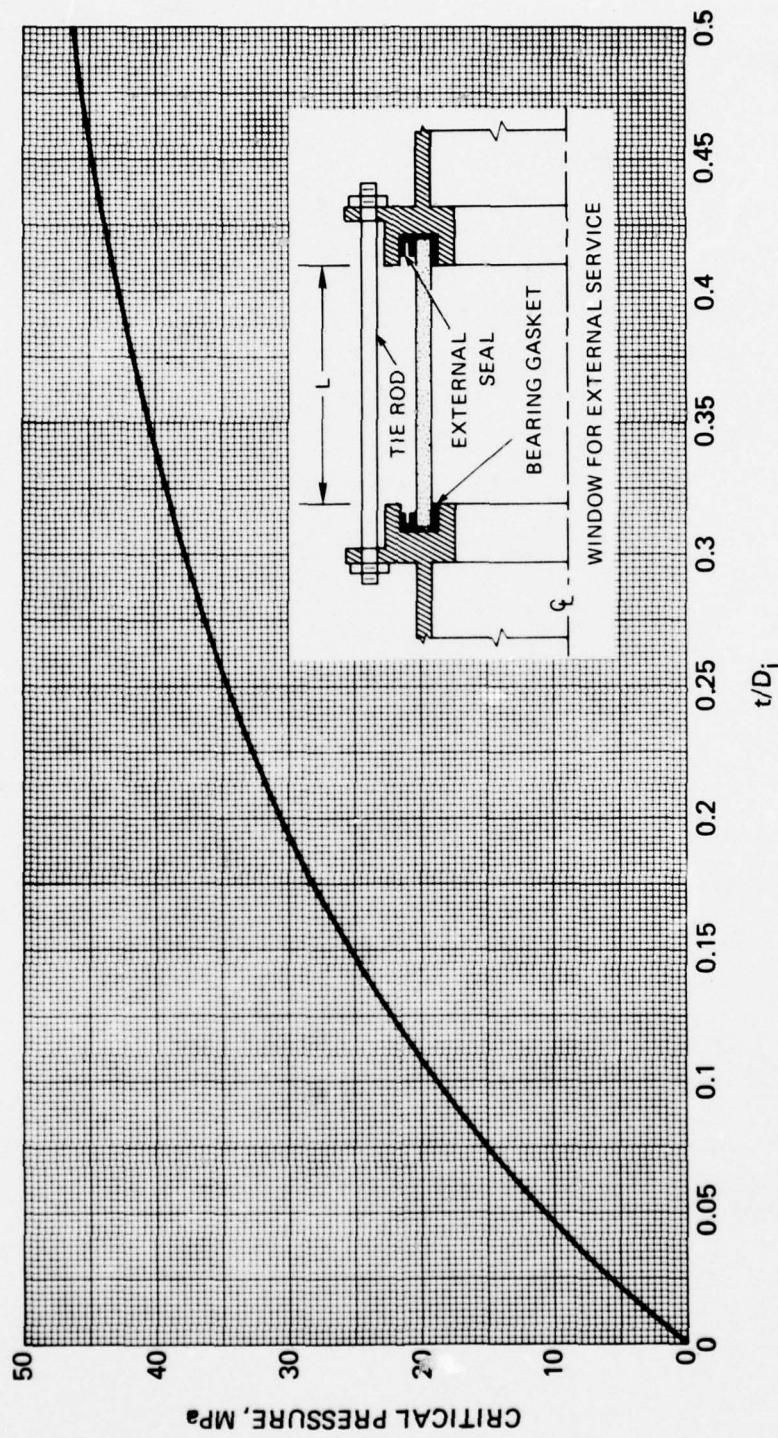
Figure B-8. Short-term critical pressure of cylindrical window pressurized externally.
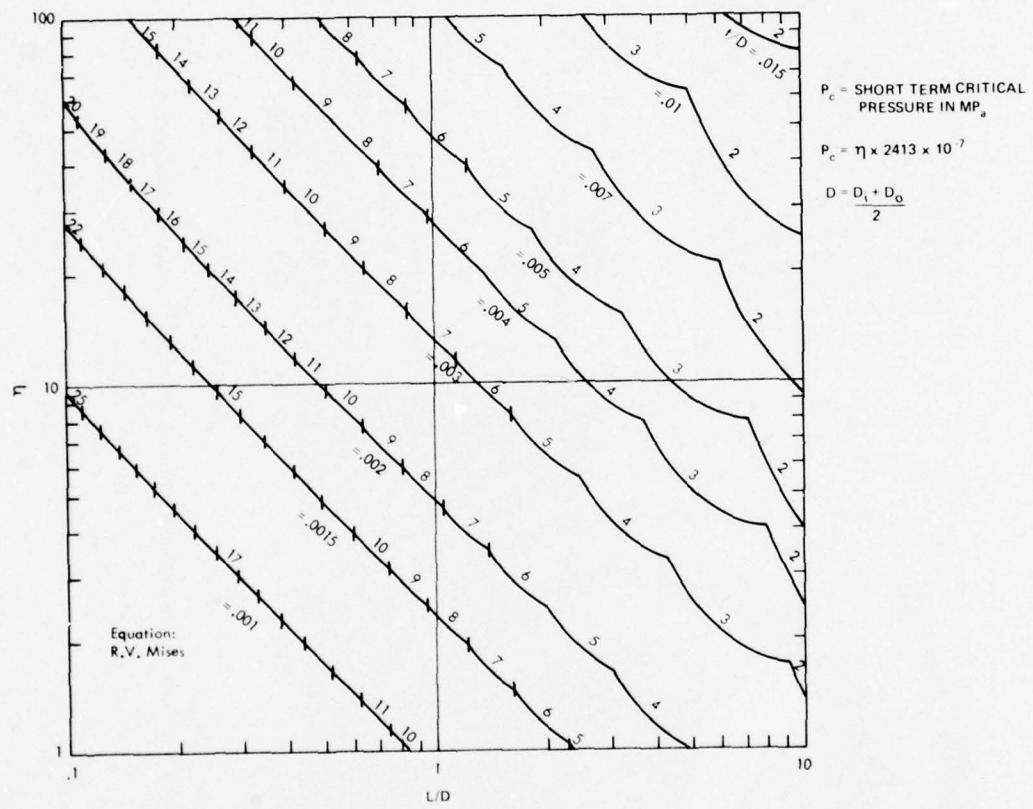
Figure B-9. Short term elastic buckling of cylindrical shells between supports under external hydrostatic pressure.

P_c = SHORT TERM CRITICAL PRESSURE IN MP_a

$P_c = \eta \times 2413 \times 10^{-7}$

$D = \dfrac{D_1 + D_0}{2}$
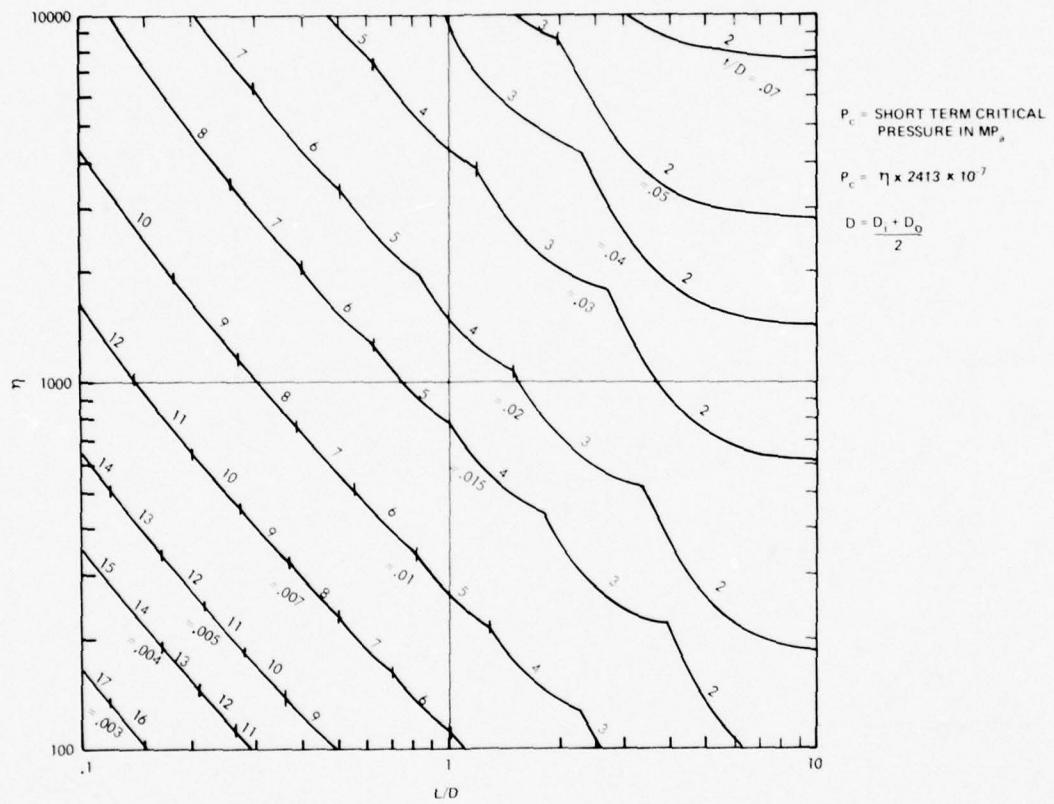
B-10. Short term elastic buckling of cylindrical shells between supports
under external hydrostatic pressure.
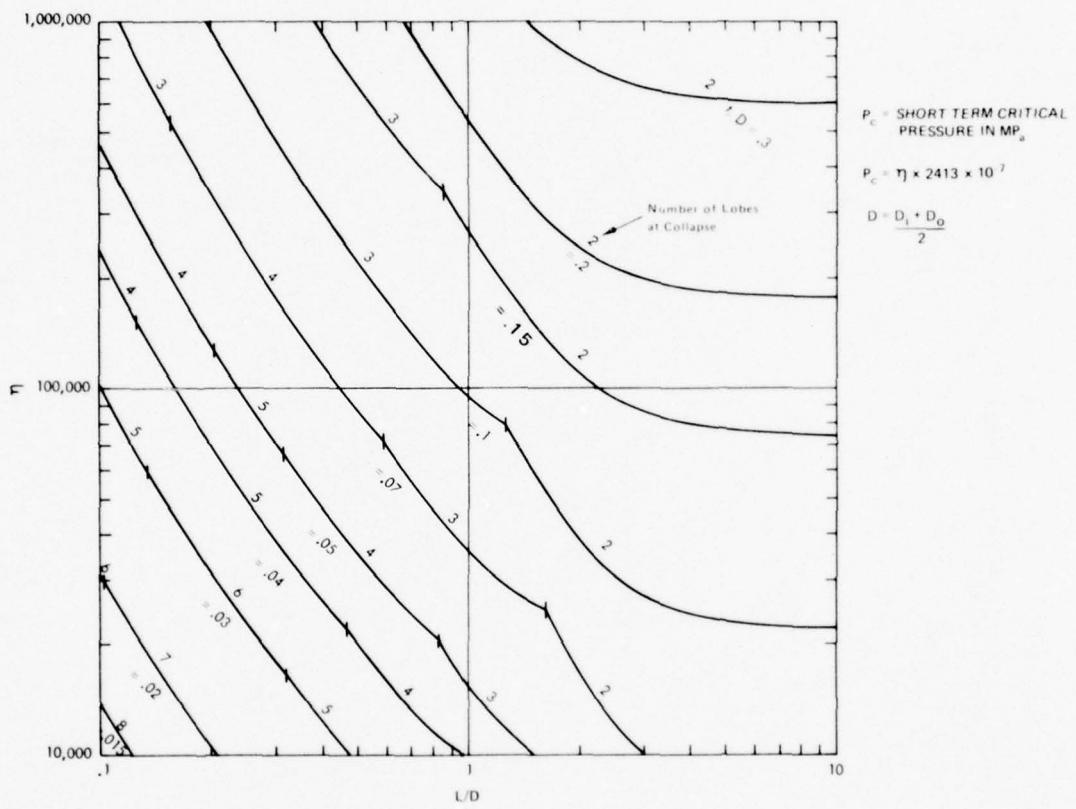
B-11. Short term elastic buckling of cylindrical shells between supports under external hydrostatic pressure.

15-56
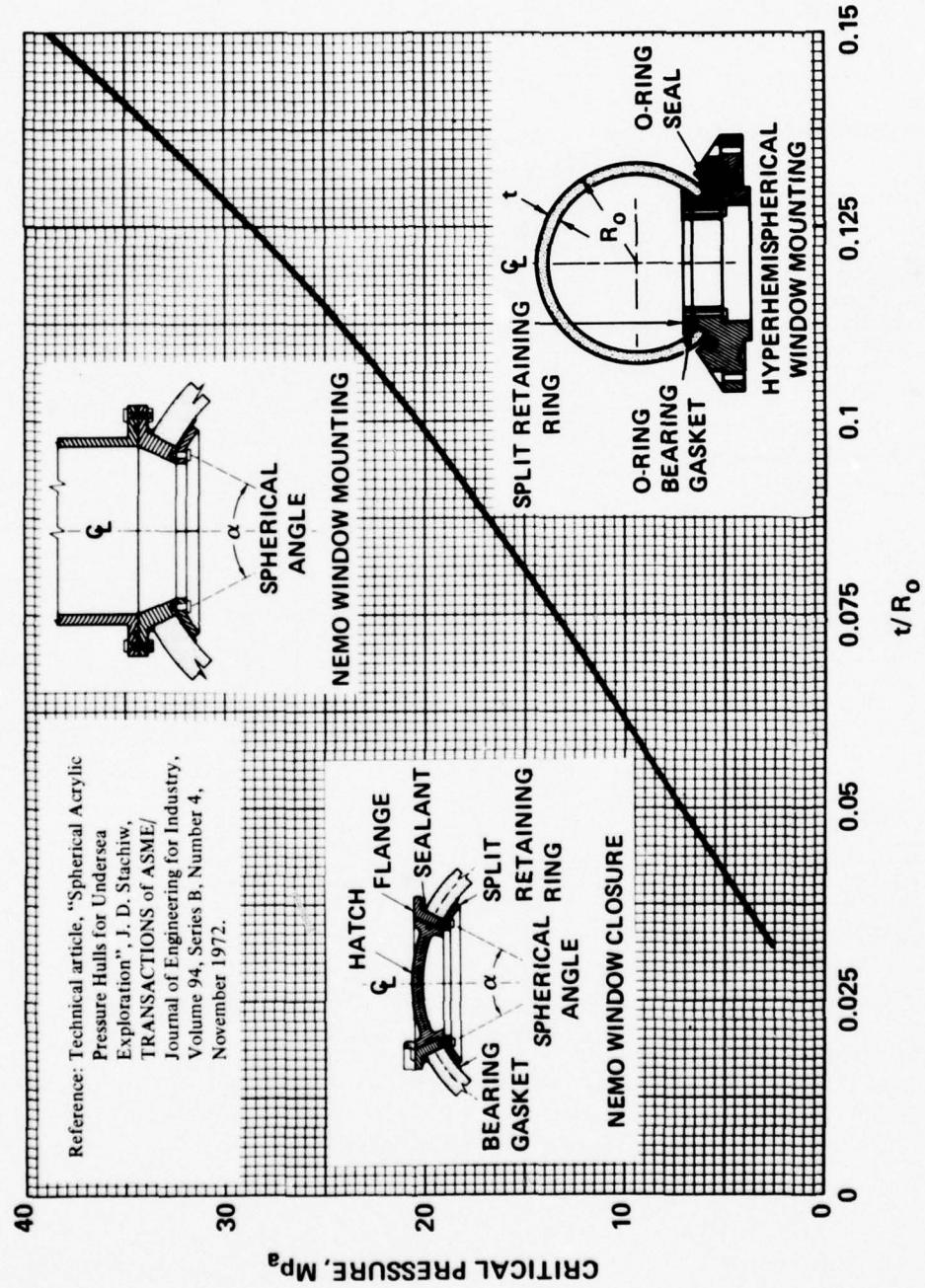
Figure B-12. Short term critical pressure of hyperhemispherical and NEMO type windows.

CONICAL FRUSTUM WINDOW
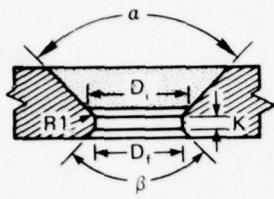
D_i/D_f RATIOS

OPERATIONAL PRESSURE RANGE	† INCLUDED ANGLE			
	60°	90°	120°	150°
N = 1	1.02	1.03	1.06	1.14
N = 2	1.04	1.06	1.12	1.28
N = 3	1.08	1.09	1.17	1.36
N = 4	1.10	1.15	1.20	1.42

SPHERICAL SHELL SECTOR WINDOW WITH CONICAL EDGE
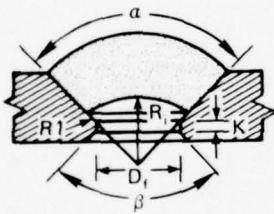
$(2R_i \sin (a/2))/D_f$ RATIOS

OPERATIONAL PRESSURE RANGE	† INCLUDED ANGLE				
	60°	90°	120°	150°	180°
N = 1	1.02	1.02	1.02	1.02	1.02
N = 2	1.03	1.03	1.03	1.03	1.03
N = 3	1.05	1.05	1.05	1.05	1.05

FLAT DISC WINDOW
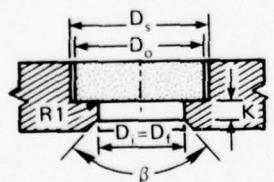
$1.250 \leqslant D_o/D_f \leqslant 1.50$

† – FOR a BETWEEN VALUES SHOWN INTERPOLATION IS REQUIRED

K – IS SELECTED ON THE BASIS OF STRUCTURAL ANALYSIS

β – IS SELECTED ON THE BASIS OF OPTICAL REQUIREMENTS

$1 \text{ mm} < R1 \leqslant 2 \text{ mm}$

Figure C-1. Seat cavity requirements.

DOUBLE BEVELED DISC WINDOW

$\dagger$ — FOR a BETWEEN VALUES SHOWN INTERPOLATION IS REQUIRED

K — IS SELECTED ON THE BASIS OF STRUCTURAL ANALYSIS

β — IS SELECTED ON THE BASIS OF OPTICAL REQUIREMENTS

$1\,mm \leqslant R1 \leqslant 2\,mm$

$\ell \leqslant 0.25t$

$n \leqslant \ell$

D_i/D_f RATIOS

OPERATIONAL PRESSURE RANGE	$\dagger$ INCLUDED ANGLE			
	$60°$	$90°$	$120°$	$150°$
N = 1	1.02	1.03	1.06	1.14
N = 2	1.04	1.06	1.12	1.28
N = 3	1.08	1.09	1.17	1.36
N = 4	1.10	1.15	1.20	1.42

Figure C-2. Seat cavity requirements.

15-59

SPHERICAL SECTOR WINDOW WITH SQUARE EDGE

$D_o = 2R_o \sin a/2$

$D_f = 2R_f \sin a/2$
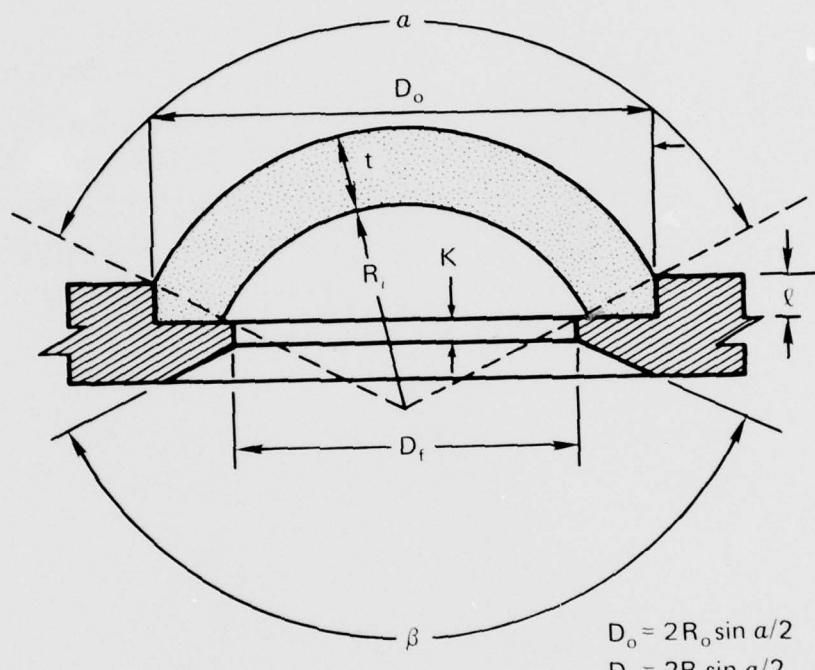
$D_f - D_f \geq 3mm\ (0.120\ inches)$

β — IS SELECTED ON THE BASIS OF OPTICAL REQUIREMENTS

K — IS SELECTED ON THE BASIS OF STRUCTURAL ANALYSIS

$\ell \geq t \sin (90° - a/2)$

Figure C-3. Seat cavity requirements.

HEMISPHERICAL WINDOW WITH EQUATORIAL FLANGE
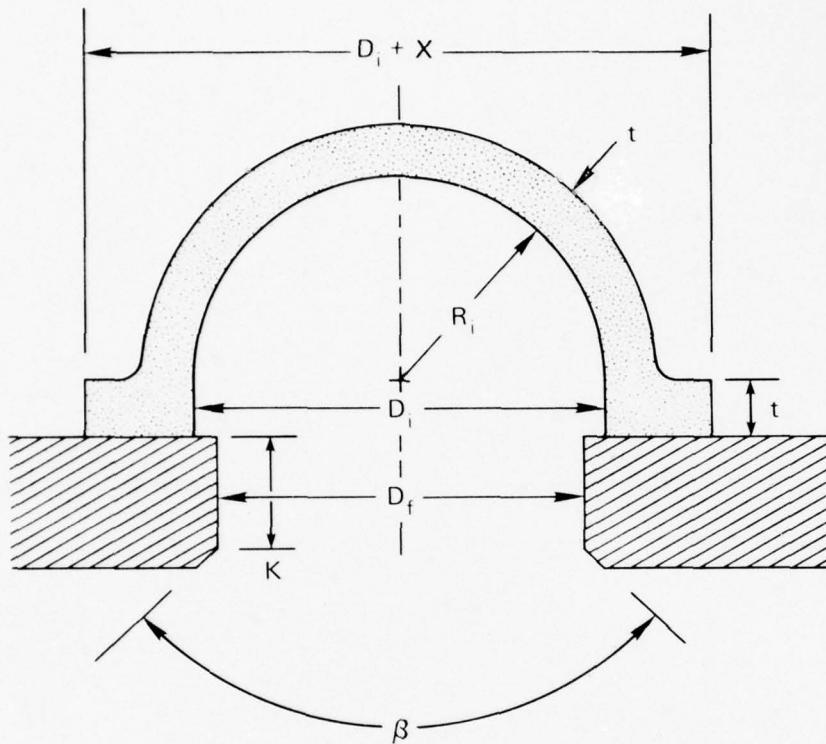
OPERATIONAL PRESSURE RANGE	D_i / D_f
N = 1	1.02
N = 2	1.03
N = 3	1.05

K — IS SELECTED ON THE BASIS OF STRUCTURAL ANALYSIS

β — IS SELECTED ON THE BASIS OF OPTICAL REQUIREMENTS

$3t \leq X \leq 4t$

Figure C-4. Seat cavity requirements.

CYLINDRICAL WINDOW

A. UNDER INTERNAL PRESSURE

ELASTOMERIC
SPACER

BEARING
GASKET

R_m

ELASTOMERIC
SEAL

$R_m \geq 1$ mm (0.040 inches)
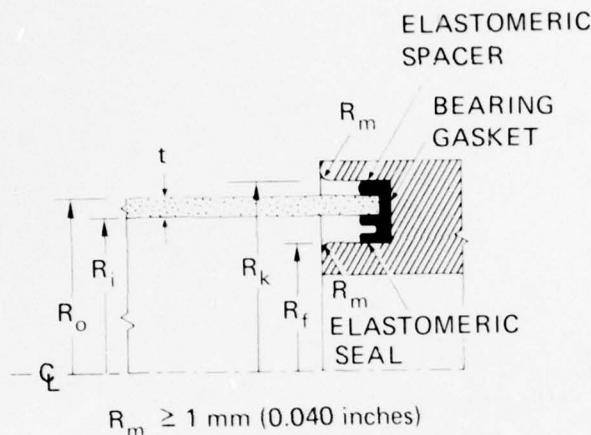
R_k — EXTERNAL RADIUS OF WINDOW SEAT; $\geq$ CALCULATED MAXIMUM R_o OF CYLINDER UNDER SUSTAINED INTERNAL DESIGN PRESSURE OF 8 hr DURATION AT DESIGN TEMPERATURE PLUS GASKET COMPRESSED 50 PERCENT

R_f — INTERNAL RADIUS OF WINDOW SEAT; $\leq$ CALCULATED R_i OF CYLINDER AT ZERO INTERNAL PRESSURE AND -30° C MINUS GASKET COMPRESSED 50 PERCENT

B. UNDER EXTERNAL PRESSURE

ELASTOMERIC
SEAL

R_m

R_m — 1mm (0.040 inches)

K — IS SELECTED ON THE BASIS OF STRUCTURAL ANALYSIS

M $\geq$ 0.05R_i

R_k — EXTERNAL RADIUS OF WINDOW SEAT; $\leq$ CALCULATED R_o OF CYLINDER UNDER ZERO EXTERNAL PRESSURE AT $+52^\circ$ C PLUS GASKET COMPRESSED 50 PERCENT

R_f — INTERNAL RADIUS OF WINDOW SEAT; $\approx$ CALCULATED R_i OF CYLINDER UNDER ZERO EXTERNAL PRESSURE AT DESIGN TEMPERATURE MINUS THICKNESS OF GASKET

HARD BEARING GASKET BONDED TO FLANGE
$R_i - R_f \leq 0.01 R_i$

Figure C-5. Seat cavity requirements.

HYPERHEMISPHERICAL WINDOW

EXTERNAL PRESSURE SEAL

FIBER REINFORCED NEOPRENE GASKET ≤ 0.7 mm

INTERNAL PRESSURE SEAL

$K_o \cdot K_i \geq 6$ mm (0.240 inches)

$n \geq 1$ mm (0.040 inches)

$c \geq 1.5$ mm (0.060 inches)

$\alpha \leq 100°$
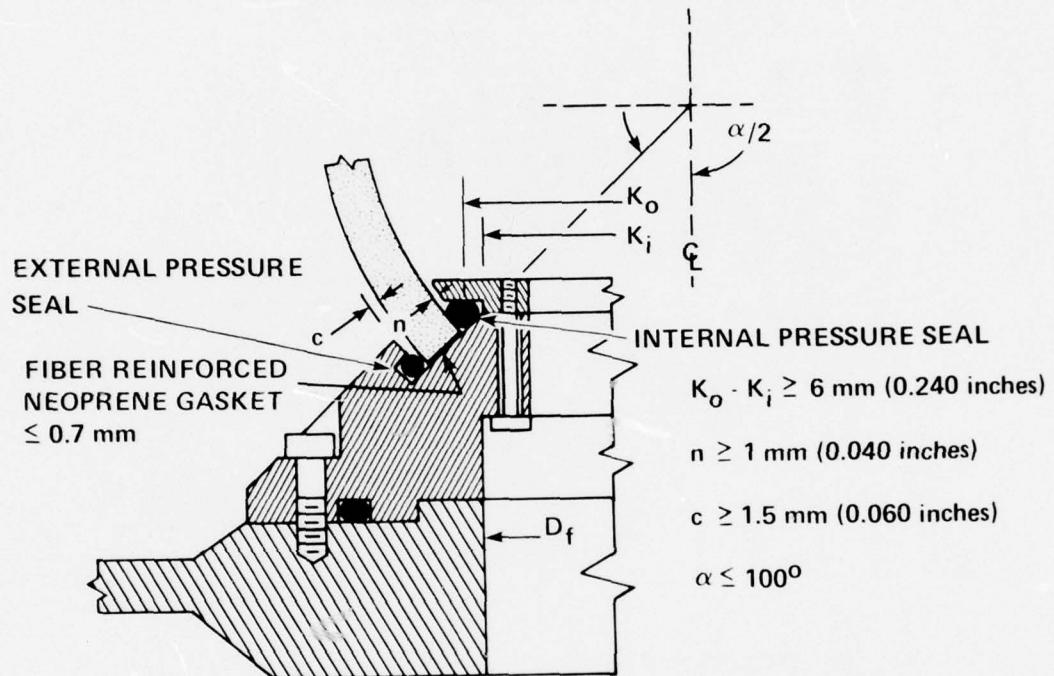
α INCLUDED SPHERICAL ANGLE OF THE OPENING

K_i INNER DIAMETER OF THE CONICAL SEAT

D_f DIAMETER OF THE OPENING IN THE PRESSURE HULL

K_o INNER DIAMETER OF THE PENETRATION IN THE WINDOW

Figure C-6. Seat cavity requirements.

NEMO WINDOW – STANDARD SEAT
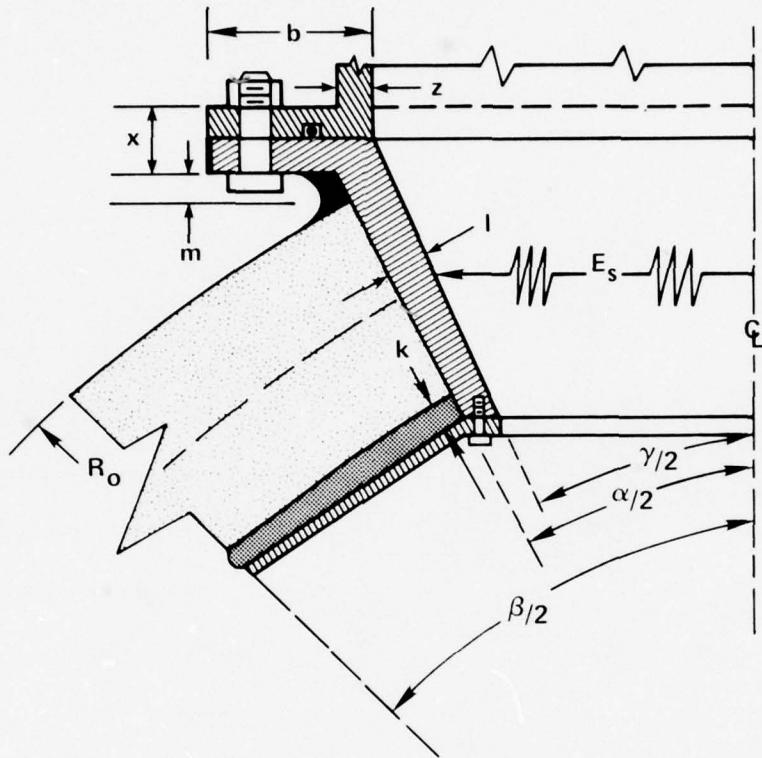
E_s ORIENTATION OF EFFECTIVE RADIAL STIFFNESS

γ SPHERICAL ANGLE OF HATCH SEAT

α SPHERICAL ANGLE OF WINDOW PENETRATION

k THICKNESS OF COMPRESSED GASKET

m ELEVATION OF HATCH RING

β SPHERICAL ANGLE OF SPLIT RETAINING RING

$\alpha \leq 50^o$; $m \geq 0.01\, R_o$; $k \geq 0.005\, R_o$; $(\alpha + 8^o) \leq \beta \leq (\alpha + 12^o)$

NOTE: x, b, z, l MUST BE PROPORTIONED IN SUCH A MANNER THAT
THE EFFECTIVE RADIAL STIFFNESS OF ALL INSERTS AT THE
PENETRATION DOES NOT EXCEED THE RADIAL STIFFNESS OF
ACRYLIC SECTOR WITH INCLUDED ANGLE α BY MORE THAN
3500 PERCENT.

Figure C-7. Seat cavity requirements.

15-64

NEMO WINDOW – SEAT WITH EXTENDED CYCLIC FATIGUE LIFE
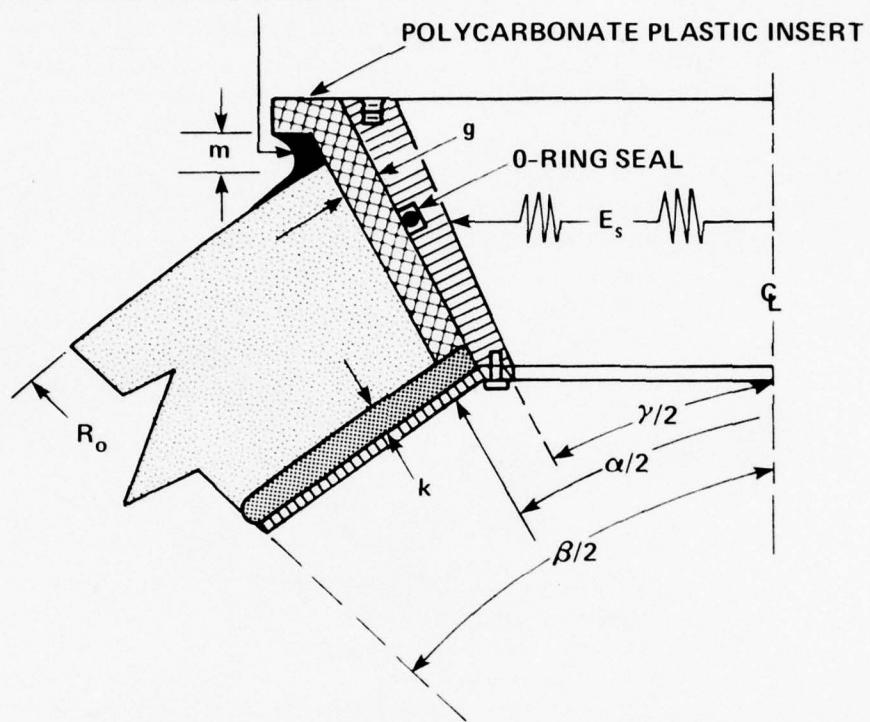
E_s ORIENTATION OF EFFECTIVE RADIAL STIFFNESS

γ SPHERICAL ANGLE OF HATCH SEAT

α SPHERICAL ANGLE OF WINDOW PENETRATION

k THICKNESS OF COMPRESSED GASKET (NEOPRENE)

m ELEVATION OF HATCH RING

β SPHERICAL ANGLE OF SPLIT RETAINING RING

g THICKNESS OF POLYCARBONATE PLASTIC GASKET

$\alpha \leq 50^{\circ}$; $m \geq 0.01\,R_o$; $k \geq 0.005\,R_o$; $(\alpha + 8^{\circ}) \leq \beta \leq (\alpha + 12^{\circ})$; $g \geq 0.03\,R_o$

NOTE: ALL INSERTS MUST BE PROPORTIONED IN SUCH A MANNER THAT THE EFFECTIVE RADIAL STIFFNESS OF ALL INSERTS IN THE PENETRATION DOES NOT EXCEED THE RADIAL STIFFNESS OF ACRYLIC SECTOR WITH INCLUDED ANGLE α BY MORE THAN 3500 PERCENT.

Figure C-8. Seat cavity requirements.

ASME Safety Standard For Pressure Vessels for Human Occupancy
Appendix A - Acrylic Viewports
Window Certification

WINDOW CERTIFICATION

1. The acrylic plastic window identified by _____
has met all the design, material, and fabrication requirements of the ASME
Safety Standard for Pressure Vessels for Human Occupancy and can be used in
viewports of pressure vessels for human occupancy with maximum allowable
working pressure of _____MPa at_____°C temperature.

2. The Design Certification, Material Certification, Parts 1 and 2, Fabri-
cation Certification and Pressure Testing Certification are complete and are
attached to this certification as enclosures 1 through 5.

_____   _____
Authorized Representative   Date
Chamber Manufacturer
(windows for new chamber)
Pressure Vessel User
(windows for replacement in existing chamber

_____
Company Name and Address

ASME SAFETY STANDARD FOR PRESSURE VESSELS FOR HUMAN OCCUPANCY
APPENDIX A - Acrylic Viewports
Window Certification Enclosure 1

WINDOW DRAWING NO. _____

DESIGN CERTIFICATION FOR ACRYLIC PLASTIC WINDOWS

Inner Diameter _____

Maximum Allowable Working Pressure _____psi_____MPa

Maximum Temperature _____°F_____°C

Window Shape _____

Included Angle _____

Conversion Factor Table No. _____

Pressure Range (N) _____

Conversion Factor (CF) _____

Short Term Critical Pressure (STCP) _____

Short Term Critical Pressure* and Figure No. _____

    Test Specimen   No. 1_____ No. 2_____

        No. 3_____ No. 4_____

        No. 5_____ STCP_____
(Note each test specimen FC-for
full scale and MC-for model scale)

    Type of Failure _____

    Tests Conducted at _____

    Tests Supervised by: _____

    Tests witnessed by authorized inspector _____

Minimum t/D_i _____

D_i _____

*If STCP is determined experimentally according to C.5 then the critical pressures
of all five windows tested, the testing laboratory, and the test supervisor should
be noted here.

Minimum t (calculated) _____

Actual t (specified on drawing) _____

D_i/D_f _____

Minimum D_f (calculated) _____

Actual D_f (specified on drawings _____

External Radius of Curvature
(spherical or cylindrical) _____

Drawing No. of Flange _____

Drawing No. of Assembly _____

Description of Pressure Vessel
(for which the window has been designed) _____

_____

_____

_____

_____

_____

_____

The viewport design complies with all of the requirements of the ASME Safety
Standards for Pressure Vessels for Human Occupancy; Appendix A, Chapters C,
D, E, F and G.

_____   _____
         Viewport Designer   Date

_____   _____
Authorized representative of chamber manufacturer   Date

_____
Name and address of chamber manufacturer

MATERIAL CERTIFICATION FOR ACRYLIC PLASTIC

Part I

The_____centimeters x_____centimeters acrylic

sheet/custom castings of_____centimeters nominal thickness

in Lot No._____have been produced by_____

under the trademark of_____.

These castings psssess typical physical properties satisfying the minimum
values specified in ASME Safety Standard for Pressure Vessels for Human
Occupancy, Appendix A, Table A-1.

_____   _____
   Authorixed Representative of   Date
      Manufacturer or Plastic

_____
Name and address of Manufacturer of Plastic

   The Material Certification, Part I, has been mailed to_____

_____on_____

ASME Safety Standard for Pressure Vessels For Human Occupancy
Appendix A Acrylic Viewports
Window Certification Enclosure 3

MATERIAL CERTIFICATION FOR ACRYLIC PLASTIC

Part II

1.   Test specimens have been (cut from castings)/(supplied already cut) by

_____.

2.   Test specimen taken from acrylic sheet/custom castings in Lot_____

of_____centimeters nominal thickness that have been produced

by_____under the trademark of_____possess

the following physical and chemical properties:

Test Method	Property	Average Values
According to paragraphs B.4 and B.5 of Appendix A - Acrylic Viewports, ASME Safety Standard for Pressure Vessels For Human Occupancy	Tensile ultimate strength	
	Elongation at break	
	Modulus of elasticity	
	Compressive yield strength	
	Modulus of elasticity	
	Compressive deformation at 4000 psi and 122°F	
	Ultraviolet transmittance (for 12.5 mm thickness)	
	Visual Clarity	
	Residual methyl methacrylate monomer	
	Residual ethyl acrylate monomer	

The experimentally proven properties satisfy the minimum values specified
in Table A-2 of the ASME safety Standard for Pressure Vessels for Human Occupancy.

_____   _____
Authorized Representative   Date
    of Material Testing Laboratory

_____
Name and address of Material Testing Laboratory

Test Data has been mailed to_____

on_____.

ASME SAFETY STANDARD FOR PRESSURE VESSELS FOR HUMAN OCCUPANCY
APPENDIX A - Plastic Viewports
Window Certification Enclosure 4

WINDOW DRAWING NO. _____

WINDOW SERIAL NO. _____

WINDOW IDENTIFICATION _____

FABRICATION CERTIFICATION FOR ACRYLIC PLASTIC WINDOWS

Material Stock Descriptions:

Manufacturer of Acrylic Plastic _____

Trade Name _____

Casting Shape _____

Nominal Thickness _____

Lot No. _____

Certified for Conformance to Table A-1 by: _____

Date _____

Certified for Conformance to Table A-2 by: _____

Date _____

Window Description:

Maximum Allowable Working Pressure Rating _____psi_____MPa

Maximum Temperature Rating _____°F_____°C

Fabrication Process Data:

Heat Shrinking Temperature (if any) _____

Duration _____

Cooling Rate (chart required _____

Joint Bonding
  Manufacturer of acrylic cement _____
  Trade name of cement _____
  Curing means and duration _____
  Average Tensile Strength _____
  Joint Quality Conforms to 8.c. (yes/no) _____
Polishing Agents _____
Cleaning Agent _____
Intermediate Annealing, Temperature (if any) _____

     Duration _____

     Cooling Rate (chart required) _____

Mandatory Final Annealing, Temperature _____

     Duration _____

     Cooling Rate (chart required _____

Actual Outside Diameter (D_o) _____

Actual Inside Diameter (D_i) _____

Actual Thickness (t max and t min) _____

Actual Included Angle (α) _____

Actual Sphericity (maximum deviation from
specified sphericity measured by a template
on the concave, or convex surface _____ %

Conforms/Deviates From Specification
For Inclusions and Scratches _____

Conforms/Deviates From Specification
For Spot Casting Repairs _____

     This window has been fabricated from material satisfying all requirements
of Chapter B. The fabrication process used in fabrication of windows satisfy
all requirements of Chapter H. The dimensions and surface finishes of the com-
pleted window satisfy all requirements of Dwg. No._____.

_____   _____
Authorized Representative of   Date
Fabricator of Windows

_____
Name and address of Fabricator of Windows

The window and fabrication certification has been shipped to_____

_____on_____.

ASME SAFETY STANDARD FOR PRESSURE VESSELS FOR HUMAN OCCUPANCY
APPENDIX A - Acrylic Viewports
Window Certification Enclosure 5

WINDOW DRAWING NO. _____

WINDOW IDENTIFICATION _____

PRESSURE TESTING CERTIFICATION

Window Description

Maximum Allowable Working Pressure _____

Maximum Design Temperature _____

Window Received; from _____

     Date _____

Test Arrangement

Windows Tested in Operational Viewport/
Simulated Viewport _____

Operational/Simulated Viewport Dwg No. _____

Window Tested According to J.3/J.8 procedure _____

Overpressure ratio, (test pressure/max
allowable working pressure) _____

Test Pressure _____ psi; _____ MPa

Pressurizing Medium Temperature Range _____ °F, _____ °C

Rate of Pressurization (average) _____

Duration of Sustained Pressurization _____

Test Observations (yes/no)

    a. Leakage   _____

    b. Permanent Deformation   _____

    c. Crazing   _____

    d. Cracking   _____

   The acrylic plastic window was pressure tested according to Chapter J.3/J.8 procedure, Appendix A of ASME Safety Standard For Pressure Vessels for Human Occupancy, and was found to perform satisfactorily without any visible permanent deformation, crazing, or cracking.

_____   _____
        Pressure Test Supervisor   Date

_____
Name and address of pressure testing laboratory.

_____   _____
Authorized representative of chamber.   Date
manufacturer (windows for new chamber,) or
user (windows for replacement existing chamber)

Window has been shipped to_____on_____.

or installed in Chamber No._____on_____.

_____   _____
        Authorized Inspector   Date

BIBLOGRAPHY

0. SNOEY, M.R. and STACHIW, J.D., "Windows and Transparent Hulls for Man in Hydrospace," Marine Technology Society Transactions, 4th Annual Converence, 1968.

(1) BEEBE, William, "Half Mile Down," Harcourt, Brace and Company, New York 1934.

(2) PICCARD, Auguste, "Earth, Sky, and Sea," Oxford University Press, New York, 1956.

(3) PICCARD, Jacques and DIETZ, Robert S., "Seven Miles Down," G.P. Putnam Sons, New York, 1961.

(4) Plexiglas Handbook for Aircraft Engineers, Rohm & Haas Company, Philadelphia, Pennsylvania, Second Edition, 1952.

(5) Materials Handbook, Corning Glass Works, Corning, New York, Sixth Edition, April 1963.

(6) STACHIW, J.D., "Critical Pressure of Conical Acrylic Windows Under Short-Term Hydrostatic Loading," ASME Transactions/Journal of Engineering for Industry, Vol. 89, No. 3, 1967.

(7) STACHIW, J.D., "Conical Acrylic Windows Under Long-Term Hydrostatic Pressure of 5000 psi," ASME Paper No. 71-Unt A, 1971.

(8) STACHIW, J.D., "Conical Acrylic Windows Under Long-Term Hydrostatic Pressure of 10,000 psi," ASME Paper No. 71-WA/Unt-3, 1971.

(9) STACHIW, J.D., "Conical Acrylic Windows Under Long-Term Hydrostatic Pressure of 20,000 psi," ASME Transactions/Journal of Engineering for Industry, Vol. 92, No. 1, 1970.

(10) STACHIW, J.D., "Procurement of Safe Viewports for Hyperbaric Chambers," ASME Transactions/Journal of Engineering for Industry, Vol. 93, No. 4, 1971.

(11) STACHIW, J.D., "Effect of Temperature and Flange Support on Critical Pressure of Conical Acrylic Windows Under Short-Term Pressure Loading," ASME Paper No. 72-OT-A, 1972, Transactions/Journal of Engineering for Industry, Vol. 94, December 1972.

(12) STACHIW, J.D., "Critical Pressure of Flat Acrylic Windows Under Short-Term Hydrostatic Loading," ASME Paper No. 67-WA/Unt-1, 1967.

(13) STACHIW, J.D., "Critical Pressure of Spherical Shell Acrylic Windows Under Short-Term Pressure Loading," ASME Transactions/Journal of Engineering for Industry, Vol. 91, No. 3, 1969.

BIBLIOGRAPHY (continued)

(14) CARDARELLI, N.F., "Antifouling Elastomeric Coverings," Symposium on Deep
      Submergence Propulsion and Marine Systems, American Institute of
      Aeronautics and Astronautics, Forest Park, Illinois, 1 March 1966.

(15) WRIGHT, C., "Development of a Large Spherical Acrylic Viewport for the
      PC8B Submarine," ASME Paper No. 71-WA/Unt-4.

(16) STACHIW, J.D., "New Approach to the Assembly of Cylindrical Hulls from
      Shell Sections," Journal of Ocean Technology, Vol. 2, No. 1, 1967.

(17) STACHIW, J.D., "Hollow Core Structures for High Pressure Hulls," Undersea
      Technology, Vol. 2, No. 2, 1961.

(18) STACHIW, J.D., "Spherical Acrylic Pressure Hulls for Undersea Exploration,"
      ASME Transactions/Journal of Engineering for Industry, Vol. 93, No. 2, 1971.

(19a) TSUJI, K. and SHELTON, R., "Fabrication of NEMO-Type Spherical Acrylic
      Capsules for Underwater Vehicles," ASME Paper 70-WA/Unt-4, 1970.

(19b) STACHIW, J.D., "Acrylic Pressure Hull for Submersible NEMO," ASME Paper
      71-Unt-2, 1971.

(19c) TROWBRIDGE, T., "Optical Properties of a Spherical Plastic Underwater
      Observatory, NEMO," ASME Paper 70-Unt-A, 1970.

(19d) SNOEY, M.R., and KATONA, M.G., "Stress Analysis of a Spherical Acrylic
      Pressure Hull," ASME Paper 70-Unt-B, 1970.

(20) SNOEY, M.R. and BRIGGS, E.M., "The NEMO Submersible," ASME Paper 70-Unt-C,
      1970.

(21) KELSEY, R.A. and DOLAN, R.B., "Johnson-Sea-Link, the First Deep Diving
      Welded Aluminum Submersible," ASME Paper 70-WA/Unt-6, 1970.

(22) MAISON, J.R. and STACHIW, J.D., "Acrylic Pressure Hull for Johnson-Sea-
      Link Submersible," ASME Paper No. 71-WA/Unt-6, 1971.

(23) MURPHY, D. and MAZZONE, W., "Transparent Hull Submersible MAKAKAI,"
      ASME Paper 72-WA/OT (number to be assigned later).

(24) STACHIW, J.D., et al, "Recommended Practices for the Design, Fabrication,
      and Prooftesting of Acrylic Plastic Windows in Man-Rated Hyperbaric
      Chambers," ASME Paper 73-WA/Oct-18, 1973.

(25) STACHIW, J.D., "Effect of Bubble Inclusions on the Mechanical Properties of
      Cast Poly-Methyl Metacrylate," ASME Transactions/Journal of Engineering
      for Industry, Vol. 94, 1972.

(26) STACHIW, J.D., "Cast Acrylic Dome for Undersea Application," Technical
      Report, TP 383, Naval Undersea Center, San Diego, California, 1974.

BIBLIOGRAPHY (continued)

(27) STACHIW, J.D., "Acrylic Hemispheres for NUC Undersea Elevator," ASME Paper 72-WH/Oct-4, 1972.

(28) STACHIW, J.D. and MAISON, J., "Flanged Acrylic Plastic Hemispherical Shells for Undersea Applications," ASME Paper 73-Oct-A, 1973.

(29) STACHIW, J.D., "Hulls for Deep Submergence Capsules," The American Ceramic Society Bulletin, 47 (2), 1968.

(30) GRAY, K.O. and STACHIW, J.D., "Glass Housing for Hydrospace Lights and Instruments," ASME Transactions/Journal of Engineering for Industry, Vol. 92, No. 1, 1970.

(31) MURPHY, D., "Development and Testing of a 56-inch Diameter Jointed Glass Pressure Hull," ASME Paper 69 WA/Unt-2, 1969.

(32) STACHIW, J.D., "Windows in the Sea," Smithsonian Institution Press, Washington, D.C., 1971.

(33) STACHIW, J.D. and BEASLEY, B., "Precision Casting Process for Acrylic Plastic Spherical Windows in High Pressure Service," ASME Paper 74-WA/Oct-70, Winter Annual Converence, 17-22 November 1974, New York, New York.

(34) STACHIW, J.D. and NICHOLS, A.E., Jr., "Cast Acrylic Plastic Dome for Undersea Applications," ASME Paper 74-WA/OCT-10, Winter Annual Conference, 17-22 November 1974, New York, New York.

(35) STACHIW, J.D., "Deep Submergence Spherical Shell Window Assembly with Glass or Transparent Ceramic Windows for Abyssal Depth Service," ASME Paper 74-WA/OCT-3, Winter Annual Converence, 17-22 November 1974, New York, New York.

(36) STACHIW, J.D., "NEMO Type Acrylic Plastic Spherical Hull for Manned Operation to 3000 ft. Depth," ASME Paper 75-WA/OcE-3, Winter Annual Conference, 1-5 December 1975, Houston, Texas.

(37) STACHIW, J.D. and BURNSIDE, O.H., "Acrylic Plastic Spherical Shell Windows Under Point Impact Loading," ASME Paper 75-WA/OcE-6, Winter Annual Converence, 1-5 December 1975, Houston, Texas.

(38) STACHIW, J.D. and SLETTEN, R., "Spherical Shell Sector Acrylic Plastic Windows with 12,000 ft. Operational Depth," ASME Paper 75-WA/OcE-2, Winter Annual Conference, 1-5 December 1975, Houston, Texas.

(39) STACHIW, J.D., "Improved Fabrication Process for Spherical Acrylic Plastic Submersible Hulls," Technical Report, TP 493, Naval Undersea Center, San Diego, California, December 1975.

BIBLIOGRAPHY (continued)

(40) STACHIE, J.D., "Spherical Sector Windows with Restrained Edges for Under-
      sea Applications, Technical Report, TP 508, Naval Undersea Center,
      San Diego, California, December 1975.

(41) STACHIW, J.D., "Acrylic Plastic Spherical Shell Windows Under Point
      Impact Loading," Technical Report, TP 486, Naval Undersea Center,
      San Diego, California, July 1975.

(42) STACHIW, J.D. and SLETTEN, R., "Flanged Acrylic Plastic Hemispherical
      Shells for Undersea Systems - Part II - Static and Cyclic Fatigue
      Life Under Hydrostatic Loading," ASME Winter Annual Meeting 1977,
      Ocean Engineering Division (to be presented as a paper).

(43) STACHIW, J.D., SMITH, N.E., and BURNSIDE, O.H., "Structural Performance
      of Acrylic Plastic Plane Disc Windows with Twin Conical Bearing Surfaces,"
      ASME Winter Annual Meeting 1977, Ocean Engineering Division (to be pre-
      sented as a paper).

(44) STACHIW, J.D. and DOLAN, R.B., "Spherical Acrylic Pressure Hulls With
      Multiple Penetrations," ASME Winter Annual Meeting 1977, Ocean Engineering
      Division (to be presented as a paper).

(45) STACHIW, J.L. and STACHIW, J.D., "Effect of Weathering and Submersion
      In Seawater on the Mechanical Properties of Acrylic Plastic," ASME
      Winter Annual Meeting 1977, Ocean Engineering Division (to be presented
      as a paper).

15.4 IN-SERVICE INSPECTION OF VIEWPORTS

15.4.1 Frequency and Method of Inspection

15.4.1.1 ANNUAL. All viewports in a pressure vessel for human occupancy must be subjected to two annual visual inspections, just prior to and immediately following the annually administered pneumatic pressure test of the vessel. These inspections must be conducted without disassembling the viewports. The primary tools of inspection will be a flashlight, a micrometer capable of being read to 0.001 inch (0.003 centimeter), and unaided vision corrected to 20/20 visual acuity. During the inspection both faces of the window must be observed directly and the bearing surfaces observed indirectly by shining the light obliquely upon the faces of the window from both sides of the window.

If the condition of the window surfaces is found to be in a deteriorated state (defined in section 15.4.2), the window must be removed from the assembly and replaced with a new window that meets the requirements of the ANSI/ASME PVHO-1 Safety Standard. Upon installation of the new window, the pressure vessel must be pneumatically tested to its rated working pressure prior to placing it in operation.

15.4.1.2 QUINTANNUAL INSPECTION. All viewports in a pressure vessel for human occupancy must be inspected every 5 years, just prior to and immediately after hydrostatic testing of the vessel to a test pressure equal to at least 1.25 × design pressure. For the inspection preceding the hydrostatic test, all viewports must be disassembled, old gaskets and seals discarded, and the surfaces of the windows and mountings inspected. Windows found to be deteriorated (see section 15.4.2), not clearly marked for the intended service (as called out in the ANSI/ASME PVHO Safety Standard), or at least 10 years old must be replaced with new windows that meet the requirements of the ANSI/ASME PVHO-1 Safety Standard.

Prior to placing windows in the vessel, the surfaces of the mountings in contact with the window's bearing surfaces or gaskets must be inspected for signs of corrosion. If corrosion is present on a surface, it must be removed by machining, grinding, or sanding; the choice of the technique depends on the severity and location of corrosion. Refinishing the corroded surfaces must produce a surface finish satisfying, or exceeding, the requirements of the ANSI/ASME PVHO-1 Safety Standard.

The new gaskets and seals must either comply with the original specifications or with the requirements of ANSI/ASME PVHO-1. Prior to assembly, the window seat in the mounting must be liberally covered with a grease that is compatible with both the acrylic plastic and gases used in that particular pressure vessel. (Dow Corning's silicon greases DC3 and DC4 and DuPont's Krytox are compatible with acrylic plastic.)

The inspection conducted immediately after the hydrostatic test must be performed in the same manner as the annual inspection (see section 15.4.1.1). However, the condition of the seals and gaskets must also be noted. If leakage of water during the test or extrusion of gaskets after the test are noted in the viewport, it must be disassembled, all gaskets replaced and reassembled, and the entire vessel repressurized to at least 1.25 × design pressure.

15.4.2 Conditions of Windows

Any of the conditions described below, when observed in a window during visual inspections (see sections 15.4.1.1 and 15.4.1.2), constitute unacceptable deterioration of the window's structural integrity and require immediate replacement of the window and its associated gaskets and seals.

15.4.2.1 CRAZING. Any visible crazing of the low-pressure face on a plane disc, plane conical frustum with $t/D_i < 0.5$, a plane disc with twin conical bearing surfaces with $t/D_i < 0.5$, and a spherical sector with plane bearing surfaces is unacceptable. Crazing on the high-pressure face of the above mentioned windows that covers more than 30 percent of the area is also unacceptable. Visible crazing is not acceptable on low- or high-pressure faces of a cylinder under internal pressures. On all other windows, including the cylinder under external pressure, crazing of high- or low-pressure surfaces cannot exceed 30 percent of the face area on which the crazing is located.

15.4.2.2 DISCOLORATION. Any perceptible change in original color, significant decrease of transmissivity in the visible spectrum, or appearance of milkiness in the acrylic plastic is unacceptable. Yellowing of bonded joints with age is acceptable.

15.4.2.3 DELAMINATION. Any visible signs of delamination or separation in a bonded joint are unacceptable.

15.4.2.4 CRACKING OF BEARING SURFACES. Any visible cracks in the plane bearing surfaces of plane discs and spherical sectors are not acceptable. Cracks in the bearing surfaces of all other windows are unacceptable, if they exceed $0.0025 \times D_i$ in depth or if they exceed $0.0015 \times D_i$ in depth and their total length exceeds $0.25 \times \pi \times D_i$.

15.4.2.5 CRACKING OF VIEWING SURFACES. Visible cracks are not acceptable on the low-pressure faces of plane discs with plane bearing surfaces, plane conical frustums with $t/D_i \leq 0.5$, plane discs with twin conical bearing surfaces with $t/D_i < 0.5$, and spherical sectors with plane bearing surfaces. Cracks in the high-pressure faces of the above windows and in the high- or low-pressure faces of all other windows are not acceptable when they exceed $0.01t$ in depth or $0.005\,t$ in depth and $0.25 \times \pi \times D_i$ in length.

15.4.2.6 SCRATCHES ON VIEWING SURFACES. Scratches deeper than 0.01 inch (0.03 centimeter) are not acceptable on the low-pressure faces of plane discs with plane bearing surfaces, plane conical frustums with $t/D_i < 0.5$, plane discs with twin conical bearing surfaces with $t/D_i < 0.5$, and spherical sectors with plane bearing surfaces.

For the same windows, scratches on the high-pressure faces are not acceptable when they exceed 0.03 inch (0.08 centimeter) in depth. On a cylinder under internal pressure, scratches exceeding 0.01 inch (0.03 centimeter) in depth are not acceptable on both high- and low-pressure faces.

Scratches deeper than 0.04 inch (0.1 centimeter) are not acceptable on the high- or low-pressure faces of plane discs with conical bearing surfaces with $t/D_i \geq 0.5$, plane discs with twin conical bearing surfaces with $t/D_i \geq 0.5$, spherical sectors with conical bearing surfaces, hyperhemispheres, NEMO-type vessels, and cylinders under external pressure.

15.4.2.7 SCRATCHES ON BEARING SURFACES. Scratches deeper than 0.02 inch (0.05 centimeter) are not acceptable on the bearing or sealing surfaces of any window.